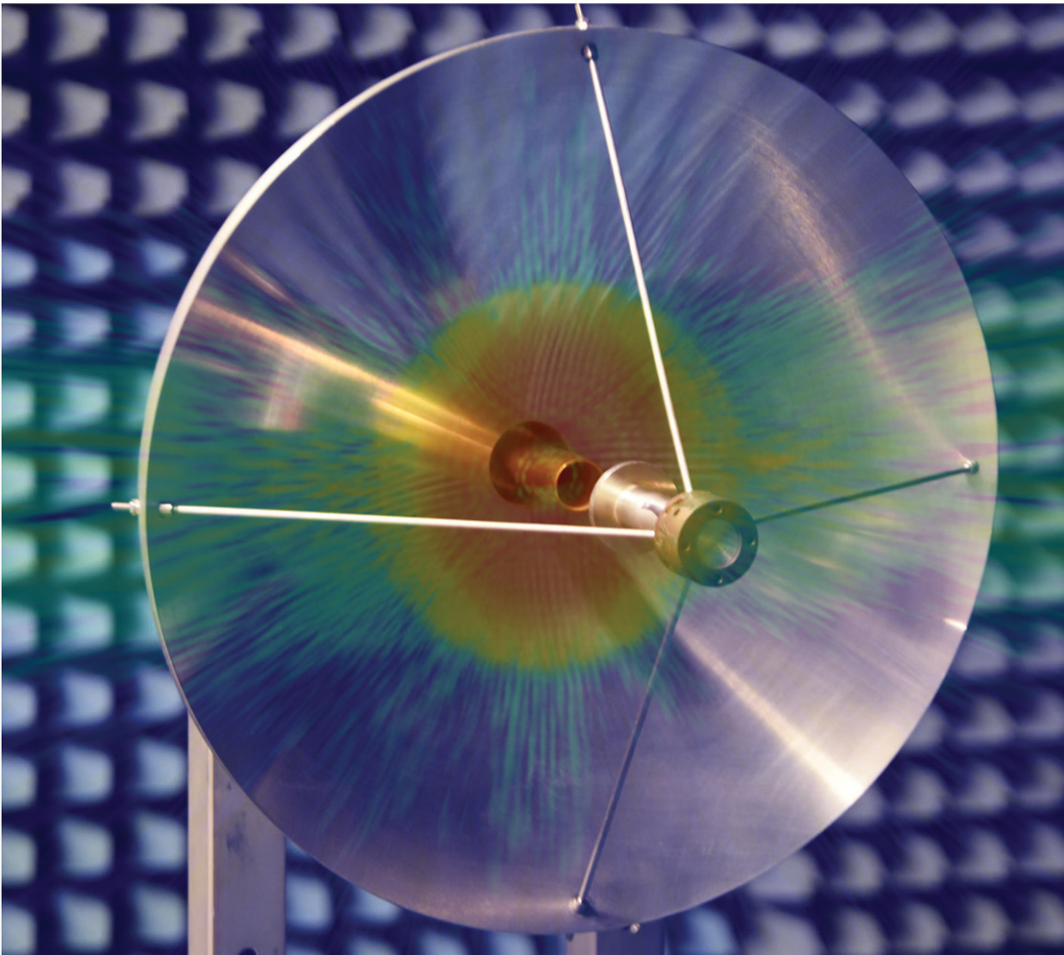


Theory and Practice of Modern Antenna Range Measurements 2nd Expanded Edition, Volume 1

Clive Parini, Stuart Gregson, John McCormick,
Daniël Janse van Rensburg and Thomas Eibert



Theory and Practice of Modern Antenna Range Measurements

Related titles on electromagnetic waves

Dielectric Resonators, 2nd Edition Kajfez & Guillon
Electronic Applications of the Smith Chart Smith
Fiber Optic Technology Jha
Filtering in the Time and Frequency Domains Blinchikoff & Zverev
HF Filter Design and Computer Simulation Rhea
HF Radio Systems and Circuits Sabin
Microwave Field-Effect Transistors: Theory, design & application, 3rd Edition Pengelly
Microwave Semiconductor Engineering White
Microwave Transmission Line Impedance Data Gunston
Optical Fibers and RF: A natural combination Romeiser
Oscillator Design and Computer Simulation Rhea
Radio-Electronic Transmission Fundamentals, 2nd Edition Griffith, Jr
RF and Microwave Modeling and Measurement Techniques for Field Effect Transistors Jianjun Gao
RF Power Amplifiers Albullet
Small Signal Microwave Amplifier Design Grosch
Small Signal Microwave Amplifier Design: Solutions Grosch
2008+ Solved Problems in Electromagnetics Nasar
Antennas: Fundamentals, design, measurement, 3rd Edition Blake & Long
Designing Electronic Systems for EMC Duff
Electromagnetic Measurements in the Near Field, 2nd Edition Bienkowski & Trzaska
Fundamentals of Electromagnetics with MATLAB, 2nd Edition Longren *et al.*
Fundamentals of Wave Phenomena, 2nd Edition Hirose & Lonngren
Integral Equation Methods for Electromagnetics Volakis & Sertel
Introduction to Adaptive Arrays, 2nd Edition Monzingo *et al*
Microstrip and Printed Antenna Design, 2nd Edition Bancroft
Numerical Methods for Engineering: An introduction using MATLAB and computational electromagnetics Warnick
Return of the Ether Deutsch
The Finite Difference Time Domain Method for Electromagnetics: with MATLAB simulations Elsherbeni & Demir
Theory of Edge Diffraction in Electromagnetics Ufimtsev
Scattering of Wedges and Cones with Impedance Boundary Conditions Lyalinov & Zhu
Circuit Modeling for Electromagnetic Compatibility Darney
The Wiener-Hopf Method in Electromagnetics Daniele & Zich
Microwave and RF Design: A systems approach, 2nd Edition Steer
Spectrum and Network Measurements, 2nd Edition Witte
EMI Troubleshooting Cookbook for Product Designers Andre & Wyatt
Transmission Line Transformers Mack and Sevick
Electromagnetic Field Standards and Exposure Systems Grudzinski & Trzaska
Practical Communication Theory, 2nd Edition Adamy
Complex Space Source Theory of Spatially Localized Electromagnetic Waves Seshadri
Electromagnetic Compatibility Pocket Guide: Key EMC Facts, Equations and Data Wyatt & Jost
Antenna Analysis and Design Using FEKO Electromagnetic Simulation Software Elsherbeni, Nayeri & Reddy
Scattering of Electromagnetic Waves by Obstacles Kristensson
Adjoint Sensitivity Analysis of High Frequency Structures with MATLAB® Bakr, Elsherbeni & Demir
Developments in Antenna Analysis and Synthesis vol1 and vol 2 Mittra
Advances in Planar Filters Design Hong
Post-processing Techniques in Antenna Measurement Castañer & Foged
Nano-Electromagnetic Communication at Terahertz and Optical Frequencies, Principles and applications Alomainy, Yang, Imran, Yao & Abbasi
Nanoantennas and Plasmonics: Modelling, design and fabrication Werner, Campbell & Kang
Electromagnetic Reverberation Chambers: Recent advances and innovative applications Guillaume Andrieu
Radio Wave Propagation in Vehicular Environments Azpilicueta, Vargas-Rosales, Falcone & Alejos
Advances in Mathematical Methods for Electromagnetics Kobayashi & Smith

Theory and Practice of Modern Antenna Range Measurements

2nd Expanded Edition

Volume 1

Clive Parini, Stuart Gregson, John McCormick,
Daniël Janse van Rensburg and Thomas Eibert

Published by SciTech Publishing, an imprint of The Institution of Engineering and Technology, London, United Kingdom

The Institution of Engineering and Technology is registered as a Charity in England & Wales (no. 211014) and Scotland (no. SC038698).

© The Institution of Engineering and Technology 2021

First published 2020

This publication is copyright under the Berne Convention and the Universal Copyright Convention. All rights reserved. Apart from any fair dealing for the purposes of research or private study, or criticism or review, as permitted under the Copyright, Designs and Patents Act 1988, this publication may be reproduced, stored or transmitted, in any form or by any means, only with the prior permission in writing of the publishers, or in the case of reprographic reproduction in accordance with the terms of licences issued by the Copyright Licensing Agency. Enquiries concerning reproduction outside those terms should be sent to the publisher at the undermentioned address:

The Institution of Engineering and Technology
Michael Faraday House
Six Hills Way, Stevenage
Herts, SG1 2AY, United Kingdom

www.theiet.org

While the authors and publisher believe that the information and guidance given in this work are correct, all parties must rely upon their own skill and judgement when making use of them. Neither the authors nor publisher assumes any liability to anyone for any loss or damage caused by any error or omission in the work, whether such an error or omission is the result of negligence or any other cause. Any and all such liability is disclaimed.

The moral rights of the authors to be identified as authors of this work have been asserted by them in accordance with the Copyright, Designs and Patents Act 1988.

British Library Cataloguing in Publication Data

A catalogue record for this product is available from the British Library

ISBN 978-1-83953-126-2 (hardback Volume 1)

ISBN 978-1-83953-127-9 (PDF Volume 1)

ISBN 978-1-83953-128-6 (hardback Volume 2)

ISBN 978-1-83953-129-3 (PDF Volume 2)

ISBN 978-1-83953-130-9 (2 volume set)

Typeset in India by MPS Limited

Printed in the UK by CPI Group (UK) Ltd, Croydon

The front cover of this volume comprises of an image of a 90GHz front fed mm-wave Cassegrain reflector antenna with a subtle overlay of the false colour plot of the reconstructed amplitude aperture illumination of the antenna as obtained from phase-less planar near-field antenna measurements.

Contents

Volume 1

About the authors	xv
List of Abbreviations	xvii
Foreword to volumes 1 and 2	xxv
Preface to volumes 1 and 2	xxvii
1 Introduction	1
1.1 The phenomena of antenna coupling	1
1.2 Characterisation via a measurement process	3
1.3 Measurable properties of antennas	6
1.3.1 Antenna gain and directivity	9
1.3.2 Antenna cross-section	10
1.3.3 Free-space radiation pattern	13
1.3.4 Polarisation	17
1.3.5 The far-field	18
1.3.6 The phase in the measurement	20
1.3.7 Reciprocity	21
1.3.8 Measurement limitations	22
1.4 The content of this text	23
References	26
2 EM theory and the mechanism behind antenna coupling	29
2.1 Maxwell's classical electromagnetic field theory	29
2.2 Electric charge and EM fields	30
2.3 Power flux in an EM field	34
2.4 Maxwell's equations	38
2.5 The electric and magnetic potentials	42
2.5.1 Static potentials	43
2.5.2 Retarded potentials	43
2.6 The inapplicability of source excitation as a measurement methodology	53
2.7 Field equivalence principle	54
2.8 Characterising vector electromagnetic fields	56

2.9	Reflection and scattering of electromagnetic fields by extended objects	58
2.10	Antenna port definition	59
2.11	Summary	61
	References	62
3	Antenna measurements	63
3.1	Antenna measurements and alignment	63
3.2	Rotation methodologies	64
3.3	Far-field ranges	66
3.4	Free-space conditions	68
3.4.1	Far-field chambers	71
3.5	Alternatives to conventional far-field ranges	73
3.5.1	Tapered anechoic chambers	73
3.5.2	The compact antenna test range	74
3.5.3	Indirect measurements	77
3.6	Antenna test range RF test equipment	85
3.6.1	RF instrumentation for test ranges	86
3.6.2	Generic near-field antenna measurement process	98
3.7	Summary	100
	References	101
4	Antenna pattern plotting: coordinate systems and polarisation bases	103
4.1	Coordinate systems and antenna measurements	103
4.1.1	Azimuth over elevation	106
4.1.2	Elevation over azimuth	108
4.1.3	Polar spherical	109
4.1.4	True-view (azimuth and elevation)	111
4.1.5	Direction cosine	114
4.1.6	Arcsine-space plotting coordinate system	116
4.1.7	Transformation between coordinate systems	118
4.1.8	Coordinate systems and elemental solid angles	120
4.1.9	One-dimensional great circle pattern cuts	120
4.2	Polarisation basis and antenna measurements	124
4.2.1	Ludwig I (Cartesian)	126
4.2.2	Polar spherical	127
4.2.3	Ludwig II (Az/EI, EI/Az)	131
4.2.4	Ludwig III (co-polar, cross-polar and cross-polar discrimination)	137
4.2.5	Conversion between polarisation bases	143
4.2.6	Elliptical polarisation, axial ratio and tilt angle	148
4.2.7	Linear and circular polarisation bases – complex vector representations	156

4.2.8	Measures of polarisation discrimination	160
4.3	Isometric rotation of coordinate systems	161
4.3.1	Illustration of the problem with antenna pattern plotting – Gauss’s Theorema Egregium	161
4.3.2	Use of direction cosine matrices in the rotation of coordinate systems	162
4.3.3	Azimuth, elevation and roll angles	168
4.3.4	Euler angles	169
4.3.5	Quaternions	171
4.3.6	Orientation of viewer plotting antenna patterns	174
4.3.7	Plotting antenna patterns on earth maps	176
	References	184
5	Compact range measurements	187
5.1	Introduction	187
5.2	Collimation of electromagnetic fields	190
5.2.1	Reflector edge diffraction	194
5.2.2	Feed spillover	205
5.2.3	Lenses as collimators	205
5.2.4	Hologram CATRs	207
5.2.5	Reflector surface errors and panel gaps	209
5.2.6	Time-gating and the absorber-less chamber	213
5.3	Types of ranges and their design issues	217
5.3.1	Single-offset reflector CATR	218
5.3.2	Dual cylindrical reflector CATR	218
5.3.3	Dual shaped reflector CATR	218
5.3.4	Tri-reflector CATR	220
5.3.5	Hologram CATR	221
5.3.6	Lens CATR	221
5.4	Quiet zones and performance evaluation	221
5.4.1	How does a CATR actually work?	223
5.4.2	Measurement of the quiet zone by field probing	233
5.4.3	Phase-less quiet zone scanning	235
5.4.4	Quiet zone evaluation using RCS of a known target	236
5.4.5	Improving measured CATR patterns	239
5.4.6	Feed scanning for static AUT measurements	245
5.5	Radiation pattern and power parameter measurement	246
5.5.1	Radiation pattern measurement	246
5.5.2	Power parameter measurement	248
5.6	Radar cross-section measurements	252
5.6.1	RCS measurement in a CATR	253
5.6.2	Sources of RCS measurement error in a CATR	257
5.6.3	RCS model towers	259
5.6.4	Time-gating for RCS	259
5.6.5	Target imaging	260

5.7	Radome testing	261
5.7.1	Radome measurements in a CATR	261
5.7.2	Positioner overview – mechanically scanned AUTs	265
5.7.3	Measurement of reflectivity, transmission efficiency, pattern distortion, boresight shift, flash lobe	266
5.7.4	Examples of radome measurement ranges	270
5.8	Satellite testing	271
5.8.1	Satellite and telecommunications payload testing in a CATR	271
5.8.2	End-to-end testing and the compensated CATR	272
5.8.3	EIRP measurements	274
5.8.4	SFD measurements	275
5.8.5	G/T measurements	275
5.8.6	Group delay measurements	276
5.9	OTA testing for 5G antennas	277
5.9.1	Simulating a communications system using OFDM	279
	References	290
6	Planar near-field antenna measurements	297
6.1	Introduction	297
6.2	Near-field measurement facility	297
6.2.1	RF sub-system	298
6.2.2	Robotics positioner system	301
6.2.3	Near-field probe	304
6.3	Limitations in the accuracy of the near-field measurement data	304
6.3.1	Mechanically based limitations	304
6.3.2	RF system limitations	305
6.4	Solution of Maxwell's equations in Cartesian coordinates	307
6.4.1	Plane wave spectrum	307
6.5	Probe pattern compensation	309
6.5.1	Effect of the probe pattern on far-field data	311
6.5.2	Scanning probe characteristics	311
6.6	Plane-polar near-field antenna measurements	313
6.6.1	Application of spectral methods to plane-polar antenna measurements	314
6.6.2	Conventional and alternate plane acquisition types	322
6.6.3	Plane-polar alignment	327
6.6.4	Remaining data acquisition factors of planar scanning	334
6.7	Sampling (interpolation theory) and aliasing	334
6.8	Finer than Nyquist sampling	341
6.9	Introduction to non-canonical near-field scanning – planar transform example	343
6.10	Electro-optical planar near-field scanning	361
6.11	Summary	364
	References	365

7 Cylindrical near-field antenna measurements	367
7.1 Introduction	367
7.2 Solution of Maxwell's equation in cylindrical coordinates	373
7.3 Solution of the scalar wave equation in cylindrical coordinates	375
7.4 Construction of vector fields	386
7.5 Derivation of cylindrical mode coefficients from cylindrical near-field data	391
7.5.1 Orthogonality properties of cylindrical wave vectors	391
7.5.2 Determining cylindrical mode coefficients from measured near electric field components	396
7.6 Derivation of asymptotic far-field parameters from cylindrical mode coefficients	401
7.7 Development of the transmission formula	409
7.7.1 The coupling equation – derivation of probe-compensated cylindrical near-field antenna measurements	409
7.7.2 Probe and test antenna	411
7.7.3 Effect of probe compensation in cylindrical near-field measurements	418
7.7.4 Calculation of probe cylindrical mode coefficients from far-field data	420
7.8 Sampling requirements for cylindrical near-field measurements	423
7.9 Implementation of cylindrical near-field to far-field transformation	430
7.10 Conical near-field antenna measurements	435
7.11 Summary	441
References	442

Index	445
--------------	------------

Volume 2

About the authors	xv
List of Abbreviations	xvii
Foreword to volumes 1 and 2	xxv
Preface to volumes 1 and 2	xxvii

8 Spherical near-field antenna measurements	459
8.1 Introduction	459
8.2 Types of SNF ranges	464
8.3 A solution to Maxwell's equations in spherical coordinates	473
8.4 Relating spherical mode coefficients to SNF data	483
8.5 Sampling requirements and spherical mode truncation	490
8.6 Development of the transmission formula	502

8.7	Near-field probe correction	507
8.8	Far-field expressions	517
8.9	Practical acquisition schemes and examples	519
8.10	Radial distance correction	523
8.11	Summary	531
	References	531
9	Antenna field transformation from non-canonical surfaces	535
9.1	Introduction	535
9.2	Measurement configuration with non-canonical surfaces	537
9.3	The reciprocity theorem	539
9.4	Mathematical formulation of the Huygens principle and equivalence principles	543
9.5	Forward transmission equation with probe correction	549
9.5.1	Voltage-equivalent current formulation	549
9.5.2	Spectral representation with propagating plane waves	552
9.5.3	Gain normalised transmission equation	554
9.5.4	Spatial and spectral probe representation	557
9.6	Types and discretisation of equivalent sources for representing the AUT	559
9.6.1	Surface current densities	559
9.6.2	Surface current densities with Love condition	561
9.6.3	Surface current densities with combined-source condition	564
9.6.4	Sources in complex space	565
9.6.5	Distributed spherical-wave or plane-wave expansion	568
9.7	Equivalent source representations of the measurement probe	572
9.8	Discretisation of the forward problem	574
9.8.1	Discretisation of the transmission equations	575
9.8.2	Discretisation of supplementary constraint equations	578
9.9	Inversion of the discretised forward problem	581
9.10	Rapid computation of the forward operator	586
9.10.1	Single-level algorithm	587
9.10.2	Multi-level algorithm	596
9.10.3	Far-field translations	604
9.10.4	Gaussian-beam translations	605
9.11	Evaluation of constraint equations and adjoint operators	607
9.12	Applications and evaluations	608
9.12.1	Pyramidal horn antenna – synthetic measurement data	609
9.12.2	Planar aperture antennas – synthetic measurement data	615
9.12.3	Double-ridged waveguide antenna – spherical and multi-planar near-field measurements	617
9.12.4	Parabolic reflector with defect – synthetic measurement data	628
9.12.5	Satellite mock-up with Ku-band reflectors – synthetic measurement data	630

9.12.6	Reflector antenna – irregular near-field measurements	634
9.13	Antenna field transformations above ground	636
9.13.1	Introduction	636
9.13.2	Inverse equivalent source formulation above ground	640
9.13.3	Post-processing of equivalent sources above different ground materials	645
9.13.4	Field transformation results above ground – synthetic measurement data	647
9.14	Summary	656
	References	657
10	Near-field range assessment	665
10.1	Introduction	665
10.2	A framework for measurement uncertainty	665
10.3	The effects of unwanted signals on vector measurements	666
10.4	The statistical nature of error signals	676
10.5	Probe/illuminator-related errors	685
10.5.1	Probe relative pattern	685
10.5.2	Probe polarisation purity	691
10.5.3	Probe alignment	693
10.6	Mechanical/positioner-related errors	695
10.6.1	AUT alignment	696
10.6.2	PNF probe (x, y) position error	697
10.6.3	PNF probe z-position (planarity) error	702
10.6.4	CNF probe ρ -position error	709
10.6.5	SNF (θ, ϕ, r) positioning uncertainty	710
10.6.6	SNF axis non-orthogonality	726
10.6.7	SNF axis (θ, ϕ) non-intersection error	727
10.7	Absolute power level-related errors	731
10.7.1	Gain standard uncertainty	731
10.7.2	Normalisation constant	732
10.7.3	Impedance mismatch	735
10.8	Processing-related errors	748
10.8.1	Aliasing	748
10.8.2	Measurement area truncation	749
10.9	RF sub-system related errors	753
10.9.1	Receiver amplitude linearity	753
10.9.2	Systematic phase	755
10.9.3	Leakage	762
10.9.4	Receiver dynamic range	763
10.10	Environmental-related errors	766
10.10.1	Probe structure reflection	766
10.10.2	Chamber reflection	770
10.10.3	Random errors	773
10.11	Combining uncertainties	773

10.12	Inter-range comparisons	774
10.13	Summary	781
	References	782
11	Mobile and body-centric antenna measurements	785
11.1	Introduction	785
11.2	Indoor far-field antenna measurements	785
11.3	Spherical near-field measurements	788
11.3.1	Over-the-air measurements	791
11.4	Low-gain antenna and <i>S</i> -parameter measurement methods	795
11.5	Corruption by cables: the use of optical fibre links	800
11.6	On-body measurements	802
11.7	Efficiency measurement using Wheeler Cap	809
11.8	UWB antenna measurements	812
11.8.1	Return loss	813
11.8.2	Radiation pattern	813
11.8.3	UWB pseudo-time domain measurements	813
11.8.4	Fidelity analysis	818
11.8.5	True time domain measurements	819
11.8.6	Mean gain	822
11.9	Special facilities	823
11.9.1	Over-the-air multipath environment simulation for MIMO testing	823
11.9.2	Reverberation chamber measurements	823
	References	825
12	Advanced antenna measurement topics	831
12.1	Introduction	831
12.2	Common topics	831
12.2.1	Probes and probe selection	831
12.2.2	Channel-balance correction for antenna measurements	846
12.2.3	Aperture diagnostics	852
12.2.4	Amplitude and phase drift correction: tie-scan correction	865
12.2.5	Alignment correction (in PNF, CNF, and SNF)	869
12.2.6	Simple semi-empirical model of an open-ended rectangular waveguide probe	877
12.2.7	Introduction to range reflection suppression	884
12.3	PNF topics	893
12.3.1	Bias leakage error	893
12.3.2	Compensation for probe translation effects in dual polarised planar near-field antenna measurements	895
12.3.3	Introduction to phase-less near-field antenna measurements	904
12.3.4	Planar mathematical absorber reflection suppression	911
12.4	CNF topics	926
12.4.1	Cylindrical mathematical absorber reflection suppression	926

12.4.2	Application of C-MARS to far-field and CATR measurements – FF-MARS	942
12.5	SNF topics	947
12.5.1	Spherical near-field electrical alignment	947
12.5.2	The radial distance to MRS ratio	955
12.5.3	Spherical mathematical absorber reflection suppression	958
12.5.4	Rotary joint wow correction for LP antennas	971
12.6	Power parameter definitions and their measurement	973
12.6.1	Directivity	973
12.6.2	Gain	978
12.6.3	Equivalent isotropically radiated power (EIRP)	988
12.6.4	Saturating flux density (SFD)	989
12.7	Summary	989
12.7.1	Summary of MARS	990
References		990
13	Electromagnetic modelling of antenna measurement ranges	995
13.1	Introduction	995
13.2	Simulation of a compact antenna test range	996
13.2.1	Point source CATR	998
13.2.2	Illumination of the CATR reflector	999
13.2.3	Calculation of the reflected electric field	1002
13.2.4	Calculation of the local surface unit normal and elemental surface area	1003
13.2.5	Electromagnetic field propagation	1004
13.2.6	Comparison of CATR CEM simulation methods with full-wave simulations	1010
13.2.7	Assessment of CATR QZ predictions	1018
13.2.8	Inclusion of feed spill-over in CATR quiet-zone	1022
13.2.9	End-to-end simulation of CATR measurement process	1022
13.2.10	Effect of amplitude taper, amplitude ripple and phase ripple on CATR measurements	1032
13.2.11	Use of CATR EM model to verify post-processing and error correction techniques	1044
13.2.12	CEM verification of scattering suppression and feed spill-over with mode filtering	1061
13.3	Full-wave three-dimensional CEM simulations	1064
13.3.1	Full-wave simulation of a PNF measurement z-cut	1064
13.3.2	Full-wave simulation of a PNF measurement xy-scan	1067
13.3.3	Simulation of a pyramidal standard gain horn	1072
13.3.4	Full-wave simulation of a spherical test system	1073
13.4	Simulation of a cylindrical near-field antenna test system	1078
13.4.1	CEM verification of scattering suppression with mode filtering	1080
13.4.2	CEM verification of improvement in signal-to-noise ratio	1089

13.4.3	CEM verification of suppression of second-order truncation effect	1093
13.5	Simulation of a spherical near-field antenna test system	1097
13.5.1	Polar mode spherical acquisition simulation with arbitrary probe	1106
13.5.2	Equatorial mode spherical acquisition simulation with an arbitrary probe	1107
13.6	Summary	1111
	References	1111
Appendix		1113
Index		1123

About the authors

Professor Clive Parini is Professor of Antenna Engineering at Queen Mary University of London and heads the Antenna & Electromagnetics Research Group. He received his BSc (Eng) degree in Electronic Engineering in 1973 and PhD in 1976 both from Queen Mary University of London. After a short period with ERA Technology Ltd, he joined Queen Mary University of London as Lecturer (1977), moving to Reader (1990) and then Professor (1999). He has published over 400 papers on research topics including array mutual coupling, array beamforming, antenna metrology, antennas for mobile and on-body communications, millimetre-wave compact antenna test ranges, millimetre-wave integrated antennas, quasi-optical systems and antenna applications for metamaterials. In 1990, he was one of three co-workers to receive the IEE Measurements Prize for work on near-field reflector metrology. He is a Fellow of the IET and a past member and Chairman of the IET Antennas & Propagation Professional Network Executive Team. He is a past member of the editorial board and past Honorary Editor for the IET Journal *Microwaves, Antennas & Propagation*. In 2009, he was elected a Fellow of the Royal Academy of Engineering.

Professor Stuart Gregson is an honorary visiting professor at Queen Mary University of London and Director of Operations & Research at Next Phase Measurements. He received his BSc degree in Physics in 1994 and his MSc degree in Microwave Solid State Physics in 1995 both from the University of Portsmouth. He received his PhD degree in 2003 from Queen Mary University of London. From his time with Airbus, Leonardo, NSI-MI and the National Physical Laboratory, he has developed special experience with near-field antenna measurements, finite array mutual coupling, computational electromagnetics, installed antenna and radome performance prediction, compact antenna test range design and simulation, electromagnetic scattering, 5G OTA measurements and has published numerous peer-reviewed research papers on these topics regularly contributing to and organising industrial courses on these subject areas. He is a Fellow of the Antenna Measurement Techniques Association, a Fellow of the Institution of Engineering and Technology, a Fellow of the Institute of Physics and is a chartered Engineer and Physicist.

Dr John McCormick has extensive experience in many areas of metrology ranging from wet chemistry laboratories to free-space electromagnetic measurement facilities. His expertise relevant to these volumes relates to his involvement over a number of decades in research and development related to naval and airborne radar systems along with RCS and EW. This experience has been gained in the course of

his working relationships with DERA, BAE Systems SELEX ES and latterly Finmeccanica where he has been engineering lead on a range of advanced programmes that required the development and implementation of diverse and novel measurement techniques. He holds degrees at BA, BSc, MSc and PhD levels, is a Fellow of the Institute of Physics, a Fellow of the Institution of Engineering Technology and is a chartered Physicist and chartered Engineer. Additionally, he takes a strong and active interest in the encouragement of public awareness of all areas of Science and Engineering especially within the school environment where he acts as a schools STEM ambassador.

Dr Daniël Janse van Rensburg is Chief Technology Officer of NSI-MI Technologies in Atlanta, GA, USA. He started his career as Professor in the Department of Electrical Engineering at the University of Pretoria, South Africa in 1992. He joined the Canadian Space Agency in Ottawa, ON, Canada, as Research Engineer in 1994 and was appointed as Senior Member of Technical Staff at COMDEV in Cambridge, ON, Canada, in 1996. He joined NSI in 1998 as Applications Engineer and upon NSI merging with MI Technologies in 2016, was named CTO of the new organization, NSI-MI Technologies LLC. He specialises in microwave antenna measurement systems, computational electromagnetics and measurement uncertainty analysis. He is a graduate of the University of Pretoria, South Africa, where he earned a PhD degree in Computational Electromagnetics in 1991. He is a Senior Member of the IEEE, Licensed Professional Engineer in Ontario, Canada and Fellow of the Antenna Measurement Techniques Association (AMTA). He was the recipient of the AMTA Distinguished Achievement Award in 2015 for his contributions to near-field technology. He remains actively involved in academia and is an Adjunct Professor in the School of Information Technology and Engineering, University of Ottawa, ON, Canada.

Professor Thomas Eibert is Professor of High-Frequency Engineering at the Technical University of Munich. He received the Dipl.-Ing. (FH) degree in electrical engineering from Fachhochschule Nürnberg, Nuremberg, Germany; the Dipl.-Ing. degree in electrical engineering from Ruhr-Universität Bochum, Bochum, Germany; and the Dr.-Ing. degree in electrical engineering from Bergische Universität Wuppertal, Wuppertal, Germany, in 1989, 1992 and 1997, respectively. From 1997 to 1998, he was with the Radiation Laboratory, Electrical Engineering and Computer Science Department, University of Michigan, Ann Arbor, MI, USA. From 1998 to 2002, he was with Deutsche Telekom, Darmstadt, Germany. From 2002 to 2005, he was with the Institute for High-Frequency Physics and Radar Techniques of FGAN e.V., Wachtberg, Germany, where he was the Head of the Department of Antennas and Scattering. From 2005 to 2008, he was Professor of Radio Frequency Technology with the Universität Stuttgart, Stuttgart, Germany. His research interests include numerical electromagnetics, wave propagation, measurement and field transformation techniques for antennas and scattering, and all kinds of antenna and microwave circuit technologies for sensors and communications. He has published more than 500 scientific papers.

List of Abbreviations

Abbreviation	Definition
3D	Three Dimensional
AAPC	Advanced Antenna Pattern Correction
AC	Alternating Current
AES	Antenna Electrical System
AESA	Active Electronically Scanned Array
AMS	Antenna Mechanical System
A-MST	Advanced Modulated Scattering Technique
AMTA	Antenna Measurement Techniques Association
APC	Antenna Pattern Comparison
AR	Axial Ratio
ARC	Antenna Range Controller
AUT	Antenna Under Test
az	Azimuth
BER	Bit Error Rate
BSS	Base Station Simulator
CAE	Computer Aided Engineering
CATR	Compact Antenna Test Range
CCR	compensated compact range
CE	Current Elements
CEM	Computational Electromagnetic Modeling
CFIE	Combined Field Integral Equation
CG	Conjugate Gradient
CM	Conformal Mesh
C-MARS	Cylindrical-MARS
CMCs	Cylindrical Mode Coefficients
CMOS	Complementary Metal Oxide Semiconductor
CNF	Cylindrical Near-Field
CNFS	Cylindrical Near-Field Scanner

C _{OFF}	Off-state Capacitance
CP	Calderon Projector
CP	Circularly Polarised
CW	Continuous Wave
CS	Combined Source
dB	Decibel
dBsm	Decibel square meters
DC	Direct Current
DFT	Discrete Fourier Transform
DGBE	Diethylene Glycol Butyl Ether
DRA	Dielectric Resonator Antenna
DUT	Device under Test
DSSS	Direct-Sequence Spread Spectrum
EA	Electro Absorptive
EDFA	Erbium Doped Fibre Amplifier
EEG	Earth Equivalent Ground
EFIE	Electric Field Integral Equation
EFT	Electromagnetic Field Theory
EHF	Extremely High Frequency
EIRP	Effective Isotropic Radiated Power
EI	Elevation
EM	Electromagnetic
EMI	Electromagnetic Interference
EMPL	Equivalent Multipath Level
EO	Electro-Optical
ESA	European Space Agency
ET	Edge Taper
EU	European Union
EUCAP	European Conference on Antennas and Propagation
F	Noise Figure
F/D	Focal length to diameter ratio
FCC	Federal Communications Commission
FDTD	Finite Difference Time Domain
FEA	Finite Element Analysis
FF	Far-Field
FF-MARS	Far-Field-MARS

FFT	Fast Fourier Transform
FIAFTA	Fast Irregular Antenna Field Transformation Algorithm
FIPWA	Fast Inhomogeneous Plane-Wave Algorithm
FMM	Fast Multipole Method
FOM	Figure-Of-Merit for Switching Times
FS	Free-space
GaAs	Gallium Arsenide
GBM	Gaussian Beam Mode
GO	Geometric Optics
GPIB	General Purpose Interface Bus
GRIN	Gradient Index
GSM	Global System for Mobile Communications, originally Groupe Spécial Mobile
GTD	Geometric Theory of Diffraction
HF	High Frequency
HFT	Chair of High-Frequency Engineering
HM	Least Squares Conjugate Gradient
HP	Horizontal linear
HVAC	Heating Ventilation and Air Conditioning
I	In-phase Receiver Channel
IBC	Impedance Boundary Condition
IDFT	Inverse Discrete Fourier Transform
IEEE	Institute of Electrical and Electronics Engineers
IESS	Inverse Equivalent Source Solvers
IET	Institution of Engineering and Technology
IF	Intermediate Frequency
IFFT	Inverse Fast Fourier Transform
IRUWB	Impulse Radio Ultra Wideband
ISAR	Inverse Synthetic Aperture Radar
ITU	International Telecommunication Union
JCMT	James Clerk Maxwell Telescope
JH	Huygens-Type Elementary Radiators
JM LOVE	Electric and Magnetic Surface Current Densities With Love Condition
JM	Electric and Magnetic Surface Current Densities Without Any Further Constraint
KH	Kirchhoff–Huygens

LF	Low Frequency
LHCP	Left Hand Circular Polarisation
LI	Ludwig 1 st definition of cross-polarisation
LII	Ludwig 2 nd definition of cross-polarisation
LIII	Ludwig 3 rd definition of cross-polarisation
LO	Local Oscillator
LP	Linearly Polarised
LPDA	Log Periodic Dipole Array
LSQR	Least Squares Conjugate Gradient
MARS	Mathematical Absorber Reflection Suppression
MC	Mirror Cube
MFIE	Magnetic Field Integral Equation
MHM	Microwave Holographic Metrology
MIMO	Multiple Input Multiple Output
MLFMM	Multilevel Fast Multipole Method
MoM	Method of Moments
MRC	Minimum Radius Cylinder
MRE	Maximum Radial Extent
MRS	Minimum Radius Sphere
MST	Modulated Scattering Technique
NASA	National Aeronautics and Space Administration
NATO	North Atlantic Treaty Organization
NBS	National Bureau of Standards
NE	Normal Error
NF	Near-Field
NFFFT	Near-Field Far-Field Transformation
N_i	Input Noise
NIST	National Institute of Standards and Technology
NPL	National Physical Laboratory
NR	Normal Residual
NRL	Naval Research Laboratory
N_o	Output Noise
OEFS	Opto-Electric Field Sensor
OEWG	Open Ended Waveguide Probe
OFDM	Orthogonal Frequency Division Multiplexing
OMT	Orthogonal Mode Transducer

OTA	Over The Air
PAMS	Portable Antenna Measurement System
PEC	Perfect Electrically Conducting
PEC	Perfectly Conducting
PCU	Power Control Unit
PDF	Probability Density Function
pHEMT	Pseudomorphic High Electron Mobility Transistor
PIN	p-type Intrinsic n-type construction for diode junction
P-MARS	Planar-MARS
PMC	Perfect Magnetically Conducting
PNF	Planar Near-Field
PNFS	planar near-field scanner
PO	Physical Optics
PTD	Physical Theory of Diffraction
PTFE	Polytetrafluoro-Ethylene
PTP	Plane-to-Plane
PWS	Plane Wave Spectrum
PWSC	Plane wave Spectrum Components
Q	Quadrature receiver channel
QML	Queen Mary, London
QZ	Quiet Zone
RA	Range Assessment
RADAR	Radio Detection and Ranging
RAL	Rutherford Appleton Laboratory
RAM	Radar Absorbent Material
RCS	Radar Cross-Section
RF	Radio Frequency
RFS	Range Fixed System
RHCP	Right Hand Circular Polarisation
RI	Range Illuminator
RMS	Root Mean Square
R_{ON}	On-state Resistance
RSA	Remote Source Antenna
RSS	Root Sum Square
RSS	Received Signal Strength
RWG	Rao–Wilton–Glisson

Rx	Receive
SAR	Specific Absorption Rate
SAR	Synthetic Aperture Radar
SC	side constraint
SD	Standard Deviation
SFD	Saturating Flux Density
SGA	Standard Gain Antenna
SGH	Standard Gain Horn
SHF	Super High Frequency
S_i	Input Signal Power
SLL	Side-Lobe Level
SM	Spherical Mesh
SMA	Subminiature A
S-MARS	Spherical-MARS
SMC	Spherical Mode Coefficient
SNF	Spherical Near-Field
SNFR	Spherical Near-Field Range
SNFS	Spherical Near-Field Scanner
SNR	Signal-to-Noise Ratio
S_o	Output Signal Power
SPHNFFFT	Spherical NF FF Transformation
SPP	Single Port Probe
SRD	Step Recovery Diode
SWR	Standing Wave Ratio
TE	Transverse Electric
T_e	Equivalent Noise Temperature
TEM	Transverse Electric and Magnetic
TIS	Total Isotropic Sensitivity
TM	Transverse Magnetic
TRP	Total Radiated Power
TT	Turntable
TUM	Technical University of Munich
Tx	Transmit
UHF	Ultra High Frequency
US	United States
UTD	Universal Theory of Diffraction

UWB	Ultra Wideband
VH	Vector-Huygens
VHF	Very High Frequency
VNA	Vector Network Analyser
VP	Vertical Linear
VSWR	Voltage Standing Wave Ratio
WF	Weak-Form
WG	Waveguide

This page intentionally left blank

Foreword to volumes 1 and 2

Foreword for the 2nd Edition of *Theory and Practice of Modern Antenna Range Measurements*

Since the publishing of the First Edition of this extensive reference book, it has been the preeminent source for the theory and practical aspects of all the measurement methods that are used to characterise the extremely broad range of antennas that have been developed as critical components in modern communication, sensing and space applications. With the completion of this Second Edition, major improvements and additions have been included to keep pace with the continuing advancements in this field. The authors have the knowledge and background to provide authoritative and practical material that is very necessary for the technical challenges that are required on modern antenna measurement facilities. The new edition has increased the scope of information and the quality of presentation and will continue to be a valuable resource for technical experts working in this field for many years.

Allen C Newell
NIST Retired, Newell Near-Field Consultants
June 2019
Boulder, Colorado, USA

This page intentionally left blank

Preface to volumes 1 and 2

At the time of writing of this text, some 147 years have passed since the publication of the *Treatise on Electricity and Magnetism* by James Clerk Maxwell. This was the text that firmly established the classical theory of electromagnetism in the mainstream of science and engineering and placed Maxwell within the pantheon of greats in the fields of science and technology. The success of this classical theory is attested to by the extraordinarily good agreement that is routinely attained between theoretical prediction and physical measurement. Its initial triumph was to not only be able to summarise all previous experiences in the fields of optics, electricity and magnetism within a small* set of self-consistent equations; but also, for the first time, to admit the possibility of electromagnetic waves. Crucially, the velocity of these waves could be deduced exclusively from electrical measurements, which when compared with the then known velocity of light, the two values were found to coincide almost exactly.

This inherent accuracy and precision has enabled successive generations of workers to construct and refine ever more complex and ingenious structures for the transmission and reception of electromagnetic waves. These waves can be used for the transmission of information by means of modulating the wave-form to contrive a signal as used in the field of telecommunications. Alternatively, these modulated (i.e. radio) waves can be utilised for the remote detection and location of planes, ships, or other targets as is employed within modern radar (Radio Detection And Ranging) systems. More recently, the way in which radio waves scatter has also been harnessed, as this additional information can be used to remotely sense properties of the physical world without the need to actually visit those locations. Thus, the sheer multitude and diversity of the applications inexorably drives the ever-increasing intricacy and sophistication of the design of the devices that are used to efficiently transmit and receive these electromagnetic waves, so accurately and rigorously postulated by James Clerk Maxwell.

The achievements of Maxwell are remembered in his home town of Edinburgh in Scotland where a statue of him seated in his academic gown holding a colour wheel stands at a busy intersection, with the proud motive 'James Clerk Maxwell Mathematical Physicist', carved into the stone pedestal on which it sits. A more modern interpretation of the term mathematical physicist might be theoretical physicist, but in fact it should be remembered that in the opening leaf of the *Treatise on*

*It was actually Oliver Heaviside who reformulated Maxwell's 20 equations, which were quite difficult to use, and reduced them to obtain the four very useful equations that are in common use today.

Electricity and Magnetism, Maxwell refers to himself as ‘Professor of Experimental Physics in the University of Cambridge’ and as if to emphasise the importance that he placed on the experimental and empirical aspects of his work he devoted the first 26 numbered paragraphs in the treatise to a preliminary to be read prior to the main text, this preliminary being entitled ‘On the measurement of quantities’. Still now, after so many years as a result of the increasing intricacy and sophistication of the devices and systems designed to utilise the concept of classical electromagnetic field theory, the problem of the measurement of electromagnetic fields remains as acute as ever.

The development and proliferation of inexpensive, powerful, digital computers with large amounts of memory in the latter part of the twentieth century has enabled the use of computer-aided engineering to become commonplace in both the design and measurement of antenna assemblies. The use of full-wave three-dimensional computational electromagnetic simulation software tools has allowed the antenna designer to accurately and precisely predict the performance of a given structure. These tools harness techniques such as the finite difference time domain, or method of moments, that simply cannot be effectively deployed without the use of a digital computer. Modern, now commercially available, software packages have provided hitherto unknown levels of detail, accuracy and precision leading to their becoming an indispensable part of the antenna design and development process. Such design and prediction capabilities have become commonplace throughout academia and industry alike and have in no small way contributed towards the emergent need for the antenna metrologist to provide a broadly comparable service.

Clearly, antennas have to be mounted and attached to structures and these can influence, in some cases significantly, the installed radiation pattern as electromagnetic waves ‘couple’ to these structures and subsequently radiate. Additionally, variations in material properties and the influence of imperfections in manufacturing mean that in nearly all practical applications the antenna radiation characteristics have to be measured before a final design can go into commercial production. The inevitable search for more efficient and accurate techniques for the characterisation of new, increasingly complex, instruments has been the catalyst for the rapid development of modern sophisticated antenna measurement techniques. These developed first from the early direct observation techniques that were harnessed during the years of the Second World War (1939–45), and which were still commonplace until only comparatively recently, to the most advanced indirect near-field techniques.

Very often, antenna metrology is considered to be a difficult discipline that is best left to a few designated ‘experts’. In part this perception is perhaps attributable to the realisation as with all science and engineering antenna metrology is fundamentally both an intellectual, and a practical activity. Thus, in order to take good measurements, the practitioner needs to be familiar with and adept at both the practical *and* theoretical aspects of the work making antenna metrology an extremely broad subject. This difficulty is further complicated as many of the concepts that are routinely used are found in the development of the theory of classical electrodynamics which, as already stated were completed in the nineteenth century[†] and which were originated centuries earlier

[†]In 1864 Maxwell published a paper entitled ‘Dynamical Theory of the Electromagnetic Field’.

than that. Furthermore, and as with any discipline that becomes firmly established (i.e. entrenched), there is a danger that the principles and concepts that lie behind the terminology its workers use can become taken for granted, thereby obscuring the subject and its meaning from all but a few experienced practitioners. This is all the more acute an issue as the development of the discipline has been sufficiently rapid over the course of the past few decades that even active workers can, at times, struggle to keep abreast of the most recent developments. This text aims to address this by adopting a coherent narrative, terminology and nomenclature throughout. In this way, it is hoped that this volume can form a useful introduction and reference to graduate students, researchers and practicing engineers alike.

The first chapters of this text present an initial examination of the properties of antennas that allow them to enhance the free-space interaction of electronic systems. This is followed by an introduction to direct far-field and indirect far-field forms of antenna measurements and their implementation. Chapter 5 presents a detailed description of the compact antenna test range which is a direct far-field measurement technique before Chapters 6–8 progress to present alternative indirect planar, cylindrical and spherical techniques, respectively. Chapter 9 is devoted to field transformations from non-canonical measurement surfaces based on general inverse-source formulations. Chapter 10 discusses near-field range error budgets which are an indispensable part of antenna metrology. Chapter 11 presents a discussion of modern mobile and body-centric antenna measurements. Finally, Chapter 12 sets out some of the most recent advances in the various measurement techniques including aperture diagnostics, phase-less antenna metrology and range multi-path suppression techniques which currently are amongst some of the most active topics for researchers.

In summary, this volume will provide a comprehensive introduction and explanation of both the theory and practice of all forms of modern antenna measurements from their most basic postulates and assumptions to the intricate details of their application in various demanding modern measurement scenarios.

The authors have not attempted to identify the originators of every concept or to provide an exhaustive literary survey or historical account as this can very often obstruct the pedagogy of a text. Additionally, except where specifically stated, it should be noted that only concepts, techniques and methodologies of which at least one of the authors has direct practical experience of implementation are included for discussion in the text. The International System of Units (SI) is used exclusively with the approximation $\mu_0 = 4\pi \times 10^{-7} \text{ NA}^{-2}$. Following the redefinition of SI base units, the kilogram, ampere, kelvin and mole, on the 20th of May 2019, the difference between this value of μ_0 and the new SI (experimental) value of μ_0 is less than 1×10^{-9} in relative value which is negligible in the context of the uncertainty budgets discussed herein. However, this assumption should be noted and re-examined periodically as it does subtly affect the permittivity of vacuum, impedance of vacuum and admittance of vacuum.

Thanks are due to a great many people who gave freely and generously of their time to review the manuscript at various stages throughout its preparation, and especially to Prof. Edward B. Joy of Georgia Tech who carefully reviewed an early draft. However, any errors or lack of clarity must, as always, remain the responsibility

of the authors alone. The authors are grateful to their wives (Claire Parini, Catherine Gregson, Imelda McCormick and Lizette Janse van Rensburg) and children (Robert Parini, Elizabeth Gregson and Suzette Janse van Rensburg) whose unwavering understanding, constant support, encouragement and good humour were necessary factors in the completion of this work. We also thank the organisations and individuals who generously provided copyright consent.

There are many useful and varied sources of information that have been tapped in the preparation of this text; however, mention must be made of the following books which have been of particular relevance and will be referred to throughout. In no special order:

- M.R. Spiegel, *Theory and Problems of Vector Analysis and an Introduction to Tensor Analysis*, Schaum Publishing Company.
- R.H. Clarke and J. Brown, *Diffraction Theory and Antennas*, Ellis Horwood Ltd.
- J.E. Hansen, *Spherical Near-field Antenna Measurements*, Peter Peregrinus, 1988.
- S.F. Gregson, J. McCormick, and C.G. Parini, *Principles of Planar Near Field Measurements*, Institution of Engineering and Technology, 2007.

Although the nomenclature and development of the theory of antenna metrology as presented within this text has not generally followed that of the National Institute of Standards and Technology (NIST), the technical publications originating from that organisation have also been a rich source of valuable information. In particular, but in no special order:

- D.M. Kerns, *Plane-Wave Scattering-Matrix Theory of Antennas and Antenna-Antenna Interactions*, National Bureau of Standards Monograph 162.
- A.C. Newell, *Planar Near-Field Antenna Measurements*, Electromagnetic Fields Division, National Institute of Standards and Technology, Boulder Colorado.
- A.D. Yaghjian, *Near-Field Antenna Measurements on a Cylindrical Surface: A Source Scattering-Matrix Formulation*, Electromagnetics Division, Institute for Basic Standards, National Bureau of Standards, Boulder, Colorado, NBS Technical Note 696, 1977.

It is the hope of the authors that this text will act as a sound reference for all aspects of modern antenna measurements and in some small way enhance the theoretical knowledge and practical skills of the reader with relation to antenna range measurements. As it is clear from careers of the greats in science and engineering, not least Maxwell's own, that it is only through the interaction of these intellectual and practical aspects of science and engineering that effective progress can be made.

Clive Parini, Stuart Gregson, John McCormick, Daniël Janse van Rensburg
and Thomas Eibert
London, Edinburgh, Atlanta and Munich
March 2020

Chapter 1

Introduction

1.1 The phenomena of antenna coupling

This text concerns itself with the ‘theory and practice of modern antenna range measurements’ and as such it is intimately concerned with the problem of the quantification, interpretation and verification of a range of physically observable phenomena that, as will be described in this text, are associated with the emission, reception and scattering of electromagnetic waves. More specifically the technologies and concepts to be discussed and explained in the text along with their use in engineering situations are bounded by a range of frequencies from about 10 MHz to 1 THz with a particular focus on the microwave and mm-wave bands.

This volume will not attempt to hypothesise or examine the variety of postulated physical mechanisms by which the interaction, which is optimised by the antennas, between the electronic systems occurs. However, as it will attempt to develop a thorough theoretical explanation of the applicability of antenna measurements, it must, at least, be consistent with physical law. Very little that is encountered within the discipline of electronic engineering is of a more relativistic nature than the operation of antennas. By definition, the interaction facilitated by the presence of antennas occurs at the speed of light, thus relativity cannot be completely ignored when considering the action of antennas. In this text only transmit (Tx) and receive (Rx) antennas that are in translational equilibrium will be considered and their velocities relative to each other will be specified to be zero. Additionally, the electromagnetic interactions will be observed from an inertial reference frame coincident with the fiducial mechanical datum of the Tx antenna. These conditions make it to a large extent possible to consider the antenna characterisation without reference to any relativistic effects associated with a multiplicity of reference frames or to any non-inertial effects. This simplifies the explanations, without invalidating them in more complex situations, and allows descriptions based on the simplified relativistically invariant equations of classical electromagnetic field theory (EFT) to be used to explain the interaction. *Note:* Only when its inclusion will simplify, expand, or illustrate certain facets of the fundamental interaction, or some detail of the measurement process or data will be quantised, non-classical nature of the electromagnetic field will be discussed. This therefore implies that the problems being discussed only require considerations of lengths that are large compared to atomic dimensions and charge magnitudes

greatly in excess of those found on elementary particles, e.g. electrons, so that recourse to quantum fields theories can be avoided. More exactly, classical concepts are characterised by assuming that the world is divisible into distinct elements, the state of each element can be described in terms of dynamic variables that can be specified with infinite precision, and that the interdependency between parts of a system can be described by exact laws that define changes within any system in terms of dynamic variables.

As a preliminary to any discussion of the theoretical models of the causes of the phenomena (see Chapter 2) or the explanation of the technologies and instruments that can be used to make the observations (see the majority of the text), it is important to realise the difference between the phenomena that can be observed and the non-observable noumena that represent the underlying reality of the observable physical phenomena [1]. The nature of the electromagnetic fields (the noumena) which are considered to be the cause of the observable phenomena is discussed in detail in Chapter 2, but it is important to realise that no direct observation of an electromagnetic field has ever been, and if modern physical science is correct will ever be made. Direct observations that relate to electromagnetic fields are confined to the observable effects that these fields can be inferred to cause, a clue to these effects being inherent to the units in which these fields are usually quantified, e.g. volts/metre or newtons/coulomb, where, e.g., voltage, acceleration and mass are directly observable physical quantities, measurements of which can be inferred to imply the existence of causal electromagnetic fields.

It has been conjectured that a short article ‘Some Thoughts on Ray Vibrations’ by Michael Faraday which appeared in the *Philosophical Magazine* in 1846 marks the birth of electromagnetic field theory. Whether this is considered to be true, and Maxwell always did consider this to be the case, it is certain that Faraday’s concept of field and the intrinsic properties of fields that allows them to manifestly influence the physical behaviour of material objects that are not in direct physical contact with each other has had a profound effect on science and engineering. Prior to Faraday’s great theoretical leap in postulating the existence of field (which appears to have been, at least in part, based upon the observations that he had made, e.g. the pattern that iron filings form in the presence of a magnetic field), no viable explanation could be advanced for the interaction of the observed phenomena that, if correctly stimulated, physically remote electrical systems can interact.

As such the recognition of and the requirement for the development of components to be used as circuit elements that enhance this coupling are based on the observation of this same phenomena that, for physically remote electronic systems if one system is suitably harmonically excited, energy and momentum can be transferred sufficiently to generate measurable voltages and currents in a second (or subsequent) remote electronic system. This is the basis of the phenomena of the antenna-enhanced coupling that will be one of the primary concerns of this text, specifically the radiative coupling between electronic systems in free space will be examined and we will only address reactive near-field aspects when they have noticeable effects on observable phenomena.

If coupling between systems that are not physically separated by large distances is required, various forms of ‘transmission lines’ can be utilised. However, large separation distances almost invariably require the use of antennas as a physical connection becomes impractical or inefficient. Communication systems contain Tx and Rx sub-systems, which necessitate the use of at least two antennas. Broadcast systems may use only a single Tx sub-system, however considerably more Rx sub-systems may be used. Radars may, or may not, use the same antenna for their Tx and Rx sub-systems and the coupling may well be profoundly affected by the scattering from some target. However, in each of these cases, in essence, we are still considering coupling between electronic sub-systems.

Careful considerations of all electronic systems which utilise antennas as a component reveal that it is the extent of this coupling that is fundamental to their operation. Replace Rx antenna with other transducer, e.g. bolometer for power detection and rectifier for rectenna (power transmission by microwave signal), and you have summed up almost every possible engineering and scientific circumstance other than those systems designed to detect transmissions from naturally occurring radiation sources, e.g. radiometers.

The extent to which electronic systems interact, as a result of this coupling, is fundamental to large swathes of electronic engineering and therefore also to our modern technological society. For many systems the existence of this coupling and its ingenuous exploitation for the transfer of information in the form of a signal is imperative to the successful operation of these technologies. This of course means that for these technologies, techniques and components must be developed that maximise this coupling between such electronic systems. As already stated, many strategies have been employed to maximise this coupling (and the subsequent transfer of information between the respective systems), but for physically isolated systems the only practical strategy for enhancing the interaction is the inclusion of circuit elements within the electronic systems that enhance this interaction; these individual circuit components being referred to as antennas.

Clearly engineering design processes for technologies based on the coupling of remote electronic systems will require a range of observations on prototype, pre-production and production systems to characterise, verify and define a range of requirements that will be necessary for successful designs to be implemented. The antenna test range is specifically designed to provide the data that the assessment of such designs requires.

1.2 Characterisation via a measurement process

The most common technique adopted to characterise, predict and quantify the coupling between electronic circuits and systems is to attempt to reduce the problem of circuit coupling to that of antenna performance. Thus, by characterising antennas in a known circuit configuration, the extent to which they enhance coupling in other situations can be predicted. This is the fundamental procedure adopted in antenna test ranges, where the inclusion of antennas in a known,

carefully controlled configuration of two coupled circuits/systems allows this measurement process to be performed. This means that the characterisation of the antennas in this circuit configuration can be used to predict the response of other circuit configurations, which include the same antennas. This characterisation is accomplished via a measurement process.

Historically measurement as a tool for rational cognition, when observations of physical phenomena are designed to extract quantitative information, has often been defined as [2]:

'the quantitative determination of a physical magnitude adopted as a standard, or by means of a calibrated instrument. The result of a measurement is thus a numerical value expressing the ratio between the magnitude under examination and a standard magnitude regarded as a unit'.

This is a commonly used definition that was originally made popular by Lord Kelvin in the nineteenth century. The passage of years has resulted in an increased level of understanding of the physical process of measurement. This, together with the introduction of 'systems centred' concepts and the development of information theory, has lead to a more generalised view of the measurement process. This yields an information conversion definition of measurement which can be stated as [2]:

'consisting of information transfer with accompanying energy transfer. Energy cannot be drawn from a system without altering its behaviour; hence all measurements affect the quantity being measured. Measurements therefore are a carefully balanced combination of physics (energy transfer) and applied mathematics (information transfer)'.

In general, when the observations of a physical phenomenon are designed to extract quantitative information about the physical phenomenon being observed, these observations are usually referred to as measurements. A range of theoretical interpretations about the nature of the measurement process have been advanced, mainly developed from the original concepts as stated by Helmholtz in 1887 in the epistemological essay 'Zahlen und Messen erkenntnistheoretisch betrachtet' [3]. However, in the last century these theoretical interpretations of the measurement process have inclined more towards the representational theory of measurement where measurement is usually defined as being [4]

'the correlation of numbers with entities that are not numbers'.

Figure 1.1 shows the elements of some physical state set (Q), e.g. potential difference, force, time and power, which are mapped onto a representational set (N), which is usually the set of real numbers by means of some measurement procedure/process (M).

Classically a physical quantity, i.e. the extent or extensive nature of a physical phenomenon, can take any real value, and this was why the mapping of the physical phenomena onto a representational set was again usually described as an isomorphism (i.e. a one-to-one mapping or correspondence) from the physical state set

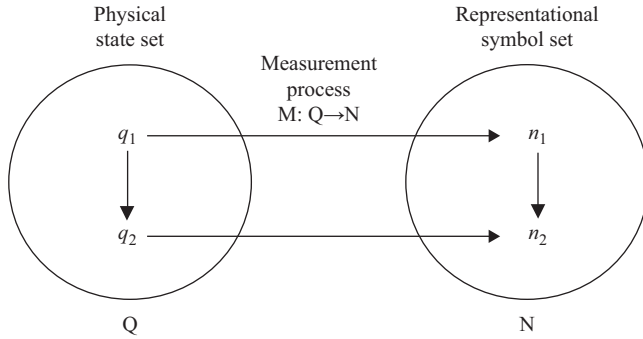


Figure 1.1 A pictorial representation of the set theoretic model of measurement

onto the real number set. It was not until the early twentieth century when the quantised nature of physical phenomena was discovered that it became understood that the physical quantities *themselves* could not take on any and all real values. However, in this text the nature of the fields under consideration will be such that in any practical situation the fields can be assumed to be capable of taking on any measurable value [5]. Nevertheless, although it had previously been thought that the physical quantities could take on any value, it was recognised that any practical measurement system could only map these physical states onto a limited range of numbers, with these numbers representing rational multiples of the resolution of the measurement scale. Thus in practice the information that could be extracted from a measurement process would be restricted to a range of numerical values where a many-to-one (i.e. homomorphism) mapping would replace the theoretical one-to-one (i.e. isomorphism) mapping of an imagined perfect measurement process. The validity of the mapping process is confirmed by the equivalence of the real value physical state sets and the limited value representational sets under the same set of automorphisms.

Since the latter part of the nineteenth century and then the twentieth century, when rigorous statistical methods were adopted in the natural sciences, a more all-encompassing concept of representational measurement has been accepted. Essentially the nature of the representation is valid if the scale mapping between the real physical state and the representational state preserves the relation between the elements of the ordered set of physical quantities in the representational set. Conventionally, the relation between the elements in the physical state set has been visible under the measurement process as a binary relation based on rational intervals of the smallest resolution of the representational set. So, e.g., if two values of a physical state set have a given ratio in the physical state set then they have the same ratio in the representational set. That is to say, a symmetry exists under the homomorphism of the scale mapping that preserves the rational interval relation between elements of the sets. However, other relations between the elements of the sets, e.g. ordinal and/or categorical relations between elements of the sets, can also be preserved under a range of homeomorphisms so measurement processes that are

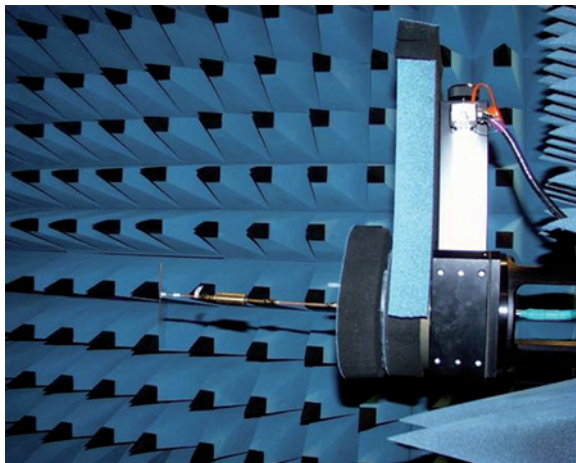


Figure 1.2 Linear dipole antenna

not based on rational intervals can also be viable. This can allow a more diverse and comprehensive range of statistical techniques to be deployed in measurement data assessment exercises.

Therefore, given that phenomena relating to the coupling of remote electronic systems can be observed and that these observations can be directly related to the action of the antennas in the electrical circuits which comprise these systems, what are the properties of the antennas that need to be assessed via a measurement process to enable viable engineering solutions to be designed, refined and tested?

1.3 Measurable properties of antennas

An antenna can be described in many ways. For instance, it is possible to describe an antenna in terms of its mass, which is clearly a critical property if the antenna is to be used in a space or aerospace application. The physical size of the antenna is also of importance in many applications where available real estate is in limited supply, for instance where antennas are installed within a mobile phone or a laptop computer, and so on. Alternatively, antennas can be categorised in terms of their physical structure. The following figures (Figures 1.2–1.6) contain examples of various different classes of antenna.

While these are all entirely valid ways of describing antennas (together with thermal temperature and colour) in this text, we are only concerned with the electrical properties of antennas, that is to say, those properties of an antenna which emerge when they are placed within an active *resonant* electrical circuit. When considered in this context, for instance, an antenna can be described as being ‘a means for radiating or receiving radio waves’ [6]. Alternatively they can be considered to be ‘an arrangement of conductors and/or dielectrics to enhance and



Figure 1.3 Slotted waveguide planar array antenna



Figure 1.4 Offset parabolic reflector antenna

control radiation'. They could equally well be thought of as being 'a transducer between free-space propagation, and guided-wave propagation'. Indeed many take a profoundly different view and consider the antenna to be purely 'a component, system, or product, which is used or sold to return profits to shareholders'. Although valid (and the likely explanation of much of the interest in antennas and the existence of the antenna industry) this last description does not advance our technical understanding. As an antenna is the part of the circuit that is the principal transducer between free-space (i.e. radiated) and guided-wave (i.e. circuit) regions, antenna behaviour can be couched in terms of either *and* in terms of the efficiency of the transformation from one to another. The free-space characteristics include properties such as free-space radiation pattern (e.g. pointing, beam-width and side

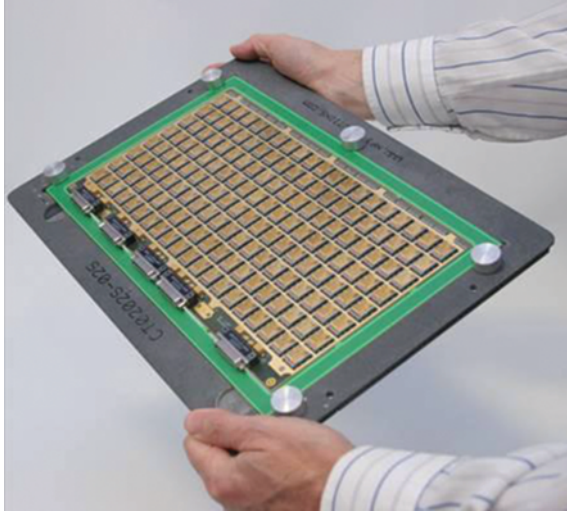


Figure 1.5 Planar patch array antenna (Courtesy of Selex ES)

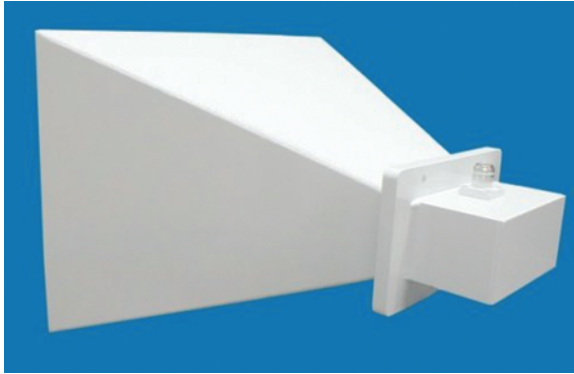


Figure 1.6 Rectangular pyramidal horn antenna

lobe level), directivity, polarisation (e.g. tilt angle, axial ratio, cross-polar discrimination) and radar cross-section (RCS), which is a wave-to-wave scattering measurement. The circuit-element characteristics include properties such as input impedance and match (cf. reflection coefficient). The transfer characteristics include quantities such as gain, efficiency, effective isotropic radiated power (EIRP), effective area and antenna noise temperature, which is a property that also depends upon the environment in which the antenna is placed. Crucially, as antennas are invariably required to operate across a range of frequencies, in order

that the antenna performance can be completely characterised, all of these properties are also needed as a function of frequency. This leads to an additional antenna property, namely that of antenna bandwidth which is the range of frequencies over which the antenna is considered to ‘operate effectively’.

Thus, with the exception of some circuit element characteristics and noise measurements, all of the above-mentioned properties of antennas are addressed (i.e. characterised) within modern antenna test ranges. However, of these properties, perhaps the three most important and specifically related to antennas are gain, free space radiation pattern and polarisation. These parameters are described in more detail in the sections that follow.

1.3.1 Antenna gain and directivity

In most electronic systems gain is related to amplification, usually expressed in terms of voltage or power depending on the types of system under discussion. For antennas, however, the concept of gain has a different meaning, one which is perhaps more closely aligned with the focusing ability of a lens. The interaction between systems facilitated by antennas requires that power is transferred between the systems from one location in space to another. It is a fundamental law of physics that energy is conserved globally and locally, and this means that for power to be transferred between remote systems there must exist a radiative power flux between the two, otherwise, isolated systems. The gain of an antenna, subject to the constraints of polarisation, as will be explained in Section 1.3.4, is defined as follows [7]:

$$G(\theta, \phi) = \frac{\text{power generated per unit angle in the direction } (\theta, \phi)}{\text{total power accepted from the source}} \quad (1.1)$$

Thus the gain relates the power flux density that an antenna radiates in a given direction relative to the total power *accepted* by the antenna. Assuming a single main or major lobe antenna pattern, the maximum gain of an antenna occurs in the direction of the main-beam (i.e. main-lobe) which, for convenience, is often referred to as simply the gain of the antenna. The power accepted by the antenna will differ from the total power that is *available* to the antenna by an amount that depends upon the impedance match of the antenna. This definition of gain results in a slightly more difficult measurement as the antenna mismatch factor must be taken into account. As will be explained in Chapter 2, the source of the power in a radiating antenna is vectorial in nature so the ability of an antenna to produce a power flux density is a function of the direction, relative to some fixed frame of reference or mechanical datum, that the power flux density is projected, hence the dependency on the angles θ and ϕ in the expression above. The gain is therefore a directive characteristic of an antenna and a directivity can also be assigned to an antenna where this can be expressed as follows [7]:

$$D(\theta, \phi) = \frac{\text{power generated per unit angle in the direction } (\theta, \phi)}{\text{total power radiated by the antenna}} \quad (1.2)$$

In the event that an antenna is lossless, the directivity and the gain would be equal. The ratio of the two quantities, namely

$$\eta = \frac{G(\theta, \phi)}{D(\theta, \phi)} \quad (1.3)$$

is defined as the radiation efficiency of the antenna. When the efficiency of the antenna is 100% and thus there is no internal dissipative (e.g. ohmic) loss, the antenna gain equals the antenna directivity thereby ensuring $0 \leq \eta \leq 1$. Thus, of the two, gain is typically the more useful parameter when describing a given antenna's overall performance.

Both gain and directivity can be expressed linearly or in decibel (dB) form where one decibel is equal to one tenth of a bell (B). As both gain and directivity can be cast in terms of power ratios (i.e. the ratio of the linear quantity and unity), the logarithmic forms can be obtained from the linear forms using

$$G_{\text{dB}} = 10 \log_{10} G \quad (1.4)$$

$$D_{\text{dB}} = 10 \log_{10} D \quad (1.5)$$

Thus, when expressed in logarithmic form, gain and directivity are related by

$$G_{\text{dB}} = D_{\text{dB}} - \eta_{\text{dB}} \quad (1.6)$$

Note, according to the IEEE standards [6], gain does not include losses arising from impedance mismatches or from polarisation mismatches. This, perhaps unintuitive, definition was decided upon because it is always possible to construct a matching network to ensure the maximum amount of power is transferred to the antenna, and similarly, as will be explained in the following text, polarisation matched antennas are assumed.

1.3.2 *Antenna cross-section*

An alternative way of expressing the effectiveness of antennas to facilitate the interaction, i.e. transfer of power in the form of voltages and currents, between coupled systems is that of antenna cross-section. This is also known as antenna effective area. As will be shown below, the effective area of an antenna is essentially a frequency independent way of expressing how well an antenna can project/accept radiation into or from a given direction. If S is the power density of the incoming plane wave in watts per square metre and $P(\theta, \phi)$ is the amount of power absorbed in watts, then the effective area can be defined by

$$P(\theta, \phi) = SA(\theta, \phi) \quad (1.7)$$

Here, the area A is in square metres and S is the power density of the plane wave in watts per square metre. In order that the maximum equivalent area for the antenna is computed, as will be explained in Section 1.3.4, it is usual to assume that the

antenna and plane wave are polarisation matched. The gain of a 100% efficient antenna, i.e. one where gain equals directivity, at a specific frequency is usually stated to be

$$D = \frac{4\pi A}{\lambda^2} \quad (1.8)$$

where D is the directivity, A is the effective area of the antenna and λ denotes wavelength.

In Section 1.1 it was noted that ‘Only when its inclusion will simplify, expand, or illustrate certain facets of the fundamental interaction, or some detail of the measurement process or data will be quantised, non-classical nature of the electromagnetic field will be discussed’. Box 1.1 contains details about the nature of the electromagnetic interaction between antennas and how it is constrained by the laws that govern the transfer of energy and momentum between all physically isolated systems, electronic or not. The contents of the box are included for the interested reader. However, as with all isolated boxes in the text it can be read in continuity of the text, in isolation from the rest of the text, or not at all, as the basic narrative of the text will be unaffected.

Box 1.1

Although the relationship between effective area, as defined above, and antenna gain can be obtained from a number of theories, including classical electromagnetic theory, perhaps the simplest explanation (involving only basic algebra) can be derived from considerations of the one of the most fundamental of physical laws, i.e. the Heisenberg uncertainty principle [8] and how this limits the localisation of any photon. Although relativistic considerations require that only photons with circular polarisation about an axis aligned with their propagation vector can exist, linear polarisation can be considered to be a superposition of equal numbers of right- and left-handed coherent photons. Circularly polarised photons have angular momentum (more commonly known as spin angular momentum and does not depend upon frequency).

Angular momentum is defined as

$$P = I\omega = mR^2\omega \quad (B1.1)$$

where I is the moment of inertia, ω is angular frequency, m is mass and R is the radius of gyration. For a zero rest mass particle, i.e. any particle that propagates at the velocity of light, e.g. any microwave photon, the energy carried by the photon can be expressed in terms of the relativistic rest mass of the photon:

$$E = hf = mc^2 \quad (B1.2)$$

Here, h is Planck's constant and c is the speed of light. Rearranging this yields

$$m = \frac{h\omega}{2\pi c^2} \quad (\text{B1.3})$$

From (B1.1)

$$R^2 = \frac{P}{m\omega} = \frac{P2\pi c^2}{h\omega^2} = \frac{h2\pi c^2}{2\pi h\omega^2} = \frac{c^2}{\omega^2} \quad (\text{B1.4})$$

From this

$$R = \frac{c}{\omega} = \frac{f\lambda}{\omega} = \frac{\omega\lambda}{2\pi\omega} = \frac{\lambda}{2\pi} \quad (\text{B1.5})$$

Thus the area swept out by the radius of gyration of such a photon is

$$A_p = \pi R^2 = \frac{\lambda^2}{4\pi} = \frac{\lambda^2 \cdot 1}{4\pi} \quad (\text{B.16})$$

This implies that A_p would be the effective area of a unity gain/directivity lossless isotropic antenna, where any emission or absorption of photons is limited to the area A_p . In terms of the uncertainty relation the photon's origin would be limited to the area A_p but there would be no knowledge of their momentum; therefore propagation in any direction would be equally likely, i.e. the probability density function for the photonic interaction would be isotropic. This means that in order for an antenna to have any level of directivity greater than unity the antenna would need to be larger than A_p . As is implied by the uncertainty relations the directivity is linearly related to the area over which emission or absorption can take place; therefore for an antenna with greater than unity directivity:

$$A = \frac{\lambda^2 D}{4\pi} \quad (\text{B1.7})$$

where, as already stated for (1.8), A is the effective area of the antenna. Thus it can be seen that the ability of any antenna to directly transfer energy and momentum in the form of voltages and currents between remote electronic systems is fundamentally limited by the basic physical principles that govern the flux of this energy and momentum across space and time.

Rearranging this expression yields

$$D = \frac{4\pi A}{\lambda^2}$$

As per (1.8), thus confirming that the directive nature of EM emissions is governed by the same laws that describe the transfer of energy and

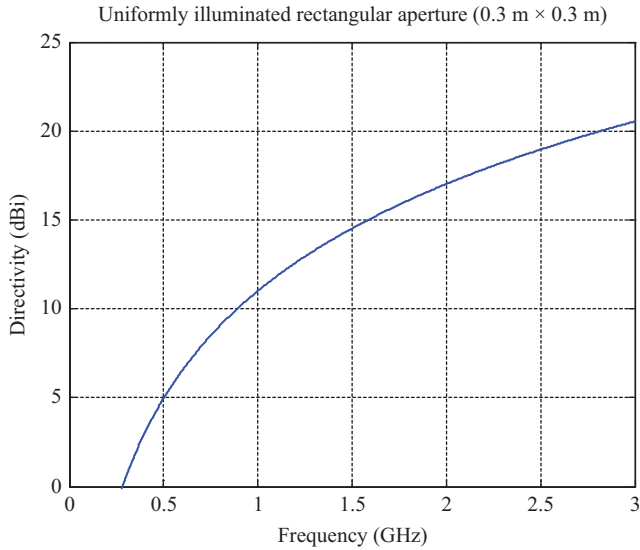


Figure 1.7 Equivalent directivity of a uniformly illuminated rectangular aperture plotted as a function of frequency

momentum between all physically isolated systems, electronic or not. *Note:* The relationship between gain/directivity and effective area for antennas can be established using a variety of different physical models, apart from the simple method that is shown above and classical electromagnetic theory, e.g. it can also be established using the tenants of statistical thermodynamics [9].

From the expression

$$D = \frac{4\pi A}{\lambda^2} \quad (1.9)$$

it can be seen that for a fixed aperture size of, for example, 30 cm by 30 cm, it is possible to plot directivity as a function of frequency.

Figure 1.7 illustrates an example of the functional relationship between antenna area, i.e. electrical size in wavelengths, and gain.

1.3.3 Free-space radiation pattern

The ability of an antenna to radiate power in a given direction is an important measurable characteristic of any antenna; however, the finite spatial extent of any practical radiating structure means that it is not possible for any antenna to radiate exclusively in one direction. At any one time an antenna will be radiating more or

less power, in a variety of different directions. Hence, the angular pattern of this radiation is another important characteristic of an antenna that can be measured in a test range.

As discussed above, antennas do not radiate equally in all directions. However, the concept of an isotropic radiator is useful as a standard relative to which any other antenna's performance can be compared but is in theory and practice impossible to construct. Therefore the variation in the ratio of the radiated power, as a function of angle relative to the fixed mechanical datum of any antenna, is an important parameter. Figure 1.8 defines a coordinate system against which this variation can be judged with the z -axis or ϕ -axis conforming to the mechanical datum, often referred to as boresight, of the Tx antenna.

Here, the variables θ and ϕ are independent and orthogonal, $\hat{\theta}$ and $\hat{\phi}$ are orthogonal unit vectors that point in the direction of increasing θ and ϕ . Figure 1.9 illustrates the relative angular position of the Tx and Rx systems as the Rx antenna moves around a circular path at a fixed value of ϕ and R with θ varying along the circular path and with the Tx antenna at its centre. For any sufficiently large fixed value of $|R|$ the extent to which power is transferred between the two antennas relative to the value at $\theta = 0$ would vary as a function of the angle θ , where R is defined as

$$\underline{R} = |\underline{R}| \sin \theta \cos \phi \hat{e}_x + |\underline{R}| \sin \theta \sin \phi \hat{e}_y + |\underline{R}| \cos \theta \hat{e}_z \quad (1.10)$$

with

$$|\underline{R}| = \sqrt{X_{AMS}^2 + Y_{AMS}^2 + Z_{AMS}^2} \quad (1.11)$$

Here, the subscript AMS is used to denote coordinates that are in the antenna measurement coordinate system.

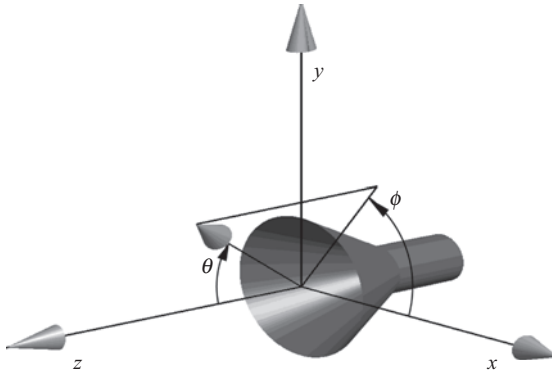


Figure 1.8 *Illustration of the antenna coordinate system, with aperture of cylindrical horn antenna located at origin*

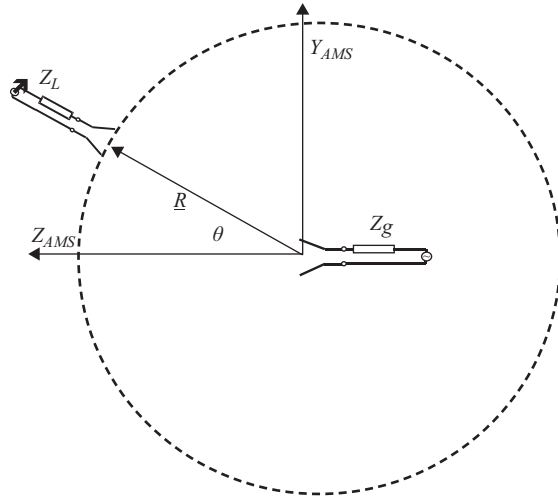


Figure 1.9 Orientation of Tx and Rx antennas, including all circuit components

Clearly this variation in relative power would also be a function of the angle ϕ so the so-called radiation pattern of the antenna would actually be a function of both θ and ϕ , the angles which define the direction of the displacement \underline{R} , the path between Tx and Rx antennas. The pattern function is an important parameter of any antenna and, assuming the magnitude of \underline{R} , i.e. the distance between the two antennas is large, for two such antennas the variation along a segment of the circular path shown could be of the form shown in Figure 1.10 where the relationship between the two parameters is represented graphically. Here, the maximum-recorded signal has been normalised to unity, i.e. zero on a dB scale.

As has been expounded above, any antenna measurement comprises the interaction of two antennas. In this case, it is clear that one of those antennas is the antenna under test (AUT), which in this case is a pyramidal horn; the question is, what is the other antenna? In this case, the second antenna, i.e. the one which is located at the observation point \underline{R} , is taken to be an infinitesimal Hertzian dipole antenna. This constitutes a single oscillating electron which is the most elemental form of ‘antenna’ and one which can be used as a reference within measurements and theoretical predictions alike. The exact reason for this choice is expounded in the following chapters. Here, the pattern has been plotted on a rectangular, i.e. Cartesian, graph with angle plotted as the abscissa and power as the ordinate. It is also common practice to present this information using a polar plot. This is illustrated in Figure 1.11 for variations in θ and in Figure 1.12 for a 3D plot.

The measurement of absolute levels of power coupled, or the levels relative to calibration standards, is also possible but again detailed discussion of this will be delayed until a simple model of radiating structures is developed in Chapter 2. There and in later chapters also, those concepts relevant to the characterisation of antennas as circuit elements that cannot be measured exclusively in antenna test

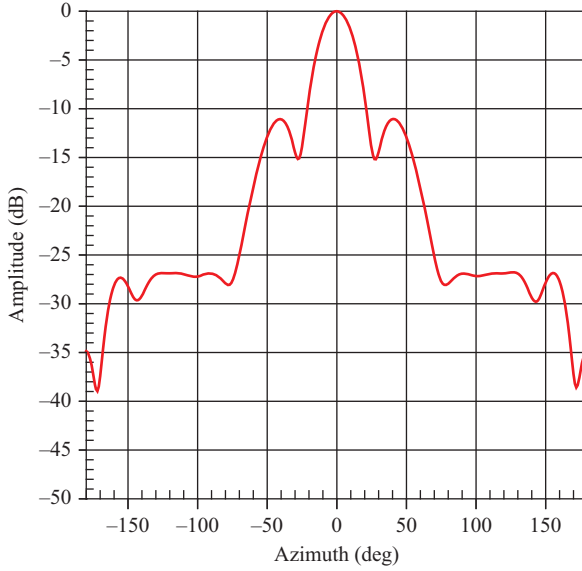


Figure 1.10 Recorded power normalised to 0 dB as Rx is moved around the circle

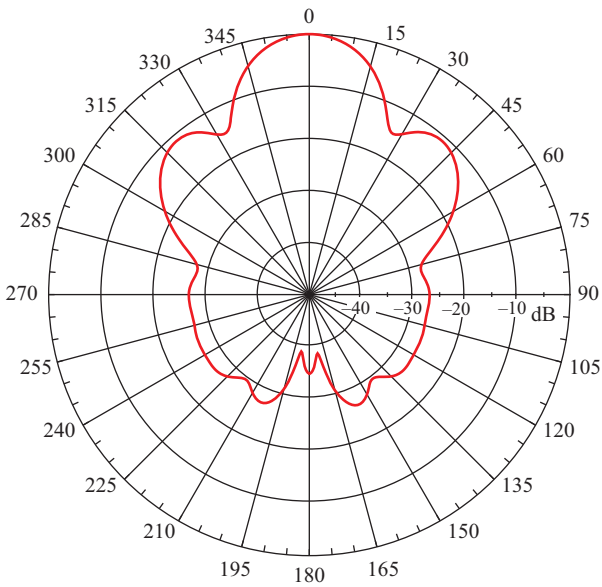


Figure 1.11 Recorded power normalised to 0 dB as Rx is moved around the circle presented in the form of a polar plot in deg.

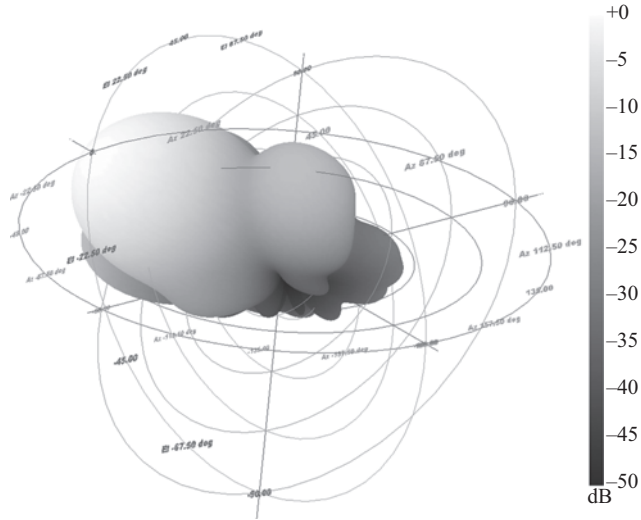


Figure 1.12 Recorded power normalised to 0 dB as Rx is moved around the far-field sphere presented in the form of a virtual 3D polar plot

ranges will be addressed. These include scattering parameters and their relevance to definitions of gain in terms of accepted as opposed to delivered power in any circuit and their possible use in scattering matrix descriptions of Tx and Rx antennas.

1.3.4 Polarisation

Having measured this pattern function, it might be assumed that everything is known about the angular variations in coupled power between the Tx and Rx systems. However, for any position of Tx and Rx, were either of the antennas to be rotated about their mechanical datum, i.e. about the ϕ -axis for the Tx antenna as per Figure 1.8, a variation in the amount of power coupled as a function of ϕ would be observed. This variation is ascribed to the polarisation of the antenna, a further illustration of the vectorial nature of the power source, and various polarisation bases that can be used to describe this polarisation will be developed over the course of the text. The concept of polarisation was discussed in Box 1.1 where it was noted that individual photons themselves exhibit the polarisation characteristics; however, for our purposes polarisation can be considered as simply another factor that influences how well two circuits can couple to one another. Thus the polarisation of an antenna is therefore defined to be the polarisation of a wave *transmitted* by the antenna and propagating in some given direction. An example of this is illustrated in Figure 1.13 which contains a typical measured response of what would be termed a linearly polarised Rx antenna's response if a Tx antenna had the same so-called initial polarisation at 0 degrees.

Polarisation is defined as the direction of the electric field. If the electric field is horizontal, the antenna is said to be horizontally polarised where the horizontal

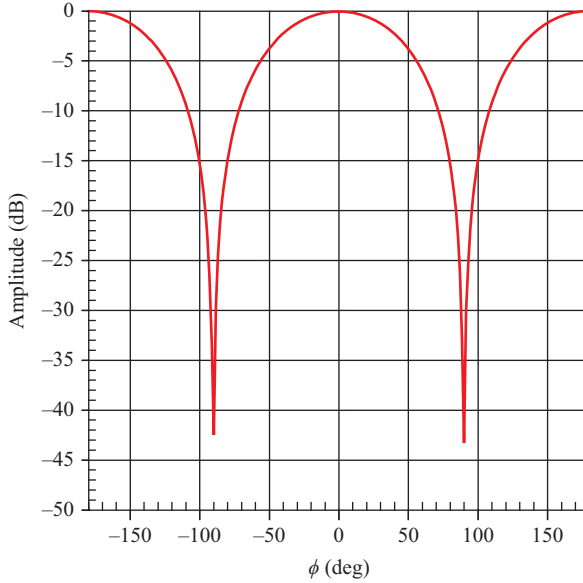


Figure 1.13 The variation in coupled power as a function of ϕ

and vertical are defined in the antenna's coordinate system. Similarly, if the electric field is vertical, the antenna is said to be vertically polarised and if the electric field is aligned at some other angle ϕ , the field is said to be slant-linear polarised. If the electric field rotates, the antenna is said to be elliptically polarised, or in a special case of this, circularly polarised. If the rotation of the electric field is clockwise when the wave is propagating towards the observer, the polarisation is left-hand clockwise, i.e. left-handed circular polarisation (LHCP). Conversely, if the electric field rotates anticlockwise (counter-clockwise) then it is right-handed circular polarisation (RHCP). These states are shown in Figure 1.14. *Note:* Other definitions of circular polarisation defined by looking from behind the antenna are often quoted and the reader should be aware that these other definitions exist. In reality an antenna is never perfectly LHCP or RHCP and is instead always elliptical. Clearly, LHCP and RHCP are orthogonal and conveniently circular polarisation can always be expressed as the sum of two orthogonal linear polarised components and conversely, linear-polarisation can always be expressed as the sum of two circularly polarised components.

1.3.5 The far-field

Both of the types of measurements discussed above, i.e. pattern and polarisation, can be made in an effort to characterise the coupling between antennas; however, one point that has been briefly mentioned will need further explanation. Figure 1.9 shows an Rx system including an antenna placed at a position along the circular path and Figure 1.11 shows the variation in the antenna pattern with angle θ . The

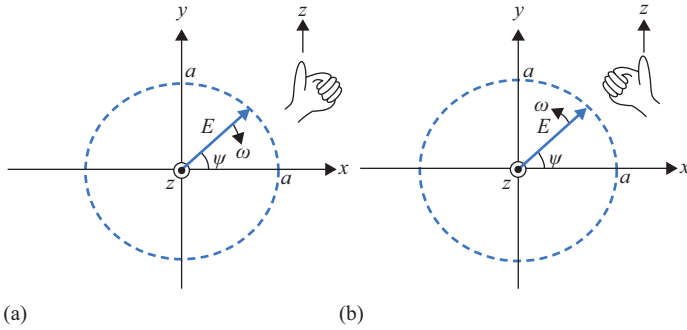


Figure 1.14 Examples of left- and right-hand circular polarisation of waves propagating towards the observer

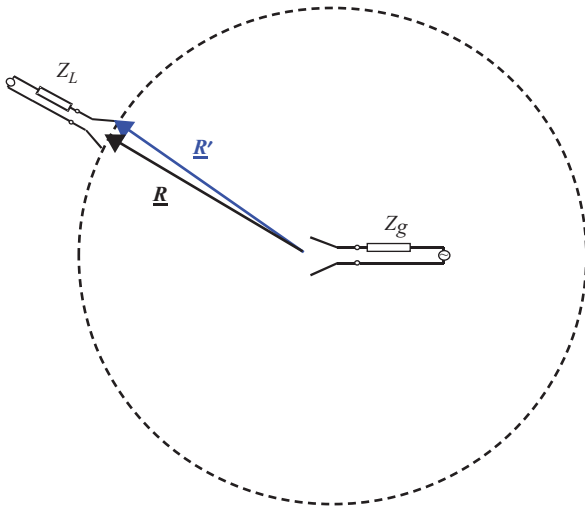


Figure 1.15 Two of the possible paths between the Tx and Rx antennas

text then goes on to state that ‘provided $|\underline{R}|$ is large enough’ the pattern will just be a function of θ and ϕ , without stating how large $|\underline{R}|$ has to be for this to be true.

When $|\underline{R}|$ is small, i.e. of the order of a few wavelengths in free space, the extent of coupling between the circuits is profoundly affected by the instantaneous distribution of charge over the surfaces of the antennas. Here, the ratio of the power coupled is strongly dependent on $|\underline{R}|$. This is the so-called reactive region around an antenna where reactive coupling dominates radiative coupling. As the distance $|\underline{R}|$ increases, the power coupled between the circuits is no longer dominated by this charge distribution; Figure 1.15 illustrates such a situation.

In this figure the displacement from Tx to Rx is again labelled \underline{R} but as the antennas are extended objects in space many displacements, e.g. \underline{R}' , are also

possible paths between the antennas, meaning that in the situation illustrated, there is *no* unique path between the two antennas. Only when $|\underline{R}|$ is infinitely large will the displacements \underline{R} and \underline{R}' be effectively the same. Therefore, only when $|\underline{R}|$ is infinitely large can we define a unique path with a definite length where all parts of the two antennas are effectively at equal distances apart; when this is so, the two antennas are in each other's true *far-field*.

In practice, since in the vast majority of engineering situations we are concerned with antennas that are at large but finite distances apart, the far-field is defined as being when all parts of the Tx antenna are effectively at the same distance from the Rx antenna. At this distance the angular field distribution is essentially, but not strictly, independent of $|\underline{R}|$. The distances at which $|\underline{R}|$ can be considered to be large enough to define a far-field region will be examined in the following chapters but it is the requirement that $|\underline{R}|$ is in theory sufficiently large and, as will be explained in the text, modern antenna test ranges are almost invariably indoor facilities with only *short* range length that is the spur for much ingenuity and innovation in the modern antenna test.

That region in which the coupling is dominated by radiation but the distance $|\underline{R}|$ is not sufficiently large to uniquely define a single path is called the radiating near-field, this is the region surrounding the antennas that will be, in many senses, the practical focus of this text. In engineering situations, as a result of how they are employed, almost invariably it is the far-field performance of antennas that is of interest. However, for practical reasons that will be examined in this text, the ability to make measurements where $|\underline{R}|$ is in fact much smaller than would normally be required is extremely important in modern antenna metrology.

1.3.6 *The phase in the measurement*

In the first paragraph of this chapter, it is stated that this text is 'intimately concerned with the problem of the quantification, interpretation and verification of a range of physically observable phenomena that, as will be described in this text, are associated with the emission, reception and scattering of electromagnetic waves'. This implies that, as will be described in Chapter 2, the radiation that facilitates the transfer of energy and momentum between remote electronic systems is based on the propagation as described in classical wave theory. So far the measurements described have been related to the magnitude of the voltages and currents that can be induced in remote systems as a result of antenna coupling, but if the propagation can be described by classical waves another aspect of the coupling will also be in evidence.

The basis of all free-space antenna measurement techniques, and indeed much of electromagnetic theory, is the assumption that the AUTs and the systems used in any test procedures behave in a linear fashion. In fact, lack of linearity will be a source of uncertainty in the measurement process that will be referred to in Chapter 10. Such linear systems can be described by linear differential equations like

$$c_n \cdot \frac{d^n f_2(t)}{dt^n} + c_{n-1} \cdot \frac{d^{n-1} f_2(t)}{dt^{n-1}} + \dots c_1 \cdot \frac{df_2(t)}{dt} + c_0 \cdot f_2(t) = f_1(t) \quad (1.12)$$

For any simple system that can support harmonic oscillations this can be truncated to a second-order equation of the form:

$$c_2 \cdot \frac{d^2 f_2(t)}{dt^2} + c_1 \cdot \frac{df_2(t)}{dt} + c_0 f_2(t) = f_1(t) \quad (1.13)$$

where the constants and functions in the equation can be related to the usual circuit parameters of an electronic system, capacitance (C), inductance (L), voltage (V), charge (q) and resistance (R), to give

$$L \cdot \frac{d^2 q(t)}{dt^2} + R \cdot \frac{dq(t)}{dt} + \frac{1}{C} \cdot q(t) = V(t) \quad (1.14)$$

This is an equation relating the circuit parameters, with a harmonic solution that will be familiar to any student of alternating current (AC) theory. However, such an equation is inadequate to describe the harmonic solutions present in a circuit at radio or microwave frequencies. If a voltage is applied to such a circuit, this voltage will be propagated through the circuit at approximately the speed of light, 3×10^8 metres per second. Thus, at 50 Hz this will produce a spatial harmonic variation in the circuit voltage which will be cyclic over some 6 000 km. Therefore, for any circuit harmonically oscillating in time at 50 Hz, it is reasonable to assume that the voltage and currents are constant at all points in the circuit at any specified time. However, at the microwave frequency of 10 GHz the associated cyclic spatial variation of the currents and voltages in any circuit will be repetitive over a distance of the order of 3 cm. At this frequency, assuming the circuit itself is at least of the order of a few centimetres in length, the currents and voltages in that circuit will vary harmonically both as a function of when and where they are observed.

A harmonic system in which such oscillations are a function of space and time will be described by a partial differential equation. Such an equation that linearly relates the rate of change of the rate of change of the variables with respect to time, to the rate of change of the rate of change of the same variables with respect to space is a wave equation. This means that measurements of the instantaneous power made at different points in the circuit at the same time will give different results and these results can be related to provide a measure of the *relative* phase of the harmonic oscillation at the different points in the circuit. These measurements, that can be used to assign a phase to the harmonic coupling, are an additional aspect of measurements that can be made on antennas. As will be discussed in the text, these measurements are the source of the in-phase and at quadrature data that will be fundamental to the near-field measurement process.

1.3.7 Reciprocity

As yet the coupling between antennas has been discussed without explicit reference to any differences that there might be in the properties of Tx and Rx antennas. It is a common fallacy to assign properties to antennas that actually belong to the systems within which they are embedded. By way of example, often antennas are described as being reciprocal devices, in fact by definition reciprocity is a property that can

only be applied to objects which are either sources or sinks for energy [10]. Thus it is correct to say that electronic systems that are reciprocal, e.g. that include generators and loads and satisfy the usual requirements of isotropy, will not have this property affected by the inclusion of antennas within them. However, to talk of antennas in the absence of well-defined waveguide ports or terminals, where load impedances and source voltages are attached, being reciprocal is to misinterpret the concept of reciprocity. In fact, almost all of the properties usually assigned to antennas, and to engineering importance, are in fact properties of systems containing antennas. Antennas do not by themselves transmit or receive energy across free space; they are simply bi-directional transducers that can be included as circuit components in electronic systems. It is systems that include antennas as components that have the emergent property that they can radiatively couple power across large ranges in free space.

Thus it should be remembered that the characterisation of antennas via measurements to quantify their performance is really the characterisation of highly specified electronic systems containing Tx and Rx antennas that can be used to predict the response of other systems in which the same or similar antennas will be utilised. Therefore it can be assumed that, unless non-reciprocal components or sub-systems are included in the overall electronic Tx and/or Rx systems that are being characterised, e.g. ferrite isolators, the response of the Tx and Rx antennas will appear reciprocal and that the measured gain, pattern and polarisation of any antenna containing system will be the same in Tx as in Rx. Modern nomenclature often refers to the entire assembly of an active electronically scanned array (AESA) as the antenna. In such an antenna there may well be non-reciprocal components and/or sub-systems. However, the actual radiating structure, the bi-directional transducers, will still have the same gain pattern and polarisation properties in Tx and Rx.

1.3.8 Measurement limitations

The ability to make any of the measurements so far described in the text has not been addressed. As will be expanded upon in Chapter 2, the action of antennas to facilitate the transfer of energy and momentum across free space between remote electronic systems involves the postulated transmission and reception of electromagnetic waves that have propagated across the intervening free space between the Tx and Rx antennas. It is vitally important in any characterisation process based on measurement that what is actually measured is truly representative of the phenomenon that is under investigation.

For example, in attempting to measure the pattern of a receiving antenna it is assumed that all of the power incident on it will emanate directly from the Tx antenna, i.e. there will be no multi-path, interference or any other electromagnetic error sources in the measurement. The assumption that what is being measured is what has been postulated unpolluted by any possible error source is also accompanied by the assumption that the test range has the capability to make the measurements with the required levels of precision and accuracy. For this to be the

case, antenna measurement will preferably take place in highly controlled and isolated environments where the action of the Tx and Rx antennas can be tightly controlled and accurately and precisely measured, hence the requirement for highly accurate characterised antenna test ranges.

1.4 The content of this text

The range of measurements detailed above can be used, along with other measurements that do not specifically need an antenna test range, to characterise antenna performance. It is exactly this requirement to be able to assume that the test range is measuring what is actually required and measuring with the required levels of accuracy that has led to the development of the modern antenna test range. The accurate characterisation of how the presence of antennas will affect the coupling of electronic circuits can be accomplished using a number of different range configurations and it is the primary purpose of this text to illustrate and explain the deployment, capability, limitations and rationale behind the use of these various modern antenna test ranges.

In Chapter 1 of this text, we have examined the phenomena of antenna coupling and, after defining what is meant by measurement, have illustrated a number of measurement parameters of antennas that are important in characterising their performance via measurement. As is explained in the Preface, and will be expanded upon in the text as a whole, the fact that these coupled antennas can facilitate the transfer of energy and momentum between remote electrical systems by exciting currents and voltages in the circuits of these systems can be used as the basis of a great many technologies that require the exchange of information in the form of a signal between widely separated electronic systems.

The most basic of these, the antenna parameters that relate to the spatial orientation of the Tx and Rx antennas, and the basic *raison d'être* behind the requirement for specialist antenna test ranges, have been examined. Other more concise and refined parameters that can be obtained from measurements in modern antenna test ranges in concert with other facilities, instrumentation and signal/data processing will be examined in the main body of the text.

Although the basis of all antenna measurements is the observable phenomena of antenna coupling and, therefore by definition the existence of a radiative interaction between Tx and Rx antennas, a full understanding of the process observed requires examination of the underlying noumena or mechanism behind the observable facts. It is not the purpose of this book to critique or examine in detail the range of hypothesised mechanisms by which the interaction facilitated by the antennas between the electronic systems occurs, some of these alternatives postulated mechanisms are listed in [11]. In this text in Chapter 2, the interaction will primarily be described in terms of the propagation of transverse, to take account of polarisation, waves propagating in a non dispersive medium, these waves being consistent with solutions to Maxwell's equations.

As it is considered essential for any deep understanding of the antenna measurement process, an examination and explanation of the basic concepts/algorithm behind, and inherent to, the classical theory of electromagnetism as summarised by Maxwell's equations are presented in Chapter 2. In a large variety of circumstances, this is a particularly successful algorithm for the description of the interaction in question, but the treatment, in this volume, will be such that other hypothesised interaction mechanisms and their attendant mathematical algorithms will not be precluded by the explanations introduced.

This is followed in Chapter 3 by a survey of far-field and quasi far-field and near-field forms of antenna measurement techniques. This includes an introduction to far-field, compact-range, and a variety of near-field scanning measurement methodologies. Discussion of the basic hardware requirements for the implementation of such measurement techniques including anechoic chambers, RF subsystems and absorber, when required robotic positioners and probe antennas, is also included along with the definition of a generic antenna measurement process.

Chapter 4 presents a detailed introduction to coordinate systems in the context of antenna measurements. These concepts are then extended to develop several the more widely encountered polarisation bases. The subject of coordinate systems is fundamental to all form of near- and far-field antenna measurements and the successful interpretation of both measured and modelled antenna patterns. Consequently, this material is presented early in on in the text so that the reader is appropriately prepared for when this knowledge is called upon within the latter chapters.

Chapter 5 concentrates on one particular type of modern antenna test range, the compact antenna test range (CATR). The different types of CATRs are discussed in terms of their inherent capability to produce the collimation of electromagnetic fields and the resultant quiet zones along with how their ability to produce these conditions can be evaluated. Particular attention is given to the applicability of CATRs to millimetre wavelength measurements, and the utility of CATRs in making scattering as well as Tx and Rx measurements is examined with respect to calibrated RCS measurements.

Chapter 6 is devoted to the technique of planar near-field scanning and its use as an antenna measurement technique. This involves, by way of explanation, illustrating the solution of Maxwell's equations in Cartesian coordinates, the development of the transmission formula and an examination of the technique of probe pattern correction.

The technique of near-field scanning is again examined in Chapter 7, but this time in a different geometry, i.e. in terms of cylindrical near-field antenna measurements. To this end a solution of Maxwell's equation in cylindrical coordinates and an appropriate transmission formula relevant to the cylindrical geometry are derived. As with planar scanning an analogous probe pattern correction formula is devised and the technique of cylindrical scanning is further developed to illustrate conical near-field antenna measurements.

In Chapter 8 the techniques of near-field scanning are again revisited but this time spherical near-field antenna measurements are explained. The different types of spherical range (ϕ/θ , θ/ϕ , arch-*role*) are illustrated and as with the

other varieties of near-field scanning a solution of Maxwell's equations in spherical coordinates along with the development of the required transmission formula and probe pattern correction is discussed.

Although the concept of measurement is briefly discussed in the opening chapters of this text, this is done in terms of the theory of representational measurement; in practice the physical limitations of any measurement system introduces ambiguity and uncertainty into the measurement process. In order to understand and quantify the extent of this uncertainty in the process, an assessment must be made of the possible, probable and certain error sources in the measurement procedure.

Chapter 9 seeks to address the need to perform near-field antenna measurements with improved flexibility as compared to the traditional approaches of canonical measurement surfaces using regular sampling. This chapter derives computationally very efficient, and very flexible, inverse equivalent source solvers for the transformation of measured near-field data into a set of equivalent sources, which can in turn be used to compute near and far-fields anywhere within the solution domain.

As near-field scanning is a measurement procedure that does not even indirectly measure many of the required characteristics of an antenna, it essentially is a process in which data is acquired from which predictions of the required characteristics can be processed, it is particularly susceptible to measurement uncertainty. Since this is the case, range assessment is an important area in the effective use of modern antenna test ranges. Chapter 10 addresses the requirement for such assessments by analysing the overall effect of the limitations in the measurement techniques in terms of the errors that may be inherent in the individual components, instruments and processes used in an antenna test range when antenna measurements are undertaken. The possible error sources are identified and techniques are advanced for their assessment and reduction/removal; this is illustrated via a detailed example of range assessment.

Chapter 11 moves away from the consideration of specific types of ranges and their performance and attributes, instead it concentrates on how these ranges can be used to advance a specific rapidly evolving area of radio-frequency technology and as such it concentrates on mobile and body centric antenna measurements. To do this, it examines the applicability of different measurement methodologies that can be deployed in modern antenna test ranges to accurately characterise a variety of antenna types that are used in this technology.

Chapter 12, attempts to summarise, explain and illustrate a number of advanced antenna measurement techniques, which are currently the most active topics for researchers; these are designed to

- correct systematic and random errors in measurement procedures,
- increase the range of useful information that can be extracted from antenna range measurement data,
- simplify and streamline signal and processing techniques that can be used in antenna range measurements,

- increase the range and diversity of measurements that can be accomplished in modern antenna test ranges.

The concluding chapter, Chapter 13 presents an introduction to several widely used EM simulation methods that can be used to examine, perturb, optimize and design a range of antenna measurement system. In this chapter, these techniques are introduced and their utility in the derivation or range uncertainty budgets, examination of error correction techniques and the simulation of complete measurement systems is presented and discussed.

Chapter 1 describes the most basic and fundamental reason for the requirement for antenna test ranges that revolve around the understanding of the coupling between antennas and how this varies as a function of the spatial and angular orientation of the Tx and Rx antennas. Any rigorous understanding of the spatial relationship between extended material objects in space, e.g. antennas, requires the specification of a frame of reference and an accompanying coordinate system relative to which displacements and orientations can be fixed. For this reason extensive appendices are included which detail and explain

- the coordinate systems used in antenna measurements,
- polarisation basis used in antenna measurements,
- transformation between the various coordinate systems and polarisation bases.

This description of the contents of this text concludes the introduction which sets the scene for the detailed descriptions that follow in the *Theory and Practice of Modern Antenna Range Measurements*; however, in order to understand the basic theoretical considerations that will guide the practical application of measurement techniques, it is necessary to be familiar with part of that underlying theory and address the nature of the noumena behind the phenomena of antenna coupling. To this end, Chapter 2 attempts to illustrate those areas of classical EFT that are required to fully understand and use modern antenna test ranges to their maximum utility.

References

- [1] Kant I., 'The ground of the distinction of all objects in general into phenomena and noumena' (Chapter 3), in Smith N.K. (trans.), *Critique of Pure Reason, First Division Transcendental Analytic, Book II Analytic of Principles*. Edinburgh: R R Clark; October 1929. pp. 257–76
- [2] Stein P.K., *Measurement Engineering*. 1st edn. Phoenix, AZ: Stein Engineering Services; 1969
- [3] Diez J.A., 'A hundred years of numbers: An historical introduction to measurement theory 1887–1990. Part I: The formation period. Two lines of research: Axiomatics and real morphisms, scales and invariance', *Studies in History and Philosophy of Science*. 1997;**28**(1):167–85
- [4] Nagel E., 'Measurement', *Erkenntnis*. 1931;**2**(1):313–35

- [5] SM358 Science Level 3. ‘The quantisation of energy’ (Chapter 1), in Bolton J., Lambourne R. (eds.), *The Quantum World. Book 1, Wave Mechanics*. Milton Keynes, UK: The Open University; 2007. pp. 10–20. ISBN 978-07492-2515-5
- [6] IEEE Std 145-1993. ‘IEEE standard definitions of terms for antennas’
- [7] Rudge A.W., Milne K., Olver A.D., Knight P. (eds.), *The Handbook of Antenna Design*. Vols. 1 and 2. Milton Keynes, UK: Peter Peregrinus; 1986. p. 19. ISBN 0-86341-052-9
- [8] SM358 Science Level 3. ‘The Heisenberg uncertainty principle’ (Chapter 4), in Bolton J., Lambourne R. (eds.), *The Quantum World. Book 1, Wave Mechanics*. London, UK: The Open University; 2007. pp. 117–20. ISBN 978-07492-2515-5
- [9] Dubost G., Dupuy J., ‘Effective area of an antenna’, *IEE Electronic Letters*. 1976; **12**(4):98, 99
- [10] Rudge A.W., Milne K., Olver A.D., Knight P. (eds.), *The Handbook of Antenna Design*. Vols. 1 and 2. London, UK: Peter Peregrinus; 1986. pp. 11, 12. ISBN 0-86341-052-9
- [11] Gregson S., McCormick J., Parini C.G., *Principles of Planar Near-Field Antenna Measurements* (Appendix A). London: IET; 2007. pp. 347–54. ISBN 978-86341-736-8

This page intentionally left blank

Chapter 2

EM theory and the mechanism behind antenna coupling

‘The modern view that emerged from Maxwell’s theory is a world with two layers. The first layer, the layer of fundamental constituents, consists of fields satisfying simple linear equations. The second layer, the layer of things that we can directly touch and measure, consists of mechanical stresses, energies and forces. The two layers are connected, because the quantities on the second layer are quadratic or bilinear combinations of the quantities on the first layer. To calculate the energies or the stresses, you take the square of the electric field strength or multiply one component of the field by another. The two-layer structure of the world is the basic reason why Maxwell’s theory seems so mysterious and difficult. The objects of the first layer are abstractions not directly accessible to our senses. The objects that we can feel and touch are on the second layer, and their behaviour is only determined indirectly by the equations that operate on the first layer. The two layer structure implies that the basic processes of nature are hidden from our view’.

—Freeman Dyson, Edinburgh 1999*

2.1 Maxwell’s classical electromagnetic field theory

If the basic processes of nature are hidden from our view and only the phenomena associated with these processes are accessible then an understanding of these abstract processes must be also based on abstract concepts. Arguably the most successful abstract concept devised by humanity to demystify the inaccessible hidden processes of nature has been formalised mathematical abstraction. This methodology of building a formal mathematical model of the underlying physical processes and mechanisms of nature as an aid to understanding, along with the validation of any hypothesis based on these models by the acquisition of objective factual evidence, is the basis of all physical science. Thus the empirically validated scientific models of the processes and mechanisms behind observed electromagnetic phenomena are the bedrock upon which all RF engineering is built.

*Quote reproduced with the permission of ‘The Society for Industrial and Applied Mathematics’ and the ‘James Clerk Maxwell Foundation’.

In this text, while attempting to explain the observed phenomena of antenna coupling in terms of the underlying electromagnetic mechanisms, all discussion of the electromagnetism will be confined to the classical representations of field concepts. This is usually sufficient for extended macroscopic objects like platforms, targets, transmission lines and antennas, the main categories of assets that are of concern in antenna and RF engineering. However, it should be borne in mind that all scientifically based theories have a range of applicability including classical EM theory, and although more accurate relativistic gauge theories of the EM interaction will not be addressed in this text, as antenna theory concerns the propagation of electromagnetic energy between physically remote antennas at the speed of light, it will not be possible to completely ignore the relativistic aspects of antenna theory. Thus as with any and all postulated theories developed to describe all physical phenomena, any description of the action of antennas must be consistent with the fundamental postulates of special relativity, these being:

1. The principle of relativity – ‘The laws of physics must be expressible in the same formal structure in all inertial frames of reference’.
2. The principle of constancy of the light speed – ‘... light is always propagated in empty/free space with a definite velocity [speed] c which is independent of the state of motion of the emitter or the observer’.

This will not invalidate the approach that has been adopted as the principal electromagnetic equations used, based on the seminal work of James Clerk-Maxwell, are themselves relativistically invariant in form and can be considered as the proto-type for all subsequently advanced gauge theories postulated to describe the fundamental forces encountered in nature. *Note:* These forces being variously described as the gravitational, the electromagnetic, the strong and the weak interactions.

2.2 Electric charge and EM fields

It is an empirical fact that under investigation electric charge appears to exist in two forms, usually but not exclusively referred to as positive and negative. Another empirically established fact is the conservation of electric charge. This means that electric charge can be neither created nor destroyed, thus any change in its distribution within space must involve the motion of charged particles.

This can be summed up by a continuity equation:

$$\nabla \cdot \underline{j} + \frac{\partial \rho}{\partial t} = 0 \quad (2.1)$$

where ρ is the charge density and \underline{j} is the current density.

It is the presence of, and the motion of, electric charge that is the source and cause of the interaction between charged particles that is summarised by the concept of an electromagnetic field.

An electromagnetic field can be thought of as constituting that ‘state of excitement’ induced in space by the presence of a possibly time-dependent distribution

of electric charge that has the potential to act on other charges that are present. To illustrate this concept, it is best initially to consider the field associated with a single charged particle, e.g. an electron, positron and beta particle. Such a physically small object has so little extension in space that, in the context of antenna engineering, it can be considered as a point charge.

The action on any point charge q_1 that is present at a point in space will be such that it alters, or tends to alter, the state of motion of other charged bodies distributed in the space around it. Thus the charge can be thought of as producing a force field in its proximity and any other charged objects in this field will interact with the field. *Note:* Although there is only one field, the electromagnetic field associated with charge distributions, historically it has been split into the concept of an electric and a magnetic field due to the different circumstances under which the manifestations of both are most easily observed.

When Alexandre Gustave Eiffel designed his famous tower in Paris, he decreed that the names of 72 of France's most illustrious scholars in the sciences should have their names engraved on the tower. Careful examination of the tower just below the first balcony will be rewarded by the sight of the engraved names of these 72 great sons of France. *Note:* This list of 72 notables was compiled in an age when the women of France, as with other Western countries, either by circumstance or prejudice, were all but totally excluded from the physical sciences [1]. However, amongst the notables listed on the tower can be seen the name of Charles–Augustin de Coulomb whose most important contribution to the physical sciences was his law of electrical attraction.

The electric field \underline{E} can be considered in terms of the Coulomb force law:

$$\underline{F} = \frac{q_1 q_2}{4\pi R^2} \underline{R} \quad (2.2)$$

where \underline{F} is the force that acts on q_1 , by definition equal and opposite to that which acts on q_2 , R is the distance between charges q_1 and q_2 , \underline{R} is the unit displacement vector in the direction defining the displacement between q_1 and q_2 , and q_1 and q_2 are two distinct point-like distributions of charge.

Thus

$$\underline{F} = q_1 \underline{E} \quad (2.3)$$

where \underline{E} is defined as

$$\underline{E} = \frac{q_2}{4\pi R^2} \underline{R} \quad (2.4)$$

As a direct result of the principle of relativity and the equivalence of inertial reference frames, all states of transitional equilibrium are equivalent. Therefore, it must be possible to define the force that acts on the test charge even if it is initially in a state of uniform motion, as opposed to being stationary, in a similar fashion.

However, although a distribution of separate charges may be individually in translational equilibrium, they may be in motion relative to each other and therefore there will be no inertial frame relative to which all of the charges constituting the

distribution are stationary. To take account of this relative motion, a second vector \underline{B} is defined which relates the force that acts on the test charge in the presence of fields at the points in space the charge instantaneously occupies when it is in motion.

From experiment, it is found that these fields apply a force \underline{F} on the charge q moving with velocity \underline{v} which is given by the Lorentz force law as

$$\underline{F} = q(\underline{E} + \underline{v} \times \underline{B}) \quad (2.5)$$

Clearly as $\underline{v} \rightarrow 0$ the Lorentz force law tends to the Coulombic formulation and additionally the vectors \underline{E} and \underline{B} will vary as a function of the inertial state of any observer. However, a range of Lorentz invariant parameters, e.g. the inner product of \underline{E} and \underline{H} , can be defined which allow transformations of the \underline{E} and \underline{B} fields between inertial reference frames. This allows the Lorentz force law to be considered a fundamental law of physics and to act as the definition of the vector quantities \underline{E} and \underline{B} .

Up to this point the field produced by the presence of, and the motion of, electric charge has been described in terms of the physically observable manifestations of the force(s) that it can exert on other charged particles. Although this is of interest in many areas of electronics and electromagnetics, it is in the ability to couple remote electronic systems that are of interest with respect to antennas, i.e. field as a source of electromotive force or EMF.

E field has been defined in terms of the force that is exerted on charged particle from (2.4) as

$$\underline{F} = q_2 \underline{E} \therefore \frac{\underline{F}}{q_2} = \underline{E} \quad (2.6)$$

From this it is clear that the units of the E field are newtons/coulomb, i.e. N/c . A volt is defined as joule/coulomb, i.e. J/c therefore $J = Vc$. Also the energy transferred to an object by a force equals the scalar product of the force and the displacement, therefore in free space $J = Nm$.

Thus

$$Nm = Vc \therefore \frac{N}{c} = \frac{V}{m} \quad (2.7)$$

Therefore for any extended object in the field, the force acting on the individual particles within the object will induce a voltage across the object and this is the source of the currents and voltages induced in remote systems. This is the physical mechanism whereby, if correctly stimulated, physically remote electrical systems can interact and produce the transfer of energy and momentum required to induce voltages and currents. *Note:* The principle of the conservation of energy requires that if voltages and currents are induced in and across a remote object/system, since a volt is a joule per coulomb, energy must be transferred from the Tx to the Rx system. So, as will be examined in Section 2.3, there must be a power flux between the Tx system and the Rx system.

The effects that will be induced in the extended objects are a function of its material constitution, size and shape, etc., but the extent of the field impinging on the object will be a function only of its remoteness from the source (which relates to the power of the source excitation) and its spatial orientation relative to the source (which relates to the pattern and polarisation of the source), the very parameters that antenna test ranges are designed to characterise.

At this point the second principle/postulate of relativity theory, the principle of the constancy of the speed of light, can be seen to impact on the predictions of EM theory as, although this speed is very high, it is not infinite, i.e. 299,792,458 m/s. Thus, at any point in time the field produced at another point in space remote from the charge distribution, which is its source, is not equal to the field that would be produced by the source charge distribution at that instant in time. This is because a certain period of time must pass before any change in the field can propagate any finite distance.

Since time elapsed is equal to distance divided by speed, it is in fact the field that would be created by the charge distribution in a period of time equal to the magnitude of the displacement of the test charge from the source divided by the speed of light.

If the point charge is moving as per the curved path in Figure 2.1, the field experienced at point P at time t when the point charge is at point B is the field that was produced at A. The field at point P at time t is determined by the position of the potential source at position A at the earlier time of $t - \tau$ where the displacement $s = c\tau = [\mathbf{r} - \mathbf{r}'(t - \tau)]$, and B is the position of the source at time t .

Thus, at any instant of time the field at a point in space mirrors the charge distribution that was present at a time in the past equal to the magnitude of the displacement from the source divided by the speed of light. This in turn means that the effect of any change in the charge distribution will take a finite amount of time to act on the test charge. Therefore any change in the field will be retarded by a period of time directly proportional to the magnitude of the displacement of the test charge from the source. The concept that the finite velocity of propagation retards the effects of the variation of any field source across space is crucial to the development of classical electromagnetic field theory.

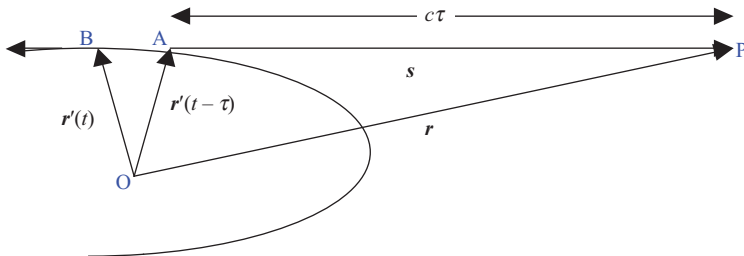


Figure 2.1 Finite temporal displacement of field due to motion of the source

2.3 Power flux in an EM field

The concept of the field at any point in space relative to the position of a moving charged particle representing the retarded field is fundamental to the classical explanation and, as will be developed in Sections 2.4 and 2.5, to why such accelerated charged particles emit radiation at all. The normal explanation of this radiation follows from Maxwell's equations through the use of retarded potentials for the field components at large distances from any source. A detailed exposition of this mechanism can be found in the authors previous text [2], and in a range of other standard texts [3,4], dedicated to the explanation of EM concepts and a detailed example is included in Box 2.2 in later sections of this chapter.

However, prior to this detailed discussion, considerable insight into the mechanisms by which such moving charged particles interact can be found in an explanation for this radiation first put forward by Noble Laureate J.J. Thomson [5]. This explanation is particularly informative as it indicates why an accelerated charge radiates, why there is an angular pattern related to this radiation and why this radiation has polarisation properties.

If we consider a positive charge stationary at the origin of a frame of reference O , at a time $t = 0$, that subsequently is subject to a small acceleration to velocity Δv (where $\Delta v \ll c$ so that the field lines still essentially describe a spherical field), in a small interval of time Δt , this can be visualised as per Figures 2.2 and 2.3.

In Figure 2.2 the charge is at point O at time $t = 0$, and field lines that actually spread out in a spherical distribution are shown merely in the plane of the page. This arrangement of field lines shows the charged particle prior to any acceleration. If the particle is subsequently accelerated to Δv after a period of time t , we can

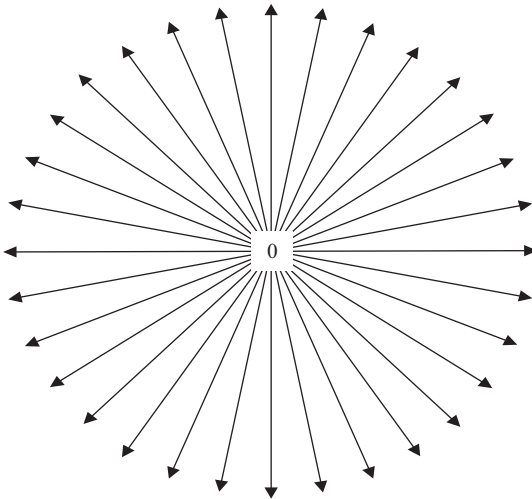


Figure 2.2 Field lines of positive charge placed at O , the origin of a frame of reference at time $t = 0$

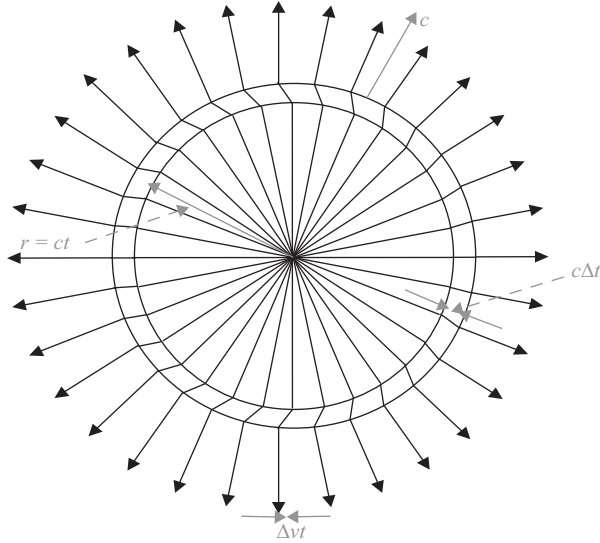


Figure 2.3 Field lines associated with a positive charge accelerated to position Δvt at time t

identify two regions of field inside and outside a sphere of radius ct . Outside of the sphere the field lines are still centred on O as, due to the finite speed of light, the field lines do not know that the source, the charged particle, has moved. Inside this sphere, at time t , the field lines are radial to the frame of reference of the moving charge and between these two regions there is a thin shell of thickness $c\Delta t$ in which the corresponding field lines join. See Figure 2.3.

Clearly within the small shell there is a region where the field lines have a component in the circumferential direction, as per Figure 2.4 in the i_θ direction. As we shall see, this sphere of field with a circumferential component can be thought of as a pulse of electromagnetic field propagating away from the source at the speed of light and thus, as we shall also see, by virtue of the charge being accelerated there is an energy loss associated with this pulse which is propagated out from the charge.

To understand why this is so, it is necessary to examine the nature of this small shell in more detail. Figure 2.4 shows the details of a small cone of field lines at an angle θ with respect to the acceleration vector of the source at time t .

The strength of the E_θ component of the field is related to the number of field lines per unit area which, from the geometry of the figure, is proportional to relative sizes of the approximate rectangle ABCD.

Thus

$$\frac{E_\theta}{E_r} = \frac{\Delta vt \sin \theta}{c\Delta t} \tag{2.8}$$

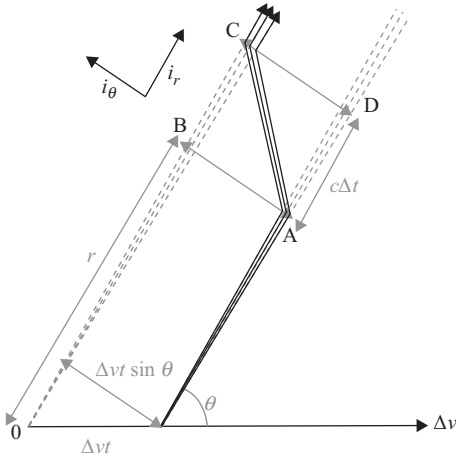


Figure 2.4 The circumferential component of the E field in the shell of thickness $c\Delta t$ at displacement r from position of the charge at time t

but

$$E_r = \frac{q}{4\pi\epsilon_0 r^2} \quad \text{where } r = ct \tag{2.9}$$

therefore

$$E_\theta = \frac{q(\Delta v/\Delta t) \sin \theta}{4\pi\epsilon_0 c^2 r} \tag{2.10}$$

However, $\Delta v/\Delta t$ is the acceleration of the source a , giving

$$E_\theta = \frac{qa \sin \theta}{4\pi\epsilon_0 c^2 r} \tag{2.11}$$

It is worth noticing at this point that the radial component of the field $E_r \propto 1/r^2$, while the field associated with the pulse falls off more slowly, i.e. $E_\theta \propto 1/r$.

For any pulse of EM radiation, the flow or energy flux per unit area per unit time is given by the Poynting vector [6], where $\underline{S} = \underline{E} \times \underline{H}$, which in terms of the magnitude of this power flux in free space is equal to $1/Z_0 E^2$, where $Z_0 = (\mu_0/\epsilon_0)^{1/2}$.

Thus the rate of loss of energy through a solid angle $d\Omega$ at distance r from the source is

$$-\left(\frac{d}{dt}(\text{energy})\right)_{rad,d\Omega} = \frac{Z_0 q^2 a^2 \sin^2 \theta}{16\pi^2 \epsilon_0^2 c^4 r^2} r^2 d\Omega \tag{2.12}$$

From the relationship between c with ε_0 and μ_0 along with cancelling the r terms, this can be simplified to

$$-\left(\frac{d}{dt}(\text{energy})\right)_{rad,d\Omega} = \frac{q^2 a^2 \sin^2 \theta}{16\pi^2 \varepsilon_0 c^3} d\Omega \quad (2.13)$$

To find the total radiation rate, this must be integrated over all solid angles, i.e. with respect to $2\pi \sin \theta d\theta$, giving

$$-\left(\frac{d}{dt}(\text{energy})\right)_{rad} = \int_0^\pi \frac{q^2 a^2 \sin^2 \theta}{16\pi^2 \varepsilon_0 c^3} 2\pi \sin \theta d\theta \quad (2.14)$$

This can be integrated to give

$$-\left(\frac{d}{dt}(\text{energy})\right)_{rad} = \frac{q^2 a^2}{6\pi \varepsilon_0 c^3} \quad (2.15)$$

This is exactly the same result, known as the Larmor equation [7], that can be obtained via the full theory working directly from Maxwell's equations. This simple model of the radiative process, illustrated in the above calculations and figures, highlights the three main areas of radiative emission that are invariably required to be estimated for more complicated sources, e.g. antennas, via a free-space EM measurements:

1. The power that is emitted, as given per (2.13) and (2.15), is as a result of an excitation that accelerates the charge.
2. The dependence of the rate of emission of radiation on the angle θ , i.e. the pattern, in this simple case is of a dipole form where $E_\theta \propto \sin \theta$ and thus there is no tangential field component and therefore no emission along the direction of the acceleration vector and the radiation is at a maximum perpendicular to this vector, as per Figure 2.3.
3. The polarisation of the radiation, i.e. the direction of the electric field vector, is parallel to the acceleration as projected onto the spherical surface at distance r again as per Figures 2.2–2.4.

The above argument, although simplified and also ignoring second-order effects like aberration, illustrates many of the facets of the actual mechanism of radiation from sources such as charged particles. *Note:* If the acceleration produced a velocity that was not very much smaller than c , many of these conclusions would be invalid.

Box 2.1

It is perhaps worth noting that this explanation as originally advanced formed part of the work for which J.J. Thomson was awarded the Nobel Prize for his

work on the conduction of electricity by gases in which he identified the electron as a classical particle in 1906. Later his son G.T. Thomson was also awarded the Nobel Prize in 1937 for his work on the wave mechanics of electron diffraction. Thus, over the course of one generation the Thomson family was awarded the Nobel Prize twice, essentially for proving that the electron was a classical particle and then for proving that it was not. Such are the vagaries of all concepts developed to describe the underlying noumena/mechanism of observable phenomena and certainly must have made conversation at the diner table in the Thomson household interesting.

2.4 Maxwell's equations

Although the later years of Oliver Heaviside's life were characterised by a descent from more or less eccentric behaviour into a pronounced pathology related to his mental health, there is little evidence to suggest that the quality of his research was degraded [8]. This is a question that can never truly be answered as the theft shortly after his death of the manuscript of his 'electromagnetic theory' means that the insights into electromagnetics of his later life have never been reported. However, the monumental work that he did in translating the 20 equations of Maxwell's original theory into the now more familiar form of four partial differential vector equations has formed the basis of almost all classical electromagnetics-based engineering for more than a hundred years. These equations essentially relate the rates of change of the vector fields with respect to time and to the spatial sense of the fields both tangential to and at a normal to the direction of the fields, as such they encapsulate all the relations between the vector fields.

Classically, the relationships between the components of any electromagnetic field are described by Maxwell's field equations and by the equations representing the properties of the medium in which that field exists. Maxwell's equations can be written in differential form as

$$\nabla \cdot \underline{D} = \rho \quad (2.16)$$

$$\nabla \cdot \underline{B} = 0 \quad (2.17)$$

$$\nabla \times \underline{E} = -\frac{\partial \underline{B}}{\partial t} \quad (2.18)$$

$$\nabla \times \underline{H} = \underline{J} + \frac{\partial \underline{D}}{\partial t} \quad (2.19)$$

The definitions and units of these quantities are as follows:

E = Electric field intensity

H = Magnetic field intensity

J = Current density

ρ = Charge density

D = Electric flux density

B = Magnetic flux density

Since only alternating, sinusoidal, time-harmonic quantities are to be considered, the time dependency of the complex representations of the electromagnetic field vectors can be taken to be of the form $e^{j\omega t}$, where to six decimal places $e = 2.718282$ and $j = \sqrt{-1}$ is the imaginary unit. Here, $\omega = 2\pi f$ is the angular frequency and f represents the temporal frequency measured in hertz. This complex exponential form of spatial and time variation of the fields is used for convenience where it is understood that the actual field quantities are obtained by taking the real part of the complex quantity, i.e.

$$E = |E_0|\cos(\omega t + \phi) = \text{Re}\{E_0 e^{j\omega t}\} \quad (2.20)$$

$$H = |H_0|\cos(\omega t + \phi) = \text{Re}\{H_0 e^{j\omega t}\} \quad (2.21)$$

Where ϕ is the phase angle of E_0 .

When using this notation the time factor is usually suppressed, i.e. the complex exponentials are cancelled on either side of the relevant expressions, and this convention is adopted throughout. Although it is conventional in electromagnetism and optics to adopt a positive time dependence, in the study of quantum mechanics and solid-state physics, the opposite time dependence is more often adopted. Clearly, as the electromagnetic field vectors are of the form $e^{j\omega t}$, the following operator substitution can be utilised:

$$D^n = \frac{\partial^n}{\partial t^n} \equiv (j\omega)^n \quad (2.22)$$

This simply states that differentiating electromagnetic field vectors with respect to time is equivalent to multiplying the field vectors by the imaginary unit and the angular velocity of the field which is assumed to be fluctuating in a sinusoidal fashion.

Crucially, the simplification afforded by restricting ourselves to considering purely monochromatic waveforms in no way restricts the analysis since any angular frequency may be considered to be a component of a Fourier series, or in the limit a Fourier integral, thus enabling this analysis to be applied to arbitrary waveforms.

Some of the field components contained within Maxwell's equations can be related to one another through the properties of the medium in which the fields exist:

$$\underline{B} = \mu \underline{H} \quad (2.23)$$

$$\underline{D} = \varepsilon \underline{E} \quad (2.24)$$

$$\underline{J} = \sigma \underline{E} \quad (2.25)$$

Here, μ is the magnetic permeability of the medium, ε is the permittivity of the medium, i.e. the dielectric constant, and σ is the specific conductivity. In general, ε and μ are complex tensors that are functions of field intensity; however, for the case of free-space antenna problems they can usually be approximated by real constants. A vacuum, in classical electromagnetic field theory, can be taken to consist of a

source and sink-free, simple linear homogeneous and isotropic free space region of space in which harmonic time varying fields are measured. In such an environment no charges are present, the current density will necessarily be zero and the resistance of the medium is infinite, i.e. zero conductivity, thus $\rho = 0$, $\underline{J} = 0$ and $\sigma = 0$. In this case, Maxwell's simultaneous differential equations reduce to two homogeneous, i.e. equated to zero, and two non-homogeneous expressions, namely

$$\begin{aligned}\nabla \cdot \underline{E} &= 0 \\ \nabla \cdot \underline{H} &= 0\end{aligned}\tag{2.26}$$

$$\nabla \times \underline{E} = -j\omega\mu\underline{H}\tag{2.27}$$

$$\nabla \times \underline{H} = j\omega\varepsilon\underline{E}\tag{2.28}$$

Eliminating the magnetic field intensity from these equations yields

$$\nabla \times \nabla \times \underline{E} = -j\omega\mu(\nabla \times \underline{H}) = \omega^2\mu\varepsilon\underline{E}\tag{2.29}$$

Thus the most general solution of Maxwell's equations in terms of the material constants and the angular frequency of the electromagnetic radiation is

$$\nabla \times \nabla \times \underline{E} - \omega^2\mu\varepsilon\underline{E} = 0\tag{2.30}$$

Similarly, eliminating the electric field intensity, the magnetic field can be expressed as

$$\nabla \times \nabla \times \underline{H} - \omega^2\mu\varepsilon\underline{H} = 0\tag{2.31}$$

These expressions are often referred to as *complex vector wave equations*, which constitute the most general forms of the wave equation. These wave equations are usually expressed in a simpler form that is particularly convenient for problems involving rectilinear Cartesian coordinate systems. Using the vector identity

$$\nabla^2 \underline{A} = \nabla(\nabla \cdot \underline{A}) - \nabla \times \nabla \times \underline{A}\tag{2.32}$$

and recalling that $\nabla \cdot \underline{E} = 0$ then

$$\nabla(\nabla \cdot \underline{E}) = \nabla(0) = 0\tag{2.33}$$

Thus the complex vector wave equation can be rewritten as

$$\nabla^2 \underline{E} + \omega^2\mu\varepsilon\underline{E} = 0\tag{2.34}$$

This is known as the vector Helmholtz equation. It is important to be aware that a solution of the homogeneous vector Helmholtz equation is not necessarily a solution of the homogeneous Maxwell's equations. Therefore, the electric field must fulfill the vector Helmholtz equation and in addition the divergence condition, cf. [9]. Similarly, as $\nabla \cdot \underline{H} = 0$ the magnetic field can be expressed as

$$\nabla^2 \underline{H} + \omega^2\mu\varepsilon\underline{H} = 0\tag{2.35}$$

The vector operator substitution used to obtain the Helmholtz equation from the general wave equation implies that we need to know how to evaluate the Laplacian of a vector in a given coordinate system. Fortunately, we do know how to perform this in Cartesian, cylindrical and spherical coordinates, although the effort required is greater for the cylindrical and spherical cases. In general, the one-dimensional transverse wave equation can be expressed as

$$\frac{\partial^2 u(x, t)}{\partial x^2} - \frac{1}{c^2} \frac{\partial^2 u(x, t)}{\partial t^2} = 0 \quad (2.36)$$

where c is taken to denote the velocity of the wave. Assuming again that the wave is sinusoidal in form this can be expressed as

$$\frac{d^2 u(x)}{dx^2} + \frac{\omega^2}{c^2} u(x) = 0 \quad (2.37)$$

Through a comparison with the Helmholtz equation, we find that the phase velocity c of the electromagnetic wave can be expressed in terms of the properties of the medium through which the wave is propagating as

$$c = \frac{1}{\sqrt{\mu\epsilon}} = f\lambda \quad (2.38)$$

where f is the frequency in hertz, λ is the wavelength in meters and c is the velocity in meters per second. Here the radical, or root, is assumed positive. For convenience, a positive constant k is defined as

$$k = \omega\sqrt{\mu\epsilon} \quad (2.39)$$

Clearly then the constant k , often termed the wave number or propagation constant, is simply related to the wavelength as

$$k = 2\pi f\sqrt{\mu\epsilon} = \frac{2\pi}{\lambda} \quad (2.40)$$

Thus the Maxwell equations can be transformed into the following vector Helmholtz, or wave, equations:

$$\nabla^2 \underline{E} + k_0^2 \underline{E} = 0 \quad (2.41)$$

$$\nabla^2 \underline{H} + k_0^2 \underline{H} = 0 \quad (2.42)$$

The velocity of an electromagnetic wave is unambiguous when considering simple solutions, i.e. plane waves. However, as the wave equation also admits solutions representing standing waves, the concept of a velocity of an electromagnetic wave can become a little ambiguous.

When assuming a Cartesian coordinate system, the electric field may be expressed as

$$\underline{E}(x, y, z) = \underline{\hat{e}}_x E_x(x, y, z) + \underline{\hat{e}}_y E_y(x, y, z) + \underline{\hat{e}}_z E_z(x, y, z) \quad (2.43)$$

The Laplacian operator ∇^2 when expressed in Cartesian coordinates can be obtained from:

$$\begin{aligned} \nabla^2 &= \nabla \cdot \nabla \\ &= \left(\frac{\partial}{\partial x} \underline{\hat{e}}_x + \frac{\partial}{\partial y} \underline{\hat{e}}_y + \frac{\partial}{\partial z} \underline{\hat{e}}_z \right) \cdot \left(\frac{\partial}{\partial x} \underline{\hat{e}}_x + \frac{\partial}{\partial y} \underline{\hat{e}}_y + \frac{\partial}{\partial z} \underline{\hat{e}}_z \right) \\ &= \frac{\partial^2}{\partial x^2} + \frac{\partial^2}{\partial y^2} + \frac{\partial^2}{\partial z^2} \end{aligned} \quad (2.44)$$

Hence we may separate the field components and write the vector Helmholtz equation as three equivalent uncoupled scalar Helmholtz equations:

$$\left[\frac{\partial^2 E_x(x, y, z)}{\partial x^2} + \frac{\partial^2 E_x(x, y, z)}{\partial y^2} + \frac{\partial^2 E_x(x, y, z)}{\partial z^2} + k_0^2 E_x(x, y, z) \right] \underline{\hat{e}}_x = 0 \quad (2.45)$$

$$\left[\frac{\partial^2 E_y(x, y, z)}{\partial x^2} + \frac{\partial^2 E_y(x, y, z)}{\partial y^2} + \frac{\partial^2 E_y(x, y, z)}{\partial z^2} + k_0^2 E_y(x, y, z) \right] \underline{\hat{e}}_y = 0 \quad (2.46)$$

$$\left[\frac{\partial^2 E_z(x, y, z)}{\partial x^2} + \frac{\partial^2 E_z(x, y, z)}{\partial y^2} + \frac{\partial^2 E_z(x, y, z)}{\partial z^2} + k_0^2 E_z(x, y, z) \right] \underline{\hat{e}}_z = 0 \quad (2.47)$$

Similar expressions also hold for $H_x(x, y, z)$, $H_y(x, y, z)$ and $H_z(x, y, z)$. Therefore all of the components of the electromagnetic field obey the scalar differential wave (Helmholtz) equation.

$$\frac{\partial^2 u(x, y, z)}{\partial x^2} + \frac{\partial^2 u(x, y, z)}{\partial y^2} + \frac{\partial^2 u(x, y, z)}{\partial z^2} + k_0^2 u(x, y, z) = 0 \quad (2.48)$$

This can readily be expressed in a more compact form as

$$\nabla^2 u + k_0^2 u = 0 \quad (2.49)$$

This differential equation can be solved by direct integration using Green's theorem to yield the Kirchhoff integral theorem.

However, a methodology that will be instructive and gives insight into the nature of the electromagnetic interaction that is often successfully adopted to evaluate the electromagnetic fields produced and subsequently radiated by moving charges is to consider the fields \underline{E} and \underline{B} to be the resultants of potentials.

2.5 The electric and magnetic potentials

Since its initial formulation in the nineteenth century, it has been widely accepted that the behaviour of the classically described forces of nature could be modelled

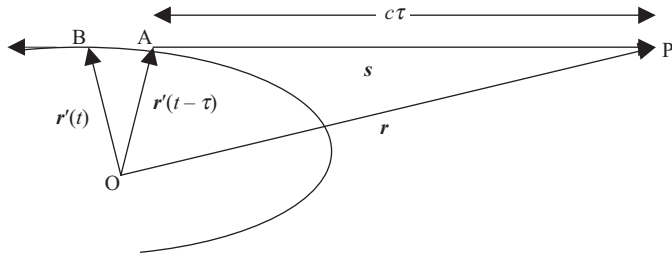


Figure 2.5 Figure showing potential at time t from point charge moving from A to B

using potentials which satisfy the Laplace equation [10]; thus it is possible to formulate electromagnetic field theory in terms of such potentials.

2.5.1 Static potentials

The electric potential ϕ is a scalar potential that is a function of position and time defined by

$$\phi(\underline{r}, t) = \frac{1}{4\pi\epsilon_0} \int \frac{\rho(\underline{r}', t)}{|\underline{r} - \underline{r}'|} dV \quad (2.50)$$

where \underline{r} is the point at which the potential is being evaluated and \underline{r}' is location of the charge density element, and the static electric field is given by

$$\underline{E} = -\nabla\phi \quad (2.51)$$

Alternatively the magnetic potential \underline{A} is defined as being a vector given by

$$\underline{A}(\underline{r}, t) = \frac{\mu}{4\pi} \int \frac{\underline{J}(\underline{r}', t)}{|\underline{r} - \underline{r}'|} dV \quad (2.52)$$

and the static magnetic field is given by

$$\underline{B} = \nabla \times \underline{A} \quad (2.53)$$

Equations (2.50) and (2.52) for the potentials give the static electric and magnetic fields; however, as explained in Section 2.2, at any point that is spatially separated from the source of the potential, i.e. the source, a finite amount of time must pass before the influence of the source can affect the potential.

2.5.2 Retarded potentials

Figure 2.1 repeated below as Figure 2.5 illustrates that, as well as the field, the potential at point P at time t is determined by the position of the potential source at position A at the earlier time of $t - \tau$ where the distance $s = c\tau = [r - r'(t - \tau)]$, and B is the position of the source at time t .

Thus, for a distributed charge of density ρ , the potential at position \underline{r} and time t due to the charge in the vicinity of \underline{r}' depends on the value of ρ at the previous time $t - [r - r']/c$; therefore the potential of the entire charge is

$$\phi(\underline{r}, t) = \frac{1}{4\pi\epsilon_0} \int \frac{\rho(\underline{r}', t - |\underline{r} - \underline{r}'|/c)}{|\underline{r} - \underline{r}'|} dV \quad (2.54)$$

This formula for the potential that is calculated to take account of the finite speed of light is referred to as the retarded scalar potential and a similar argument can be followed to establish a retarded vector potential.

$$\underline{A}(\underline{r}, t) = \frac{\mu}{4\pi} \int \frac{\underline{J}(\underline{r}', t - |\underline{r} - \underline{r}'|/c)}{|\underline{r} - \underline{r}'|} dV \quad (2.55)$$

Therefore (2.51) does not apply for time-dependent systems and must be modified to take account of the finite but constant speed of light to be

$$\underline{E} = -\nabla\phi - \frac{\partial \underline{A}}{\partial t} \quad (2.56)$$

Since the curl of any grad $\equiv 0$, this satisfies Maxwell's third equation as

$$\nabla \times \underline{E} = -\nabla \times (\nabla\phi) - \frac{\partial}{\partial t}(\nabla \times \underline{A}) \quad (2.57)$$

$$\nabla \times \underline{E} = -\frac{\partial}{\partial t}(\nabla \times \underline{A}) = -\frac{\partial \underline{B}}{\partial t} \quad (2.58)$$

which is in agreement with (2.18). Additionally, (2.53) is still correct for time-dependent systems as the div of any curl $\equiv 0$

$$\nabla \cdot (\nabla \times \underline{A}) = \nabla \cdot \underline{B} = 0 \quad (2.59)$$

and from (2.16)

$$\epsilon^{-1} \nabla \cdot \underline{D} = -\nabla^2 \phi - \frac{\partial}{\partial t}(\nabla \cdot \underline{A}) = \epsilon^{-1} \rho \quad (2.60)$$

If $1/v^2 \cdot \partial^2 \phi / \partial t^2$ is inserted into (2.60), where v is the propagation velocity

$$-\nabla^2 \phi - \frac{\partial}{\partial t}(\nabla \cdot \underline{A}) + \frac{1}{v^2} \frac{\partial^2 \phi}{\partial t^2} = \frac{\rho}{\epsilon} + \frac{1}{v^2} \frac{\partial^2 \phi}{\partial t^2} \quad (2.61)$$

which is rearranged to give

$$\nabla^2 \phi - \frac{1}{v^2} \frac{\partial^2 \phi}{\partial t^2} = -\frac{\rho}{\epsilon} - \frac{1}{v^2} \frac{\partial^2 \phi}{\partial t^2} - \frac{\partial}{\partial t}(\nabla \cdot \underline{A}) \quad (2.62)$$

This can be simplified to give

$$\nabla^2 \phi - \frac{1}{v^2} \frac{\partial^2 \phi}{\partial t^2} = -\frac{\rho}{\varepsilon} - \frac{\partial \underline{F}}{\partial t} \quad (2.63)$$

where

$$\underline{F} = \nabla \cdot \underline{A} + \frac{1}{v^2} \frac{\partial \phi}{\partial t} \quad (2.64)$$

By substitution into (2.19) in a similar fashion, it can be shown that

$$\nabla^2 \underline{A} - \frac{1}{v^2} \frac{\partial^2 \underline{A}}{\partial t^2} = -\mu \underline{J} + \nabla \cdot \underline{F} \quad (2.65)$$

Both of these equations can be simplified if we make

$$\underline{F} = \nabla \cdot \underline{A} + \frac{1}{v^2} \frac{\partial \phi}{\partial t} = 0 \quad (2.66)$$

Equations (2.63) and (2.65) then become

$$\nabla^2 \phi - \frac{1}{v^2} \frac{\partial^2 \phi}{\partial t^2} = -\frac{\rho}{\varepsilon} \quad (2.67)$$

$$\nabla^2 \underline{A} - \frac{1}{v^2} \frac{\partial^2 \underline{A}}{\partial t^2} = -\mu \underline{J} \quad (2.68)$$

Clearly if the condition set out in (2.66), where $F = 0$, is met then (2.67) and (2.68) are decoupled in that (2.67) now defines ϕ in terms of charge density without reference to current density and (2.68) does likewise for \underline{A} and current density. The condition that $F = 0$, referred to as the Lorentz condition, can in fact always be satisfied due to the nature of the definitions of ϕ and \underline{A} .

If \underline{A} is transformed to \underline{A}'

$$\underline{A} \rightarrow \underline{A}' = \underline{A} + \nabla \chi \quad (2.69)$$

and

$$\phi \rightarrow \phi' = \phi + \frac{\partial \chi}{\partial t} \quad (2.70)$$

where χ is a function of position and time.

Since

$$\underline{E}' = \underline{E} + \nabla \frac{\partial \chi}{\partial t} - \frac{\partial}{\partial t} \nabla \chi = \underline{E} \quad (2.71)$$

and

$$\underline{B}' = \underline{B} + \nabla \times (\nabla \chi) = \underline{B} \quad (2.72)$$

the use of either ϕ or ϕ' , or \underline{A} or \underline{A}' is arbitrary as \underline{E} and \underline{B} will remain unchanged. Transformations such as (2.69) and (2.70) are referred to as gauge transformations and potentials that satisfy the Lorentz condition are said to belong to the Lorentz gauge.

The retarded potentials (2.54) and (2.55) are solutions of the decoupled (2.67) and (2.68) in combination with the Lorentz condition; therefore they provide a consistent method for the solution of Maxwell's equations. They allow the sources ρ and \underline{j} to be the inputs that can be used to calculate ϕ and \underline{A} , which in turn allows the calculation of \underline{E} and \underline{B} . This may appear to be a long and convoluted methodology for the calculation of fields from their charge and current density sources, but it is usually a much easier process than attempting to evaluate \underline{E} and \underline{B} directly from Maxwell's equations. As an example, the full derivation of the Larmor equation, (2.15) in the text, is included in Box 2.2 for those with an interest in examining the nature and extent of the stages of the complete solution to the power emitted by a moving charge.

Box 2.2

The charge and current densities of a moving point charge are singular and described by

$$\rho(\underline{r}, t) = q\delta[\underline{r} - \underline{r}_p(t)] \quad (\text{B2.1})$$

$$\underline{J}(\underline{r}, t) = q\underline{v}(t)\delta[\underline{r} - \underline{r}_p(t)] \quad (\text{B2.2})$$

where q is the charge, $\underline{r}_p(t)$ is the instantaneous location of the charge and $\underline{v}(t) = d\underline{r}_p(t)/dt$.

Using the Green's function for any arbitrary wave equation

$$G(\underline{r} - \underline{r}', t - t') = \frac{1}{4\pi|\underline{r} - \underline{r}'|} \partial \left(t - t' - \frac{|\underline{r} - \underline{r}'|}{c} \right) \quad (\text{B2.3})$$

and (2.67) and (2.68) from the main text shown below as (B2.4) and (B2.5):

$$\nabla^2 \phi - \frac{1}{v^2} \frac{\partial^2 \phi}{\partial t^2} = -\frac{\rho}{\epsilon} \quad (\text{B2.4})$$

and

$$\nabla^2 \underline{A} - \frac{1}{v^2} \frac{\partial^2 \underline{A}}{\partial t^2} = -\mu \underline{J} \quad (\text{B2.5})$$

solutions of the form

$$\phi(\underline{r}, t) = \frac{q}{4\pi\epsilon_0} \int dV' \int dt' \frac{1}{|\underline{r} - \underline{r}'|} \partial[\underline{r}' - \underline{r}_p(t')] \partial[f(t')] \quad (\text{B2.6})$$

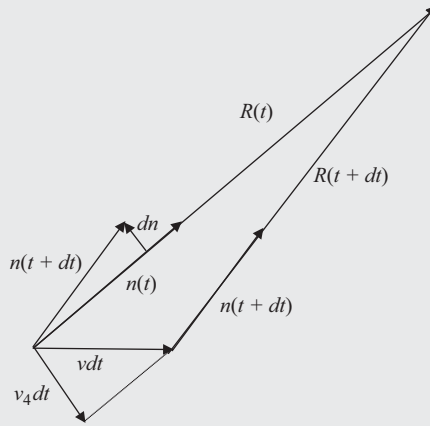


Figure B2.1 The change in the unit vector \hat{n} caused by the velocity \underline{v}

and

$$\underline{A}(\underline{r}, t) = \frac{\mu_0 q}{4\pi\epsilon_0} \int dV' \int dt' \frac{\underline{v}(t')}{|\underline{r} - \underline{r}'|} \partial[\underline{r}' - \underline{r}_p(t')] \partial[f(t')] \quad (\text{B2.7})$$

can be advanced where

$$f(t') = t' - t + \frac{\underline{r} - \underline{r}'}{c} \quad (\text{B2.8})$$

Carrying out the volume integrals gives

$$\phi(\underline{r}, t) = \frac{q}{4\pi\epsilon_0} \int \frac{1}{|\underline{r} - \underline{r}_p'|} \partial[f(t')] dt' \quad (\text{B2.9})$$

and

$$\underline{A}(\underline{r}, t) = \frac{\mu_0 q}{4\pi\epsilon_0} \int \frac{\underline{v}(t')}{|\underline{r} - \underline{r}_p'|} \partial[f(t')] dt' \quad (\text{B2.10})$$

where more explicitly for this case

$$f(t') = t' - t + \frac{\underline{r} - \underline{r}_p(t)}{c} \quad (\text{B2.11})$$

As for any such integrals the delta function can be simplified as:

$$\int g(t') \partial[f(t')] dt' = \int g(t') [f(t')] \frac{1}{\left| \frac{df(t')}{dt'} \right|} df = \left| \frac{g(t')}{\left| \frac{df}{dt'} \right|} \right|_{f=0} \quad (\text{B2.12})$$

where t' is now understood as a solution for t' satisfying $f(t') = 0$.

This is in general an implicit equation for t' , giving the time derivative of $f(t')$ as

$$\frac{df}{dt'} = 1 - \frac{\hat{n}(t') \cdot \underline{v}_p(t')}{c} = 1 - \hat{n}(t') \cdot \underline{\beta}(t') \quad (\text{B2.13})$$

where $\hat{n}(t')$ is a unit vector along the relative distance $\underline{r} - \underline{r}_p(t')$, i.e.

$$\hat{n}(t') = \frac{\underline{r} - \underline{r}_p(t')}{|\underline{r} - \underline{r}_p(t')|} \quad (\text{B2.14})$$

and

$$\underline{\beta} = \frac{\underline{v}}{c} \quad (\text{B2.15})$$

The observing time t and the time t' are related by

$$\left[1 - \hat{n}(t') \cdot \underline{\beta}(t')\right] dt' = dt \quad \text{or} \quad \frac{dt}{dt'} = 1 - \hat{n}(t') \cdot \underline{\beta}(t') \quad (\text{B2.16})$$

Therefore, after performing the time integration

$$\phi(\underline{r}, t) = \frac{q}{4\pi\epsilon_0} \cdot \frac{1}{1 - \hat{n}(t') \cdot \underline{\beta}(t')} \cdot \frac{1}{|\underline{r} - \underline{r}_p(t')|} = \frac{q}{4\pi\epsilon_0} \cdot \frac{1}{k(t') |\underline{r} - \underline{r}_p(t')|} \quad (\text{B2.17})$$

and

$$\underline{A}(\underline{r}, t) = \frac{\mu_0 q}{4\pi} \cdot \frac{1}{1 - \hat{n}(t') \cdot \underline{\beta}(t')} \cdot \frac{\underline{v}(t')}{|\underline{r} - \underline{r}_p(t')|} = \frac{q}{4\pi\epsilon_0} \cdot \frac{\underline{v}(t')}{k(t') |\underline{r} - \underline{r}_p(t')|} \quad (\text{B2.18})$$

where this gives

$$k(t') = 1 - \hat{n}(t') \cdot \underline{\beta}(t') \quad (\text{B2.19})$$

These are the Liénard–Wiechert potentials as formulated originally in 1898* using these the field can be calculated from (2.56) in the main text, shown below as (B2.20) explicitly for \underline{r} and t

$$\underline{E}(\underline{r}, t) = -\nabla\phi - \frac{\partial \underline{A}}{\partial t} \quad (\text{B2.20})$$

Making use of the result from integration by parts that

$$\begin{aligned} \int g(t') \frac{d}{df} \partial[f(t')] dt' &= \int g(t') \frac{d}{df} \frac{d}{dt'} [f(t')] dt' = - \left[\frac{1}{df/dt'} \frac{d}{dt'} \left(\frac{g(t')}{df/dt'} \right) \right]_{f(t')=0} \\ &= - \left[\frac{i}{k(t')} \frac{d}{dt'} \left(\frac{g(t')}{k(t')} \right) \right]_{f(t')=0} \end{aligned} \quad (\text{B2.21})$$

then

$$\nabla \phi = \frac{q}{4\pi\epsilon_0} \int \nabla \left(\frac{1}{r - r_p(t')} \partial[f(t')] \right) dt' \quad (\text{B2.22})$$

If $R(t') = |r - r_p(t')|$ and using the definition of \hat{n} this can be written as

$$\nabla \phi = \frac{q}{4\pi\epsilon_0} \int \hat{n} \frac{\partial}{\partial R} \left(\frac{1}{R} \partial[f(t')] \right) dt' \quad (\text{B2.23})$$

giving

$$\nabla \phi = - \frac{q}{4\pi\epsilon_0} \int \left[\frac{\hat{n}}{R^2} \partial[f(t')] - \frac{\hat{n}}{cR} \frac{d}{df} \partial[f(t')] \right] dt' \quad (\text{B2.24})$$

which when integrated gives

$$\nabla \phi = - \frac{q}{4\pi\epsilon_0} \left[\frac{\hat{n}}{kR^2} + \frac{1}{ck} \frac{d}{dt'} \left(\frac{\hat{n}}{kR} \right) \right] \quad (\text{B2.25})$$

A similar process can be followed for \underline{A} giving

$$\frac{\partial \underline{A}}{\partial t} = \frac{q}{4\pi\epsilon_0} \frac{1}{ck} \frac{d}{dt'} \left(\frac{\underline{\beta}}{kR} \right) \quad (\text{B2.26})$$

Thus the electric field \underline{E} is

$$\underline{E}(r, t) = \frac{q}{4\pi\epsilon_0} \left[\frac{\hat{n}}{kR^2} - \frac{1}{ck} \frac{d}{dt'} \left(\frac{\hat{n}}{kR} \right) \right] - \frac{q}{4\pi\epsilon_0} \left[\frac{1}{ck} \frac{d}{dt'} \left(\frac{\underline{\beta}}{kR} \right) \right] \quad (\text{B2.27})$$

which simplifies to

$$\underline{E}(r, t) = \frac{q}{4\pi\epsilon_0} \left[\frac{\hat{n}}{kR^2} + \frac{1}{ck} \frac{d}{dt'} \left(\frac{\hat{n} - \underline{\beta}}{kR} \right) \right] \quad (\text{B2.28})$$

At this point it is necessary to take into account the vector nature of this equation and the nature of the variation in the field that produces an energy flux, i.e. power, with respect to the position of the accelerated charge.

The unit vector \hat{n} points along the distance vector $\underline{R} = \underline{r} - \underline{r}_p(t')$, thus it can only change its direction through a velocity component that is at a normal to \underline{R} , as can be seen in Figure B2.1. Thus

$$d\hat{n} = -\frac{v_{\perp}}{R} dt' \therefore \frac{d\hat{n}}{dt'} = -\frac{v_{\perp}}{R} \quad (\text{B2.29})$$

Also since $k(t') = 1 - \hat{n}(t') \cdot \underline{\beta}(t')$

$$\begin{aligned} \frac{d}{dt'} \left(\frac{1}{kR} \right) &= -\frac{1}{(kR)^2} \frac{d}{dt'} \left[\left(1 - \hat{n} \cdot \underline{\beta} \right) R \right] \\ &= -\frac{1}{kR^2} \left[v_{\perp} \cdot \underline{\beta} - \left(\hat{n} \cdot \dot{\underline{\beta}} \right) R - c \left(1 - \hat{n} \cdot \underline{\beta} \right) \hat{n} \cdot \underline{\beta} \right] \end{aligned} \quad (\text{B2.30})$$

giving

$$\frac{d}{dt'} \left(\frac{1}{kR} \right) = -\frac{c}{(kR)^2} \left(\beta^2 - \hat{n} \cdot \underline{\beta} - \frac{1}{c} R \left(\hat{n} \cdot \dot{\underline{\beta}} \right) \right) \quad (\text{B2.31})$$

If we substitute the results of (B2.29) and (B2.31) into (B2.28), this gives

$$\underline{E}(\underline{r}, t) = \frac{q}{4\pi\epsilon_0} \left[\frac{\hat{n} - \underline{\beta}}{(kR)^2} - \frac{\hat{n} - \underline{\beta}}{k(kR)^2} \left(\beta^2 - \hat{n} \cdot \underline{\beta} - \frac{1}{c} R \left(\hat{n} \cdot \dot{\underline{\beta}} \right) \right) - \frac{\dot{\underline{\beta}}}{ck^2R} \right] \quad (\text{B2.32})$$

as before, assuming that this is a solution for t' when

$$f(t') = t' - t + \frac{r - r_p(t)}{c} = 0 \quad (\text{B2.33})$$

This simplifies to

$$\underline{E}(\underline{r}, t) = \frac{q}{4\pi\epsilon_0} \left[\frac{1 - \beta^2}{(k^3 R^2)} \left(\hat{n} - \underline{\beta} \right) + \frac{1}{k^3 R} \hat{n} \times \left[\left(\hat{n} - \underline{\beta} \right) \times \dot{\underline{\beta}} \right] \right] \quad (\text{B2.34})$$

This equation has two distinct terms, one which is proportional to $1/R^2$ and one which is proportional to $1/R$. The first term does not include the acceleration term $\dot{\underline{\beta}}$.

$$\underline{E}_{Coulomb} = \frac{q}{4\pi\epsilon_0} \left[\frac{1 - \beta^2}{(k^3 R^2)} \left(\hat{n} - \underline{\beta} \right) \right]_{f(t')=0} \quad (\text{B2.35})$$

It relates to the radial field and therefore has no impact on the power radiated by the source. The second term

$$\underline{E}_{rad} = \frac{q}{4\pi\epsilon_0} \left[\frac{1}{ck^3R} \hat{n} \times \left[\left(\hat{n} - \underline{\beta} \right) \times \dot{\underline{\beta}} \right] \right]_{f(t')=0} \quad (\text{B2.36})$$

includes the $\dot{\underline{\beta}}$ term and is proportional to $1/R$ and is the radiation field due to the charge being accelerated. If the acceleration is tangential to the velocity where $\dot{\underline{\beta}} \times \underline{\beta} = 0$, as per the example used in Section 2.3 of this chapter, this term reduces to

$$\underline{E}_{rad} = \frac{q}{4\pi\epsilon_0} \left[\frac{\hat{n} \times \left(\hat{n} \times \dot{\underline{\beta}} \right)}{ck^3R} \right]_{f(t')=0} \quad (\text{B2.37})$$

The angular distribution of this radiation at the observing time t will be

$$\frac{dP(t)}{d\Omega} = c\epsilon_0 |\underline{E}_{Rad}|^2 R^2 \quad (\text{B2.38})$$

thus

$$\begin{aligned} \frac{dP(t)}{d\Omega} &= c\epsilon_0 \frac{q^2}{(4\pi\epsilon_0)^2} \left[\frac{\hat{n} \times \left(\hat{n} \times \dot{\underline{\beta}} \right)}{ck^3R} \right]^2 R^2 \\ &= \frac{c\epsilon_0 q^2}{(4\pi\epsilon_0)^2 c^2} \left[\frac{\hat{n} \times \left(\hat{n} \times \dot{\underline{\beta}} \right)}{k^3} \right]^2 \frac{R^2}{R^2} \end{aligned} \quad (\text{B2.39})$$

This can be further simplified to

$$\frac{dP(t)}{d\Omega} = \frac{1}{4\pi\epsilon_0} \frac{q^2}{4\pi c} \left[\frac{\hat{n} \times \left(\hat{n} \times \dot{\underline{\beta}} \right)}{k^3} \right]_{f(t')=0}^2 \quad (\text{B2.40})$$

If we denote the angle between $\dot{\underline{\beta}}$ and \hat{n} as θ , remembering that \hat{n} is a unit vector of magnitude one, then

$$\left[\hat{n} \times \left(\hat{n} \times \dot{\underline{\beta}} \right) \right]^2 = \dot{\beta}^2 \sin^2 \theta \quad (\text{B2.41})$$

Additionally from (B2.19) and the fact that $\hat{n} \cdot \underline{\beta} = \beta \cos \theta$ gives

$$\frac{dP(t)}{d\Omega} = \frac{1}{4\pi\epsilon_0} \frac{q^2}{4\pi c} \left[\frac{\dot{\beta}^2 \sin^2 \theta}{(1 - \beta \cos \theta)^6} \right]_{f(t')=0} \quad (\text{B2.42})$$

This is the rate of energy at time t which may not be the same as at the retarded time t' , to alter this formulation to take this into account. In order to calculate the rate of energy at $P(t')$, it is necessary to calculate what is termed the differential energy, i.e. $d\xi/d\Omega$, the energy radiated during the time between t' and $t' + dt'$, given that by definition $d\xi = P(t')dt'$. As per Figure 2.3 in the main text the radiation is sandwiched between two concentric spherical surfaces with a volume

$$dV = R^2 c dt' (1 - \beta \cos \theta) \quad (\text{B2.43})$$

Therefore the differential energy is

$$\frac{d\xi}{d\Omega} = \frac{1}{2} \epsilon_0 |\underline{E}_{rad}|^2 R^2 c dt' (1 - \beta \cos \theta) \quad (\text{B2.44})$$

and also

$$\begin{aligned} \frac{dP(t')}{d\Omega} &= \frac{1}{4\pi\epsilon_0} \frac{q}{4\pi c} \left[\frac{\dot{\beta}^2 \sin^2 \theta}{(1 - \beta \cos \theta)^6} \times (1 - \beta \cos \theta) \right]_{f(t')=0} \\ &= \frac{1}{4\pi\epsilon_0} \frac{q}{4\pi c} \left[\frac{\dot{\beta}^2 \sin^2 \theta}{(1 - \beta \cos \theta)^5} \right]_{f(t')=0} \end{aligned} \quad (\text{B2.45})$$

As already stated in Section 2.3 (where $\Delta v \ll c$ so that the field lines still essentially describe a spherical field), in the non-relativistic limit where $|\beta| \ll 1$ the radiation will be directed predominantly in a direction perpendicular to the acceleration, thus $\theta = \pi/2$, giving the total radiation power as

$$P \approx \frac{1}{4\pi\epsilon_0} \frac{q^2 \dot{\beta}^2}{4\pi c} \int \sin^2 \theta d\Omega = \frac{1}{4\pi\epsilon_0} \frac{2q^2 \dot{\beta}^2}{3c}, \quad \text{when } |\beta| \ll 1 \quad (\text{B2.46})$$

From the definition of β in (B2.15) with a representing the acceleration not scaled in terms of c , this can be rewritten as

$$P = \frac{q^2 a^2}{6\pi\epsilon_0 c^3} \quad (\text{B2.47})$$

This is the same as (2.15) in the main text (the ‘Larmor equation’).

Note: Although this is a much more complicated methodology to arrive at the same result as shown in Section 2.3, a number of assumptions and constraints used in that derivation are not mandatory. Thus this full derivation can be modified to predict the power when v is not very much smaller than c , the field lines do not describe a spherical field and thus when the primary direction of radiation is not at a normal to the acceleration and is therefore without these specific assumptions a universally valid description of the power radiated by accelerated charges.

* Landua L.D., Lifshitz E.M. *The Classical Theory of Fields* (in Russian), M. Hamermeash (trans.), 4th rev. edn. Oxford: Pergamon Press; 1973.

Given that a knowledge of the sources ρ and \underline{j} can be used as inputs for the calculation of ϕ and \underline{A} , which in turn allows the further calculation of \underline{E} and \underline{B} , the fields induced by the sources, it would appear that in attempting to characterise antennas, measurements of charge and current density (in the form of currents and voltages) would be the starting point for any attempt to quantify their performance.

2.6 The inapplicability of source excitation as a measurement methodology

The application of a methodology based on a knowledge of ρ and \underline{j} that provides an algorithm for the calculation of the free-space electromagnetic field propagation away from or to an antenna structure in terms of currents and charge distributions excited on a geometrical structure is widely used in antenna design. As basic circuit theory and methods designed to cope with guided wave paths in systems are based on the concepts of current and voltage, the interface of these techniques with antenna design methods is extremely fortuitous.

However, in terms of metrology the concept of excitation currents on a structure have considerable limitations. The direct probing of the surface of any radiating structure to determine charge and current distributions, as a result of the constraints associated with the transfer of signal along a conducting path from any single or array of sensors, is an extremely intrusive measurement methodology. Although to some extent all measurement procedures are intrusive, in general the end result of such an RF surface probing procedure is a very considerable alteration in the existing state of the system in the course of the measurement procedure.

This alteration can in theory be compensated for via the use of theoretical models. However, if the measurement procedure results are essentially the results of a modelling procedure that is no more accurate than the original modelling procedure included as part of the design process, then measurements cannot be used to confirm the accuracy or effectiveness of any design.

The accuracy of any compensating mathematical processing can also be brought into question due to its possible inconsistency with theory. In that, as a result of space contraction, and therefore the non-invariance of volume under the Lorentz transformation, current and charge density are not separately relativistically invariant quantities. Therefore any extrapolation from raw measurement data

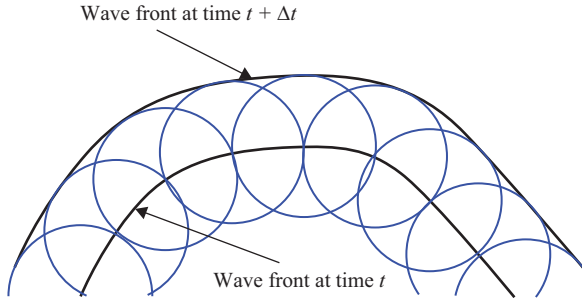


Figure 2.6 Huygen's principle

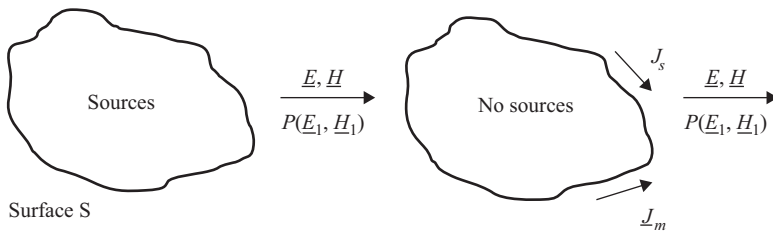


Figure 2.7 The field equivalence principle

from only one of these two processed measured data may be done without a firm basis in the physical processes involved. However, an alternative strategy can be used to determine the radiated fields from an electromagnetic source that can be more amenable to the constraints of metrology.

2.7 Field equivalence principle

The field equivalence principle is the process of replacing the actual sources that create an electromagnetic field over some closed surface S , with equivalent sources located on that same surface. It is in fact a theoretical statement of Huygen's principle that any wave front can be viewed as being made up of secondary sources of spherical waves. Each point on a primary wave front can be considered to be a new source of a secondary spherical wave and that a secondary wave front can be constructed as the envelope of these secondary spherical waves, at the same frequency as illustrated in Figure 2.6.

Figure 2.7 defines the field equivalence principle, where a set of electric and magnetic current sources create the radiated electric, \underline{E} , and magnetic, \underline{H} , fields over an arbitrary closed surface S . The wave fronts that create the radiated field \underline{E}_1 , \underline{H}_1 at point P in the left-hand diagram can be alternatively created by equivalent electric and magnetic current sources \underline{J}_s and \underline{J}_m on the surface S of the right-hand diagram, so creating the same radiated field at point P and indeed everywhere

outside the enclosing surface S which now contains no sources. In order that the total field throughout the whole of the volume space (both internal and external to S) is a valid solution to Maxwell's equations, the equivalent sources must conform to the proper boundary conditions at S between the internal and external E and H field at the surface S as well as the radiation condition at infinity. By postulating a null field inside S, the equivalent surface currents are given by (2.73) and (2.74):

$$\underline{J}_s = \hat{a}_n \times \underline{H}(\underline{s}) \tag{2.73}$$

$$\underline{J}_m = -\hat{a}_n \times \underline{E}(\underline{s}) \tag{2.74}$$

where the unit vector \underline{a}_n represents the surface normal and $\underline{E}(\underline{s})$ and $\underline{H}(\underline{s})$ represent the tangential electric and magnetic fields at the surface S.

A particularly valuable modification to the field equivalence comes about when we note that the zero field within S cannot be disturbed by changing the material properties within S, e.g. that of a perfect electric conductor. In this case at the moment the electric conductor is introduced the electric current on the surface S, \underline{J}_s , is short-circuited. This leaves just the magnetic current, \underline{J}_m , over the surface S and it radiates in the presence of the perfect electric conductor to give the correct fields \underline{E}_1 and \underline{H}_1 at point P in Figure 2.7. Similarly the dual of this process can be enacted such that the material properties are replaced by a perfect magnetic conductor, so short-circuiting the magnetic current, \underline{J}_m , thus leading to a purely electric current \underline{J}_s radiating in the presence of a perfect magnetic conductor.

The utility of the field equivalence approach comes when we consider an infinite surface; this can be a closed surface S or, as will be described in the text, an infinity flat plane, since here the problems reduce to determining how a magnetic surface current, \underline{J}_m , radiates in the presence of a continuous conductor of infinite extent. From image theory this problem is reduced to that shown in Figure 2.8.

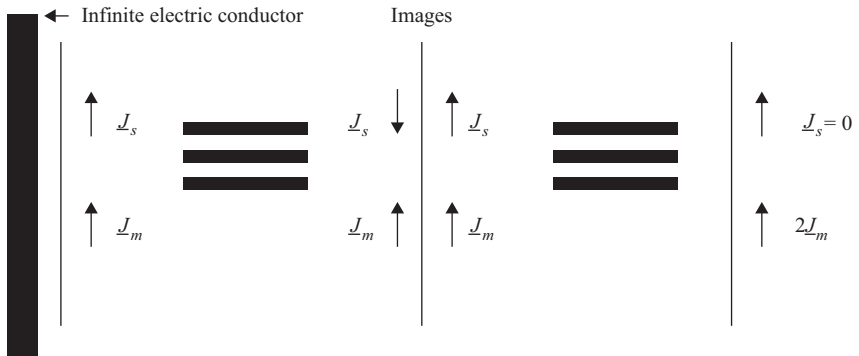


Figure 2.8 Application of image theory to the radiating magnetic current in presence of a perfect infinite electric conductor

Figure 2.8, where in (a) the presence of the electric conductor short-circuits \underline{J}_s , and the removal of the infinite electric conductor by image theory (b) leads to the doubled magnetic surface current in an unbounded medium (c), from which the radiating fields can be determined to the right of the conducting plane. By duality the use of a perfect magnetic conductor reduces the problem to that of a doubled electric surface current radiating in an unbounded medium.

As will be expanded upon in later chapters, the above process of equivalent fields leads to a convenient way forward for a whole class of antenna measurement techniques in that we can measure the electric field on a surface close to the antenna's physical structure. From this process we can derive the generating magnetic current on this scanned plane, which can then be used to determine the far-field characteristics of the antenna.

2.8 Characterising vector electromagnetic fields

The choice of spherical coordinates for the far-field is near universal, the choice of coordinate system to represent the antenna in order to calculate its radiation pattern very much depends on the structure of the antenna. Considerable mathematical simplifications in calculating the radiation pattern of a given antenna can be achieved by choice of a *matching* coordinating system. For example, the use of cylindrical coordinates to calculate the radiation of a circular open-ended waveguide offers considerable simplification over the use of a rectangular aperture coordinate frame. In this section we will illustrate the process of determining the radiated field by considering the z -directed Hertzian dipole and this will also serve to define the concept of the plane wave.

The fundamental solution for the wave equation in vector potential A (2.62) is the retarded vector potential of (2.49) at a single source point with current \underline{J}_s

$$\underline{A}(\underline{r}, t) = \frac{\mu}{4\pi} \frac{\underline{J}_s(\underline{r}', t - |\underline{r} - \underline{r}'|/c)}{|\underline{r} - \underline{r}'|} \quad (2.75)$$

This is clearly a function of both source point and field point and defines the 'action at a distance' property of the electromagnetic wave. Equation (2.67) is often called the Green's function because by definition a Green's function is the solution to a differential equation for a unit source. We will now consider the radiation from this infinitesimal small (with respect to the radiation wavelength) current element, often termed the Hertzian dipole (Figure 2.9). For this dipole we have a constant current

$$\underline{J}_s(\underline{r}', t - |\underline{r} - \underline{r}'|/c) = J_0 \hat{\underline{a}}_z e^{-jkr} \quad (2.76)$$

and so the vector potential can be written as

$$\underline{A} = \hat{\underline{a}}_z \frac{\mu J_0 l}{4\pi r} e^{-jkr} \quad (2.77)$$

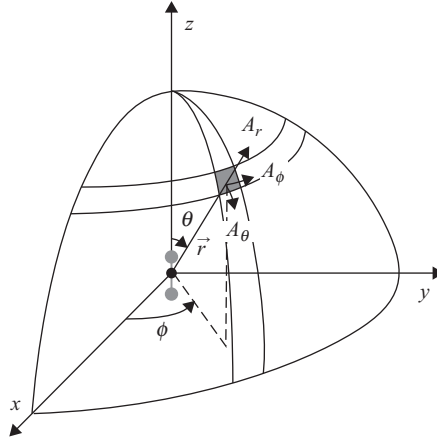


Figure 2.9 Coordinate system for infinitesimal dipole over its length l

Since the far-field is to be expressed in spherical coordinates, the vector identity

$$\begin{bmatrix} A_r \\ A_\theta \\ A_\phi \end{bmatrix} = \begin{bmatrix} \sin \theta \cos \phi & \sin \theta \sin \phi & \cos \theta \\ \cos \theta \cos \phi & \cos \theta \sin \phi & -\sin \theta \\ -\sin \phi & \cos \phi & 0 \end{bmatrix} \begin{bmatrix} A_x \\ A_y \\ A_z \end{bmatrix} \quad (2.78)$$

yields

$$\underline{A} = (\hat{a}_r \cos \theta - \hat{a}_\theta \sin \theta) \frac{\mu J_o l}{4\pi r} e^{-jkr} = \underline{A}_r(\theta, r) + \underline{A}_\theta(\theta, r) \quad (2.79)$$

As j_s is located in the z direction, it is independent of the far-field angle ϕ and so $\delta/\delta\phi = 0$, thus

$$\underline{H} = \nabla \times \underline{A} \quad (2.80)$$

gives the magnetic field at the observation point r . Expressing the cross-product in spherical coordinates with $\delta/\delta\phi = 0$ gives

$$\underline{H} = \frac{1}{r} \left[\frac{\partial(rA_\theta(\theta, r))}{\partial r} - \frac{\partial A_r(\theta, r)}{\partial \theta} \right] \hat{a}_\phi \quad (2.81)$$

yielding only an H_ϕ component in the far-field.

For the electric field we have

$$\underline{E} = \frac{1}{j\omega\epsilon} (\nabla \times \underline{H}) \quad (2.82)$$

with $H_r = H_\theta = \delta/\delta\phi = 0$, which yields

$$E_r = \frac{1}{j\omega\epsilon r} \frac{1}{\sin\theta} \left[\frac{\partial(H_\phi \sin\theta)}{\partial\theta} \right] \quad (2.83)$$

$$E_\theta = \frac{1}{j\omega\epsilon r} \left[\frac{\partial(rH_\phi)}{\partial r} \right] \quad (2.84)$$

Evaluating the three non-zero field components gives

$$H_\phi = \frac{jkJ_oI\sin\theta}{4\pi} \left[\frac{1}{r} + \frac{1}{jkr^2} \right] e^{-jkr} \quad (2.85)$$

$$E_r = \frac{Z_oJ_oI}{2\pi} \left[\frac{1}{r^2} + \frac{1}{Jkr^3} \right] \cos\theta e^{-jkr} \quad (2.86)$$

$$E_\theta = \frac{jkZ_oJ_oI\sin\theta}{4\pi} \left[\frac{1}{r} + \frac{1}{jkr^2} - \frac{1}{k^2r^3} \right] e^{-jkr} \quad (2.87)$$

Near to the dipole $1/r^2$ and $1/r^3$ terms dominate, whereas in the far-field only $1/r$ terms are significant. Thus the far-fields are given by

$$H_\phi = \frac{jkJ_oI\sin\theta}{4\pi r} e^{-jkr} \quad (2.88)$$

$$E_\theta = \frac{jkZ_oJ_oI\sin\theta}{4\pi r} e^{-jkr} \quad (2.89)$$

and we note that $E_\theta/H_\phi = Z_o$ is the free-space wave impedance. Thus the infinitesimal dipole radiates a spherical wave in the radial direction r .

It should be noted that computing the average power flow (Poynting vector) in the case of the near-field ($1/r^2$ and $1/r^3$ terms only) results in zero power flow indicating the field is reactive. For the far-field case real power flow is achieved.

2.9 Reflection and scattering of electromagnetic fields by extended objects

The interaction of electromagnetic fields with extended objects is at its most fundamental related to the interaction of individual charged particles with the field. In extended objects other parameters are in play that constrain the motion, displacement and localisation of these charged particles and thus alter the induced currents and voltages across these extended bodies. Such that when the electromagnetic field impinges on an extended material object the material object can be characterised by values of ϵ , μ and σ which relate the atomic and molecular properties of the material from which the object is composed to the overall macroscopic response of the object to the impinging field.

The variations in the ϵ , μ and σ values for the object from those of the free space in which the incident radiation is travelling can be thought of as the cause of

the interactions which will alter the propagating field. When considered in terms of classical EM theory, these variations are most effectively described by the Stratton–Chu equations for scattered fields [3].

The overall reaction of these extended bodies to electromagnetic irradiation can take the form of absorption, transmission, refraction, diffraction and reflection, dependent on the physical properties of the objects. Almost all (and all that will be of concern in this text) of these different reactions to irradiation can be described in detail using classical electromagnetic field theory.

Modern antenna test ranges can be utilised to investigate many of these properties that are of interest, as will be examined in later chapters particularly those related to the scattering of EM waves and the associated scattering or radar cross-section that these objects project to incident EM radiation.

However, the interaction with these fields is not only a function of the material properties of the objects, engineering solutions can be provided that turn objects, e.g. metallic structures that should totally reflect incident radiation, into absorbers of radiation, i.e. Rx antennas and via reciprocity also Tx antennas. In order to understand how it is that extended objects like antennas can be used to induce currents and voltages in circuits as a result of themselves being irradiated when used in Rx and how they can be excited to induce fields in their vicinity when excited via a circuit, it is necessary to examine the concept of antenna port or terminal.

2.10 Antenna port definition

In our discussion of antenna principles we invariably have to refer to electric (E) and magnetic (H) field intensities, and even though we can at times replace these for convenience with equivalence currents conceptually these two parameters remain fundamental to the radiation discussion. From them we can determine antenna polarisation and calculate all radiation parameters of interest. However, despite the very fundamental nature of these two parameters, as already described, we cannot measure these directly and we have to rely on an indirect method of measurement. To illustrate, consider Figure 2.10, where a transmitting antenna (a) is depicted as the AUT with a receiving antenna (b) acting as field sensor. In

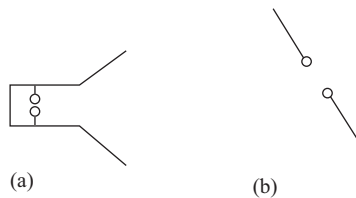


Figure 2.10 Antenna under test (AUT) depicted as (a) and probe antenna depicted as (b)

practice we measure the complex voltage at the port of antenna (b) and relate that to the electric field intensity radiated by antenna (a).

In order to measure this complex voltage at the port of antenna (b), we conceptually perform a line integral of the electric field intensity due to antenna (a) from conductor 1 to conductor 2 along a path of integration designated by Γ in Figure 2.11.

$$V = \left[\int_2^1 \underline{E}_a \cdot d\underline{l} \right] \quad (2.90)$$

In order to obtain a unique voltage measurement, the integration must be path independent. The requirement for the voltage measurement to be path independent or unique is what defines a proper set of terminals. If we consider Figure 2.11 as a more general case, where we enclose our AUT within a closed surface and we have two conductors protruding from this surface that we wish to define as the AUT terminals, then a voltage measurement performed across these two conductors must satisfy

$$\left[\int \underline{E}_a \cdot d\underline{l} \right]_{\Gamma_1} = - \left[\int \underline{E}_a \cdot d\underline{l} \right]_{\Gamma_2} \quad (2.91)$$

or

$$\oint \underline{E} \cdot d\underline{l} = - \frac{\partial}{\partial t} \int_{S_c} \underline{B} \cdot d\underline{s} = 0 \quad (2.92)$$

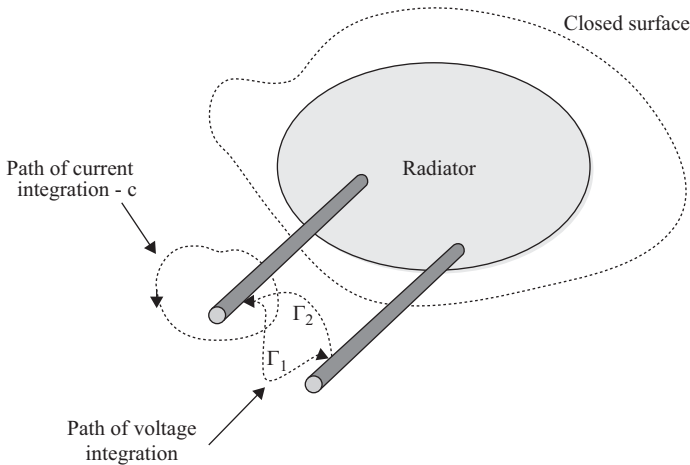


Figure 2.11 A generic AUT contained within a closed surface with two conductors protruding from this surface that we define as the AUT terminals

where \underline{B} is the magnetic flux density and this condition requires that there is no component of \underline{B} normal to the surface enclosed by the circuit integral. This condition holds when the field in the terminal region is conservative or as a specific example transverse electromagnetic (TEM).

Once a proper set of terminals have been defined, a complex current measurement can be performed as a closed circuit integral of the magnetic field intensity as

$$I = \oint_c \underline{H} \cdot d\underline{l} \quad (2.93)$$

Using the complex voltage and current measured in this fashion, the complex terminal impedance is readily calculated. A very practical example of a TEM field condition is a coaxial line and it is therefore common to see coaxial ports on antennas and these can be used as well-defined terminals as a result.

The question does arise, what to do with antennas where one is faced with a rectangular or circular waveguide port? In these instances it is common practice to attach a coax to waveguide port to the waveguide port to establish a convenient TEM terminal. *Note:* In cases where the frequency band of operation precludes the use of a coax to waveguide adapter, some solid-state frequency down-conversion process invariably converts from the waveguide modes (a non-conservative field environment) to a TEM or quasi-TEM environment where a unique voltage measurement is feasible.

Thus an extended material object, an antenna, when integrated into a circuit via its terminals, can produce a current in the circuit as a result of its terminal voltage. This is the basic transducer action that an Rx antenna performs when it transforms a free-space electromagnetic field into a current generating EMF in a circuit; thus by reciprocity a Tx antenna can develop an electromagnetic field in free space as a result of an applied EMF across its terminals.

2.11 Summary

This chapter has detailed a theory that describes the interaction of antennas through free space as a process of the propagation of electromagnetic waves; these waves being directly related to the acceleration of charged particles. A description of these waves was then provided based on Maxwell's equations and the derivation of the scalar Helmholtz equations. Then a description of the basis of the fields that produce these waves as being related to retarded potentials was expounded.

The basic physical principles of charges, forces and fields, along with the symmetries inherent in energy and momentum conservation, allow the development of a theory of classical electromagnetic fields that can be modelled concisely by Maxwell's equations. Using these equations and simplifications and assumptions based on them, it is possible essentially to describe all EM interactions that are of interest to antenna engineers. This includes the fundamental action of

antennas as transducers between free-space fields and the guided wave paths in circuits.

Thus this theory describes the unobserved mechanism behind the observation that electronic systems can be made to induce currents and voltages in other remote systems that have no connection other than radiative fields in free space if suitable antennas are included in the remote Tx and Rx systems/circuits. As such, it highlights the importance of antennas as circuit elements and given the limitations of direct voltage and current-based measurements with respect to antenna excitations it points to the conclusion that the field equivalence principle should be used when attempting to characterise the current and voltage distributions on the surfaces of antennas.

Given that for engineering purposes antennas need to be characterised and free-space measurements of fields appear to be the most viable way forward in this, the next chapter will begin to describe the variety and type of measurement setups that have traditionally been used to identify and quantify the properties of various antennas via these free-space measurements.

References

- [1] Mozans H.J., *Women in Science*. London: CreateSpace; 2012. ISBN-10: 147008066
- [2] Gregson S., McCormick J., Parini C.G., *Principles of Planar Near Field Antenna Measurements*. Herts, UK: IET; 2007. ISBN 978-86341-736-8
- [3] Stratton J.A., *Electromagnetic Theory*. New York, NY: McGraw-Hill; 1942. ISBN-10: 1443730548
- [4] Kraus J.D., *Electromagnetics*. New York, NY: McGraw-Hill; 1991. ISBN 0-07-035621
- [5] Thomson J.J., *Notes on Recent Researches in Electricity and Magnetism*. Ithaca, NY: Cornell University Library; 1893. ISBN-10: 1429740531
- [6] Collin R.E., Zucker F.J., *Antenna Theory Part 1*. New York, NY: McGraw-Hill; 1969. ISBN-10: 0070117993
- [7] Larmor J., 'A dynamical theory of the electric and luminiferous medium'. *Philosophical Transactions of the Royal Society A*. 1897;**190**:205–300
- [8] Llyod J., Mitchinson J., *The Book of the Dead*. London: Faber and Faber; 2009. ISBN: 978-0-571-24491-1
- [9] Gregson S.F., Parini, C.G., McCormick, J., *Principles of Planar Near-Field Antenna Measurements*. UK: IET Press, IET EM Waves Series 53, Section 4.6, pp. 81–83; 2007. ISBN: 978-0-86341-736-8
- [10] Polyanin, A.D., *Handbook of Linear Partial Differential Equations for Engineers and Scientists*. Boca Raton, FL: Chapman & Hall/CRC Press; 2002. ISBN 58488-299-9

Chapter 3

Antenna measurements

3.1 Antenna measurements and alignment

From Chapter 1, it is clear that the purpose of all free space antenna measurements is to establish the extent to which one electronic system/sub-system will interact with another system. By characterising antennas in a known circuit configuration, the extent to which they enhance coupling in other situations can be predicted. This is the fundamental procedure adopted in antenna test ranges, where the inclusion of antennas in a known, carefully controlled configuration of two coupled circuits/systems, represented by an antenna under test (AUT) and a range antenna, allows this measurement process to be performed.

In Chapter 1, it is also made clear that the extent to which antennas couple is directly related to their physical orientation and displacement relative to each other; thus, the main parameters of antenna performance that can be used to characterise the extent of this coupling between an AUT and a range antenna are

- Gain
- Free space radiation pattern
- Polarisation

Figure 1.8 is included again as Figure 3.1 to help illustrate how these parameters are characterised in modern antenna test ranges, where the antenna in the figure is the AUT and the z direction points directly at the range antenna.

Gain: This (specifically main beam gain when the antenna has a single main lobe) characterises the magnitude of the coupling of the AUT to the range antenna in the configuration shown in Figure 3.1, where the main beam of the range antenna is tangential to the z -axis but aligned with a displacement in the $-z$ direction, the *boresight* vector aligned at a normal to the AUT aperture and aligned with the z -axis.

Free space radiation pattern: This characterises how the magnitude (and phase) of the coupling between the AUT and the range antenna varies as a function of the angular displacement of the AUT from the z direction in Figure 3.1. In this figure, this would involve the AUT being rotated to different pointing angles defined by θ and ϕ and would mean that the vector describing the boresight direction of the AUT is moved to a range of different angular orientations.

Polarisation: This characterises how the magnitude of the coupling varies at any angular orientation, defined by θ and ϕ , as the AUT is itself rotated around the

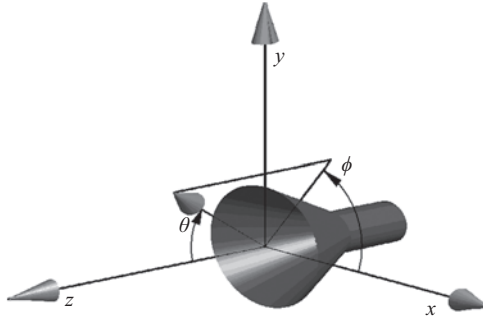


Figure 3.1 AUT coordinate system

vector that defines its boresight at that orientation. This characterisation can also be acquired by rotating the range antenna.

With these measurements undertaken, it will be possible to produce a calibrated measurement – in terms of gain and free space radiation pattern, the important parameters of any AUT – for any specifically defined polarisation basis. See Chapter 4 for a more detailed description of the various polarisation bases that can be adopted. From these measurement definitions, it is also clear that in order to fully characterise these interactions, via a measurement process, the two antennas will have to be realigned and rotated relative to each other to make the full range of measurements possible. Or, some form of measurement process that predicts their response if they were to be moved relative to each other needs to be employed.

3.2 Rotation methodologies

In order to align and move antennas in a test range to correspond to the different orientations required for the measurements to be performed, the use of antenna positioners will be required. Figure 3.2 illustrates a small, slotted waveguide array mounted on a seven-axis positioner that allows the movement and alignment of the AUT into a range of measurement configurations.

Using these axes, the AUT can be manoeuvred into a number of historically used configurations, with convenient, associated coordinate systems in which antenna measurements have usually been performed.

In Figure 3.2, the small, slotted waveguide antenna is mounted directly onto a polariser axis, above an elevation axis, above the translation axis, above an azimuth axis, above a second elevation axis, above a second azimuth axis above a final translational axis. Clearly, the inclusion of so many axes on the antenna positioner allows the movement of the AUT in a variety of distinct ways. Rotation using the polariser to vary the ϕ -angle and an azimuth axis to vary θ -angle measurements in a (ϕ, θ) coordinate system can be performed.



Figure 3.2 Seven-axis positioner (Courtesy of Leonardo MW)

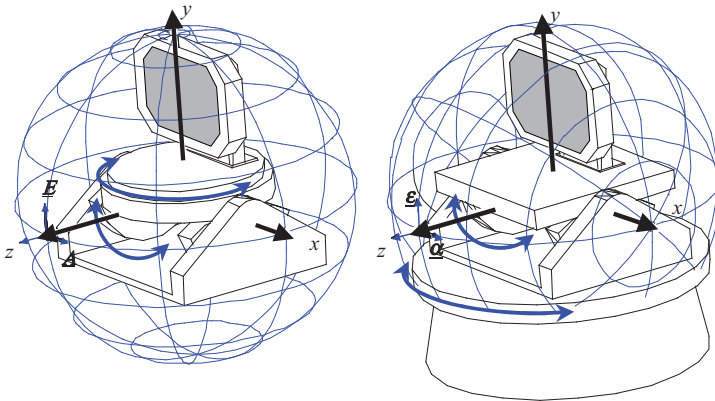


Figure 3.3 Azimuth over elevation and elevation over azimuth positioning for AUT Tx and Rx measurements

Figure 3.3 illustrates how measurements in other commonly used coordinate systems can be accomplished with a variety of axes included in an antenna positioner system.

When considering the range antenna to be the Tx antenna in the range, the measurements that can be made in the various geometries shown in the figure depend on the ability of the range antenna to produce a plane wave that is incident on the AUT. This is because in most practical circumstances where the AUT will be used, it can be assumed that the Tx and Rx antennas will be far

apart in each other's far-field, or other more cost-effective methods of establishing the required levels of coupling would be adopted, e.g. fixed solid transmission line.

Although there are a great many ways in which the plane wave illumination of the AUT can be achieved in practice, their mechanisms can be divided into two categories, direct and indirect collimation. Those that rely upon direct collimation include free space ranges, reflection ranges, i.e. compact antenna test ranges (CATR) and refraction, i.e. dielectric lens ranges. Indirect techniques include all forms of near-field ranges, i.e. planar, cylindrical and spherical. All types of ranges that will be further discussed in detail later in the text.

3.3 Far-field ranges

The most basic direct method to generate the plane wave is from a portion of a spherical wavefront. This can be achieved by having a source antenna at a long distance from the AUT and so the AUT aperture sees a nearly plane wave when R is large, as per Figure 3.4. Please see Chapter 4 below for a detailed discussion of these coordinate systems.

To ensure near-plane wave conditions at the AUT aperture, the phase taper across the AUT aperture is usually controlled to be a maximum variation of 22.5° (the

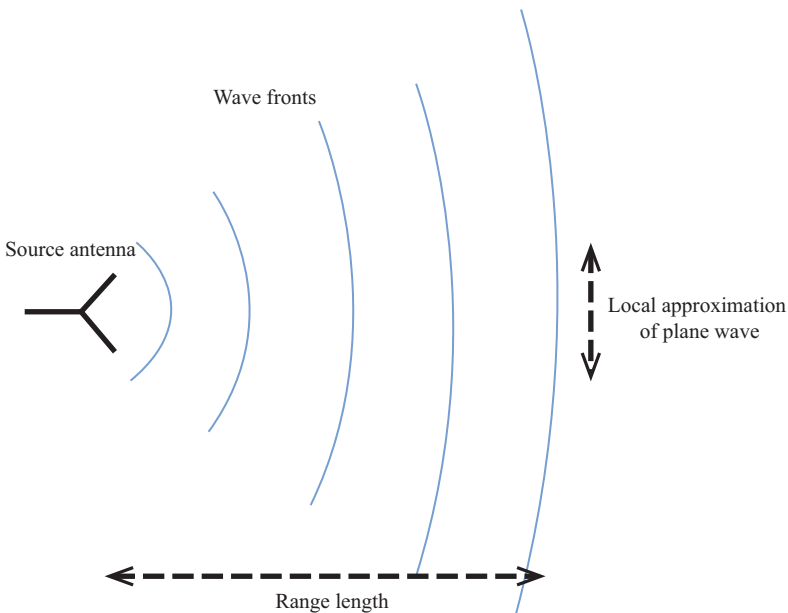


Figure 3.4 *Plane-wave created from far-field source*

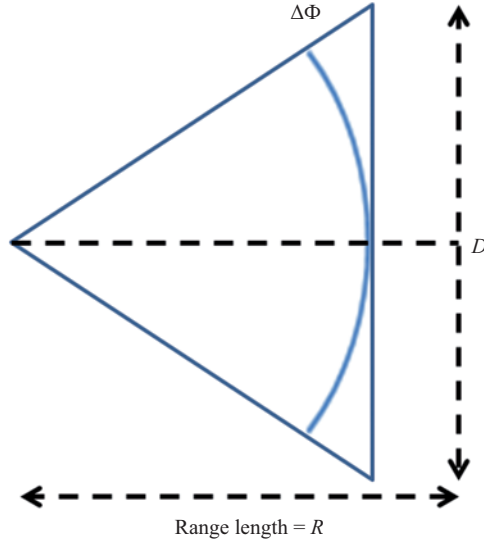


Figure 3.5 Far-field phase taper geometry

acceptable allowable phase variation can be selected to give the required accuracy in measured gain and AUT pattern). Referring to Figure 3.5, this can be expressed as

$$\Delta\Phi = \frac{2\pi}{\lambda} \left(\sqrt{R^2 + \left(\frac{D}{2}\right)^2} - R \right) \quad (3.1)$$

$$\Delta\Phi = \frac{2\pi R}{\lambda} \left(\left(1 + \left(\frac{D}{2R}\right)^2 \right)^{1/2} - 1 \right) \quad (3.2)$$

Taking the first term of the Taylor series yields

$$\Delta\Phi \approx \frac{\pi D^2}{4\lambda R} \quad (3.3)$$

If $\Delta\Phi < \pi/8$ or 22.5° , then we get the approximate far-field distance

$$R \geq \frac{2D^2}{\lambda} \quad (3.4)$$

This length of R is approximately equivalent to the displacement where only one unique path exists between the AUT and the range antenna, as per Chapter 1, wherein the limit if only one path existed then $\Delta\Phi = \text{zero}$. *Note:* this argument has been constructed in terms of the AUT being in Rx but considerations of reciprocity show that it is equally valid in Tx.

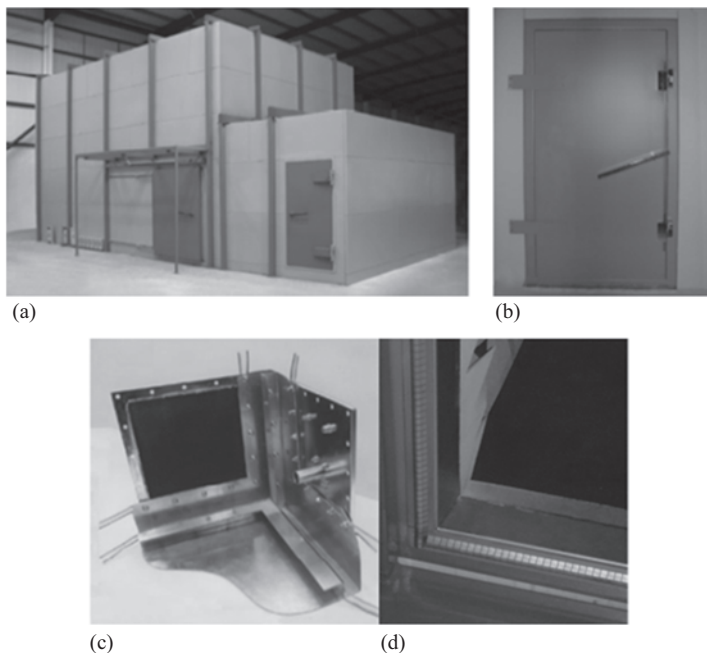


Figure 3.6 (a) Fully screened chamber, (b) details of door, (c) details of corner construction and cable entry and (d) door seal detail

Clearly from (3.4), to allow accurate measurements to be undertaken the distance associated with the displacement between the AUT and the range antenna will need to be considerable, e.g. for a 33 dBi circular antenna at 10 GHz the AUT and range antenna may need to be displaced from each other by over 12 m, for higher gain antennas, this distance can be many tens or hundreds of metres. This implies that antenna far-field test ranges either need to be outdoors or established in very large building structures.

If constructed outdoors, antenna ranges are subject to all the vagaries of weather interference, vegetation, wildlife and a host of other factors that can degrade the measurements; therefore, almost exclusively modern antenna test ranges are indoor ranges. Given that antennas are designed to be used in a free space environment, it therefore falls upon the range designer to attempt to replicate these free-space conditions in an enclosed environment.

3.4 Free-space conditions

The first consideration related to producing a pseudo-external environment relates to the susceptibility of the test range to external interference. To this end, test ranges are usually constructed within fully screened enclosures such as shown in Figure 3.6.

Such enclosures/chambers provide a high level of magnetic, electric and microwave shielding and this allows test facilities to be placed in environments where there may be high levels of residual radio frequency (RF) energy. Additionally, as well as mitigating the effects of interference impinging on any test procedures taking place in the range, the shielding also stops the egress of any signals from within the test range into the surrounding environment.

Shielding removes any interference that the range may produce in the surrounding environment; this may be an important consideration from the standpoint of health and safety as it allows high power levels to be used in the test procedures. It also allows the security aspects of any waveform or signal pattern that is used in the test procedures to be kept confidential.

Typical shielding values when tested to IEEE299 are

- –100 dB @ 1–500 MHz in the electric field
- –100 dB @ 1–18 GHz in microwave (far-field)

Given that it will be necessary to enclose the test range in a screened chamber, the proximity of these conducting walls of the chamber will mean that in any test procedure where one of the antennas in the range is in Tx and the other in Rx, the direct path between the two antennas will not be the only path that a signal could follow to couple the response of the range antenna and AUT. The presence of the conducting walls will, via reflections from the walls, provide a number of other paths that a signal from Tx to Rx can follow. *Note:* this signal that travels from Tx to Rx not via the direct path between the two antennas is usually referred to as multipath.

To remove the influence of multipath and further enhance the ability of indoor ranges to mirror the external environment, radar adsorbent material (RAM) needs to be included in the design of the range. This means that the chamber must be designed to be anechoic to electromagnetic waves over the bandwidth that it is to be used for measurements.

In practice, the anechoic environment is not perfect, as typical high-quality, wide-band RAM with a thickness of four wavelengths has a normal incidence mono-static reflection coefficient of –40 dB. The bi-static reflection coefficient of most RAM will increase as the angle of incidence becomes larger whilst the mono-static backscatter is always present.

A measure of RAM performance is its reflectivity, which is the ratio of the received signal with absorber to that of the signal received when the absorber is replaced by a metal plate, see Figure 3.7.

Typical values of reflectivity range from –20 to –50 dB for normal incidence. This depends on the pyramid size relative to the operational wavelength. The degradation of reflectivity with angle means that careful consideration should be made about the size and positioning of AUTs in ranges during measurements to ensure that multipath is not introduced into the measurement results.

Thus, in practice, the anechoic environment is not perfect and consideration must be given to the reflection characteristics of the pyramidal RAM material used in its specification. Essentially, the electrical thickness of the material determines

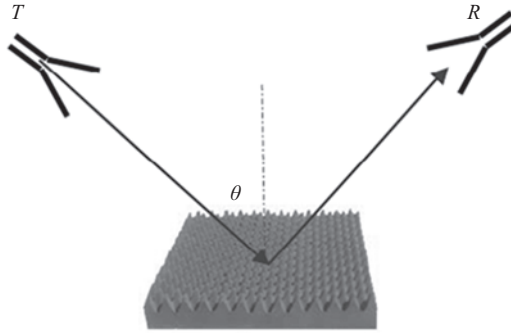


Figure 3.7 Measurement of RAM reflectivity

how much RF energy is absorbed, with the usual approximation used to determine this at normal to boresight being

$$R_0(t) = -13.374 \ln(t) - 26.515 \quad (3.5)$$

where t is the thickness of the RAM material in wavelengths (see Ref. [1]).

This equation is generally considered to be valid over the range where $0.25\lambda \leq t \leq 20\lambda$.

However, as will be further described, in most chamber designs at least part of the included RAM material will not be at a normal to the incident RF radiation. To address the variation in the reflectivity of RAM materials as a function of angle, a series of polynomial expressions have been developed that attempt to predict the response of RAM material at a range of different angles. The generic form of the polynomial is

$$R_\theta(t, \theta) = R_0(t) + A_1(t)\theta + A_2(t)\theta^2 + A_3(t)\theta^3 + A_4(t)\theta^4 + A_5(t)\theta^5$$

where the coefficients in the polynomial are divided into two sections that related to the thickness of the RAM material [2].

For $0.25\lambda \leq t \leq 2\lambda$,

$$A_1(t) = 1.5252 - 4.8249t + 6.9479t^2 - 3.8332t^3 + 0.7333t^4$$

$$A_2(t) = -0.0754 + 0.24782t - 0.3984t^2 + 0.2285t^3 - 0.0442t^4$$

$$A_3(t) = 0.0016 - 0.00502t + 0.00938t^2 - 0.00577t^3 + 0.001155t^4$$

$$A_4(t) = -1.58 \times 10^{-5} + 4.91 \times 10^{-5}t - 1.015 \times 10^{-4}t^2 \\ + 6.58 \times 10^{-5}t^3 - 1.35 \times 10^{-5}t^4$$

$$A_5(t) = 5.84 \times 10^{-8} - 1.78 \times 10^{-7}t + 4.02 \times 10^{-7}t^2 \\ - 2.71 \times 10^{-7}t^3 + 5.7 \times 10^{-8}t^4$$

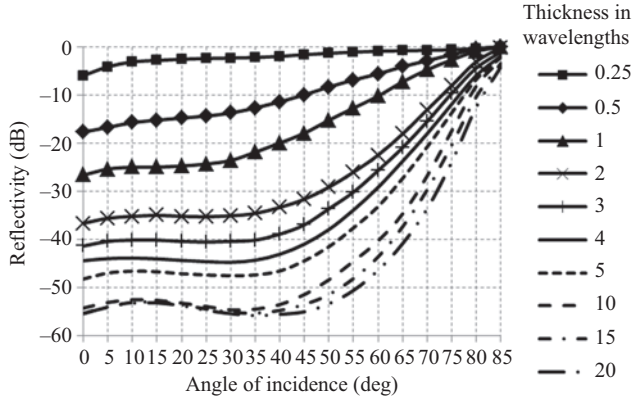


Figure 3.8 Bi-static reflectivity as a function of angle for different RAM thicknesses in λ

and for $2\lambda \leq t \leq 20\lambda$,

$$A_1(t) = 0.1751 + 0.149t - 0.0119t^2 + 0.00028t^3$$

$$A_2(t) = -0.0105 - 0.00824t + 0.0007t^2 - 1.61 \times 10^{-5}t^3$$

$$A_3(t) = 0.00029 + 0.000123t - 1.13 \times 10^{-5}t^2 + 2.57 \times 10^{-7}t^3$$

$$A_4(t) = -1.69 \times 10^{-6} - 4.77 \times 10^{-7}t + 5.08 \times 10^{-8}t^2 - 1.14 \times 10^{-9}t^3$$

$$A_5(t) = 0$$

Figure 3.8 illustrates the output from these polynomials for a range of RAM thicknesses from 0.25λ to 20λ and angles up to 85° off-normal incidence.

There are a number of additional limitations related to the polynomial approximation

- It is only valid out to $\theta = 85^\circ$.
- It is only valid up to $t = 20\lambda$, beyond 20λ the reflectivity can be assumed to be constant.
- At large values of θ and t , the approximation can overestimate the reflectivity by as much as 10 dB.

However, even given these limitations, the polynomial approximation is a valuable tool in defining the requirements for any far-field anechoic chamber.

3.4.1 Far-field chambers

For far-field chambers, a common rule of thumb used to define the dimensions of the chamber is that the width and height of an anechoic chamber should be three times the diameter, D , of the minimum sphere that contains the AUT during the test. While the test range antenna should be separated from the AUT by at least $2D^2/\lambda$, where D is a specific number of wavelengths, i.e. $D = n\lambda$.

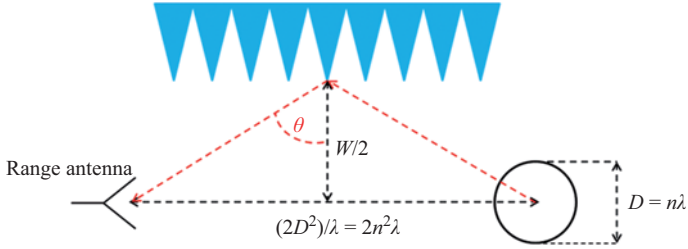


Figure 3.9 Basic geometrical requirements for far-field chambers

Figure 3.9 shows the geometry of a far-field measurement facility where W is the width of the chamber which will equal the height of the chamber.

From Figure 3.9

$$\frac{2n^2\lambda}{W} = \tan(\theta) \tag{3.6}$$

Solving for $W/2$

$$\frac{W}{2} = n^2 \cot(\theta) \tag{3.7}$$

This will give the minimum required distance between the centre of the range and the tips of the RAM material taking into account that the distance between the edge of the minimum sphere and the tips of the pyramidal RAM must be at least 2λ at the lowest frequency of use.

Since the reflectivity of the RAM material is a function of the angle θ the different values of θ will give different levels of multi-path in the chamber. The required width of the chamber for any given level of reflectivity can be calculated from consideration of (3.7).

If the required level of reflectivity can be acquired at an angle θ , then the overall width of the chamber can be calculated from

$$W = (2n^2 \cot(\theta) + 2t)\lambda \tag{3.8}$$

where θ is the angle at which the required level of reflectivity is acquired and t is the thickness of the RAM material in wavelengths.

The overall required length of the chamber can be determined via the addition of a number of terms

- $2n^2\lambda$ is the distance between the range antenna and the AUT,
- $n\lambda$ is the minimum sphere the AUT moves through,
- $4\lambda = 2\lambda + 2\lambda$ is the downrange separation from the tips of the RAM from the range antenna and AUT,
- $K\lambda$ is the size of the range antenna and
- $2t\lambda$ is the thickness of the RAM material at both ends of the chamber.

Thus, the required length of the chamber, L , is given by

$$L = (2n^2 + n + 4 + 2t + K)\lambda \quad (3.9)$$

Therefore, from knowledge of the size of the AUT and the minimum sphere, it will move through during the measurement procedure, along with details of the RAM material to be used, and the level of reflectivity that is acceptable the minimum width, height and length of a chamber to be used for far-field measurements can be calculated.

3.5 Alternatives to conventional far-field ranges

3.5.1 Tapered anechoic chambers

From (3.9), it is clear that for long wavelengths the physical size of the chamber required will be very large. As an alternative at these lower frequencies, a tapered chamber can be used. Rather than trying to reduce the reflections from the sidewalls, as is attempted in a conventional rectangular far-field chamber, in a tapered chamber the specular reflection from the sidewalls is used in the illumination of the AUT. The chamber is shaped to enhance the specular reflections from the sidewalls with the generic design based on a number of empirical rules [3]. The generic design of such a chamber is illustrated in Figure 3.10.

- The RAM on the back wall of the chamber should have a reflectivity suitable for the requirements of the quiet zone.
- The rectangular section of the chamber should be cubic with the width (W) and the height, H , defined by

$$W = H = QZ + 4\lambda + t\lambda \quad (3.10)$$

where QZ is the size of the quiet zone, λ is the wavelength and t is the number of wavelengths in the back-wall absorber to provide the required level of attenuation for the quiet zone.

Note: The height of the chamber is required to be the same as its width so that reflections from the walls ceiling and floor will be approximately the same and the

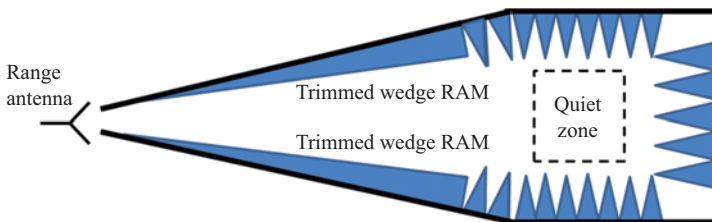


Figure 3.10 Generic tapered chamber design

length of the tapered region should be twice the height of the rectangular section of the chamber.

The size of the test/quiet zone within the rectangular section of the chamber is therefore related to the height of the chamber and the requirement to separate the AUT from the RAM material by 2λ .

Thus, in practice, the requirement to replicate a free space environment merely by placing the antennas sufficiently far apart to produce an approximately plane wave incident on the AUT means that large chambers completely lined with RAM, exhibiting very high levels of isolation from the external environment are required to make far-field antenna measurements indoors.

3.5.2 *The compact antenna test range*

To deal with larger higher gain antennas in the enclosed volumes available in indoor ranges, other methods of producing a plane wave have to be adopted. One of the most successful of these is the concept of the CATR. In a compact antenna test range, as originally patented by Johnson at Georgia Tech in (1967) [4], the test antenna is placed within an anechoic chamber on a positioner as already described. However, in the case of a CATR, the distance between the AUT and the range antenna is not the factor that describes or determines the nature of the field incident on either the AUT or the range antenna. Figure 3.11 illustrates using a simple ray diagram the basic concept of a two reflector CATR, viewed from above.

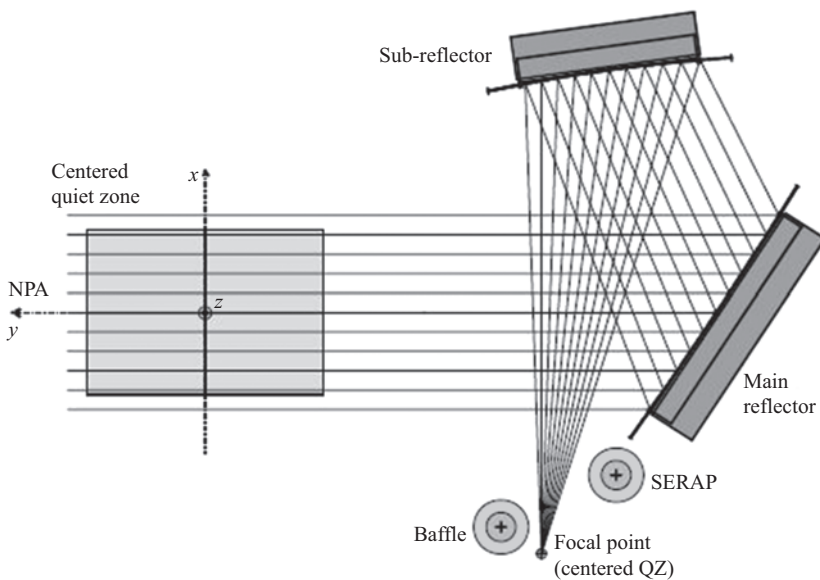


Figure 3.11 *Ray diagram plan view of a twin reflector CATR*

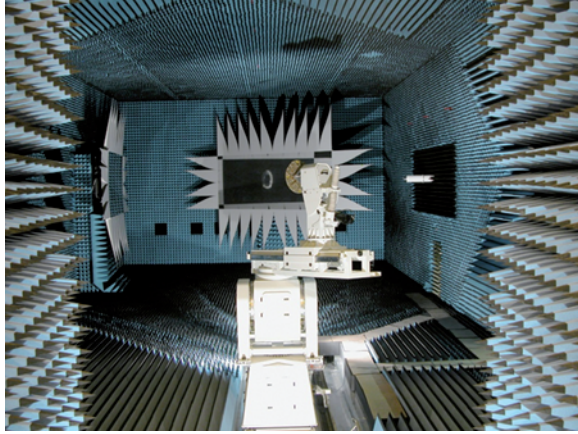


Figure 3.12 View of an antenna mounted on a positioner in a CATR enclosed in a $24\text{ m} \times 14\text{ m} \times 11\text{ m}$ anechoic chamber (Courtesy of Leonardo MW)

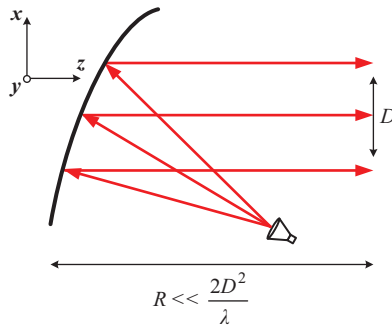


Figure 3.13 Ray diagram plan of single reflector CATR

From the figure, it can be seen that a range/feed antenna placed at the focal point of the range when in Tx will have the wave front that is produced in its main beam sequentially reflected via a main and sub-reflector into an area in the range referred to as the quiet zone. The nature of the curvature and positions on the reflectors as well as the edge geometry of the reflectors ensures that the field produced in the quiet zone is comprised of plane waves. Thus, the CATR produces the type of wave fronts that would be incident on the AUT if it were placed very much further away from the feed than is in fact the case.

Figure 3.13 shows an example of such CATR where, as in Figure 3.12, the plane wave is collimated into the quiet zone, the location of the antenna positioner, placed in the test zone so that the AUT can be tested. This description relates primarily to the action of the AUT in Rx where the range antenna located at the feed point is in Tx. However, it is clear from the figures that the collimating action

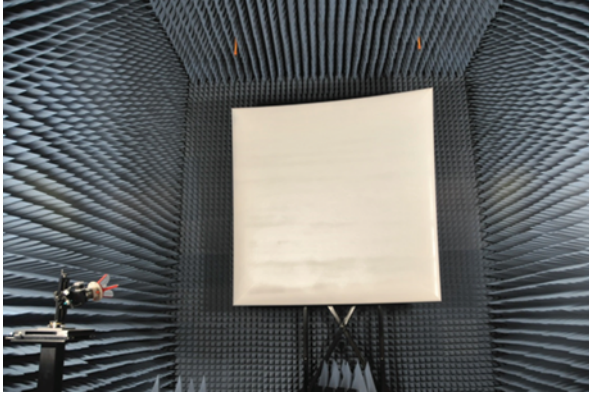


Figure 3.14 Single reflector CATR (Courtesy of NSI-MI Technologies LLC)

of the reflectors would be reciprocated if the AUT were transmitting and the collimated beam would then be incident on the feed point, allowing testing of the AUT in Tx and Rx.

Figures 3.11 and 3.12 show a CATR where the collimated beam is produced via the reflections from a sub-reflector that collimates the beam in the azimuth plane and a main reflector that collimates it in the elevation plane. It is possible to collimate in both planes simultaneously as per the range pictured in Figures 3.13 and 3.14. As will be examined in Chapter 4, the inclusion of more than two reflectors to produce the beam is also possible, and the advantages and constraints associated with the choice of designs, in terms of numbers and types of reflectors as well as the geometrical arrangement of reflectors is discussed and illustrated in Chapter 4.

It can be seen from Figures 3.12 and 3.14 that the edges of the two reflectors are very different. As will be described in detail later in this text, such reflectors are designed to convert the spherical wave-front of a point source into a plane wave, but the finite extent of the reflector means that they will produce diffracted fields from the rims of the reflector. Figures 3.12 and 3.14 illustrate the two main methods adopted to reduce these diffracted fields, which provide the reflectors with serrated edges or rolled edges. The rolled edge following on as an extension from Johnson's original patented CATR concept and the serrated or petal edge being mainly developed by Joy and patented in 1994 [5]. *Note:* unfortunately, for Ed Joy the US government owns the patent.

As with a far-field range, the nature of the chamber needed will enclose such a CATR is directly related to the geometry of the range. The size of the reflector or reflectors is the principal factor that determines the size of the range.

For a single reflector range the length of the range required can be estimated from

$$L = C + \frac{5}{4}F + \frac{1}{2}QZ + (2 + t)\lambda \quad (3.11)$$

where L is the length of the range, F is the focal length of the range, QZ is the size of the quiet zone, t is the number of wave lengths in the thickness of the end wall absorber and C is the clearance factor to allow for the inclusion of the reflector in the chamber.

The required width of the chamber can be estimated from

$$W = WR + (4 + n)\lambda \quad (3.12)$$

where W is the width of the chamber and WR is the width of the reflector.

The height of the chamber is approximated by

$$H = HR + (2 + K + 2n)\lambda \quad (3.13)$$

where H is the height of the chamber, HR is the height of the reflector and K is the clearance factor for the height of the reflector above the floor and space for feeds.

Note if the range antenna for the range was mounted on the wall a coverage factor $K1$, would need to be utilised in the width calculation and removed from the height calculation.

For a twin reflector range, K plus an additional secondary coverage factor to take account of the secondary reflector would need to be added to the width or height calculation.

A similar collimating effect can be achieved with a lensing structure; although the nature of lenses that operate at microwave frequencies means that lens-based ranges tend to have much lower realisable bandwidths than those assembled from reflectors. Additional difficulties in manufacturing physically large structures with the required levels of isotropy and homogeneity also limit the effective utilisation of lensing compact ranges.

However, overall this means that the effect of introducing a collimating structure (e.g. reflectors, lenses or other collimating methods that will be discussed in Chapter 5) into an isolated anechoic chamber allows the characterisation of antennas with near-field/far-field interface distances that are much larger than the actual dimensions of the chambers. Thus, the CATR provides the capability of making measurements on a variety of antennas that would normally require very long-range lengths in conventional far-field ranges.

3.5.3 Indirect measurements

In Section 3.1, it was explained that in order to quantify the main antenna characteristics that are of importance ‘the two antennas will have to be moved and realigned relative to each other to make the full range of measurements possible. Or some form of measurement process that predicts their response if they were to be moved relative to each other needs to be employed’. So far, our discussion has only involved direct measurement methodologies where the antennas have been moved and realigned relative to each other so that a plane wave is incident on either the AUT or the range antenna dependant on which antenna is in Tx.

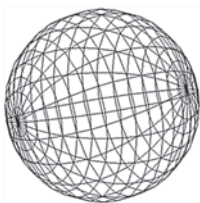
In fact, other indirect methodologies exist whereby an AUT can be characterised when no actual plane wave is present. These methods originally pioneered in the so-called swimming pool in the basement of Electronics Research Building of the Georgia Tech. Engineering Experimentation Station [4] involves the synthesis of a plane, circular or cylindrical wave response from a sequence of other measurements. Measurement methodologies that are based on the synthesis of these wave responses are collectively referred to as scanning measurements.

In Section 2.6, it was shown that if we can determine the near-field on a surface close to a radiating antenna we can subsequently determine the radiated far-field. We shall, in subsequent chapters, see in detail the mathematical processes by which these transformations can be undertaken in the most efficient way and consider the limitations imposed by scanning measurement techniques and how such limitations can be mitigated. In this section, we consider the basic geometries required for measuring the near electric field to provide a data set that can be processed to predict the far-field response of AUTs.

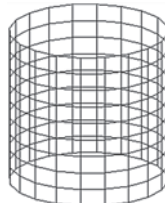
Three commonly employed coordinate systems are utilised for taking near-field antenna measurements: spherical, cylindrical and planar. These three geometries are generally considered preferable since not only is the vector Helmholtz equation separable in each of these systems, but also, in practice, positioner sub-systems that employ them can be conveniently constructed. These system geometries are shown schematically in Figure 3.15.

In principle, spherical, cylindrical and planar techniques are endeavouring to derive a complex vector field function at a large distance from the antenna, via the sampling of similar complex data over a well-understood surface at a much smaller distance. This facilitates the testing of electrically large antennas in a controlled indoor environment.

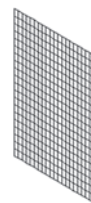
In all cases, the acquisition of the near complex vector field is accomplished by placing the range antenna, which is usually described as a probe in near-field measurements, at a particular position and polarisation, pointing in a particular direction and allowing the electric field which surrounds the probe to generate an observable excitation current. The difference in potential between the probe and a reference is sampled in phase and at quadrature. Provided that two such orthogonal



Spherical near-field
acquisition geometry



Cylindrical near-field
acquisition geometry



Planar near-field
acquisition geometry

Figure 3.15 Near-field acquisition surface geometries

complex voltages are sampled over a well-defined surface at regular intervals, the principal of modal expansion can be utilised to determine the amplitudes and phases of an angular spectrum of plane, cylindrical or spherical waves. This enables the computation of the electric and magnetic fields at any distance from the AUT, and hence the computation of the fields when infinitely far removed from the radiator, which results in a far-field vector pattern.

Despite the obvious similarities between the theoretical descriptions at the generic level, the differing geometries result in a significant divergence in the specific implementation of each measurement technique.

3.5.3.1 Spherical near-field ranges

In order for the spherical near-field range, a development of the original ‘two dimensional phase centre range’ [6] to characterise the propagating near-field component, a test probe is held at rest, while the AUT is nodded in ϕ and rotated in θ . Here, θ and ϕ are conventional spherical coordinates. Figure 3.16 illustrates how rotation of the AUT relative to the probe using commonly used antenna positioners can be used to produce measurements over a spherical surface. Thus, the rotational movements of the AUT effectively result in the path of travel of the probe describing a spherical surface that is attached to the AUT.

From a measurement of the complex voltages acquired on this spherical surface, as will be described in detail in Chapter 8, a full prediction of the far-field characteristics of the AUT can be obtained. Pictured in Figure 3.17 is an example of such a range.

Similar considerations that relate to the depth of RAM on the end walls in wavelengths, te , the space needed for the probe installation, PD , and the minimum

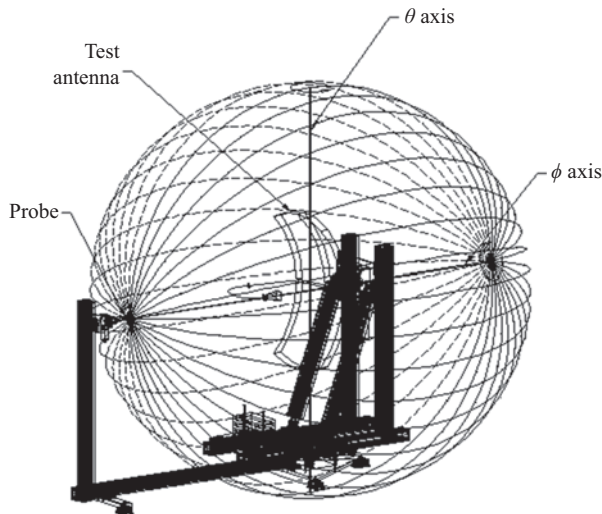


Figure 3.16 Spherical near-field antenna measurement configuration

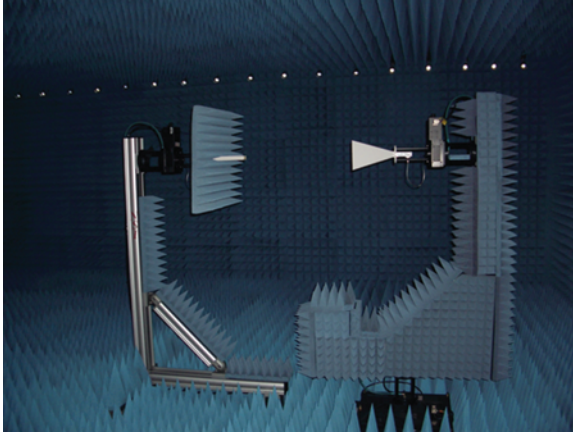


Figure 3.17 Practical implementation of spherical scanning (Courtesy of NSI-MI Technologies LLC)

sphere through which the antenna moves through in wavelengths, n , apply for the dimensions of the chamber required to make spherical near-field measurements. Assuming 4λ is the distance between the probe and the AUT the minimum length, L , for a chamber can be calculated from

$$L = PD + (n + 6 + te)\lambda \quad (3.14)$$

For the chamber width (W)

$$W = (n + 4 + ts)\lambda \quad (3.15)$$

where ts is the depth of the RAM on the side walls in wavelengths.

In estimating the height required for the chamber, H , the dimensions of the positioner holding the AUT, HP , must also be taken into consideration giving

$$H = HP + (n + 4 + ts)\lambda \quad (3.16)$$

From these considerations of RAM thicknesses required, space for the AUT, probe maximum dimensions and a realistic estimate of probe AUT displacement, the dimensions required for chambers deploying spherical near-field measurement equipment can be estimated. However, these calculations will give the minimum sizes and increased dimensions may well be useful in terms of installation of antennas and other equipment in the chamber.

3.5.3.2 Planar near-field measurements

The implementation of the geometry of planar near-field scanner, PNFS, does not involve the movement of the AUT at all. To accomplish the near-field data acquisition in PNFS, it is the probe that is moved (scanned), across the aperture of the AUT. This is illustrated in Figure 3.18 where it can be seen that by moving the

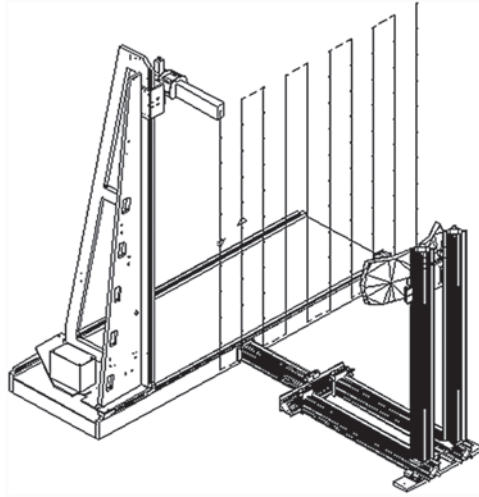


Figure 3.18 Planar near-field range configuration

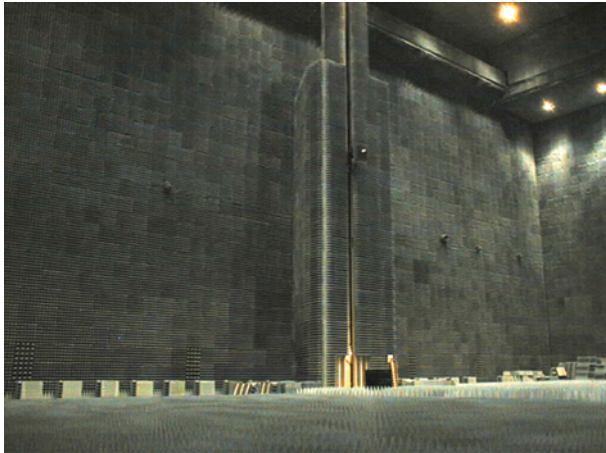


Figure 3.19 Practical implementation of planar scanning

probe on a plane relative to the AUT, near-field data in the form of complex voltages can be obtained that can, as will be explained in subsequent chapters, be used to provide a prediction of the far-field characteristics of the AUT.

Pictured in Figure 3.19 is an example of such a range showing the probe mounted on carriages that allows its movement across, x direction, and up and down, y direction on a plane.

The geometry of a chamber designed for use with a planar scanner is primarily defined by the extent of the scan plane and the angle out to which the pattern is required along with the spacing of the AUT from the scan plane. The relationship between these variables is illustrated in Figure 3.20.

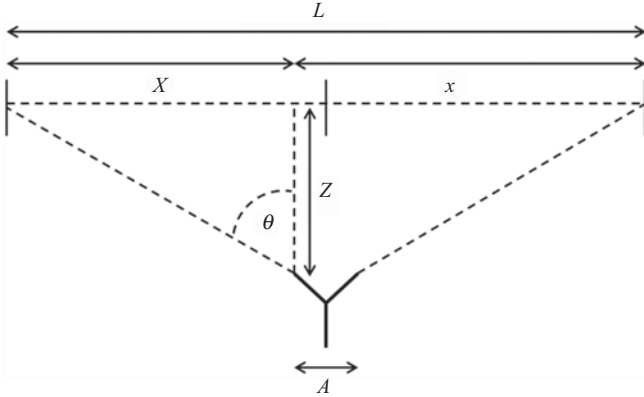


Figure 3.20 Geometry of a planar near-field scanner

If the displacement of the AUT from the plane Z is defined in numbers of wavelength, i.e. $Z = k\lambda$ and the size of the AUT is also defined in terms of the wavelength, i.e. $A = n\lambda$, then the extent of the scan plane required for and pattern prediction out to angle θ is

$$L_p = (n + 2k \tan(\theta))\lambda \quad (3.17)$$

Allowing 2λ as a separation between tips of the RAM material and the scanner with an additional clearance factor of C_s to take account of the scanner structure out with the plane the width required for the chamber, W , is

$$W = L + (4 + 2t)\lambda + C_s \quad (3.18)$$

The length required for the scanner chamber, L_c , can be calculated from details of the depth required for the scanner structure, D_s , and the depth of the AUT (Da); thus, the minimum length of the range can be defined as

$$L = D_s + Da + (4 + k + t)\lambda \quad (3.19)$$

Additionally, a minimum chamber height can be seen to be comprised of factors that relate to the vertical size of the scan plane, L_v , the height of the scanning probe, H_p , at the bottom of the scan plane

$$H = L_v + H_p + (2 + ts)\lambda \quad (3.20)$$

3.5.3.3 Cylindrical near-field measurements

As can be seen in Figure 3.21, the cylindrical near-field scanning technique utilises a hybrid measurement configuration in which the AUT is rotated in azimuth, whilst a scanning probe is moved linearly in z . Thus, data comprising complex voltages can be acquired on a cylindrical surface and then

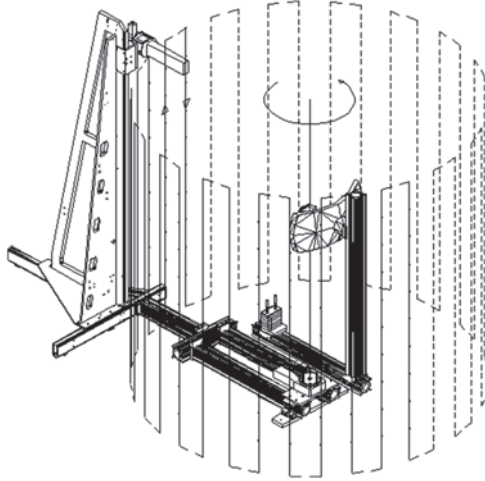


Figure 3.21 Cylindrical near-field configuration

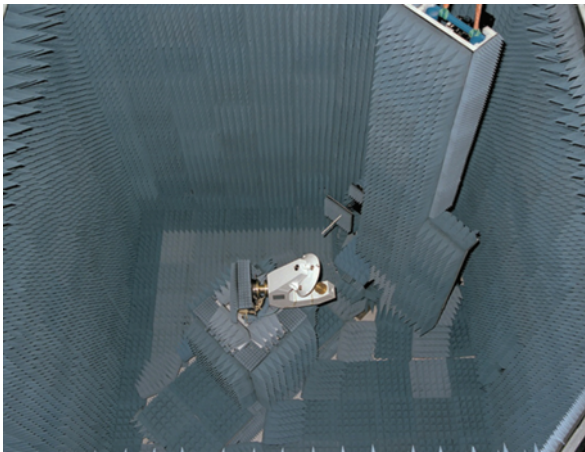


Figure 3.22 Practical implementation of cylindrical scanning (Courtesy of NSI-MI Technologies LLC)

subsequently processed to provide a prediction of the far-field characteristics of the antenna.

Pictured in Figure 3.22 is an example of such a range which shows the AUT mounted on a positioner that can rotate beside the probe, mounted on a carriage that can move linearly up and down (in the y direction defined in the range).

The arrangement of RAM material and the chamber design required for such a cylindrical system can be readily seen to be a combination of the design requirements for a planar and spherical test ranges.

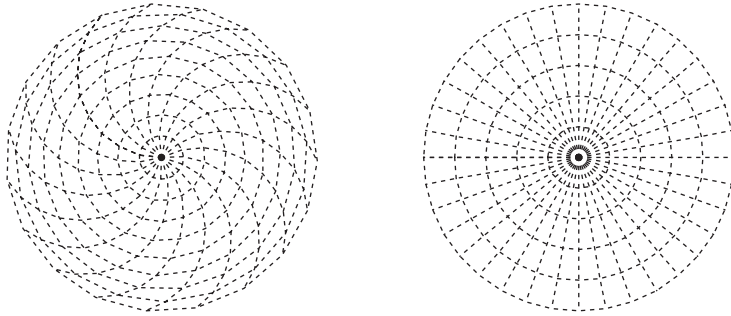


Figure 3.23 Plane bi-polar and plane polar data acquisition geometries

3.5.3.4 Other geometries for scanning measurements

Planar, cylindrical and spherical are the most widely used configurations for near-field scanning measurements as they correspond to realisable antenna positioner combinations and, as will be described in detail in the following chapters, are suitable for the development of transformation algorithms that allow ease of prediction of the far-field parameters from the measured near-field data. Other geometries have been used, and a combination of antenna characteristics and range capability can make some of these other configurations preferable.

The data required in planar measurements could, as per Figure 3.18, be acquired using a raster or rectilinear scan. Figure 3.23 shows two other geometries that can be used in the acquisition of data, plane bi-polar and plane polar.

As will be explained in Chapter 6, both of these geometries have advantages and limitations. Additionally, using these measurements, geometries data acquired in more than one scan of an antenna can be used to predict the far-field characteristics of the AUT, this will be elaborated on in Chapter 12 [7]. Again, as will be further elaborated on in Chapters 6 and 12, individual scans acquired on tangential or angularly displaced planes can be used to provide accurate far-field predictions of antenna performance [8]. So, these alternative measurement geometries may have advantages over conventional rectilinear raster scanning in certain circumstances.

Other geometries not associated with these conventional scanning geometries are also possible, e.g. Chapter 7 will describe in detail cylindrical measurements, and also the measurement schemes that rely on data being acquired on conical and conic frustum surfaces [8,9]. Lastly, Chapter 9 will develop more general measurement techniques for processing near-field data acquired over non-canonical surfaces.

All these measurement techniques therefore depend on the acquisition of data at fixed points relative to the AUT from which via a subsequent processing stage the response that the antenna would make in a far-field data acquisition can be predicted. This means that the positions at which the data must be obtained must again be defined rigorously and the mechanical systems that move and rotate the probes and AUTs must be extremely accurately, precisely and sensitively

controlled. The requirement in all these different techniques for accurate sampling of the near-field characteristics on a surface at a sampling interval not more than $\lambda/2$ at the highest frequency to be measured means that there are certain generic similarities between all the near-field techniques.

3.6 Antenna test range RF test equipment

The requirement for isolation and RAM materials in the range is based on the presence of RF radiation in the range and it is the ability of the AUT and the antenna test range antennas to couple via this RF radiation that is actually tested in the range. Thus, the generation control and measurement of this RF power flux as a function of the two antennas displacement and orientation relative to each other is fundamental to the action of the range as a test facility. Therefore, a sensitive, accurate, precise RF system of the same nature as that shown in Figure 3.24 will be required in the range to provide the basis of the measurements.

As can be seen from the figure, a typical RF test system is essentially a two-arm microwave interferometer where a range antenna and AUT are inserted into the test arm. In practice, this is realised with a standard vector network analyser (VNA) measurement system controlled via a central computer. The configuration shown could be based around a VNA operating in remote mixing mode where the VNA will act as the receiver and may also act as one of the sources. For physically small systems, it is possible to work without remote mixing if cables are short as remote mixing is merely a way of redistributing the receiver within the chamber to minimise cable losses and improve the system dynamic range.

Although a swept signal generator can be used for local oscillator (LO) and RF sources, it is more common to use a synthesiser as a signal source. The RF output from this source is fed via a (typically) 20 dB directional coupler to the transmit port of the AUT usually using coaxial cable or waveguide. The test mixer is connected to the single port of the range antenna by means of a short coaxial cable or waveguide and is often padded with a 10 dB attenuator to reduce the effect of multiple reflections between the range antenna and the mixer using the LO cable. This mixer is fed with a LO signal, so that an intermediary frequency (IF) can be passed to the receiver.

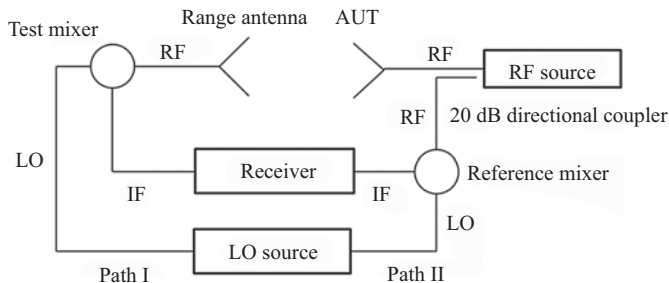


Figure 3.24 The fundamental basis of range RF system

Note: A VNA combines the sources, down converter and receiver in a single instrument.

When using a swept LO source this is phase locked usually by means of a reference signal. Using a synthesiser for the LO is more popular nowadays and the external clock option permits the source synthesiser clock to act as the master for both synthesisers. Occasionally, third, fifth or even seventh harmonic mixing is utilised to reduce the attenuation resulting from an electrically long LO test path. However, this is undesirable as the sensitivity of the RF system is inevitably degraded, e.g. utilising third harmonic mixing can result in a reduction in the sensitivity of the receiver of 20 dB. For high microwave frequencies and millimetre wave operation, a more complex configuration is often necessary as will be explained in the following text.

The reference mixer similarly mixes down the reference RF signal obtained from the directional coupler. The lengths of the two LO paths are usually balanced; i.e. path I and path II are of equal length to minimise the impact of phase variations resulting from thermal fluctuations and from small frequency changes in the RF source. The concept is that if the two path lengths are the same, the relative phase variation between the respective RF paths will be zero, irrespective of how the temperature fluctuates within the facility.

One arm of the interferometer contains the range antenna and the AUT and the other arm of the interferometer is a reference path. Provided any actual physical movement of the AUT does not alter or degrade the fidelity of the Tx/Rx signal, then any variation in the measured signal should be directly related to the extent to which the two antennas couple as a function of angle and polarisation.

To allow this overall measurement concept to be undertaken in antenna test facilities, a variety of specific instruments will need to be specified, acquired and integrated to allow the development of effective measurement procedures.

3.6.1 RF instrumentation for test ranges

For simple facilities designed to undertake antenna measurements, there will usually be requirements for

- Receivers
- Sources
- Mixers
- Multipliers
- Amplifiers
- Probes
- RF cables
- Couplers
- Switches
- Attenuators

These are described further in the following sections.

3.6.1.1 Receivers and sources

The important instrument characteristics related to the requirements for a receiver relate to

- Noise floor
- Sampling speed
- IF bandwidth
- Compression level

All of these characteristics will need to be taken account of in defining the requirements for any test range. Figure 3.25 illustrates the input power in dBm and the output response along with the important features of the receiver response (dynamic range 1 dB compression point) that need to be considered.

As described in Chapter 1, not only the amplitude of the voltage produced by the coupling, but also its phase is fundamental to the antenna measurement process. This is usually accomplished by the use of a synchronous detector in the receiver, sometimes referred to as quadrature channel detector, quadrature detector, I/Q demodulator or a coherent detector. Figure 3.26 illustrates that very basic concept of such a detector, where the measured signal F_{sig} is mixed with oscillator signal, F_{os} using a 90° phase change to provide the quadrature data.

Such a detector used in concert with the rest of a receiver can produce the required data for the characterisation of antennas.

For sources overall available bandwidth, switching speed, stability, harmonics levels and noise performance are the important characteristics to be considered.

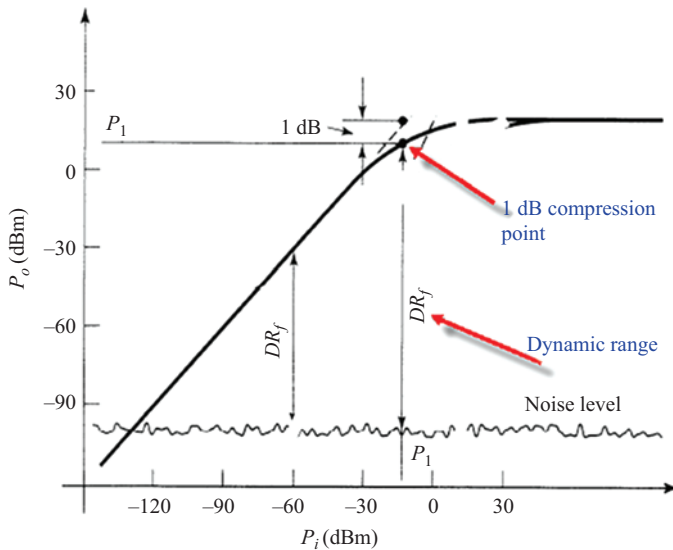


Figure 3.25 Important receiver characteristics

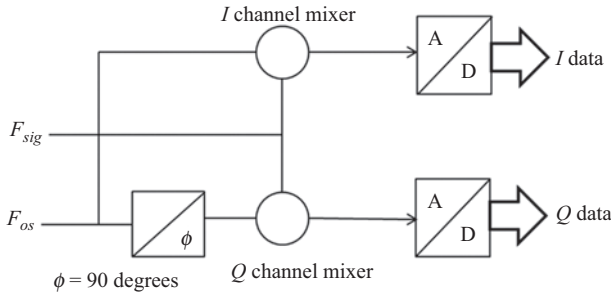


Figure 3.26 Synchronous/coherent detection

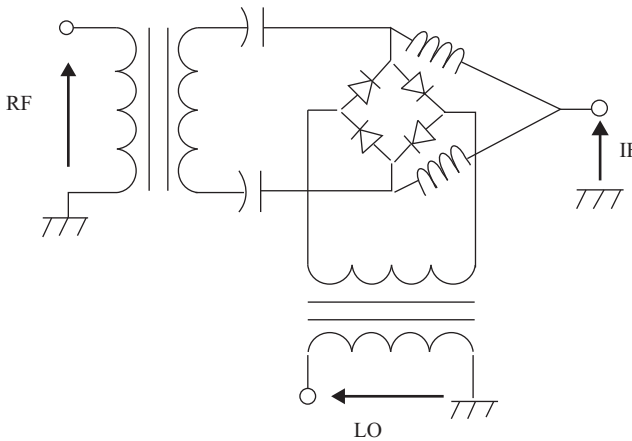


Figure 3.27 RF to IF mixer configuration

Down conversion from the RF frequency may also be required giving a more manageable (in terms of measurement and system loss) IF frequency.

3.6.1.2 Down conversion mixers and up conversion multipliers

Antenna measurements often involve high levels of free space loss associated with the movement of RF signals through phase stable cabling that is invariably relatively high loss at RF frequencies. Therefore, down conversion to a much lower loss IF frequency is a practice often adopted in antenna test ranges.

The most common strategy employed to allow this down conversion to an IF is the inclusion of remote mixers as shown in Figure 3.24. A direct sampling at the RF frequency is possible; however, at higher microwave frequencies, the losses in the cabling in the RF system will be such that the inclusion of remote mixing in the system will become necessary.

Essentially, a mixer is a set of diodes, embedded in a configuration of biasing circuitry as shown in Figure 3.27.

A monotonic RF signal as per Figure 3.28 is the RF input.

An LO frequency, as per Figure 3.29, that is close to the RF frequency is also input. This LO signal is heavily compressed so that it is non-linear and is over-driven to the extent that it is close to a square wave.

The bias on the diodes in the mixer is switched by the incoming RF with a sampling rate determined by the biasing produced by the highly clipped LO signal acting as a square wave switching control.

The resultant IF output is as per Figure 3.30. This waveform has a linear envelope that is at a much lower frequency than the RF input. If subsequent high-frequency filtering is implemented on this signal, it will produce a linear lower frequency output that will contain all the essential signal information embedded in the original RF signal. However, as a result of its much lower frequency, it will suffer far less loss in the RF cabling.

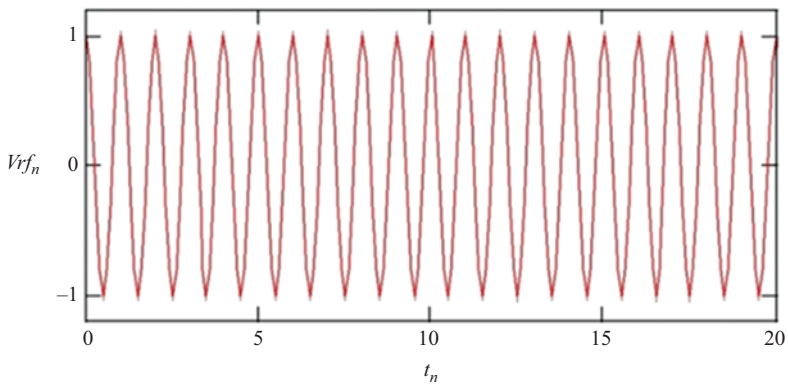


Figure 3.28 RF mixer input

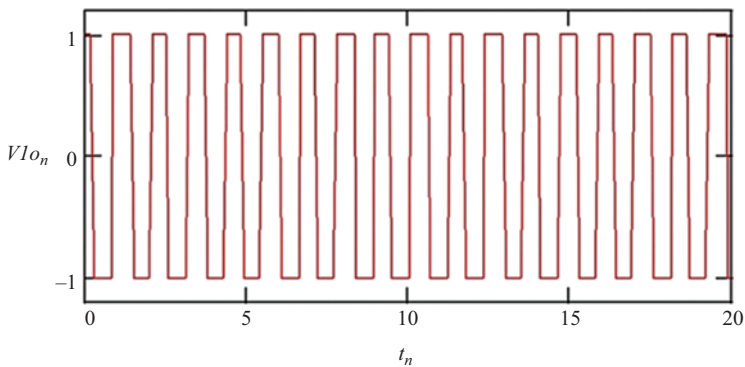


Figure 3.29 LO mixer input

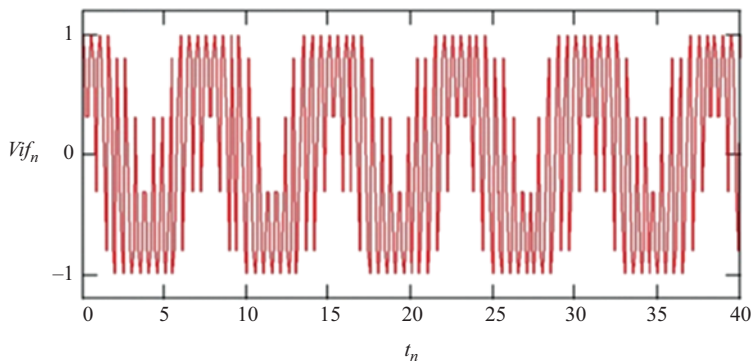


Figure 3.30 Unfiltered IF output

The inclusion of mixers to produce a distributed sub-system where cable losses are reduced to a minimum is a common solution for antenna test ranges where noise levels need to be minimised and dynamic range needs to be optimised. This is especially relevant for electrically large systems since cable losses become prohibitive and the locations of the components comprising the RF subsystem are critical. By using remote mixers, the use of lower frequency cables with lower loss becomes feasible and this approach dramatically increases the available power level at the transmitting antenna and the sensitivity of the receiver. Additionally, by utilising remote frequency conversion and providing frequencies in the interferometer arms that are much lower than the RF frequency, existing lower frequency instrumentation can often be used.

There are limitations as to the extent to which frequency conversion can be accomplished using just a distributed sub-system. If there is a requirement to move to higher frequencies in the millimetre wave range, other solutions will be required. The inclusion of multipliers in the system allows the use of conventional RF measurement instrumentation that may only be instrumented, for example, to only 18, 26 or 40 GHz, to make measurements at much higher frequencies.

RF multipliers are devices that generate an output signal that is a harmonic product of the input frequency and as such can be used close the point of transmission to up convert microwave frequency signals.

Such frequency multiplying modules can have implications on the mechanical design on measurement systems, and Figure 3.31 shows that the additional mass and volume required to implement this solution does impact the design and specification of measurement systems.

Note: Figure 3.31 shows details of a probe-type range antenna and frequency multiplier modules that are deployed in a near-field-scanning configuration.

While the use of down conversion to an IF frequency and multiplication will reduce the levels of loss in the system, the requirement to Tx and Rx RF frequencies in the system will often mean that amplification is required at points in the measurement system.

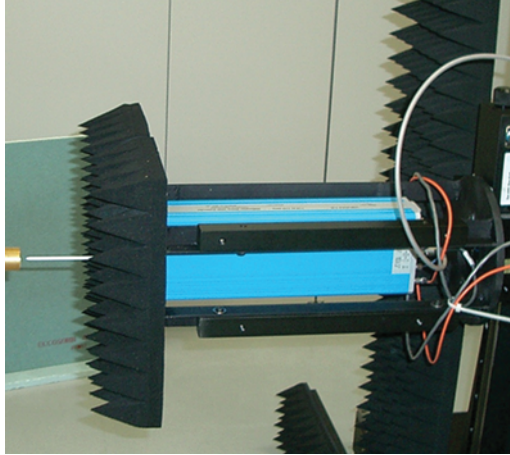


Figure 3.31 Frequency multiplier modules mounted behind a probe-type range antenna on a range antenna carriage (Courtesy of NSI-MI Technologies LLC)

3.6.1.3 Amplifiers

The most important characteristics of such an amplifier are gain and its noise figure. The gain is the ratio of the input to output RF power where a maximum input power that will invoke a linear response is defined. With an input power above this level, the amplifier will be in compression, and the response will no longer be linear. In many RF systems, this non-linear condition is the condition in which the amplifiers are used. In this case, it will be necessary to ensure that the input power is greater than the linear threshold and the output power will be the maximum that the amplifier is specified to emit.

The noise figure, F , is a measure of the degradation of the signal to noise ratio between the input and output of the amplifier.

This is defined as

$$F = \frac{S_i/N_i}{S_o/N_o} \geq 1 \quad (3.21)$$

where S_i is the input signal power, S_o is the output signal power, N_i is the input noise power and N_o is the output noise power.

The noise figure of such an RF component is sometimes defined in terms of an equivalent noise temperature, T_e , rather than a noise figure. The relationship between the noise figure and the equivalent noise temperature is

$$T_e = (F - 1)T_o \quad (3.22)$$

where T_o is 290 K.

3.6.1.4 Probes

In earlier sections, it was stated that in near-field measurements the range antenna is usually described as a probe. This is because in all near-field measurements the range antenna/probe is required to have certain common desirable characteristics.

The near-field measurement technique places several requirements upon the characteristics of the scanning probe. Typically, these are

1. Time-invariant gain and mechanically rigidity.
2. No pattern nulls in the forward hemisphere, i.e. low directivity, i.e. electrically and physically small.
3. Wide bandwidth.
4. Low scattering cross-section and reflection coefficient – i.e. well matched with a small return loss. Unfortunately, this requirement cannot usually be satisfied over a wide bandwidth.
5. Good polarisation purity.
6. Good front to back ratio to minimise sensitivity to probe placing and multiple reflections. This is at odds with item 2.

Typical near-field probes can include cylindrical waveguide, rectangular waveguide, corrugated horns and pyramidal horns. Two common probe antennas are the dual-port choked cylindrical waveguide probe and an open-ended rectangular waveguide probe. Figure 3.32 shows rectangular waveguide probes with one mounted protruding from an attached RAM.

One of the most significant contributions, albeit an extremely systematic one, to the overall error budget of conventional near-field measurement techniques is inaccuracy in the characterisation of the near-field probe. Conventionally, as the measured main-component pattern is proportional to the main-component range antenna pattern, errors in the corrected main polarisation pattern arising from probe characterisation errors will be a one-to-one mapping. That is, for near-field measurements, they have the same magnitude and direction as the errors in the probe pattern.

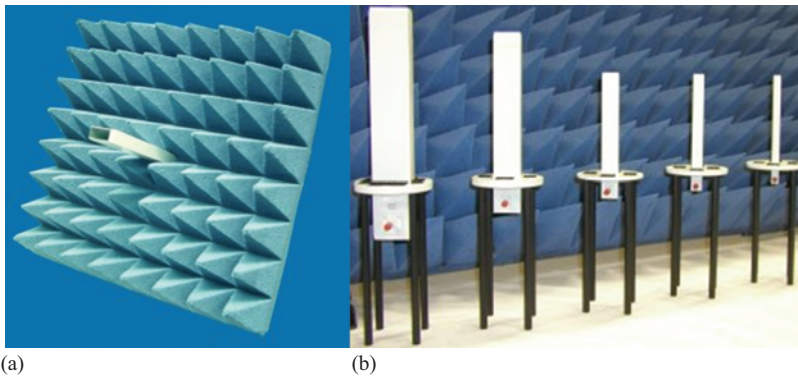


Figure 3.32 *Near-field scanning probes (Courtesy of NSI-MI Technologies LLC). a) shown with absorber collar and b) a family of probes shown without the absorber collars*

A generalised three-antenna technique is usually used for precise calibration of the on-axis gain and polarisation of a near-field probe, and the resulting gain values can be generally certified to have an uncertainty of approximately 0.10 dB [10]. Once known, the probe gain can then be used to determine the gain of the AUT as part of the near-field measurement process.

3.6.1.5 Couplers

Microwave couplers are devices that divert a fraction of the signal on one transmission line to another transmission line. The signal exiting the output port of the first transmission line is called the ‘through’ (sometimes called the ‘direct’) signal since it is directly connected to the input port and the signal exiting the other transmission line is called the ‘coupled’ signal. If the coupled signal is traveling in the same direction as the through signal, the coupler is called a ‘forward-wave’ coupler. If in opposition, it is called a ‘backward-wave’ coupler. Because these coupled signals are related to the direction of the through signals, couplers are called directional couplers.

Note: if the outputs of the coupled and through ports are equal in amplitude, the coupler is often referred to as a hybrid coupler.

In antenna measurements, a coupler is used to couple a certain portion of the Tx signal with this coupled portion being used as the reference path through the interferometer.

Such couplers are four port devices, where port 1 is the input port, port 2 is the output/through port, port 3 is the coupled port and port 4 is the isolated port. Ideally, power into port 1 will only appear at ports 2 and 3, with no power at port 4, but in real couplers, some power leaks to port 4. For an incident signal at port 1 of power P_1 (and output powers P_2 , P_3 and P_4 at ports 2, 3 and 4, respectively), then

- Insertion loss (IL) = $-10 \log(P_2/P_1) = -20 \log(|S_{21}|)$
- Coupling (C) = $-10 \log(P_3/P_1) = -20 \log(|S_{31}|)$
- Isolation (I) = $-10 \log(P_4/P_1) = -20 \log(|S_{41}|)$
- Directivity (D) = $-10 \log(P_4/P_3) = 20 \log(|S_{31}/S_{41}|)$

Additionally, phase unbalance and amplitude imbalance between the coupled port and the through port over the operating frequency band. Both of these characteristics can be used to define the bandwidth of the coupler.

The choice of coupler to be used in a measurement system will depend on the relative signal levels required and the bandwidth over which it will be used.

3.6.1.6 Switches

Considerations related to the switching speeds that may be required limits the choice of switching mechanism in RF measurement systems. MEMS are generally considered too slow for such systems so FETs and pin diode switches are usually adopted.

Frequency considerations can be important in deciding which variety of switch to use in the measurement system. PIN diodes have a lower frequency limitation due to carrier lifetime meaning that they are ineffective at lower frequencies and

essentially will not operate at all for DC. However, PIN diodes have a significant high-frequency advantage over FETs at high frequencies because of their low off-state capacitance, C_{OFF} , for a given on-resistance, R_{ON} .

The microwave industry uses a figure of merit, FOM , to rate the switching characteristics of different switch elements. Multiplying R_{ON} times C_{OFF} gives a number with units in seconds. This is usually quoted in terms of frequency as

$$FOM = 1/2\pi C_{OFF}R_{ON} \quad (3.23)$$

The higher the FOM , the easier to achieve any required bandwidth. Typical values for a PIN diode, off-capacitance can be of the order of 50 fF, with on-resistance as low as 1.7 Ω at 20 mA. The FOM for such a PIN diode would be 1 872 GHz. For a typical FET used in a switch, an on-resistance of 1.5 Ω and an off-capacitance of 400 fF giving a FOM 265 GHz.

A useful ‘rule of thumb’ that can be adopted to ensure that your switch can cope with your required bandwidth is, if you divide the switching FOM by 10, this will give you a good estimate of the highest frequency that the device can be made to perform as a switch. As can be seen, using this rule, a typical PIN switch can operate to frequencies much higher than a typical FET switch.

FETs can have advantages in terms of control and isolation but in measurement systems, switching speed is the overriding concern so PIN diode switches are usually adopted for such systems.

3.6.1.7 Attenuators

Attenuators are passive resistive elements that are designed to reduce the gain. They can be added to the RF path in a measurement system if there is a requirement to reduce signal strength at any point, e.g. to reduce the signal strength to ensure that amplifiers are working in their linear region and their output is not compressed.

Adding an attenuator in the RF path in front of an amplifier will adversely affect the noise figure, and care must be taken if adding it after an amplifier to ensure that the attenuator can cope with the amplified signal power.

Therefore, care must be exercised in placing attenuating elements in the RF path to minimise noise and ensure linearity in response is conserved [11].

3.6.1.8 RF cables

The primary concerns that relate to cables in RF systems are ohmic and dielectric loss combined as insertion loss and additionally return loss. High frequency cables have considerably more loss than 18 or 20 GHz cables; hence, the requirement for IF frequencies. Figure 3.33 illustrates the insertion loss per unit length of typical cables as a function of frequency for typical cables.

Return loss in cabling is directly related to the types and quality of the connectors used so to ensure low return loss certain varieties of connectors are more suited to limited ranges of frequencies. Figure 3.34 illustrates the frequency ranges that are applicable to specific types of connector.

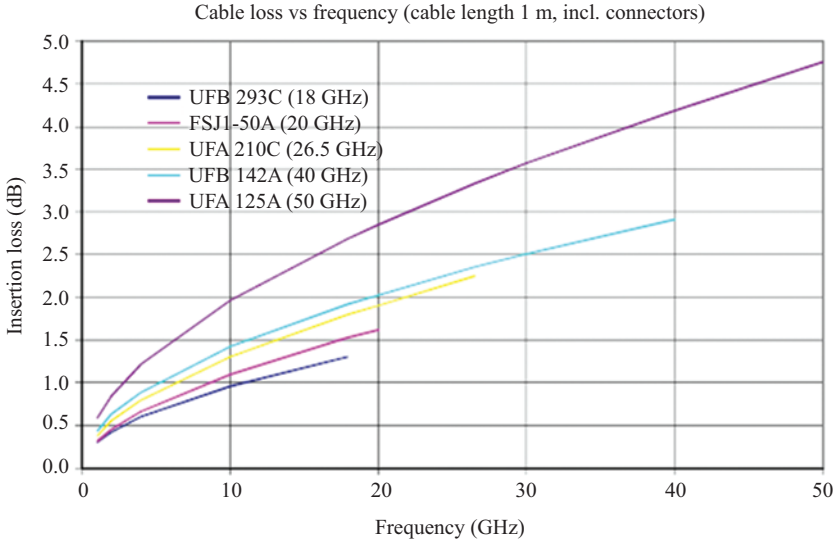


Figure 3.33 Cable loss vs frequency (cable length 1 m, including connectors)

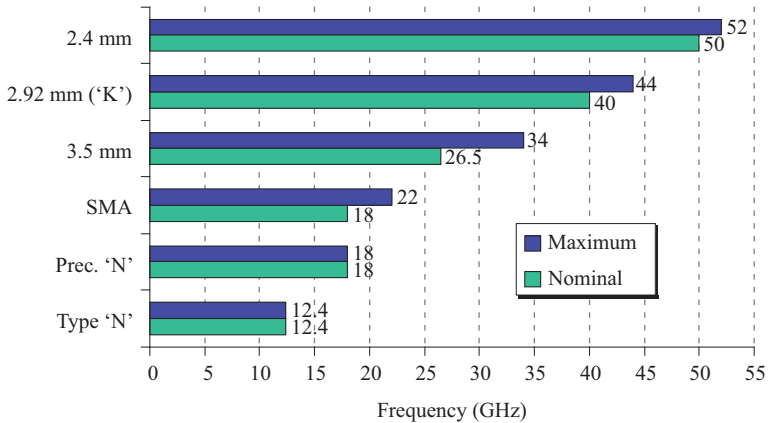


Figure 3.34 Connector frequency ranges

3.6.1.9 Integrated facility instrumentation

A clear understanding of the types of measurements that are to be undertaken is required to specify the requirements for the RF instrumentation to be used in a measurement facility and the exact nature of these instruments deployed will mirror this requirement. Figures 3.35 and 3.36 illustrate a typical microwave measurement

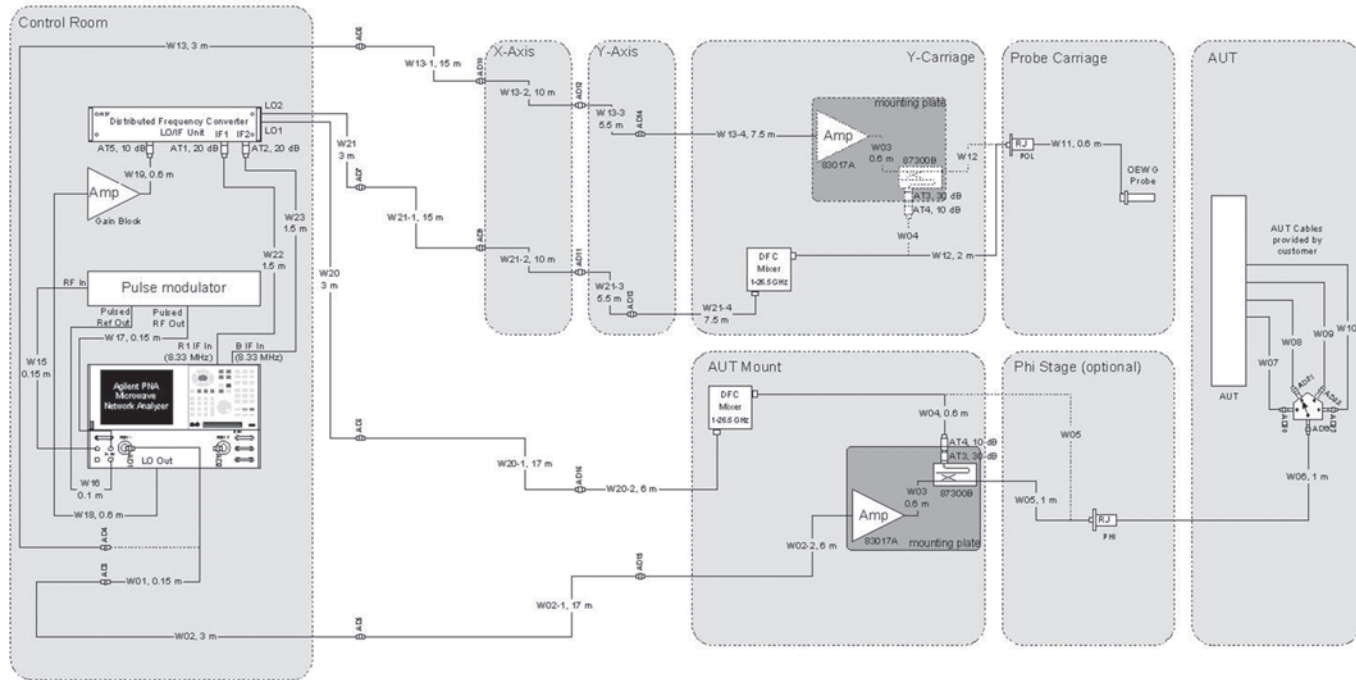


Figure 3.35 Typical microwave measurement facility RF subsystem (Courtesy of NSI-MI Technologies LLC)

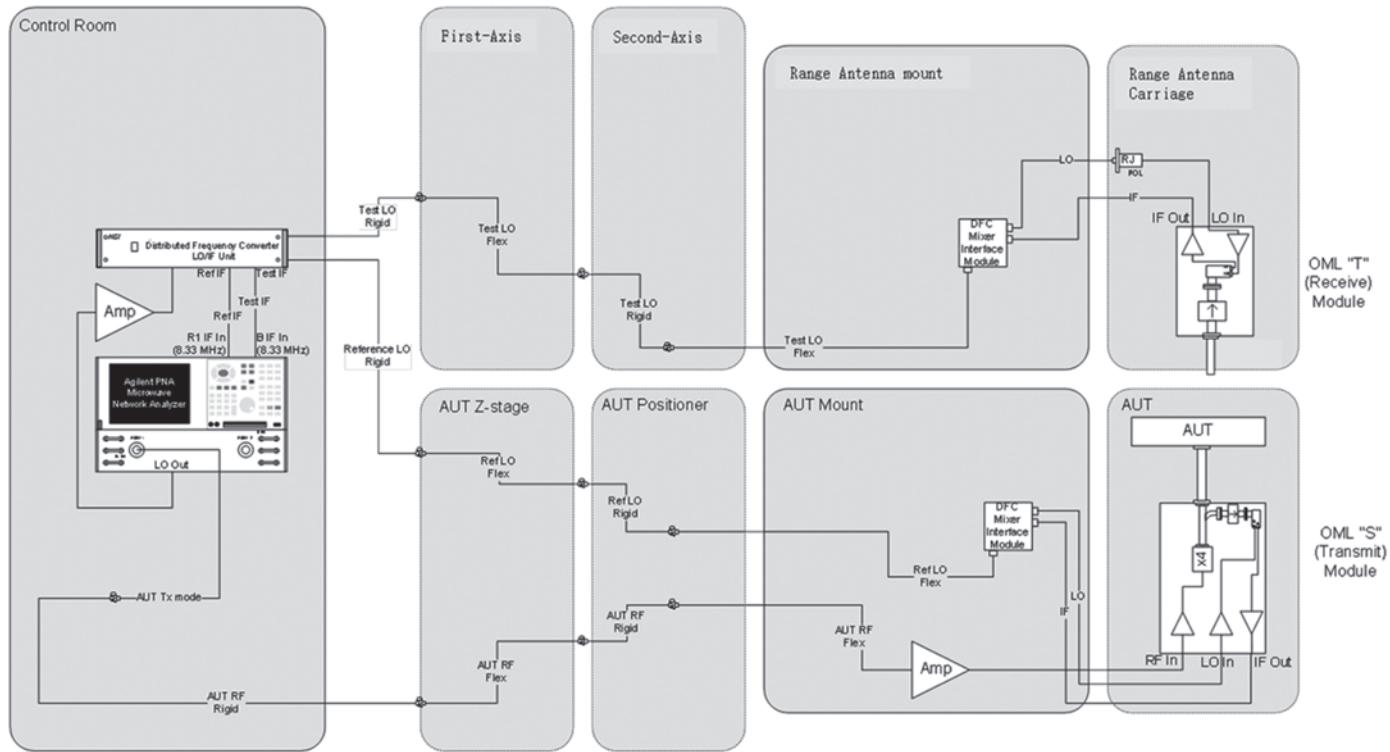


Figure 3.36 mm wave measurement configuration based on frequency multipliers (Courtesy of NSI-MI Technologies LLC)

facility set up and a millimetre wave measurement configuration based on frequency multipliers. Both of these configurations illustrate a type of design process that can be adopted in the specification of measurement facilities by dividing the requirement for the overall RF system into compartments related to addressing specific areas of the design.

3.6.2 *Generic near-field antenna measurement process*

The measurement of the antenna radiation pattern relative to the antenna mechanical interface necessitates the accurate determination of the alignment of the mechanical interface, which is associated with the antenna, relative to the range co-ordinate system during the acquisition of the near-field data. The known alignment is then compensated for during the transformation process. Once the alignment data has been captured, the near-field scanning process is performed. Following this, the measured near-field data is processed to yield corrected far-field results. These results are typically presented in Ludwig's third (co-polar and cross-polar) polarisation basis [12,13] referenced to a specified *electrical bore-sight system* (the system which defines the co-polar direction) which may or may not be coincident with the *antenna plotting system* (the output system in which the field quantities are tabulated). The measurement of absolute gain is a topic in itself, and is an area that will be described in later chapters. Typically, in near-field measurements, the substitution method using a calibrated standard is implemented. Figure 3.37 illustrates schematically the general near-field measurement process that is common to all near-field measurement procedures in the form of an overview.

Near-field measurements present other difficulties. The sampling of data over a finite measurement surface, as in planar and cylindrical near-field measurements results in the failure to sample a portion of the propagating near-field. This introduces truncation errors in the resulting far-field data that restricts the measured antenna pattern coverage to less than 180° . The failure to account for the multiple reflections between the probe and AUT within the theoretical description of near-field measurements results in the appearance of a series of concentric circles in the calculated far-field pattern, which constitute a microwave equivalent of Newton's rings. Furthermore, they introduce a loss in accuracy with which the gain can be determined.

Additional uncertainties are introduced by incorrect reporting of the position at which the amplitude and phase measurements have been taken. Such positional errors typically result from timing errors within the control subsystem, as well as from mechanical imperfections within the robotics of the positioner subsystem.

In general, if the antenna under consideration is linear, of finite extent, operates at a single fixed frequency, radiates a constant power and, assuming that Maxwell's equations accurately describe the region of space in which the antenna and measuring equipment is situated, then the approximations involved within the formulation are

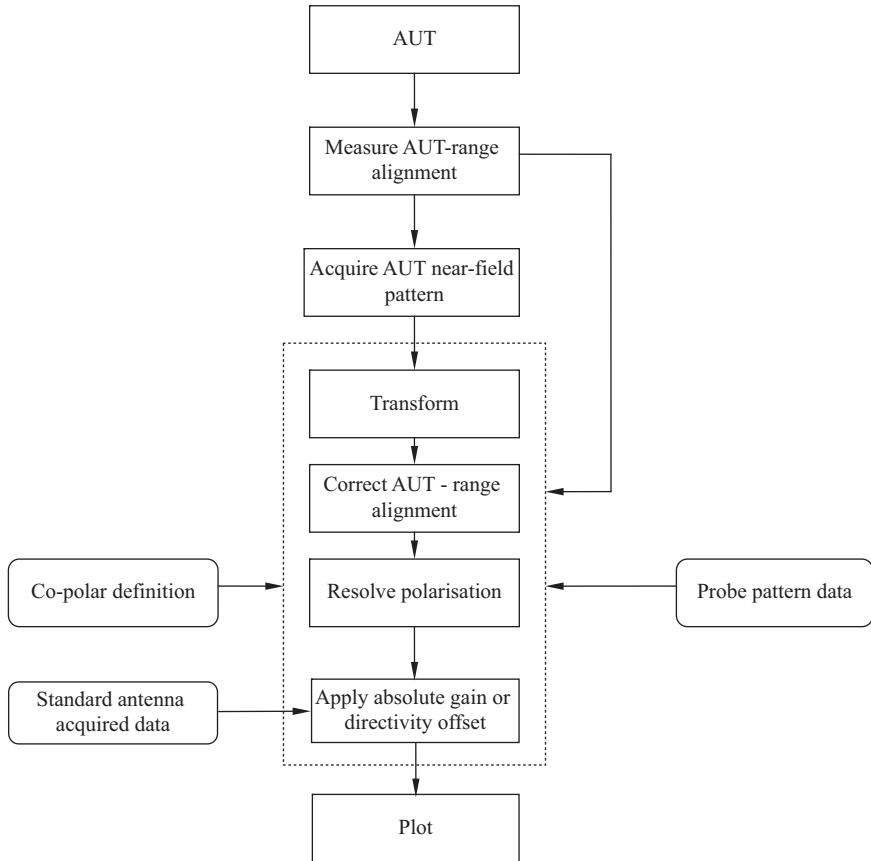


Figure 3.37 Generic near-field measurement process

1. The fields outside the finite sampling interval are zero.
2. The AUT is aligned to the scanner with infinite precision.
3. The robotics subsystem positions the probe at the designated points in space with infinite precision.
4. The RF interferometer measures the impinging signal with infinite precision.
5. There are no multiple reflections between the AUT and the probe.
6. There are no truncation or rounding errors introduced by data processing.
7. There are no reflections (multipath) from the chamber enclosing the measurement.

Although in practice all of these approximations are incorrect, the extent to which each of these possible error sources impacts on the accuracy of the predictions is closely related to the extent to which these approximations can be considered empirically adequate. Clearly, if there is extensive multi-path in the chamber in which the measurements are made, this will impact on the integrity of

the measurement. However, if the error signal resultant from the multi-path is very low compared to the direct path signal then the assumption that there is no multi-path may be valid. It is the job of the range designer to ensure that, while it may be true that none of these approximations is completely valid, their impact on the accuracy, precision and sensitivity of any measurements is minimised.

3.7 Summary

Although the practical use of antennas is mainly in an outdoor environment where there are large separations between Tx and Rx antennas, modern antenna test ranges attempt to make measurements in indoor facilities where Tx and Rx antennas are in close physical proximity to each other. Such indoor facilities have the advantages of security, control of the environment and ease of access for equipment and personnel. However, in order to make measurements in indoor facilities that mirror what would be expected on large outdoor ranges, a number of engineering solutions are required. These solutions involve isolating the test range from its immediate environment, which usually involves placing the range in a metallic chamber or some other enclosure to ensure the signals generated inside the chamber stay inside the chamber and signals generated outside the chamber do not interfere with the measured signals generated inside the chamber.

A metallic isolating structure will be the source of reflections, which will cause multi-path in the chamber; this can be mitigated by careful design and the inclusion of RAM within the test range. The placing of positioners within such an anechoic chamber will allow the movements and/or rotations of range antennas and AUTs to provide the main antenna characteristics, gain, pattern and polarisation that are required from measurements.

Measurements of the complex voltages that vary with angle and polarisation are acquired via the use of an interferometry-based RF system that samples in phase and at quadrature. This system is usually being based on the use of various RF sources and a vector network analyser.

The basic interferometer-based concept in practice requires the use of a variety of different devices, amplifiers, attenuators, mixers, etc., and these must be specified to meet the requirements of the envisaged test procedures.

The requirement for the antennas to be in each other's far-field so that plane wave illumination is achieved and the resultant spatial demands that result from this can be mitigated in a number of ways. First, the inclusion of reflecting or refracting structures that can produce a collimated plane wave in a much shorter distance than would be possible conventionally in a so-called 'compact antenna test range' can substantially reduce the real estate requirements for a test range.

Alternatively, measurements that depend on the synthesis of a plane wave response from a number of near-field measurements that can be subsequently processed to produce a prediction of the required far-field response are also possible. The use of readily available positioner systems and the ease of subsequent

processing recommend three preferred geometries on which such measurements can be accomplished: spherical, planar and cylindrical geometries.

All of these geometries have their limitations and advantages but they all share the same basic inherent measurement procedure which differs from conventional far-field measurements, in that a transformation from near-field to far-field data is required along with the removal of the impact of the measurement probes inherent pattern.

This chapter has summarised the basic techniques and equipment in use in modern antenna test ranges to characterise AUTs and subsequent chapters describe in the required level of detail each of these measurement methodologies starting with compact antenna test range measurements.

References

- [1] Rodriguez V., “Basic Rules for Indoor Anechoic Chamber Design”, *IEEE Antennas and Propagation Magazine*, 2016, pp 82–93.
- [2] Rodriguez V., Barry E., “A polynomial Approximation for the Prediction of Reflected Energy from Pyramidal RF Absorbers”, *Proceedings AMTA 2016*, pp 155–160.
- [3] King R. W. P., Smith G. S., Owens M., Wu T. T., “Antennas in Matter: Fundamental Theory and Applications”, Cambridge, MA, MIT Press, 1981.
- [4] Joy E. B., “A Brief History of the Development of Near-Field Measurement Technique at the Georgia Institute of Technology”, *740 IEEE Transactions on Antennas and Propagation*, 1988, 36(6): pp 740–745.
- [5] Joy E. B., “Low side lobe reflectors”, US Patent 5,341,150, August 1994.
- [6] Joy E. B., “A Practical Method for Measurement the Complex Polarisation Ratio of Arbitrary Antennas”, *IEEE Transaction on Antennas and Propagation*, 1973, AP-21(4): pp 432–435.
- [7] Gregson S. F., Parini C. G., McCormick J., “Developments of Wide Angle Antenna Pattern Measurements using a Probe Corrected Polyplanar Near-Field Measurement Technique”, *IEE Proceedings Microwave Antennas and Propagation*, 2005, 152(6): pp 563–572.
- [8] Gregson S. F., Parini C. G., McCormick J., “Proposal for a Novel Near Field Antenna Measurement Technique Employing Conic Frustum Geometry”, LAPC, Loughborough, March 2008.
- [9] Gregson S. F., Hindman G. E., “Conical Near-Field Antenna Measurements”, *IEEE Antennas and Propagation Magazine*, 2009, 51(1): pp 193–201.
- [10] Newell A. C., Stubenrauch C. F., “Effect of Random Errors in Planar Near Field Measurements”, *IEEE Transactions on Antennas and Propagation*, 1988, 36(6): pp 769–773.
- [11] www.microwaves101.com/encyclopedias/attenuators#intro

- [12] Ludwig A. C., “The Definition of Cross Polarisation”, IEEE Transactions on Antennas and Propagation, January 1973, AP-21(1): pp 116–110.
- [13] Gregson S., McCormick J., Parini C. G., “Principles of Planar Near Field Antenna Measurements”, IET Publications, 2007, ISBN 978-86341-736-8, section 4.9.

Chapter 4

Antenna pattern plotting: coordinate systems and polarisation bases

4.1 Coordinate systems and antenna measurements

Antenna measurement data is collected over a tabulating surface as a function of position relative to the antenna under test (AUT). In the far-field, where most antenna pattern comparisons are performed, this reduces to the problem of representing data as a function of one or more angles with the electrically large measurement radius being arbitrary but fixed. In general, even when taking conventional far-field data, the antenna measurement engineer seldom uses a single rotation stage as two-dimensional pattern data is generally required. However, as will be illustrated below, the data collection/visualisation coordinate system directly affects how data is mapped to the surface: planar, cylindrical, spherical or other types. Thus, far-field measurements are usually mapped or converted to spherical surfaces from which directivity, polarisation and patterns are calculated and projected. Often the collected coordinate system is not the same as the final-mapped system, requiring special formulas for proper conversion. In addition, projecting this data in two- and three-dimensional polar or rectangular plots presents other problems in interpreting the antenna pattern data. Implicit within this is the assumption that the tabulating grids are plaid, monotonic and equally spaced. Whilst not necessary from a theoretical standpoint, these conditions greatly simplify the recording process for a robotic positioner as well as simplifying the tasks of numerical integration, differentiation and interpolation. The following sections present a concise description of the most important coordinate systems and then go on to discuss methods for representing the relationships between them. This section presents a summary of many of the most commonly encountered coordinate system formulas and shows how they relate to one another.

Antenna measurements are made to show the performance of an antenna: gain, pattern, directivity, cross-pol, etc. Data collection of performance characteristics come in the form of printed patterns, exported files and interactive computer displays. Various formats have been designed to allow the user to quickly compare antenna performance to expected results. These comparisons are often in the form of overlaid patterns, pass-fail specification lines or require additional computation by other computer programs. It is particularly important to understand the details of the measurement coordinate system prior to comparing between measurement data

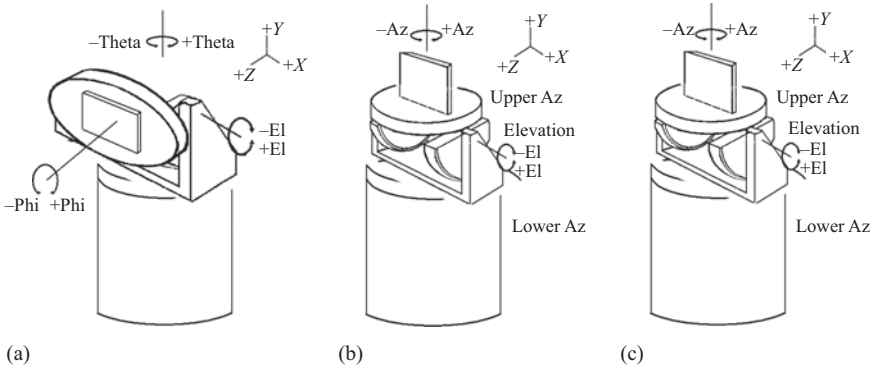


Figure 4.1 Roll-over-elevation-over-azimuth positioner system

to expected results or data taken on another range. The rotation of the antenna and/or the probe when making measurements will directly affect the form of the patterns produced. In addition, natural polarisation vectors are produced by a positioner system and these can be quite different if compared to those taken using an alternative positioner configuration. Figure 4.1 shows a classical roll-over-elevation-over-azimuth positioner. This is a very common positioner configuration as it supports three standard types of spherical coordinate systems.

Figure 4.1(a) shows the AUT mounted on the top roll axis with the elevation axis fixed at 90° . This constitutes a standard Theta-Phi coordinate system. Figure 4.1(b) and 4.1(c) shows how the antenna is mounted for the two other standard coordinate systems. Each system consists of two movable axes defined for that system and one fixed axis that is not part of the acquisition system. Each system has a natural pole orientated in a different direction, that is to say, aligned with a different axis. The pole is where the AUT does not change its pointing angle in space when one of the two defined axes is rotated, i.e. a singularity. Table 4.1 shows how the positioner axes are configured to produce each coordinate system.

Figure 4.2 shows the angles a far-field probe makes with respect to the AUT as it is rotated. *Note:* it is important to remember that there is a difference between the angle the antenna points in space and the angle made between the probe and positioner. In Figure 4.2(a)–(c), the cardinal cuts, which are equivalent, can be seen to be plotted in bold. The meshes that can be seen were formed by incrementing the two rotating axes by a constant angular amount where the order of incrementation is unimportant.

Proper antenna positioner rotation is important to make sure that the range is properly defined. Far-field positioners often include encoders whose polarity can be changed based on various needs. The standard definition for positioners is that when looking from the front of the rotation platen, a clockwise rotation should produce a positive-going angle (e.g. -170 to -150 or $+10$ to $+20$). In the case of the elevation positioner, positive angles will expose the upper side of the AUT to

Table 4.1 Coordinate system definition for 3-axis positioner system

System	Pole	Upper Az	Elevation	Lower Az
θ, ϕ	Z-axis	ϕ	Fixed at 90°	θ
Az/El	Y-axis	Az	Elevation	Fixed at 0°
El/Az	X-axis	Fixed at 0°	Elevation	Azimuth

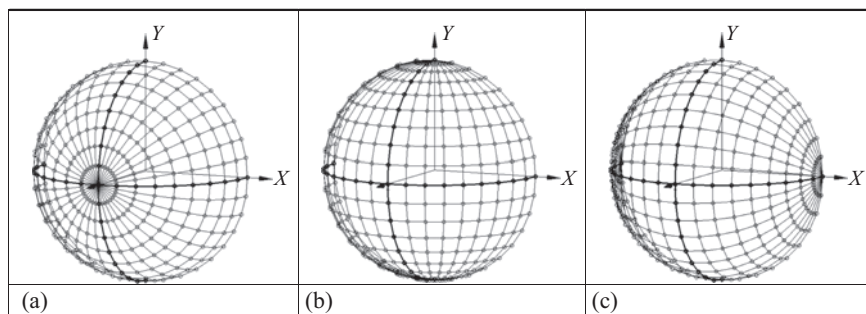


Figure 4.2 Spherical rotation systems: (a) polar spherical θ, ϕ ; (b) azimuth over elevation; and (c) elevation over azimuth

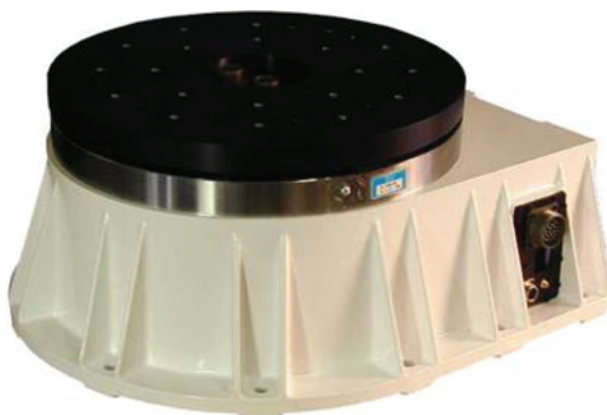


Figure 4.3 Angle convention for rotation stages

the source antenna. Figure 4.3 shows the rotation of each axis to produce a positive angle.

Three-dimensional antenna measurements are made by rotating two axes to sweep out a full sphere or section thereof and recording the amplitude and/or phase at defined locations. In practice, it is usually not possible to measure the complete sphere without some blockage due to the positioner itself. Nonetheless, a complete

sphere can be measured by rotating one axis through 180° and the other through 360° . *Note:* Some configurations, such as elevation-over-azimuth, may have additional restrictions due to the mechanical makeup of the positioner. In the positioner configuration shown in Figure 4.1(c), the elevation axis is restricted to $-45^\circ < \text{El} < +90^\circ$.

4.1.1 Azimuth over elevation

In order to illustrate how different the patterns can be interpreted, first let us consider a map of the Earth plotted in each of the three main spherical coordinate systems. In each case, the $H = V = 0$ point is on the equator in the Atlantic ocean off the West coast of Africa. As shown in Figure 4.4, the image between azimuth = $\pm 180^\circ$ and elevation = $\pm 90^\circ$ is easily recognisable as a Mercator projection [1], i.e. azimuth equates to longitude whilst elevation equates to latitude. The image beyond elevation = $\pm 90^\circ$ shows the alternate sphere (thus the data plotted forms a double sphere). In this figure the false-colour denotes altitude.

This map corresponds to an Az/El positioner system whose pole is at the Y -axis. Note the distortion at the North and South poles. This is because the point at elevation = $\pm 90^\circ$ is the same point in space irrespective of the azimuth angle. By plotting the data in this way, each of the poles (which represents a single point in space) has been stretched out until it becomes a line that is equal in length to the equator. This causes the map to be deformed significantly near the poles. In

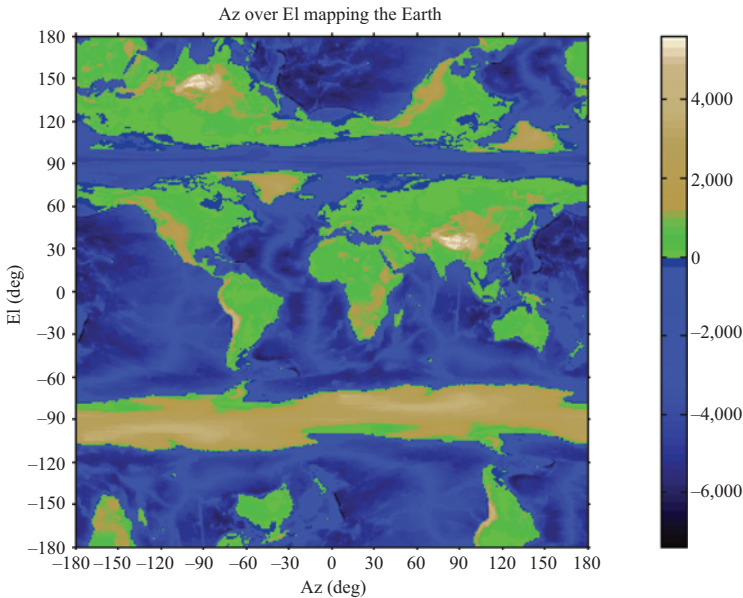


Figure 4.4 Earth mapped using an Az/El positioner system

creating this map, the goal is to create a map where the H and V axes are plaid, monotonic and equally spaced. This is described with the following expressions:

$$H = H_0 + \Delta H(n - 1) \quad (4.1)$$

$$V = V_0 + \Delta V(p - 1) \quad (4.2)$$

Here, n and p are positive integers, $n = 1, 2, 3, \dots, N$ and $p = 1, 2, 3, \dots, P$, with V_0 and H_0 being the starting values of the grid in the h - and v -plotting axes, respectively; ΔH and ΔV are the incrementing values in the h - and v -plotting axes, respectively. In general, a straightforward reliable method for transforming from one coordinate system to another is by means of equating Cartesian direction cosines. Direction cosines use three direction angles α , β and γ to identify a point in space. The point is described by a vector \underline{r} measured from the origin to the point. Direction cosines relate the vector \underline{r} to Cartesian coordinates where

$$\underline{r} = r_0 (u\hat{\underline{e}}_x + v\hat{\underline{e}}_y + w\hat{\underline{e}}_z) \quad (4.3)$$

Here, u , v and w are called the direction cosines are the weightings for each orthogonal unit vector and r_0 is the magnitude of the position vector \underline{r} . They are described by the following expressions:

$$u = \cos \alpha \quad (4.4)$$

$$v = \cos \beta \quad (4.5)$$

$$w = \cos \gamma \quad (4.6)$$

Here, each of the angles α , β and γ is measured from the positive x -, y - and z -axes, respectively. Note, in a subsequent section on polarisation, the variable α is used instead to denote the azimuth angle in an elevation over azimuth coordinate system. The interpretations of the respective nomenclatures are clear from the context of the different meanings and as they never occur together in the same expressions or section of this text. Using these expressions, a straightforward conversion can be performed between any of the antenna measurement coordinates systems. This is accomplished by normalising the length of the vector \underline{r} so that $|\underline{r}| = 1$ and then relating the angles in each antenna coordinate system to the three direction cosines.

As shown in Figure 4.1(b), the rotation of the azimuth angle is made around the elevation angle. This means that a pole is produced at two elevation points -90° and 90° . The pole is along the y -axis, thus $El = -\beta + 90^\circ$ and Az will be a combination of α and γ angles in the following way:

$$u = \sin Az \cos El \quad (4.7)$$

$$v = \sin El \quad (4.8)$$

$$w = \cos Az \cos El \quad (4.9)$$

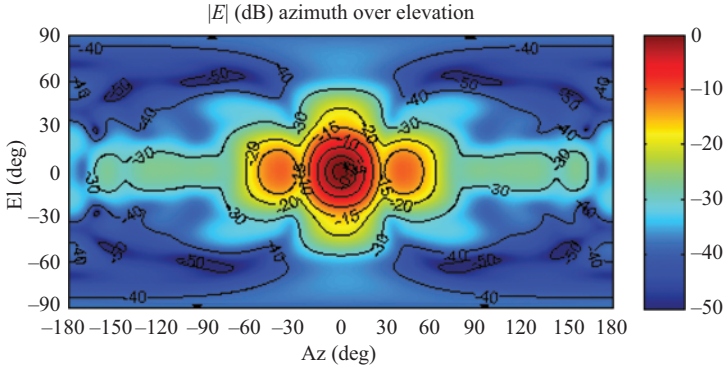


Figure 4.5 Pattern of an SGH plotted using an azimuth over elevation coordinate system

By way of illustration, Figure 4.5 contains a false colour checkerboard plot of radiated power of a standard gain horn (SGH) that has been plotted using a regular azimuth over elevation coordinate system. One of the difficulties associated with using this coordinate system in practice is that as a consequence of the positioner stack-up, the AUT is typically not located at the origin of the measurement coordinate system meaning that it is translated in space during the acquisition.

It is worth noting that the definitions used here for Az/El (and El/Az developed in the following section) differ to those used by some proprietary simulation software packages where these naming conventions are exchanged. This can cause confusion to the uninitiated and the reader is wise to refer to the associated documentation to confirm which convention is used.

4.1.2 Elevation over azimuth

Figure 4.6 contains a plot equivalent to Figure 4.5 for the case of an elevation over azimuth projection; however, here the distortion appears near the X -axis pole (azimuth = $\pm 90^\circ$).

As shown in Figure 4.1(c), the rotation of the elevation angle is made around the azimuth angle. This means that a pole is produced at two azimuth points -90° and 90° . The pole is along the X -axis; thus, $Az = -\gamma + 90^\circ$ and Az will be a combination of α and γ angles in the following way:

$$u = \sin Az \quad (4.10)$$

$$v = \cos Az \sin El \quad (4.11)$$

$$w = \cos Az \cos El \quad (4.12)$$

By way of illustration, Figure 4.7 contains a grey-scale plot of an SGH that has been plotted using a regular elevation over azimuth coordinate system.

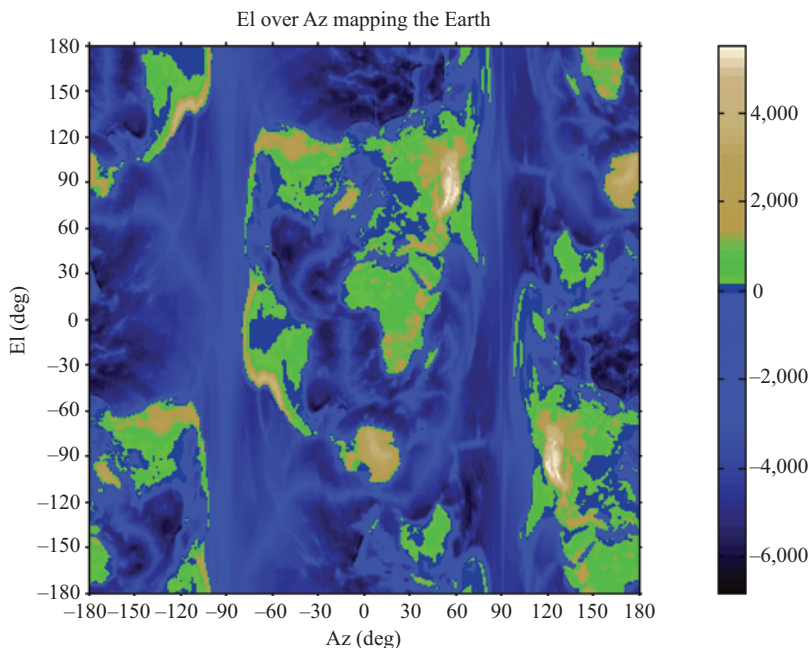


Figure 4.6 Earth mapped using an El/Az positioner system

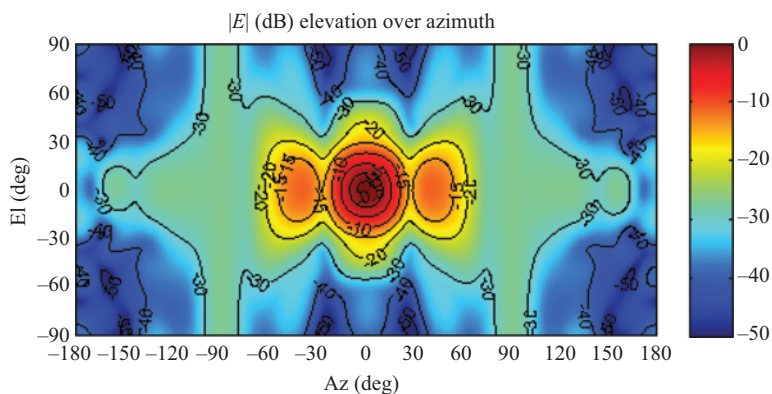


Figure 4.7 Pattern of an SGH plotted using an elevation over azimuth coordinate system

4.1.3 Polar spherical

In the third case, there are two ways to show the map. One is to display the θ -axis along the horizontal axis of the plot, with the ϕ -axis as the vertical axis of the plot forming a rectangular plot as shown in Figure 4.8. In this case, distortion appears greatest along the Z-axis pole ($\Theta = 0^\circ, \pm 180^\circ, \dots$).

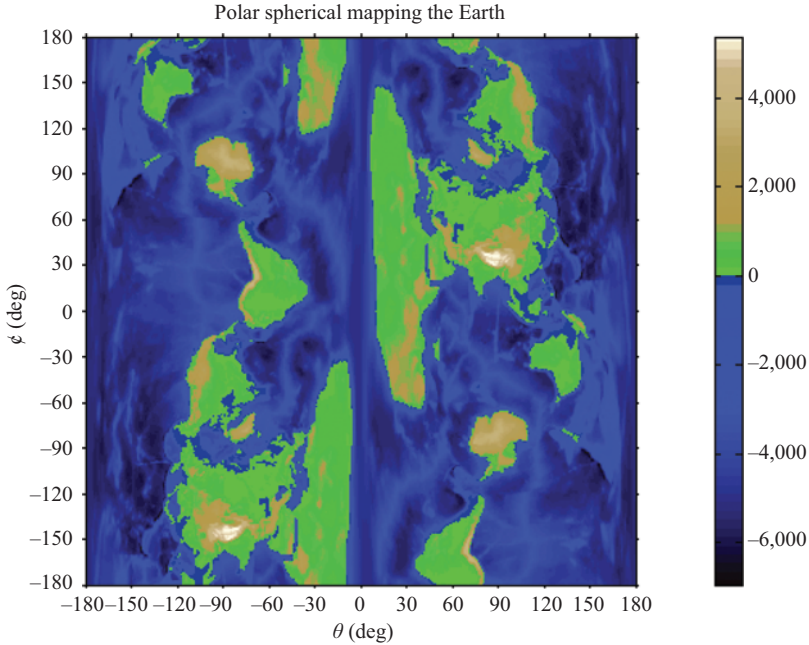


Figure 4.8 Earth mapped using a polar spherical phi over theta positioning system

From Figure 4.8, it is clear that the full sphere pattern can be represented in at least four different ways:

1. $0 \leq \theta \leq \pi, -\pi \leq \phi \leq \pi,$
2. $-\pi \leq \theta \leq 0, -\pi \leq \phi \leq \pi,$
3. $-\pi \leq \theta \leq \pi, 0 \leq \phi \leq \pi,$ and
4. $-\pi \leq \theta \leq \pi, -\pi \leq \phi \leq 0.$

Clearly, by allowing θ and ϕ to vary by more than modulo 2π or to allow the spherical angles to be centered about a value other than zero, an infinite number of other (typically unhelpful) representations become available. As shown in Figure 4.1(a), the rotation of the ϕ angle is made around the θ angle. This means that a pole is produced at the Theta points $0^\circ, 180^\circ, 360^\circ, \dots$. The pole is along the Z-axis, and the spherical angles are related to the direction cosines in the following way:

$$u = \sin \theta \cos \phi \quad (4.13)$$

$$v = \sin \theta \sin \phi \quad (4.14)$$

$$w = \cos \theta \quad (4.15)$$

Table 4.2 Direction cosines for three spherical coordinate systems

System	\underline{u}	\underline{v}	\underline{w}
$\theta-\phi$	$\sin(\theta) \cos(\phi)$	$\sin(\theta) \sin(\phi)$	$\cos(\theta)$
Az/El	$\cos(El) \sin(Az)$	$\sin(El)$	$\cos(El) \cos(Az)$
El/Az	$\sin(Az)$	$\cos(Az) \sin(El)$	$\cos(El) \cos(Az)$

For antenna measurement, this arrangement has the advantage that it moves the AUT through only a small portion of the test zone, and it places the blockage that results from the AUT mount entirely in the back hemisphere. Moving the AUT by only a small amount minimises errors associated with imperfections in the illumination of the test zone and can, in some instances, render probe pattern correction unnecessary. Occasionally, one comes across the concept of an ‘equatorial’ spherical measurement system. This is identical to the polar spherical case only here the main beam of the antenna points to the equator, rather than towards the positive z -axis (through the pole). In summary, the three coordinate systems can be summarised in a single table as shown in Table 4.2.

When interpreting these plots, it is important to note that (obviously) the Earth’s continents have not changed, this is a given. Their relative spacing to one another is also the same. It is the spherical projection onto a flat piece of paper that distorts the image. This distortion is an unavoidable consequence of trying to represent a three-dimensional object on a two-dimensional piece of paper. Flat maps could not exist without map projections because a sphere cannot be laid flat over a plane without distortion. This can be seen mathematically as a consequence of Gauss’s Theorema Egregium [2] which essentially states that it is not possible to bend a finite-sized, i.e. *not* infinitesimal, non-elastic, piece of paper onto the surface of a sphere.

Overlaying one of the projections onto another, as in the case of overlaying antenna patterns from ranges with different positioning systems, is worthless in identifying differences between the patterns except on, or *very* near, the Cardinal cuts. To compare data at other cuts between the three systems, a conversion, i.e. transformation, must be implemented between one coordinate system and another.

By way of illustration, Figure 4.9 contains a false colour plot of an SGH that has been plotted using a regular polar spherical coordinate system.

4.1.4 True-view (azimuth and elevation)

For any given direction in space, as referenced to a given frame of reference, it is possible to use an infinite number of different, but equivalent, spherical angles to describe the relationship. However, in most areas of application, the spherical angles are limited to modulo 360, or equivalently modulo 2π . However, even if the range of the spherical angles is limited, it is still possible to describe a given direction in more than one way. An implicit assumption has been made within text

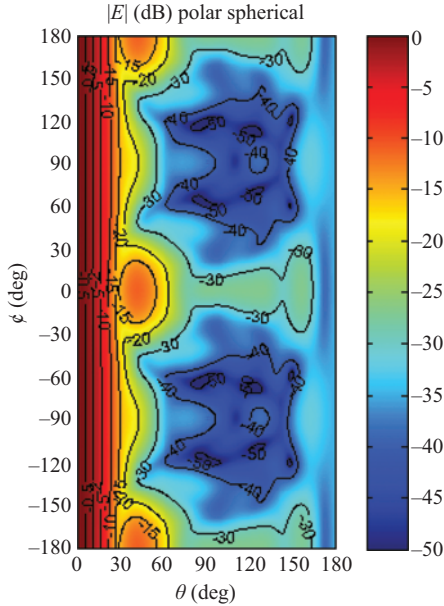


Figure 4.9 Pattern of an SGH plotted using a polar spherical coordinate system

concerning the range of the angles (variables) θ and ϕ . These are

$$0 \leq \theta \leq 180 \tag{4.16}$$

$$-180 \leq \phi \leq 180 \tag{4.17}$$

An alternative but equally valid choice is

$$-180 \leq \theta \leq 180 \tag{4.18}$$

$$0 \leq \phi \leq 180 \tag{4.19}$$

Typically, this is convenient for displaying cuts, as only one value of ϕ is required to specify an entire great circle cut. Conversion between the two systems is facilitated through

$$\theta \rightarrow -\theta \tag{4.20}$$

$$\phi \rightarrow \phi + \pi \tag{4.21}$$

These relationships can be justified from Figure 4.10.

This observation provides an alternative possibility of plotting which is to show the θ cuts in the form of a polar diagram. Figure 4.11 shows the θ cuts plotted radially with each cut being rotated by an amount determined by the ϕ angle. Here,

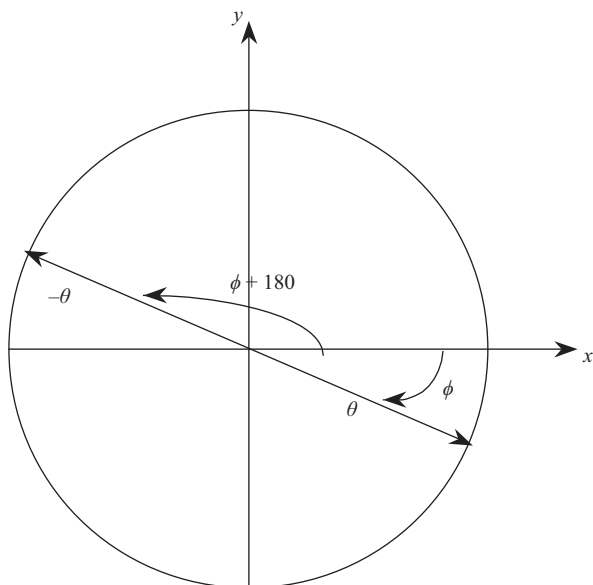


Figure 4.10 Conventional and alternate spherical angles

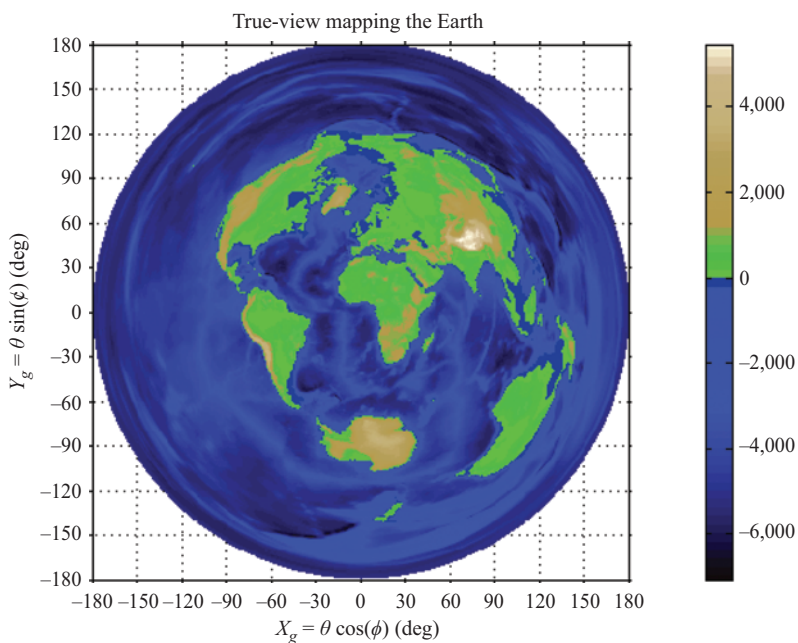


Figure 4.11 Earth mapped using a polar spherical phi over theta positioning system and plotted in polar form

parts of the pattern with θ angles <0 correspond to the alternate sphere with the mapping between spheres being as stated.

The true-view, that is polar plotting of the polar spherical coordinate system, differs from the previous plots as this is not achieved by plotting the measured data using a rectangular, i.e. raster, format. Relaxing the rigid connection between the plotting system and positioner enables the introduction of other alternative plotting systems that can potentially offer advantages when interpreting the patterns. Thus, unlike the coordinate systems described above, the true-view coordinate system is instead a polar representation of the polar spherical (θ, ϕ) coordinate system. Thus, the x - and y -axes of the plot, denoted by X_g and Y_g , respectively, are related to the spherical angles through

$$\theta = \sqrt{X_g^2 + Y_g^2} \quad (4.22)$$

$$\phi = \arctan\left(\frac{Y_g}{X_g}\right) \quad (4.23)$$

Here, \arctan is used to denote the four-quadrant arctangent function which has a range of $-\pi$ to π . Thus,

$$u = \sin\left(\sqrt{X_g^2 + Y_g^2}\right) \cos\left(\arctan\left(\frac{Y_g}{X_g}\right)\right) \quad (4.24)$$

$$v = \sin\left(\sqrt{X_g^2 + Y_g^2}\right) \sin\left(\arctan\left(\frac{Y_g}{X_g}\right)\right) \quad (4.25)$$

$$w = \cos\left(\sqrt{X_g^2 + Y_g^2}\right) \quad (4.26)$$

By way of illustration, Figure 4.12 contains a false colour plot of an SGH that has been plotted using a regular true-view coordinate system.

4.1.5 *Direction cosine*

Relaxing the rigid connection between the plotting system and the positioner enables the introduction of other alternative plotting systems that can potentially offer advantages when interpreting the patterns. By way of illustration, Figure 4.13 contains an Earth map when plotted using a direction cosine coordinate system. This system is essentially the same as the k -space coordinate system since the two are related to a linear scaling of the free-space propagation constant k_0 . However, the direction cosine system has the inherent advantage that the system is not dependent upon (scaled by) the frequency of the radiated field. The direction cosine coordinate system has no direct analogy with an arrangement of rotation stages. However, we are still not completely free to choose the values of u , v and w since

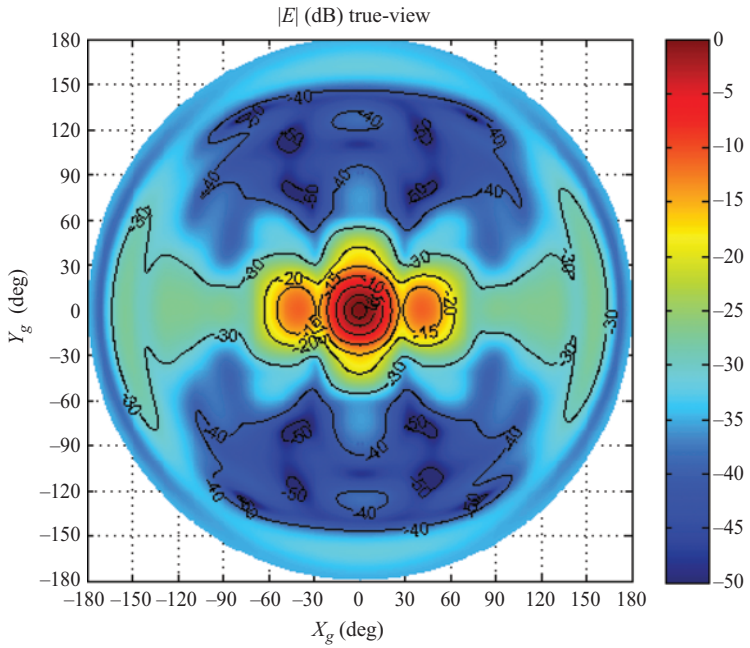


Figure 4.12 Pattern of an SGH plotted using a true-view coordinate system

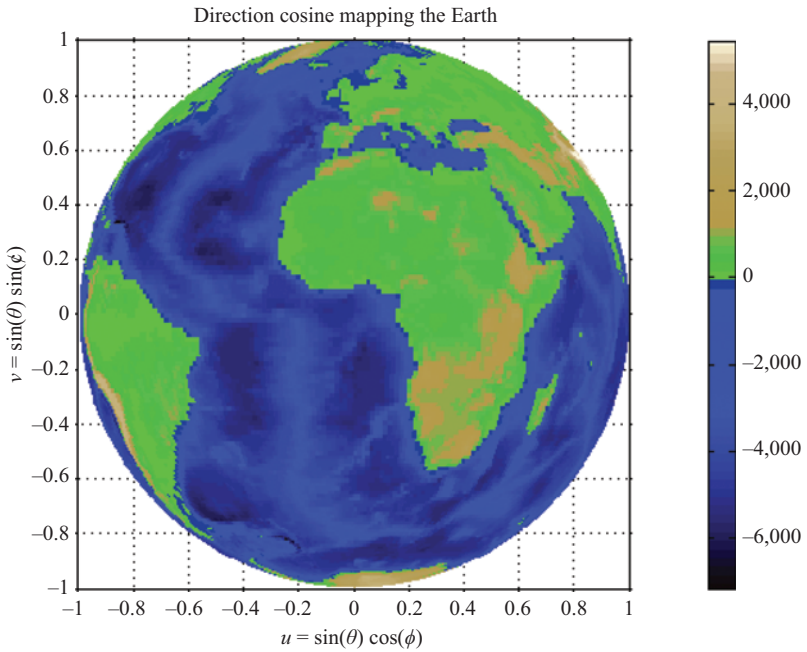


Figure 4.13 Earth mapped using a direction cosine plotting system

the length of the unit vector which these components represent has, by definition, a length of unity. Thus,

$$1 = u^2 + v^2 + w^2 \quad (4.27)$$

Clearly, the direction cosine system corresponds to an orthographic projection in which the sphere is projected onto a tangent, or secant, plane. Here, only a half-space is visible at any one time and points on the plot for which

$$u^2 + v^2 > 1 \quad (4.28)$$

correspond to real ϕ angles and complex θ angles. If this system is used to plot the angular spectrum of plane waves, then the propagating field will be contained within the parts of the pattern when $u^2 + v^2 \leq 1$, i.e. visible space, and the reactive field will be contained with parts of the pattern when $u^2 + v^2 > 1$. Thus, when plotting true asymptotic far-field patterns, the field will be identically zero outside the unit circle. Here, u and v are related to the spherical coordinates by

$$u = \sin \theta \cos \phi \quad (4.29)$$

$$v = \sin \theta \sin \phi \quad (4.30)$$

For the forward half-space,

$$w = \cos \theta = \sqrt{1 - u^2 - v^2} \quad (4.31)$$

For the back half-space,

$$w = \cos \theta = -\sqrt{1 - u^2 - v^2} \quad (4.32)$$

By way of illustration, Figure 4.14 contains a grey-scale plot of an SGH that has been plotted using a regular direction cosine coordinate system.

4.1.6 *Arcsine-space plotting coordinate system*

Another useful plotting system, which is sometimes favoured by designers of active electronically scanned array antennas, can be obtained by taking the arcsine of the x and y plotting axes. This is illustrated in Figure 4.15. In this case, anything outside of the unit square corresponds to invisible space.

Again, the θ_{xy} coordinate system has no direct analogy with an arrangement of rotation stages and is instead most closely related to the direction-cosine system as

$$u = \sin X_g \quad (4.33)$$

$$v = \sin Y_g \quad (4.34)$$

$$w = \sqrt{1 - u^2 - v^2} \quad (4.35)$$

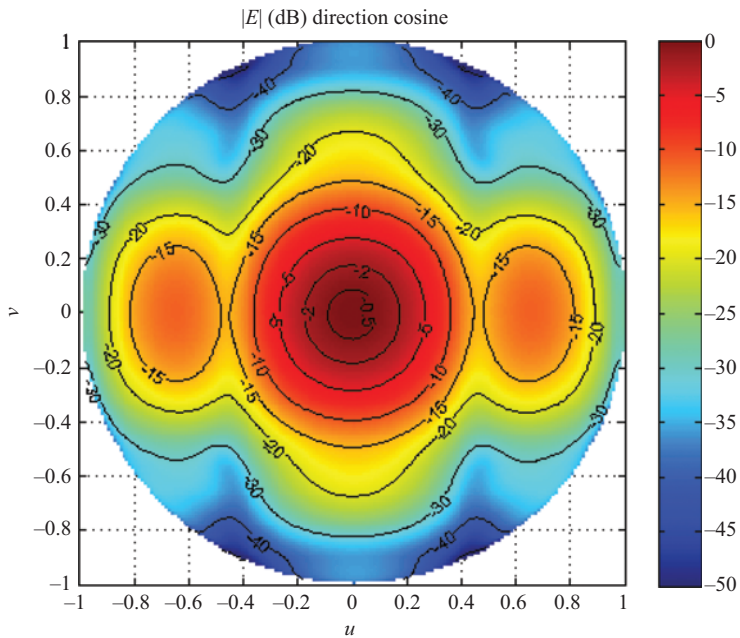


Figure 4.14 Pattern of an SGH plotted using a direction cosine coordinate system

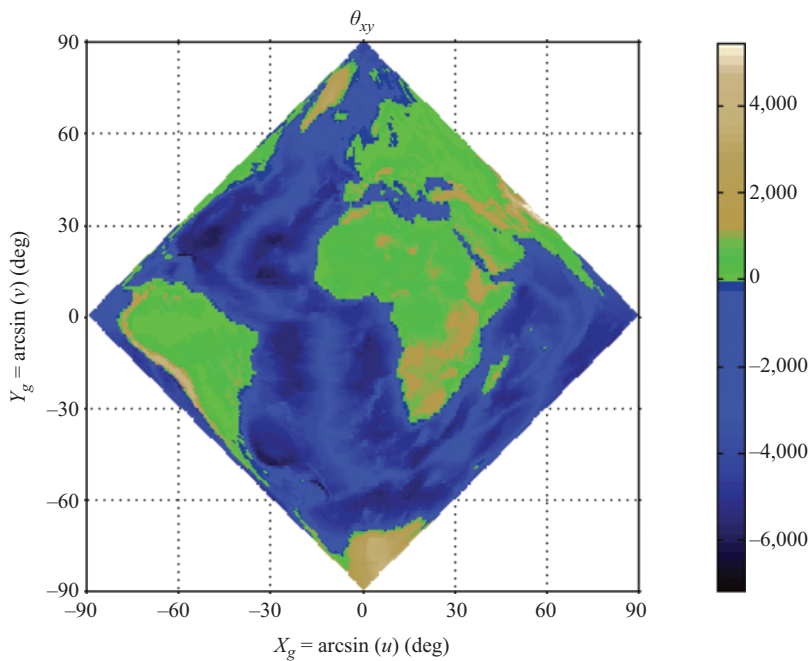


Figure 4.15 Earth mapped using an arcsin-space plotting coordinate system

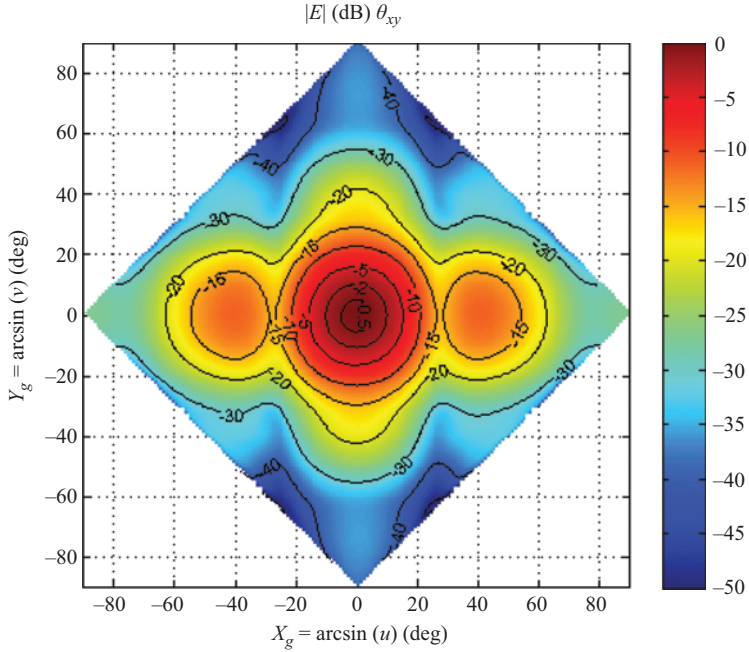


Figure 4.16 Pattern of an SGH plotted using an arcsin-space coordinate system

By way of illustration, Figure 4.16 contains a false colour plot of an SGH that has been plotted using a regular arcsin-space coordinate system.

4.1.7 Transformation between coordinate systems

It is often the case that an antenna engineer is presented with antenna pattern data tabulated in one of the coordinate systems described above and is required perhaps for the purposes of comparison to re-plot that data in a different plotting system. This can be interpreted as being the numerical analogue of exchanging variables within analytical expressions. To help facilitate this, Table 4.3 comprises a summary of the various coordinate systems discussed above and illustrates how each of the parameters can be related to one another.

For example, the spherical angles can be related to the azimuth over elevation angles as

$$\theta = \arccos(w) = \arccos(\cos(Az) \cos(El)) \tag{4.36}$$

$$\phi = \arctan\left(\frac{v}{u}\right) = \arctan\left(\frac{\tan(El)}{\sin(Az)}\right) \tag{4.37}$$

Table 4.3 Transformation between coordinates

Coordinate system	x-Axis	y-Axis	z-Axis
Direction cosine	u	v	w
k -Space	k_x/k_0	k_y/k_0	k_z/k_0
Azimuth over elevation	$\sin(Az)\cos(EI)$	$\sin(EI)$	$\cos(Az)\cos(EI)$
Elevation over azimuth	$\sin(Az)$	$\cos(Az)\sin(EI)$	$\cos(Az)\cos(EI)$
Polar spherical	$\sin \theta \cos \phi$	$\sin \theta \sin \phi$	$\cos \theta$
True-view (azimuth and elevation)	$\sin(\sqrt{Az^2 + EI^2}) \cos(\tan^{-1}(\frac{EI}{Az}))$	$\sin(\sqrt{Az^2 + EI^2}) \sin(\tan^{-1}(\frac{EI}{Az}))$	$\cos(\sqrt{Az^2 + EI^2})$
θ_{xy}	$\sin X_g$	$\sin Y_g$	$\sqrt{1 - \sin^2 X_g - \sin^2 Y_g}$

Here, as usual, we take advantage of the two argument arctangent function so that quadrant ambiguity can be eliminated. Or conversely, the azimuth and elevation angles can be related to the spherical angles as

$$Az = \arctan\left(\frac{u}{w}\right) = \arctan(\tan \theta \cos \phi) \tag{4.38}$$

$$El = \arcsin(v) = \arcsin(\sin \theta \sin \phi) \tag{4.39}$$

Indeed, by transforming via the direction cosines, it is possible to convert from any one set of coordinates to any other set of coordinates. As a note of caution, however, when calculating the inverse tangent it is important that the four-quadrant inverse tangent is used. This function will return angles over a full $\pm 180^\circ$ range rather than over the more limited $\pm 90^\circ$ range that returned by the conventional inverse tangent function.

4.1.8 *Coordinate systems and elemental solid angles*

When evaluating far-field parameters, it is often important to have an expression for the elemental solid angle each of the coordinate systems that the antenna pattern is tabulated in. One example where this would be useful is when calculating the total radiated power or the directivity of an antenna. The expression for the elemental solid angle for each of the systems described above can be seen presented in Table 4.4.

Thus, we have been able to describe a point in space with a particular antenna coordinate system and convert it to any other antenna coordinate system by equating the respective direction cosines.

4.1.9 *One-dimensional great circle pattern cuts*

One further complication arises when plotting great circle θ -cuts for arbitrary but fixed ϕ -angles. The conventional cardinal cuts are illustrated in Figures 4.17 and 4.18. Here, to the left of the figure, the AUT can be seen depicted as a red square is

Table 4.4 Expressions for the elemental solid angle

Coordinate system	Coordinates	$d\Omega$
Direction cosine	(u, v)	$\frac{1}{\cos \theta} du dv$
Azimuth over elevation	(Az, El)	$\cos(El) dAz dEl$
Elevation over azimuth	(Az, El)	$\cos(Az) dAz dEl$
Polar spherical	(θ, ϕ)	$\sin(\theta) d\theta d\phi$
True-view	(Az, El)	$\text{sinc}(\theta) dAz dEl$

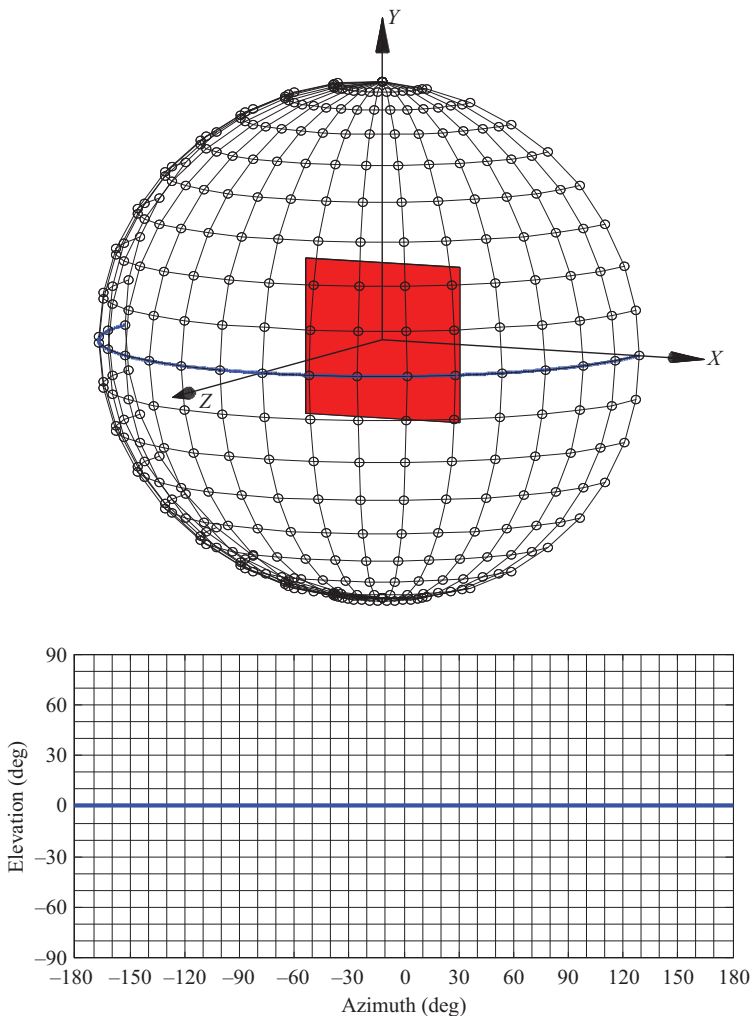


Figure 4.17 Illustration of the horizontal cardinal cut in three-dimensional space and on an azimuth over elevation plotting system

shown placed at the centre of the far-field plotting sphere. The great circle cut is depicted as the blue trace. To the right-hand side of the figure, the cut is presented again as a blue trace; however, here it is plotted on a regular azimuth over the elevation coordinate system. Figures 4.19 and 4.20 are equivalent plots only here, two inter-cardinal plots are shown for various ϕ -angles. Here, it can be seen that almost none of the points on the cut coincide with points on the regular plaid azimuth over elevation grid as the inter-cardinal cut corresponds to a sinusoidal trajectory in the azimuth over elevation domain.

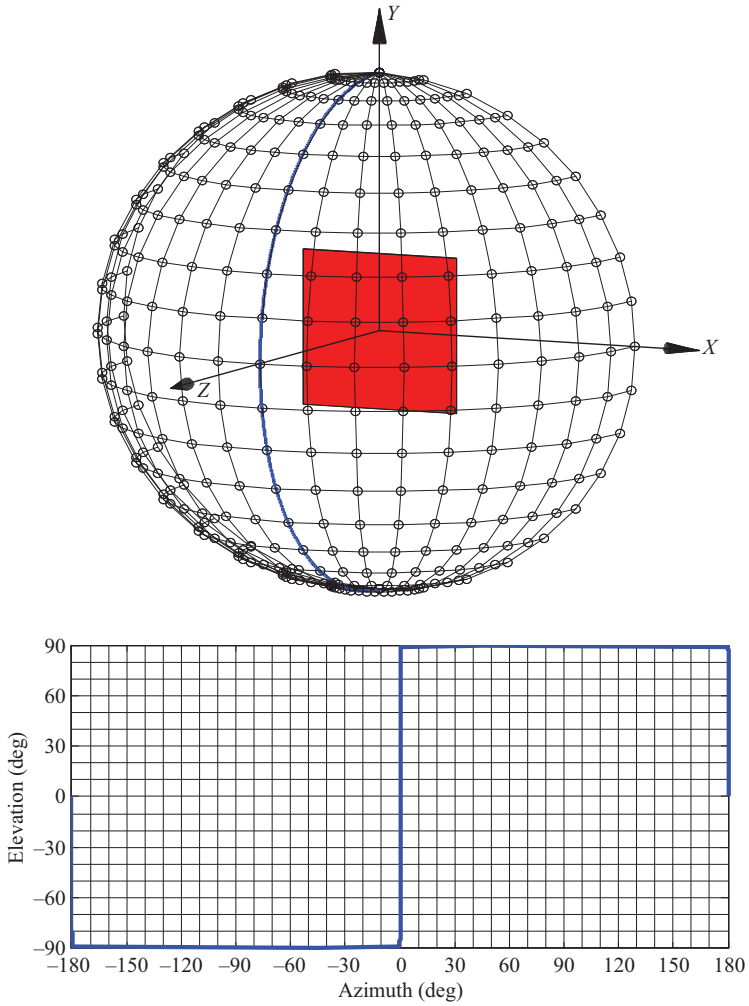


Figure 4.18 Illustration of vertical cardinal cut in three-dimensional space and on an azimuth over elevation plotting system

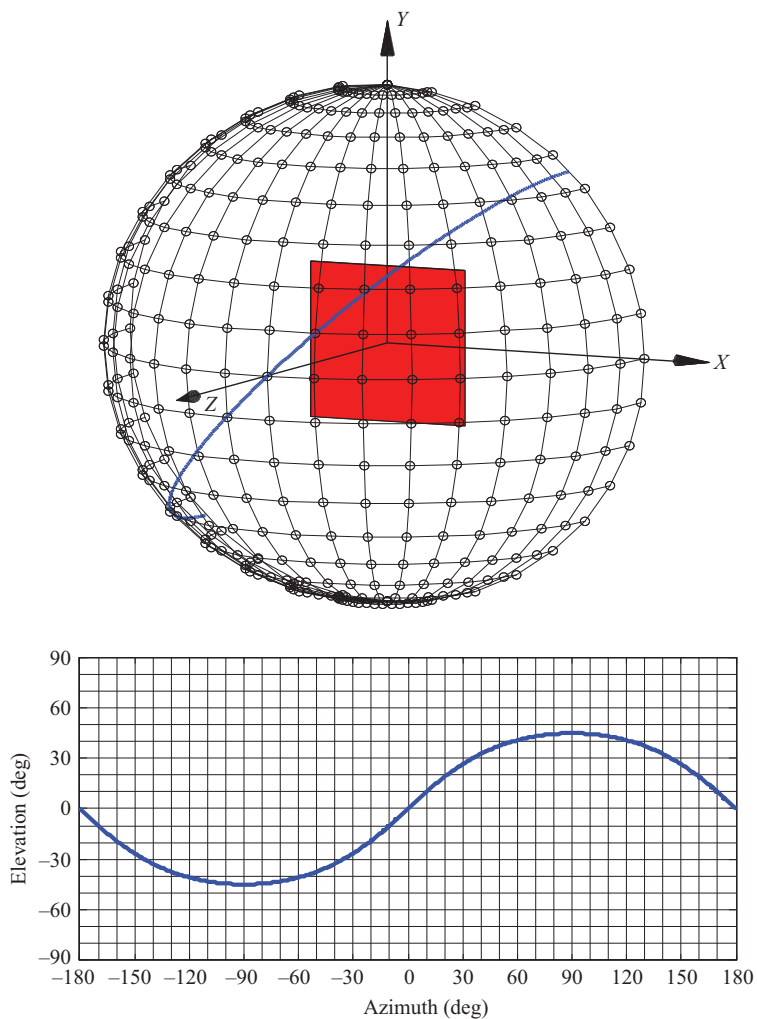


Figure 4.19 Illustration of an inter-cardinal cut in three-dimensional space and on an azimuth over elevation plotting system, smaller ϕ -angle

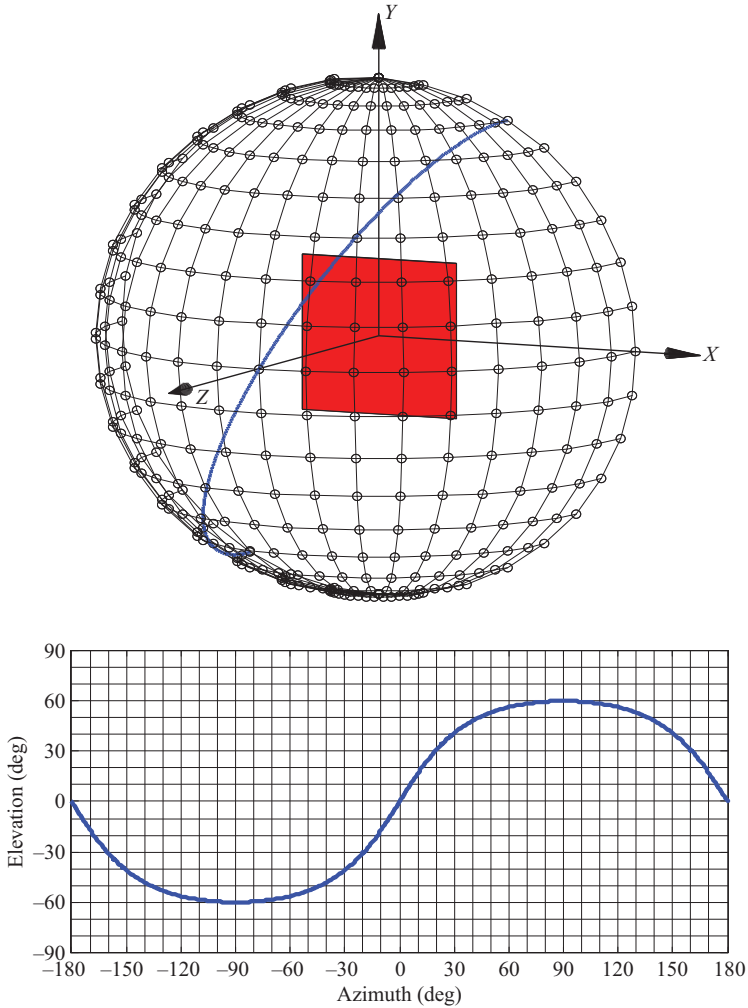


Figure 4.20 Illustration of an inter-cardinal cut in three-dimensional space and on an azimuth over elevation plotting system, larger ϕ angle

4.2 Polarisation basis and antenna measurements

As shown above, in the near zone, the electric, or magnetic, field is completely characterised by specifying three vector components, whilst the far-field is defined unambiguously by specifying two transverse vector components since the vector component in the direction of propagation is identically zero due to the plane wave condition. It is customary to define cross polarisation as ‘the polarisation orthogonal to a reference polarisation’. Unfortunately, this leaves the direction of the reference polarisation undefined and thus ambiguous for all but circularly polarised waves. The

definitions presented below can be used to resolve this ambiguity. In the far-field, that is when the field point is very far removed from the antenna, a radiator will produce an electric field perpendicular to the direction of propagation in some orientation on a plane. That orientation can be described using two spherical angles, similar to those used above to represent the direction of propagation, that is

$$\underline{E}(r, \theta, \phi) = [A(\theta, \phi)\hat{e}_\theta + B(\theta, \phi)\hat{e}_\phi] e^{-jk_0 r} \quad (4.40)$$

$$\underline{E}(r, Az, El) = [A(Az, El)\hat{e}_{Az} + B(Az, El)\hat{e}_{El}] e^{-jk_0 r} \quad (4.41)$$

$$\underline{E}(r, \alpha, \varepsilon) = [A(\alpha, \varepsilon)\hat{e}_\alpha + B(\alpha, \varepsilon)\hat{e}_\varepsilon] e^{-jk_0 r} \quad (4.42)$$

Here, A and B are complex quantities and the suppressed time dependency of the complex representations of the electromagnetic field vectors can be taken to be of the form $e^{j\omega t}$, i.e. an assumed positive time dependency. In the asymptotic (true) far-field, any two unit vectors can be used to describe the polarisation. There are two special cases for A and B that are important to consider and those are Case 1, linearly polarised (A or $B = 0$). In this case, the resulting electric field is indicative of a field that is polarised in one direction with respect to the direction of propagation. Case 2, elliptical polarisation (A and B are 90° out-of-phase with each other). In this case, the resulting field appears to rotate around the direction of propagation. In the special case of elliptical polarisation where the magnitudes of A and B are equal, circular polarisation results.

When an antenna pattern is measured either in receive or in transmit mode, its pattern is a function of the polarisation of the far-field probe that is used to measure it. For example, if the far-field probe, or source antenna as it is sometimes called, is predominantly polarised as that matching the AUT (co-polarised), then the pattern will have higher values than when it is imperfectly matched to the AUT polarisation (cross-polarised). With the far-field probe antenna downrange, pointing at the AUT positioner, at least two orientations of the probe are required to completely characterise the AUT's polarisation. For convenience, the two orientations should be orthogonal to each other and perpendicular to the direction of propagation. In most ranges, this is done by making a measurement and rotating the probe by 90° about its boresight direction and repeating the measurement. If only a linear co-polar and cross-polar pattern are required, the operator may decide to locate the peak of the pattern and then rotate the probe's angle so that the lowest value is received. This angle is the cross-polar angle. The co-polar pattern is then measured 90° from this angle.

If a complete characterisation of the polarisation is required, then the operator must measure both the amplitude and the phase for the two orthogonal polarisations. With these two measurements and a perfect far-field probe, any polarisation can be synthesised. If the probe's polarisation is not perfect, additional correction must be performed to correct for the probe's polarisation effects. Although this correction is straightforward, it is not part of this discussion.

Each positioner configuration has a natural basis of polarisation vectors. As with the pattern tabulating (plotting) angles, these vectors can be converted to other

bases using a series of transformations. Polarisation patterns include direction information about the antenna's performance in a particular orientation. For example, perhaps it is desired to know how sensitive the antenna is to signals oriented along the horizon as opposed to those vertical. In general, the AUT's pattern will not have the same polarisation at all angles. In fact, at some angles, the polarisation could be directly opposite of the desired pattern. Some of these become design issues if cross-pol pattern rejection is of major concern. Understanding, polarisation conversion and comparison between ranges using different positioner configurations is very important in determining cross-pol performance.

4.2.1 Ludwig I (Cartesian)

The Cartesian polarisation basis, Ludwig's definition I [3], corresponds to resolving the electric field onto three unit vectors aligned with each of the three Cartesian axes. This can be expressed as

$$\underline{E}(\hat{r}) = E_x(\hat{r})\hat{e}_x + E_y(\hat{r})\hat{e}_y + E_z(\hat{r})\hat{e}_z \quad (4.43)$$

This definition is valid in the near and far zones. Here, the unit vectors in the x -, y -, and z -directions are denoted by

$$X - \text{unit vector} = \hat{e}_x \quad (4.44)$$

$$Y - \text{unit vector} = \hat{e}_y \quad (4.45)$$

$$Z - \text{unit vector} = \hat{e}_z \quad (4.46)$$

These are scalar unit vectors where

$$\hat{e}_x \cdot \hat{e}_x = \hat{e}_y \cdot \hat{e}_y = \hat{e}_z \cdot \hat{e}_z = 1 \quad (4.47)$$

And,

$$\hat{e}_x \cdot \hat{e}_y = \hat{e}_x \cdot \hat{e}_z = \hat{e}_y \cdot \hat{e}_z = 0 \quad (4.48)$$

To illustrate how to find, for example, the x -component of a field vector using the dot product we see that

$$\underline{E} \cdot \hat{e}_x = \left(E_x \hat{e}_x + E_y \hat{e}_y + E_z \hat{e}_z \right) \cdot \hat{e}_x = E_x \quad (4.49)$$

This concept is used when evaluating each of the field components defined in the following section and the generalised definition of the dot product is also employed when defining circular polarisation bases as will be illustrated below. This arrangement is illustrated in Figure 4.21 which shows the x -axis orientated red unit vectors and the y -axis orientated blue unit vectors which are depicted as arrows placed over the surface of a unit sphere, the z -directed unit vectors have been omitted from the plot. This illustrates that this definition is effectively

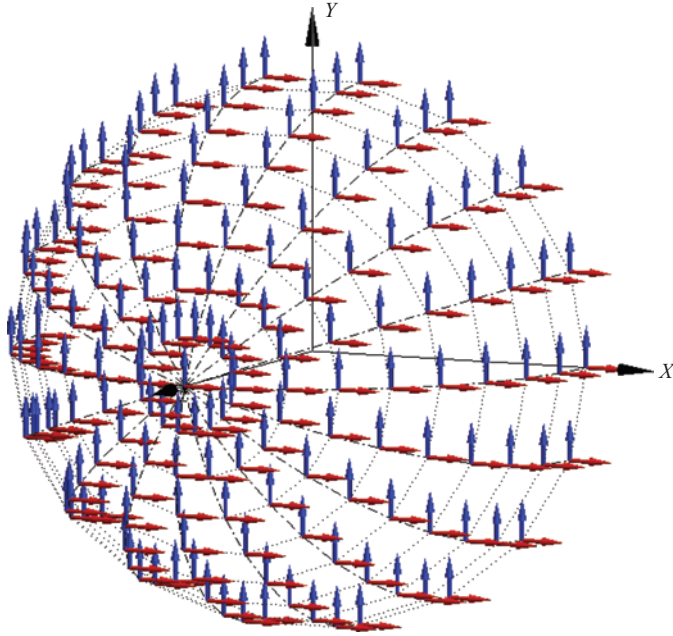


Figure 4.21 Cartesian polarisation basis (LI), E_x , E_y

defining the polarisation on a flat-screen normal to the boresight direction of the AUT. Clearly around the boresight direction, the co-polar and cross polarisation is as one would normally measure. The dotted grid lines represent lines of constant θ and ϕ upon which the conceptual far-field vector pattern function is tabulated.

By way of illustration, Figures 4.22–4.24 contain a false colour grey-scale plot of an SGH that has been plotted using a regular azimuth over elevation coordinate system having been resolved onto a Ludwig I Cartesian polarisation basis.

4.2.2 Polar spherical

If instead the electric field is resolved onto a spherical polarisation basis, then it is possible to define three further polarisation bases, each corresponding to placing the pole along the x -, y - or z -axes, respectively, with each corresponding to one of the positioner arrangements described above. For the case of the polar spherical polarisation basis, the electric field is resolved onto three unit vectors, one aligned to each of the three spherical unit vectors, $\hat{e}_\theta, \hat{e}_\phi, \hat{e}_r$. This is illustrated in Figure 4.25 where the red arrows represent the \hat{e}_θ -orientated unit vectors and the blue arrows represent the \hat{e}_ϕ -orientated unit vectors. The \hat{e}_r -orientated unit vectors are not plotted, as there is no field in this direction since in the far-field all radiation is transverse and wave propagation is in the radial direction. As before, the blue grid lines represent lines of constant azimuth and elevation upon which the far-field vector pattern function is tabulated.

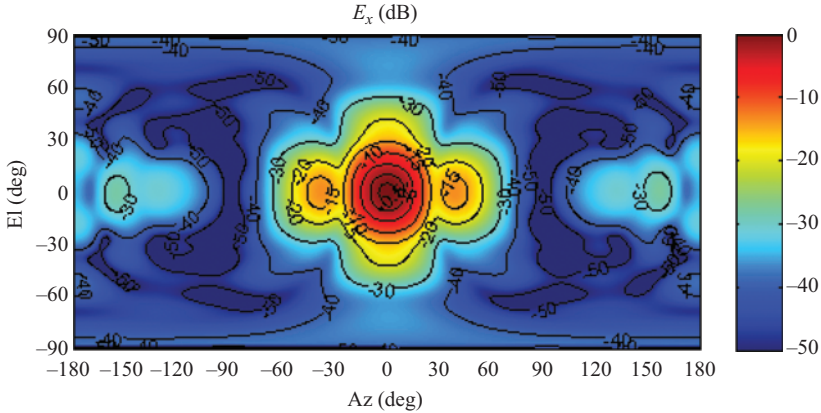


Figure 4.22 *x*-Polarised field component of an SGH plotted using an azimuth over elevation coordinate system

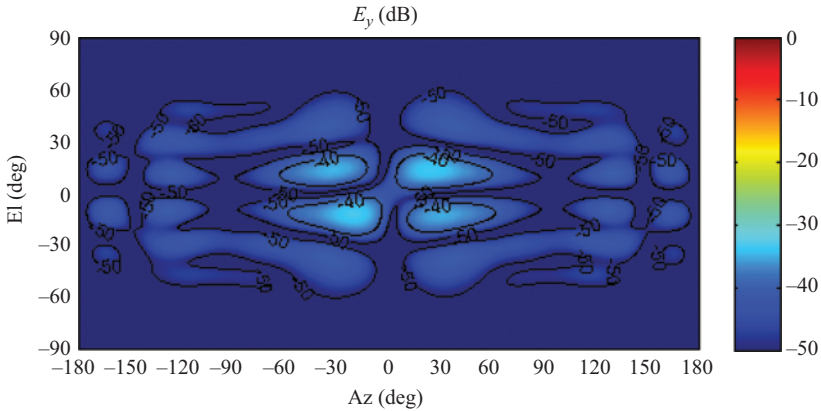


Figure 4.23 *y*-Polarised field component of an SGH plotted using an azimuth over elevation coordinate system

Here, the pole of the azimuth over elevation tabulation grid lies north and south where the $\pm y$ -axis pierces the unit sphere. Unfortunately, this polarisation basis displays a soft singularity, i.e. a discontinuity, in the z -direction in both the forward and back hemisphere, where $\theta = n\pi$ and $n = 0, 1, 2, \dots$. Thus, to implement this definition, a choice must be made as to the orientation of \hat{e}_θ and \hat{e}_ϕ at the poles. Typically, \hat{e}_θ is chosen to be aligned to either $\phi = 0^\circ$ or $\phi = 90^\circ$ and \hat{e}_ϕ is chosen to be mutually orthogonal to \hat{e}_θ and \hat{e}_r . Within this text, the $\phi = 0^\circ$ convention has been adopted. When the electric field is decomposed onto these unit vectors and the

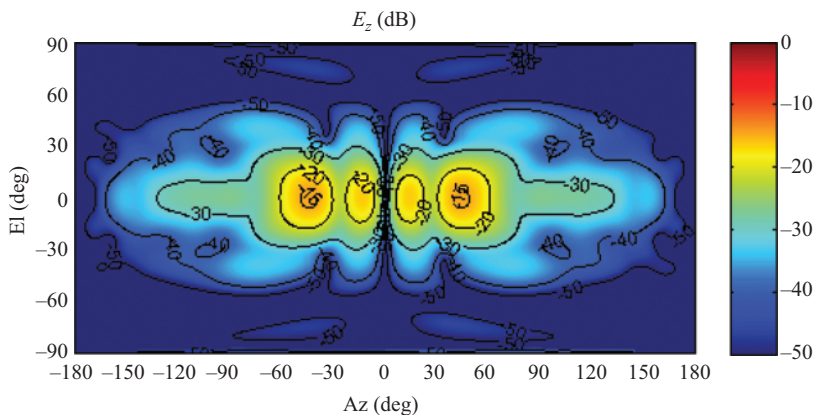


Figure 4.24 *z*-Polarised field component of an SGH plotted using an azimuth over elevation coordinate system

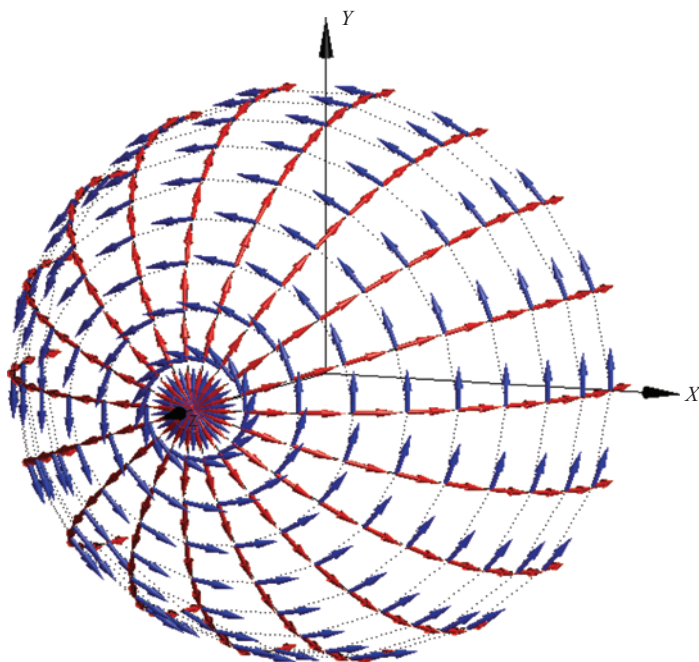


Figure 4.25 Polar spherical polarisation basis (E_θ, E_ϕ)

radial component is assumed zero, the total field can be expressed mathematically as follows:

$$\underline{E}(\hat{r}) = E_\theta(\hat{r})\underline{\hat{e}}_\theta + E_\phi(\hat{r})\underline{\hat{e}}_\phi \tag{4.50}$$

If the position vector to a point can be expressed as $\underline{r} = \underline{r}(u_1, u_2, u_3)$, a tangent vector to the curve $u_1 = u_1(x, y, z)$ at that point for which $u_2 = u_2(x, y, z)$ and $u_3 = u_3(x, y, z)$ are constant is, $\partial \underline{r} / \partial u_1$. Thus, a unit tangent vector in this direction is

$$\underline{\hat{e}}_1 = \frac{\frac{\partial \underline{r}}{\partial u_1}}{\left| \frac{\partial \underline{r}}{\partial u_1} \right|} \quad (4.51)$$

Similar expressions can be written down for the remaining unit vectors $\underline{\hat{e}}_2$ and $\underline{\hat{e}}_3$. Thus, if the position of the point in space is expressed in spherical coordinates (Table 4.2), then

$$\underline{r} = \sin \theta \cos \phi \underline{\hat{e}}_x + \sin \theta \sin \phi \underline{\hat{e}}_y + \cos \theta \underline{\hat{e}}_z \quad (4.52)$$

then

$$\frac{\partial \underline{r}}{\partial \theta} = \cos \theta \cos \phi \underline{\hat{e}}_x + \cos \theta \sin \phi \underline{\hat{e}}_y - \sin \theta \underline{\hat{e}}_z \quad (4.53)$$

Thus,

$$\left| \frac{\partial \underline{r}}{\partial \theta} \right| = \sqrt{\cos^2 \theta \cos^2 \phi + \cos^2 \theta \sin^2 \phi - \sin^2 \theta} = 1 \quad (4.54)$$

Hence, the unit vector in the direction of increasing θ that is tangential to the surface of a sphere

$$\underline{\hat{e}}_\theta = \cos \theta \cos \phi \underline{\hat{e}}_x + \cos \theta \sin \phi \underline{\hat{e}}_y - \sin \theta \underline{\hat{e}}_z \quad (4.55)$$

Similarly,

$$\frac{\partial \underline{r}}{\partial \phi} = -\sin \theta \sin \phi \underline{\hat{e}}_x + \sin \theta \cos \phi \underline{\hat{e}}_y \quad (4.56)$$

$$\left| \frac{\partial \underline{r}}{\partial \phi} \right| = \sqrt{\sin^2 \theta \sin^2 \phi + \sin^2 \theta \cos^2 \phi} = \sin \theta \quad (4.57)$$

Hence,

$$\underline{\hat{e}}_\phi = -\sin \phi \underline{\hat{e}}_x + \cos \phi \underline{\hat{e}}_y \quad (4.58)$$

The relationship between the Cartesian and spherical field components can be expressed in matrix notation as

$$\begin{bmatrix} E_\theta \\ E_\phi \end{bmatrix} = \begin{bmatrix} \cos \theta \cos \phi & \cos \theta \sin \phi & -\sin \theta \\ -\sin \phi & \cos \phi & 0 \end{bmatrix} \cdot \begin{bmatrix} E_x \\ E_y \\ E_z \end{bmatrix} \quad (4.59)$$

As the three-column by two-row matrix is both orthogonal and correctly normalised to unity, the inverse matrix is equal to the matrix transpose and the converse transformation can be expressed again in matrix notation as follows:

$$\begin{bmatrix} E_x \\ E_y \\ E_z \end{bmatrix} = \begin{bmatrix} \cos \theta \cos \phi & -\sin \phi \\ \cos \theta \sin \phi & \cos \phi \\ -\sin \theta & 0 \end{bmatrix} \cdot \begin{bmatrix} E_\theta \\ E_\phi \end{bmatrix} \quad (4.60)$$

This results in there not being a convenient principal co-polar and cross-polar field value, i.e. definition, around the AUT boresight as this definition involves placing the pole of the polarisation basis along the z-axis. Although inconvenient in many ways, this is the polarisation basis that is most closely associated with the useful phi-over-theta ‘model tower’ positioning system, it is commonly encountered when making either near- or far-field spherical antenna pattern measurements.

By way of a further illustration, Figures 4.26 and 4.27 contain a grey-scale plot of an SGH that has been plotted using a regular azimuth over elevation coordinate system having been resolved onto a polar spherical polarisation basis.

4.2.3 Ludwig II (Az/El, El/Az)

If the electric field is resolved onto a spherical polarisation basis, then it is possible to define three polarisation bases, each corresponding to placing the pole along the x-, y- or z-axes, respectively, with each corresponding to one of the positioner arrangements described above. The z-axis aligned case was discussed in the preceding section. Ludwig’s definition II [3], therefore, has two useful definitions in terms of a ‘co-polar’ and ‘cross-polar’ value on boresight. The azimuth-over-elevation polarisation basis being the first of these which places the poles in the

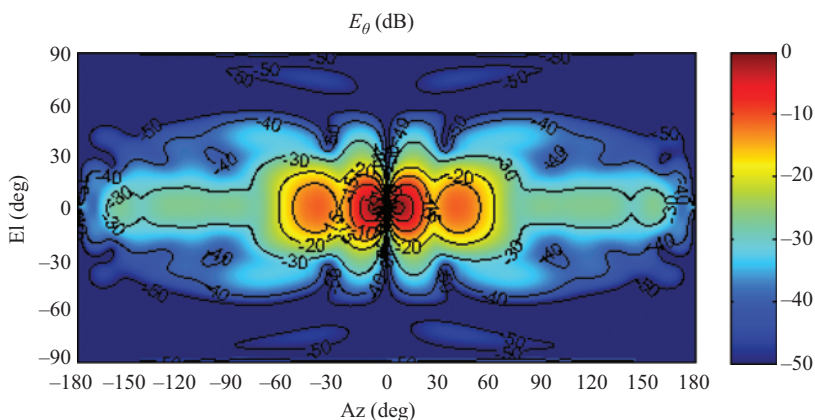


Figure 4.26 θ -Polarised field component of an SGH plotted using an azimuth over elevation coordinate system

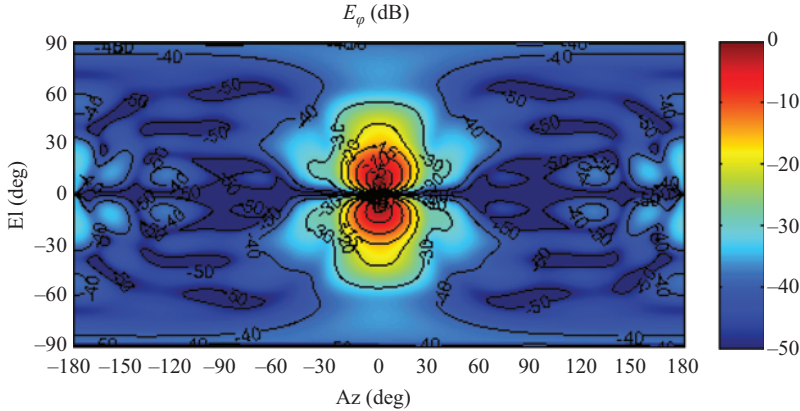


Figure 4.27 ϕ -Polarised field component of an SGH plotted using an azimuth over elevation coordinate system

y -axis and can be expressed as

$$\underline{E}(\hat{r}) = E_{az}(\hat{r})\hat{e}_{az} + E_{el}(\hat{r})\hat{e}_{el} \quad (4.61)$$

Again, as we are primarily concerned with representing far-field antenna patterns, the radial orientated field component is not considered, as this is identically zero which is a direct consequence of the plane-wave condition. This arrangement is illustrated schematically in Figure 4.28, which shows the vertical (blue) and horizontal (red) unit vectors depicted as arrows placed over the surface of a unit sphere and correspond to the case where the pole is placed along the y -axis. The \hat{e}_r -orientated unit vectors are not plotted.

Clearly, around the boresight direction, the two components are naturally orthogonal and consistent with Ludwig I. Using the same procedure to obtain the transformation between the field components as before (Table 4.2), we find that as

$$\underline{r} = \sin Az \cos El \hat{e}_x + \sin El \hat{e}_y + \cos Az \cos El \hat{e}_z \quad (4.62)$$

Then,

$$\frac{\partial \underline{r}}{\partial Az} = \cos Az \cos El \hat{e}_x - \sin Az \cos El \hat{e}_z \quad (4.63)$$

Thus,

$$\left| \frac{\partial \underline{r}}{\partial Az} \right| = \sqrt{\cos^2 Az \cos^2 El + \sin^2 Az \cos^2 El} = \cos El \quad (4.64)$$

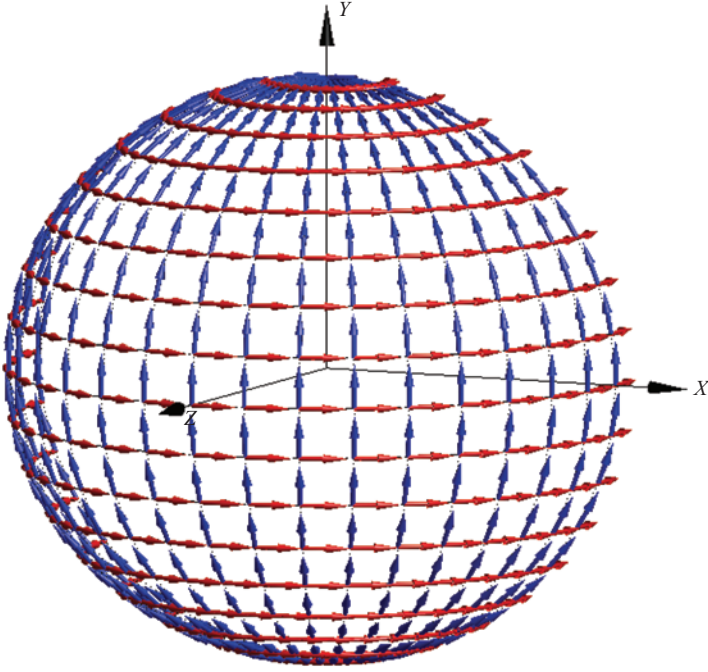


Figure 4.28 Ludwig second polarisation basis (LII) Az/El

Hence, the unit vector in the direction of increasing azimuth that is tangential to the surface of a sphere

$$\underline{\hat{e}}_{Az} = \cos Az \underline{\hat{e}}_x - \sin Az \underline{\hat{e}}_z \quad (4.65)$$

Similarly,

$$\frac{\partial \underline{r}}{\partial El} = -\sin Az \sin El \underline{\hat{e}}_x + \cos \phi El \underline{\hat{e}}_y - \cos Az \sin El \underline{\hat{e}}_z \quad (4.66)$$

$$\left| \frac{\partial \underline{r}}{\partial El} \right| = \sqrt{\sin^2 Az \sin^2 El + \cos^2 El + \cos^2 Az \sin^2 El} = 1 \quad (4.67)$$

Hence,

$$\underline{\hat{e}}_{El} = -\sin Az \sin El \underline{\hat{e}}_x + \cos El \underline{\hat{e}}_y - \cos Az \sin El \underline{\hat{e}}_z \quad (4.68)$$

The relationship between the Cartesian and azimuth over elevation spherical field components can be expressed in matrix notation as

$$\begin{bmatrix} E_{Az} \\ E_{El} \end{bmatrix} = \begin{bmatrix} \cos Az & 0 & -\sin Az \\ -\sin Az \sin El & \cos El & -\cos Az \sin El \end{bmatrix} \cdot \begin{bmatrix} E_x \\ E_y \\ E_z \end{bmatrix} \quad (4.69)$$

As the three-column by two-row matrix is both orthogonal and correctly normalised to unity, the inverse matrix is equal to the matrix transpose and the converse transformation can be expressed again in matrix notation as follows:

$$\begin{bmatrix} E_x \\ E_y \\ E_z \end{bmatrix} = \begin{bmatrix} \cos Az & -\sin Az \sin El \\ 0 & \cos El \\ -\sin Az & -\cos Az \sin El \end{bmatrix} \cdot \begin{bmatrix} E_{Az} \\ E_{El} \end{bmatrix} \quad (4.70)$$

Figures 4.29 and 4.30 contain a grey-scale plot of an SGH that has been plotted using a regular azimuth over elevation coordinate system having been resolved onto an azimuth over elevation polarisation basis.

There is another possible system which comes under the Ludwig II definition and that is the elevation over azimuth polarisation basis [3]. This is depicted in Figure 4.31.

Again around the boresight direction, the co-polar and x-polar components are naturally orthogonal and consistent with Ludwig I. Using the usual procedure (Table 4.2) to obtain the transformation between the field components as before, we find that as

$$\underline{r} = \sin a \underline{\hat{e}}_x + \cos a \sin \underline{\hat{e}}_y + \cos a \cos \underline{\hat{e}}_z \quad (4.71)$$

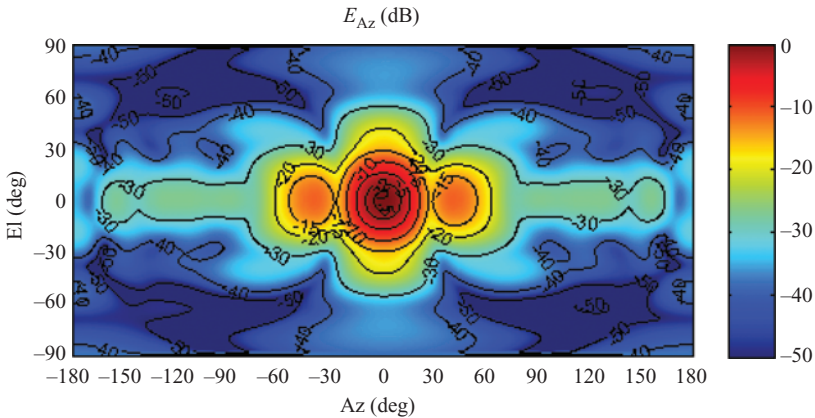


Figure 4.29 *Azimuth-polarised field component of an SGH plotted using an azimuth over elevation coordinate system*

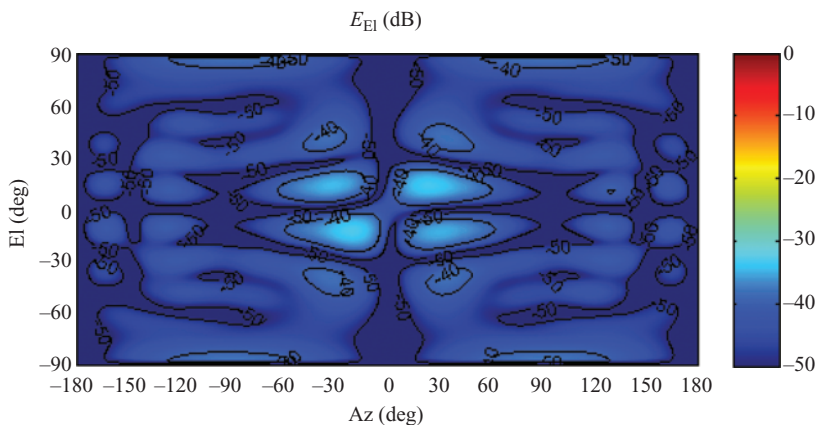


Figure 4.30 Elevation-polarised field component of an SGH plotted using an azimuth over elevation coordinate system

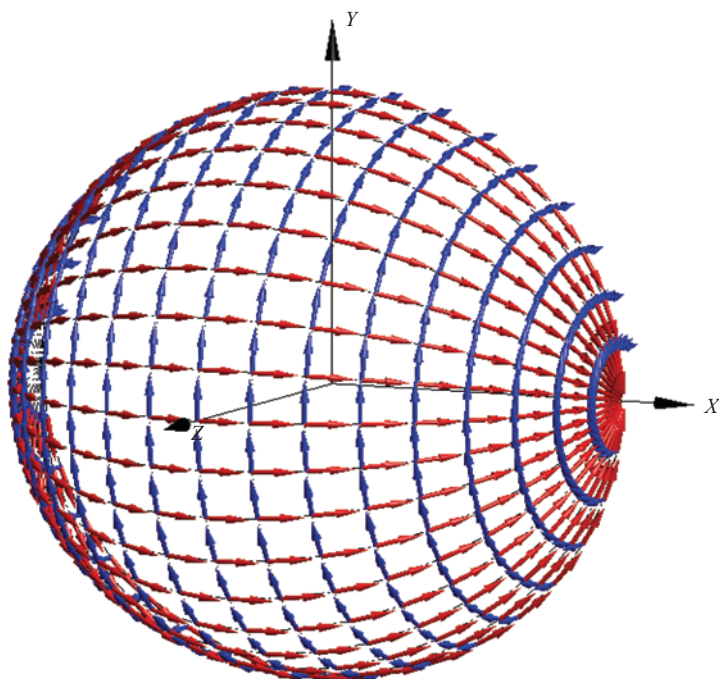


Figure 4.31 Ludwig second polarisation basis (LII) El/Az

Then,

$$\frac{\partial \underline{r}}{\partial \alpha} = \cos \alpha \underline{\hat{e}}_x - \sin \alpha \sin \varepsilon \underline{\hat{e}}_y - \sin \alpha \cos \varepsilon \underline{\hat{e}}_z \quad (4.72)$$

Thus,

$$\left| \frac{\partial \underline{r}}{\partial \alpha} \right| = \sqrt{\cos^2 \alpha + \sin^2 \alpha \sin^2 \varepsilon + \sin^2 \alpha \cos^2 \varepsilon} = 1 \quad (4.73)$$

Hence, the unit vector in the direction of increasing azimuth that is tangential to the surface of a sphere

$$\underline{\hat{e}}_\alpha = \cos \alpha \underline{\hat{e}}_x - \sin \alpha \sin \varepsilon \underline{\hat{e}}_y - \sin \alpha \cos \varepsilon \underline{\hat{e}}_z \quad (4.74)$$

Similarly,

$$\frac{\partial \underline{r}}{\partial \varepsilon} = \cos \alpha \cos \varepsilon \underline{\hat{e}}_y - \cos \alpha \sin \varepsilon \underline{\hat{e}}_z \quad (4.75)$$

Thus,

$$\left| \frac{\partial \underline{r}}{\partial \varepsilon} \right| = \sqrt{\cos^2 \alpha \cos^2 \varepsilon + \cos^2 \alpha \sin^2 \varepsilon} = \cos \alpha \quad (4.76)$$

Hence, the unit vector in the direction of increasing elevation that is tangential to the surface of a sphere

$$\underline{\hat{e}}_\varepsilon = \cos \varepsilon \underline{\hat{e}}_y - \sin \varepsilon \underline{\hat{e}}_z \quad (4.77)$$

The relationship between the Cartesian and elevation over azimuth spherical field components can be expressed in matrix notation as

$$\begin{bmatrix} E_\alpha \\ E_\varepsilon \end{bmatrix} = \begin{bmatrix} \cos \alpha & -\sin \alpha \sin \varepsilon & -\sin \alpha \cos \varepsilon \\ 0 & \cos \varepsilon & -\sin \varepsilon \end{bmatrix} \cdot \begin{bmatrix} E_x \\ E_y \\ E_z \end{bmatrix} \quad (4.78)$$

As the three-column by two-row matrix is both orthogonal and correctly normalised to unity, the inverse matrix is equal to the matrix transpose and the converse transformation can be expressed again in matrix notation as follows:

$$\begin{bmatrix} E_x \\ E_y \\ E_z \end{bmatrix} = \begin{bmatrix} \cos \alpha & 0 \\ -\sin \alpha \sin \varepsilon & \cos \varepsilon \\ -\sin \alpha \cos \varepsilon & -\sin \varepsilon \end{bmatrix} \cdot \begin{bmatrix} E_\alpha \\ E_\varepsilon \end{bmatrix} \quad (4.79)$$

Figures 4.32 and 4.33 contain a grey-scale plot of an SGH that has been plotted using a regular azimuth over elevation coordinate system having been resolved onto an elevation over azimuth polarisation basis.

Outside boresight both Ludwig I and II deviate from what one would normally measure and indeed use in a practical scenario. Clearly, it is preferable to utilise a

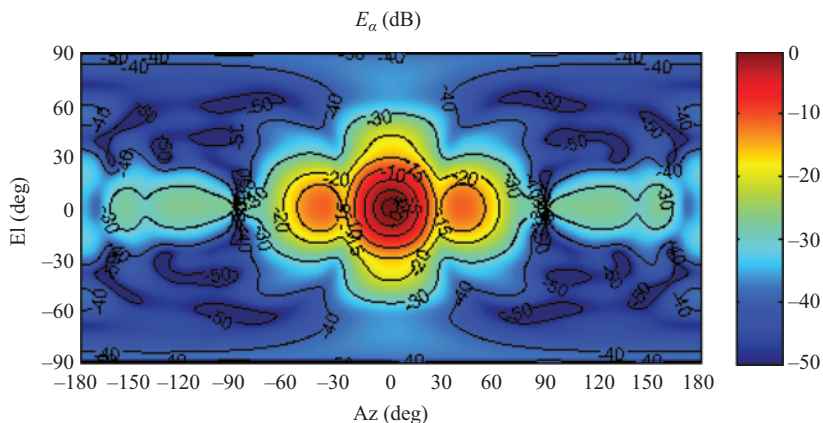


Figure 4.32 α -Polarised field component of an SGH plotted using an azimuth over elevation coordinate system

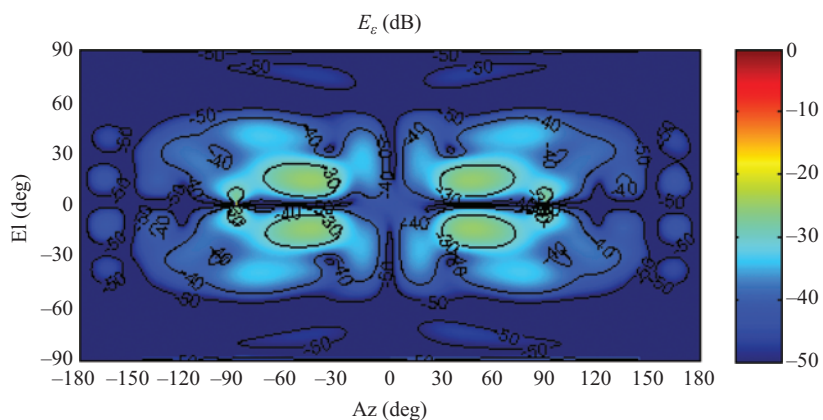


Figure 4.33 ϵ -Polarised field component of an SGH plotted using an azimuth over elevation coordinate system

definition that applies over all angles and the resolution of this difficulty motivated the adoption of Definition III.

4.2.4 Ludwig III (co-polar, cross-polar and cross-polar discrimination)

This definition was formulated mathematically by Ludwig after its usage had become commonplace in the antenna measurement community [3]. This definition corresponds physically to rolling the range antenna [remote standard antenna (RSA)] in χ as the AUT is rotated in ϕ . It has the inherent advantage that it removes the soft singularity at $\theta = 0$ present within the polar spherical definition. Here, the

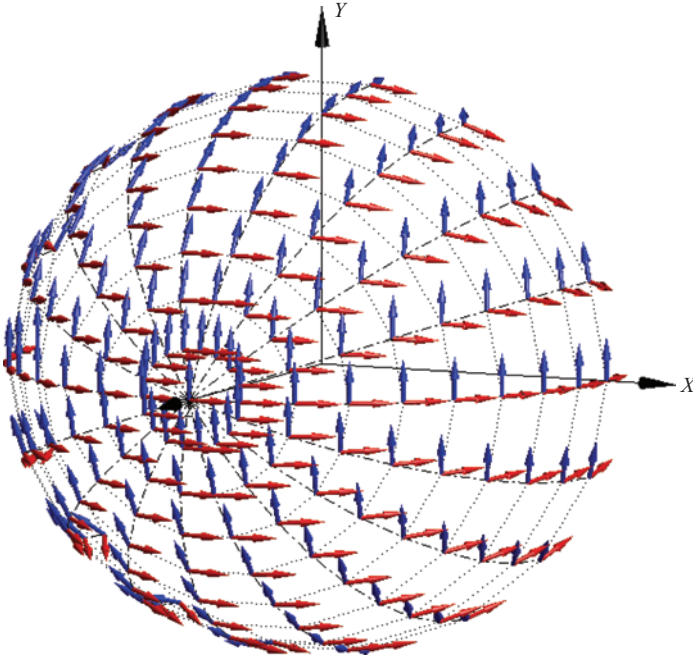


Figure 4.34 Ludwig III x-co-polar polarisation basis

electric field is resolved onto three unit vectors, one aligned to each of the three unit vectors, \hat{e}_{co} , \hat{e}_{cross} , \hat{e}_r . This is illustrated in Figure 4.34 where the red arrows represent the x-co-polar \hat{e}_{co} -orientated unit vectors and the blue arrows represent the \hat{e}_{cross} -orientated unit vectors. Here, an ‘x-co-polar’ definition has been assumed. The \hat{e}_r -orientated unit vectors are not shown as in the far-field all radiation is transverse and propagates in the radial direction. Again, the dotted grey grid lines represent lines of constant θ and ϕ upon which the conceptual far-field vector pattern function is tabulated.

For the RSA and the AUT to remain polarisation matched, the RSA must be rotated through an angle $-\phi$ as the AUT is rotated through an angle ϕ . Thus, let the polarisation-matched orientation be \hat{e}_{co} , and an orientation that is mutually orthogonal to this and the direction of propagation be \hat{e}_{cr} . When the electric field is decomposed onto these unit vectors the total field can be expressed mathematically as follows:

$$\underline{E} = E_{co}\hat{e}_{co} + E_{cr}\hat{e}_{cr} \tag{4.80}$$

where

$$\hat{e}_{cross} = \hat{e}_r \times \hat{e}_{co} \tag{4.81}$$

and obviously by design

$$\underline{\hat{e}}_{co} \cdot \underline{\hat{e}}_{cross} = 0 \quad (4.82)$$

The so-called co-polar and cross-polar unit vectors are related to the spherical unit vectors through

$$\underline{\hat{e}}_{co} = \cos \phi \underline{\hat{e}}_{\theta} - \sin \phi \underline{\hat{e}}_{\phi} \quad (4.83)$$

$$\underline{\hat{e}}_{cr} = \sin \phi \underline{\hat{e}}_{\theta} + \cos \phi \underline{\hat{e}}_{\phi} \quad (4.84)$$

Since, when expressed in matrix notation this is clearly an orthogonal and unit normalised matrix the matrix inverse is equal to matrix transpose hence

$$\underline{\hat{e}}_{\theta} = \cos \phi \underline{\hat{e}}_{co} + \sin \phi \underline{\hat{e}}_{cr} \quad (4.85)$$

$$\underline{\hat{e}}_{\phi} = -\sin \phi \underline{\hat{e}}_{co} + \cos \phi \underline{\hat{e}}_{cr} \quad (4.86)$$

As

$$\underline{E} = E_{\theta} \underline{\hat{e}}_{\theta} + E_{\phi} \underline{\hat{e}}_{\phi} \quad (4.87)$$

Thus,

$$\underline{E} = E_{\theta} (\cos \phi \underline{\hat{e}}_{co} + \sin \phi \underline{\hat{e}}_{cr}) + E_{\phi} (-\sin \phi \underline{\hat{e}}_{co} + \cos \phi \underline{\hat{e}}_{cr}) \quad (4.88)$$

Hence,

$$\underline{E} = (E_{\theta} \cos \phi - E_{\phi} \sin \phi) \underline{\hat{e}}_{co} + (E_{\theta} \sin \phi + E_{\phi} \cos \phi) \underline{\hat{e}}_{cr} \quad (4.89)$$

Finally,

$$E_{co} = E_{\theta} \cos \phi - E_{\phi} \sin \phi \quad (4.90)$$

$$E_{cr} = E_{\theta} \sin \phi + E_{\phi} \cos \phi \quad (4.91)$$

The relationship between the spherical and Ludwig III field components can be expressed in matrix notation as

$$\begin{bmatrix} E_{co} \\ E_{cross} \end{bmatrix} = \begin{bmatrix} \cos \phi & -\sin \phi \\ \sin \phi & \cos \phi \end{bmatrix} \cdot \begin{bmatrix} E_{\theta} \\ E_{\phi} \end{bmatrix} \quad (4.92)$$

Again, as the two-column by two-row matrix is both orthogonal and correctly normalised to unity the inverse matrix is equal to the matrix transpose and the converse transformation can be expressed again in matrix notation as follows:

$$\begin{bmatrix} E_{\theta} \\ E_{\phi} \end{bmatrix} = \begin{bmatrix} \cos \phi & \sin \phi \\ -\sin \phi & \cos \phi \end{bmatrix} \cdot \begin{bmatrix} E_{co} \\ E_{cross} \end{bmatrix} \quad (4.93)$$

Thus, the soft singularity encountered on boresight ($\theta = 0$) is removed. However, this is achieved at the expense of doubling the severity of the singularity encountered at

$$\theta = \pm\pi, \pm3\pi, \pm5\pi, \dots \tag{4.94}$$

As this is in the opposite direction of the boresight direction, this is generally of little practical consequence. Often, these equations are modified so that a reference angle is included that represents the angle from the x -axis to the major axis of the polarisation ellipse thus

$$\begin{bmatrix} E_{co} \\ E_{cross} \end{bmatrix} = \begin{bmatrix} \cos(\phi - \phi_0) & -\sin(\phi - \phi_0) \\ \sin(\phi - \phi_0) & \cos(\phi - \phi_0) \end{bmatrix} \cdot \begin{bmatrix} E_\theta \\ E_\phi \end{bmatrix} \tag{4.95}$$

Here, ϕ_0 is the reference angle and enables, for example, a y -axis co-polar reference to be chosen in cases where that definition is convenient. Figure 4.35 shows an example of this where the co-polar polarisation basis has been rotated by 40° to illustrate a ‘slanted’ co-polarisation definition. Comparison with Figure 4.34 enables the effect of the generalised rotated polarisation reference as shown in Figure 4.35 to be seen more clearly.

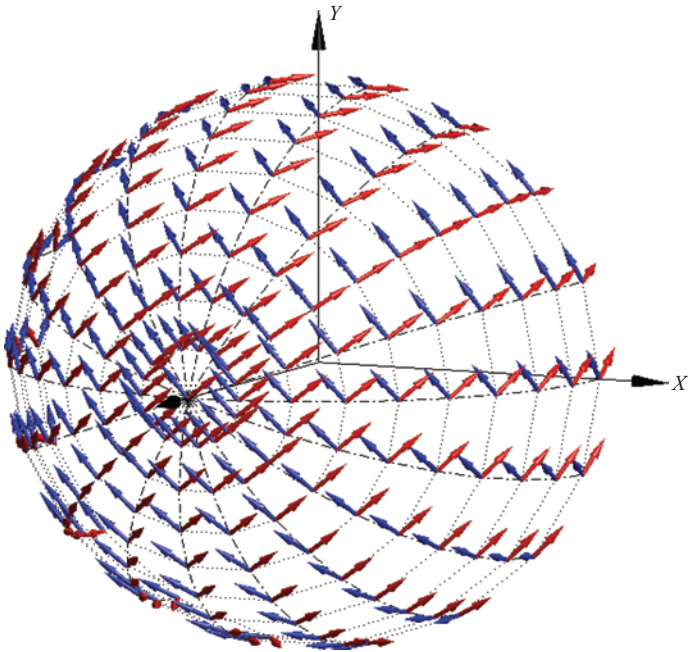


Figure 4.35 *Ludwig III rotated-co-polar polarisation basis*

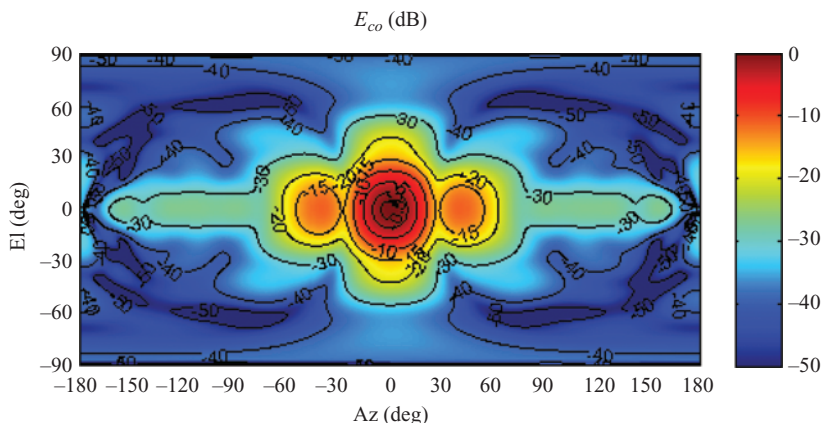


Figure 4.36 Co-polarised field component of an SGH plotted using an azimuth over elevation coordinate system

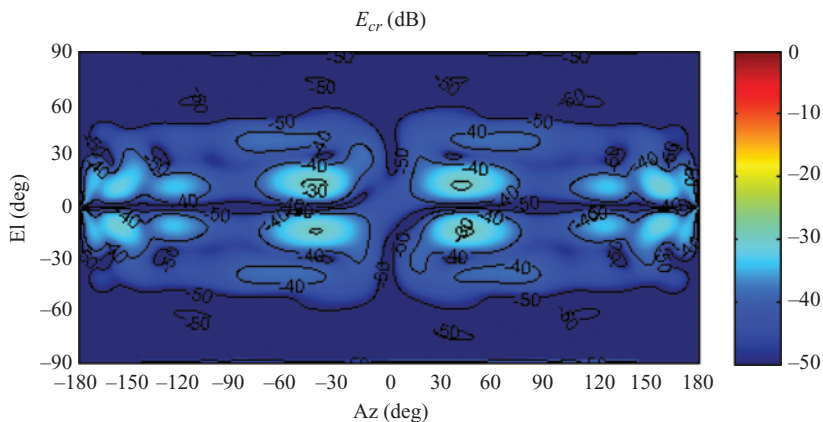


Figure 4.37 Cross-polarised field component of an SGH plotted using an azimuth over elevation coordinate system

Figures 4.36 and 4.37 contain a false colour plot of an SGH that has been plotted using a regular azimuth over elevation coordinate system having been resolved onto a Ludwig III co-polar and cross-polar polarisation basis where the co-polar reference direction is aligned with the x -axis.

The above definition assumes that the co-polar reference direction is aligned with the positive x -axis, i.e. horizontal axis. This definition can easily be modified to accommodate a vertically polarised reference direction by introducing a ϕ -offset in the definition whereby the relationship between the spherical and Ludwig III

field components can be expressed in matrix notation as

$$\begin{bmatrix} E_{co} \\ E_{cross} \end{bmatrix} = \begin{bmatrix} \cos(\phi - \phi_0) & -\sin(\phi - \phi_0) \\ \sin(\phi - \phi_0) & \cos(\phi - \phi_0) \end{bmatrix} \cdot \begin{bmatrix} E_\theta \\ E_\phi \end{bmatrix} \tag{4.96}$$

Here, ϕ_0 is used to denote the reference direction measured from the positive x -axis to the major axis of the polarisation ellipse. Thus, when $\phi_0 = \pi/2$, the co-polar reference is vertically polarised. This definition relies upon the principle that the main beam direction, i.e. the antenna boresight, is aligned with the z -axis. Although we have removed the soft singularity on boresight, we have achieved this at the price of increasing the severity of the polarisation issue in the opposite direction, and this is illustrated in Figure 4.38. This issue is not normally problematic as for many antennas there is very little field propagating in this direction and so it is seldom noticed.

When considering mechanically or electrically scanned antennas or a single spacecraft with many antennas each orientated such that their respective main beams point in different directions this may not in fact be the case and this is the motivation for the development of a more general LIII definition. This can be implemented in a straightforward way, although in this case it is necessary to apply the isometric rotations to the Cartesian, that is, Ludwig I, field components. A detailed description of the rotation process is now given as

1. Define the polarisation boresight system as a rotation from the nadir-centred azimuth over elevation plotting system.

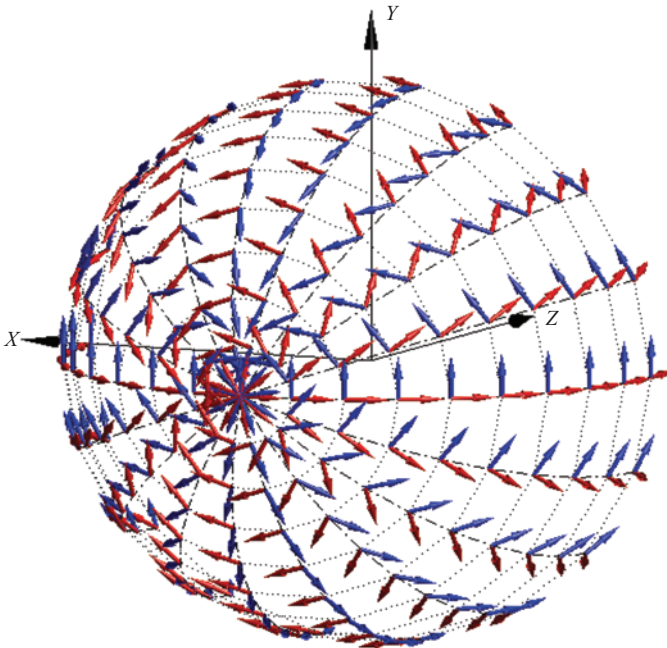


Figure 4.38 *Ludwig III co-polar and cross-polar polarisation basis viewed from behind*

2. Transform Cartesian field components into the new rotated basis specified by the polarisation boresight.
3. Transform the Cartesian direction cosines of the field point into the new rotated system.
4. Calculate the new spherical angles, θ and ϕ , of the data point in the new system.
5. Calculate spherical field components in the rotated coordinate system from the rotated Cartesian field components.
6. Calculate Ludwig III co-polar and cross-polar field components in the rotated system.

Circular polarisation will be considered in detail in the following sections; however, it is worthwhile to note that many workers make the conversion from linear to circular polarisation using the LIII co-polar and cross-polar field components. The reason for this is that the fields and the tilt angle are well defined in the direction of greatest interest.

The differences between the various definitions of cross-polarisation that are presented in the above sections are subtle and without an attendant definition being provided with the plotted antenna patterns it is often far from apparent as to which definition has been used. It is also clear that the cross-polarised patterns show greater differences and this can become confusing when comparing between patterns if great care is not taken.

4.2.5 Conversion between polarisation bases

It is often the case in practice that an antenna pattern is acquired using one of the polarisation definitions above and for the purposes of post-processing or pattern comparison, it is required to convert that data into an alternative definition of cross-polarisation. This section considers that task and provides formulae for implementing this change of polarisation basis.

As with the conversion of direction vectors, the procedure for converting polarisation basis is perhaps most readily accomplished by first resolving the fields onto a triad of Cartesian field components before and then resolving the fields onto the required basis. This strategy is used to derive the analytic transformations that are presented in the following sections for convenience.

4.2.5.1 Conversion from polar spherical to azimuth over elevation bases

The transformation from polar spherical to LII azimuth over elevation field components can be accomplished by coupling together the relevant matrix equations thus

$$\begin{bmatrix} E_{Az} \\ E_{El} \end{bmatrix} = \begin{bmatrix} \cos Az & 0 & -\sin Az \\ -\sin Az \sin El & \cos El & -\cos Az \sin El \end{bmatrix} \cdot \begin{bmatrix} \cos \theta \cos \phi & -\sin \phi \\ \cos \theta \sin \phi & \cos \phi \\ -\sin \theta & 0 \end{bmatrix} \cdot \begin{bmatrix} E_{\theta} \\ E_{\phi} \end{bmatrix} \quad (4.97)$$

Multiplying yields a two-by-two matrix multiplied by a column vector. The elements of the square matrix are

$$\begin{aligned}
 A_{1,1} &= \cos Az \cos \theta \cos \phi + \sin Az \sin \theta \\
 &= \cos^2 Az \cos El \cos \phi + \frac{\sin^2 \theta \cos \phi}{\cos El} \\
 &= (\cos^2 Az \cos^2 El + \sin^2 \theta) \frac{\cos \phi}{\cos El} \\
 &= \frac{\cos \phi}{\cos El}
 \end{aligned} \tag{4.98}$$

$$\begin{aligned}
 A_{2,1} &= -\sin Az \sin El \cos \theta \cos \phi + \cos El \cos \theta \sin \phi + \cos Az \sin El \sin \theta \\
 &= -\frac{\sin^2 \theta \sin \phi \cos \theta \cos^2 \phi}{\cos El} + \cos El \cos \theta \sin \phi + \frac{\cos \theta \sin^2 \theta \sin \phi}{\cos El} \\
 &= (-\sin^2 \theta \cos^2 \phi + 1 - \sin^2 \theta \sin^2 \phi + \sin^2 \theta) \frac{\cos \theta \sin \phi}{\cos El} \\
 &= (1 - \sin^2 \theta \{\cos^2 \phi + \sin^2 \phi - 1\}) \frac{\cos \theta \sin \phi}{\cos El} \\
 &= \frac{\cos \theta \sin \phi}{\cos El}
 \end{aligned} \tag{4.99}$$

$$A_{1,2} = -\cos Az \sin \phi = -\frac{\cos \theta \sin \phi}{\cos El} \tag{4.100}$$

$$\begin{aligned}
 A_{2,2} &= \sin Az \sin El \sin \phi + \cos El \cos \phi \\
 &= \left(\frac{\sin^2 \theta \sin^2 \phi}{\cos El} + \cos El \right) \cos \phi \\
 &= \frac{\cos \phi}{\cos El}
 \end{aligned} \tag{4.101}$$

This therefore reduces to the desired final expression

$$\begin{bmatrix} E_{Az} \\ E_{El} \end{bmatrix} = \frac{1}{\cos El} \begin{bmatrix} \cos \phi & -\cos \theta \sin \phi \\ \cos \theta \sin \phi & \cos \phi \end{bmatrix} \cdot \begin{bmatrix} E_{\theta} \\ E_{\phi} \end{bmatrix} \tag{4.102}$$

where

$$\cos El = \sqrt{1 - \sin^2 El} = \sqrt{1 - \sin^2 \theta \sin^2 \phi} \tag{4.103}$$

The inverse transformation can be expressed by evaluating the matrix inverse yielding

$$\begin{bmatrix} E_{\theta} \\ E_{\phi} \end{bmatrix} = \frac{1}{\cos^2 \phi + \cos^2 \theta \sin^2 \phi} \begin{bmatrix} \cos \phi \cos El & \cos \theta \sin \phi \cos El \\ -\cos \theta \sin \phi \cos El & \cos \phi \cos El \end{bmatrix} \cdot \begin{bmatrix} E_{Az} \\ E_{El} \end{bmatrix} \tag{4.104}$$

From trigonometric identities, we can simplify the common denominator as follows:

$$\begin{aligned}
 \cos^2 El &= 1 - \sin^2 \theta \sin^2 \phi \\
 &= 1 - (1 - \cos^2 \theta) \sin^2 \phi \\
 &= 1 - \sin^2 \phi + \cos^2 \theta \sin^2 \phi \\
 &= \cos^2 \phi + \cos^2 \theta \sin^2 \phi
 \end{aligned} \tag{4.105}$$

This therefore yields the simplified final result

$$\begin{bmatrix} E_\theta \\ E_\phi \end{bmatrix} = \frac{1}{\cos El} \begin{bmatrix} \cos \phi & \cos \theta \sin \phi \\ -\cos \theta \sin \phi & \cos \phi \end{bmatrix} \cdot \begin{bmatrix} E_{Az} \\ E_{El} \end{bmatrix} \tag{4.106}$$

4.2.5.2 Conversion from polar spherical to elevation over azimuth bases

A similar procedure can be used to obtain the conversion expressions that relate the polar spherical field components to the elevation over azimuth field components, whereby

$$\begin{bmatrix} E_\alpha \\ E_\varepsilon \end{bmatrix} = \begin{bmatrix} \cos \alpha & -\sin \alpha \sin \varepsilon & -\sin \alpha \cos \varepsilon \\ 0 & \cos \varepsilon & -\sin \varepsilon \end{bmatrix} \cdot \begin{bmatrix} \cos \theta \cos \phi & -\sin \phi \\ \cos \theta \sin \phi & \cos \phi \\ -\sin \theta & 0 \end{bmatrix} \cdot \begin{bmatrix} E_\theta \\ E_\phi \end{bmatrix} \tag{4.107}$$

Multiplying yields a two-by-two matrix multiplied by a column vector. The elements of the square matrix are

$$\begin{aligned}
 A_{1,1} &= \cos \alpha \cos \theta \cos \phi - \sin \alpha \sin \varepsilon \cos \theta \sin \phi + \sin \alpha \cos \varepsilon \sin \theta \\
 &= \cos \alpha \cos \theta \cos \phi - \frac{\sin^2 \theta \cos \phi \cos \theta \sin^2 \phi}{\cos \alpha} + \frac{\sin^2 \theta \cos \phi \cos \theta}{\cos \alpha} \\
 &= (\cos^2 \alpha - \sin^2 \theta \sin^2 \phi + \sin^2 \theta) \frac{\cos \theta \cos \phi}{\cos \alpha} \\
 &= (1 - \sin^2 \theta \cos^2 \phi - \sin^2 \theta \sin^2 \phi + \sin^2 \theta) \frac{\cos \theta \cos \phi}{\cos \alpha} \\
 &= (1 - \sin^2 \theta \{ \cos^2 \phi + \sin^2 \phi - 1 \}) \frac{\cos \theta \cos \phi}{\cos \alpha} \\
 &= \frac{\cos \theta \cos \phi}{\cos \alpha}
 \end{aligned} \tag{4.108}$$

$$\begin{aligned}
 A_{2,1} &= \cos \varepsilon \cos \theta \sin \phi + \sin \varepsilon \sin \theta \\
 &= \frac{\cos^2 \theta \sin \phi}{\cos \alpha} + \frac{\sin^2 \theta \sin \phi}{\cos \alpha} \\
 &= \frac{\sin \phi}{\cos \alpha}
 \end{aligned} \tag{4.109}$$

$$\begin{aligned}
 A_{1,2} &= -\cos \alpha \sin \phi - \sin \alpha \sin \varepsilon \cos \phi \\
 &= -(\cos^2 \alpha + \sin^2 \alpha) \frac{\sin \phi}{\cos \alpha} \\
 &= -\frac{\sin \phi}{\cos \alpha}
 \end{aligned} \tag{4.110}$$

$$A_{2,2} = \cos \varepsilon \cos \phi = \frac{\cos \theta \cos \phi}{\cos \alpha} \tag{4.111}$$

This therefore reduces to the desired final expression

$$\begin{bmatrix} E_\alpha \\ E_\varepsilon \end{bmatrix} = \frac{1}{\cos \alpha} \begin{bmatrix} \cos \theta \cos \phi & -\sin \phi \\ \sin \phi & \cos \theta \cos \phi \end{bmatrix} \cdot \begin{bmatrix} E_\theta \\ E_\phi \end{bmatrix} \tag{4.112}$$

where α and ε are the azimuth and elevation angles, respectively, and

$$\cos \alpha = \sqrt{1 - \sin^2 \alpha} = \sqrt{1 - \sin^2 \theta \cos^2 \phi} \tag{4.113}$$

The inverse transformation can be expressed as

$$\begin{aligned}
 \begin{bmatrix} E_\theta \\ E_\phi \end{bmatrix} &= \frac{1}{\cos^2 \theta \cos^2 \phi + \sin^2 \phi} \\
 &\cdot \begin{bmatrix} \cos \theta \cos \phi \cos \alpha & \sin \phi \cos \alpha \\ -\sin \phi \cos \alpha & \cos \theta \cos \phi \cos \alpha \end{bmatrix} \cdot \begin{bmatrix} E_\alpha \\ E_\varepsilon \end{bmatrix}
 \end{aligned} \tag{4.114}$$

From trigonometric identities, we can simplify the common denominator as follows:

$$\begin{aligned}
 \cos^2 \alpha &= 1 - \sin^2 \alpha = 1 - (1 - \cos^2 \theta) \cos^2 \phi \\
 &= 1 - \cos^2 \phi + \cos^2 \theta \cos^2 \phi = \sin^2 \phi + \cos^2 \theta \cos^2 \phi
 \end{aligned} \tag{4.115}$$

Hence,

$$\begin{bmatrix} E_\theta \\ E_\phi \end{bmatrix} = \frac{1}{\cos \alpha} \begin{bmatrix} \cos \theta \cos \phi & \sin \phi \\ -\sin \phi & \cos \theta \cos \phi \end{bmatrix} \cdot \begin{bmatrix} E_\alpha \\ E_\varepsilon \end{bmatrix} \tag{4.116}$$

4.2.5.3 Conversion between LII definitions

Often a requirement exists to transform between spherical polarisation bases. This can be readily accomplished by multiplying out the respective matrices. Let us first consider transforming between azimuth over elevation and elevation over azimuth field components

$$\begin{aligned}
 \begin{bmatrix} E_\alpha \\ E_\varepsilon \end{bmatrix} &= \begin{bmatrix} \cos \alpha & -\sin \alpha \sin \varepsilon & -\sin \alpha \cos \varepsilon \\ 0 & \cos \varepsilon & -\sin \varepsilon \end{bmatrix} \\
 &\cdot \begin{bmatrix} \cos Az & -\sin Az \sin El \\ 0 & \cos El \\ -\sin Az & -\cos Az \sin El \end{bmatrix} \cdot \begin{bmatrix} E_{Az} \\ E_{El} \end{bmatrix}
 \end{aligned} \tag{4.117}$$

Multiplying out the matrices results in a two-by-two matrix multiplied by a column vector. The elements of the square two-by-two matrix are

$$\begin{aligned}
 A_{1,1} &= \cos \alpha \cos Az + \sin \alpha \cos \varepsilon \sin Az \\
 &= \cos \alpha \cos Az + \frac{\cos El \sin Az \cos Az \cos El \sin Az}{\cos \alpha} \\
 &= (\cos^2 \alpha + \cos^2 El \sin^2 Az) \frac{\cos Az}{\cos \alpha} \\
 &= (\cos^2 \alpha + \sin^2 \alpha) \frac{\cos Az}{\cos \alpha} = \frac{\cos Az}{\cos \alpha}
 \end{aligned} \tag{4.118}$$

$$A_{2,1} = \sin \varepsilon \sin Az = \frac{\sin Az \sin El}{\cos \alpha} \tag{4.119}$$

$$\begin{aligned}
 A_{1,2} &= -\cos \alpha \sin Az \sin El - \sin \alpha \sin \varepsilon \cos El + \sin \alpha \cos \varepsilon \cos Az \sin El \\
 &= -\cos \alpha \sin Az \sin El - \frac{\cos^2 El \sin Az \sin El}{\cos \alpha} + \frac{\cos^2 El \sin Az \cos^2 Az \sin El}{\cos \alpha} \\
 &= -(\cos^2 \alpha + \cos^2 El - \cos^2 El \cos^2 Az) \frac{\sin Az \sin El}{\cos \alpha} \\
 &= -(\cos^2 \alpha + \cos^2 El(1 - \cos^2 Az)) \frac{\sin Az \sin El}{\cos \alpha} \\
 &= -(\cos^2 \alpha + \cos^2 El \sin^2 Az) \frac{\sin Az \sin El}{\cos \alpha} \\
 &= -(\cos^2 \alpha + \sin^2 \alpha) \frac{\sin Az \sin El}{\cos \alpha} \\
 &= -\frac{\sin Az \sin El}{\cos \alpha}
 \end{aligned} \tag{4.120}$$

$$\begin{aligned}
 A_{2,2} &= \cos \varepsilon \cos El + \sin \varepsilon \cos Az \sin El = \frac{\cos^2 El \cos Az}{\cos \alpha} + \frac{\sin^2 El \cos Az}{\cos \alpha} \\
 &= \frac{\cos Az}{\cos \alpha}
 \end{aligned} \tag{4.121}$$

Hence, the final result is

$$\begin{bmatrix} E_\alpha \\ E_\varepsilon \end{bmatrix} = \frac{1}{\cos \alpha} \begin{bmatrix} \cos Az & -\sin Az \sin El \\ \sin Az \sin El & \cos Az \end{bmatrix} \cdot \begin{bmatrix} E_{Az} \\ E_{El} \end{bmatrix} \tag{4.122}$$

This inverse transform can be obtained from taking the inverse of this. Let

$$a = \frac{\sin A \sin E}{\cos \alpha} \tag{4.123}$$

$$b = \frac{\cos A}{\cos \alpha} \tag{4.124}$$

Thus,

$$\begin{bmatrix} E_\alpha \\ E_\epsilon \end{bmatrix} = \begin{bmatrix} a & -b \\ b & a \end{bmatrix} \cdot \begin{bmatrix} E_{Az} \\ E_{El} \end{bmatrix} \quad (4.125)$$

So that

$$\begin{bmatrix} E_{Az} \\ E_{El} \end{bmatrix} = \begin{bmatrix} a & -b \\ b & a \end{bmatrix}^{-1} \cdot \begin{bmatrix} E_\alpha \\ E_\epsilon \end{bmatrix} = \frac{1}{a^2 + b^2} \begin{bmatrix} a & b \\ -b & a \end{bmatrix} \cdot \begin{bmatrix} E_\alpha \\ E_\epsilon \end{bmatrix} \quad (4.126)$$

Recalling the relations between the coordinate angles, $\sin \alpha = \sin Az \cos El$, $\cos^2 \alpha = 1 - \sin^2 Az \cos^2 El$ and recalling the trigonometric identity, $\cos^2 \theta + \sin^2 \theta = 1$, it can be seen that

$$\begin{aligned} a^2 + b^2 &= \frac{\sin^2 Az \sin^2 El + \cos^2 Az}{\cos^2 \alpha} \\ &= \frac{\sin^2 Az(1 - \cos^2 El) + \cos^2 Az}{1 - \sin^2 Az \cos^2 El} \\ &= \frac{\sin^2 Az - \sin^2 Az \cos^2 El + \cos^2 Az}{1 - \sin^2 Az \cos^2 El} \\ &= \frac{1 - \sin^2 Az \cos^2 El}{1 - \sin^2 Az \cos^2 El} = 1 \end{aligned} \quad (4.127)$$

Hence, the required result is found to be

$$\begin{bmatrix} E_{Az} \\ E_{El} \end{bmatrix} = \frac{1}{\cos \alpha} \begin{bmatrix} \sin Az \sin El & \cos Az \\ -\cos Az & \sin Az \sin El \end{bmatrix} \cdot \begin{bmatrix} E_\alpha \\ E_\epsilon \end{bmatrix} \quad (4.128)$$

4.2.6 *Elliptical polarisation, axial ratio and tilt angle*

The term polarisation is used to describe the behaviour (that is to say, the path of travel of the tip) of the instantaneous electric field vector as a function of time at a fixed point in space. By removing the time dependence from the electric field expression, these equations can be used to determine the locus of \underline{E} , that is to say, the path of travel of the tip of the electric, or magnetic field, vector. To derive circular polarisation performance for an AUT, one can transform mathematically the linear polarisation results. The following section presents the development of a method for accomplishing this task. Let us first choose two orthogonal electric field components in a plane so that we can write

$$\frac{E_\theta}{E_1} = \cos \omega t \quad (4.129)$$

$$\frac{E_\phi}{E_2} = \cos(\omega t + \gamma) = \cos \omega t \cos \gamma - \sin \omega t \sin \gamma \quad (4.130)$$

Thus,

$$\frac{E_\phi}{E_2} = \frac{E_\theta}{E_1} \cos \gamma - \sin \omega t \sin \gamma \quad (4.131)$$

Hence,

$$\left(\frac{E_\phi}{E_2} - \frac{E_\theta}{E_1} \cos \gamma \right)^2 = \sin^2 \omega t \sin^2 \gamma \quad (4.132)$$

Expanding yields

$$\left(\frac{E_\phi}{E_2} \right)^2 - 2 \frac{E_\theta E_\phi}{E_1 E_2} \cos \gamma + \left(\frac{E_\theta}{E_1} \right)^2 \cos^2 \gamma = \sin^2 \omega t \sin^2 \gamma \quad (4.133)$$

Using trigonometric identities,

$$\left(\frac{E_\phi}{E_2} \right)^2 - 2 \frac{E_\theta E_\phi}{E_1 E_2} \cos \Delta\phi + \left(\frac{E_\theta}{E_1} \right)^2 (1 - \sin^2 \gamma) = \sin^2 \omega t \sin^2 \gamma \quad (4.134)$$

Thus,

$$\left(\frac{E_\phi}{E_2} \right)^2 - 2 \frac{E_\theta E_\phi}{E_1 E_2} \cos \gamma + \left(\frac{E_\theta}{E_1} \right)^2 - \left(\frac{E_\theta}{E_1} \right)^2 \sin^2 \gamma = \sin^2 \omega t \sin^2 \gamma \quad (4.135)$$

$$\left(\frac{E_\phi}{E_2} \right)^2 - 2 \frac{E_\theta E_\phi}{E_1 E_2} \cos \gamma + \left(\frac{E_\theta}{E_1} \right)^2 - \cos^2 \omega t \sin^2 \gamma = \sin^2 \omega t \sin^2 \gamma \quad (4.136)$$

Hence,

$$\left(\frac{E_\phi}{E_2} \right)^2 - 2 \frac{E_\theta E_\phi}{E_1 E_2} \cos \gamma + \left(\frac{E_\theta}{E_1} \right)^2 - \sin^2 \gamma = 0 \quad (4.137)$$

which is in the same form as the equation for an ellipse, namely,

$$Ax^2 + Bxy + Cy^2 + Dx + Ey + F = 0 \quad (4.138)$$

Thus, the tip of the instantaneous field vector traces out a curve which is the shape of an ellipse. Here, the coefficients are

$$A = \frac{1}{E_1^2} \quad (4.139)$$

$$B = -\frac{2 \cos \gamma}{E_1 E_2} \quad (4.140)$$

$$C = \frac{1}{E_2^2} \quad (4.141)$$

$$F = -\sin^2 \gamma \quad (4.142)$$

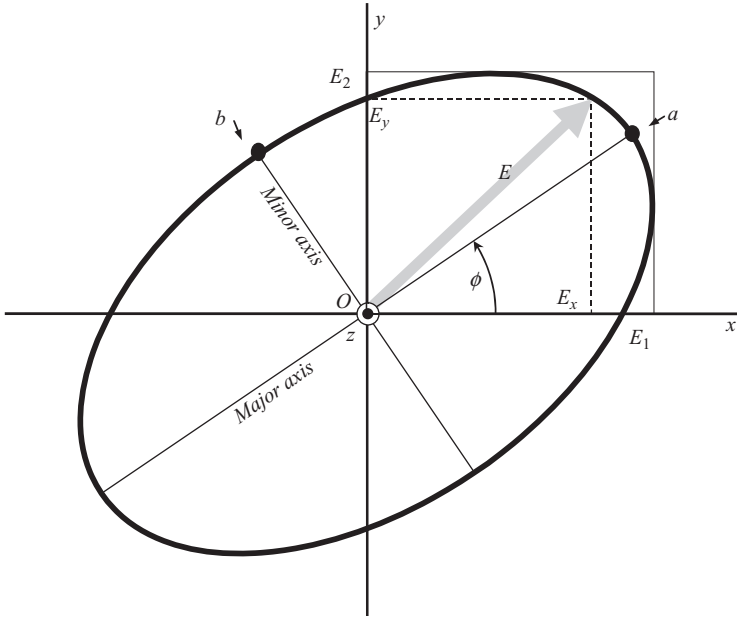


Figure 4.39 Polarisation ellipse showing semi-major and semi-minor axes. E denotes the instantaneous electric field at some time t

Here, there is no x - or y -term, which implies that the ellipse is not translated in the x - or y -axis as $D = E = 0$. However, there is an xy term, i.e. $B \neq 0$, which implies that the ellipse could be rotated. In general, the coordinate axes will not align with the principal axes of the polarisation ellipse. The amount of rotation is called the tilt angle and can be calculated from the complex components of the \underline{E} field. This is represented schematically in Figure 4.39. Thus, by also calculating the semi-major and semi-minor axes of the polarisation ellipse, the complete polarisation properties of the field can be expressed in terms of the parameters of the polarisation ellipse.

Expressions for the tilt angle and the semi-major and semi-minor axes can be obtained from the \underline{E} field in a straightforward way. As

$$E_\phi = E_2 \cos(\omega t + \gamma) \tag{4.143}$$

This can be written as

$$\begin{aligned} E_\phi(\underline{r}, t) &= E_2(\underline{r})[\cos \omega t \cos \gamma + \sin \omega t \sin \gamma] \\ &= p_\phi(\underline{r}) \cos \omega t + q_\phi(\underline{r}) \sin \omega t \end{aligned} \tag{4.144}$$

where

$$p_\phi(\underline{r}) = E_2(\underline{r}) \cos \gamma \tag{4.145}$$

$$q_\phi(\underline{r}) = E_2(\underline{r}) \sin \gamma \tag{4.146}$$

In general, we can write

$$\underline{E}(\underline{r}, t) = \underline{p}(\underline{r}) \cos \omega t + \underline{q}(\underline{r}) \sin \omega t \quad (4.147)$$

So,

$$p_\theta(\underline{r}) = E_1(\underline{r}); q_\theta(\underline{r}) = 0 \text{ yields } E_\theta(\underline{r}, t) \quad (4.148)$$

Thus, $\gamma = 0$ gives linear polarisation and $\gamma = \pm 90^\circ$ gives circular polarisation (for $E_1 = E_2$) and elliptical polarisation otherwise. We can write

$$\underline{E}(\underline{r}, t) = \text{Re}[U(\underline{r})e^{-j\omega t}] \quad (4.149)$$

$$\underline{U}(\underline{r}) = \underline{p}(\underline{r}) + j\underline{q}(\underline{r}) \quad (4.150)$$

Now looking at \underline{E} point $r = r_0$ as time varies, end point of \underline{E} describes an ellipse defined by \underline{p} and \underline{q} . Now, we can write

$$(\underline{p} + j\underline{q}) = (\underline{a} + j\underline{b})e^{j\phi} \quad (4.151)$$

Here, ϕ is any scalar. Thus, we can write

$$\underline{a} = \underline{p} \cos \phi + \underline{q} \sin \phi \quad (4.152)$$

$$\underline{b} = -\underline{p} \sin \phi + \underline{q} \cos \phi \quad (4.153)$$

If we now choose ϕ so that \underline{a} and \underline{b} are perpendicular to each other, the orthogonality relation yields

$$\underline{a} \cdot \underline{b} = (\underline{p} \cos \phi + \underline{q} \sin \phi) \cdot (-\underline{p} \sin \phi + \underline{q} \cos \phi) = 0 \quad (4.154)$$

We can now write

$$\underline{E}(\underline{r}, t) = (\underline{a} + j\underline{b})e^{-j(\omega t - \phi)} = \underline{a} \cos(\omega t - \phi) + \underline{b} \sin(\omega t - \phi) \quad (4.155)$$

Taking Cartesian axes with origin at r_0 and with x and y directions along a and b yields

$$E_x = a \cos(\omega t - \phi) \quad (4.156)$$

$$E_y = b \sin(\omega t - \phi) \quad (4.157)$$

which is the parametric equation of an ellipse with semi-major axis = a , semi-minor axis = b and tilt angle = ϕ . Thus, solving for these three parameters will fully specify the ellipse. By simple geometry, it can be shown that p and q are thus semi-radii of the ellipse measured in the θ and ϕ directions, see Figure 4.39.

Simplifying the dot product of \underline{a} and \underline{b} yields

$$\left(-\underline{p}^2 + \underline{q}^2\right) \cos \phi \sin \phi + \underline{p} \cdot \underline{q} (\cos^2 \phi - \sin^2 \phi) = 0 \quad (4.158)$$

$$\frac{1}{2} \left(-\underline{p}^2 + \underline{q}^2\right) \sin 2\phi + \underline{p} \cdot \underline{q} \cos 2\phi = 0 \quad (4.159)$$

Hence, we obtain the desired result

$$\tan 2\phi = \frac{2\underline{p} \cdot \underline{q}}{\underline{p}^2 - \underline{q}^2} \quad (4.160)$$

If γ is used to denote the angle between the vectors \underline{p} and \underline{q} , then this can be expressed as

$$\tan 2\phi = \frac{2pq \cos \gamma}{\underline{p}^2 - \underline{q}^2} \quad (4.161)$$

Thus, the tilt angle ϕ , in radians, is obtained from

$$\phi = \frac{1}{2} \arctan \left(\frac{2pq \cos \gamma}{\underline{p}^2 - \underline{q}^2} \right) \quad (4.162)$$

where γ is the phase angle between the vectors p and q . The tilt angle is measured from the x -axis and is un-rotated when $\phi = 0$. The maximum field would be measured when the measuring frame of reference is a rotation by ϕ and the minimum would be recorded 90° away from this.

Next, we wish to determine the semi-major and semi-minor axes of the polarisation ellipse. To accomplish this, let us now consider

$$(\underline{a})^2 = (\underline{p} \cos \phi + \underline{q} \sin \phi)^2 \quad (4.163)$$

Expanding yields

$$a^2 = p^2 \cos^2 \phi + q^2 \sin^2 \phi + 2\underline{p} \cdot \underline{q} \cos \phi \sin \phi \quad (4.164)$$

or

$$a^2 = p^2 \cos^2 \phi + q^2 \sin^2 \phi + \underline{p} \cdot \underline{q} \sin 2\phi \quad (4.165)$$

Expanding yields

$$a^2 = \frac{p^2}{2} (\cos 2\phi + 1) + \frac{q^2}{2} (1 - \cos 2\phi) + \underline{p} \cdot \underline{q} \sin 2\phi \quad (4.166)$$

Simplifying yields

$$a^2 = \frac{1}{2} (p^2 + q^2) + \frac{1}{2} (p^2 - q^2) \cos 2\phi + \underline{p} \cdot \underline{q} \sin 2\phi \quad (4.167)$$

Returning to the expression for the rotation and considering the tangent of an angle yields a useful trigonometric identity, namely,

$$\tan^2 \phi = \frac{\sin^2 \phi}{1 - \sin^2 \phi} \quad (4.168)$$

Thus,

$$\tan^2 2\phi = \frac{4(\underline{p} \cdot \underline{q})^2}{(p^2 - q^2)^2} \quad (4.169)$$

Hence,

$$\frac{\sin^2 2\phi}{1 - \sin^2 2\phi} = \frac{4(\underline{p} \cdot \underline{q})^2}{(p^2 - q^2)^2} \quad (4.170)$$

$$(p^2 - q^2)^2 \sin^2 2\phi = 4(\underline{p} \cdot \underline{q})^2 - 4 \sin^2 2\phi (\underline{p} \cdot \underline{q})^2 \quad (4.171)$$

$$(p^2 - q^2)^2 + 4(\underline{p} \cdot \underline{q})^2 = \frac{4(\underline{p} \cdot \underline{q})^2}{\sin^2 2\phi} \quad (4.172)$$

Thus, we obtain the first of our two necessary substitutions

$$\sin 2\phi = \frac{2(\underline{p} \cdot \underline{q})}{\sqrt{(p^2 - q^2)^2 + 4(\underline{p} \cdot \underline{q})^2}} \quad (4.173)$$

The second can be obtained from the first using

$$\frac{2\underline{p} \cdot \underline{q}}{p^2 - q^2} = \frac{1}{\cos 2\phi} \frac{2(\underline{p} \cdot \underline{q})}{\sqrt{(p^2 - q^2)^2 + 4(\underline{p} \cdot \underline{q})^2}} \quad (4.174)$$

Hence, we find the second of our two substitutions

$$\cos 2\phi = \frac{p^2 - q^2}{\sqrt{(p^2 - q^2)^2 + 4(\underline{p} \cdot \underline{q})^2}} \quad (4.175)$$

Thus, if these substitutions are used to simplify the expression of a^2 , we obtain

$$a^2 = \frac{1}{2}(p^2 + q^2) + \frac{1}{2} \frac{(p^2 - q^2)^2}{\sqrt{(p^2 - q^2)^2 + 4(\underline{p} \cdot \underline{q})^2}} + \frac{2(\underline{p} \cdot \underline{q})^2}{\sqrt{(p^2 - q^2)^2 + 4(\underline{p} \cdot \underline{q})^2}} \quad (4.176)$$

or

$$a^2 = \frac{1}{2} \left[(p^2 + q^2) + \frac{(p^2 - q^2)^2 + 4(\underline{p} \cdot \underline{q})^2}{\sqrt{(p^2 - q^2)^2 + 4(\underline{p} \cdot \underline{q})^2}} \right] \quad (4.177)$$

Hence,

$$a^2 = \frac{1}{2} \left[(p^2 + q^2) + \sqrt{(p^2 - q^2)^2 + 4(\underline{p} \cdot \underline{q})^2} \right] \quad (4.178)$$

This can be expressed in terms of the angle between the vectors \underline{p} and \underline{q} as

$$a^2 = \frac{1}{2} \left[(p^2 + q^2) + \sqrt{p^4 + q^4 - 2p^2q^2 + 4p^2q^2 \cos^2 \gamma} \right] \quad (4.179)$$

$$a^2 = \frac{1}{2} \left[(p^2 + q^2) + \sqrt{p^4 + q^4 + 2p^2q^2(-1 + 2 \cos^2 \gamma)} \right] \quad (4.180)$$

Thus, the final result is

$$a = \sqrt{\frac{1}{2} \left[(p^2 + q^2) + \sqrt{p^4 + q^4 + 2p^2q^2 \cos 2\gamma} \right]} \quad (4.181)$$

where the positive radical is chosen. Following a similar procedure, we can obtain a similar result for b . Thus,

$$b^2 = p^2 \sin^2 \phi + q^2 \cos^2 \phi - \underline{p} \cdot \underline{q} \sin 2\phi \quad (4.182)$$

So that

$$b^2 = \frac{1}{2} (p^2 + q^2) - \frac{1}{2} (p^2 - q^2) \cos 2\phi - \underline{p} \cdot \underline{q} \sin 2\phi \quad (4.183)$$

Hence,

$$b^2 = \frac{1}{2} \left[(p^2 + q^2) - \sqrt{(p^2 - q^2)^2 + 4(\underline{p} \cdot \underline{q})^2} \right] \quad (4.184)$$

Thus, as required,

$$b = \sqrt{\frac{1}{2} \left[(p^2 + q^2) - \sqrt{p^4 + q^4 + 2p^2q^2 \cos 2\gamma} \right]} \quad (4.185)$$

where again the positive radical is chosen. Here, p and q are thus semi-radii of the ellipse measured in the θ and ϕ directions. Following the IEEE standard, the axial ratio is the ratio of the major axis to the minor axis of the polarisation ellipse. Thus,

when denoted with AR , the axial ratio is defined to be the ratio of a and b

$$AR = \frac{a}{b} \tag{4.186}$$

which is clearly equivalent to

$$AR = \frac{E_{\max}}{E_{\min}} \tag{4.187}$$

Here, $1 \leq |AR| \leq \infty$. This is often presented in a logarithmic form

$$AR|_{dB} = 20 \log_{10}(|AR|) \tag{4.188}$$

Often the inverse is calculated as this avoids the divide by zero that would be encountered at points in space where the field is perfectly linearly polarised. In this case from the law of logarithms, the AR in dB can be seen to be the negative of the IEEE definition. Thus, it is possible to describe the polarisation ellipse unambiguously as it has a shape that is quantified by the axial ratio, and an orientation which is specified by the tilt angle. Other representations of the polarisation state can be used [4]; however, the axial ratio and tilt angle are perhaps the most commonly encountered parameters. Although the derivation presented above is based upon the assumption of a plane wave, this nonetheless yields a very general result since over local regions of interest many waves (including spherical waves) behave as though they were plane waves.

For plane waves, the two cases of particular interest are those of plane and circularly polarised waves. For the case of linear polarisation, the phase difference, γ , between the two components is a multiple of 180° and the polarisation ellipse degenerates into a straight line (that is to say, an infinitely thin ellipse), which in general is tilted by an angle ϕ from the x -axis. Thus, for the special case of linearly polarised fields,

$$\phi = \frac{1}{2} \arctan\left(\frac{2pq}{p^2 - q^2} \cos(\pm m\pi)\right) \tag{4.189}$$

where m is an integer and the tilt angle can be expressed as

$$\phi = \frac{1}{2} \arctan\left(\frac{2pq}{p^2 - q^2} (-1)^m\right) \tag{4.190}$$

For the case of circular polarisation $p = q$ and the phase difference between the two components is an odd multiple of 90° and the polarisation ellipse degenerates into a circle. Thus, $\gamma = m\pi/2$ where again m is any non-zero integer. Two cases are admitted by the positive and negative rotation of the electric field vector as a function of time.

It is important to be aware that the same value of semi-major and semi-minor radii and therefore axial ratio, will be obtained irrespective of the orthogonal spatial polarisation basis that the field is resolved on to when calculating the values of a and b . Therefore, any of the orthogonal spatial polarisation basis described above

can be used, for example, $E_x, E_y; E_\theta, E_\phi$; and so on. However, and as ever, it is advantageous to choose a polarisation basis that is free from singularities in the direction of greatest interest.

4.2.7 *Linear and circular polarisation bases – complex vector representations*

The various spatial polarisation bases that have been discussed above, that is to say, the various Ludwig definitions of cross-polarisation, etc., can be used to represent linear *or* circular temporal polarisations states of the field. However, when considering an antenna whose radiation is predominately circularly polarised, alternative temporal polarisation bases are often adopted so as to simplify the visualisation of the fields. Whilst there is no difficulty encountered when plotting the axial ratio or tilt angle as a function of position (in either one or two dimensions), the cognitive interpretation of fields (either electric or magnetic) can become highly challenging and some form of simplification is clearly very attractive. As the complexity arises from the rotating nature of the tip of the electric (or magnetic) field vector, by removing this time dependency (and therefore spatial singularity) from the fields would provide the simplification necessary. That is to say, if the fields were plotted relative to a unit vector that rotated with the same angular velocity as the field itself, then this difficulty can be resolved, cf. LIII definition [3]. As two orthogonal bases are required, it is possible to define a second vector that rotates in the opposite direction at the same rate. It turns out that mathematically, this can be conveniently accomplished through the use of complex unit vectors. Complex vector algebra offers a convenient framework for the analysis of time-harmonic fields and as such this subject has been treated mainly within books on electromagnetics in the context of time-harmonic fields. The following section develops the concept of complex vector algebra, a circularly polarised basis, and the necessary transformations.

When defining linear polarisation bases, the evaluation of a given field component was based upon the definition of the scalar product that was formed between a complex field vector and a real unit vector. When constructing circular components we are required to evaluate the scalar product between complex vectors. Here, complex vectors are merely vectors whose components are complex numbers such that a complex vector is defined as a combination of two real vectors such that

$$\underline{A} = \underline{A}_{re} + j\underline{A}_{im} \quad (4.191)$$

The complex conjugate of a complex vector is denoted with a superscript asterisk and is defined as

$$\underline{A}^* = (\underline{A}_{re} + j\underline{A}_{im})^* = \underline{A}_{re} - j\underline{A}_{im} \quad (4.192)$$

Usefully, if \underline{A} corresponds to a time-harmonic vector, then \underline{A}^* corresponds to a time-harmonic vector that rotates in the opposite direction. The algebra of complex

vectors adhere too many of the rules known from real vector algebra; however, there are some differences that need expounding. For real, non-zero, vectors it is possible to define parallel vectors such that $\underline{a} \times \underline{b} = 0$ and perpendicular vectors such that $\underline{a} \cdot \underline{b} = 0$. However, for complex vectors, the usual definition of the dot product can lead to ambiguity. For example, the dot product of a vector with itself can be zero without the vector itself being the zero vector and this clearly yields complications for the concepts of length and angle. This difficulty can be resolved if the definition of the dot product is modified such that it is understood that one of the vectors is conjugated [5], and in this case, the *second* vector is modified. Clearly, if \underline{a} and \underline{b} happen to be real, then this definition reduces to the standard definition of the dot product. Thus, many geometric properties can be retained, all be it at the cost of giving up the commutative property of the inner product, that is if \underline{a} and \underline{b} are complex, $\underline{a} \cdot \underline{b}^* \neq \underline{b} \cdot \underline{a}^*$ as $\underline{a} \cdot \underline{b}^* = (\underline{b} \cdot \underline{a}^*)^*$. Here, the superscript asterisk is used to denote the complex conjugate. This makes the definition for the real-valued squared magnitude of a complex vector

$$|\underline{a}|^2 = \underline{a} \cdot \underline{a}^* \quad (4.193)$$

Using this definition, and as before, the complex polarisation vectors can be defined so that they form an orthogonal set such that

$$\hat{\underline{e}}_R \cdot \hat{\underline{e}}_R^* = \hat{\underline{e}}_L \cdot \hat{\underline{e}}_L^* = 1 \quad (4.194)$$

And,

$$\hat{\underline{e}}_R \cdot \hat{\underline{e}}_L^* = 0 \quad (4.195)$$

Here, the unit vectors for right-hand, and left-hand, circular components are defined as follows, where a $+j\omega t$ time convention has been assumed

$$\hat{\underline{e}}_R \equiv \frac{(\hat{\underline{e}}_x - j\hat{\underline{e}}_y)}{\sqrt{2}} \quad (4.196)$$

$$\hat{\underline{e}}_L \equiv \frac{(\hat{\underline{e}}_x + j\hat{\underline{e}}_y)}{\sqrt{2}} \quad (4.197)$$

The total field can be formed from the linear combination of the two orthogonal components

$$\underline{E} = E_R \hat{\underline{e}}_R + E_L \hat{\underline{e}}_L \quad (4.198)$$

Thus, to illustrate how to find, for example, the *R*-component of a field vector using the dot product, we see that

$$\underline{E} \cdot \hat{\underline{e}}_R^* = (E_R \hat{\underline{e}}_R + E_L \hat{\underline{e}}_L) \cdot \hat{\underline{e}}_R^* = E_R \hat{\underline{e}}_R \cdot \hat{\underline{e}}_R^* = E_R \quad (4.199)$$

Thus, if we wish to find the R -component of a field from the linear components, we use a similar strategy

$$E_R = \underline{E} \cdot \hat{\underline{e}}_R^* = (E_x \hat{\underline{e}}_x + E_y \hat{\underline{e}}_y) \cdot \hat{\underline{e}}_R^* = (E_x \hat{\underline{e}}_x + E_y \hat{\underline{e}}_y) \cdot \frac{(\hat{\underline{e}}_x + j\hat{\underline{e}}_y)}{\sqrt{2}} \quad (4.200)$$

Thus, for a $+j\omega t$ time convention,

$$E_R = \frac{E_x + jE_y}{\sqrt{2}} \quad (4.201)$$

Similarly,

$$E_L = \underline{E} \cdot \hat{\underline{e}}_L^* = (E_x \hat{\underline{e}}_x + E_y \hat{\underline{e}}_y) \cdot \hat{\underline{e}}_L^* = (E_x \hat{\underline{e}}_x + E_y \hat{\underline{e}}_y) \cdot \frac{(\hat{\underline{e}}_x - j\hat{\underline{e}}_y)}{\sqrt{2}} \quad (4.202)$$

Thus, for a $+j\omega t$ time convention,

$$E_L = \frac{E_x - jE_y}{\sqrt{2}} \quad (4.203)$$

It is important to note the difference in the signs of the imaginary parts of the equations for the circular unit vectors and the equations for the circular field components which results from the definition of the dot product used when treating complex vectors. Many texts do not make this important distinction. If a different time convention had been adopted, the difference would have still been present although the expressions would have been the conjugates of those developed above. The inverse transformations of unit vectors can be easily obtained. Adding

$$\hat{\underline{e}}_R + \hat{\underline{e}}_L = \frac{(\hat{\underline{e}}_x - j\hat{\underline{e}}_y)}{\sqrt{2}} + \frac{(\hat{\underline{e}}_x + j\hat{\underline{e}}_y)}{\sqrt{2}} = \frac{2\hat{\underline{e}}_x}{\sqrt{2}} \quad (4.204)$$

or, for a $+j\omega t$ time convention,

$$\hat{\underline{e}}_x = \frac{(\hat{\underline{e}}_R + \hat{\underline{e}}_L)}{\sqrt{2}} \quad (4.205)$$

Subtracting

$$\hat{\underline{e}}_R - \hat{\underline{e}}_L = \frac{(\hat{\underline{e}}_x - j\hat{\underline{e}}_y)}{\sqrt{2}} - \frac{(\hat{\underline{e}}_x + j\hat{\underline{e}}_y)}{\sqrt{2}} = \frac{-2j\hat{\underline{e}}_y}{\sqrt{2}} \quad (4.206)$$

or, for a $+j\omega t$ time convention,

$$\hat{\underline{e}}_y = \frac{j(\hat{\underline{e}}_L - \hat{\underline{e}}_R)}{\sqrt{2}} \quad (4.207)$$

Computing the transform from circular to linear components

$$E_x = \underline{E} \cdot \hat{\underline{e}}_x^* = (E_R \hat{\underline{e}}_R + E_L \hat{\underline{e}}_L) \cdot \hat{\underline{e}}_x^* = (E_R \hat{\underline{e}}_R + E_L \hat{\underline{e}}_L) \cdot \frac{(\hat{\underline{e}}_R + \hat{\underline{e}}_L)}{\sqrt{2}} \quad (4.208)$$

Hence, for a $+j\omega t$ time convention,

$$E_x = \frac{E_R + E_L}{\sqrt{2}} \quad (4.209)$$

Similarly,

$$E_y = \underline{E} \cdot \hat{\underline{e}}_y^* = (E_R \hat{\underline{e}}_R + E_L \hat{\underline{e}}_L) \cdot \hat{\underline{e}}_y^* = (E_R \hat{\underline{e}}_R + E_L \hat{\underline{e}}_L) \cdot \frac{j(\hat{\underline{e}}_L - \hat{\underline{e}}_R)}{\sqrt{2}} \quad (4.210)$$

Hence, for a $+j\omega t$ time convention,

$$E_y = \frac{j(E_L - E_R)}{\sqrt{2}} \quad (4.211)$$

As set out above, the axial ratio is defined as

$$AR = \frac{a}{b} = \frac{E_{\max}}{E_{\min}} \quad (4.212)$$

Thus, when expressed in terms of circular polarised fields, the axial ratio can be seen to be easily obtained from

$$AR = \frac{|E_R| + |E_L|}{|E_R| - |E_L|} \quad (4.213)$$

Here, the sign of the denominator defines the sense of the hand of polarisation. As a and b are both radii, they are always positive real numbers and as such they are not able to provide the hand of polarisation. Note that when expressing the axial ratio in a logarithmic form, we must first take the absolute value of AR as one cannot evaluate the logarithm of a negative number. Thus, in this case, the sense of polarisation must be specified separately.

In the past, the testing of circularly polarised antennas on far-field ranges was often accomplished by continuously rotating a linearly polarised source antenna while the far-field radiation pattern was measured [6]. This rotation was fast when compared to the motion of the AUT positioner so that the probe will turn through at least one complete rotation for each far-field measurement point on the great circle cut. The intent therefore is to vary the signal source in such a way that the full polarisation ellipse can be traced out at each far-field pattern angle.

This procedure has two principal advantages. It yields a real-time direct measurement of the axial ratio of the AUT and can be accomplished with the use of a scalar network analyser. This form of the far-field plot is still popular in some quarters and can be easily obtained from two complex orthogonal linear field components which thereby enable such results to be obtained from near-field

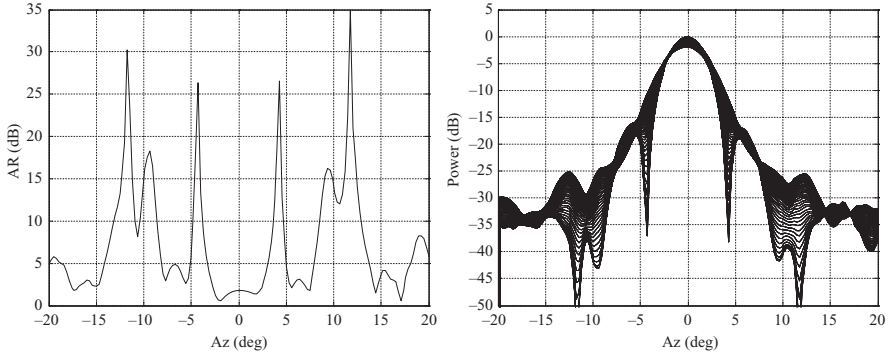


Figure 4.40 Comparison of axial ratio cut and a traditional spin linear measurement

measurements. The measured spin-linear value can be obtained from the semi-major and semi-minor axes using

$$r = \sqrt{(a \sin(\chi))^2 + (b \cos(\chi))^2} \tag{4.214}$$

Here, χ has been used to denote the spinning polarisation angle and the positive radical is chosen. Thus, the signal that a purely linearly polarised antenna would receive when expressed in dB form is

$$\text{rotating linear} = 20 \log_{10}(r) \tag{4.215}$$

As AR is defined to be the ratio of the major to the minor axis and as the maximum envelope is $20 \log_{10}(a)$ and the minimum envelope is $20 \log_{10}(b)$ then, from the law of logarithms, it is clear that axial ration, AR, will be the difference between these values when expressed in dB form. In the preparation of Figure 4.40, the χ angle was varied over a full 360° range for each far-field angle. By way of comparison, an axial ratio plot of the same pattern cut is presented in Figure 4.40.

From inspection, it can be seen that the axial ratio values correspond exactly to the difference in the envelope of the synthesised spin linear measurement.

4.2.8 Measures of polarisation discrimination

Often, it is desirable to determine the polarisation purity of an antenna, typically in order that its applicability for use with a frequency reuse scheme can be quantified. In such circumstances, it is preferable to know how much smaller, or larger, the cross-polar signal is than the co-polar signal thus the relative cross-polar power, i.e. the cross-polar discrimination, is calculated. Here, the relative cross-polar field is taken to be a scalar quantity that can be related to the Ludwig III co-polar and cross-polar fields through the following expression:

$$E_{relcross} = \frac{E_{cross}}{E_{co}} \tag{4.216}$$

4.3 Isometric rotation of coordinate systems

In the preceding sections, a number of different coordinate systems and polarisation bases have been developed. Transformations between these various coordinate systems and polarisation basis were developed. Whilst this provides the practicing antenna engineer with a great deal of flexibility when presenting data and comparing between measurements taken in different facilities using different assumptions and conventions, it is always possible that through experimental error or simply as a result of the orientation of the antenna when it was tested that these frames of references still do not equate. In such circumstances, a need for techniques for rotating patterns and polarisation basis is clearly motivated. Such techniques are developed and illustrated in the following sections. We start however with an illustration of the difficulty of representing the surface of a three-dimensional object on a two-dimensional piece of paper before developing the mathematical apparatus needed to implement these sorts of transformations.

4.3.1 Illustration of the problem with antenna pattern plotting – Gauss’s Theorema Egregium

There is a fundamental problem that is associated with representing the surface of a three-dimensional spherical object on a two-dimensional flat piece of paper. It has long been known that, with the Earth being spherical, any flat representation generates distortions such that shapes and areas cannot both be conserved simultaneously, distances can never all be preserved for anything other than an infinitely small region, cf. K.F. Gauss, ‘General Investigations of Curved Surfaces of 1827 and 1825’, The Princeton University Library, Translated 1902. Thus, the mapmaker must choose a suitable map projection according to the space to be mapped and the intended purpose of the map. The same is true when visualising antenna radiation patterns. To illustrate the effect of representing angular antenna pattern data on a two-dimensional pattern plot, a number of illustrations are presented that show the Earth plotted as a sphere placed in front of a plane. This example was selected as an example that is likely to be familiar to many readers. The surface of the sphere is mapped onto the plane so that both can be seen. Here, the altitude is represented with a false colour map. This is a direct analogue of the problem that the antenna engineer faces when presenting results of their pattern measurements or simulations. In this case, the Earth map has been projected onto the surface of a vertical circular cylinder. This is then ‘unrolled’ and is shown placed behind the globe. The difficulty with this approach is that the map becomes progressively more distorted as one moves away from the equator and travels towards to north or south poles. This is clear as the length of the equator on the globe and the length of the equator on the flat map are equal. However, the north-pole corresponds to an infinitesimal point on globe, whereas it is stretched out into a line that is of equal length to the equator. This distortion means that areas and shapes are not preserved on the flat map. As may perhaps be expected, Figure 4.41 shows the Earth map presented with the sphere nominally aligned. The pattern on the plane is similar to the Gall Peters projection.

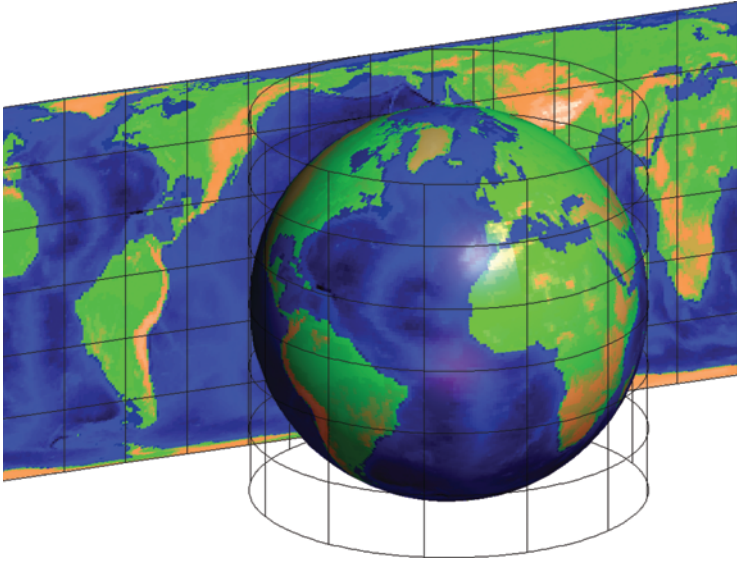


Figure 4.41 Globe nominally aligned – no rotation

To illustrate the effect that applying a rotation to an antenna pattern, in Figure 4.42, the Earth has been rotated by 90° in azimuth. Clearly, the Earth itself is unchanged, however, its representation in the flat two-dimensional surface has altered. Here, it is clear that the pattern has shifted horizontally with a periodic boundary condition at the left- and right-hand sides of the plane. That being said, the planar map projection is merely a translated version of that shown in Figure 4.41.

Figure 4.43 presents a similar case only here the Earth has been rotated in elevation. Again, the Earth itself has not changed however in this case the two-dimensional representation is very different as here; points on the plane are moved towards and away from the poles in the plotting coordinate system. This makes the interpretation of the two-dimensional information far more challenging than was previously the case in Figure 4.41.

Lastly, Figure 4.44 presents a result in which the Earth has been rotated by 90° in roll. Here, points that were hitherto at the pole on the planar plot have been shifted to the equator and vice versa. Again, it is clear that the Earth itself has not changed, other than the fact that it has been rotated with respect to the plotting coordinate system. Instead, it is the two-dimensional representation that has changed significantly. This plot also nicely illustrates that a 90° rotation in roll is not equivalent to a transposition of the two-dimensional pattern plot, cf. Figure 4.41.

4.3.2 Use of direction cosine matrices in the rotation of coordinate systems

Passive transformation matrices are matrices that post-multiply a point vector to produce a new point vector and is merely a change in the coordinate system. The

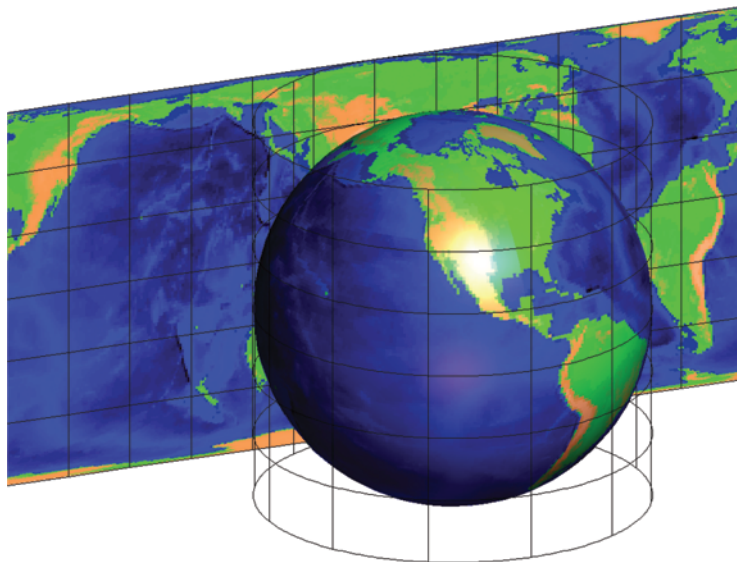


Figure 4.42 Globe rotated by 90° in azimuth

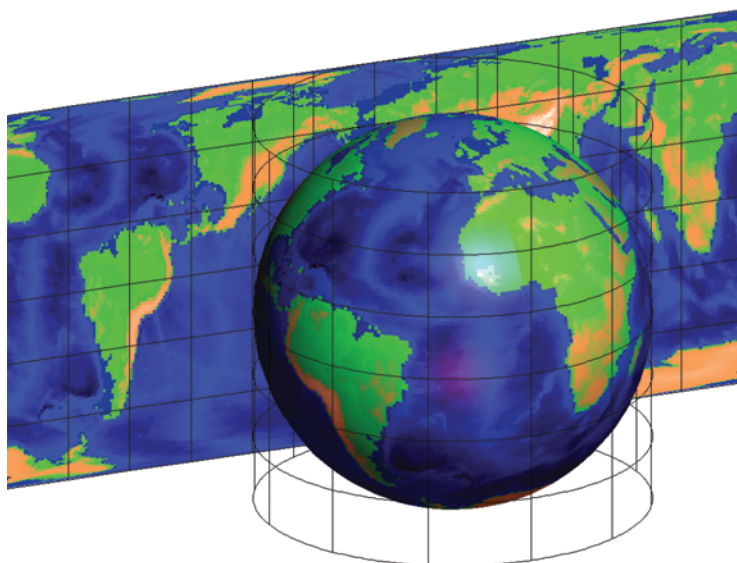


Figure 4.43 Globe rotated by 20° in elevation

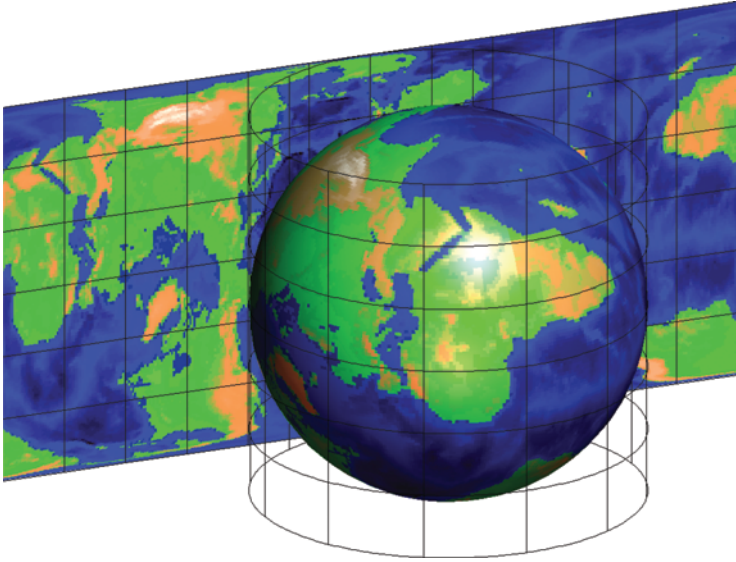


Figure 4.44 *Globe rotated by 90° in roll*

relationship between two coordinate systems can be defined with the use of a four-by-four homogeneous transformation matrix, namely,

$$\begin{bmatrix} x' \\ y' \\ z' \\ 1 \end{bmatrix} = \begin{bmatrix} A_{1,1} & A_{1,2} & A_{1,3} & A_{1,4} \\ A_{2,1} & A_{2,2} & A_{2,3} & A_{2,4} \\ A_{3,1} & A_{3,2} & A_{3,3} & A_{3,4} \\ 0 & 0 & 0 & 1 \end{bmatrix} \cdot \begin{bmatrix} x \\ y \\ z \\ 1 \end{bmatrix} \quad (4.217)$$

or

$$\begin{bmatrix} x' \\ y' \\ z' \\ 1 \end{bmatrix} = [A] \cdot \begin{bmatrix} x \\ y \\ z \\ 1 \end{bmatrix} \quad (4.218)$$

Here, the elements $A_{1,4}$, $A_{2,4}$ and $A_{3,4}$ represent a translation between the origins of the respective frames of reference. The three-by-three sub-matrix

$$\begin{bmatrix} A_{1,1} & A_{1,2} & A_{1,3} \\ A_{2,1} & A_{2,2} & A_{2,3} \\ A_{3,1} & A_{3,2} & A_{3,3} \end{bmatrix} = \begin{bmatrix} \hat{e}_{x'} \cdot \hat{e}_x & \hat{e}_{x'} \cdot \hat{e}_y & \hat{e}_{x'} \cdot \hat{e}_z \\ \hat{e}_{y'} \cdot \hat{e}_x & \hat{e}_{y'} \cdot \hat{e}_y & \hat{e}_{y'} \cdot \hat{e}_z \\ \hat{e}_{z'} \cdot \hat{e}_x & \hat{e}_{z'} \cdot \hat{e}_y & \hat{e}_{z'} \cdot \hat{e}_z \end{bmatrix} \quad (4.219)$$

contains the rotational information relating these frames of reference. This can also be expressed in terms of the cosine of the angles between the various combinations of unit vectors. This is also why these are termed direction cosine matrices.

Specifically then,

$$\begin{bmatrix} A_{1,1} & A_{1,2} & A_{1,3} \\ A_{2,1} & A_{2,2} & A_{2,3} \\ A_{3,1} & A_{3,2} & A_{3,3} \end{bmatrix} = \begin{bmatrix} \cos \theta_{1,1} & \cos \theta_{1,2} & \cos \theta_{1,3} \\ \cos \theta_{2,1} & \cos \theta_{2,2} & \cos \theta_{2,3} \\ \cos \theta_{3,1} & \cos \theta_{3,2} & \cos \theta_{3,3} \end{bmatrix} \quad (4.220)$$

In essence, we are merely projecting each of the unit vectors of one coordinate system onto each of the unit vectors of the other. Therefore, each row can be considered to represent a vector describing the orientation of the unit vector of the primed coordinate system in terms of the un-primed coordinate system. Similarly, each of the columns can be considered to represent a vector describing the orientation of the unit vector of the un-primed coordinate system in terms of the primed coordinate system. As the rotations that we are considering are isometric, that is to say, the distance of a point from the origin in one system will be exactly the same in each coordinate system, i.e. it is invariant under the transformation. This can be expressed mathematically as

$$l = \sqrt{x^2 + y^2 + z^2} = \sqrt{x'^2 + y'^2 + z'^2} \quad (4.221)$$

Similarly, the length of a vector will also remain invariant under these transformations. Clearly then, a unit vector will have a unit length in every system. Thus, the magnitude of each of the row vectors will be one. Similarly, the magnitude of the column vectors will also be one. This can be expressed conveniently as

$$1 = \sqrt{A_{i,1}^2 + A_{i,2}^2 + A_{i,3}^2} \quad \text{where } i = 1, 2, 3 \quad (4.222)$$

and

$$1 = \sqrt{A_{1,i}^2 + A_{2,i}^2 + A_{3,i}^2} \quad \text{where } i = 1, 2, 3 \quad (4.223)$$

Also, as the un-primed unit vectors will be mutually orthogonal, which will also be the case for the primed unit vectors, then knowledge of any two row vectors will enable the third to be obtained by taking the cross product of the other two. Also, as the unit vectors in each coordinate system are orthogonal, only two of any three vectors can be chosen arbitrarily, the third being recoverable from the cross product of the other two. Here, this implies that knowledge of any two rows will enable the third to be determined and similarly, knowledge of any two columns will enable the third to be deduced. For example,

$$A(3, 1) = A(1, 2)A(2, 3) - A(1, 3)A(2, 2) \quad (4.224)$$

$$A(3, 2) = A(1, 3)A(2, 1) - A(1, 1)A(2, 3) \quad (4.225)$$

$$A(3, 3) = A(1, 1)A(2, 2) - A(1, 2)A(2, 1) \quad (4.226)$$

The determinate of this sub-matrix can be calculated and any significant deviation from a value of unity can be treated as being indicative of a bad direction

cosine matrix. Occasionally, a good direction cosine matrix is reported as faulty if the number of significant figures used to represent the matrix is insufficient. Typically, all direction cosine matrices should be treated as being of type double precision in order that truncation and rounding errors remain acceptably small. This follows from noting that typically the smallest angular increment observable from a rotary position encoder is $\pm 0.01^\circ$, or when expressed in terms of a direction cosine this deviates from unity in the eighth decimal place. Furthermore, the act of multiplying out one or more direction cosine matrices can further compromise the data, as the cumulative rounding error can increase appreciably. Conversely, the inverse transformation can be accomplished with

$$\begin{bmatrix} x' \\ y' \\ z' \\ 1 \end{bmatrix} = [A]^{-1} \cdot \begin{bmatrix} x \\ y \\ z \\ 1 \end{bmatrix} \quad (4.227)$$

The adoption of a four-by-four matrix, with its inherent redundancy, is preferable as the matrix inverse, and thus the inverse transformation, only exists for square matrices. An added advantage of this definition is that the four-by-four alignment matrices can be obtained directly from most engineering computer-aided design packages. By way of illustration, rotations about the x -, y - and z -axes are represented, respectively, by the three matrices [7]

$$R_x = \begin{bmatrix} 1 & 0 & 0 & 0 \\ 0 & \cos \theta_x & \sin \theta_x & 0 \\ 0 & -\sin \theta_x & \cos \theta_x & 0 \\ 0 & 0 & 0 & 1 \end{bmatrix} \quad (4.228)$$

$$R_y = \begin{bmatrix} \cos \theta_y & 0 & -\sin \theta_y & 0 \\ 0 & 1 & 0 & 0 \\ \sin \theta_y & 0 & \cos \theta_y & 0 \\ 0 & 0 & 0 & 1 \end{bmatrix} \quad (4.229)$$

$$R_z = \begin{bmatrix} \cos \theta_z & \sin \theta_z & 0 & 0 \\ -\sin \theta_z & \cos \theta_z & 0 & 0 \\ 0 & 0 & 1 & 0 \\ 0 & 0 & 0 & 1 \end{bmatrix} \quad (4.230)$$

The derivation of the rotation matrix can either be obtained from the use of trigonometric identities or from geometry. Figure 4.45 illustrates this for the case of a positive rotation about the positive z -axis.

Thus, from trigonometry, it can be seen that

$$x' = x \cos \theta_z + y \sin \theta_z \quad (4.231)$$

$$y' = -x \sin \theta_z + y \cos \theta_z \quad (4.232)$$

$$z' = z \quad (4.233)$$

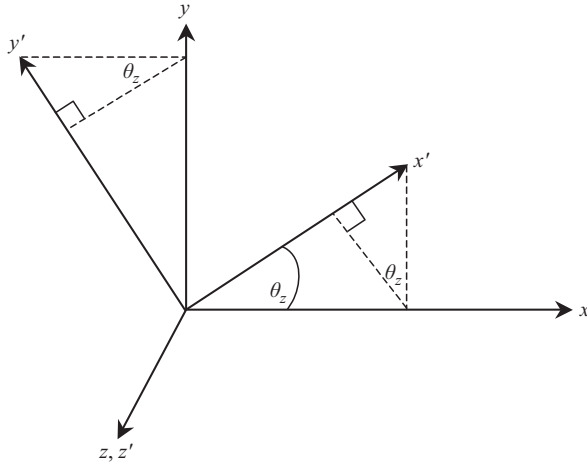


Figure 4.45 Illustration of a positive rotation about the positive z-axis

A similar construction can be used for rotations about the x- and y-axes. Translation of T_x , T_y and T_z in the x-, y- and z-axes, respectively, can be implemented using

$$T = \begin{bmatrix} 1 & 0 & 0 & T_x \\ 0 & 1 & 0 & T_y \\ 0 & 0 & 1 & T_z \\ 0 & 0 & 0 & 1 \end{bmatrix} \tag{4.234}$$

A series of transformation matrices may be concatenated into a single matrix through matrix multiplication. If A_1 , A_2 and A_3 are transformation matrices to be applied in order, matrix A is the product of the three matrices. Thus,

$$((P \cdot A_1) \cdot A_2) \cdot A_3 \equiv P \cdot ((A_1 \cdot A_2) \cdot A_3) = P \cdot A \tag{4.235}$$

where the multiplication is non-commutative and

$$A = (A_1 \cdot A_2) \cdot A_3 \tag{4.236}$$

In this way, *any* sequence of rotations can be constructed by sequentially multiplying out the necessary rotations and translations. Often the only rotational relationship between two systems is considered. This is often the case when considering far-field patterns. In this case, the three-by-three sub-matrix can be considered alone and is used instead of the homogeneous four-by-four transformation matrix. The utilisation of the three-by-three direction cosine matrix has an important benefit. As the direction cosine matrix is orthogonal and normalised the matrix whose elements are all real, the inverse is identically equal to the matrix transpose. This means that obtaining the inverse transformation is essentially reduced to a

matter of reordering of the elements within the matrix, which is both trivial and numerically robust.

When direction cosine matrices are used, the determinant of the matrix should be calculated and any significant deviation from unity can be treated as being indicative of a bad direction cosine matrix, as the matrix should be normalised to unity. Occasionally, a good direction cosine matrix can be reported as faulty if the number of significant figures used to represent the matrix is insufficient. Typically, all direction cosine matrices should be treated as being of type double precision in order that truncation and rounding errors remain acceptably small. This follows from noting that say the smallest angular increment observable from a rotary position encoder is say $\pm 0.01^\circ$, or when expressed in terms of a direction cosine this deviates from unity in the eighth decimal place. Furthermore, the act of multiplying out one or more direction cosine matrices can further compromise the data, as the cumulative rounding error can increase appreciably.

Crucially, although almost any number of different angular definitions are available for describing the relationship between coordinate systems, they can be related, i.e. equated, to one another via the direction cosine matrix without knowledge of the rotation or the order in which they were applied.

4.3.3 *Azimuth, elevation and roll angles*

Any number of angular definitions for describing the relationship between the two coordinate systems are available. Such rotations are termed passive as each successive rotation is applied to the newly rotated system. However, if the angles azimuth, elevation and roll are used, where the rotations are applied in this order, we may write the equivalent direction cosine matrix as

$$[A] = [A_1] \cdot [A_2] \cdot [A_3] \quad (4.237)$$

Specifically,

$$[A_1] = \begin{bmatrix} \cos(\text{roll}) & \sin(\text{roll}) & 0 \\ -\sin(\text{roll}) & \cos(\text{roll}) & 0 \\ 0 & 0 & 1 \end{bmatrix} \quad (4.238)$$

$$[A_2] = \begin{bmatrix} 1 & 0 & 0 \\ 0 & \cos(\text{el}) & -\sin(\text{el}) \\ 0 & \sin(\text{el}) & \cos(\text{el}) \end{bmatrix} \quad (4.239)$$

$$[A_3] = \begin{bmatrix} \cos(\text{az}) & 0 & -\sin(\text{az}) \\ 0 & 1 & 0 \\ \sin(\text{az}) & 0 & \cos(\text{az}) \end{bmatrix} \quad (4.240)$$

These transformation matrices can be easily derived either from geometry or from trigonometric identities. Here, in accordance with the rules of linear algebra, the first rotation matrix is written to the right. When multiplied out $[A]$ can be

explicitly expressed as $A_{row,column}$

$$A_{1,1} = \cos(roll) \cos(az) + \sin(roll) \sin(el) \sin(az) \quad (4.241)$$

$$A_{1,2} = \sin(roll) \cos(el) \quad (4.242)$$

$$A_{1,3} = \cos(roll) \sin(az) - \sin(roll) \sin(el) \cos(az) \quad (4.243)$$

$$A_{2,1} = -\sin(roll) \cos(az) + \cos(roll) \sin(el) \sin(az) \quad (4.244)$$

$$A_{2,2} = \cos(roll) \cos(el) \quad (4.245)$$

$$A_{2,3} = -(\sin(roll) \sin(az) + \cos(roll) \sin(el) \cos(az)) \quad (4.246)$$

$$A_{3,1} = -\cos(el) \sin(az) \quad (4.247)$$

$$A_{3,2} = \sin(el) \quad (4.248)$$

$$A_{3,3} = \cos(el) \cos(az) \quad (4.249)$$

where the rotations are understood to have been performed in the following order:

1. rotate about the negative y -axis through an angle azimuth,
2. rotate about the negative x -axis through an angle elevation, and
3. rotate about the z -axis through an angle Roll.

When $Az = 0$, $El = 0$ and $Roll = 0$, the direction cosine matrix will be the identity matrix and specifies that no rotations are to be applied, i.e.

$$[A] = \begin{bmatrix} 1 & 0 & 0 \\ 0 & 1 & 0 \\ 0 & 0 & 1 \end{bmatrix} = [I] \quad (4.250)$$

Clearly, from this matrix, it can be seen that these angles can be obtained from the matrix $[A]$ as

$$az = \arctan\left(\frac{-A_{31}}{A_{33}}\right) \quad (4.251)$$

$$el = \arcsin(A_{32}) \quad (4.252)$$

$$roll = \arctan\left(\frac{A_{12}}{A_{22}}\right) \quad (4.253)$$

Many other definitions for rotating frames of reference exist. These include the triad of Euler angles (see below), or the yaw pitch, and roll angles. However, the azimuth, elevation and roll definition is most convenient, for example, when presenting data tabulated in a regular azimuth over the elevation coordinate system.

4.3.4 Euler angles

As an alternative to the azimuth, elevation and roll rotations described above the triad of Euler angles are often utilised to represent the relationship between two frames of [8]

1. rotate about the z -axis through an angle ϕ ,
2. rotate about the new y -axis through an angle θ , and
3. rotate about the new z -axis through an angle χ .

These angles are often used when rotating spherical mode coefficients when working with spherical near-field measurements. Specifically, if the angles ϕ , θ and χ are used, where the rotations are applied in this order, we may write the equivalent direction cosine matrix as

$$[A] = [A_1] \cdot [A_2] \cdot [A_3] \quad (4.254)$$

where

$$[A_1] = \begin{bmatrix} \cos(\chi) & \sin(\chi) & 0 \\ -\sin(\chi) & \cos(\chi) & 0 \\ 0 & 0 & 1 \end{bmatrix} \quad (4.255)$$

$$[A_2] = \begin{bmatrix} \cos(\theta) & 0 & -\sin(\theta) \\ 0 & 1 & 0 \\ \sin(\theta) & 0 & \cos(\theta) \end{bmatrix} \quad (4.256)$$

$$[A_3] = \begin{bmatrix} \cos(\phi) & \sin(\phi) & 0 \\ -\sin(\phi) & \cos(\phi) & 0 \\ 0 & 0 & 1 \end{bmatrix} \quad (4.257)$$

When multiplied out, $[A]$ can be explicitly expressed as $A_{row,column}$

$$A_{1,1} = \cos \chi \cos \phi \cos \theta - \sin \chi \sin \phi \quad (4.258)$$

$$A_{1,2} = \cos \phi \sin \chi + \cos \chi \cos \theta \sin \phi \quad (4.259)$$

$$A_{1,3} = -\cos \chi \sin \theta \quad (4.260)$$

$$A_{2,1} = -\cos \phi \cos \theta \sin \chi - \cos \chi \sin \phi \quad (4.261)$$

$$A_{2,2} = \cos \chi \cos \phi - \cos \theta \sin \chi \sin \phi \quad (4.262)$$

$$A_{2,3} = \sin \chi \sin \theta \quad (4.263)$$

$$A_{3,1} = \cos \phi \sin \theta \quad (4.264)$$

$$A_{3,2} = \sin \phi \sin \theta \quad (4.265)$$

$$A_{3,3} = \cos \theta \quad (4.266)$$

Here, the three angles are referred to as Euler angles. Conversely, the three Euler angles can be determined from the direction cosine matrix as

$$\theta = \arccos(A_{33}) \quad (4.267)$$

If $\theta \neq 0$, then

$$\chi = \arctan\left(\frac{A_{23}}{-A_{13}}\right) \quad (4.268)$$

$$\phi = \arctan\left(\frac{A_{32}}{A_{31}}\right) \quad (4.269)$$

Again, the four-quadrant arctangent is used to evaluate the angles. However, if $\theta = 0$, then a zero divide by zero ambiguity is introduced. In this case, we must use

$$\chi = 0 \quad (4.270)$$

$$\phi = \arctan\left(\frac{A_{12}}{A_{22}}\right) \quad (4.271)$$

Clearly, when the θ rotation is zero, the ϕ and χ rotations are equivalent and hence either rotation may be used. A conversion between the azimuth, elevation and roll angles and the three Euler angles can be accomplished readily by equating the elements of their respective direction cosine matrices.

4.3.5 Quaternions

It is well known that complex numbers can be related to two-dimensional geometry, most notably, by virtue of the Euler relation

$$e^{j\phi} = \cos \phi + j \sin \phi \quad (4.272)$$

where

$$|e^{j\phi}| = 1 \quad (4.273)$$

The multiplication of a complex number by a complex exponential can be shown to be equivalent to a rotation of the coordinate axes. Hence, we can rotate a point in a two-dimensional coordinate system by an angle ϕ where the x coordinate is represented by the real part of the complex number a and the y coordinate by the imaginary part. The rotation is implemented by multiplying the complex number a by a complex exponential

$$a' = ae^{j\phi} \quad (4.274)$$

Here, the primed complex number a' represents the point in the rotated frame of reference, the real part of a' represents the x -component and the imaginary part denotes the y -component in the rotated system. The quaternion is in essence an extension of this idea where the rotation is applied in a higher dimensional space.

Mathematically, quaternions can be considered to be a non-commutative extension of complex numbers. It is not the purpose of this section to give a complete development of quaternions as this is beyond the scope of this text;

instead, the discussion will be limited to the use of quaternions in implementing coordinate transforms. By way of an analogy, complex numbers are represented as a sum of real and imaginary parts. Similarly, a quaternion can also be written as a linear combination of real and hyper-complex parts

$$Q = q_0 + q_1i + q_2j + q_3k \quad (4.275)$$

Here, i, j and k are quaternion units and have the property that

$$i^2 = j^2 = k^2 = ijk = -1 \quad (4.276)$$

Thus, as a complex number can be represented as a point on a two-dimensional plane, a quaternion can be considered to be a point in a four-dimensional space. A quaternion can be computed from a direction cosine matrix using

$$q_0 = \frac{1}{2} \sqrt{1 + A_{11} + A_{22} + A_{33}} \quad (4.277)$$

$$q_1 = \frac{1}{4q_0} (A_{23} - A_{32}) \quad (4.278)$$

$$q_2 = \frac{1}{4q_0} (A_{31} - A_{13}) \quad (4.279)$$

$$q_3 = \frac{1}{4q_0} (A_{12} - A_{21}) \quad (4.280)$$

Conversely, a direction cosine matrix can be constructed from a quaternion using

$$A_{11} = 2q_0^2 - 1 + 2q_1q_2 \quad (4.281)$$

$$A_{12} = 2q_1q_2 + 2q_0q_3 \quad (4.282)$$

$$A_{13} = 2q_1q_3 - 2q_0q_2 \quad (4.283)$$

$$A_{21} = 2q_1q_2 - 2q_0q_3 \quad (4.284)$$

$$A_{22} = 2q_0^2 - 1 + 2q_2^2 \quad (4.285)$$

$$A_{23} = 2q_2q_3 + 2q_0q_1 \quad (4.286)$$

$$A_{31} = 2q_1q_3 + 2q_0q_2 \quad (4.287)$$

$$A_{32} = 2q_2q_3 - 2q_0q_1 \quad (4.288)$$

$$A_{33} = 2q_0^2 - 1 + 2q_3^2 \quad (4.289)$$

As is the case for vectors the length, or norm, of a quaternion is utility. This can be calculated from

$$|Q| = \sqrt{Q^*Q} = \sqrt{QQ^*} \quad (4.290)$$

Here, the superscript asterisk is used to denote the complex conjugate of Q so that $Q^* + Q = 2q_0$. Thus,

$$|Q| = \sqrt{q_0^2 + q_1^2 + q_2^2 + q_3^2} \quad (4.291)$$

If P_q and Q_q are quaternions and are expressed using the vector form of a quaternion, then

$$P_q = p_0 + \underline{P} \quad (4.292)$$

$$Q_q = q_0 + \underline{Q} \quad (4.293)$$

When expressed in this form, the quaternions can be multiplied together using

$$R_q = P_q Q_q = p_0 q_0 - \underline{P} \cdot \underline{Q} + p_0 \underline{Q} + q_0 \underline{P} + \underline{P} \times \underline{Q} \quad (4.294)$$

Here, a dot denotes the scalar dot product and the cross denotes the vector cross product. When expanded out and expressed in element form this equates to

$$r_0 = p_0 q_0 - p_1 q_1 - p_2 q_2 - p_3 q_3 \quad (4.295)$$

$$r_1 = p_0 q_1 + p_1 q_0 + p_2 q_3 - p_3 q_2 \quad (4.296)$$

$$r_2 = p_0 q_2 + p_2 q_0 + p_3 q_1 - p_1 q_3 \quad (4.297)$$

$$r_3 = p_0 q_3 + p_3 q_0 + p_1 q_2 - p_2 q_1 \quad (4.298)$$

As was the case for the multiplication of direction cosine matrices, quaternion multiplication is equivalent to the concatenation of several sequential rotations. As was the case for direction cosine matrices, multiplications are non-commutative, i.e.

$$P_q Q_q \neq Q_q P_q \quad (4.299)$$

Inverting a quaternion rotation produces the inverse rotation and the inverse of a quaternion is equal to the complex conjugate of that quaternion thus

$$Q_q^{-1} = (q_0 + q_1 + q_2 + q_3)^{-1} = q_0 - q_1 - q_2 - q_3 \quad (4.300)$$

Thus, computing an inverse rotation using the quaternion representation requires less effort than accomplishing the same task using direction cosine matrices, as the latter involves a matrix inversion. All rotations can be represented by a single rotation about an axis in space. The axis and angle of that rotation can be calculated from the quaternion using

$$\phi = 2 \arccos(q_0) \quad (4.301)$$

$$\underline{v} = v_1 \hat{e}_x + v_2 \hat{e}_y + v_3 \hat{e}_z = \frac{1}{\sin(\phi/2)} [q_1 \hat{e}_x + q_2 \hat{e}_y + q_3 \hat{e}_z] \quad (4.302)$$

Here, ϕ is used to denote the angle of rotation and \underline{v} represents the axis of the rotation. Conversely, the quaternion can be computed from the angle and axis of rotation using

$$q_0 = \cos\left(\frac{\phi}{2}\right) \quad (4.303)$$

$$q_1 = v_1 \sin\left(\frac{\phi}{2}\right) \quad (4.304)$$

$$q_2 = v_2 \sin\left(\frac{\phi}{2}\right) \quad (4.305)$$

$$q_3 = v_3 \sin\left(\frac{\phi}{2}\right) \quad (4.306)$$

In addition to being a more efficient recording method, quaternions have the advantage that computing inverse rotations is made significantly easier than is the case for direction cosine matrices. Also, whilst the multiplication of two direction cosine matrices can, in the presence of truncation and rounding errors, produce a direction cosine matrix that is not a rotation, i.e. the components naturally drift which violates the orthonormality constraints. Quaternions have no such problem, i.e. the multiplication of two quaternions will always yield a rotation, all be it, perhaps, the wrong rotation. It is also a comparatively simple matter to adjust for numerical drift, one merely needs to compute the norm of the quaternion and then divide each component by it. This takes far fewer operations than matrix orthonormalisation which would be required in order to attempt to correct a direction cosine matrix.

4.3.6 *Orientation of viewer plotting antenna patterns*

When making a projection, another important concept is that of a viewing angle. This is related to the horizontal and vertical axes of the plot. The viewing angle is related to where the H - and V -axes are centered and how they are aligned to the original coordinate system. The plot centre (H_0 , V_0) is the angle relative to the original coordinate system and is not just a shift in the rotation of the sphere. Because of this, the pattern at the centre of the plot could be distorted (e.g. $H = 90^\circ$, $V = -90^\circ$ in an azimuth over the elevation coordinate system). The angles are allowed to wrap but the distortion at the poles of the plotting system will still apply. To illustrate this, Figure 4.46 contains a plot of the Earth tabulated on a regular azimuth over elevation coordinate system. However, in this case, the Earth has been rotated through -90° about the positive x -axis so that Antarctica, which is Earth's most southerly continent, is now plotted at the equator of the plotting coordinate system. Essentially, this is similar to viewing the Earth from sub-satellite latitude = -90° , sub-satellite longitude = 0° . Note also that although Earth map has been rotated, the poles of the plotting system are still located at $\pm 90^\circ$ in elevation and the equator is still at 0° and $\pm 180^\circ$ in elevation.

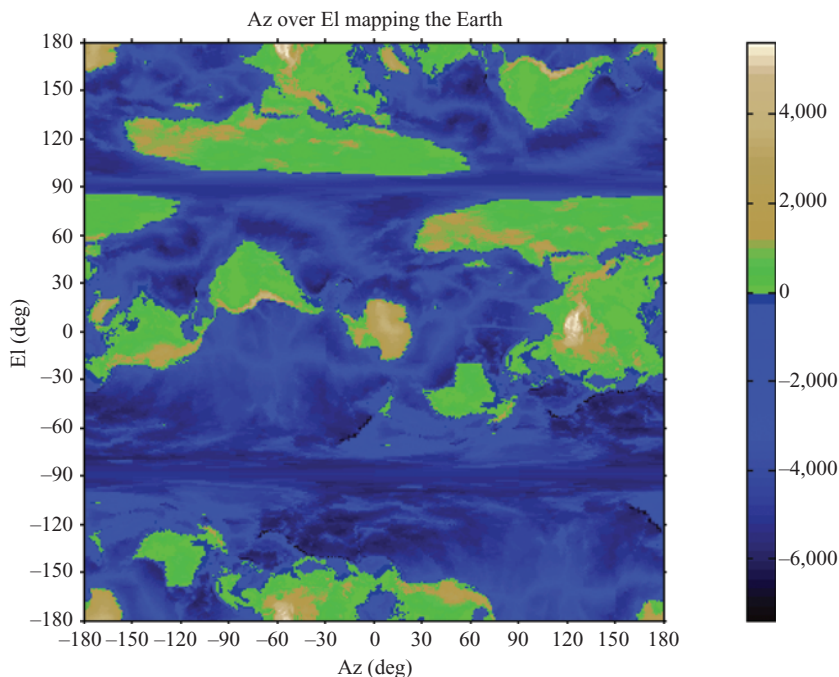


Figure 4.46 Earth mapped using an Az/El positioner system with the Earth rotated about the x -axis by -90°

Such isometric rotations are easily implemented by using a transformation matrix, as developed above, to rotate the triad of direction cosines. In this instance, a rotation of ψ about the positive x -axis can be expressed as

$$\begin{bmatrix} u' \\ v' \\ w' \end{bmatrix} = \begin{bmatrix} 1 & 0 & 0 \\ 0 & \cos \psi & \sin \psi \\ 0 & -\sin \psi & \cos \psi \end{bmatrix} \cdot \begin{bmatrix} u \\ v \\ w \end{bmatrix} \tag{4.307}$$

An antenna pattern is not a physical boundary as are the continents of the world. It is a transparent ‘snapshot’ of the pattern at a particular radius. For this reason, the observer can view the pattern that the antenna makes on the sphere from inside the sphere or from outside it. This orientation will change the H - and V -axes slightly based on how they are related to the original angles. It is necessary then to add two additional constants to the formulas discussed above. These constants are designated as l and m . They are only permitted to take on the values ± 1 depending upon where the observer is situated with respect to the AUT. The three possible cases are as follows:

- $l = 1, m = 1$, observer facing the AUT. Thus, looking in the $-Z$ direction (into the page), the $+X$ -axis is horizontal and increases towards the right and the $+Y$ -axis is vertical and increases upwards.

- $l = -1, m = 1$, observer standing behind the AUT. Thus, looking in the $+Z$ direction (into the page), the $+X$ -axis is horizontal and increases towards the left and the $+Y$ -axis is vertical and increases upwards.
- $l = 1, m = -1$, observer standing behind the AUT. Thus, looking in the $+Z$ direction (into the page), the $+X$ -axis is horizontal and increases towards the right and the $+Y$ -axis is vertical and increases downwards.

Case 2 is commonly used within the space industry when plotting antenna patterns over Earth maps to demonstrate antenna performance compliance with a given coverage region, which are often specified in terms of geopolitical boundaries. Case 3 is commonly used within the RCS measurement community as targets are routinely mounted upside down on low RCS pylons. In our maps of the world concept, Case 1 would be looking from space at the earth. Case 2 would be looking from the centre of the earth out with ones feet pointing at the South Pole. Case 3 would be looking from the centre of the earth out with your feet pointing at the North Pole. Again, this can be expressed compactly using the l and m integers in terms of a transformation matrix

$$\begin{bmatrix} u' \\ v' \\ w' \end{bmatrix} = \begin{bmatrix} l & 0 & 0 \\ 0 & m & 0 \\ 0 & 0 & 1 \end{bmatrix} \cdot \begin{bmatrix} u \\ v \\ w \end{bmatrix} \quad (4.308)$$

4.3.7 *Plotting antenna patterns on earth maps*

The performance specification of a space telecommunications antenna intended for use on a satellite stationed in geostationary orbit is often defined in terms of a gain iso-level coverage contour plotted over an Earth map. In this way, a satellite operator can specify the radiated power flux density across a particular region of interest which perhaps follows a coastline or a geopolitical boundary. As a consequence of this, there is a clear need to be able to plot maps of the Earth in the same coordinate system as that is used to visualise the antenna radiation pattern. This section is devoted to developing a procedure for creating these sorts of combined, i.e. hybrid, plots.

Figure 4.47 shows the Earth-centred Earth fixed (ECEF) coordinate system which is generally used for mapping the Earth. This convention represents positions as x, y , and z coordinates with the point $x = y = z = 0$ defined as being the centre of mass of the Earth. The axes are aligned with the international reference pole and international reference meridian which are fixed with respect to the Earth with the z -axis passing through true north. The x -axis intersects the sphere of the Earth at 0° latitude (i.e. at the equator) and 0° longitude (i.e. at the prime meridian) which is defined by convention to pass through Greenwich, London, in the UK. This is shown in Figure 4.48.

This means that ECEF rotates with the Earth and therefore coordinates of a point fixed on the surface of the earth do not change as a function of time. The angle measured up from the equator is defined as being the latitude and has a

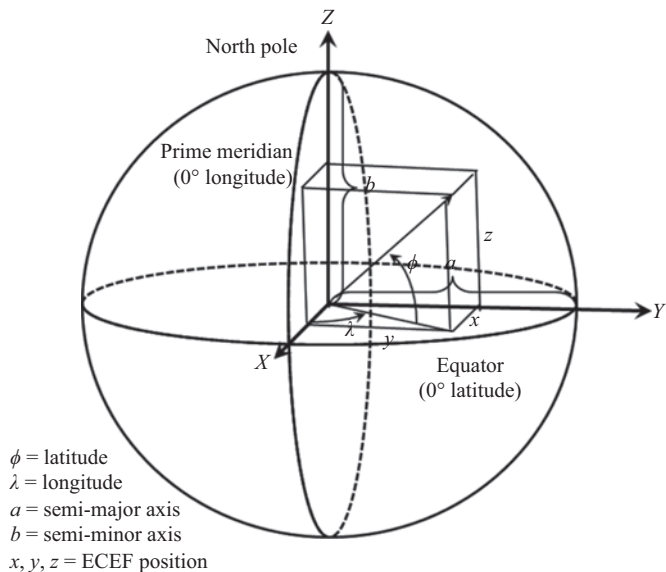


Figure 4.47 Geometry defining latitude and longitude for an ECEF coordinate system



Figure 4.48 Photograph of the prime meridian, i.e. longitude 0°, taken at the Royal Observatory, Greenwich in London. Note that there is some dispute as to whether this mark is exactly located along the prime meridian. That being said, it is a nice illustration

range of $-90^\circ \leq \text{latitude} \leq 90^\circ$ with negative angles referring to the southern hemisphere and positive angles referring to the northern hemisphere. Conversely, the angle measured in the equatorial plane is defined to be the longitude. For this coordinate system, there is no natural reference for a zero and so the zero datum line, as described above is taken by convention as being the line through Greenwich England. Conventionally, ϕ is used to denote latitude, λ is used to denote longitude and a is taken to be the radius of the semi-major axis, i.e. the equatorial radius.

Initially, we shall assume that the Earth is a perfect sphere. This is however a far less gross assumption for our particular application than may first appear the case. To illustrate this, it is worth recalling that the peak of Mount Everest is approximately 8.850 km above sea level and conversely, the deepest known point in Earth's oceans is the Challenger Deep in the Mariana Trench which is circa 10.994 km below sea level. As the Earth's equatorial radius is 6,378.137 km, this means that the peak-to-peak surface roughness of the Earth is less than $\pm 0.18\%$ of the radius. By way of a comparison, in the UK, a snooker ball is specified as having a diameter of 52.5 mm within a tolerance of ± 0.05 mm, or equivalently a peak-to-peak surface roughness of approximately $\pm 0.19\%$. So were the Earth to be shrunk down to the size of a snooker ball, the snooker ball would have the more irregular surface profile.

Now that we have defined the coordinate system in which we shall work, we return to the specific consideration of a satellite stationed in the geostationary orbit about the Earth. A geostationary orbit is a circular Earth geosynchronous orbit above the Earth's equator with a radius of 42,164 km and rotating in the same direction as that of the Earth's rotation with an orbital period equal to the Earth's rotational period, i.e. one sidereal day. An object in this sort of orbit appears to be motionless, i.e. located at a fixed position in the sky, for any observer on the Earth. This is advantageous as any ground-based antennas that communicate with the geostationary satellite do *not* need to rotate in order to track them over time. That being said, not all satellites are stationed perfectly over the intersection of the equator and the prime meridian. For cases such as these, a sub-satellite latitude and a sub-satellite longitude must be introduced to accommodate this. The sub-satellite longitude can be introduced as a simple subtraction from the longitudinal coordinate, i.e.

$$\lambda = \text{long} - \text{ss-long} \quad (4.309)$$

Here, long denotes the longitude of the point on the Earth's surface and the ss-long denotes the sub-satellite longitude of the spacecraft. Conversely, the sub-satellite latitude can be obtained through an isometric rotation of the ECES coordinate system about the y -axis as will be shown below. Thus, and as a first approximation, if we assume that the Earth is a perfect sphere and from inspection of Figure 4.49, then we can see that the relationship between the latitude and longitude components and a set of Cartesian coordinates centred at the origin of the sphere can be expressed as

$$x = a \cos(\phi) \cos(\lambda) \quad (4.310)$$

$$y = a \cos(\phi) \sin(\lambda) \quad (4.311)$$

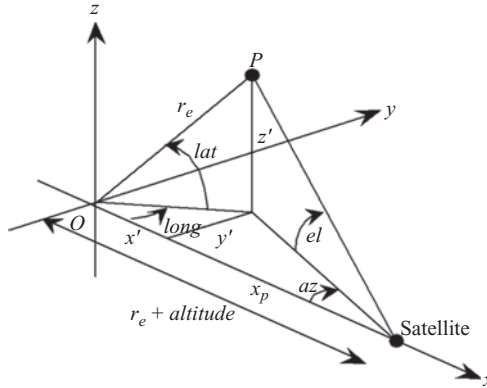


Figure 4.49 Geometry for latitude, longitude to azimuth, elevation coordinate transformation. Here, the geometry of the ECEF coordinate system has been adopted

$$z = a \sin(\phi) \tag{4.312}$$

The Earth's equatorial radius a , or semi-major axis, is the distance from its centre to the equator. As noted above, the sub-satellite latitude can be introduced using the rotation:

$$\begin{bmatrix} x' \\ y' \\ z' \end{bmatrix} = \begin{bmatrix} \cos(\text{sslatt}) & 0 & \sin(\text{sslatt}) \\ 0 & 1 & 0 \\ -\sin(\text{sslatt}) & 0 & \cos(\text{sslatt}) \end{bmatrix} \cdot \begin{bmatrix} x \\ y \\ z \end{bmatrix} \tag{4.313}$$

Circular Earth geosynchronous orbits have a radius of 42,164 km. Clearly, the orbit radius, r_{Orbit} of a satellite can be related to the altitude h above the Earth's spherical surface and the radius of the Earth a through

$$r_{Orbit} = a + h \tag{4.314}$$

Hence, the altitude above the Earth's surface, h , can be seen to be 35,786.0 km. This is needed as we wish to convert from an Earth-centred coordinate system to one that is centred about the geostationary satellite. The geometry for this is presented schematically in Figure 4.49.

From inspection of Figure 4.49, we can see that

$$x_p = r_{orbit} - x' \tag{4.315}$$

$$y_p = y' \tag{4.316}$$

$$z_p = z' \tag{4.317}$$

Hence, the distance from the satellite to the point on the Earth's assumed spherical surface described by the latitude and longitude coordinate is

$$r_p = \sqrt{x_p^2 + y_p^2 + z_p^2} \tag{4.318}$$

From trigonometry, the equivalent azimuth and elevation angles can be expressed as

$$El = \arcsin\left(\frac{z_p}{r_p}\right) \tag{4.319}$$

$$Az = \arctan\left(\frac{y_p}{x_p}\right) \tag{4.320}$$

This therefore provides the conversion from latitude and longitude to azimuth and elevation for a satellite stationed at sub-satellite latitude and sub-satellite longitude pointing to the centre of the Earth assuming that the Earth is a perfect sphere. Thus, providing a map of the Earth is available in latitude and longitude coordinates, as is often the case, it is possible to plot this in the antenna coordinate system. An example of this can be seen presented in Figure 4.50. Here, the Earth is viewed from geostationary altitude and subtends approximately $\pm 8.7^\circ$. Although sufficient for many applications, this model does not take account of the fact that the Earth is more accurately modelled as being an oblate spheroid, that is to say, the radius at the equator is greater than the radius at the pole. Figure 4.50 contains a

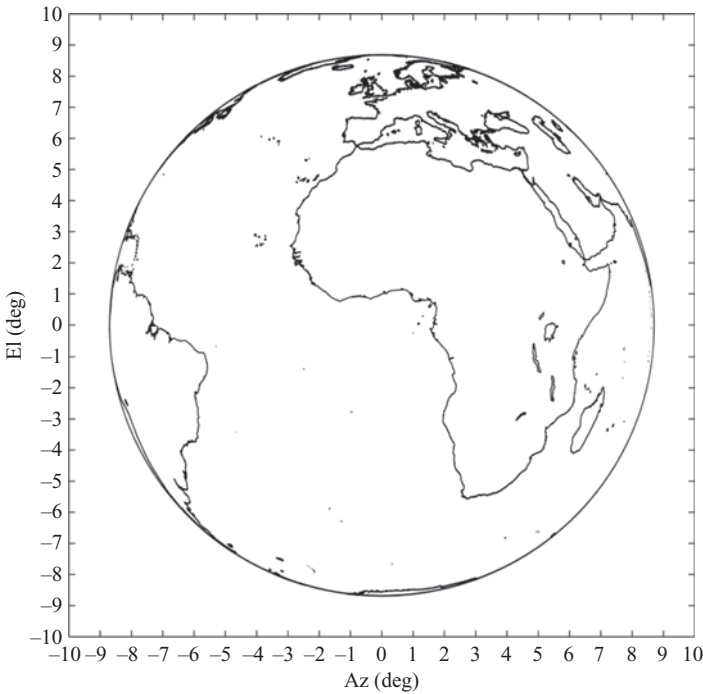


Figure 4.50 Earth viewed from geostationary altitude. The solid line is an oblate spheroid model of the Earth, and the dashed line is a perfect spherical model of the Earth

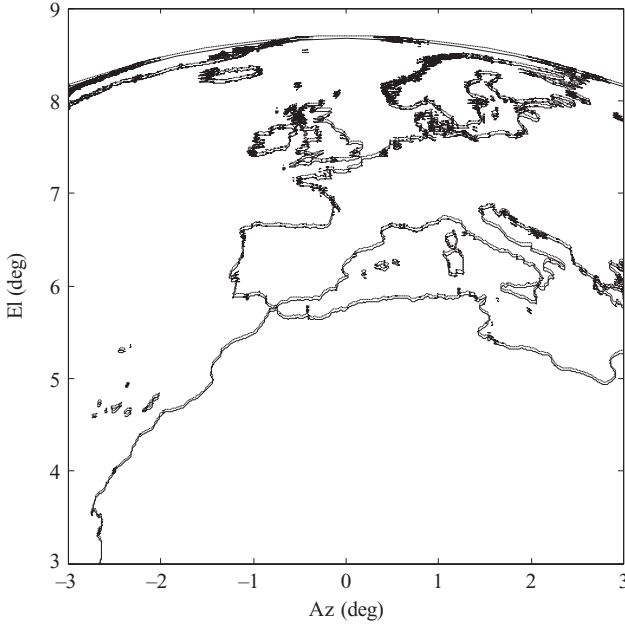


Figure 4.51 Earth viewed from geostationary altitude at with reduced axes limits to highlight differences between Earth models. The solid line is an oblate spheroid model of the Earth, and the dashed line is a perfect spherical model of the Earth

secondary mapping of the Earth which is denoted with the solid black line only here, an oblate spheroid model has been utilised. As expected, for small latitudes the two models agree well, as the equatorial radii are equal. However for larger latitudes differences do become more evident, i.e. the lines look ‘thicker’.

This difference is more pronounced in Figure 4.51 which has reduced the axes of the plot to focus on northern Europe. For many applications, this difference is unimportant however for cases considering large elevations this difference may be crucial.

As illustrated above, it is preferable to use an oblate spheroid model of the Earth when preparing these sorts of plots. We can implement this using the World Geodetic System 84 (WGS84) ellipsoid model [9], which is the reference system used by the global positioning system. In this model, we assume that the equatorial radius $a = 6,378.137$ km, as we did before; however, we also assume that the polar radius $b \approx 6,356.752314245$ km. For an oblate spheroid, the ellipticity can be computed using

$$e = \sqrt{\frac{a^2 - b^2}{a^2}} \quad b < a \quad (\text{oblate spheroid}) \quad (4.321)$$

Thus, for the WGS84 ECEF model, $e = 8.1819190842622\text{e}-2$, where e has been defined analogously to eccentricity for the two-dimensional case. For the sake

of completion, the inverse flattening $(1/f) = 298.257223563$ where the flatness can be obtained from the ellipticity using

$$f = 1 - \sqrt{1 - e^2} \quad (4.322)$$

It can be shown that we can calculate the prime vertical radius of curvature using [9]

$$N = \frac{a}{\sqrt{1 - (e \sin(\phi))^2}} \quad (4.323)$$

We can then convert from geodetic to ECEF Cartesian coordinates using [9]

$$x = (N + h) \cos(\phi) \cos(\lambda) \quad (4.324)$$

$$y = (N + h) \cos(\phi) \sin(\lambda) \quad (4.325)$$

$$z = ((1 - e^2)N + h) \sin(\phi) \quad (4.326)$$

Here, h denotes altitude of the surface of the Earth above the surface of the oblate spheroid, which has been assumed to be zero when preparing Figures 4.50 and 4.51. From comparison with the spherical case, it is apparent that the change in shape is implemented through a scaling of the radius of the Earth which varies as a function of latitude. The transformation from Cartesian components to azimuth and elevation coordinates can be implemented using the same transformation as was developed for the spherical Earth model case shown above. Although we have illustrated the plotting procedure for the case of an azimuth over elevation antenna pattern plotting coordinate system, we are not constrained to using that one system and we can in fact utilise any coordinate system we wish by converting between the systems using the transformation that we developed within the preceding sections. By way of an illustration of the consequence of using non-zero sub-satellite latitude and longitude, Figures 4.52 and 4.53 present example plots of the Earth as seen from the geostationary altitude from two different positions.

There is one last subtlety that one needs to take account of when plotting an antenna pattern together with an Earth map and that is the orientation of the AUT when viewing the pattern data. The coordinate system definitions presented within the preceding sections plot the pattern while viewing the face of the antenna. For the purposes of plotting antenna patterns over earth maps, we must view the pattern data as though we are standing behind the antenna and are looking in the same direction as the mechanical boresight direction of the antenna so that in principle we could see both the antenna pattern and the Earth. We therefore use an antenna plotting system (APS) coordinate axes which, as usual, forms a right-handed set. However, when plotting we assume that we are looking in the $+z$ -APS direction towards the far-field, with the x - and y -axes are orientated as follows:

- $+x$ -APS: horizontally towards the left and
- $+y$ -APS: vertically upwards.

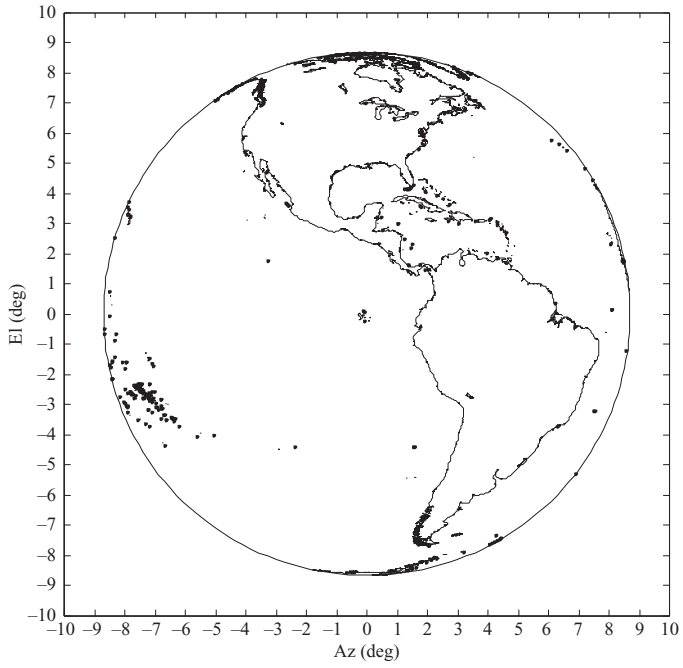


Figure 4.52 Earth map plotted with SS Lat = -90° , SS Long = 0° with an oblate spheroid model

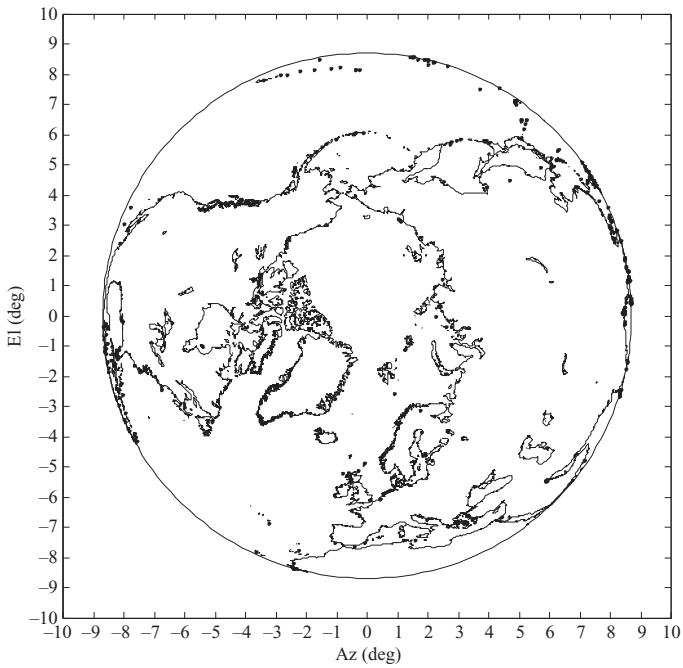


Figure 4.53 Earth map plotted with SS Lat = 0° , SS Long = 90° with oblate spheroid model

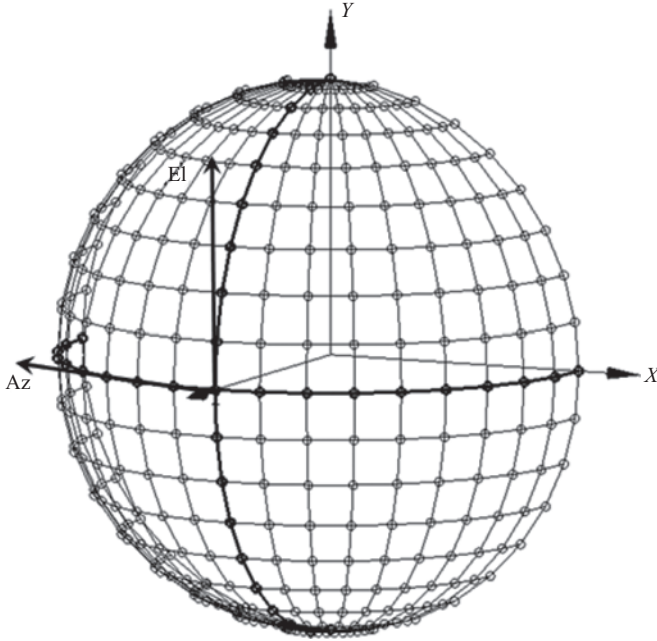


Figure 4.54 *Over elevation coordinate system for pattern plotting with Earth maps. Azimuth and elevation plotting angles shown together with APS axes*

Additionally, azimuth is measured away from the $+z$ -APS axis within the xz -APS plane and increases towards the *negative* x -APS. Elevation is unchanged from the usual definition (cf. Figure 4.54).

Thus, the relationship between the azimuth and elevation angles and the direction cosines can be expressed as

$$u_{APS} = -\sin(Az) \cos(El) \quad (4.327)$$

$$v_{APS} = \sin(El) \quad (4.328)$$

$$w_{APS} = \cos(Az) \cos(El) \quad (4.329)$$

This system is used for plotting the far-field antenna pattern data of typically spaceborne antennas and especially when those antenna patterns are to be plotted over Earth maps. Other plotting coordinate systems would be similarly modified through the introduction of a negative sign on the x -component. This has the effect of flipping the antenna pattern from left to right (in the vertical axis) as though one were looking through the page from the backside.

References

- [1] J.P. Snyder, "Map Projections: A Working Manual", Geological Survey (U.S.), Report Number 1395, p. 37, 1987.

- [2] K.F. Gauss, "General Investigations of Curved Surfaces of 1827 and 1825", The Princeton University Library, Translated 1902.
- [3] A.C. Ludwig, "The Definition of Cross-Polarization", *IEEE Trans. Antennas Propagation*, vol. AP-21 no. 1, pp. 116–119, Jan. 1973.
- [4] W.L. Stutzman, "Polarization in Electromagnetic Systems", Artech House, Inc., 1993, ISBN 0-89006-508-X, pp. 31–32.
- [5] G.B. Arfken, H.J. Webber, "Mathematical Methods for Physicists", International Edition, Fourth Edition, Academic Press, 1995, ISBN 0-12-059816-7, p. 572.
- [6] C.A. Balanis, "Antenna Theory Analysis and Design", Second Edition, John Wiley and Sons, Inc., 1997, ISBN 0-471-59268-4, p. 879.
- [7] J. McGregor, A. Watt, "The Art of Microcomputer Graphics for the BBC Micro/Electron", Addison-Wesley Publishing Company, 1984, ISBN 0-201-14435-2, p. 313.
- [8] J.E. Hansen, "Spherical Near-Field Antenna Measurements", Peter Peregrinus Ltd., Institution of Electrical Engineers, Electromagnetic Waves Series 26, 1988, ISBN 0-86341-110-X, p. 343.
- [9] Department of Defence World Geodetic System 1984, p. 4-4, National Imagery and Mapping Agency, June, 2004.

This page intentionally left blank

Chapter 5

Compact range measurements

5.1 Introduction

The basic concept of the compact antenna test range (CATR) was described in Chapter 3 (Section 3.5.1). If we consider the AUT as a receiver, the spherical radiated field from the CATR horn feed is collimated and transformed into a plane wave by a lens, a planar array or a reflector. The AUT is placed in this pseudo plane wave region which forms in the radiating near-field region of the reflector, lens or array. The radiation characteristics of the test antenna can be obtained by recording the received fields for different orientations of the test antenna as in a conventional far-field range.

The AUT couples to this ‘plane wave’ creating the measured radiation pattern, and so the quality of the plane wave defines the accuracy to which the AUT radiation pattern can be determined. This region of pseudo plane wave is called the *quiet zone* (or *test zone*) and is determined by the volume of field where the sum of taper and ripple in amplitude and phase within that volume is confined to peak-to-peak variations of ± 0.5 dB and $\pm 5^\circ$ (Figure 5.1). The scattering characteristics of the AUT (or other object) can be obtained by receiving the scattered signal back at the CATR horn feed. This enables radar cross-section (RCS) measurements to be performed in a compact, indoor, secure, environment. The ability to perform accurate RCS measurements has been one of the reasons why the compact range has been so very successful.

The first attempts to make antenna test ranges in the laboratory were made using lenses. In 1950, Woonton, Borts and Caruthers [1] used a metal plate lens as the collimating device. This had a 35λ square aperture, but the results were not satisfactory and the failure was attributed to diffraction off the metal edges. The pioneer of the compact range using a reflector as the collimating device was Johnson, working at Georgia Institute of Technology. He filed a patent in 1967 [2] and first described the range in 1969 [3], with more results being published by him and co-workers in 1973 [4] and 1975 [5]. Initially Johnson constructed two configurations – a line-source range consisting of a parabolic cylinder reflector with a large Hogg horn feed and a point-source range with a small rectangular horn feed. Development of the line-source feed did not proceed far due to the disadvantages of single polarisation and of needing to change the physical size of the line-source feed for different frequencies. The point-source ‘compact range’ was very

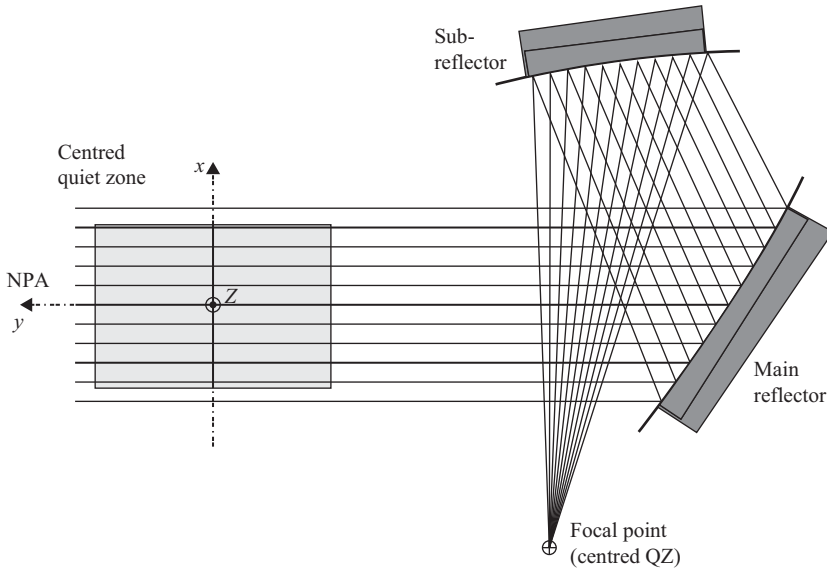


Figure 5.1 Main elements of a CATR

successful and has formed the basis of most of the subsequent developments. Johnson's designs were developed by Scientific Atlanta who started marketing the range in about 1974 [6,7]. Their range used an offset parabolic reflector made of metal-coated machined fibreglass with a size of about 5 m wide by 3.5 m high which gave a quiet zone of about 1.5 m diameter. The range had a shaped edge in order to reduce edge diffraction and was the forerunner for classic single-offset CATR we know today (Figure 5.2). These designs inherently have a poor utilisation of the reflector surface, with typical quiet zones about one third the size of the main reflector. In 1976, Vokurka [8], at Eindhoven University of Technology, developed a compact range using two cylindrical parabolic reflectors. By collimating the beam in orthogonal planes with two reflectors with large effective focal lengths, it was easier to make accurate cylindrical reflectors and a high area utilisation factor was achieved; Figure 5.3 shows a modern development of this concept.

Since early days the compact range has become a very popular antenna measurement solution as it offers

- efficient use of real estate for a given quiet zone size,
- low path loss as the beam from the main reflector is collimated and does not suffer $1/R^2$ loss,
- secure operation in a controlled indoor environment (temperature controlled, 'clean room' capability, freedom from external EM interference),
- RCS measurement capability,

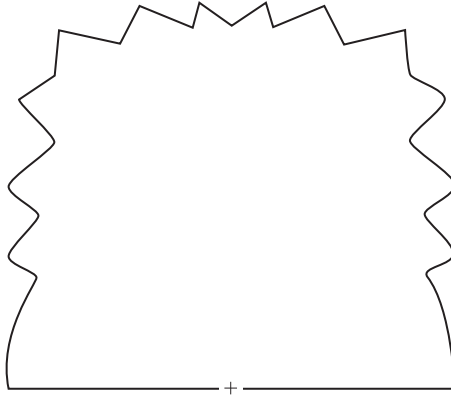


Figure 5.2 Reflector edge treatment employed by the Scientific Atlanta model 5750 range marketed in the late 1970s

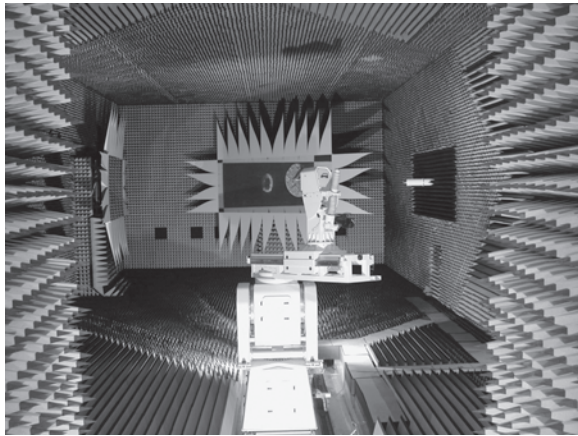


Figure 5.3 View of an antenna mounted on a positioner in a CATR enclosed in a $24\text{ m} \times 14\text{ m} \times 11\text{ m}$ anechoic chamber (Courtesy of SELEX ES)

- flexible instrumentation including operating in both transmit or receive AUT configurations,
- inherent wideband operation, since based on ray optics the system is limited mainly by the surface accuracy and edge treatment of the reflectors,
- operation at millimetre wavelengths.

In the next section we will look at the various ways in which we can collimate the field from the CATR feed to generate the pseudo plane wave we require.

5.2 Collimation of electromagnetic fields

The principle of the CATR is to take the spherical wave emanating from the feed horn and convert this to a plane wave. The simplest way to achieve this is to use a single-offset reflector antenna as shown in Figure 5.4. Here a high-performance feed (e.g. corrugated feed horn) illuminates the paraboloidal reflector with the feed phase centre located at the focal point of the reflector. On reflection the spherical wave of the feed is converted to a ‘plane wave’ offering a uniform phase front in the quiet zone. This uniform phase comes about from geometric optics that shows that (Figure 5.4)

$$\overline{FP} + \overline{PA} = 2F + \Delta l \tag{5.1}$$

where F is the focal length (where \overline{FP} indicates the magnitude of the distance from F to P , etc.). Hence the phase across the aperture is constant but the amplitude varies as $1/\rho^2$ (where ρ is the distance from the focal point to a point P on the reflector surface). This is by virtue of the paraboloid being a spherical wave to plane wave transformer.

This is illustrated in Figures 5.5–5.7 where the down range electric field amplitude and phase are plotted for a single offset reflector. The horizontal scale is measured in focal lengths and clearly indicates why the industry standard location for the QZ centre of ($5/3F = 1.667$) is used. It is also clear from these plots that the QZ is a volume, and although generally, the QZ is largely determined by the transverse field taper and ripple (as in Figure 5.6), and it is important to understand that the QZ is a volume and hence there needs to be a down range “Quiet” field

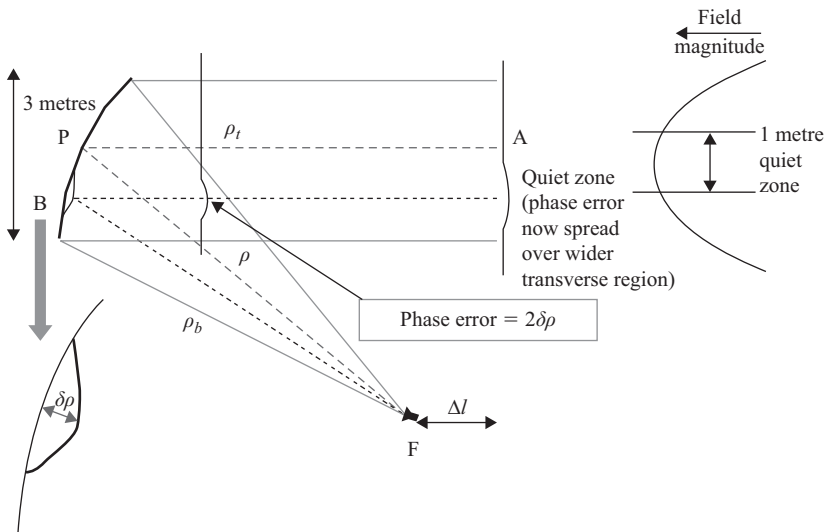


Figure 5.4 The single-offset CATR, showing effect of reflector surface error

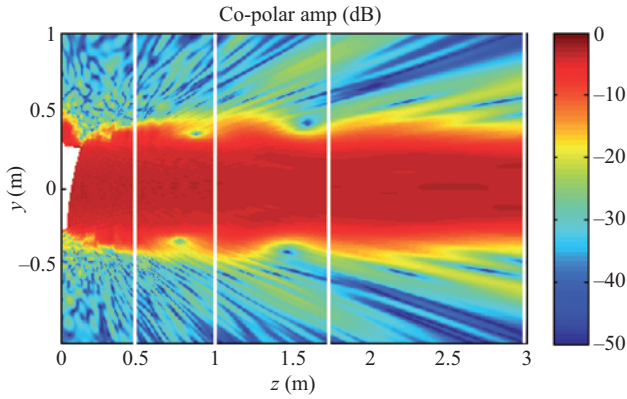


Figure 5.5. Down range electric field amplitude from a single offset CATR (reflector shown on the left). The Z-axis is plotted in units of focal length of the CATR reflector, and the Y-axis is measured in units of D which is the tip-to-tip reflector size in the vertical direction

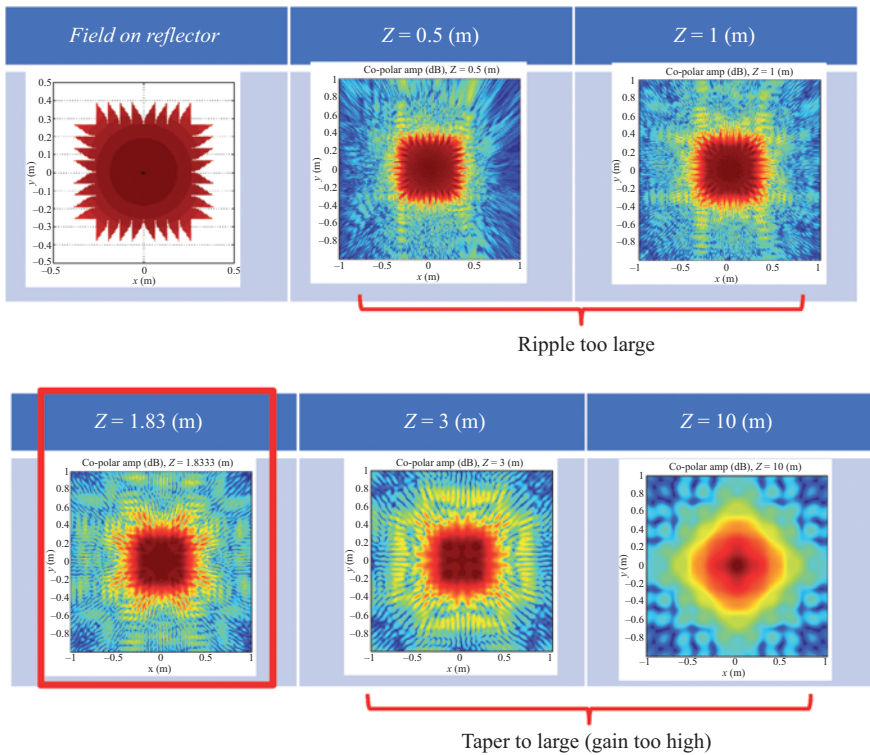


Figure 5.6. Transverse electric field amplitude plots for different down range distances shown in Figure 5.5

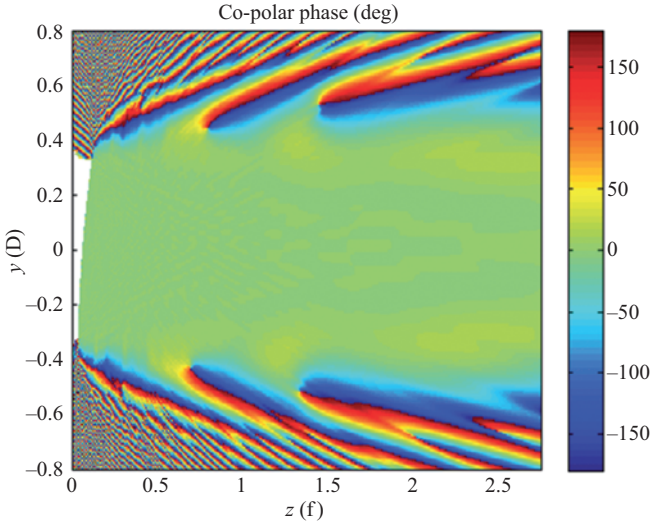


Figure 5.7. Down range electric field phase from a single offset CATR (reflector shown on the left). The Z-axis is plotted in units of focal length of the CATR reflector, and the Y-axis is measured in units of D which is the tip-to-tip reflector size in the vertical direction. The $\exp(-jk_0z)$ term removed and field phase normalised to 0°

region where the field has low ripple and remains collimated, which for the single offset case is centred around $5/3F$.

Figure 5.4 shows that with the feed boresight pointed to the centre of the offset reflector (point P), the signal amplitude at the bottom of the reflector will be proportional to ρ_b and at the top to ρ_t offering a small additional amplitude taper to the feed pattern that projects onto the top half of the reflector. This asymmetry in amplitude can be improved by aiming the feed antenna higher than the centre point of the reflector. The resulting aperture field amplitude is shown to the right of the figure. In order to conform with the desire to have the quiet zone at ± 0.5 dB, it is clear that only the central region (typically about one third) of the reflector can be deployed as a CATR quiet zone. Neglecting extraneous effects such as edge diffraction and feed spill-over the phase in the quiet zone is constant; however, as shown by point B in Figure 5.4, if the reflector surface is not a pure paraboloid then a small indentation of depth $\delta\rho$ will result in a phase distortion at the quiet zone of $2\delta\rho$. Thus, if $2\delta\rho$ represents 5° of phase shift in the quiet zone then $\delta\rho$ must be 0.007λ in size, which means the rms error needs to be kept to 0.01λ . This is a significant limitation to the use of CATRs at millimetrewave frequencies, and we will return to this later in this chapter.

However, surface error is not the only source of quiet zone amplitude and phase error as Figure 5.8 illustrates. Here we show the different sources of energy that can reach point A in the quiet zone. Critically we have the contribution due to

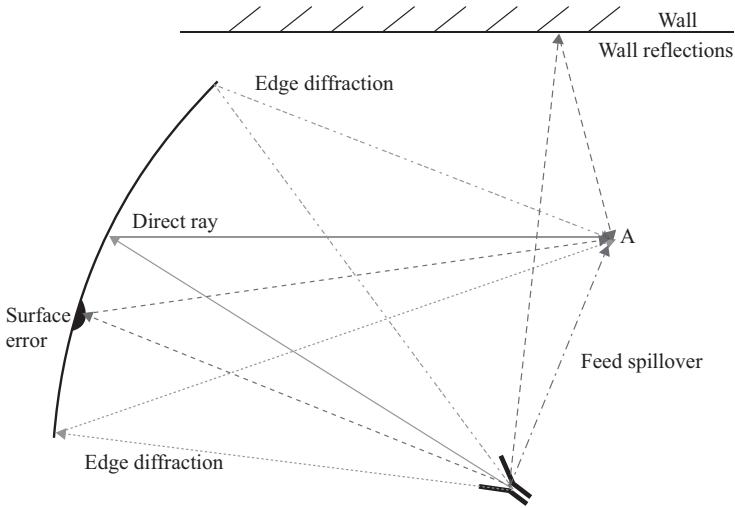


Figure 5.8 Sources of quiet zone error

edge diffraction at the reflector edges, as well as contributions from reflections from non-perfect absorber, that lines the whole chamber that encloses the CATR as well as the direct ray from the feed that ‘spills over’ into the quiet zone and also contributes to the signal at A.

This situation can become more complicated when a dual reflector CATR is used (Figure 5.9), where diffraction reflection effects as well as multiple diffraction will further add to the number of possible interfering sources reaching a given point in the quiet zone. Here we briefly look at each of these sources of error and in the following sections we will consider how these various effects can be mitigated in a given design.

Reflector edge diffraction: This can be reduced by redirecting the diffracted energy away from the quiet zone by such techniques as serrating (castillations) the reflector edges (see Figure 5.2) or by using a blended rolled edge. Alternatively, the magnitude of the energy hitting the edge can be reduced by decreasing the level of the edge illumination through choice of feed; however, for a simple feed an increased edge taper will reduce the size of the quiet zone as the narrower feed pattern is projected into the quiet zone (see Figure 5.4) so an engineering compromise is needed. Alternatively a more complex shaping of the energy hitting the main reflector can be achieved by using a multi-shaped reflector feed system.

Feed spillover: This can be overcome by careful feed design, use of absorber baffles or use of a multi-shaped reflector feed system.

Wall reflections: This is largely down to size of pyramidal absorber used (see Chapter 3), but also on the shape of the chamber walls as all absorber

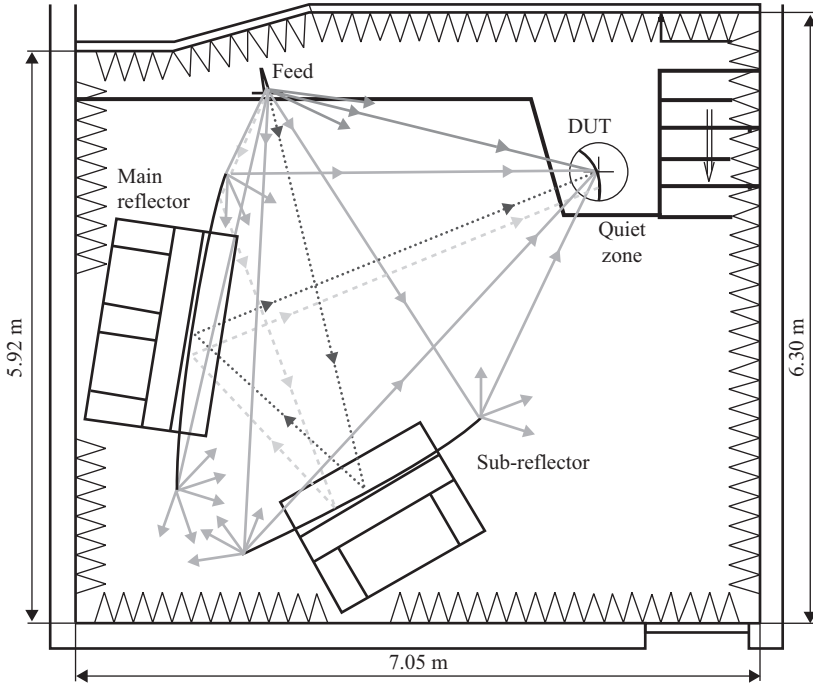


Figure 5.9 Dual reflector CATR sources of quiet zone error caused by non-optimised serrations (used with permission from Prof. Dietmar Fasold, Munich University of Applied Sciences, Munich, Germany)

operates with the best reflectivity at normal incidence. As in any anechoic chamber the size of the pyramidal absorber used determines its low frequency performance.

Time-gating: A completely alternative approach is to not worry about mitigating these effects and to use a time-gating receiver technique to remove these signals, which have either a shorter time of flight from feed to quiet zone (e.g. feed spillover) or a longer time of flight (e.g. edge diffraction). This is covered in more detail in Section 5.2.6.

5.2.1 Reflector edge diffraction

There are several methods of minimising this effect and these will be considered in detail.

5.2.1.1 Serrated edge reflectors

The problem of reflector edge diffraction was quickly recognised as a critical effect in successfully designing a CATR, as demonstrated by the early designs of CATR such as the Scientific Atlanta model 5750 range marketed in the late 1970s (see Figure 5.2). The concept of the serrated edge is that the continually changing edge

angle spreads the diffracted energy over a wider region in the quiet zones and so avoids constructive mixing of the individual diffraction points which is seen on a simple straight or curved reflector edge. The first attempt at analysing this was by Beekman [9]; the near-field zone of a serrated edge aperture having a rectangular rim shape was calculated using a scalar Fresnel transform. The triangular shape of the serrations used allowed an analytic evaluation of the 2D integrals involved in defining the Fresnel transform. A dramatic improvement of the serrated edge case over the untreated counterpart was demonstrated. For example, it was shown that an amplitude ripple of almost 4.5 dB was transformed to only a 0.2 dB ripple when serrations were introduced. This is shown in the reproduced result from this paper in Figure 5.10. This nicely demonstrates that enlarging the serrations (and so the overall aperture size) enlarges slightly the quiet zone size. Figure 5.11 (also from [9]) shows how the transverse quiet zone at different down range distances (thus defining the quiet zone *Volume*) is controlled by the serrations. Work along similar lines dealing with a circular projected aperture envelope has been reported in [10–13]. The conclusions were similar in that the serrated aperture provides the better performance in terms of near-field uniformity.

In [14] the shape of serrations was studied by both theoretical modelling of different shapes and the experimental verification by measuring the RCS of thin strips of CATR reflector with the desired shaped serration at each end. From the RCS measurements the maximum plane wave spectral components of the quiet

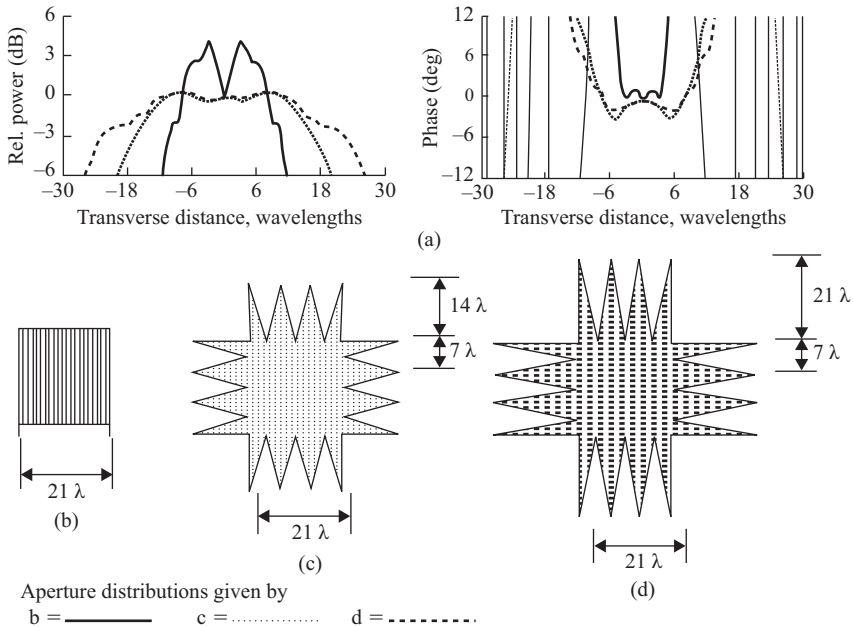


Figure 5.10 Fresnel diffraction patterns at a distance of 64λ from the aperture plane (adapted from [9]). Aperture size is 45λ

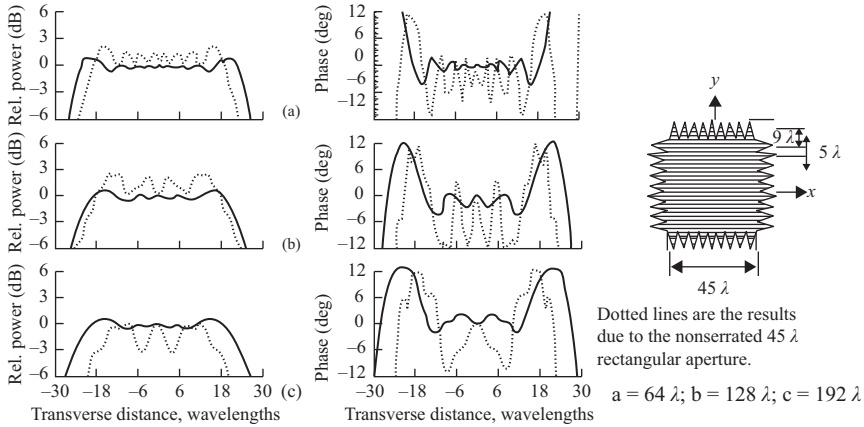


Figure 5.11 Fresnel diffraction patterns due to the serrated aperture distribution, shown inset, for three different down range distances z (from [9])

zone were determined and used as a performance measure. The research showed that at low frequencies where the serrations were only around 5λ in length, triangular serrations worked best. However, at higher frequencies with serrations in excess of 10λ , a cosine to the power 1.6 shape was the better choice. Serrations aim to smooth the transition between reflector with maximum current and free space at reflector edge with no current. As the electrical size of the serrations increases, the lowest quiet zone ripple is achieved by making the current distribution at the edge continuous for all derivatives which is offered by a cosine squared shape. The cosine to the power 1.6 is thus an engineering compromise for the typical range of operation of a CATR.

However, in [11] the vectorial nature of the fields involved was neglected and the study concentrated on a single CATR reflector size of 50λ . Two main criticisms can be levelled at these studies. First, when comparing serrated and unserrated edge apertures, the serrations were assumed to ‘add on’ to the unserrated aperture. When considering a retrofit of an existing facility, this approach is sound; however, from a design and chamber volume point of view, this comparison is unfair since in this case the unserrated aperture is always smaller than its serrated counterpart. The second problem is due to the fact that in none of the above studies was the possibility of imposing an edge taper on the unserrated reflector used in any comparison. This issue was addressed by one of us (Parini) and is reported in [15] and summarised below.

The physical optics (PO) method of modelling can be used, since with this method it is easy to accommodate the impact of serrations and at the same time provide reasonable accuracy.

Two examples of projected apertures for serrated rim reflector CATRs are shown in Figure 5.12 where the value of serration length used (30%) was selected to be representative of practical CATRs. A CATR with a nominal projected

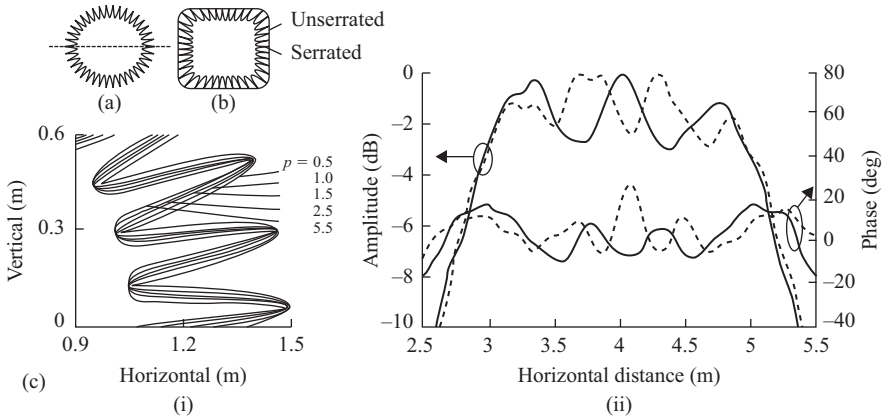


Figure 5.12 (i) Superquadratic rim shapes (a) circular, (b) rectangular, (c) serration shape against parameter p . (ii) Comparison of PO-calculated quiet zones for straight rim ($ET = -7$ dB) and serrated rim ($ET = -1$ dB) circular aperture CATR diameter = 3 m, $z = 6$ m. — serrated rim; - - - straight rim

aperture of 3 m diameter and a focal length of 5.4 m was used in the study operating at 3 GHz, this being a small 30λ aperture. Results for the circular aperture of Figure 5.9 [15] with an edge taper of -1 dB do indeed show that the uniformity of the transverse quiet zone phase (taken at $z = 6$ m) is substantially improved with the serrated rim where 70° of phase ripple was reduced to 20° . However, a too low or too high a value for the serration steepness factor (p) provides no improvement in the amplitude quality, as compared with the straight edge case with a similar amount of edge taper.

For large p values, increased amounts of almost straight rim sections reappear between the serration peaks (Figure 5.12(i)) with the direct consequence of a gradual reinforcement of the edge diffracted field coherence. Additionally, these straight sections were located at a reduced distance from the apertures centre, which could explain the increase in amplitude ripple. However, for p values in the range 1–3, an improvement of as much as 2 dB in quiet zone amplitude ripple could be observed. A value of $p = 2.5$ was selected for subsequent calculations. The quiet zone is far less sensitive to changes in N , the total number of serration periods. These observations were made by studying the quiet zone field along both the horizontal and vertical transverse axes. In [12] and [13] the effect of randomised lengths of the serrations (i.e. not all uniform), the root depths between serrations and the width of the serrations were studied by Joy for general low side lobe antennas and the CATR. The ‘flower petal’ shape serrations shown in Figure 5.13 was patented in 1994 (US patent #5,341,150). The conclusion was that there was no great advantage to randomising the serrations as compared to uniform serrations for a CATR.

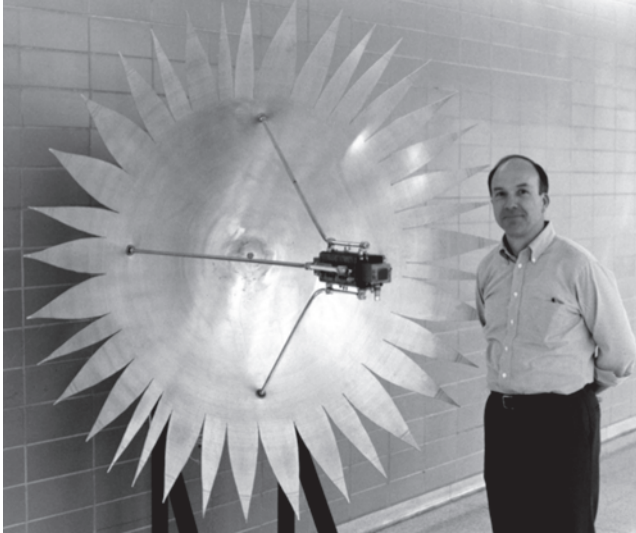


Figure 5.13 Randomised 'flower petal' serrations as used on a low side lobe reflector antenna, pictured with Ed Joy

Serrations provide spatial tapering of the field towards the reflector rim but this could equally well be done by changing the feed of the equivalent straight rim reflector to provide a similar edge illumination taper. When the edge taper is close to -7 dB, comparable results to the serrated case can be obtained, and this is illustrated in Figure 5.12(ii) for a horizontal scan. The -10 dB field extent is similar in both the horizontal and the vertical scan, which can be used as an indication of the similarity between the amplitude and spatial tapering for the corresponding examples.

Similar results can be seen for the superquadratic aperture shape (Figure 5.12(i)b) with the straight rim aperture performing better than the circular aperture when they have the same edge taper. The larger edge taper at the corners of the superquadratic rim, combined with the fact that the noncircular aperture is larger than its circular counterpart, is the main contributions to the improvement. For the case of the straight rim with -7 dB edge taper, the amplitude and phase of the superquadratic aperture satisfy the commonly used quality criteria (± 0.5 dB and $\pm 5^\circ$), yielding a quiet zone with 0.9 m lateral extent. The equivalent circular aperture would not be able to satisfy this criterion at 3 GHz. The results for the superquadratic aperture suggest that an alternative to serrations for reducing diffraction would be to use an aperture shape which directs the edge diffraction energy away from the test zone. An indication that this suggestion is valid can be seen by considering the case of the Queen Mary University of London (QML) CATR which has a sector-shaped aperture (Figure 5.14). At a frequency of 3 GHz and edge taper -7 dB, the theoretical co-polar field scans perform similarly to the square projected aperture CATR. As with the superquadratic aperture, the QML CATR has straight sides and an orientation relative

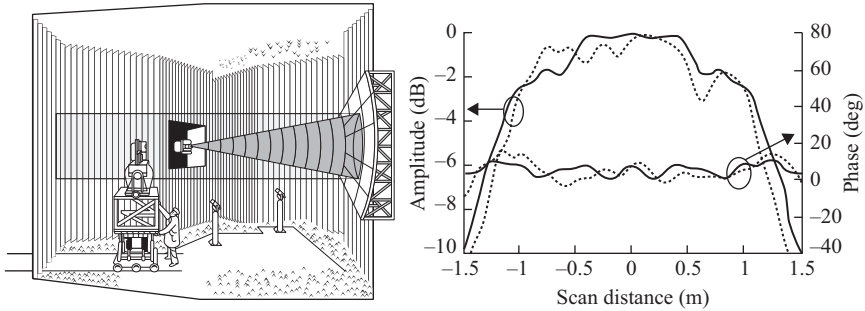


Figure 5.14 Left: sector-shaped CATR at Queen Mary University of London (QML). Right: quiet zone amplitude and phase for sector-shaped QML CATR with $ET = -7$ dB, $z = 6$ m; — vertical scan; - - - horizontal scan

to the feed which directs the edge diffraction energy away from the quiet zone. A direct result of this is that a quiet zone scan along the vertical has a higher degree of uniformity than along the horizontal.

In summary when the envelope of a CATR reflector projected aperture is kept constant, the inclusion of serrations improves the low frequency performance of the CATR. The improvement offered can be thought of as a consequence of the spatial tapering induced, and hence the introduction of an equivalent amount of illumination tapering in an untreated edge reflector will produce quiet zone fields of similar quality. In this sense spatial tapering (serrations) and feed tapering are electrically equivalent methods to reduce edge diffraction. The geometric optics (GO) field component for a CATR with a strongly illuminated serrated rim is uniform over a larger lateral extent than for the equivalent performance unserrated rim, since for the later case edge diffraction is reduced by using a stronger edge taper from a simple feed. If a more complex feed is employed, which can shape the illumination more effectively near to the reflector edge (using a system of shaped reflectors for instance), then serrations become unnecessary. Having established the equivalence between illumination tapering and serrations, the superiority of one approach over the other can be judged primarily from practical and financial considerations. In this sense the serration approach may have an advantage, if the best low frequency performance is required, since at the low frequency limit a feed providing the necessary illumination taper will be large and expensive to manufacture.

In [21] the concept of the R-card is proposed where double-sided resistive cards (or plates) are strategically located around the edges of the CATR reflector to effectively shape the aperture illumination; however, the authors are not aware of any practical implementation of this technique for a CATR.

5.2.1.2 Blended rolled edges

The concept of the blended rolled edge was first devised by Burnside and reported in [16]. This uses a smooth transition from the parabolic reflector surface that

collimates the feed spherical wave to the quiet zone, to an elliptic surface that progressively steers the energy away from the quiet zone (Figure 5.15). There are several ways that this edge can be constructed ranging from direct transition from parabola to ellipse as well as blending from ellipse to parabola via cosine and cosine squared transition functions, these are compared in Figure 5.16. A good description of the mathematical process is described in [17].

To demonstrate the effectiveness of this solution in [13], Burnside compared the diffraction from a 24λ paraboloidal reflector with a knife edge and a blended rolled edge using geometric theory of diffraction (GTD) showing a significantly low quiet zone ripple (Figure 5.17). In [18] a direct comparison between the blended rolled edge and the serrated edge was undertaken for a $20 \lambda \times 20 \lambda$ reflector surface with the addition of either a 10λ long serration or a 10λ blended rolled edge (so the overall reflector with edge treatment was in both cases $40 \lambda \times 40 \lambda$). Figure 5.18 shows a comparison of the transverse quiet zone at a down range distance of 70λ for both the blended rolled edge and the serrated edge along with the ideal GO field with no diffraction. These were calculated using the PO technique with the physical theory of diffraction (PTD). The closeness of the blended rolled edge to that of the ideal case is clear. How this translates to pattern measurements is illustrated in Figure 5.19, which shows the backscatter signal from a $12 \lambda \times 12 \lambda$ diagonal plate simulated in both the serrated and blended rolled edge CATR. The error in the serration pattern occurs when the ‘main beam’ of the AUT looks at the serrations and so the stray diffraction signals are amplified by the main beam, and this signal level can be comparable to that of the true side lobes generated by the CATR plane wave illuminating the AUT. A typical blended rolled edge reflector is shown in Figure 5.20, and this is generally much more expensive and difficult to make than a serrated reflector as the blending from parabola to ellipse must be smooth to ensure that no diffraction occurs at the boundary. In addition, the

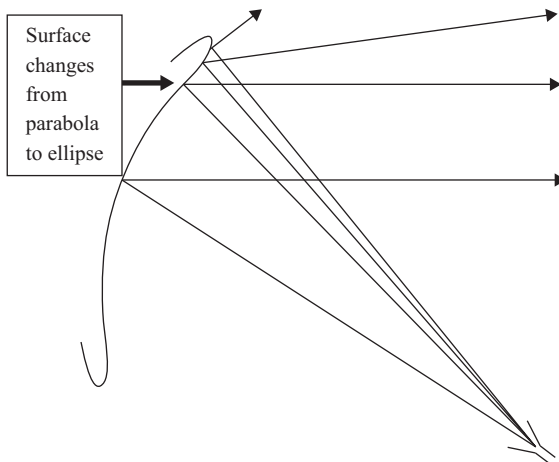


Figure 5.15 Concept of the blended rolled edge CATR reflector

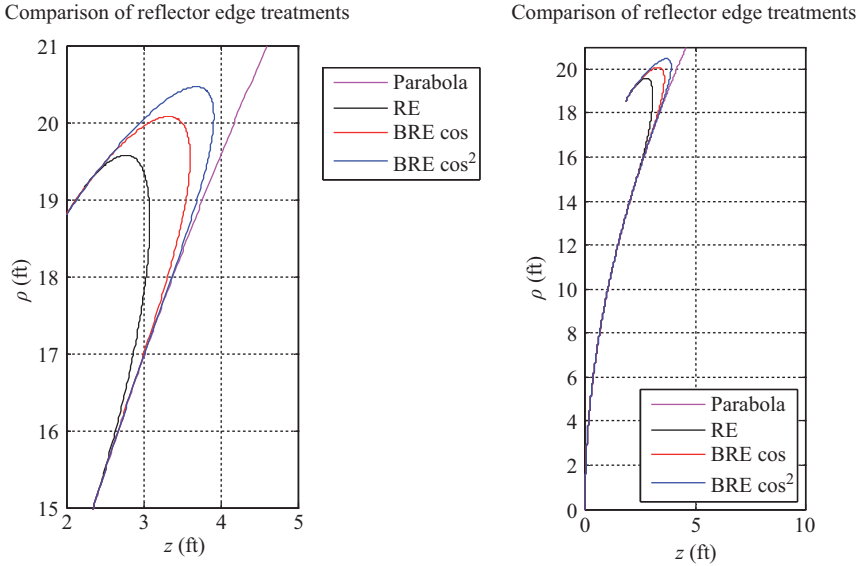


Figure 5.16 Comparison of several types of blended rolled edge. RE = direct to ellipse; BRE cos = blending between parabola and ellipse via a cosine blending function; BRE cos² = blending between parabola and ellipse via a cosine squared blending function

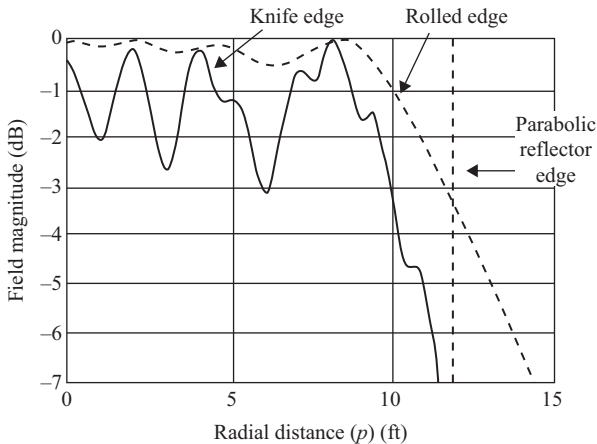


Figure 5.17 Blended rolled edge quiet zone vs knife edge reflector [16]

inevitable panel construction must ensure that surface currents flow freely and no ‘panel gap’ effect is seen (this issue is covered in Section 5.2.5). In practice, the benefit is usually not so great as illustrated by these simulated measurements as the redirected energy of the blended rolled edge needs to be effectively absorbed by

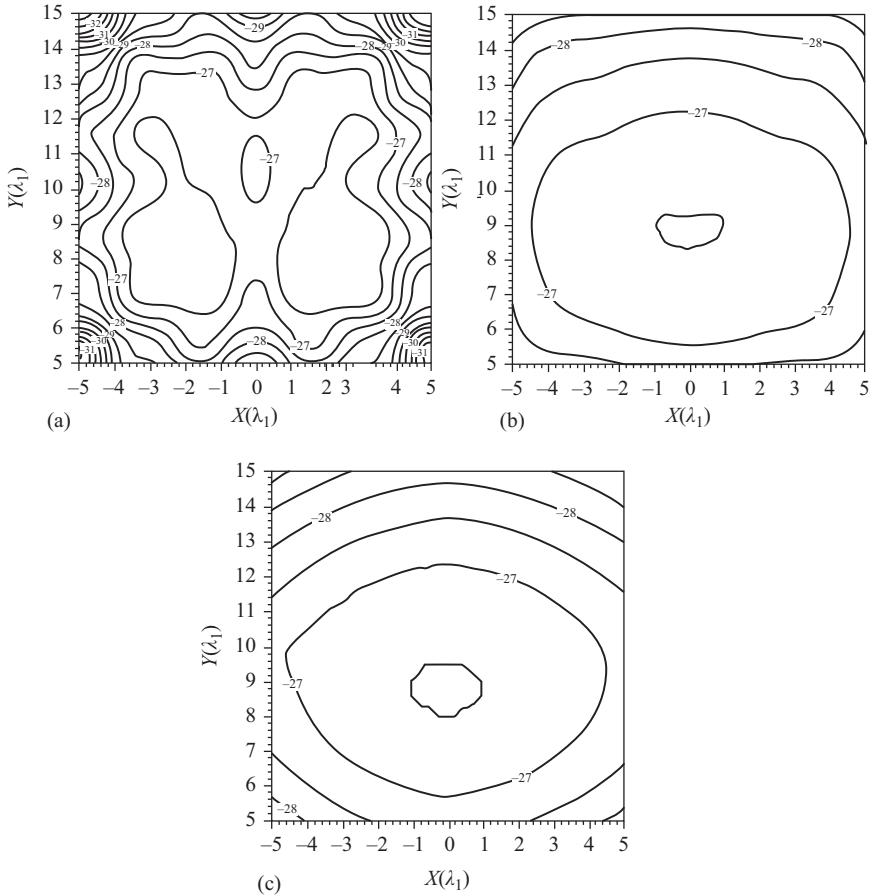


Figure 5.18 Simulated quiet zone contours for serrated edge and blended, rolled edge-compact range reflectors of 40λ by 40λ . (a) Serrated edge reflector. (b) Blended, rolled edge reflector. (c) Ideal geometric optics field (contour lines separated by 0.5 dB) [18]

the anechoic chamber walls for the full benefit to be achieved. A comparison of the ray paths resulting from the focal point feed illumination of a parabola for both serrations and blended rolled edge treatment is shown in Figure 5.21.

5.2.1.3 Shaped feed illumination

An alternative approach that is viable for high-frequency operation (millimetrewaves) is to shape the illumination that reaches the main reflector so that the illumination across the major part of the reflector is uniform but rapidly falls off to -20 dB or less at the reflector edges. The concept is illustrated in Figures 5.22 and 5.23, where a pair of shaped sub-reflectors is used to shape the illumination that hits

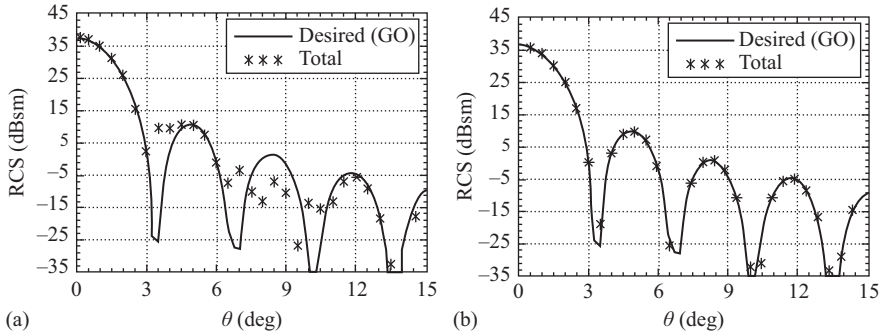


Figure 5.19 Simulated backscattered fields of diagonal flat plate 'measured' using the (a) serrated edge and (b) blended rolled edge reflector [18]

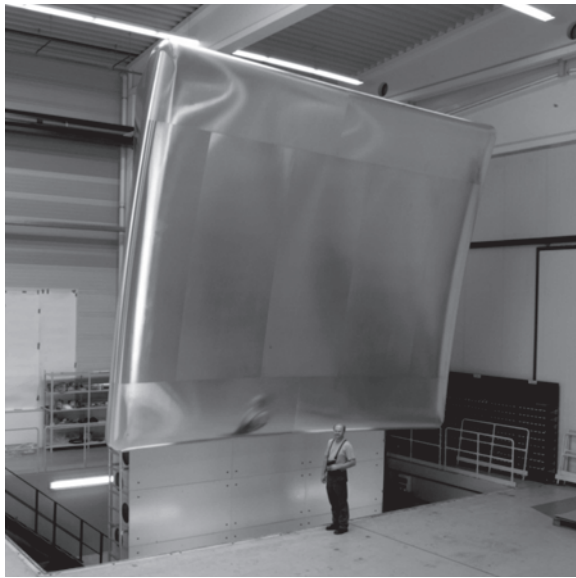


Figure 5.20 Blended rolled edge reflector 6 m (including rolled edge), quiet zone of 3 m diameter, rolled edge 1.5 m width and lowest frequency of 500 MHz (Courtesy of MVG-Orbit/FR)

the main reflector. This has two benefits, first that the reflector can be made with no edge treatment, and second that the quiet zone size can be up to 70% of the main reflector diameter, compared to the 30% of a conventional single-offset reflector. This is particularly desirable for millimetrewave compact ranges where very high surface accuracy reflectors (e.g. $8\ \mu\text{m}$ rms for 300 GHz operation) are required and the cost of manufacture is strongly linked to the main reflector diameter.

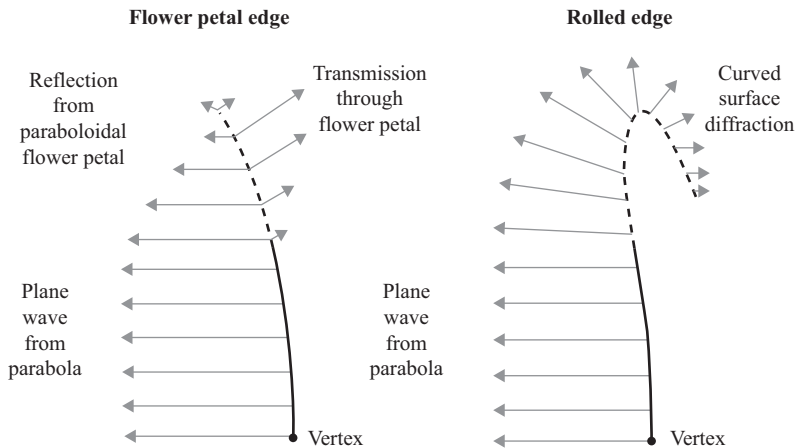


Figure 5.21 Ray paths resulting from focal point feed illumination of a parabola for both serrations and blended rolled edge treatment (Courtesy of Ed Joy)

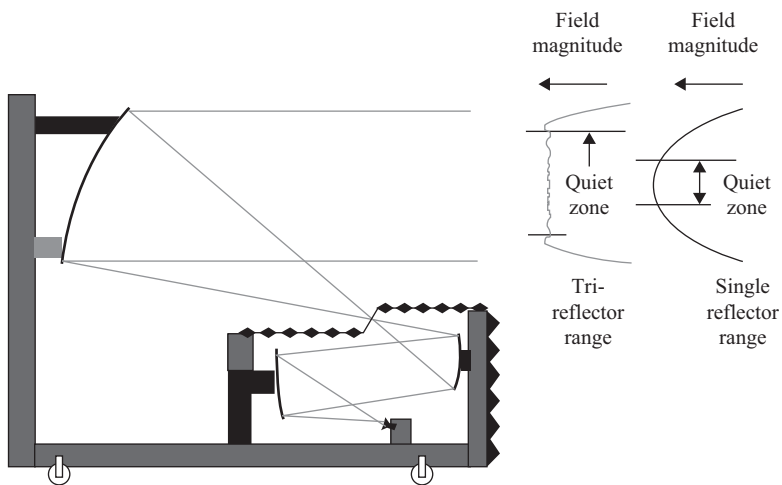


Figure 5.22 Tri-reflector CATR which takes the Gaussian feed pattern of a corrugated horn, shaped by dual reflectors to give an optimal illumination at the main reflector

However, the influence of the shape of the amplitude taper across the quiet zone on the measured AUT patterns should not be neglected, particularly when very low side lobe antennas are to be measured. In [19] the effect of a ‘single hump’ transverse quiet zone amplitude distribution was compared to a ‘double hump’ (with dip in the middle) distribution, both having the same peak-to-peak

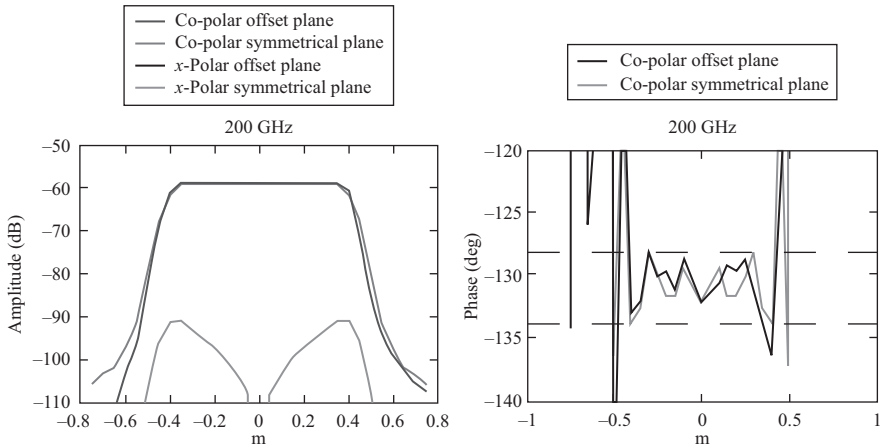


Figure 5.23 Simulated performance of tri-reflector CATR with 1 m diameter main reflector operating at 200 GHz [20]

ripple of just 0.25 dB. Theoretical results obtained when ‘measuring’ a 40 dB side lobe level Chebyshev distribution AUT indicated that the single hump produced a first side lobe decrease of 1 dB and a gain loss of 0.04 dB, but the double hump produced a first side lobe increase of 5 dB and a gain loss of 0.12 dB. Clearly this illustrates that just setting a global maximum quiet zone amplitude ripple may not be sufficient to guarantee accuracy of measurement for very low side lobe AUTs. In such cases, simulation of the AUT measurement in a given CATR is vital, and this topic is considered in Section 5.4.

5.2.2 Feed spillover

As shown in both Figures 5.8 and 5.9, energy from the feed can be directly received in the quiet zone. This is demonstrated in Figure 5.24 by the simulation taken from [21] for a single-offset reflector quiet zone cut taken in the vertical (offset) plane. If this is compared with the similar horizontal plane cut (Figure 5.25), we see a reduced ripple frequency in the quiet zone plots. This is due to the fact that for the vertical plane the PWS contribution from the spillover has high angular spectrum, whereas for the horizontal cut the PWS contribution from spillover is centred around the low angular spectrum origin.

The use of absorber baffles to isolate the direct path from feed to quiet zone is a popular solution and can be seen for the single-offset case in the QML range (Figure 5.14) and for the Airbus Defence and Space dual reflector CATR in Figure 5.26.

5.2.3 Lenses as collimators

Up till now we have only considered the reflector as the means of collimating the electromagnetic energy into the required pseudo plane wave; however, as we know

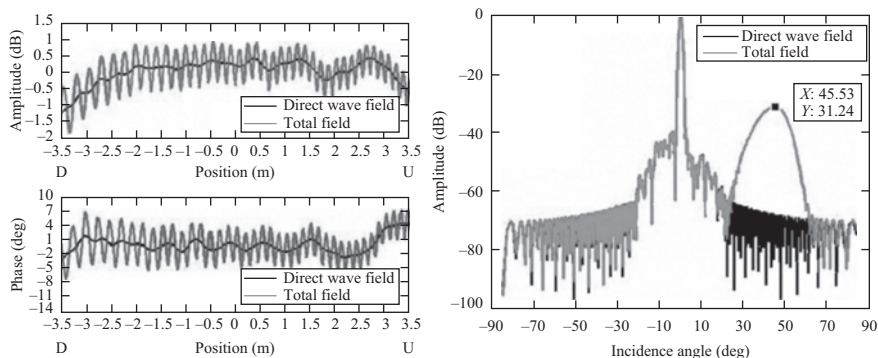


Figure 5.24 Simulation of feed spillover in vertical plane for single-offset CATR, left: quiet zone amplitude and phase; right: corresponding plane wave spectrum (PWS) [21]

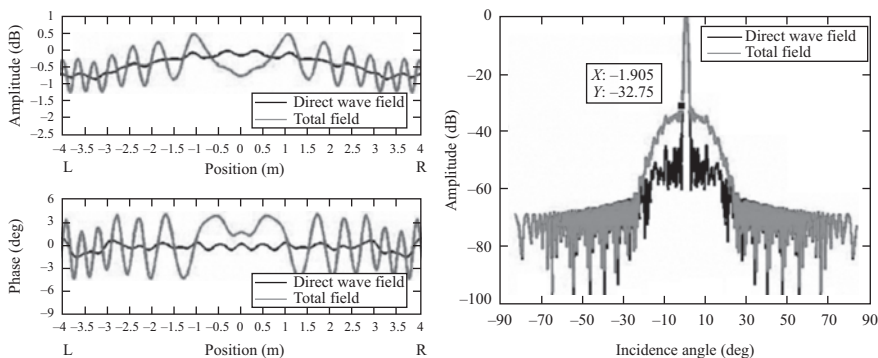


Figure 5.25 Simulation of feed spillover in horizontal plane for single-offset CATR, left: quiet zone amplitude and phase; right: corresponding plane wave spectrum (PWS) [21]

from basic optics a lens can be deployed equally well. In 1953, Mentzer [23] used a foam dielectric lens of 33λ in diameter and a relative permittivity of 1.03. However, the low permittivity meant that the focal length to diameter ratio was about 10 so that the antenna range was not very compact. In the late 1970s, Olver and Saleeb demonstrated that a lens type compact range using foam dielectric was possible [24]. Menzel and Huder [25] later showed that a solid PTFE dielectric lens could be used to measure antennas at 94 GHz. This had a diameter of 0.5 m, a spherical contour and a thickness of 20 mm. A tolerance analysis shows that the accuracy of the lens contour only has to be about 0.5 mm to give the same phase error as a reflector with 0.1 mm error. This is because firstly the error appears only once in the transmission path for the lens, but twice for the reflector, and secondly, this error is weighted by a factor of $\sqrt{\epsilon_r} - 1$, which is about 0.4 in the case of

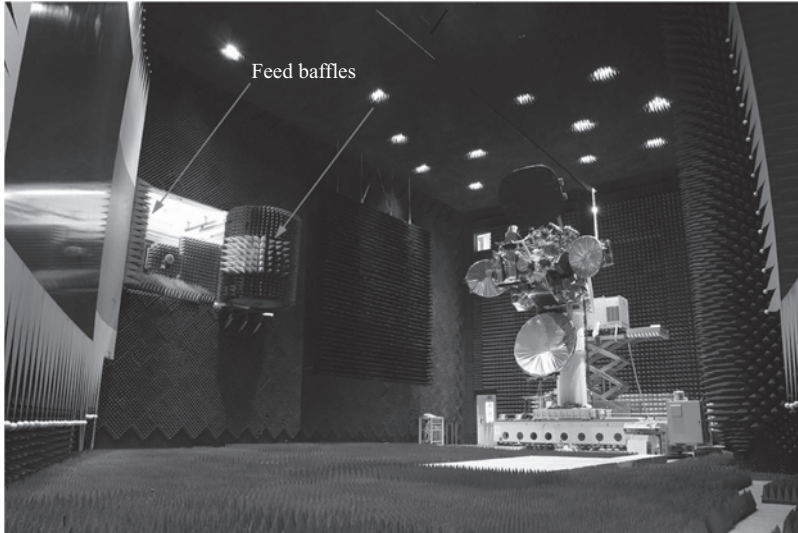


Figure 5.26 Airbus Defence and Space CATR showing cylindrical absorber baffles to isolate feed from quiet zone. Copyright 2004, Airbus Defence and Space

PTFE. In this case a very long focal length was used resulting in a range length of 4.5 m. It was successfully used to measure a 30 cm diameter antenna at 94 GHz, where the far-field distance would be 56.4 m, so it was an effective way of fitting such an antenna in a reasonably sized anechoic chamber. No quiet zone measurements were reported for this case. In 1991, workers at Helsinki University of Technology reported [26] a lens CATR with a shaped polyethylene ($\epsilon_r = 2.32$) lens for 110 GHz (Figure 5.27), where the shaping provided a uniform amplitude distribution in the quiet zone. In order to make the quiet zone amplitude ripple from edge diffraction small, saw tooth serration around the lens was used and shown theoretically to have quiet zone peak-to-peak ripple of 0.27 dB, with preliminary measurements showing a ripple of 2.0 dB.

A critical factor in any lens design is the homogeneity of the material forming the lens as any local non-homogeneity will lead to quiet zone phase ripple in the same way that surface errors do. The advantage of the lens is the high area utilisation, lower edge diffraction (prior to treatment), no direct radiation from the feed and good cross-polarisation; however, the ability to manufacture with high homogeneity severely limits the practicality of this approach.

5.2.4 Hologram CATRs

A successful development of the lens work at Helsinki University of Technology was the development of the holographic CATR. Here a transmission-type binary amplitude hologram is used as a collimating element to form a plane wave for

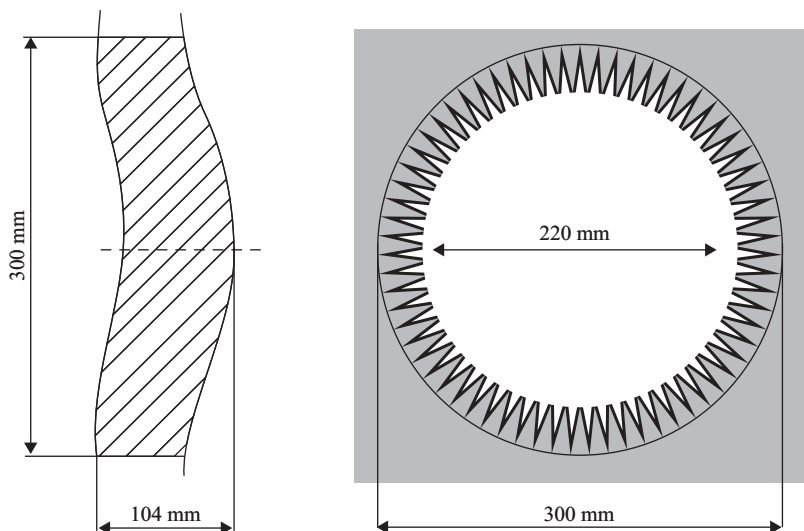


Figure 5.27 Shaped dielectric lens CATR with cosine shaped saw tooth serrations. Lens focal length = 94.7 cm [26]

antenna testing. The hologram is a computer-generated interference pattern etched on a thin metal-plated dielectric film, which is stretched on a supporting frame. An example of this work is given in [27] where a 3.0 m diameter hologram was constructed for operation at 322 GHz; a diagram of the system is shown in Figure 5.28. The hologram is designed to generate the plane wave to an angle of 33° from the hologram normal in order to prevent the unwanted diffraction modes propagating along the normal from disturbing the quiet zone. The performance of a $0.6 \text{ m} \times 0.6 \text{ m}$ prototype hologram made from three pieces of $50 \mu\text{m}$ thick copper-plated Mylar film ($0.2 \text{ m} \times 0.6 \text{ m}$ in size) joined together using a soldering technique was shown to have a 300 mm diameter quiet zone with amplitude and phase ripple of 1.5 dB and 10° peak-to-peak. The full 3.0 m diameter hologram CATR was again made from three sections due to the limitation in manufacturing single piece holograms any larger than $1.35 \text{ m} \times 3.2 \text{ m}$. The performance of the full system was limited by an amplitude error in the hologram modelling, but measurements were undertaken on a 1.5 m diameter 322 GHz AUT [28].

The same group extended this work by constructing a 1.0 m diameter hologram for 644 GHz operation, using a $50 \mu\text{m}$ thick copper-plated Mylar film as the substrate material [29]. The hologram was manufactured using direct laser writing of the pattern followed by wet etching. The quiet zone field generated by the hologram had measured peak-to-peak amplitude and phase ripples of approximately 2 dB and 15° .

In [30], the use of a dual reflector feed system (see Section 5.2.1.3) to shape the amplitude that illuminates the holograms enables a nearly constant slot width in the hologram pattern, which simplifies the hologram manufacturing by eliminating

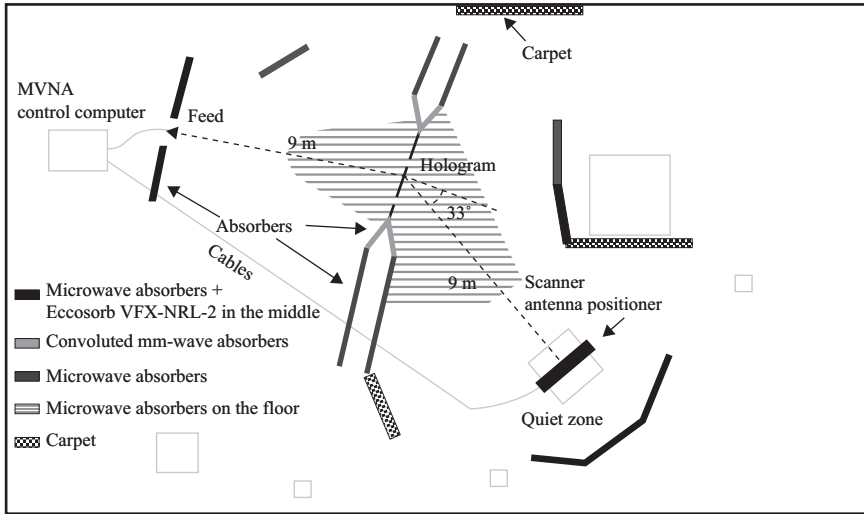


Figure 5.28 Hologram CATR [27]

the narrow slots in the edge of the hologram pattern, required when a simple corrugated feed horn is used. Wider slots are easier to etch correctly and they are more tolerant to over-etching.

For millimetrewave and sub-millimetrewave operation, the hologram CATR is a viable alternative to very high precision reflector antennas. The disadvantage of the hologram is its narrow bandwidth and single polarisation operation. The narrow bandwidth is due firstly to the fact that as the frequency changes from the design frequency the direction of the hologram beam moves, and secondly the quiet zone amplitude ripple increase, thus a bandwidth limitation of only a few per cent is practical. However, the much lower cost of manufacturing the hologram means that a range of holograms could be built to suit a given measurement campaign.

5.2.5 Reflector surface errors and panel gaps

In the introduction to Section 5.2 we have already indicated the issue of reflector surface errors that need to be kept to about 0.01λ . For millimetrewave CATR operation this becomes a significant issue, e.g. a 300 GHz CATR; this translates to a $10 \mu\text{m}$ surface accuracy. Such accuracy is expensive to achieve over a large reflector size, particularly if a single-offset configuration is conserved where the quiet zone is only about 30% of the main reflector diameter. At QML, a tri-reflector CATR has been developed (see Figure 5.22 [20]) that uses a 1.0 m diameter spherical main reflector with surface accuracy of $8 \mu\text{m}$ rms and achieves a quiet zone size of 0.7 m by the use of a dual shaped reflector feed system (sub-reflectors also with $8 \mu\text{m}$ surface accuracy). The spherical reflector can be used to exploit the symmetry and hence enable it to be machined on a lathe. For such large focal lengths, the difference between the sphere and the offset paraboloid is small and the

phase error can be corrected for within the design of the dual reflector feed system. Larger main reflectors are possible and one could conceive of a 1 THz CATR with $1.0\ \mu\text{m}$ surface accuracy and 8.2 m diameter main reflector. Such a reflector could be constructed using optical mirror technology, where currently the largest single mirror of useable diameter 8.2 m forms part of the Subaru Telescope located at the Mauna Kea Observatory on Hawaii (part of the National Astronomical Observatory of Japan). This reflector is made from ultra-low thermal expansion glass, is 20 cm thick and weighs 22.8 tons [31]. By using the same construction for such a mirror with 8.2 m diameter and $0.25\ \mu\text{m}$ rms surface accuracy (typical after fine grinding and prior to polishing) and metalising, the fine ground mirror surface would lead to a suitable CATR main reflector. This would enable a 5.7 m diameter quiet zone (based on 70% of the main reflector) when used with a dual reflector feed system.

High-precision panels to form an offset reflector have been used by QML to build a millimetrewave CATR in the early 1990s (see Figure 5.29) [32]. The panels used in the construction of this CATR reflector surface were developed by the Rutherford Appleton Laboratory (UK) for the James Clerk Maxwell Telescope (JCMT) based at the Mauna Kea Observatory on Hawaii. This is a millimetrewave radio-telescope with a 15 m diameter Cassegrain dual reflector antenna. The 5.4 m focal length primary surface consists of 276 lightweight aluminium panels arranged in 7 rings and the individual panels have average rms surface accuracies of about $15\ \mu\text{m}$. The high-precision sector-shaped panels are made using a stretch form process. A thin aluminium skin is stretched over a numerically machined former. A layer of aluminium honeycomb, pre-crushed onto the former and bonded to the facing skin, maintains the surface shape. A second honeycomb layer gives increased rigidity and beneficial thermal properties. The complete sandwich is

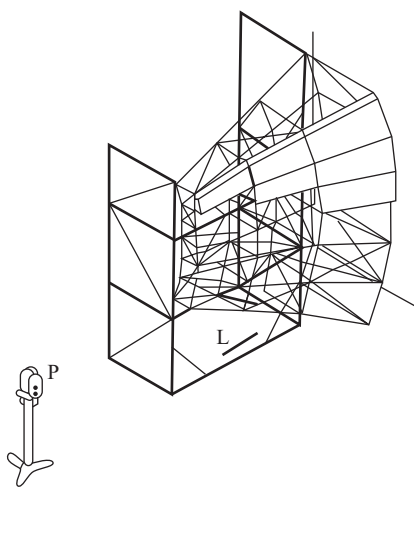


Figure 5.29 *QML panelled single-offset millimetrewave CATR [32]*

bonded together with epoxy adhesive. Each panel weighs about 6.8 kg and has dimensions of 1 m long and averages 0.5 m in width. The structure shown in Figure 5.29 is 3.0 m wide and between 2.0 m and 4.3 m high and made of 18 panels formed from the third, fourth and fifth rings of the telescope structure. To keep the overall height of the structure low, the plane of offset is horizontal with range boresight parallel to the ground and 3.0 m above it. The panels are supported on a space-frame backing structure with three-point mounting permitting panel adjustment via micrometer adjusters with 10 μm accuracy. The panels were aligned using a theodolite-based scheme, as shown in Figure 5.29, and achieved an estimated surface accuracy of 70 μm rms. The single-offset reflector enables a 3.0 m diameter projection on its surface leading to a 1.0 m diameter quiet zone based on the use of a simple corrugated horn feed.

In [33] the GO/UTD technique was employed to study the effects of inter-panel gap edge diffraction. The conclusions of this work were that at millimetrewaves gap edge diffraction can impair the CATR ‘quiet zone’ quality. When an antenna is tested in a panelled CATR with untreated gaps then spurious lobes are induced in its measured pattern. These lobes are centred at angles where the gaps are subtended by the AUT main beam. The severity of the gap-induced effects is determined primarily from the width of the gap and from the panel misalignment. The latter is the dominant factor when its magnitude exceeds the figure of $\lambda/60$ as demonstrated below. At 183 GHz, a typical measured value for the strength of the spurious lobes was found to be around -30 dB. To rectify this situation a thin metallic tape can be used to cover the gaps and an extensive analysis of the performance based on this solution was presented in [34].

Figure 5.30 shows the modelled effect of both a gap and a panel misalignment at 180 GHz, while Figure 5.31 shows the effect of 10 μm thick, 40 mm wide conducting metal tape on a perfect surface, with that for a tape covered gap with 60 μm panel misalignment, with and without tape pillowing. The effect on the measured radiation pattern of taped and untaped panel gaps can be seen in Figure 5.32, where a 226 mm diameter aperture Cassegrain antenna operating at 186 GHz was measured in the QML panelled CATR.

The degree of alignment between adjacent panels is very important. Under tape treatment a figure of panel edge misalignment of about $\lambda/60$ will result in spurious lobes with strength near to -50 dB for a measurement scenario similar to the one of Figure 5.32. The amount of tape pillowing is generally proportional to the width of the gap which the tape covers. Hence, panels manufactured accurately enough to allow for a gap width around 1 mm or smaller should be used, rather than the 2–3 mm used for the QML range. Experimentally spurious lobes with a level of around -45 dB have been observed when a 10 mm wide tape covered a 2 mm wide panel gap. This figure is about 7 dB higher than the value that would be expected as a result of scattering from its edges only. Tape deformation and panel edge misalignment are contributing to this discrepancy. Although conducting metal tape can be used, the quality of the continuity of the current flow across the gap is often unknown and would be an additional factor in any design. It is clear that the effect

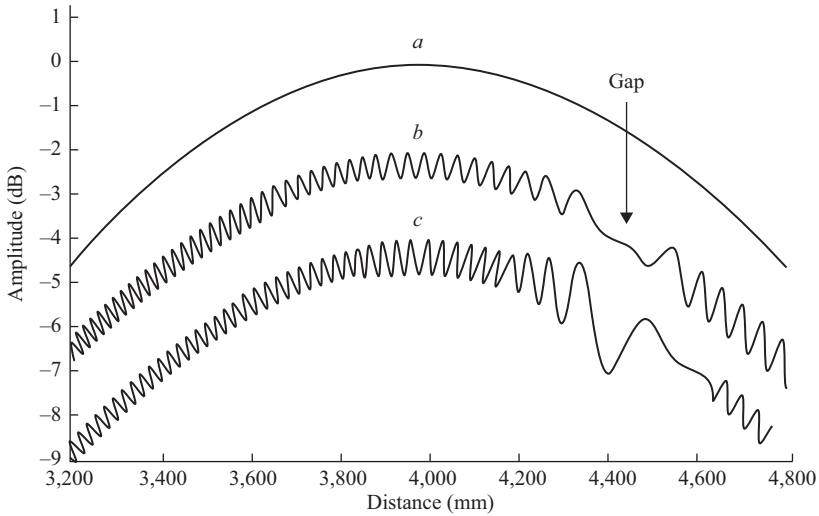


Figure 5.30 Quiet zone scan in a 2 panel CATR with and without panel misalignment at 180 GHz. *a* = reference case of perfect reflector; *b* = 3 mm gap width; *c* = 3 mm gap width plus 60 micron ρ error in panel alignment (for definition of ρ see Figure 5.4) [34]. Curves shifted for clarity

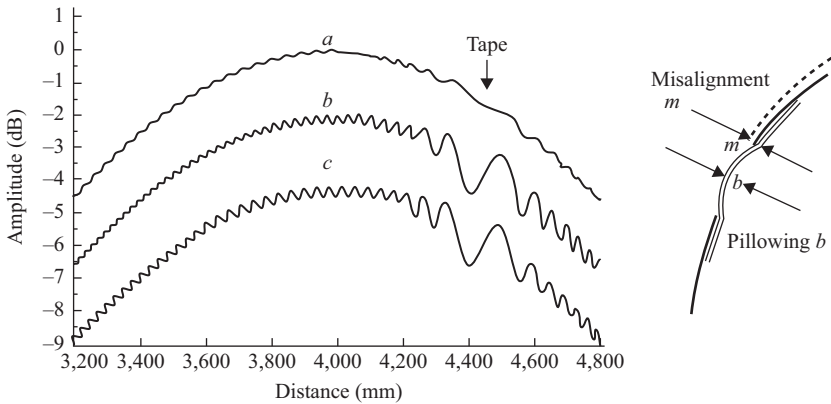


Figure 5.31 As Figure 5.30, with *a* = 10 micron thick 40 mm wide tape on a perfect surface, *b* = that for a tape covered gap with $m = 60 \mu\text{m}$ panel misalignment (see inset figure), *c* = as *b* but with tape pillowing of $b = 150 \mu\text{m}$ [34]

of the gaps can be mitigated but not removed by this technique, although the MARS technique (see Section 5.4.5.1) may offer a possible processing solution.

It should be noted that the panel gaps considered above are electrically large (in excess of 1 wavelength) and in the case where the panel gaps are fractions of a

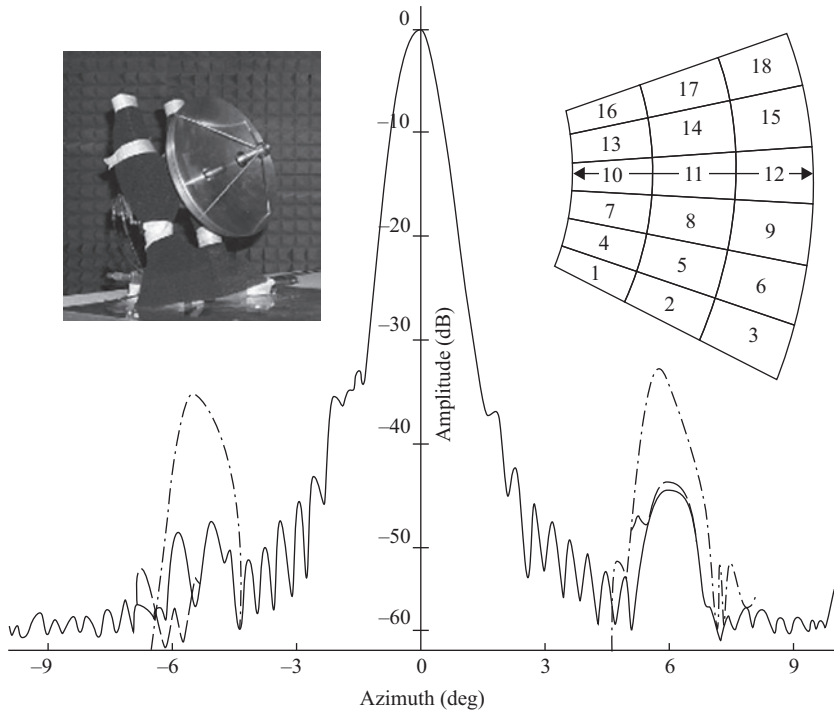


Figure 5.32 Radiation pattern of 226 mm diameter Cassegrain antenna (inset top left) in the panelled QML CATR (inset top right), with AUT aperture pointing at centre of panel 11. - - - - = measured with bare gaps; — = measured with taped gaps, = theoretical prediction with tape treatment [34]

wavelength the effect on the quiet zone and hence AUT measurement error is much reduced. In [35] the effect of panel gaps with dimensions less than 0.3λ was modelled as slot antennas and shows the polarisation sensitivity of the gaps. As an example the paper considers the Fort Hauachuca (Arizona) outdoor compact range shown in Figure 5.33, which has a 15 m test zone and panel gaps in the range 0.5–1 mm, and operates up to 40 GHz. The analysis indicated that the additional cross-polar amplitude ripple would be increased by about 0.3 dB peak-to-peak and the co-polar amplitude ripple was negligible.

5.2.6 Time-gating and the absorber-less chamber

It is clear from Figure 5.8 that many of the sources of quiet zone error result from signal paths that have clearly longer or shorter ray path lengths from the CATR feed to the quiet zone. This implies that a time-gating solution to managing the quiet zone ripple would be viable as illustrated in Figure 5.34, where a short pulse



Figure 5.33 Fort Huachuca (Arizona) outdoor panelled compact range (Courtesy of Ed Joy)

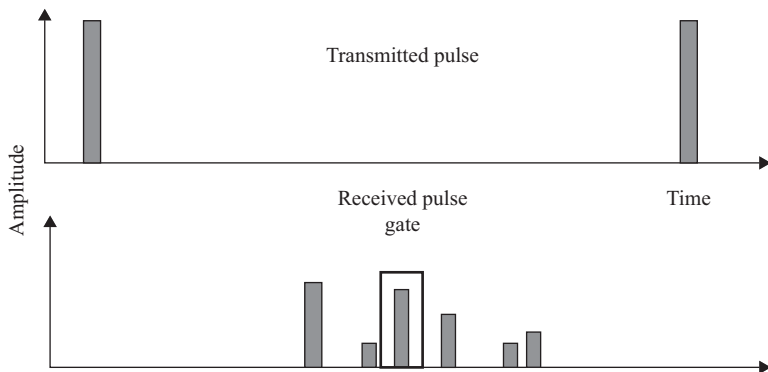


Figure 5.34 Time-gating in a CATR

is transmitted by the CATR feed and the desired direct path is identified and the other responses are time gated out.

There are essentially two approaches to time-gating, hardware time-gating and software time-gating. For software time-gating (often called pseudo time-gating), a

vector network analyser (VNA) sweeps across a wide range of frequencies for each antenna pattern point, a fast Fourier transform (FFT) is then applied to the frequency sweep (called the *frequency span*) and the time domain plot (as shown in Figure 5.34) is obtained. For most modern VNAs this is available as a hardware/software option with the FFT being undertaken in hardware to provide a near real-time time domain plot. A software gate can then be applied to the time domain plot (Figure 5.34) and the resulting gated response is then subject to an inverse FFT to recover the frequency domain response of the AUT from just the direct path. The effective ‘pulse width’ of such a system is approximately equal to $1/(\text{frequency span})$, and the maximum time span that this can achieve is then approximately equal to $1/\Delta f$, where $\Delta f = \text{frequency span}/(N - 1)$ and $N =$ the number of frequency samples taken across the frequency span (typically 101–10 001). So an 8–12 GHz sweep with 10 001 points would give a pulse width of 250 ps, Δf of 0.4 MHz and a maximum time span of 2.5 μs . The pulse width translates in free space to 75 mm in range distance, which is thus the smallest path difference that can be resolved. The maximum time span dictates the alias free range which translates in free space to a distance of 750 m. The user needs to be aware of the following issues:

- The AUT must have a bandwidth which supports the frequency span required. Should the AUT limit the bandwidth of the signal received/transmitted, the resulting frequency span will not permit the required time-gating.
- Windowing improves the dynamic range of the time domain measurement by modifying (filtering) the frequency domain data prior to conversion to the time domain to produce an impulse stimulus with lower side lobes.
- Gate shape controls the flatness, roll-off rate and side lobe level of the gate.

These and other issues can be found in a variety of texts, e.g. [36].

For hardware time-gating this can be achieved in one of two ways. Firstly, using a VNA and RF modulator switch controlled via VNA and external pulse generator (Figure 5.35). Gating is achieved usually at IF via internal gate switching, typically with a time resolution of 50 ps. Secondly, using a dedicated pulse radar system which could be reproduced to some extent by a pico-second pulse generator and digital sampling oscilloscope as in Figure 5.36. For this latter case a 50 ps pulse would cover the frequency range to 20 GHz ($1/\text{pulse width}$) with a typical pulse repetition frequency of 250 kHz (4 ms period). In [36] this concept has been taken to the extreme where antenna measurements were performed in a single-offset CATR with no absorber surrounding the system and no reflector edge treatment.

The offset reflector antenna of the CATR was a commercially available Ku-band direct-broadcast satellite antenna of diameter 165 cm with $F/D = 0.6$, and a WR90 open-waveguide antenna was used as a feed. The system achieved a quiet zone volume of about 55 cm with a magnitude taper of 1 dB and a quiet zone ripple of ± 0.5 dB and $\pm 5^\circ$ at 12 GHz. Using a 30 ps pulse the system was successfully used to measure a 60 cm diameter Ku-band antenna as well as a 25 cm diameter Ka-band antenna.

It is important to realise the full implications of time domain measurements and this is addressed in [37] in relation to the coherence time of the AUT. In receive

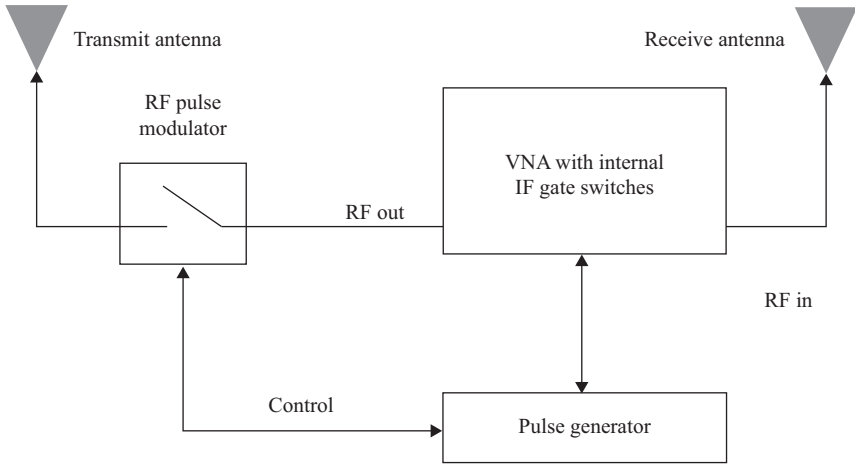


Figure 5.35 Hardware time-gating using VNA

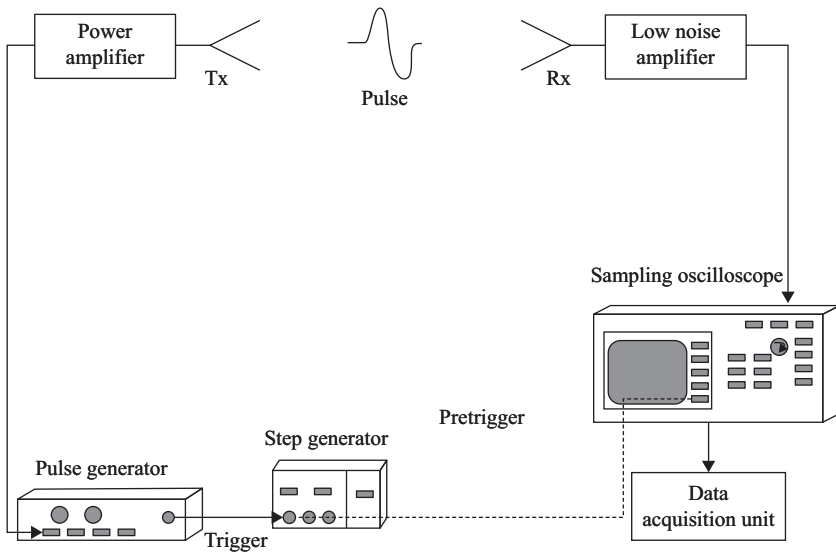


Figure 5.36 Hardware time-gating using a pico-second pulse generator and digital sampling scope

mode the radiation pattern of an antenna is essentially an interference pattern of the incoming plane waves incident on its aperture. This is illustrated in Figure 5.37, where in order to obtain a perfect radiation pattern, the coherent length of the receiving waves must be greater than or equal to the physical path length difference that is seen by the incident waves within the antenna structure. When a finite time

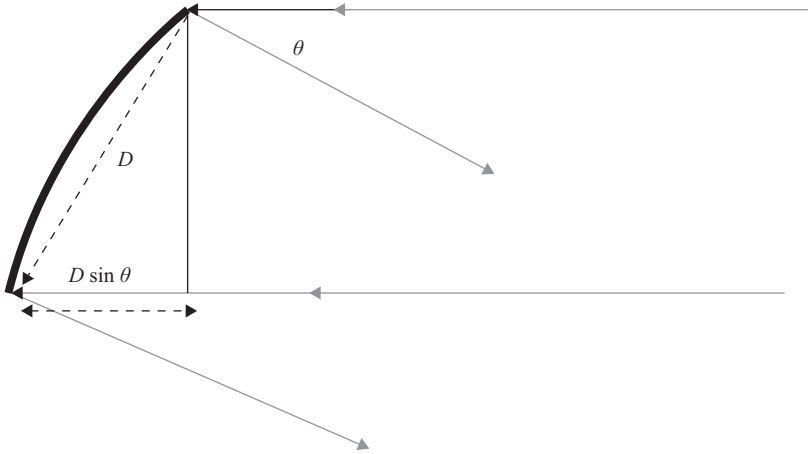


Figure 5.37 Coherence length in an AUT

pulse is imposed, it can be regarded as the coherence time of the incident plane waves, which means that when the corresponding coherent distance becomes less than the target physical path length difference within the AUT conventional CW interference no longer takes place and the resulting measured *pattern* is distorted. For the antenna of Figure 5.37 this occurs at a radiation pattern angle of θ_m for the time pulse of width Δt , where

$$\theta_m = \sin^{-1} \left(\frac{c\Delta t}{D} \right) \quad (5.2)$$

For pattern angles that exceed this value, the diffraction pattern of the antenna will be significantly distorted. This has been experimentally demonstrated for a 60 cm diameter reflector antenna fed with an open-ended waveguide [Figure 5.38(a)]. It is apparent that with a 1 ns gate there are large discrepancies between the time-gating pattern and the CW pattern, also the far-out side lobes from about 45° onwards are distorted significantly. As predicted, there is improvement when the gate width is increased to 2 ns. The pulse width was subsequently increased up to 4 ns and a measurement errors summary is shown in Figure 5.38(b), demonstrating the importance of careful pulse width in time domain antenna pattern measurement. It is important to note that this effect applies to hardware gating for the transmit pulse and for both hardware and pseudo time-gating for the choice of gate width. It is also a critical issue in RCS measurement and this is addressed in Section 5.6.4.

5.3 Types of ranges and their design issues

In the previous section a wide range of different CATR configurations have been described in order to achieve a collimated plane wave in a quiet zone region. In this section we will classify the various CATR configurations and comment on their

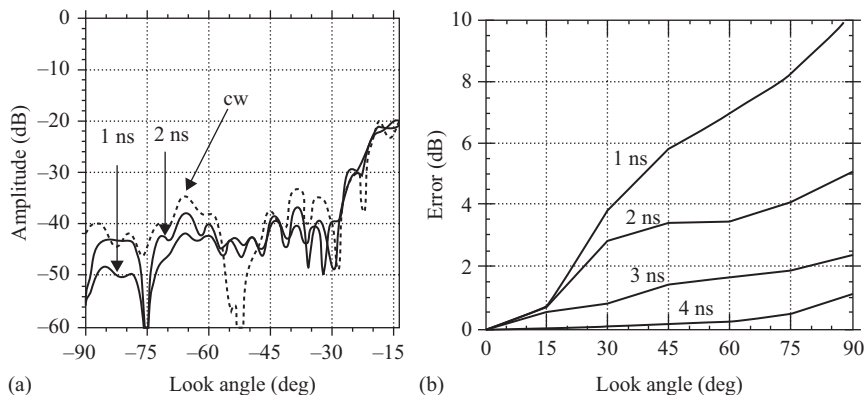


Figure 5.38 (a) Measured 60 cm diameter front fed reflector antenna at 9 GHz, (b) errors for different time pulses (or gate widths) for this antenna [38]

main design issues. We have limited the review to CATRs that have been practically implemented and reported in the open literature.

5.3.1 Single-offset reflector CATR

This is by far the most widely used CATR offering a simple low-cost solution. The main issue is that with a simple feed horn the edge taper and edge illumination level compromise results in a quiet zone that is approximately one third the diameter of the CATR reflector. In addition, because a single-offset reflector has inherent cross-polarisation in the offset plane, the cross-polar performance is likely to be at best -30 dB and that is only when a long focal length is used. Reflector edge treatment is vital and both serrations and blended rolled edges (e.g. Figure 5.20) have been successfully used. It has also been demonstrated that CATR operation without edge treatment can be achieved using a commercial communications offset antenna along with a time domain gated approach [37].

5.3.2 Dual cylindrical reflector CATR

In this approach the issue of manufacturing large reflector antennas with high surface accuracy of at least $\lambda/50$ and ideally $\lambda/100$ (to give the desired $\pm 5^\circ$ quiet zone performance at high frequency) is approached by constructing a pair of cylindrical antennas that provide collimation first in the horizontal plane and then in the vertical plane, as shown in Figure 5.39. Using such an approach exploits the fact that it is easier to make highly accurate reflector surface when there is just one plane of curvature.

5.3.3 Dual shaped reflector CATR

Here both reflector surfaces are shaped which offers the following advantages:

- Low differential path loss when using large focal lengths.

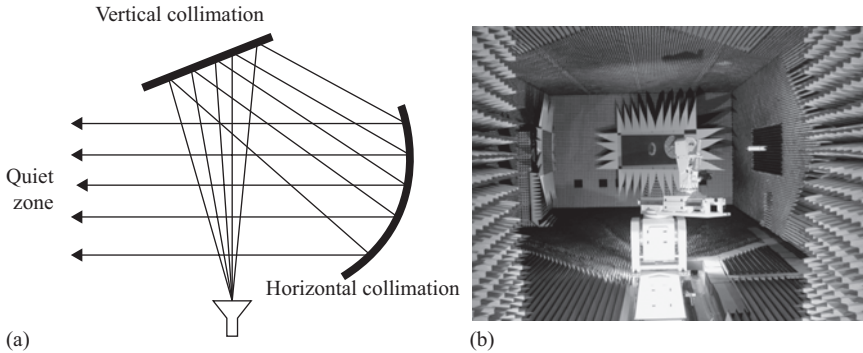


Figure 5.39 (a) Dual cylindrical CATR ray diagram, (b) dual cylindrical CATR (Courtesy of SELEX ES)

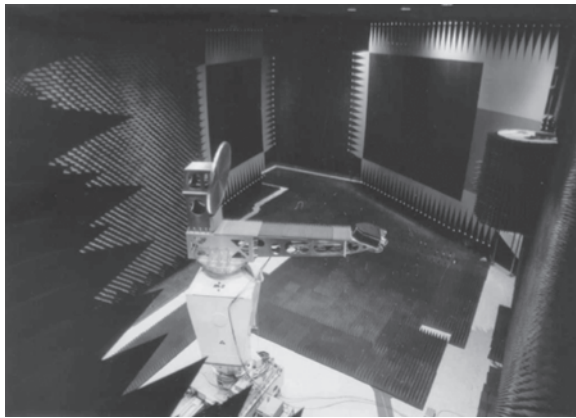


Figure 5.40 Dual shaped CATR at Airbus Defence and Space offering a $5\text{ m} \times 8\text{ m}$ quiet zone at 1.5 GHz to 500 GHz. Reflector surface accuracy = 20 microns. Copyright 2003, Airbus Defence and Space

- Zero cross-polarisation from the reflectors when the Mizugutch condition is used (here the cross-polar from one reflector cancels that from the second reflector). The only cross-polarisation comes from the feed and diffraction effects.
- Reduced edge effects due to shaping.

Because of the excellent cross-polar performance (typically < -40 dB peak in the quiet zone), such systems are often employed to measure space craft antennas, and an example is shown in Figure 5.40 [39]. To achieve such a performance an optimised range feed with < -50 dB cross-polarisation in the field of view is required (see Figure 5.41).

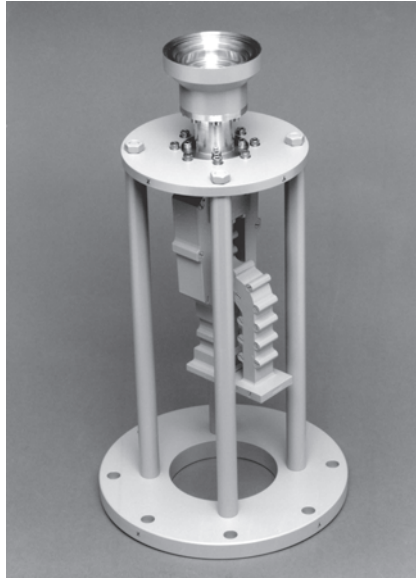


Figure 5.41 Feed system from Airbus Defence and Space CATR system shown in Figure 5.37. Copyright 2000, Airbus Defence and Space

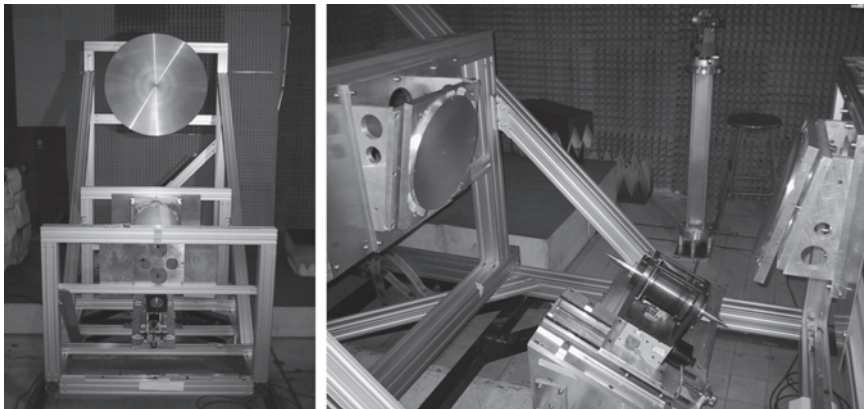


Figure 5.42 Tri-reflector CATR for operation up to 350 GHz with 1 m diameter spherical main reflector and 700 mm diameter quiet zone

5.3.4 Tri-reflector CATR

This system employs a dual reflector quasi-optical feed system to provide a shaped illumination on the main reflector for millimetrewave operation (see Section 5.2.1.3). The system developed at Queen Mary University of London is shown in Figure 5.42.

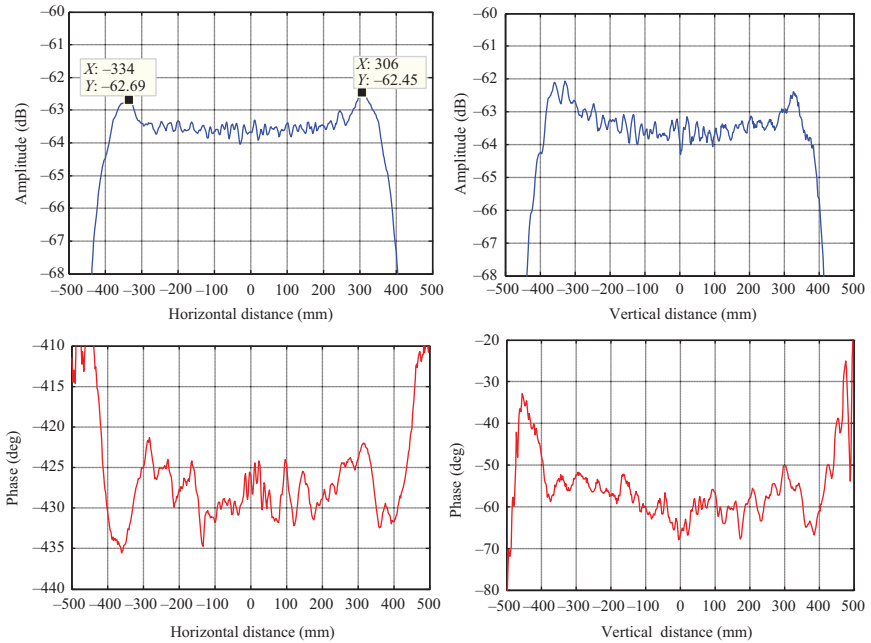


Figure 5.43 173-GHz tri-reflector CATR measured QZ: left, horizontal; right, vertical; top, amplitude; bottom, phase

This uses a spherical 1 m diameter main reflector with 8 μm surface accuracy and a pair of 350 mm diameter shaped sub-reflectors also with 8 μm surface accuracy.

Measured QZ transverse scans of amplitude and phase for an identical system are shown in Figures 5.43 and 5.44 at frequencies of 173 and 285 GHz, respectively.

5.3.5 Hologram CATR

This technique has been described in Section 5.2.4 and the system used at 322 GHz at Helsinki University of Technology is shown in Figure 5.45.

5.3.6 Lens CATR

These are reviewed in Section 5.2.3 but although several lens CATR designs have been reported in recent years [40], none to our knowledge have been implemented and reported in the open literature.

5.4 Quiet zones and performance evaluation

The use of the uniformity of the quiet zone in determining the maximum size of test antenna that can be measured in a given CATR has been the accepted method since

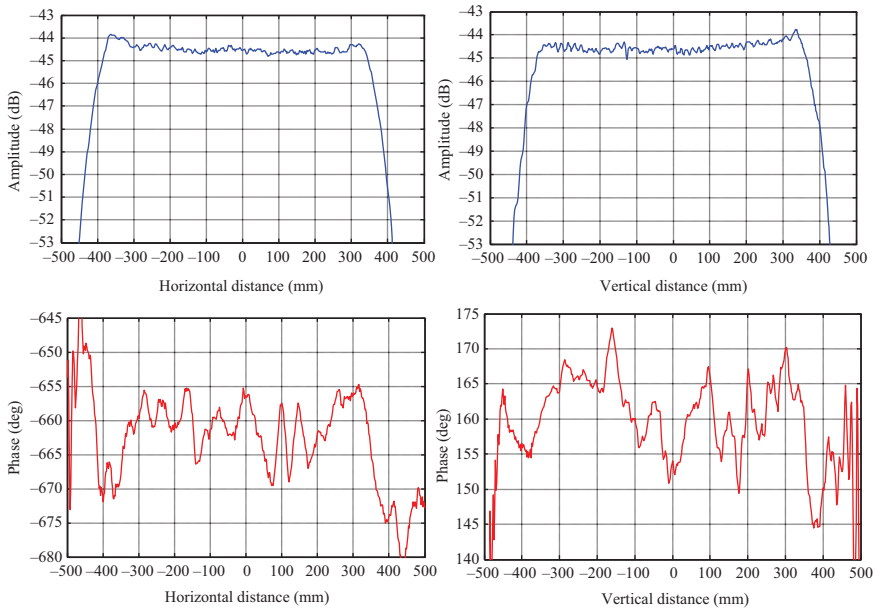


Figure 5.44 285-GHz-tri-reflector CATR measured QZ: left, horizontal; right, vertical; top, amplitude; bottom, phase

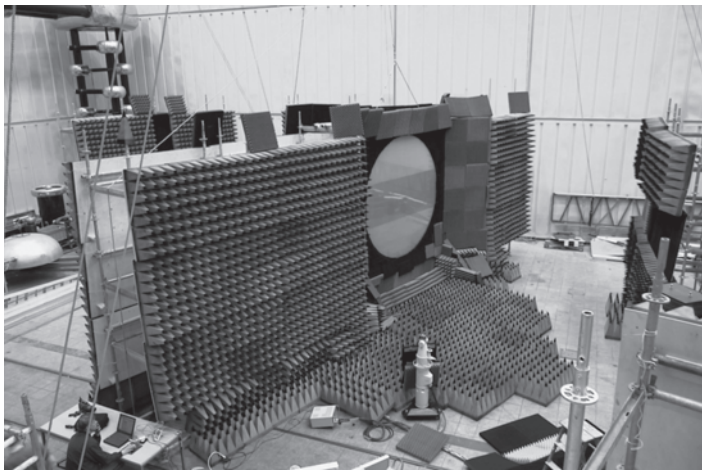


Figure 5.45 Hologram CATR for operation at 322 GHz using a 3 m diameter hologram, MilliLab, Radio Laboratory, Helsinki University of Technology [28]

its inception. The definition of a quiet zone as one having ripple less than ± 0.5 dB in amplitude and $\pm 5^\circ$ in phase has become a near universal standard. In Section 5.4.1, we take a critical look at this ‘measure of quality’ by understanding exactly how a CATR works by using a full 3D simulation of the antenna pattern-measurement process. In subsequent sections we look at the various ways in which the quiet zone ripple of a CATR facility can be evaluated. Finally we look at ways in which a given pattern measurement can be improved by such techniques as multiple scans and post-processing.

5.4.1 *How does a CATR actually work?*

In general, a user of a CATR is primarily interested in the accuracy to which the radiation pattern of a given antenna can be measured in a given facility. Such questions as ‘what is the error bound on the sixth side lobe?’ are often posed. Specifying the quiet zone ripple does not answer this, but an answer is possible using simulated pattern measurements by employing a realistic CATR model. In this section we attempt to answer these questions as well as understand how a CATR operates by using a full 3D analysis of the electromagnetic coupling between the CATR antenna and the AUT. Such a simulation can be used for the purpose of studying the impact of the various operating parameters, optimising existing facilities or comparing candidate CATR configurations in terms of the pattern measurement accuracy offered.

The CATR is essentially a ‘plane wave synthesiser’, so coupling between the CATR and the AUT can be best expressed in terms of the plane wave spectra (PWS) of the transmitting (T) CATR and the receiving (R) test antenna. Candidate test antennas are assumed to be either focused apertures or at least ones where their pattern possesses an identifiable ‘limited-size’ main beam. Thus the bulk of the transmitted energy, or the peak sensitivity in the receiving case, is taking place over a limited-size angular region. For the CATR, such an assumption is automatically satisfied due to the very nature of the collimation process. In its most general form the coupling equation expresses the power transfer between a transmitter and a receiver, the domain of integration spanning the whole spectral space which is computationally difficult. However, a considerable restriction of this angular domain can be achieved by invoking the following arguments:

1. The first sub-domain to be included is a spectral region S1 over which the bulk of the transmitted energy is taking place. For a focused aperture this region can be identified as the spectral space occupied by the main beam of the transmitter PWS plus perhaps a small number of adjacent side lobes.
2. The second sub-domain to be included is a region S2 over which the peak receiver sensitivity occurs. For a focused aperture this region is simply the spectral space around the main beam of the receiver PWS plus again a small number of adjacent side lobes.
3. The third sub-domain that should be included is a region S3 around the stationary points of the Green’s function associated with the physical separation

between CATR and test antenna. This is essential since the exponential factor affects directly the way that the transmitted energy is distributed in space. The behaviour of this term becomes the dominant factor that determines the coupling as the separation distance between receiver and transmitter approaches, or exceeds, the Rayleigh value.

The coupling integral can then be efficiently evaluated numerically about these three regions. The PWS involved in the coupling calculation can be directly derived from the far-field patterns, if these are available. Alternatively they can be found through Fourier transformation from aperture fields. Full details of the analysis process can be found in [41], and here it is used to first give an understanding of CATR operation and then to understand what drives the measurement error process for a given size of AUT in a given CATR.

The specific CATR configurations which will be used here are the circular aperture (of diameter 3 m) with straight or serrated rim and the sector-shaped rim used in the QML CATR of Figure 5.29. The PWS of the CATR collimator, required for the coupling calculations, are derived through the Fourier transformation of the tangential electric field which exists on a planar aperture $4\text{ m} \times 4\text{ m}$ in size placed at the position $z = 1.6\text{ m}$. These fields have been calculated with the PO method. A sampling interval of $\lambda/2$ was used with the test antenna being placed at $z = 6\text{ m}$ and set to face the centre of the collimator aperture. The AUTs are taken as circular apertures having a Taylor distribution, as it is possible to control the strength of a prescribed number of almost equi-level side lobes that are adjacent to the main beam. It was found that if the coupling integral sub-domains (S1 to S3) were given the appropriate size so as to accommodate the AUT main beam plus two near-in side lobes, then the RMS error was of the order of -60 dB .

For an AUT diameter of 1 m, the co-polar pattern for a circular aperture CATR with edge taper (ET) = -7 dB is shown in Figure 5.46. From the error curve, it is obvious that a spurious lobe is formed at the angle where the test antenna 'looks' at the CATR edges. The value of the induced error is about -30 dB , and in this case has caused an error of 5 dB in the side lobes of the measured pattern but the beamwidth of the test antenna is not affected. If the value of the CATR edge taper is decreased to -1 dB , the only noticeable effect is a proportional increase in the value of the error peak to -24 dB . This behaviour shows that, with a relatively small test antenna, the CATR measurement is predominantly edge-diffraction limited.

Pattern measurements and quiet zone measurements have a distinct difference in the way in which edge diffraction is presented. During quiet zone measurements, the field is measured in such a way that all (or nearly all, depending on the probe gain) possible diffraction sources contribute to the value of the field at a given point. During pattern measurements, on the other hand, only the diffraction sources 'looked at' by the test antenna are contributing to the induced error at a given angle. The ability of the test antenna to discriminate (filter) between the various diffraction sources means that the error induced on the pattern measurement is weaker than that suggested from quiet zone measurements.

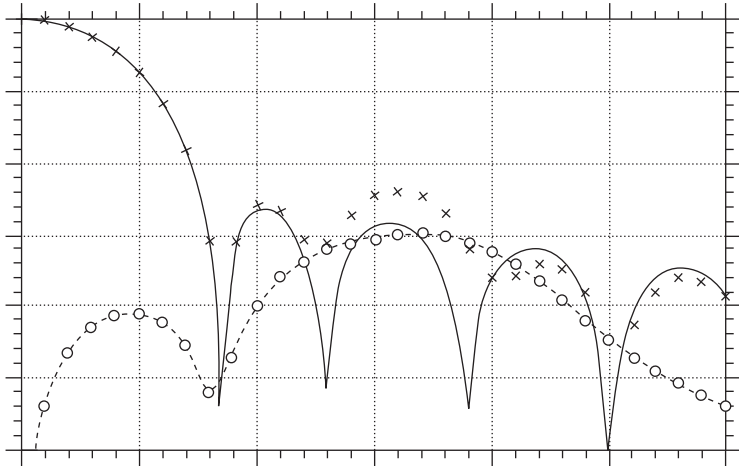


Figure 5.46 Simulated measurement of an 1 m diameter AUT in a 3 m single-offset circular rim CATR with straight rim. Frequency 3 GHz, CATR edge taper = -7 dB. — = ideal pattern, $\times \times \times \times$ = 'measured' pattern, error pattern shown as $--o--o$

The distribution of the diffraction-induced spurious lobe is affected by the size of the AUT. The creation of an error due to edge diffraction is made clear by the situation depicted in Figure 5.47, where the AUT is transmitting. The bulk of the energy leaving the AUT will be mainly confined along a tubular beam with an increasingly large cross-section with distance. Fundamental Gaussian-beam-mode (GBM) theory [43] is particularly successful in giving a simple, yet realistic, picture of how the transmitted energy is travelling at close and intermediate distances away from the test antenna. If this beam illuminates the edge E of the CATR (Figure 5.47), then strong edge diffraction will be generated with a wide angular distribution and so a diffracted field component will reach the CATR feed leading to the introduction of a diffraction-induced error in the pattern. For a fixed transmit power, the field strength of the point in the GBM impinging on the CATR reflector edge will be inversely proportional to the test-antenna diameter. From UTD analysis, the strength of the edge diffraction is directly proportional to the field strength of the particular ray intercepting the edge. When an antenna with an increasing size is tested in a CATR, the edge-related spurious lobe induced will decrease in peak strength but will distribute more widely in the measured pattern. This is demonstrated in Figure 5.48, where a simulated-pattern measurement of a test antenna with 1.5 m diameter and Taylor distribution is shown. Comparison with Figure 5.46 shows that the spurious-lobe beamwidth, defined by e^{-1} points, is $\Delta\theta = 6.1^\circ$ if the AUT diameter is 1 m, and $\Delta\theta = 8.1^\circ$ if the AUT diameter is 1.5 m.

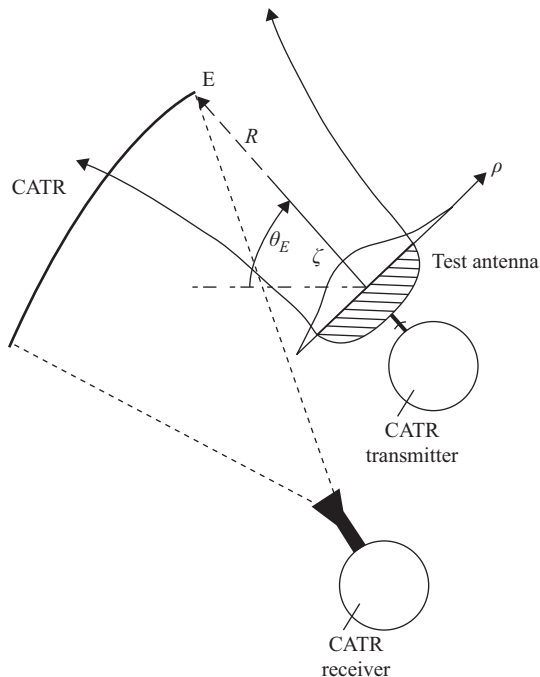


Figure 5.47 CATR edge illumination considered in the reciprocal mode of operation

To confirm the validity of the simulated-pattern-measurement process, a GBM analysis of the situation depicted in Figure 5.46 was performed which yielded values of $\Delta\theta = 6.5^\circ$ and $\Delta\theta = 8.5^\circ$ respectively. Considerable agreement is observed between the values derived, giving confidence in the simulation process.

Where the AUT diameter was 1.0 m, a decrease in the absolute value of the CATR edge taper resulted in a universal increase of the error induced. For a 1.5 m aperture test antenna (Figures 5.48 and 5.49), the error induced in some parts of the pattern (above 8° , approximately) does indeed increase for $ET = -1.0$ dB, but at lower angles the error decreases. Around boresight, an increase in the beamwidth and a decrease in the level of the near-in side lobes is seen when $ET = -7$ dB. This behaviour suggests that the prime source of error is the amplitude taper of the CATR GO field. For $ET = -7$ dB, the projection of the CATR GO taper onto the AUT aperture means that, as it is rotated, increasingly larger portions of its aperture are falling inside the more uniform parts of the field and hence the effects due to the GO-amplitude taper are minimised. It is clear from the simulated measurement of the 1.5 m diameter AUT that its boresight characteristics are affected by the GO-amplitude taper, while at larger angles the pattern is affected primarily by edge diffraction.

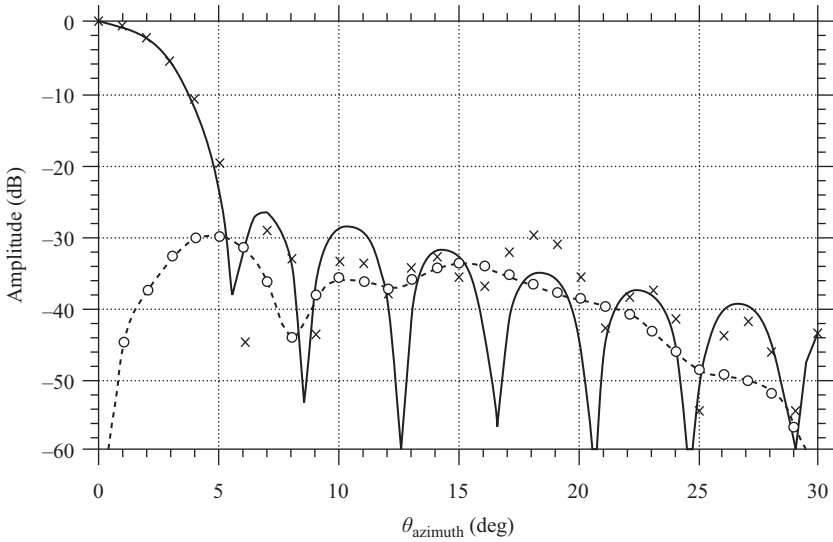


Figure 5.48 Simulated measurement of a 1.5 m diameter AUT in a 3 m single-offset CATR with straight rim at 3 GHz and $ET = -7$ dB. _____ = ideal pattern; $\times \times \times \times$ = simulated measurement; $\circ \circ \circ \circ$ = error pattern

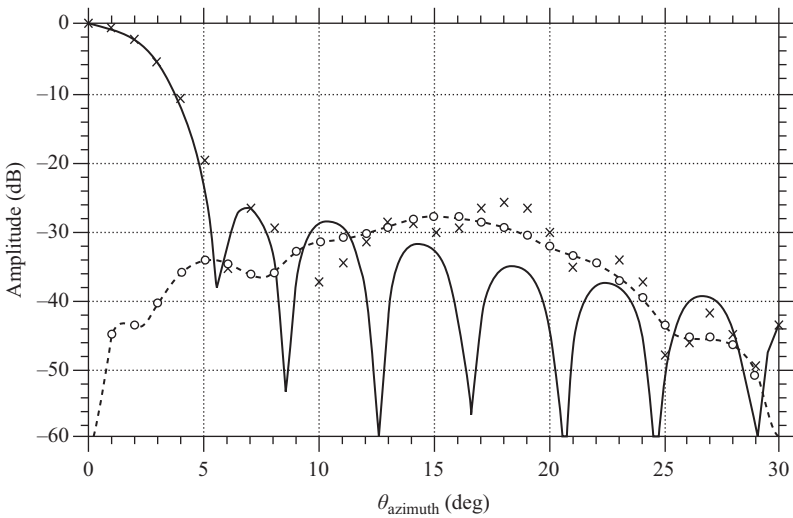


Figure 5.49 Simulated measurement of a 1.5 m diameter AUT in a circular rim 3 m single-offset CATR with straight rim at 3 GHz and $ET = -1$ dB. _____ = ideal pattern; $\times \times \times \times$ = simulated measurement; $\circ \circ \circ \circ$ = error pattern

In Section 5.2.1.1 it has been demonstrated that there is an equivalence in quiet zone quality between a straight-rim CATR with $ET = -7$ dB and a serrated-rim CATR with $ET = -1.0$ dB. This is confirmed by pattern simulation of a 1 m diameter AUT when the co-polar pattern error is plotted for the two cases (Figure 5.50). It is also evident that in both cases the error due to the CATR GO-amplitude taper, expected near boresight, is very small. The extended flatness of the error curve in the serrated-rim example shows that the improvement offered is achieved by the dispersion of the edge-diffracted energy over a wider angular domain. Moreover, this dispersion mechanism suggests that it is likely that the mainbeam region will be more in error than for the example of a straight-rim CATR. Hence, the suggestion that the serrated-rim CATR offers superior performance based on the quiet zone field performance is not founded for small AUT when a pattern simulation is performed. This clearly demonstrates the importance of using the pattern-simulation process in assessing CATR performance.

When an antenna with diameter of 1.5 m (half the CATR size) is tested in a straight-rim CATR with -7 dB edge taper, the measurement errors are primarily attributed to the GO-field non-uniformity. The example of the simulated pattern error measured in the serrated rim CATR is compared in Figure 5.51. As a result of the small illumination taper used in the serrated-rim example, the AUT boresight characteristics are reproduced with better accuracy than where a straight-rim CATR is used. There is now a clear advantage of using a serrated-rim CATR when large antennas are tested. The peak error for the serrated-rim CATR has a level

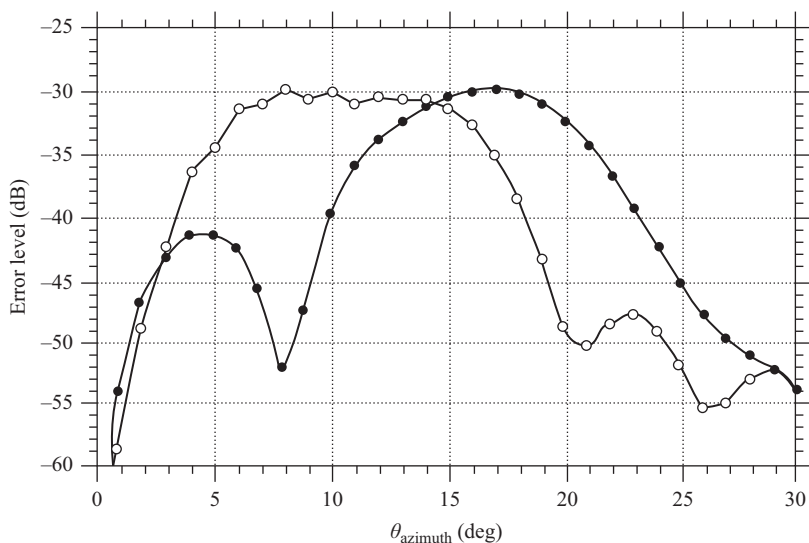


Figure 5.50 Comparison of simulated co-polar pattern measurement error for straight and serrated-rim CATR for 1 m AUT. ● = straight rim $ET = -7$ dB; ○ = serrated rim $ET = -1$ dB

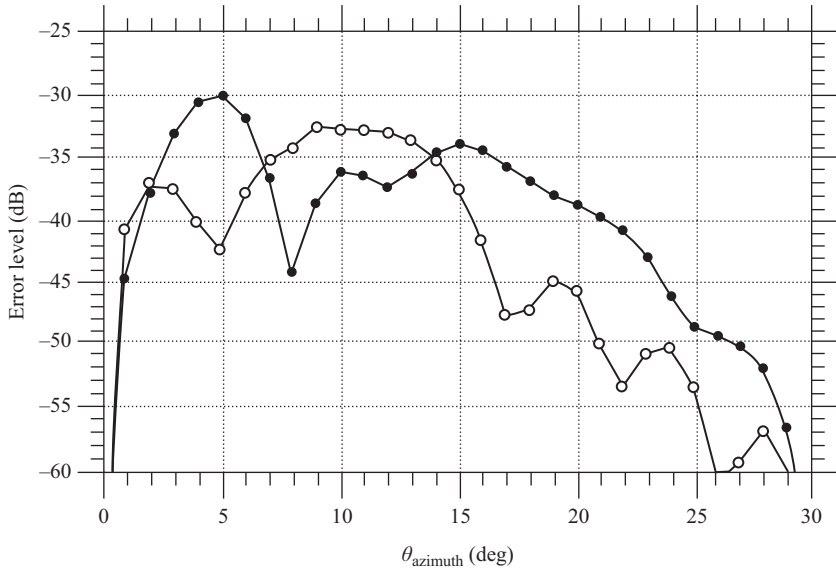


Figure 5.51 Comparison of simulated co-polar pattern measurement error for straight- and serrated-rim CATR for 1.5 m AUT. ● = straight rim $ET = -7$ dB; ○ = serrated rim $ET = -1$ dB

dominated by edge diffraction and it can be seen (Figure 5.51) that the value of this peak error is almost equal to the error due to edge diffraction in the straight-rim example. In conclusion, the advantage of serrated-rim CATRs over the straight-rim implementations is not that there is somehow the potential of an improved edge-diffraction suppression, but rather that, whatever level is achieved, it is not made at the expense of the general GO-field uniformity. Thus larger antennas can be measured in a serrated-rim CATR.

Two-dimensional modelling of the coupling integral can also be performed offering a computationally rapid evaluation of performance; it cannot, of course, handle the two polarisations which are present simultaneously in a realistic test antenna. It has been demonstrated [44] that, when the CATR rim is irregular, the quiet zone characteristics cannot be represented accurately from a simple 2D model under similar prime illumination characteristics. The same is to be expected for pattern measurements. However, when the rim has a regular shape, or when an equivalent prime illumination can be derived, the two-dimensional model can provide useful information in a simple and fast way. To verify the two-dimensional approach, the pattern measurement error between the 3D and the 2D models was compared for the example of the QML CATR (Figure 5.52). For the 3D model the QML CATR was considered during azimuth-pattern-cut measurements. In the 2D model, the plan view of this facility (i.e. a simple offset paraboloid) was used. The strong edge illumination and the low frequency (3 GHz) of operation provide a good test concerning the capabilities of the 2D method to predict the diffraction

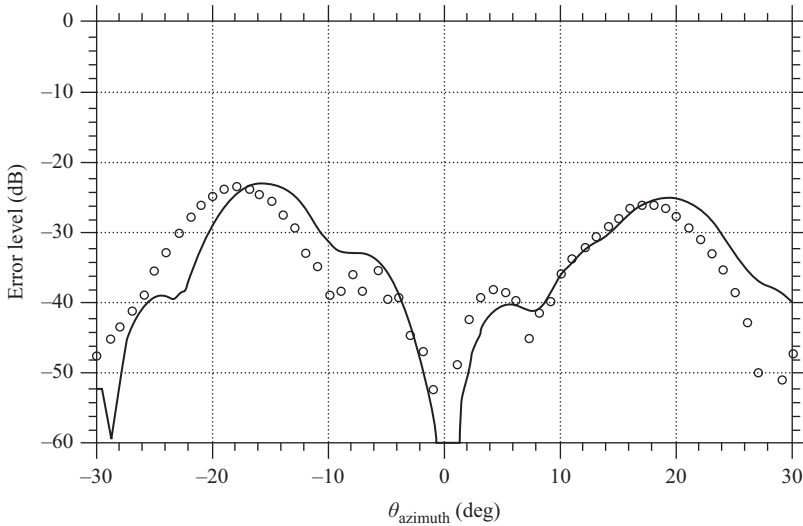


Figure 5.52 Comparison between two- and three-dimensional pattern-measurement error predictions for the QML CATR at 3 GHz with $ET = -1$ dB. _____ = 2D; ○○○ = 3D

effects accurately. Close agreement is observed between the two error patterns, giving confidence in the 2D calculations as a method of providing the correct magnitude for the measurement error and its general trends.

The computational speed of the 2D simulation of CATR pattern measurements allows the exhaustive performance testing of any facility which is amenable to a 2D modelling process. As an example, a 2D facility derived from the QML CATR of Figure 5.29 was studied in this way. The induced pattern error is a combined result of edge diffraction and the amplitude taper introduced by the prime illumination characteristics of the CATR. The ‘ripple’ specification of the quiet zone cannot discriminate between these error sources, but during pattern measurements they do appear in distinct ways. The relative significance of these error mechanisms is determined by two factors: the illumination characteristics of the feed and the relative size of the AUT. By considering AUTs with a size varying from 0.5 m to 1.5 m operating in a 2D model of the QML CATR, the change in pattern-error distribution was studied. Since diffraction effects will be worse at the lowest frequency of operation, a value of 6 GHz (the facility’s lowest operating frequency) was used. The AUT aperture distribution was a cosine on a pedestal, with edge illumination of -10 dB, placed at $z = 6$ m ($= 2D_{CATR}$), and facing the centre of the collimator’s projected aperture. The patterns resulting from the simulation showed that, for AUTs below a D_{AUT}/D_{CATR} of $1/3$, edge diffraction was clearly the dominant factor. Increasing the illumination taper improved the quality of the pattern measurement. As the size of the AUT is increased, the emphasis gradually shifts towards errors due to the amplitude taper, while at the same time the room for

compromise between the two types of error decreases. For the largest D_{AUT}/D_{CATR} studied (1/2), there was almost an equal amount of increase in boresight errors (GO-taper induced) for a corresponding decrease in the errors due to edge diffraction.

The detailed distribution of the induced error is dependent on the intrinsic characteristics of the AUT, and in [41] this was studied for a given diameter AUT with different aperture distributions. There was considerable similarity in the general trends of the error distribution between the different AUT aperture distributions, with the peak level being largely independent of the test-antenna type. This is an important result, since the pattern-error function obtained under simulation with, for example, the Taylor aperture distribution is applicable to a wide range of other AUT aperture distributions which could be generally classed as those that produce a focused beam. Thus realistic CATR pattern-error estimation can be made without the need to consider each individual test antenna's aperture distribution. It therefore is possible, for a given CATR, to produce measured pattern-error curves as shown in Figure 5.53 for the QML CATR of Figure 5.29. Here the pattern measurement error is represented by two indicators: the peak error and the RMS error calculated over the $\pm 50^\circ$ angular range. These error indicators are presented as functions of the electrical size of the CATR, the relative size of the AUT, and the CATR edge taper. An AUT located at $z = 2D_{CATR}$, with uniform illumination, has been used to produce these results. These curves can be used as a powerful aid in the design of a single-offset reflector CATR.

The definition of the acceptable performance for a CATR is directly related to the amount of error we are prepared to tolerate. The adoption of envelope curves restricting the allowable error strength and distribution is a very appropriate way to define the CATR performance. The standard procedure of adopting the ± 0.5 dB and $\pm 5^\circ$ ripple in the uniformity of the quiet zone as an acceptable performance is clearly an indirect measure of range performance, and so too conservative, underestimating the accuracy that a given CATR can achieve. However, let us try to interpret this allowable ripple in terms of an acceptable measurement error. If we make the simplistic (2D) assumption that the ± 0.5 dB ripple in the quiet zone is a consequence of the interference between a desired uniform plane wave front plus two spurious plane waves coming from the direction of the CATR edges, then the peak error pattern allowed would correspond to two edge sources of about -31 dB. Returning to the pattern-simulation results, if we require that the -31 dB target should be met for antennas having a D_{AUT}/D_{CATR} of at least 1/3, then the lower frequency limit of the CATR operation can be identified. With this definition in mind, it has been found that the electrical size of the collimator should be about 40λ in order that an appropriate selection of edge illumination can bring the peak error to the acceptable value. For the QML CATR example, this would require an edge taper of -15 dB, a value difficult to meet with a simple compact feed. Taking this into consideration, a more realistic value should be over 50λ , where the requirements for edge illumination would now be met with a smaller value of edge taper in the range between -8 dB and -10 dB.

The power of the pattern-simulation method can be illustrated in the following example. For the QML CATR operating at 6 GHz (60λ diameter collimator) [44],

the ripple over the zone spanning 30λ ($D_{AUT}/D_{CATR} = 0.5$) is 2.5 dB and $\pm 5^\circ$, which would lead one to expect that pattern errors would be unacceptably high, based on the ± 0.5 dB and $\pm 5^\circ$ ripple criterion. However, we see that pattern simulation (Figure 5.53) demonstrates that the peak pattern error would be -30 dB and the RMS error would be below -40 dB when a CATR edge taper of -8 dB was employed. In many cases this level of error would be acceptable, indicating that antennas with D_{AUT}/D_{CATR} larger than $1/3$ can be measured successfully. For a CATR using a single-feed-per-frequency band, an optimum selection of its illumination characteristics will result in an error with a peak value balanced among the different sizes of the candidate test antennas. From Figure 5.53 we can see that, for a collimator with a size of 60λ , the optimum feed will produce an edge taper of -8 dB. Similar curves to Figure 5.53, calculated at higher frequencies, showed that the balance shifts towards smaller values of edge taper, -4 dB being about optimum for the QML CATR operating at 18 GHz.

In summary, the accuracy of an AUT radiation pattern measured in a single-offset-reflector CATR is limited by two factors: the edge diffraction, which usually manifests as a fast-changing ripple in the quiet zone, and the amplitude taper imposed by the feed. Diffraction from the CATR edges affects the pattern region which corresponds to angles where the test-antenna main beam is directed towards them. Both co-polar and cross-polar patterns are likely to be affected by the edge diffraction. Amplitude taper, on the other hand, affects mostly the boresight region of the AUT pattern. Direct effects of the amplitude taper are the broadening of the main beam and a level decrease for the boresight side lobes. The power of the pattern measurement simulation process is that it permits the error in the measured pattern to be quantified, so extending the size and decreasing the frequency of test antennas which can be measured with quantifiable accuracy by a given CATR facility. Although we have concentrated on the single-offset CATR, the method can be extended to simulate other CATR configurations.

In Chapter 13 (Section 13.2), we consider more extensively both the modelling of a CATR quiet zone (QZ) and the end-to-end simulation of the CATR measurement process. This chapter compares five different modelling methods for the CATR quiet zone and concludes that the 'Current Element' or 'Physical Optics' approaches offer the best agreement. In Section 13.2, we describe the mathematics of each of the five modelling methods considered and from this the reader could then write software to analyse their own CATR QZ. Alternatively, commercial reflector antenna software packages such as GRASP [45] or FEKO can undertake the QZ modelling process. Such modelling enables QZ volume to be determined as well as effects such as feed spill-over. Modern computing facilities mean that these 3D modelling techniques are now completely viable on a modest desk-top computer. Indeed, in Section 13.2.9, we demonstrate the viability of full end-to-end simulation of the CATR measurement process using the reaction theorem, enabling full-sphere simulated measured data for a given CATR AUT combination. In Section 13.2.10, we demonstrate that we can employ this method to create a 'perfect' CATR QZ and then investigate the effects on a 'measured' AUT of: QZ amplitude taper, QZ amplitude and phase ripple, effect of the spatial frequency of

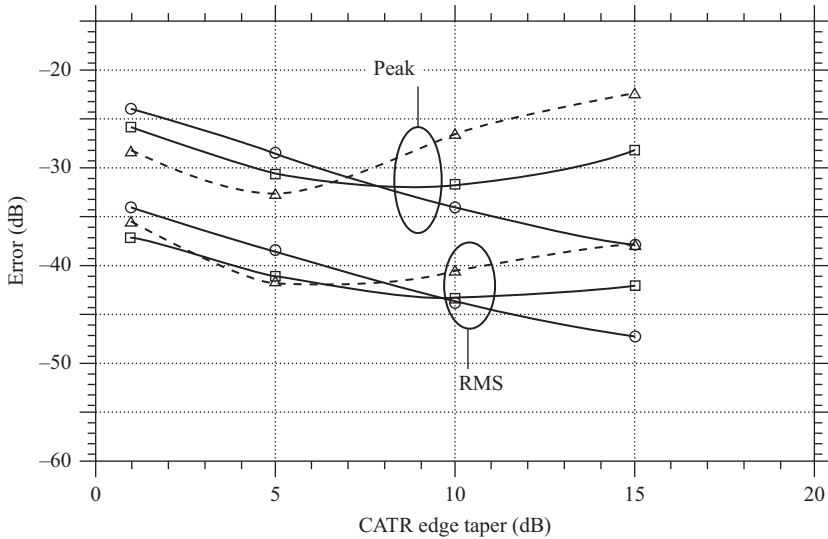


Figure 5.53 Predicted radiation-pattern-error curves for the QML CATR as a function of edge taper. CATR diameter = 60λ (6 GHz). $\circ = D_{AUT}/D_{CATR} = 1/6$; $\square = D_{AUT}/D_{CATR} = 1/3$; $\Delta = D_{AUT}/D_{CATR} = 1/2$

the QZ ripple, and AUT position within the QZ volume. Indeed, we are able to demonstrate that, for the case where we have a 1 dB amplitude taper, 1 dB amplitude ripple and 10° phase ripple in the QZ, this has the effect on a AUT -20 dB side lobe that approximates to a ± 1 dB error value, which is the accepted rule of thumb that is often stated (and never derived from theory) that originates from what one typically sees in practice.

Although we make a strong case here for pattern simulation, quiet zone ripple has been shown to be a conservative choice in fixing the performance envelope of a given CATR facility, and is very much the industry standard. In Section 5.4.2 we consider ways in which the quiet zone ripple can be measured, as to date this remains the universal performance criterion.

5.4.2 Measurement of the quiet zone by field probing

This is the standard method of evaluating the quiet zone for a compact range. Here some form of transverse field scanner, which could be a planar scanner or a plane-polar scanner, is used to measure the amplitude and phase of the quiet zone as a function of transverse position. Planar scanners used for near-field scanning are ideal for purpose [Figure 5.54(a)]; however, for larger ranges a plane-polar approach is often preferred [see Figure 5.54(b)]. The probe antenna needs to be electrically small and have a radiation pattern that predominantly looks in the forward hemisphere. An open-ended waveguide is often used (see Figure 5.55), where the probe assembly can be seen to consist of a chamfered rectangular

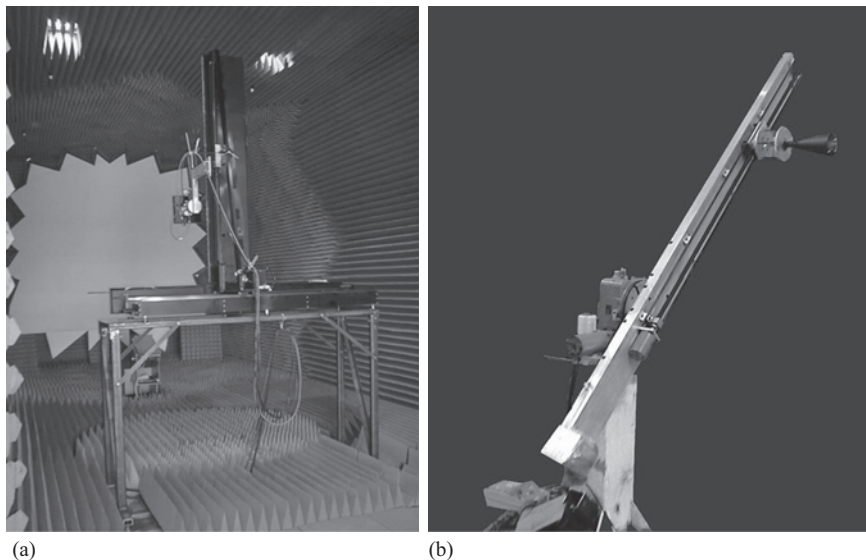


Figure 5.54 (a) Planar field probe, (b) plane polar field probe (Courtesy of NSI-MI Technologies LLC)

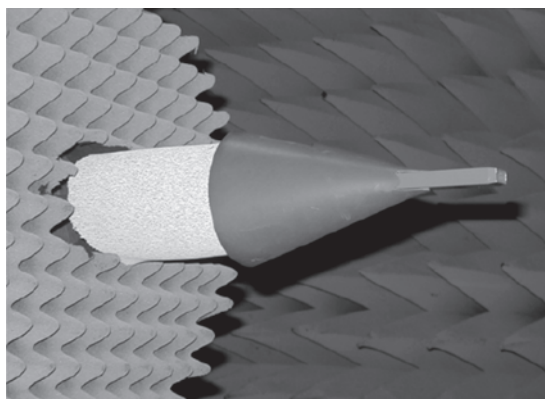


Figure 5.55 Field probe (Courtesy of SELEX)

waveguide section and a *swam* cone. The cylindrical section is included to displace the flat circular RAM sheet that is used to screen the CATR, from the waveguide probe.

It is important to cover as much of the scanner as possible with RAM and it is interesting to note that for the 650 GHz hologram CATR at *Millilab*, Finland (see Section 5.2.4), the plane-polar probe was covered in carpet (Figure 5.56), which

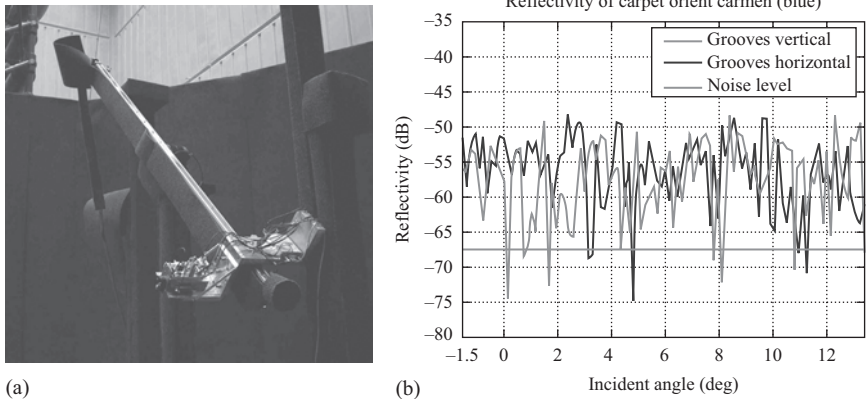


Figure 5.56 (a) 650 GHz plane-polar probe at Millilab hologram CATR facility showing use of carpet as an effective absorber [47], (b) reflectivity measurement of carpet as a function of incident angle from normal [48]

makes an excellent absorber at the frequency with maximum reflectivity of about -48 dB, as shown in Figure 5.56(b).

Spherical quiet zone probing can also be undertaken, and has the advantage of using the existing range spherical positioner. The method is described in [46] and consists of using a probe antenna (e.g. open-ended waveguide) mounted on the spherical positioner and scanning the field in theta and phi. Conversion of this data to the plane wave spectrum can then be used to identify the direction of a scatter. Spherical probing of the test zone has the advantage of documenting energy arriving into the test zone for all angles.

The process of scanning the quiet zone enables one to determine the volume of the quiet zone (by successive transverse scans moving down range of the CATR) using the ± 0.5 dB and $\pm 5^\circ$ ripple criteria. It also enables the correct alignment of the CATR reflectors and the CATR feed.

5.4.3 Phase-less quiet zone scanning

When millimetrewave systems are used it becomes increasingly difficult to scan the phase due to cable effects; this is also true for very large CATR facilities operating a microwave frequencies. In [49] an effective CATR phase-less testing algorithm for superquadratic apertures based on the Jacobi–Bessel expansion of the aperture field is reported. The process finds the amplitude and phase of the field radiated by the CATR in the quiet zone from the knowledge of its amplitude on two transverse measurement planes S_1 and S_2 suitably located in the near-field zone of the CATR aperture. To reduce the computational complexity and to improve the conditioning of the problem, the number of unknowns is kept as low as possible by means of an effective aperture field representation, involving orthogonal functions

matching the aperture shape. In this method the Jacobi–Bessel representation of the aperture field distribution is adopted yielding aperture field expansions truncated to the minimum number of unknown coefficients $M \times N$. These unknown coefficients, which represent the CATR aperture, are evaluated to best match the measured data on S_1 and S_2 . The method was tested in simulation using the QML single-offset CATR (Figure 5.29) with the measurement planes S_1 and S_2 being taken at $Z_1 = 200 \lambda$ and $Z_2 = 260 \lambda$ shown in Figure 5.57, where only S_1 is located within the quiet zone. To make the simulation as realistic as possible, the direct field radiated by the feed towards the measurement planes was added to the one scattered by the collimator and a uniformly distributed noise added to the data with SNR = 35 dB. To analyse the performance of the approach, the CATR phase and amplitude field was numerically simulated over five additional quiet zone test planes of Z_3 to Z_7 of Figure 5.57. The resulting reconstructed amplitude and phase quiet zone plots are shown in Figure 5.57(b), with the maximum amplitude and phase error across all five planes Z_3 to Z_7 being <0.3 dB and $<3^\circ$ respectively. These results are modelled and as far as the authors know the method has not been practically compared with directly scanned results, but this offers an attractive alternative for millimetrewave CATR evaluation where phase measurement is a major problem.

5.4.4 Quiet zone evaluation using RCS of a known target

Here a reference target with known RCS response is rotated in azimuth and elevation within the quiet zone. A comparison with the target’s well-known RCS response provides a measure of the quality of the quiet zone. Applying the Fourier transform to the RCS data provides the amplitude and phase distribution across the reference target in the quiet zone. From this plane wave spectral components (PWSC) can be determined which can be used as an alternative measure of CATR quiet zone quality offering fuller information than a simple quiet zone transverse scan. A variety of targets have been used for this method including a straight metal

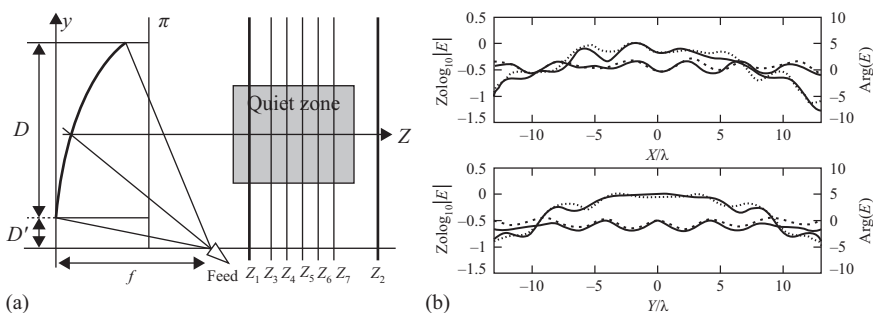


Figure 5.57 (a) Single-offset CATR, (b) reconstructed quiet zone in x (top) and y (bottom). Simulated = —, predicted = - - -, in both graphs amplitude is the upper pair and phase is the lower pair [49]

rod [50] and a flat diagonal plate [51]. The method is demonstrated in [50] where a reference target of a metal bar that is approximately twice the length of the transverse quiet zone is measured for RCS at a down range location in the middle of the quiet zone volume. Such a measurement can be made simultaneously at all frequencies of interest making for a relatively rapid measurement. From the RCS measurements and the known RCS of the target, the transverse fields and PWSC are determined. Once the PWSC are known the transverse fields at other down range distances can be determined (by taking into account the phase factor for the new down range location), and indeed the down range field as a function of down range distance, offering a complete volumetric characterisation of the quiet zone.

In [52] the 6 m × 5 m test zone of the ESA CATR was evaluated by measuring the RCS of a 2 m diameter flat plate with 0.02 mm rms surface error. The plate was constructed from an aluminium sandwich construction with high density honeycomb material inside to ensure a rigid low-weight structure. When the flat plate is illuminated by a non-planar wave from the CATR, the complex scattered field is a function of its azimuth (α) and elevation angles (β):

$$S(u, v) = \iint_A E_{2W}(x, y) e^{j(u \cdot x + v \cdot y)} dx dy \quad (5.3)$$

where $E_{2W}(x, y)$ is the illuminating field of the plate, A is the surface area of the plate, and $u = 2k \sin(\alpha)$ and $v = 2k \cos(\alpha) \sin(\beta)$. This equation can be inverted giving the 2D test zone field across the plate:

$$E_{2W}(x, y) = 4\pi^2 \iint_A S(u, v) e^{-j(u \cdot x + v \cdot y)} dudv \quad (5.4)$$

The one-way quiet zone field is thus obtained from

$$E_{1W}(x, y) = \sqrt{E_{2W}(x, y)} \quad (5.5)$$

In the ESA CATR the measured RCS of the flat plate was taken at 12 GHz and the data transformed as above to obtain the quiet zone field over the 2 m diameter plate. The amplitude and phase deviations were approximately 0.7 dB and 8° within a test zone diameter of 1.5 m. The truncation associated with the plate size of 2 m limits the accuracy of the quiet zone field near the edges of the plate. However, for small millimetrewave CATRs where the plate can be made larger than the CATR quiet zone, this offers another attractive alternative to the difficulties (and cost) of planar scanning at millimetrewaves.

In [51] a diagonal flat plate (which offers low SAR side lobes in the two principal planes) is used via ISAR (inverse synthetic aperture radar) to ‘image’ the quiet zone and hence can be used as a diagnostic tool to locate and possibly remedy undesirable range reflections. A stray signal response will peak up when the plate is oriented such that the stray signal is specularly reflected back in the plane wave direction (CATR boresight). The size of the plate can be optimised to enable the

null of the flat plate RCS to lie in the direction of the CATR reflector edge in order to accurately diagnose its treatment [53]. The ISAR concept is covered in Section 5.6.5.

A flat plate can also be valuably deployed to determine the accurate beam pointing of an electrically large CATR reflector, in particular for millimetrewave applications. The basic principle is to measure the monostatic or bistatic RCS of the flat plate (constructed from a large plate glass mirror metallised on the front surface) and from that pattern determine the direction of the pattern boresight in turntable azimuth and elevation coordinates. Figure 5.58 shows this using a bistatic set-up, where by taking a series of raster cuts (azimuth plots stepped in elevation) around the main beam of the RCS pattern, a contour plot of the main beam can be generated. By spline fitting ellipses to a range of contour levels, determining the centroid of the ellipse in each case, the average centroid determines the beam pointing. The problem is then one of transferring the position of the flat plate on the turntable to that of the AUT on the same turntable. The approach to be used requires that the AUT and flat plate be simultaneously mounted on the turntable with their respective beam pointing directions separated by approximately 180° in azimuth, as shown in Figure 5.58. It is then required to know the pointing of the flat plate relative to a fixed reference point on the AUT. In the case of space-based instruments these have alignment mirror cubes mounted on them in order that the orientation of the instrument can be accurately aligned to that of the spacecraft body. By using the AUT's mirror cube (MC) in conjunction with one mounted on the flat plate, the exact position of the plate surface relative to the AUT's MC can be determined.

The procedure involves using an auto-collimating telescope to align the pointing of the flat plate MC with that of the AUT's MC. This is undertaken by setting an externally mounted auto-collimating telescope to be aligned with the AUT's MC (this being best done by using the turntable azimuth and elevation

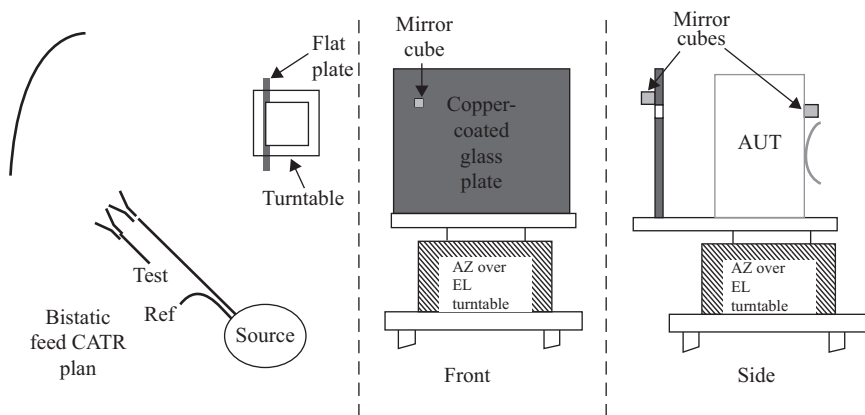


Figure 5.58 Flat plate boresight determination measurement technique

adjustment set to fine adjust). The turntable is then rotated in azimuth until the flat plate MC comes into view and then adjusting the flat plate elevation angle using the mechanical adjustment on the mirror mount along with the azimuth turntable until the telescope auto-collimates with the MC. The flat plate and instrument MCs now have identical elevation pointing and their azimuth difference is determined by the amount of azimuth rotation of the turntable $= x^\circ$. The RF pointing axis of the range has now been transferred to the instrument MC by the single azimuth angle x° . The main sources of error in this technique are the accuracy to which the telescope can auto-collimate with the MCs, and the accuracy of flat plate and AUT RF pointing measurements. Measurements with the QML CATR at 90 GHz have indicated MC transfer errors (RSS) of order 0.0007° and an overall accuracy of about 1% of the flat plate half power beamwidth.

5.4.5 Improving measured CATR patterns

In this section we look at several approaches of improving the measured radiation patterns in a CATR.

5.4.5.1 Mathematical absorber reflection suppression (MARS)

This mathematical post-processing technique (described in detail in Chapter 10) can be deployed to antenna pattern data taken using a far-field or CATR facility using only a single great circle cut to efficiently correct far-field, frequency domain data. We have seen in this chapter that reflections in a CATR can often be the largest source of measurement error within the error budget of a given facility. This mode orthogonalisation and filtering technique that has proved so successful in near-field ranges (planar, cylindrical, spherical) is applied to 2D far-field measurements in [54]. This technique requires only a minimum amount of information about the AUT and measurement geometry, and is able to suppress reflections in a direct far-field one-dimensional antenna range measurement.

It is well known that the 2D far-fields of an antenna can be represented as a linear superposition of orthogonal cylindrical mode coefficients (CMCs) and this permits the application of cylindrical mode orthogonalisation and filtering algorithms to suppress reflections within measurements made using non-cylindrical systems [55,56]. This observation permits the MARS technique to be applied to the CATR. Contrary to usual antenna measurement practice, the MARS technique deliberately displaces the AUT from the centre of rotation. This has the effect of making the differences in the illuminating field far more pronounced than would otherwise be the case, and it is exactly this greater differentiation that makes their identification and subsequent extraction viable. Figure 5.59(a) shows an AUT installed within a typical spherical geometry measurement system, centred about the origin of the range coordinate system, and the conceptual smallest sphere that circumscribes the majority of the current sources which is centred on the intersection of the rotational axes. Conversely, Figure 5.59(b) shows an equivalent MARS measurement where the AUT has been displaced away from the centre of

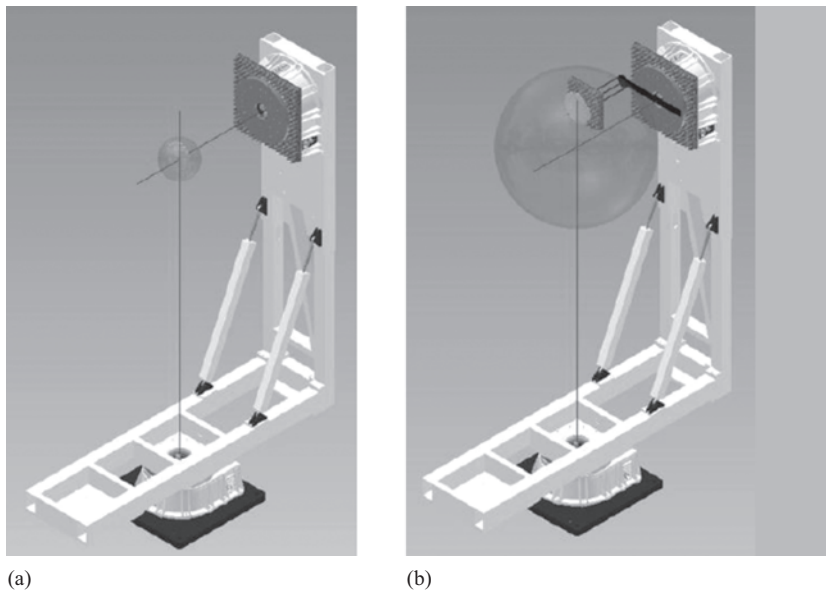


Figure 5.59 (a) AUT measured conventionally at rotation origin with smaller MRE. (b) AUT measured with offset from rotation origin with larger MRE

rotation and the maximum radial extent (MRE) has been correspondingly increased. Once the far-field great circle pattern cut has been acquired and the AUT has been mathematically translated back to the origin of the measurement coordinate system by means of a differential phase change, the equivalent CMCs can be deduced from the measured fields.

The CMCs for the now ideally centrally located AUT are then recovered, so any mode representing fields outside the ideal conceptual minimum MRE can be filtered out thereby removing contributions that are not associated with the AUT. Thus from standard cylindrical theory it is possible to filter out all higher order modes without affecting the integrity of the underlying antenna pattern function. CMCs associated with the AUT are confined to a narrow band that is tightly distributed about the $n = 0$ CMC. As the total power radiated by the AUT must be conserved, the amount of power per mode must increase as the total number of modes associated with the AUT decreases. As the amount of noise per mode can be seen to be roughly constant with respect to the maximum level, the effective system SNR of the measurement is significantly increased. Crucially, and as has been observed previously with all other MARS implementations, although the AUT has been translated back to the origin of the measurement coordinate system, this is not the case for the scatterers which are spatially extended and are represented by many higher order modes. In effect, the contributions in the CMC domain of the AUT and the scatterers are separated so that they do not interfere and are in essence

orthogonalised from one another. The asymptotic MARS processed far-field pattern can be obtained from a simple summation of CMCs. As these transforms and their inverse operations can be evaluated with the FFT, this makes the F-MARS algorithm very efficient in terms of computational effort. The mathematical details of this technique are covered in Section 12.4.2, and here we apply the technique to the QML CATR of Figure 5.29, the process being fully reported in [54].

To demonstrate the method repeat measurements were taken of the far-field great circle azimuth cut of a medium gain (aperture diameter 127 mm) X-band corrugated horn. A single parametric change was introduced into the measurement; this change consisted of introducing a 0.6 m by 0.6 m flat reflecting plate into the chamber that was located in the same horizontal plane as the AUT and was chosen as it constituted a worst case configuration as the specular reflection of the main beam of the corrugated horn directly illuminated the CATR reflector. This arrangement is shown in Figure 5.60, where the AUT is displaced backward from the centre of rotation by 195 mm. Figure 5.61 shows the great-circle far-field co-polar amplitude and phase patterns of the AUT where the *reference* trace is taken without the reflecting plate. Conversely, the *measured* trace is taken with the reflecting plate installed within the chamber and clearly shows the effects of the additional scattering as an additional large amplitude side lobe at around 50° .

Figure 5.62 shows the CMCs for the case of Figure 5.61, and illustrates the strong peak from the plate as well as the filtered region used to reconstruct the radiation pattern. From inspection of the F-MARS processed patterns, it can be seen that the effects of the spurious scatterer have been effectively suppressed in both the amplitude and phase plots as the respective traces are clearly in good agreement. Corrugated horns are generally renowned for their excellent symmetry.

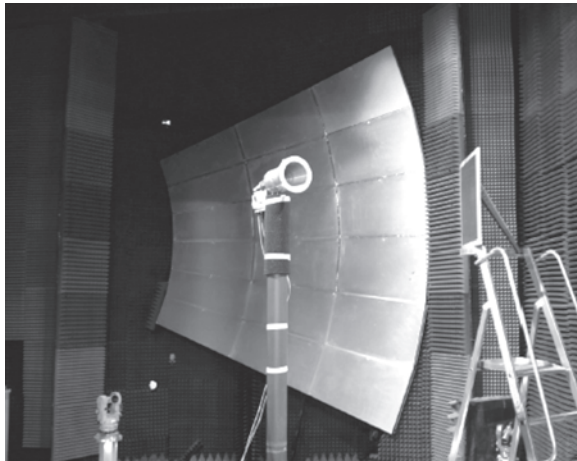


Figure 5.60 X-band corrugated horn AUT installed within QML CATR shown together with 0.6 m by 0.6 m reflecting plate, shown to right of picture

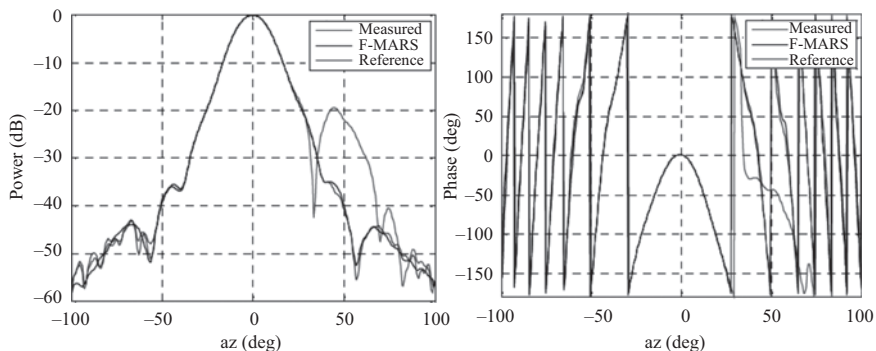


Figure 5.61 Far-field plot of X-band corrugated horn power pattern measured with and without reflecting plate plotted against F-MARS processed pattern, frequency 10.2 GHz. Left: amplitude plot; right: phase plot

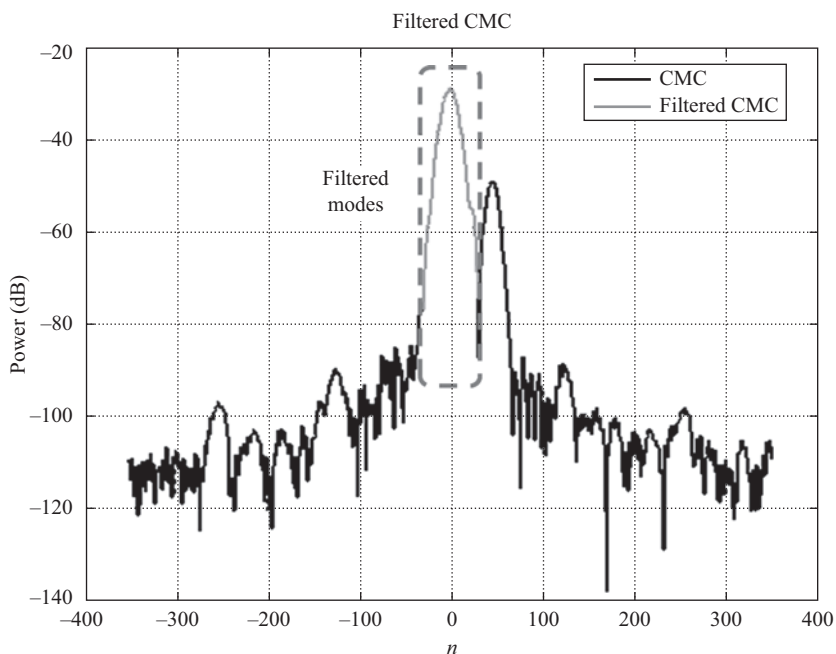


Figure 5.62 CMC's for case shown in Figure 5.61

It is clear that the F-MARS processed patterns demonstrated a very high deal of symmetry as $f(A_z)$ is approximately equal to $f(-A_z)$, where f denotes the amplitude or phase function.

Figure 5.63 shows the F-MARS processed far-field great circle cuts of the corrugated horn that were taken with, and without, the 0.6 m by 0.6 m flat reflecting

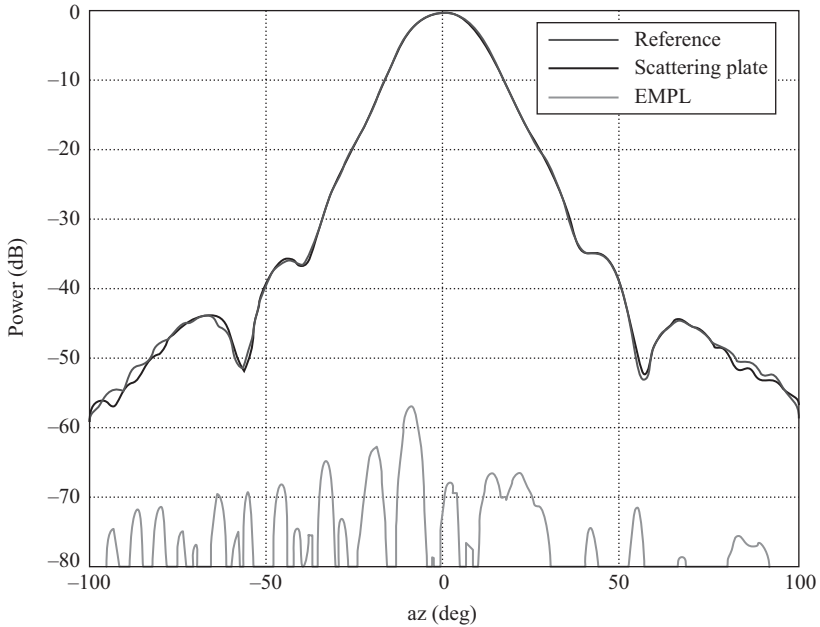


Figure 5.63 Comparison of F-MARS processed AUT patterns with and without flat reflecting plate installed within the QML CATR

plate together with the equivalent multipath level (EMPL) that is used to quantitatively represent the similarity between the respective measurements. Clearly the patterns are in encouraging agreement and this is further demonstrated by the EMPL, which is below -70 dB in the region where the specular reflection had greatest impact. Interestingly, the wide angle high angular frequency ripple that is known to result from diffraction from the edges of the CATR main offset reflector has also been suppressed by the F-MARS processing, cf. pattern ripple for $|az| > 60$. Although the results presented above show pattern data limited to the range $|az| < 100^\circ$, which is merely a sector of a great circle, the F-MARS technique itself is capable of processing pattern data over a complete $\pm 180^\circ$ angular range.

Far-field MARS processing can be used with a very high degree of confidence since all the steps in the measurement and analysis are consistent with the well-established principles of standard cylindrical near-field theory and measurement technique. The offset of the AUT and the resulting finer sample spacing are estimated using conventional rules, and the mathematical translation of the AUT to the origin is rigorous and is described in Chapter 5. The selection of the mode cut-off for the translated pattern is based on the physical dimensions of the AUT and its translated location. The final result with MARS processing can be degraded if the translation of the AUT is incorrectly applied, or the mode filter is too tight, i.e. abrupt. The results of far-field MARS processing will reduce but cannot entirely eliminate the effect of scattering in a CATR.

Chapter 13 addresses the electromagnetic modelling of antenna measurement ranges, and in Section 13.2.11 the CATR modelling process to verify scattering suppression using MARS was used. We also demonstrate that QZ amplitude and phase ripple suppression is also possible (with sufficiently high QZ ripple spatial frequency) with MARS, as is feed spill-over suppression.

5.4.5.2 Antenna pattern comparison (APC) methods

The APC process of taking several sets of antenna amplitude pattern cuts at slightly different AUT transverse and down range distances, with the corrected pattern being obtained by averaging the measured patterns has been used for many years [57,58]. Because the spurious signal arrives from a different direction than the desired plane wave, the relative phase difference between the spurious signal and the desired plane wave is different at each measurement position. Thus the effect of the spurious signals can be compensated for by averaging across all the measured antenna patterns. For a CATR, APC using small changes (less than $\lambda/2$) in AUT position within the quiet zone can be used to compensate the errors caused by standing waves between the transmitter and focusing element as well as errors caused by other spurious signals such as edge diffraction and absorber reflections. Most CATR AUT positioning systems (e.g. roll-over-azimuth) only provide a horizontal slide at the bottom of the AUT positioning system, perpendicular to the plane wave propagation. This thus limits APC to horizontal displacement only in such cases. In [59] the use of CATR feed displacement to achieve APC is described which overcomes the problem of lack of vertical AUT movement, as this is replaced by the more simple to achieve vertical movement of the CATR feed.

A method described in [60] for CATR use (particularly for millimetrewave operation) is based on determining the desired AUT measurement positions in the quiet zone by determining them from the location of the peaks and troughs of a measured quiet zone amplitude scan of the CATR. In [61] a similar process is described where the CATR feed is moved instead of the AUT. Here, by moving the feed in both vertical and horizontal directions from the nominal CATR reflector focus, the quiet zone impinging on the AUT is changed and so averaging can again take place. However, there is an additional complexity here in that as the feed is moved so is the direction of the pseudo plane wave that comes from the CATR. Thus the pointing of each of the measured AUT patterns needs to be corrected before the APC averaging process can be done. This pointing correction can be calculated from the geometry of the CATR reflector system.

Advanced APC is offered as being superior to the traditional APC method because both amplitude and phase data are used to estimate the error vector, in turn reducing the number of measurements required (to a minimum of three). In the AAPC method [62], the main field is represented by the complex vector E_d , and the vector sum of the extraneous field components is represented by the complex vector E_r . The error vector is calculated from a circle-fitting technique based on some minimisation criterion, typically least squares. The method then assumes the frequency and polarisation of E_d and E_r are identical. However, the most critical assumption is that only one extraneous source is present, *the single interfering wave*

paradigm. Corral in [63] critically studies the method and concludes that for a given pointing direction of the AUT in a CATR, there needs to be one dominant error source for the method to be successful, and so is really applicable to high gain AUTs. The method has been successfully used in, for example, the ESA CATR (see [52]).

Compared to simple APC, these processes require considerable post-processing and appear to be more complicated than applying the F-MARS method.

5.4.6 Feed scanning for static AUT measurements

For very large AUTs (e.g. antenna mounted on a spacecraft) it is not always possible to move the AUT to undertake conventional CATR pattern measurements. Planar near-field measurement is one solution to this, and poly-planer near-field overcomes the restriction of the need for very large scanning planes [64]. However, it is possible to provide some static AUT measurement with a CATR by scanning its feed, and hence changing the direction of the pseudo plane wave hitting the AUT. The concept is depicted in Figure 5.64 for the case of a dual reflector CATR, where the long equivalent focal length offers the best capability.

The effects of the feed displacement means that the incoming plane wave arrives at a different direction to the AUT and hence the AUT antenna pattern can be measured. The relationship between feed movement and the CATR pseudo plane wave can be calculated from the geometry of the CATR reflector system. However, the CATR quiet zone ripple characteristics also change with feed movement. The deviation of the wave front from a plane is independent of the frequency; however, the actual quiet zone phase and amplitude are a function of the

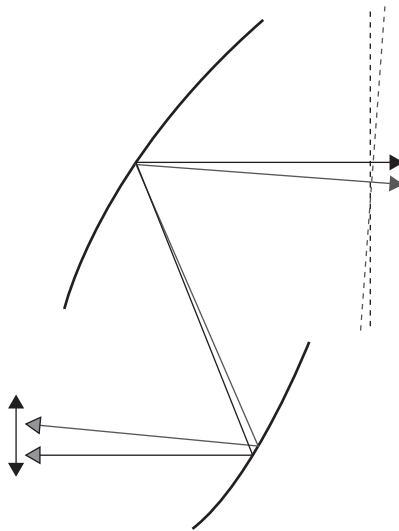


Figure 5.64 Feed scanning in a dual reflector CATR

frequency. This means that the maximum allowable feed displacement depends on the size of the AUT and on the axial position of the AUT in the test zone. The larger the AUT, the smaller the scan range; the closer it is to the CATR reflector, the larger the scan range.

The relative phase at the AUT varies strongly with the feed displacement because the distance between antenna and feed changes as the feed moves, so the phase has to be corrected for this effect. Both horizontal and vertical scans can be obtained, and the preferred direction of the feed displacement for horizontal scans is along the focal line of the sub-reflector since in that case the latter is not defocused, resulting in a cylindrical phase error in the test zone. A vertical feed displacement gives a vertical scan, but with both horizontal and vertical phase errors in the antenna aperture [61].

Since the CATR of Figure 5.64 has a large focal length, the phase and amplitude errors for a certain scan angle are small. The feed has to be moved by considerable distances, which is helpful in accurate positioning of the feed and which allows several feeds to be used simultaneously to illuminate an AUT with two beams simultaneously (see, e.g., [39]).

As an example [61] describes a dual reflector CATR with a main reflector of $2.07 \text{ m} \times 1.90 \text{ m}$ in front-view, excluding the serrations. The AUT is about $1.65 \text{ m} \times 1.50 \text{ m}$, so there is a margin of about 0.2 m on all sides to the GO boundaries. The available scan range for a 1 m diameter circular antennas is 6.4° in azimuth and 3.8° in elevation. The required feed displacement for this scan range is 76 cm horizontally and 27 cm vertically. The maximum amplitude variation across the AUT aperture was a maximum of 0.2 dB and the maximum phase was 43° at 60 GHz .

5.5 Radiation pattern and power parameter measurement

In this section we will look at the process of measuring the far-field radiation pattern of an antenna using the CATR. We will also consider how other antenna ‘power’ parameters can be measured in the CATR such as Directivity, Gain, Effective Isotropic Radiated Power (EIRP) and Saturating Flux Density (SFD).

5.5.1 Radiation pattern measurement

As far as measurement of the radiation pattern of an AUT is concerned, we make use of the fact that the CATR provides a pseudo plane wave across the AUT aperture and so use a conventional azimuth over elevation (or elevation over azimuth) turntable to directly take the pattern measurements as is the convention in a far-field range. Specific issues that arise in the CATR are multiple reflections between the AUT and CATR reflector feed horn particularly around the boresight direction, which manifests itself as a ripple around the boresight of the radiation pattern. The effect can be quantified as in the case for antenna pattern comparison (APC) (see Section 5.4.5.2) by monitoring the boresight received signal as the

down range distance is moved incrementally through a distance of half a wavelength.

Because the ‘path-loss’ in a CATR is low (see Section 5.1), there is a real possibility of reflections from the front surface of the AUT support structure or the turntable system acting as an open resonator with the CATR reflector and feed. Careful attention to the use of absorbers to mitigate this effect is vital for successful radiation pattern measurement in a CATR. The use of time domain gating, either direct or using swept frequency methods, offers a valuable solution to this issue, and indeed the time domain response can be helpful in identifying sources of reflection within the CATR chamber (see Section 5.2.6).

The CATR is a valuable facility for measuring active antennas such as phased array radars, where the CATR acts as the receiver. In this case care needs to be taken concerning power levels if the radar system is to be tested at full power as the focusing property of the CATR reflectors means that very high power densities can occur around the CATR feed area and the edges of the sub-reflector [65]. To determine where *high power absorber* needs to be placed in a given CATR configuration, a full 3D EM model of the range is required (see Section 5.4.1).

In the above sections we have looked at various sources of error during the measurement of the radiation pattern in a CATR. In any given measurement campaign, it may not be possible to devise or implement measurement techniques that can effectively remove or suppress all systematic errors. There will certainly be limitations on the numbers of repetitions of measurements that can be made to reduce random nondeterministic errors. The formation of an error budget for a given facility is a valuable tool and consists of a quantitative assessment of the impact of the combination of individual error sources on the measurement. Thus an accurate and complete examination of the measurement errors associated with a given set of measurements in a CATR facility can be used to assign an expected uncertainty, via extrapolation, to other measurements made in the same facility. The primary error sources for antenna measurements in a CATR are the following:

- Alignment of AUT (geometrical)
- Multi-path (geometrical)
- Test zone quality (geometrical)
- RF path dynamic/static variation (geometrical)
- RF system linearity (RF system fidelity)
- RF system dynamic range (RF system fidelity)
- Leakage and cross talk (RF system fidelity)
- Channel imbalance (RF system fidelity)
- System drift (environmental)
- Random errors (environmental)

The most practical empirical methodology for assessing the ability of any test facility to make measurements and to establish its error budget is by way of repetition of the measurement procedure. This repetition can be accomplished without alteration in the measurement configuration, to simply address repeatability and precision, or with the inclusion of parametric variations to assess sensitivity. Such a

study was undertaken in [65] for the SELEX CATR facility in Edinburgh (Figure 5.3), and a sample plot is shown in Figure 5.65 for percentage error against dB below the peak of the radiation pattern, i.e. from the plot a feature in the pattern at -40 dB below peak would have an error of the order of $\pm 10\%$. The figure shows that without the use of any advanced measurement techniques (see Section 5.4.5 as well as Chapter 12), a main beam error of some ± 0.4 dB could be expected.

5.5.2 Power parameter measurement

In this section we address four power parameters that are often the end goal of an entire measurement campaign. Since these parameters are so important and there are subtle differences that often lead to confusion, a complete discussion is warranted at this point in the book. Of course these parameters can be measured in a variety of ways, certainly not just in a CATR; however, since this CATR chapter is the first ‘Method’ chapter we chose to address these definitions here. The parameters of interest are Directivity, Gain, EIRP and Saturating Flux Density (SFD), and the first three of these are formally defined in the *IEEE Standard Definitions of Terms for Antennas* as [66]:

- **Directivity** (of an antenna) (in a given direction). The ratio of the radiation intensity in a given direction from the antenna to the radiation intensity averaged over all directions. The average radiation intensity is equal to the total power radiated by the antenna

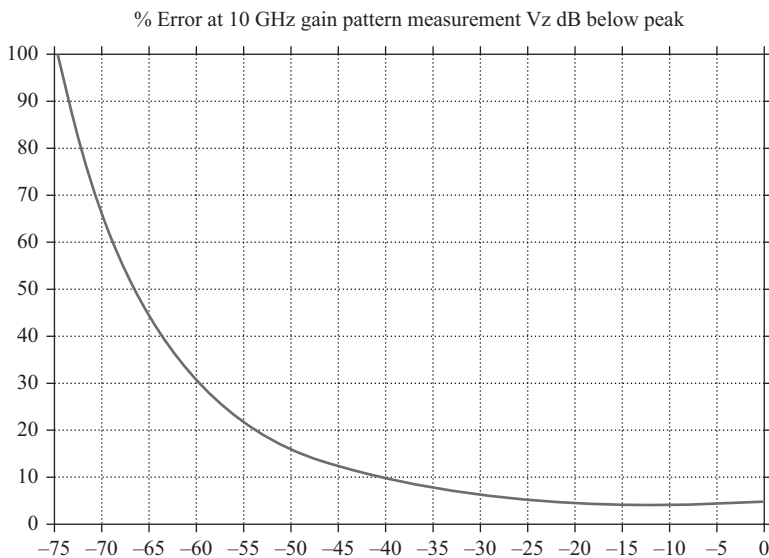


Figure 5.65 Percentage error as a function of dB below peak for SELEX CATR facility, 10 GHz [65]

divided by 4π . If the direction is not specified, the direction of maximum radiation intensity is implied.

- **Gain** (in a given direction). The ratio of the radiation intensity, in a given direction, to the radiation intensity that would be obtained if the power accepted by the antenna were radiated isotropically. The radiation intensity corresponding to the isotropically radiated power is equal to the power accepted by the antenna divided by 4π . If an antenna is without dissipative loss, then in any given direction, its gain is equal to its directivity. If the direction is not specified, the direction of maximum radiation intensity is implied.
- **The Equivalent Isotropically Radiated Power (EIRP)** of an antenna in a given direction is the gain of a transmitting antenna multiplied by the net power accepted by the antenna from the connected transmitter. This is also known as effective isotropically radiated power.

There is no formal definition for SFD, but this parameter can loosely be described as the receive equivalent of EIRP and is described in [67] as follows:

- **The Saturating Flux Density (SFD)** is the flux density required to saturate the system receiver and is expressed in terms of the input power into and the gain of the transmitting antenna.

In the case of Directivity (and Gain) one can also refer to partial Directivity (or Gain) and this can be described as the quantity derived for a given polarisation. So in a given direction, it is that part of the radiation intensity corresponding to a given polarisation divided by the total radiation intensity averaged over all directions. The (total) Directivity (or Gain) of an antenna, in a specified direction, is the sum of the partial Directivities (or Gain) for any two orthogonal polarisations.

Another term often encountered in industry is that of **Realised Gain**. Since the formal definition of Gain does not include losses arising from impedance mismatches, **Realised Gain** accounts for this and is often the more sought-after parameter in practice. Figure 5.66 illustrates the relationship between the Directivity, Gain and Realised Gain parameters schematically. Directivity is unique as it can be determined purely from the antenna pattern itself and is calculated from the full-sphere measurement. Gain takes into account losses within the antenna (loss due to heat) and is therefore always less than or equal to (only if the antenna is lossless) the Directivity. Realised Gain further takes into account any power loss due to port impedance mismatch and is less than or equal to (only if the antenna is connected to a line impedance matched to the conjugate of its port impedance) the Gain.

Chapter 12 contains formal definitions of all these four power parameters and presents the methods available to measure these parameters using both far-field and near-field techniques.

For the case of gain measurement in a CATR, the options are as follows.

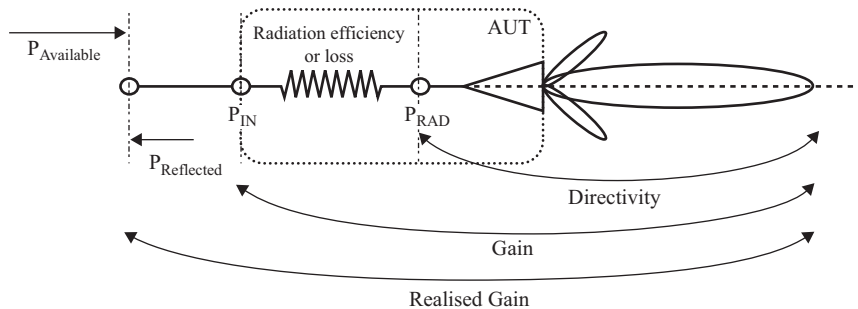


Figure 5.66 Schematic representation of Directivity, Gain and Realised Gain

5.5.2.1 Gain measurement using the substitution technique

This is by far the most commonly used method in industry today and involves comparing the antenna under test to a calibrated standard gain antenna. The theory behind this is given in Chapter 12 (Section 12.6.2) and for the CATR it involves noting the peak boresight signal level R_r (dB) for the reference antenna, then replacing this with the antenna under test so that the apertures of both antennas are centred on the same point in the range. The peak boresight signal level R_t (dB) for the AUT is then noted and the AUT dB gain is then given by $G_t = G_r + (R_t - R_r)$, where G_r is the dB gain of the reference antenna. To improve accuracy this process is repeated with the reference and test antenna apertures co-located at several different points in the transverse quiet zone plane and taking the average of the measured gains. Accuracy is at its best when the AUT and reference antenna have similar size apertures and hence gains. It should always be remembered that matching of the AUT and reference antenna impedance to the line impedance is important and it is simple to test for this if a swept frequency response at the boresight position of the antenna is taken. The mismatch will manifest itself as a standing wave between the AUT and CATR. This can be much reduced by placing an attenuator at the output port of both the AUT and reference antennas (preferably a waveguide attenuator), so reducing the standing wave. Correct alignment of the polarisation of the AUT and reference antennas with that of the CATR is also important for maximum accuracy. An extensive study of the uncertainties for calibration of standard gain horns from measured directivity and estimated loss can be found in [68] together with uncertainties for the gain transfer method on a CATR. This study indicates that gain uncertainty (95% confidence level) from radiation pattern-based directivity measurements can be as good as 0.08 dB and for the gain transfer method 0.15 dB.

5.5.2.2 The three-antenna gain method

This is a well used method for conventional far-field ranges and can be adapted for use in a CATR. It has the advantage of not requiring a calibrated gain reference antenna, but requires at least two of the antennas to not be circularly polarised, see

Section 12.6.2 as well as [69]. In this case the AUT, a second antenna and the CATR feed form the three antennas applying so the CATR feed will be replaced by one of the two other antennas during the test procedure. The replacement feed must have its phase centre positioned at the focal point of the CATR reflector and the feed pointing alignment is also critical if the resulting quiet zone is not to have an unwanted phase taper across it. The use of a different feed to that for which the CATR was designed will also clearly affect the quiet zone size and performance, a lower gain feed will result in more edge diffraction and hence more quiet zone ripple, a higher gain feed will result in a reduced quiet zone size which may well not then be ‘plain’ over the AUT aperture, hence adding significant measurement error. For all these reasons the only viable way a CATR can be used for the three-antenna method is to have two near identical CATR feed horns for antennas 1 and 2 with the AUT making up the third. As discussed in Section 5.5.2.1, making the measurement at several points in the quiet zone and averaging the results will improve the accuracy. Reference [70] reports a study of using the three-antenna method at 34 GHz and well illustrates the problems associated with not using two identical CATR feed horns in the process.

5.5.2.3 Direct gain measurement

This is based on using the Friis transmission formula and the direct measurement of power with a suitable power meter. The Gain is given by

$$G_{AUT} = P_r/P_t \left[\frac{1}{G_{feed}} \right] \left[\frac{\lambda}{4\pi R} \right]^{-2} \quad (5.6)$$

where G_{AUT} is the gain of the AUT, G_{feed} is the gain of the CATR feed, P_r is the receive power of the AUT, P_t is the transmit power at the CATR horn input, the distance R between the test antenna and the CATR feed reduces to the distance from the CATR feed to main reflector (i.e. the spherical wave path) and provides the equivalent distance with spherical attenuation. For the case of a single-offset CATR (Figure 5.67), this is the distance R shown and is related to the focal length.

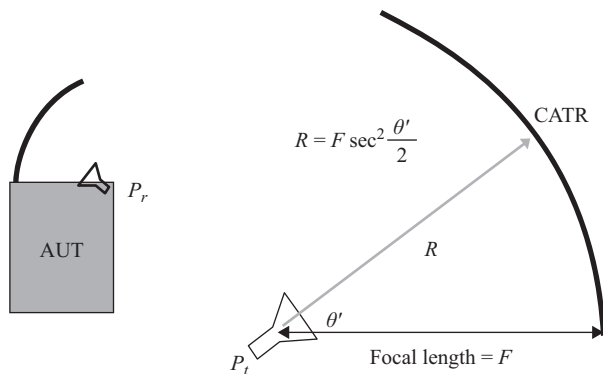


Figure 5.67 Single-offset CATR geometry

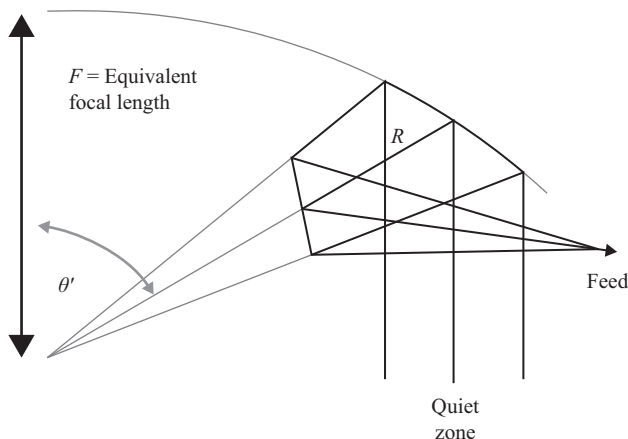


Figure 5.68 Dual offset CATR geometry

For multi-reflector CATRs this distance needs to be determined from its optical geometry and thus the equivalent focal length of the system; see for example the case for a dual reflector system in Figure 5.68. A typical set-up is shown in Figure 5.67, with P_r and P_t measured using a power meter or preferably a VNA, the latter offering gain as a function of frequency.

5.5.2.4 EIRP measurement

Since $EIRP = G_t P_t$, where G_t is the AUT transmit gain, then

$$EIRP = P_{r-catr} / G_{feed} (4\pi R / \lambda)^2 \quad (5.7)$$

where P_{r-catr} is the power received by the CATR feed from the transmitting AUT and the remaining terms are as in (5.6). See also Section 12.6.3.

5.5.2.5 Saturating flux density measurement

SFD is flux density to saturate the AUT transponder so

$$SFD = G_t P_t \left[\frac{1}{4\pi R^2} \right] \quad (5.8)$$

where G_t is the gain of the CATR feed, P_t is the transmit power at the CATR feed and R is as in (5.6). See also Section 12.6.4.

5.6 Radar cross-section measurements

It is no understatement that the development of the CATR revolutionised the measurement of RCS. The ability to have a large pseudo plane wave illuminating a target in a compact and fully controlled, secure and repeatable environment was the

key to this revolution and some very large facilities capable of taking complete aircraft now exist.

5.6.1 RCS measurement in a CATR

Here we give a brief review of RCS; for a detailed description the reader should consult one of the many texts such as [71]. The magnitude of the scattering from a given object is a function of both its shape and the surface characteristics. Ignoring the complications inherent in the minimum signal to noise constraints on system response, the impact of pulse-based integration and processing as well as the statistical nature of the scattering response from all but very simple targets and any polarisation-based complications the basis of RCS can be seen from the simplified bistatic radar equation:

$$P_r = \frac{P_t G_t}{4\pi R_t^2} \sigma \frac{A_r}{4\pi R_r^2} \quad (5.9)$$

where P_t , G_t and R_t are the transmitting power, gain and range, A_r and R_r the effective receiving antenna area and range, with σ being the RCS which in itself can be expressed as

$$\sigma = A\rho^2 G \quad (5.10)$$

where A is the target area, ρ its reflectivity and G the targets *gain* in the receive direction.

For a monostatic RCS using a CATR, (4.9) becomes

$$P_r = \frac{P_t G_f^2}{(4\pi)^3 R^4} \sigma \lambda^2 \quad (5.11)$$

where G_f is the CATR feed gain and R becomes the distance from feed to reflector centre (in the case of a single-offset CATR and as described in Section 5.5.2.3), thus accounting for the spherical wave loss since as the path from reflector to target is collimated and so suffers no $1/R^4$ loss.

It is worth noting at this point that this collimation property has been another important factor to the success of the CATR for RCS measurements, since for the alternative far-field approach a distance between target (of diameter D) to source antenna needs to be $4D^2/\lambda$ rather than the radiation pattern far-field criteria of $2D^2/\lambda$ because of the double path for the RCS signal.

As an example for a CATR operating at 10 GHz with $R = 6$ m, $G_f = 10$ dB can detect a target with RCS of 10^{-5} m² using a receiver offering a minimum discernable signal level of -100 dBm with a transmit power of 24.5 dBm. However, for large CATR facilities, kilowatt transmit powers are required. The undesirable sources of reflection and scattering in a CATR (shown in Figure 5.8) are added to by the fact that the return path to the feed adds additional sources of error as illustrated in Figure 5.69 and all these are sources of error (so called ‘Clutter’) for RCS measurements. This is particularly true for targets that have low RCS at small

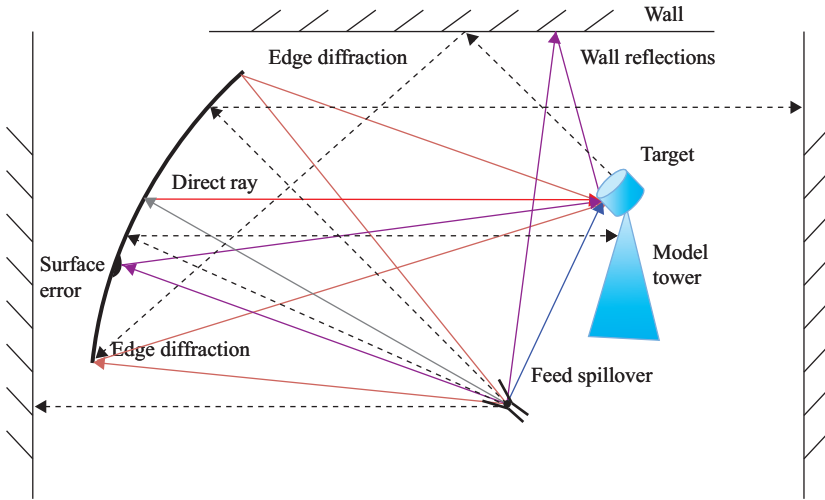


Figure 5.69 Additional sources of error (---) in a monostatic RCS range due to the return path to the feed

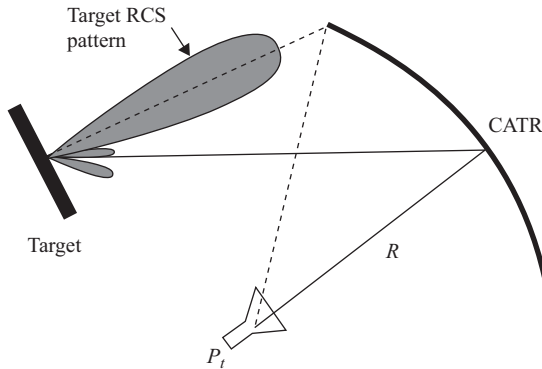


Figure 5.70 RCS of flat plate corrupted by edge diffraction from CATR reflector

angles away for the maximum (such as a flat plate) and Figure 5.70 illustrates a worst case where a flat plate peak RCS return points to the CATR edge diffracted signal creating a strong error signal compared to the true very low RCS return from the plate at this angle. It can be seen in this figure that the path length of the error signal is similar to the direct ray path, so time-gating would not help here. However, for many other of the additional error sources shown in Figure 5.69, time-gating is a valuable tool for the RCS measurement range (see Section 5.2.6).

Subtracting the background is a popular solution for clutter reduction, where the signal is recorded as the model tower is rotated without the target and this is then vector subtracted from the same data with the target present as a post-

processing exercise (nowadays nearly in real time). Of course the entire complement of chamber and hardware must be stable over time and temperature for this method to work. To use it one assumes that there is no ‘shadowing’ of the chamber by the mounted target so that the background is not affected by the presence of the target. An example of how both background subtraction and time-gating can improve a target is shown in Figure 5.71 for the NASA Almond target (shown in Figure 5.72), which exhibits an RCS that varies between -24 dBsm and -45 dBsm in azimuth at X-band. Clearly without background subtraction small RCS targets cannot be clearly defined.

All practically achievable RCS measurements that are undertaken are essentially substitution measurements in that initial measurements are made using a target of known scattering cross-section and then the results of these measurement are used to calibrate the data acquired for the target under test. This means that a range of calibration targets are required if quantitative RCS measurement are to be made.

Often the simplest possible targets are used for such calibration, a sphere with a uniform response in all directions and at all frequencies being the optimum. This is shown in Figure 5.73 mounted on a low RCS column. Often the use of a sphere is not possible due to the nature of the RCS mount, e.g. a pylon with a mounted positioner will not be compatible with a sphere, in this case a squat cylinder is usually used as it has a uniform response in azimuth and if sufficiently squat a wide

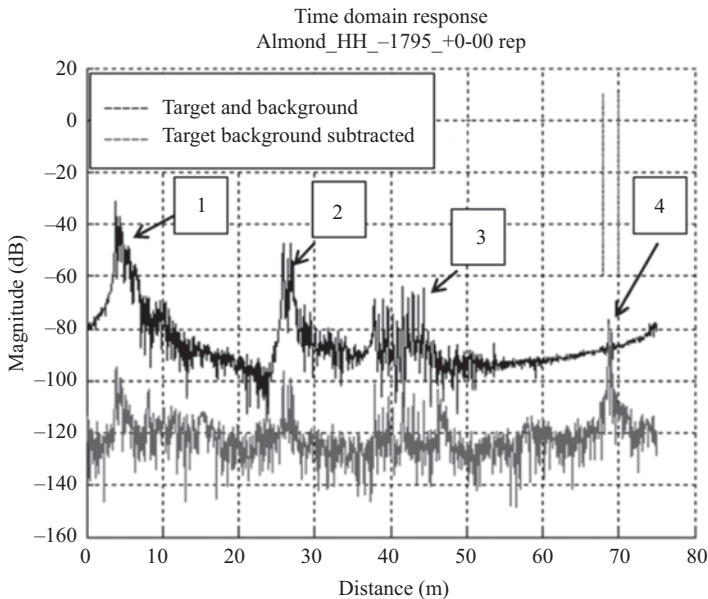


Figure 5.71 Time domain RCS measurement of NASA Almond target:
 1 = coupling between Tx and Rx antennas, 2 = scattering from CATR sub-reflector, 3 = scattering from CATR main reflector, 4 = target response (Courtesy of SELEX ES)

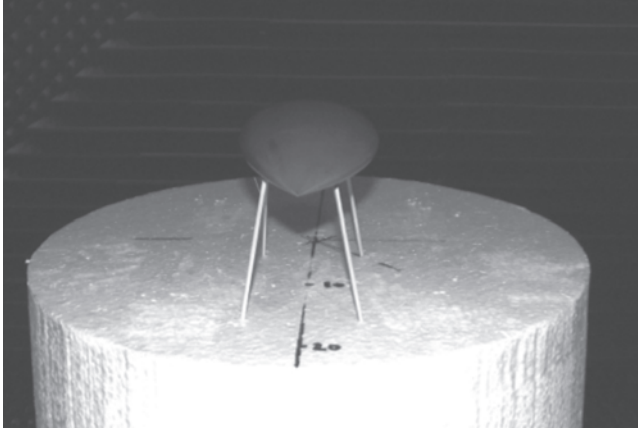


Figure 5.72 *NASA Almond in position on low RCS, (40 dBsm) column in the SELEX ES CATR (Courtesy of SELEX ES)*

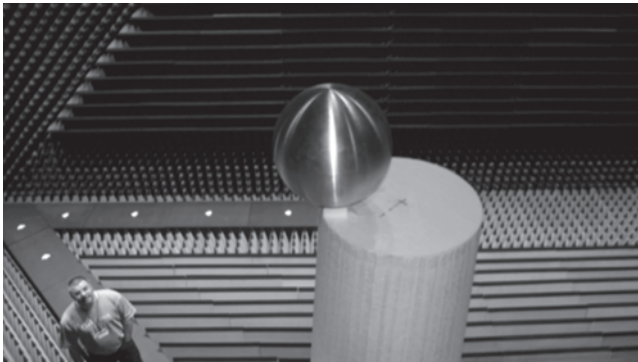


Figure 5.73 *Spherical calibration target on top of low RCS column (Courtesy of SELEX ES)*

main beam in elevation. However, other targets with equally predictable scattering cross-sections can be used, e.g. dihedrals, trihedrals (corner reflectors) and flat plates can all be used. Corner reflectors are an example of targets that are said to be re-entrant, since they efficiently trap and re-radiate energy; use of these as calibration targets can lead to anomalies in phase and time domain windowing if not properly compensated for.

The polarisation of a target's backscatter depends on the target structure and in general differs from the polarisation of the incident signal. For example a thin straight wire can be distinguished from a sphere by measuring the backscattered signal as the transmit polarisation is rotated. The return from the sphere will be constant with polarisation rotation but the wire will vary between a maximum and minimum value. Thus for a complete knowledge of the target's RCS, the *polarisation matrix* must be determined by measuring the RCS in all possible

polarisation combinations. Taking V to be vertical polarisation and H to be horizontal polarisation, then transmitting on horizontal and receiving on vertical is called an HV measurement, so the full polarisation matrix is HH, VV, HV, VH [72]. Most RCS CATR measurement systems provide this polarisation measurement matrix capability automatically via switching between the orthogonal output ports of the transmit and receive horns as well as using multiport receivers. A typical RCS measurement set-up using a 4-port VNA as the core receiver is shown in Figure 5.74. It is of course possible to use a 2-port VNA along with a 2-port PIN switch to switch between the V-pol and H-pol measurements at the expense of measurement time and possibly some accuracy dependent on the repeatability of the positioner as scans would need to be done twice since measurements are generally done with continuous movement of one axis (so called ‘on the fly’). A detailed look at errors such as this can be found in Chapter 12.

5.6.2 Sources of RCS measurement error in a CATR

The primary error sources for RCS measurements in a CATR are the following:

- Alignment within the chamber (geometrical)
- Multi-path (geometrical)
- Test zone quality (geometrical)
- RF system linearity (RF system fidelity)
- RF system dynamic range (RF system fidelity)
- Leakage and cross talk (RF system fidelity)
- Channel imbalance (RF system fidelity)
- Polarisation purity (RF system fidelity)
- Standards (environmental)
- Backscatter, chamber and mount (environmental)
- System drift (environmental)
- Random errors (environmental)

Again we refer to the study undertaken in [65] for the SELEX ES CATR facility in Edinburgh (Figure 5.3; see also Figure 5.76), where the simple configuration used to develop the RCS budget involved the use of two RCS standards one of approximately -11 dBsm and the other with a RCS response that varied around 15 dBsm as a function of frequency. All measurements were made in CW mode and a software gate was used to isolate the target response in the time domain. The targets were mounted on a 4.5 m expanded polystyrene column initially in the centre of the test zone and background subtraction was used to reduce the impact of the mount and the chamber-intrinsic RCS, which were anticipated to be approximately -40 dBsm and -65 dBsm, respectively. The RCS set-up ensured that RCS levels of approximately 25 dBsm could be acquired without signal compression and if single polarisation measurements were to be acquired only, single polarised quasi monostatic feeds were deployed. Typical results were [65] as follows:

- At 8 GHz a 20 dBsm target could be measured to within $(+0.34, -0.37)$ dBsm, $(108 - 92)$ m², 100 m² $\pm 8\%$.

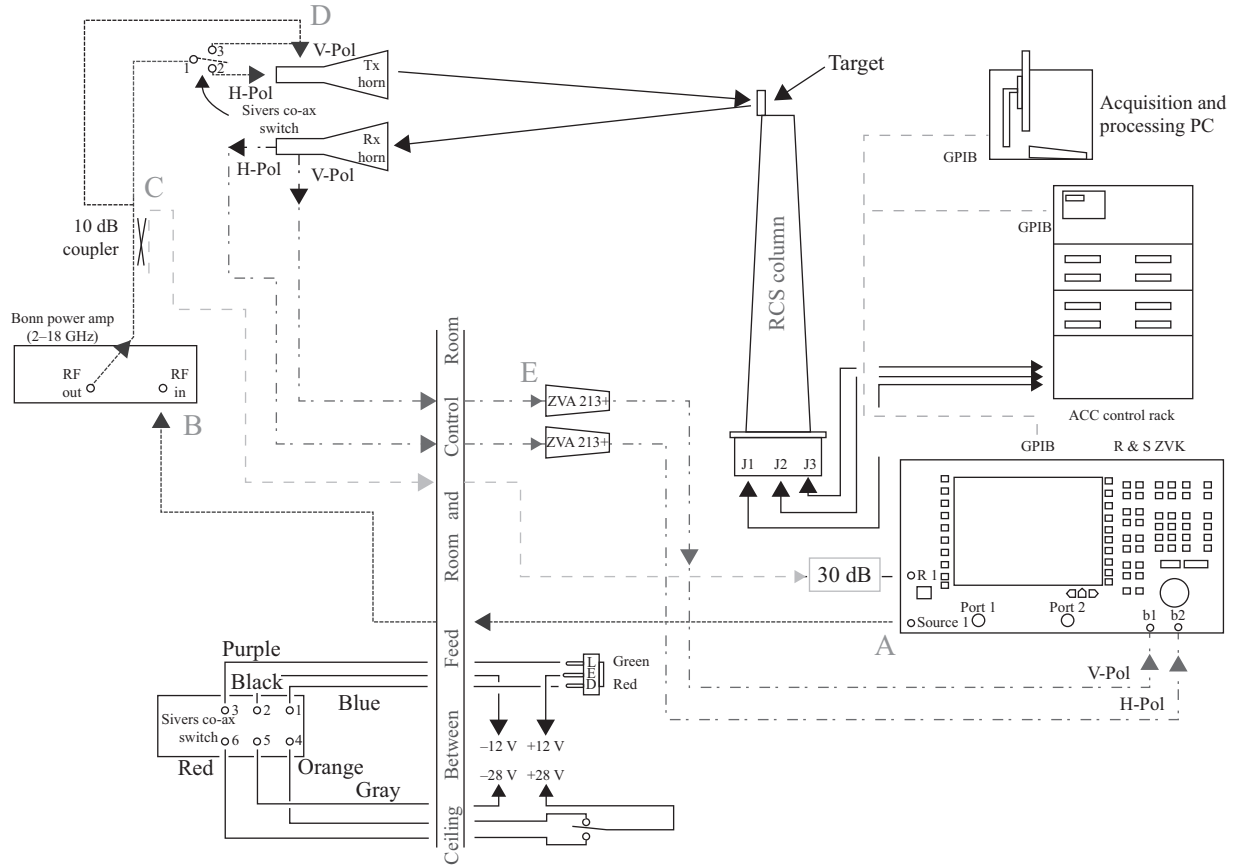


Figure 5.74 Standard RCS measurement set up SELEX ES, this can vary if specific frequencies and or RCS levels are required (Courtesy of SELEX ES)

- At 9 GHz a 0 dBsm target could be measured to within (+0.36, -0.40) dBsm, $(1.09 - 0.91) \text{ m}^2$, $1 \text{ m}^2 \pm 9\%$.
- At 10 GHz a -20 dBsm target could be measured to within (+0.60, -0.70) dBsm, $(0.0111 - 0.0085) \text{ m}^2$, $0.01 \text{ m}^2 \pm 11\%$.
- At 11 GHz a -40 dBsm target could be measured to within (+1.57, -2.49) dBsm, $(0.000144 - 0.0000564) \text{ m}^2$, $0.0001 \text{ m}^2 \pm 44\%$.
- At 12 GHz a -50 dBsm target could be measured to within (+2.87, -12.00) dBsm, $(0.0000194 - 0.000000631) \text{ m}^2$, $0.00001 \text{ m}^2 \pm 94\%$.

Figure 5.75 illustrates a typical RCS response over a 1 GHz window for a specific squat cylinder target, showing both measured and predicted result.

5.6.3 RCS model towers

A vast amount of material exists in the open literature of the design of model towers (or pylons). If only a target is to be supported then a low-reflection foam support can be used (Figure 5.73); if the target is large or heavy or requires active connection via cables then a hollow non-rotating metallic tilted tower often with ogive cross-section is used to minimise reflection back to the CATR feed (see, e.g., Figure 5.76). Alternatively absorber covered rotating cylindrical columns can be used. In extreme cases wires or ‘strings’ have been used.

5.6.4 Time-gating for RCS

To achieve high levels of rejection for clutter signals closely spaced in time to the signal of interest, one requires pulses with very rapid rise times of several nanoseconds or less. This in turn requires high instantaneous bandwidth for the transmit and receive channels, being as much as 200 MHz. To achieve the equivalent of a CW measurement with pulses, one must make the length of the pulse cover the target. The leading edge of the pulse should be allowed to travel the full length of the target, L_t , and return to the front of the target (a time of $2\tau_L$, where $\tau_L = L_t/c$) to

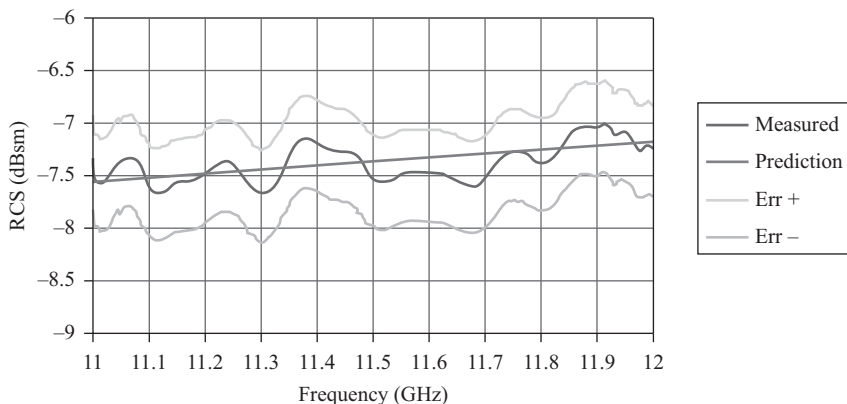


Figure 5.75 Measured and predicted RCS of squat cylinder vs frequency for the SELEX CATR facility [65]

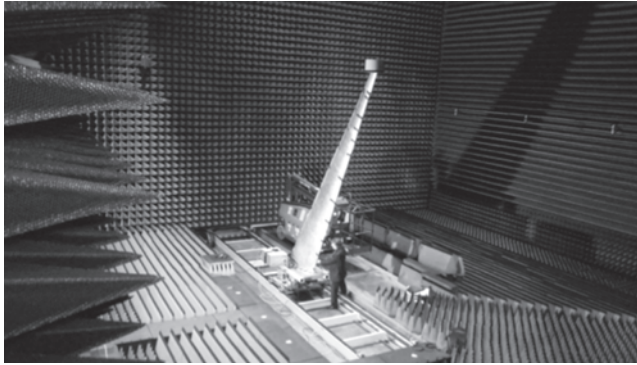


Figure 5.76 Tilted ogive large RCS pylon during installation in the SELEX ES CATR (Courtesy of SELEX ES)

form the complete radar signature; only then, once this composite signal has reached the receiver, does one want to open the receive gate of the radar receiver. Thereupon it is left open for a period of time τ_s , corresponding to the sampling window of the receive gate. The requirement for the pulse width may be written mathematically as

$$\tau_P \geq \tau_R + 2\tau_L + \tau_s + \tau_F \quad (5.12)$$

where τ_R and τ_F are the rise and fall times of the gated CW pulse [73].

In making RCS measurements with time-gated waveforms, one must choose the height of the model tower to make the distance of the target above the ground, h_t , sufficiently large that the ground bounce ray does not illuminate the target during the time interval when the target return signal is being formed. Thus

$$h_t \geq 0.5(2L_t + c\tau_s) \quad (5.13)$$

where c is the speed of light.

Equations (5.12) and (5.13) also set the minimum height and width for the rectangular CATR chamber dimensions, so the target should be at least two target dimensions away from the side walls and ceiling.

Typical performance parameters for a gated CW radar system instrumentation used in RCS measurements are given in Table 5.1 [73], which can achieve a sensitivity of -70 dBsm at frequencies below 18 GHz. Clutter levels of -60 to -65 dBsm are attainable in chambers of sufficient size.

5.6.5 Target imaging

An excellent summary of target imaging was given by Hess in [73], which has the various data acquisition and processing routines as listed below:

- **RCS vs Aspect Angle:** Set the frequency to a fixed value and scan the azimuth and/or elevation axes of the target rotator. This is the classical RCS pattern measurement.

Table 5.1 Typical performance parameters of a gated CW radar instrumentation system for CATR use [73]

Frequency range	2–40 GHz
Pulse repetition frequency	Up to 5 MHz
Transmit and receive on/off ratio	120 dB
Transmit and receive isolation	130 dB
Transmit pulse width	10–499 ns
Receive gate width	10–499 ns
Receive delay	30–499 ns
Rise/fall time	<2 ns
Jitter	0.03% plus 25 ps

- **RCS vs Frequency:** Set the azimuth and elevation position angles of the target to fixed values and step or sweep frequency through a range of values.
- **RCS vs Range (Range Walk):** Set the azimuth and elevation position angles and step the gate delay through a set of values starting at zero and ending with the range length beyond the target. This is used to identify range artefacts and to confirm the choice of range gate delay setting in the two measurement procedures above.
- **RCS vs Cross Range:** By performing a Fourier transform on an ‘RCS vs Azimuth’ data trace, one obtains an ‘RCS vs Cross Range’ data trace, where the cross range coordinate is in units of distance measured laterally across the target on a horizontal line that is perpendicular to the range axis.
- **RCS vs Down Range:** By performing an inverse Fourier transform on an ‘RCS vs Frequency’ data trace, one obtains an ‘RCS vs Radial Distance’ along the range axis.
- **RCS Image Formation or Inverse Synthetic Aperture Radar (ISAR) Imaging:** By performing a two-dimensional Fourier transform on a data set that is RCS vs Azimuth Angle & Frequency, one obtains a two-dimensional data set that is RCS vs cross range distance and down range distance. This resulting data set is termed an ‘Image of the Target’ because it can be readily compared with a perspective optical view of the target. See, e.g., Figure 5.77.

An example of achievable performance is demonstrated in [74] where clutter levels below -75 dBsm were achieved using a gated CW radar on a large 8.1 m focal length CATR. This employed imaging with background subtraction to distinguish clearly three small -61 dBsm spheres resting upon a foam column at Ku-band.

5.7 Radome testing

5.7.1 Radome measurements in a CATR

The term ‘Radome’ originates from ‘Radar Dome’ which was a weather protective dome-shaped covering for ground-based radar antennas, but is nowadays used to refer to any protective covering for an antenna in both civil and military

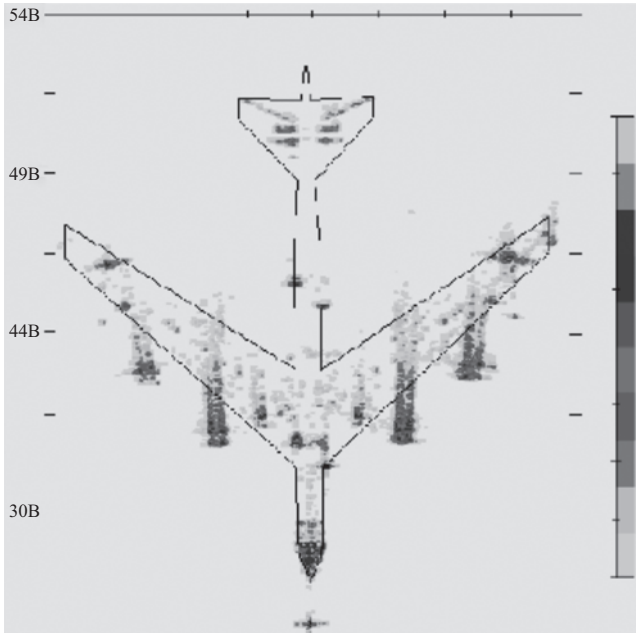


Figure 5.77 2D RCS image with envelope of aircraft outlined [73]

applications. Typical radome applications include aircraft radar, missiles, satellite communications, and mobile base-station antennas, and in many cases, the radome offers both weather protection and performing an aerodynamic function.

The radome obviously has to offer a high degree of transparency to the electromagnetic waves operating frequency band of the enclosed antenna, and so they are usually made from a plastic composite material (e.g. fibre-glass). Since the radome has non-unity dielectric constant and a finite thickness, the electromagnetic wave from the enclosed antenna will be distorted resulting in changes in the beam direction, reduction in peak amplitude, distortion of the antenna radiation pattern and changes to the antenna VSWR. Figure 5.78 illustrates how the direction of the antenna beam can be changed by the radome presence, and Figure 5.79 shows the effect of a ‘nose-cone’ radome on the boresight ray path.

Radomes can be placed into two categories, the first are lightweight radomes with primary function of providing weather protection (keeping water and dirt away from the enclosed antenna); they generally have low impact on the enclosed antennas performance. Such radomes have application in communications and aircraft-mounted surveillance radars.

The second category could be called ‘radomes for fire control radars’, these are usually mounted as nose-cone radars on supersonic platforms and require radomes with considerable mechanical resilience; these always have a significant impact on antenna performance in terms of: insertion loss, return loss, blockage; and

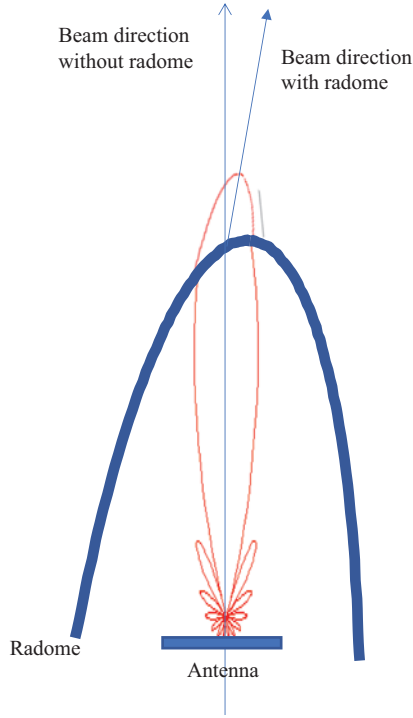


Figure 5.78 Change of beam direction due to radome structure

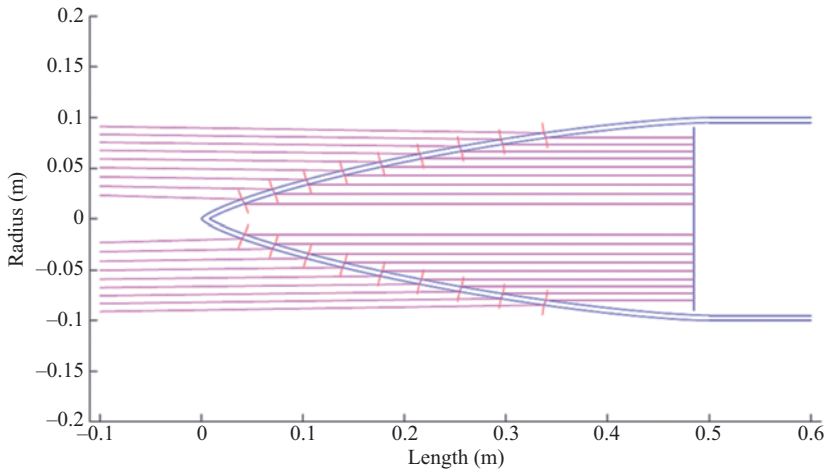


Figure 5.79 Ray tracing of path through a 'nose-cone' radome on boresight

aberration. These are usually composite radomes, often of a C sandwich design (multilayer structure) and will have insertion loss in terms of power that will reduce main beam gain. Additionally as the radome will have a geometry that meets the aerodynamic and structural requirements of the platform, the beam will pass through areas of the radome at different angles and different thicknesses. The different insertion phases associated with these thicknesses and direction will effectively introduce a differential phase across the antenna beam with resultant impacts on null depths and beam pointing angle, i.e. aberration.

Antenna measurements with radome mounted imply installed performance measurements; therefore, realistic radomes should be used. In practice, on airborne platforms, radome are liberally festooned with addition furniture such as pitot tubes, lightning strips, and refuelling nozzles, all of which introduce blockage that will impact on antenna performance.

Clearly, since a lot of design effort goes into optimising the performance of a given antenna, it is vitally important to know what effect a given radome has on the antenna performance and this is usually determined by a comparison of the *with* and *without* radome measurement of the antenna parameters. For a simple fixed microwave back-haul application where the radome does not move with respect to the antenna, this is a relatively simple procedure to undertake with and without test of the main antenna parameters.

However, in the case where the antenna scans, either electrically or mechanically, inside a radome (such as an aircraft weather radar or a fire control radar), there will be different levels of radome distortion depending on the relative pointing of the antenna within the radome. For fire control radars, extreme care is needed to ensure that *with* and *without* radome measurement comparisons are valid as the results are usually used to verify look-up tables installed in the radar that are used to correct the beam steering angle to take account of aberration; this look-up table needs to be accurate to some small number of milli-radians. Hanging a structurally strong radome that may weight many tens of kilograms off the front of an antenna will exert a considerable moment about the mounting point of the antenna. This will alter the angle of the mechanical datum of the antenna and so measurements intended to characterise aberration angles will be compromised by this additional change in the datum angle. Therefore, mounts have to be devised that do not alter the centre of gravity of the AUT whether it is measured with or without the radome present. For a radome to be fully characterised in this way requires the use of separate translation/rotation stages for the antenna and its radome. Assuming this can be done insertion loss measurements are simple comparisons and pattern measurements will indicate the extent to which blockage is degrading the pattern. However, the extent of blockage aberration, the magnitude and direction of flash lobes will be a function of the angles through which the antenna beam is pointing. Therefore, to fully characterise the response of the antenna installed behind a radome is a huge task. This means that most radome measurements are diagnostic in form or designed to validate already produced prediction of the antennas performance behind a radome by fully characterising a

limited range of scenarios by measurement that can then be compared to extensive comprehensive modelled results.

The standard radome test parameters are:

Reflectivity: Change in VSWR at the antenna input port with and without the radome present.

Transmission efficiency: Percentage of transmission power that passes through the radome determined by with and without measurement.

Pattern distortion: Change in the radiation pattern of the antenna with and without the radome installed. Pattern parameters to be measured are beam width, side lobe level, image lobes, and tracking null fill-in.

Beam deflection: Boresight and tracking null shift with and without radome.

The CATR offers an efficient, environmentally controllable test facility for a radome measurement. However, the CATR quiet zone volume needs to be sufficiently large to be able to enclose the radome and antenna in all the radome scanning positions.

5.7.2 Positioner overview – mechanically scanned AUTs

A radome positioner system is shown in Figure 5.80 where independent control of the radome position is provided and the antenna has its own two-axis positioner termed a *gimbal mount*. An example of a gimbal mount is shown in Figure 5.81, where the centre of rotation of gimbal corresponds to the centre of actual antenna's mount. Gimbals are often constructed from direct drive motors offering very fast

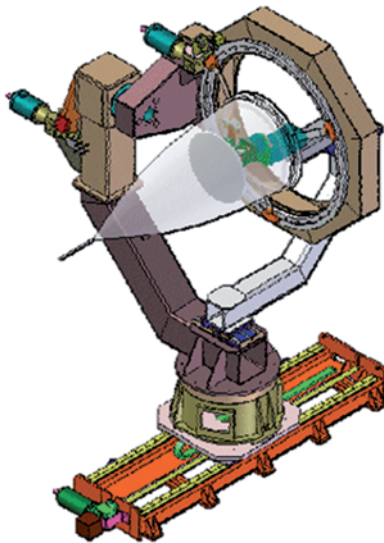


Figure 5.80 Radome test positioner which provides independent control of radome orientation from the gimbal mounted AUT (Courtesy NSI-MI Technologies LLC)

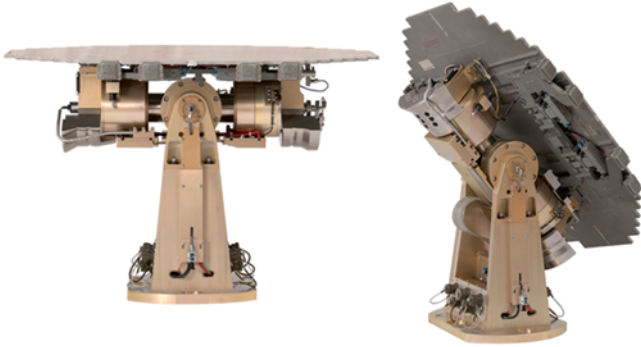


Figure 5.81 2-Axis gimbol positioner with direct drive motors and $\pm 70^\circ$ of travel in both axes (Courtesy NSI-MI Technologies LLC)

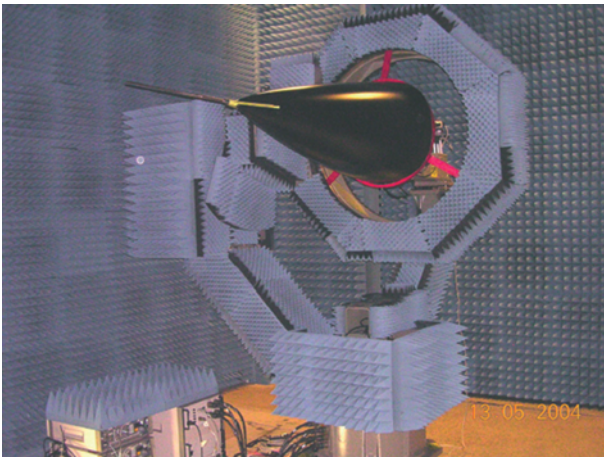


Figure 5.82 Radome positioner of Figure 5.80 with RAM and radome mounted in a CATR (Courtesy NSI-MI Technologies LLC)

rates of movement and wide angles of coverage. An example of an aircraft radome mounted on a radome test positioner is shown in Figure 5.82 (with radome) and Figure 5.83 (without radome).

There are various ways that the antenna parameters can be measured using the radome test positioner; however, in this text we shall concentrate on using the CATR as it is one of the more efficient and commonly encountered approaches.

5.7.3 Measurement of reflectivity, transmission efficiency, pattern distortion, boresight shift, flash lobe

5.7.3.1 Reflectivity

This is a measure of the change in magnitude of the reflection coefficient at each antenna port with and without the radome installed for a given position of antenna

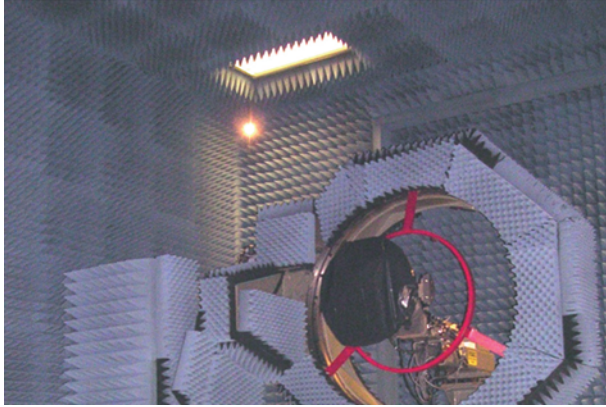


Figure 5.83 Radome positioner of Figure 5.82 with radome removed to view gimbal mounted antenna (Courtesy NSI-MI Technologies LLC)

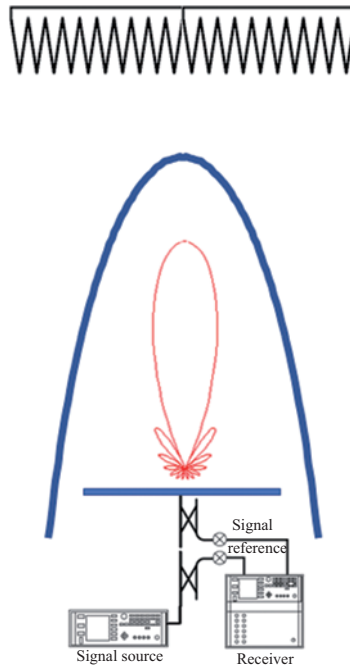


Figure 5.84 Reflectivity measurement taken with and without radome

with respect to radome. The measurement setup is illustrated in Figure 5.84 for the case with the radome installed. This method can employ either high-quality absorber and/or the use of background subtraction of the case without the radome. For a fixed antenna and radome structure (e.g. for the case of a communications

antenna), this is a relatively simple measurement that is performed as a function of frequency. For a scanning antenna within a radome, the measurements need to be made over a range of scan angles with respect to radome, whilst simultaneously ensuring that the absorber is kept normal to the antennas main beam direction. In this case, the return loss of the radome cannot be effectively measured but the main impact of this return loss is clear in range measurements. The geometry of the radome means that the reflections from the radome walls will produce flash lobes in the antenna pattern. These flash lobes will impact on system performance particularly in terms of range Doppler processing for medium and high PRF radar.

5.7.3.2 Transmission efficiency

Here, we compare the measured boresight power level with and without the radome taking into account any skewing of the boresight direction resulting from diffraction, absorption and reflection as the field passes through the radome. The relative change in angle of arrival is measured in the boresight shift measurement described below. For a scanning antenna within a radome, measurements need to be made over a range of scan angles with respect to radome. The measurement is illustrated in Figure 5.85. The requirement to measure a 2D solid angle for a large number of scan angles is one of the more time consuming aspects of radome testing that lends itself to characterisation with a CATR as opposed to, for example, spherical near-field measurement. It is possible to use a near-field system and cylindrical near-field test systems have been used for this application however the additional time

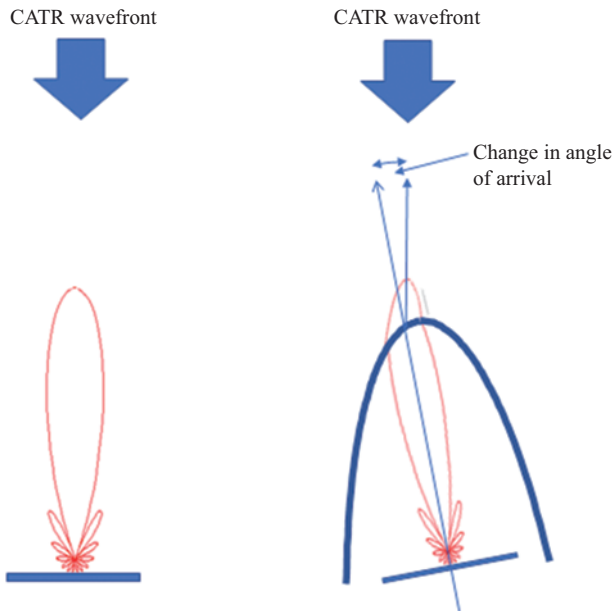


Figure 5.85 *Transmission efficiency measurement taken with and without radome*

required to perform the two-dimensional near-field acquisition tends to be a detractor.

5.7.3.3 Pattern distortion

This is a measure of the full 3D radiation pattern with and without the radome to determine the effect on the radiation pattern main beam and side lobes. For a scanning antenna within a radome measurements need to be made over a range of scan angles with respect to radome.

5.7.3.4 Boresight shift

Here, we start with the gimbal mounted tracking antenna without radome aligned to the CATR wavefront. The radome is then added and then as the radome is rotated the CATR wavefront is tracked with the antenna gimbal. The azimuth and elevation angles of the tracker determine the boresight shift for different radome orientations with respect to the CATR wavefront.

5.7.3.5 Flash lobe

With the antenna plus radome in transmit mode flash lobes result from a component of the reflected ray from the radomes inner surface (made up of reflections from the inner and out surface) finding its way via transmission through the radome and hence adding to the far-field radiation pattern. This can result from either direct transmission of the internally reflected ray or through multiple internal bounces before exiting the radome. An illustration of flash lobes can be seen in Figure 5.86 where the radiation pattern of a 900 mm array antenna is shown with and without an ogive radome with the antenna main beam pointing along its nose. This effect is most commonly encountered when using ogive radomes and is a function of the

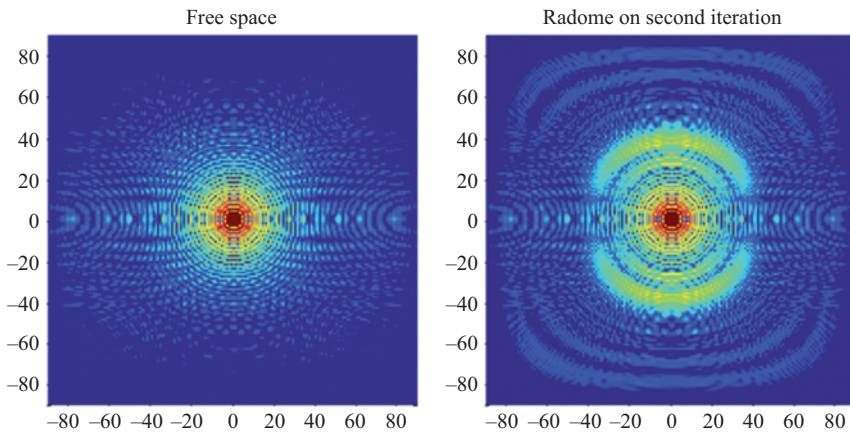


Figure 5.86 Left: radiation pattern of 900 mm array antenna. Right: antenna with beam pointing along the nose of a 3 m ogive radome of diameter 1,200 mm [75]

scan angle, radome surface profile, polarisation of incident field and the frequency. The main rings close to the main beam correspond to the first flash lobe region. The second flash lobe region due to second-order internal bounce is clearly discernible as a set of fainter secondary rings that are visible at wider pattern angles. Here, the measurement is undertaken as in Section 5.7.3.3. The position of the first flash lobe can, in many cases involving ogive radomes, be estimated as being twice that of the scan angle of the antenna. This means that as the antenna scans, quite quickly, the flash lobes shift out and appear in the back half-space beyond $\theta = 90^\circ$, meaning that very often large, possibly near full sphere, angular spans are needed to fully characterise the behaviour of the antenna radome assembly.

5.7.4 *Examples of radome measurement ranges*

Radomes can take a variety of forms depending on their specific application. For a nose-cone type radome, an example of a typical test system is shown in Figure 5.82. Conversely, an example of an airborne radome for satellite communications applications is shown in Figure 5.87. Often custom mechanical support equipment is required containing a gimbaled test antenna to support the radome during the measurements. As illustrated in the above sections, a large number of measurements need to be made to accommodate the various combinations of antenna and radome orientations. Stability of the RF system and the CATR during the measurement process is vital for accurate measurements. Mechanical repeatability of ‘with and without’ radome measurements is also vital and a measurement campaign that optimises the minimum amount of radome mounting and demounting that is desirable whilst ensuring RF stability (which is particularly critical for the transmission efficiency measurements). The presentation of results can be particularly challenging and often a contour, i.e. iso-level, graph of a measurement parameter plotted over the unrolled surface of the radome is used (Figure 5.88).

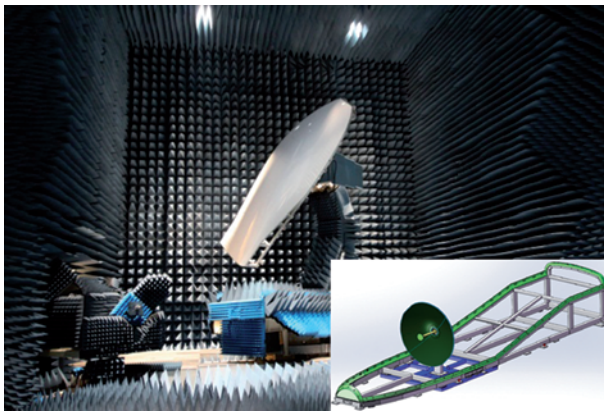


Figure 5.87 *Airborne satellite communications radome in CATR. Inset: the gimbaled antenna on radome test rig [76]*

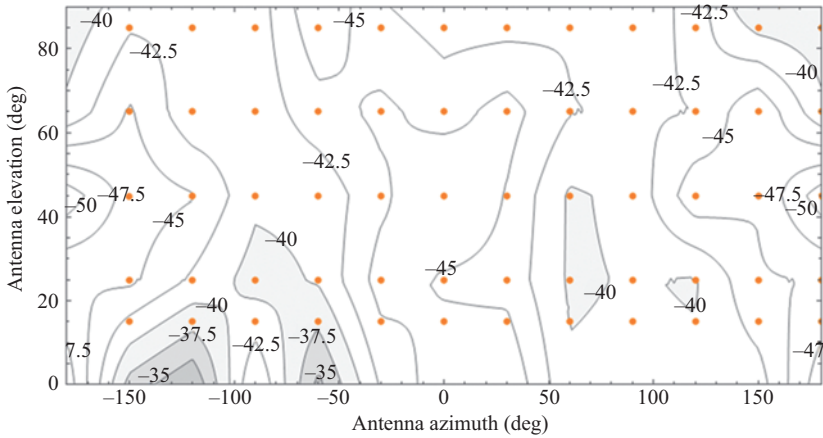


Figure 5.88 Typical contour graph for one parameter over the surface of a radome after evaluation of all the radiation patterns [77]

5.8 Satellite testing

5.8.1 Satellite and telecommunications payload testing in a CATR

The measurement of a fully assembled satellite payload parameters is highly suited to being undertaken in a compensated CATR (CCR). This form of CATR offers the low cross-polarisation required for the polarisation isolation measurement, and the long focal length of the system offers quiet zone transverse scanning to accommodate the simultaneous illumination of the antenna farm normally located on both sides of the spacecraft body.

For the measurement of the antenna patterns, the spacecraft is usually measured unpowered via an antenna test port integrated into the spacecraft design. The AUT of interest is located at the QZ centre, which is achieved by transversely moving the spacecraft on the multi-axis AUT positioner (Figure 5.89). Antenna patterns are then taken with a raster scan using the azimuth and elevation axes of the AUT positioner. Usually, a dual-polarised feed (Figure 5.41) is used to measure both polarisations simultaneously. A fast, synthesised source and range receiver is used to accommodate multi-frequency measurements during the motion scans. The antenna gain can be measured in the CCR using the ‘direct gain measurement’ method as described in Section 5.5.2.3.

The RF boresight of an antenna mounted on a spacecraft has to be aligned to that of the spacecraft body to a high precision (of order 0.01° – 0.02°). This is usually achieved optically using a theodolite and mirror cubes mounted on the spacecraft body. With the antenna placed in the measured AUT RF boresight direction, the theodolites measure the location of the spacecraft with respect to the CCR range axis to thus determine the pointing. The CCR range axis having been

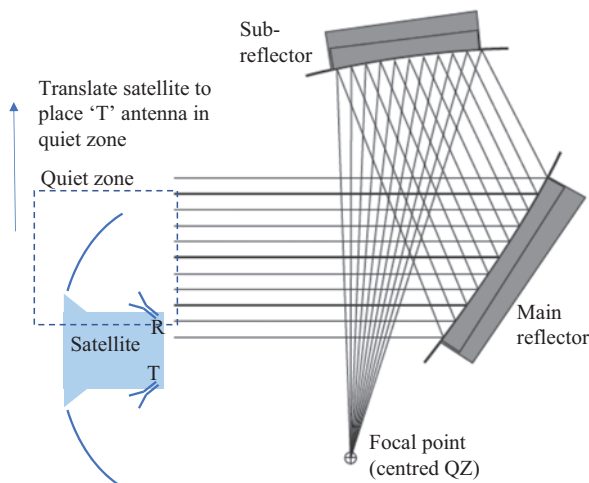


Figure 5.89 Satellite antenna pattern measurement setup in a compensated CATR

previously measured, for a given feed position, using, for example, the RCS of a flat plate as described in Section 5.4.4.

Recently, measurement facilities that combine both CCR and planar NF measurement systems in the same chamber have been constructed, for example, the European Space Agency HERTZ facility. Reference [78] compares the payload measurement process using both CCR and Planar NF, and Van Rensburg [79] discusses the process of group delay measurement in a planar NF facility. In the following sections, we consider the measurement of the various payload parameters that are more commonly encountered. Several useful publications that cover this topic in further detail are [78,80–82].

5.8.2 End-to-end testing and the compensated CATR

Because of the long effective focal length of the CCR, it is possible, by movement of the CCR feed, to scan the QZ to cover antenna farms located on either side of the spacecraft body [83], as shown in Figure 5.90. This facility thus enables complete end-to-end testing of the powered spacecraft (TWT's in linear mode) by placing a synthesised source of known power at the 'R' feed port in Figure 5.90 and then receiving the frequency translated signal from the spacecraft on the CCR 'T' feed port. As in the direct measurement of gain, we use the knowledge of the CCR's spherical path loss distance for both the T and R feed ports to calculate the free space losses for the two different frequencies for the satellites transmit and receive paths. From this, we can calculate the amplitude frequency response (AFR) [80]

$$AFR = P_T P_R G_T G_R \left(\frac{\lambda_T \lambda_R}{(4\pi)^2 R_T R_R} \right)^2 \quad (5.14)$$

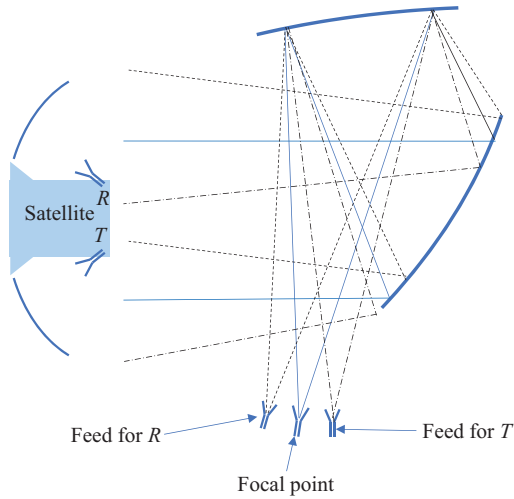


Figure 5.90 Scanned quiet zones for air-to-air link testing

where P_T is the power transmitted at CCR feed port R (power meter), P_R is the power received at CCR feed port T (power meter/spectrum analyser), G_T is the gain of CCR port R feed, G_R is the gain of CCR port T feed, R_T is the spherical wave path for CCR from the feed R port, R_R is the spherical wave path for CCR to the feed T port and λ_T and λ_R are wavelength of satellite transmit and receive frequencies, respectively.

As these equations are measuring power, the measurement needs to be first calibrated for cable and system losses.

For the case shown in Figure 5.90, the overall spacecraft does not fit within the CCR ‘boresight’ QZ and so the CCR feeds are substantially offset to relocate the QZ. For the case where the spacecraft does fit within the boresight QZ, only a small CCR feed offset is required in order to just give space for the location of the two feeds. In the former case, it is thus likely that the QZ phase front will not be aligned to the spacecraft antenna boresight, so the beam pointing loss associated with this off-boresight illumination needs to be corrected for in P_T and P_R in (5.14).

Using the same measurement satellite and CCR setup, the gain over frequency (G/F) can be measured using a vector network analyser (VNA), as shown in Figure 5.91. G/F describes the system gain consisting of uplink antenna, transponder, and downlink antenna and it is commonly measured over a certain channel bandwidth. G/F is defined as the ratio of the transmitted and received power (the S_{21} parameter of the NWA) which has to be corrected for the gain of the range antennas as well as for the free space loss on uplink and downlink paths and the losses in the measurement system [78],

$$\frac{G}{F} = S_{21} \left(\frac{1}{G_T G_R} \right) \left(\frac{(4\pi)^2 R_T R_R}{\lambda_T \lambda_R} \right)^2 \quad (5.15)$$

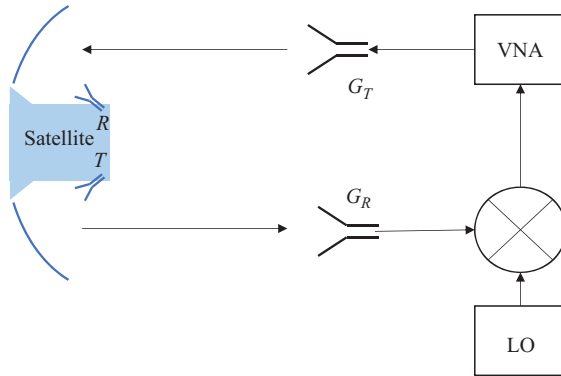


Figure 5.91 Gain over frequency setup (CCR reflectors of Figure 5.90 not shown for simplicity)

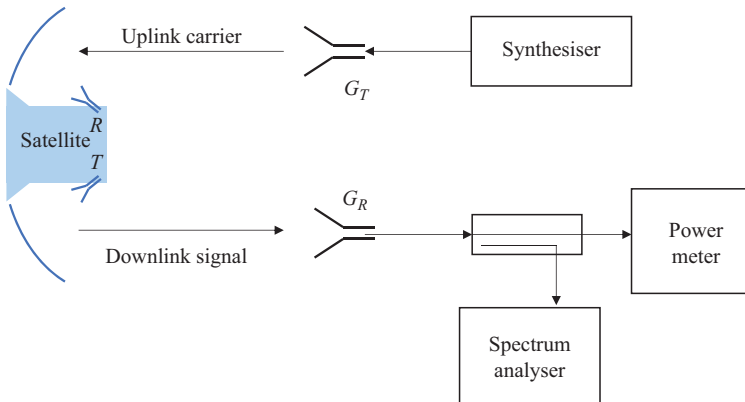


Figure 5.92 EIRP measurement setup (CCR reflectors of Figure 5.90 not shown for simplicity)

As in the AFR case above, the ratio of $P_R/P_T = S_{21}$ needs to be corrected for any beam pointing loss associated with off-boresight illumination of the spacecraft antennas by the CCR feed displacements. Again the measurement needs to be first calibrated for cable and system losses (which include in this case the loss through the mixer).

5.8.3 EIRP measurements

The effective isotropic radiated power (EIRP) is the maximum power that can be transmitted by the satellite over a certain antenna and using a certain transponder. This can be measured in an air-to-air configuration in the CCR, and in Figure 5.92, the synthesised source is used to drive the chosen receive antenna and transponder combination into saturation. The satellite transmit antenna boresight is then aligned

to the CCR T port wavefront direction using the AUT positioner and the down link signal received by the CCR is connected to a power meter. A spectrum analyser is also connected by a directional coupler in order to monitor the linearity of the received signal.

The point of saturation describes the point of the maximum output power of the TWT amplifier which is found at the peak of a nonlinear curve. The most sensitive method to determine this point is to transmit an AM modulated carrier and detect this with a spectrum analyser to detect the maximum AM suppression of the first sidebands of the carrier signal as retransmitted by the satellite down link [82]. To reach saturation, the satellites chosen TWT gain is increased in small power level steps via satellite electrical ground support equipment (EGSE) command until the point of maximum AM-suppression is reached. The fine tuning can be performed by increasing or decreasing the transmitted uplink power level. The EIRP is then given by

$$\text{EIRP} = (4\pi R_R / \lambda_T)^2 P_R / G_R \quad (5.16)$$

Since the uplink path is used just to saturate the transponder, if only one radiated channel is available a test coupler built into the payload receiver could be used in order to drive the payload into saturation. Again the measurement needs to be first calibrated for cable and system losses.

5.8.4 SFD measurements

The saturating flux density (SFD) is the power density that is required at the uplink antenna of the satellite to drive a given transponder into saturation. The setup is the same as Figure 5.92 but now the satellite receive antenna is aligned to the CCR R port wavefront direction using the AUT positioner. The SFD is then given by

$$\text{SFD} = P_T G_T (1/4\pi R_T^2) \quad (5.17)$$

Since the downlink path is used just to detect saturation of the transponder, if only one radiated channel is available a test coupler built into the payload transmitter could be used in order to detect saturation. Again, the measurement needs to be first calibrated for cable and system losses and the value of P_T determined via a calibrated power meter.

5.8.5 G/T measurements

The gain over noise temperature (G/T) gives the figure of merit of the satellite receiver. It is determined with the satellite receive antenna aligned with the boresight of the CCR port R wavefront using three power measurements in the case of a fixed gain transponder. The measurement setup is shown in Figure 5.93, first the noise power of the measurement equipment P_1 is measured, second the noise power of the equipment and the satellite P_2 is measured, and finally the overall noise power is measured together with the carrier signal resulting in P_3 .

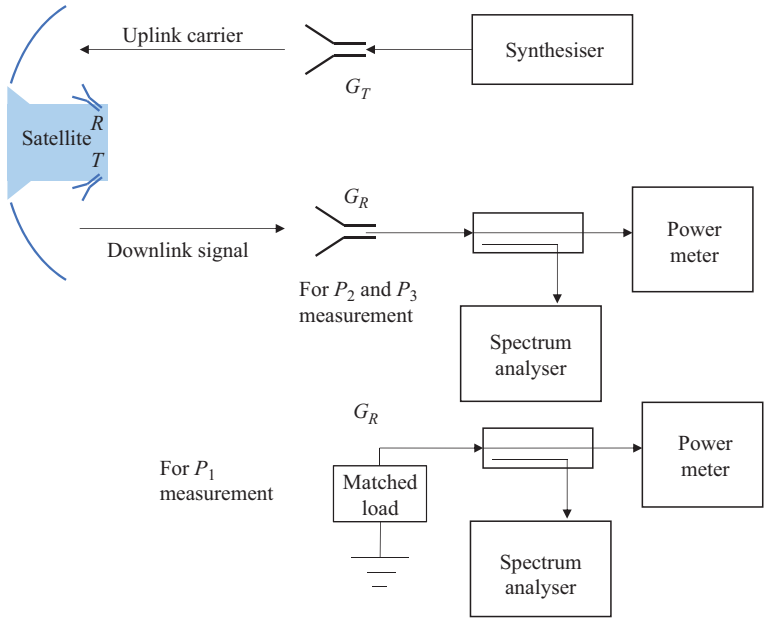


Figure 5.93 *G/T measurement setup*

In Figure 5.93, the synthesiser provides an uplink signal via the CCR R port, the downlink is then received at the CCR T port, amplified, and then connected to a spectrum analyser for down conversion and measurement of the IF power. To measure P_1 the CCR T port, antenna is removed and terminated in a matched load, thus measuring the noise of the measurement system. With the CCR T port antenna reconnected, and the satellite configured with the transponder connected to the transmit antenna power P_2 is measured. Finally, with the carrier present and transmitted through the transponder power $EIRP$ and P_3 is measured. In all three power measurements, the same bandwidth B is used via the spectrum analyser and power meter. The G/T is then given by

$$\frac{G}{T} = \frac{kB}{EIRP} \frac{P_3 - P_2}{P_2 - P_1} \left(\frac{4\pi R_R}{\lambda_R} \right)^2 \tag{5.18}$$

where the EIRP is measured and calculated as in Section 5.8.3 for the particular transponder operating point.

5.8.6 Group delay measurements

Group delay (GD) is defined as the negative of the rate of change of transmission phase angle with respect to frequency. Ideally, the GD of a component or system should be the same for all frequency components if distortion at the output is to be avoided. GD can be considered to represent the delay of the envelope of the

modulating signal and serves as a transfer function to characterise signal dispersion. Mathematically, GD can be expressed as

$$\text{GD}(f) = -\frac{1}{2\pi} \frac{d\Phi(f)}{df} \quad (5.19)$$

where $\Phi(f)$ defines the insertion phase (the phase of S_{21}) in radians at frequency f . For practical numerical cases, (5.19) can be approximated by a sided difference where the frequency step is made as small as is practical,

$$\text{GD}(f) = -\frac{1}{2\pi} \frac{\Phi(f_1) - \Phi(f_0)}{f_1 - f_0} \quad (5.20)$$

Alternatively, and providing the frequency points are monotonic and equally spaced, a more accurate numerical derivative can be obtained by taking central differencing (with sided-differences being taken at the extremities of the data arrays) [79]

$$\text{GD}(f) = -\frac{1}{2\pi} \frac{\Phi(f_1) - \Phi(f_{-1})}{f_1 - f_{-1}} \quad (5.21)$$

The measurement setup is the same as the G/F case (Figure 5.91) except that we measure the angle (Φ_{21} in radians) of S_{21} rather than the magnitude. We need to first calibrate out all the system GD and then measure and remove the GD of both CCR horns using the following formulation to determine the GD of the satellite system:

$$\text{GD}(f) = -\frac{1}{2\pi} \frac{\Phi_{21}(f_1) - \Phi_{21}(f_0)}{f_1 - f_0} - \text{GD}_T(f) - \text{GD}_R(f) \quad (5.22)$$

The calibration out of the GD due to the mixer shown in Figure 5.91 is an import issue and can be relatively easily undertaken using modern VNA's, the details of this process are outside the scope of this text but can be found in reference [84].

5.9 OTA testing for 5G antennas

The fifth generation (5G) mobile network promises to deliver multi-Gbps data capacity [85]. Achieving this requires the widespread adoption of several new technologies with the use of higher frequency, millimetre wave, bands and more complex massive MIMO (multiple input multiple output) architectures being principal among them [85,86]. As the intended circa 10–20-fold increased in data capacity is one of the most prominent promises of the 5G roll-out, absolute data throughput is perhaps the primary figure of merit (FOM) used for the verification of network performance [85]. The adoption of OTA communication system-level performance metrics and the tighter integration between the physically smaller massive MIMO array antenna and the increasingly complex active electronics

means that widespread interest in classical antenna performance parameters is waning. Instead, focus is shifting towards alternative communication system level parameters such as far-field error vector magnitude (EVM), bit error rate (BER), and signal-to-interference-plus-noise-ratio, which predicate the use of quadrature amplitude modulation (QAM) waveforms of varying orders and more directly relate to data rates [86].

This, therefore, represents a very significant shift for the far-field antenna measurement community where hitherto monochromatic CW, or at most a pulsed CW, RF signal was used almost exclusively. The requirement for broadband orthogonal frequency-division multiplexing (OFDM) with QAM schemes when combined with the requirement that system performance be determined in far-field mode has resulted in the recent, and very significant, resurgence of interest in the CATR. CATRs have the inherent advantage that they offer a way to determine real-time, broadband, far-field performance at a very much reduced, fixed, range length. This is of particular importance for 5G applications where testing the higher-frequency, larger apertures required by active mm-wave massive-MIMO antennas results in far-field distances that are very much larger than those which were previously required when working with prior generations of networks at sub-6 GHz frequencies and which cannot otherwise be conveniently realised economically indoors. This is illustrated in Table 5.2 where far-field distances for typical 26 and 39 GHz MIMO antennas are tabulated.

We have seen in this chapter (as well as Section 13.2) that CATR modelling is a well-established, mature discipline capable of determining quiet-zone quality and measurement uncertainties for a range of typical antenna parameters for a known antenna under test (AUT)/CATR combination. However, it has not previously been possible to equate this to the effect that this would have on OTA system-level properties such as EVM and BER. Here, we present the results of a recent study that extended the work of Section 13.2 to include these system performance metrics

Table 5.2 Far-field distances for typical MIMO antennas (entries in green indicate those that could be achieved economically in an indoor far-field chamber)

Frequency (GHz)	Array dimension (cm)	Far-Field distance (m)	Path loss (dB)
26	10	1.7	66
	15	3.9	73
	20	6.9	78
39	10	2.6	73
	15	5.9	80
	20	10.4	85

to enable the design and optimisation of a CATR test system that is capable of providing sufficient reliability, repeatability and an acceptable level of measurement uncertainty for a given 5G OTA testing application. Preliminary results are presented and discussed.

5.9.1 Simulating a communications system using OFDM

OFDM is a very flexible and efficient modulation technique that is at the heart of all major wireless and wired standards used today including 5G. Examples of standards that use OFDM are 4G, LTE, 5G, WiMAX, Video Broadcast and ADSL.

OFDM separates the channel bandwidth into multiple narrow-band subcarriers to transmit the information. A single data stream is split across several separate narrowband channels at different frequencies. The original data stream of bits is transmitted in parallel but at lower speed in each sub-stream when compared to the original. Thus, we need to simulate the behaviour of the CATR and AUT combination at *each of these frequencies* to be able to simulate a 5G application.

In Section 13.2, we presented frequency domain modelling technique and this can be extended by repeating the simulations at various frequencies to cover a communications bandwidth, which typically might be 400 MHz. Over such a band, we would expect to see that the CATR:

- Feed pattern remains fairly stable with frequency.
- Amplitude taper therefore is fairly stable with frequency.
- Amplitude and phase ripple will vary with frequency (due to edge diffraction effects).
- AUT antenna gain will vary with frequency (typically increases for an aperture antenna).
- AUT location of side lobes changes with frequency.

So, to model the communications link, we need to repeat the simulation of coupling (S_{21}) at boresight (or any other fixed angle) across a band of frequencies, which could be 200 or so over the 400 MHz bandwidth. Now, 200 complete CEM CATR AUT simulations are computationally intensive. However, we have found that implementing the processing in parallel on a typical PC can lead to circa $600\times$ speed up, leading to single frequency modelling times for a 100 wavelength CATR and 25 wavelength AUT of the order of 7 s. This thus makes simulating several hundred frequencies completely viable, giving several hundred S_{21} values over the communications band.

Modern communication systems typically use QAM schemes. So, each OFDM sub-carrier, i.e. signal, is modulated with for example 256 QAM.

Figure 5.94 shows a typical constellation diagram for both QPSK and 256 QAM in the presence of noise. Whilst it is possible to create these from the S_{21} CATR AUT simulations what is actually needed is a figure of merit for the whole link. EVM is a measure of the modulator or demodulator performance of an impaired signal. The EVM is a modulation-quality metric that measures the error between the transmitted signal and the ideal signal, calculated as the magnitude

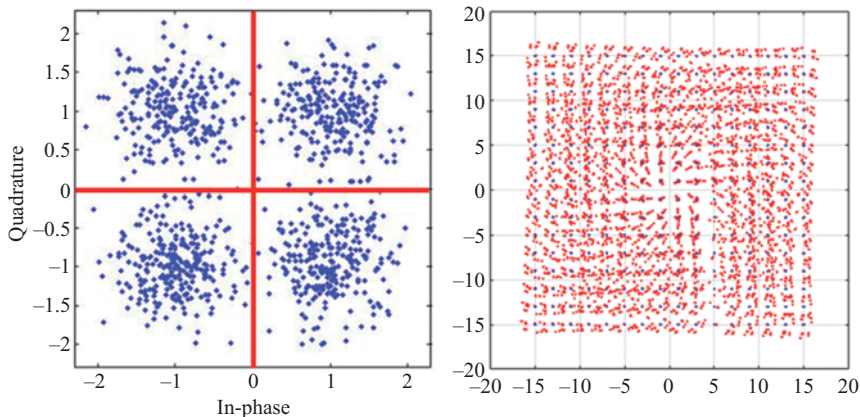


Figure 5.94 Constellation diagram for (left) QPSK with noise added; (right) 256 QAM with noise added

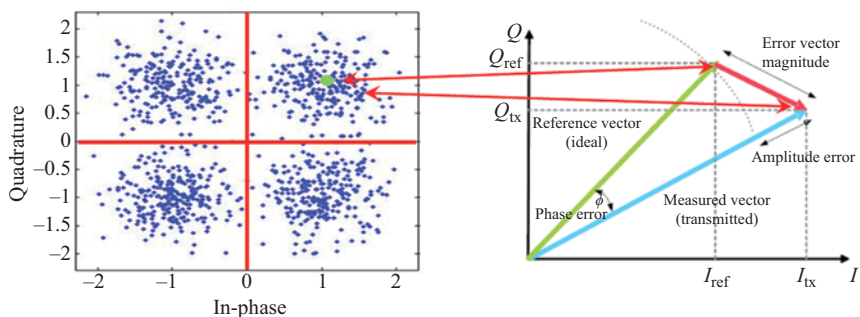


Figure 5.95 Illustration of EVM for one symbol in the constellation diagram

of the vector difference between the transmitted and reference vectors, represented on a complex plane (i.e. constellation diagram). In practical measurements, a modulated reference data stream (or vector set r_k , where $k = 0, \dots, N$ symbols) is transmitted through the transmit chain. The distorted signal m_k at the antenna output port is then detected, demodulated and quantified on the constellation diagram corresponding to the modulation scheme used in the test vector, against the reference data (see Figure 5.95). In this example, we choose to modulate the signal using OFDM and 256 QAM, and this is illustrated in Figure 5.96.

To see how this signal is affected by the signal being transmitted through the CATR and received by the AUT, we need to determine the complex S_{21} of this transmission path so that the magnitude and phase change experienced by each sub-carrier frequency can be established. A typical S_{21} result for the CATR AUT measurement is shown in Figure 5.97. Here, a simple linear

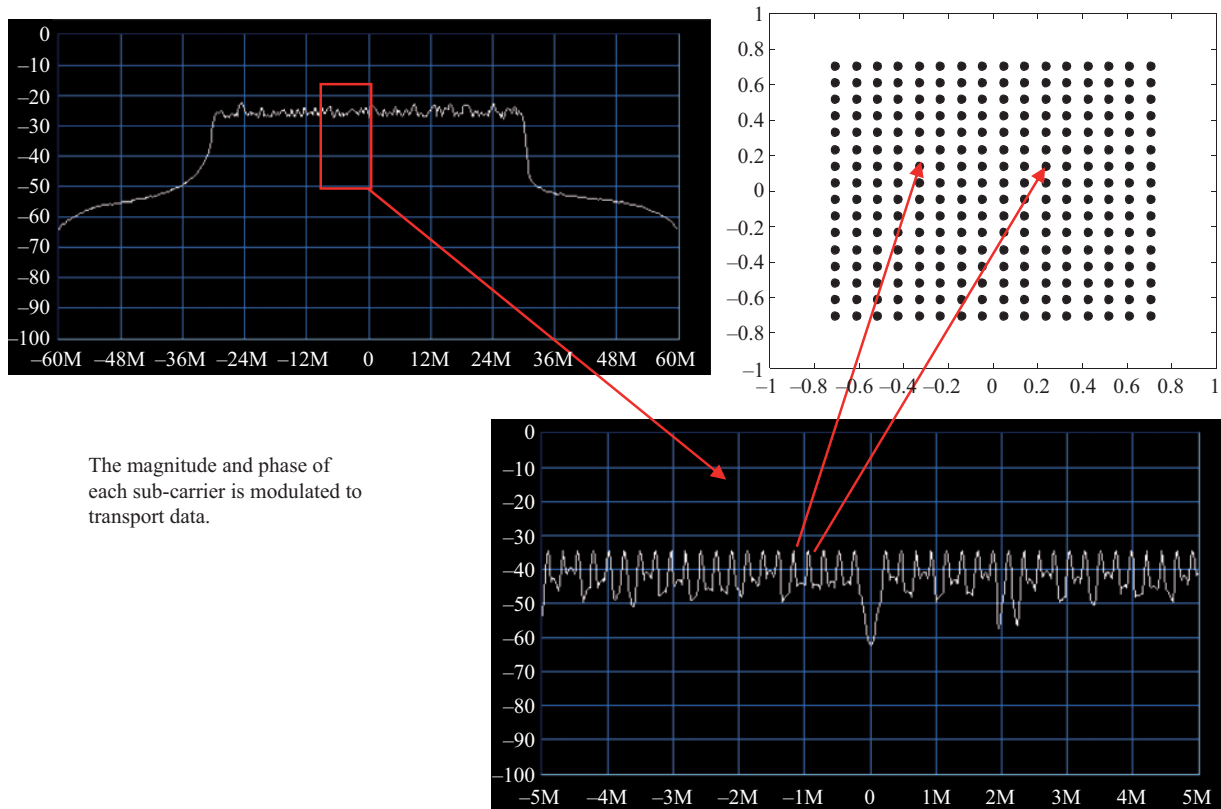


Figure 5.96 Orthogonal frequency-division multiplexing (OFDM) and Quadrature amplitude modulation (QAM) provide 256 QAM modulation as the basis for the EVM test signal

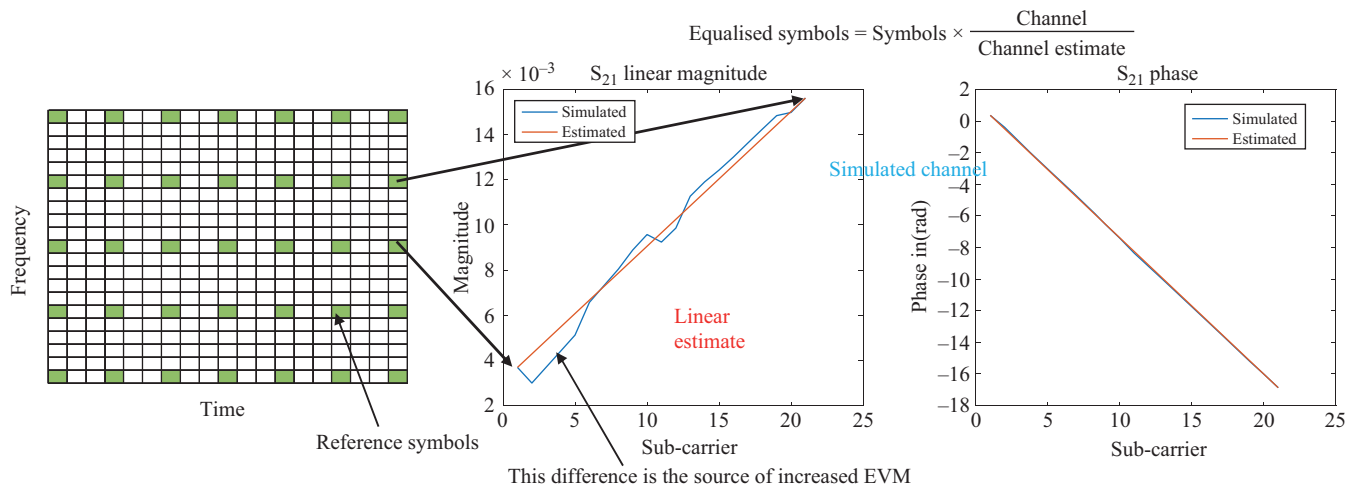


Figure 5.97 S_{21} of CATR AUT measurement channel showing the simulated result and a simple linear estimation for the equalisation process required in order to recover the signal

estimation is used for the equalisation process which is required in order to recover the signal.

The test signal we will use to determine the EVM is an image, as the human eye is very sensitive at discerning errors. Our image signal is a 512×512 RGB (red green blue, 8 bits per colour) modulated with 256 QAM (8 bits per symbol) with image data mapped byte by byte onto the symbols. Each symbol error produces an error in one colour channel of a pixel. Each frequency in the input file is treated as a separate sub-carrier. Symbols are transmitted by sequentially looping through the available sub-carriers until all the data has been transmitted. The received signal has to be equalised to remove the influence of the channel and recover the original data. Transmission attenuates the signal (reduces the size of the constellation diagram) and changes the phase of the signal (rotates the constellation diagram); therefore, we need to equalise the received signal to recover the transmitted information. Thus, quality of the equalisation used directly affects the result and the estimated EVM value. If we take the simple linear equalisation shown in Figure 5.97, the difference between this and the actual S_{21} is the source of the EVM at each sub-carrier. To calculate a single EVM number, we take the RMS value over all the symbols forming the transmitted image. This is defined in Figure 5.98.

We can therefore assess the impact of CATR plus AUT on a measurement by

- Calculating EVM (%) – RF measure of performance.
- Calculating bit error rate (%) – digital measure of performance.
- Data throughput $\sim R(1 - \text{BER}/100)$, where R is the data rate (if any errors occur, then we need to resend and throughput drops further).
- Calculate image structural similarity index (normalised measure) for measuring image quality [87]. This is an objective, quantitative, holistic way of ‘looking’ at the recovered image.

Figure 5.99 shows examples of perfect and imperfect transmission through the CATR and AUT system (we here use the standard test image ‘lake’ [88]). To illustrate the change in EVM through the CATR plus AUT system, we mechanically rotate the AUT so the received signal is away from boresight. In Figures 5.100–5.104, we rotate the AUT in azimuth for 0° , 10° , 20° , 30° and 40° ,

$$\text{EVM}_{\text{RMS}} = \frac{\sqrt{\frac{1}{N} \sum_{k=1}^N (e_k)^2}}{\sqrt{\frac{1}{N} \sum_{k=1}^N (I_k^2 + Q_k^2)}} * 100$$

Difference between ideal and received symbols

$N = \text{Number of symbols}$

Ideal symbols

Figure 5.98 Definition of EVM used in our calculations

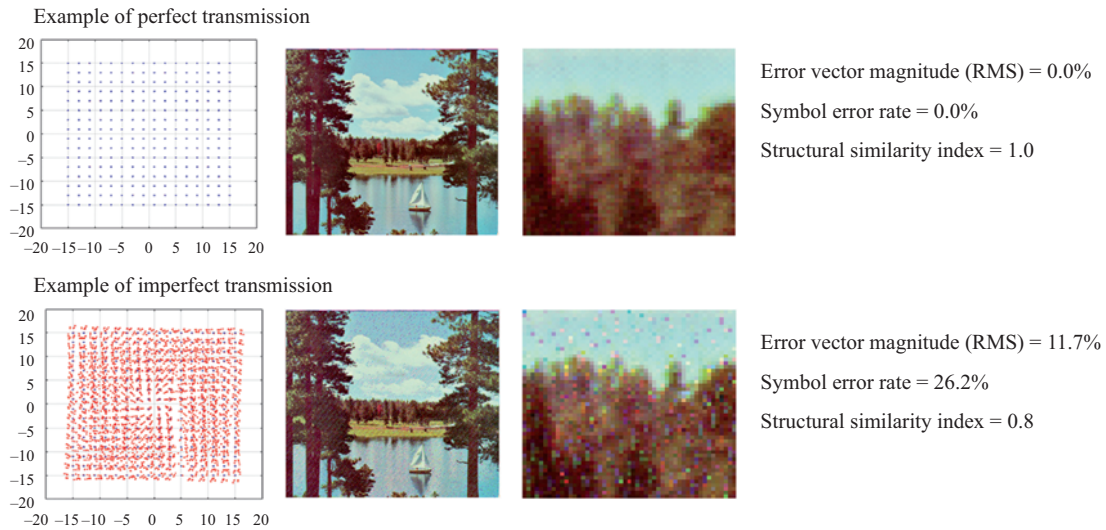


Figure 5.99 Examples of perfect and imperfect transmission through CATR/AUT system

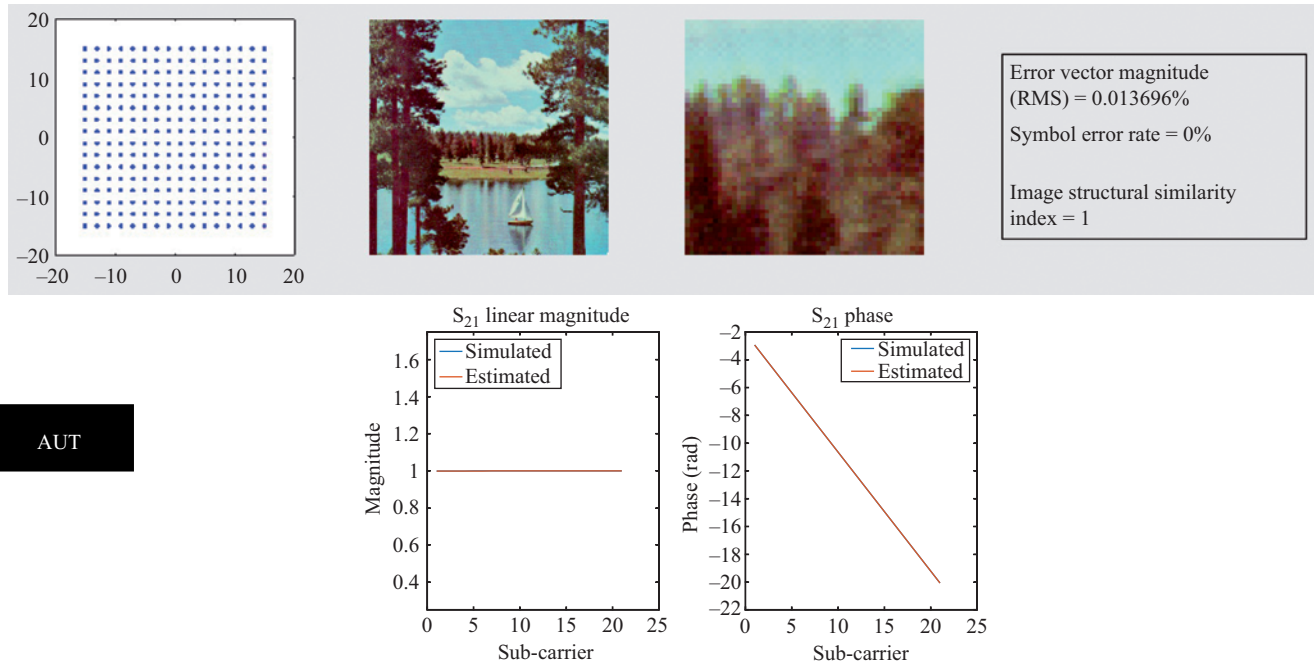
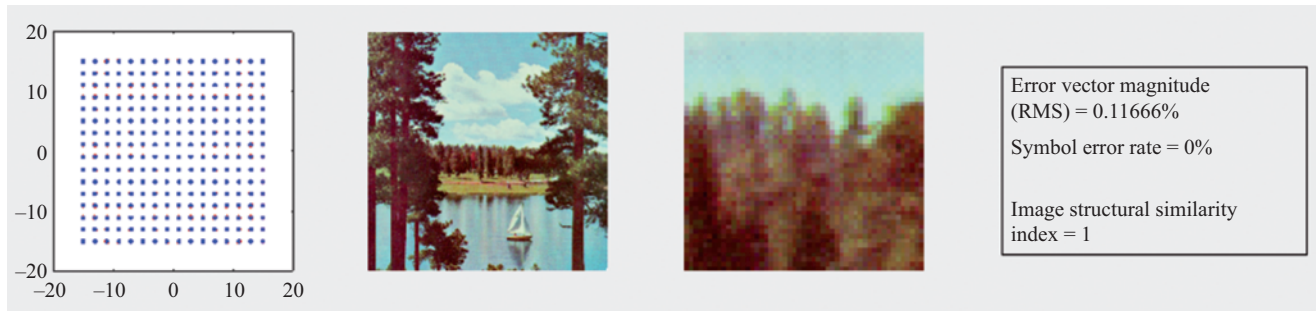


Figure 5.100 Simulated OTA performance of CATR plus AUT with AUT at boresight. At the bottom of the figure is the amplitude and phase response of the channel and the linear equalisation applied



AUT

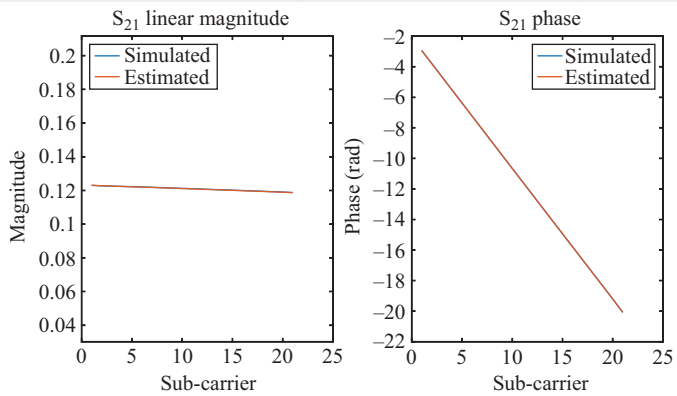


Figure 5.101 Simulated OTA performance of CATR plus AUT with AUT 10° rotation. At the bottom of the figure is the amplitude and phase response of the channel and the linear equalisation applied



AUT

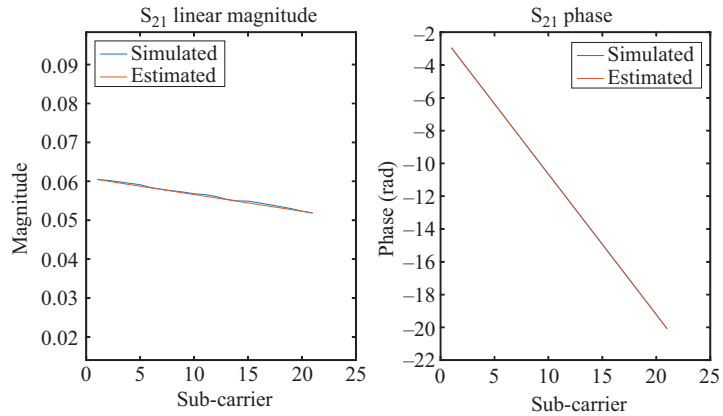


Figure 5.102 Simulated OTA performance of CATR plus AUT with AUT 20° rotation. At the bottom of the figure is the amplitude and phase response of the channel and the linear equalisation applied

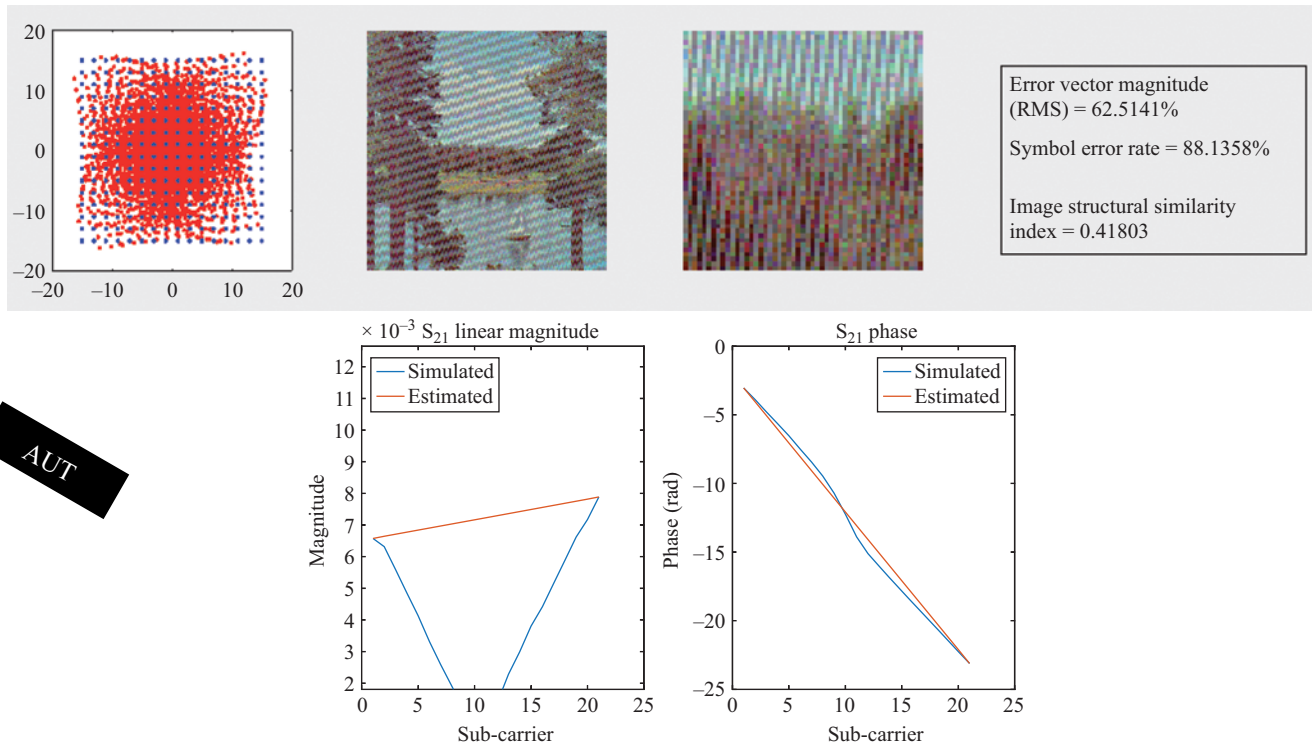
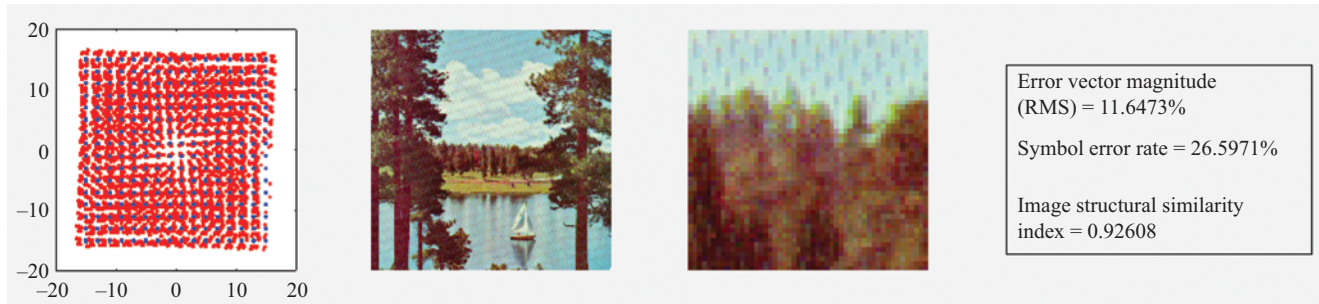


Figure 5.103 Simulated OTA performance of CATR plus AUT with AUT 30° rotation. At the bottom of the figure is the amplitude and phase response of the channel and the linear equalisation applied



AUT

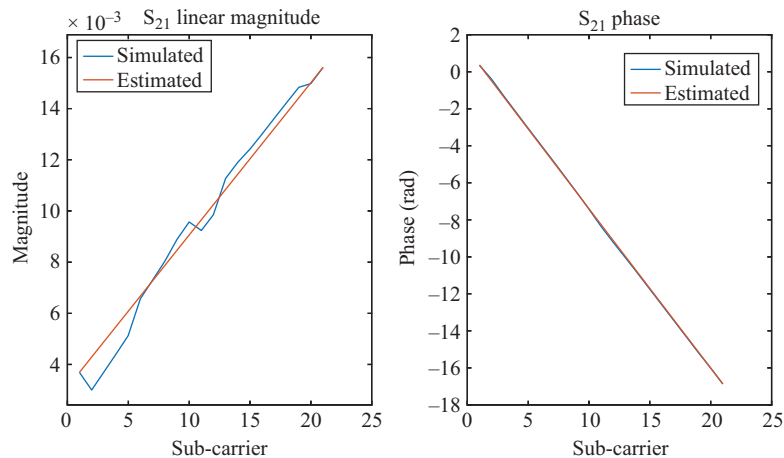


Figure 5.104 Simulated OTA performance of CATR plus AUT with AUT 40° rotation. At the bottom of the figure is the amplitude and phase response of the channel and the linear equalisation applied

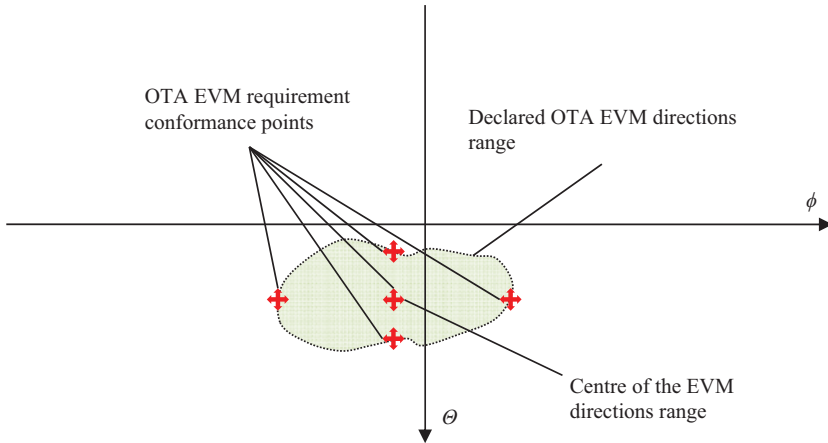


Figure 5.105 Specified EVM conformance level within a communications cell

respectively. The results for 30° are particularly bad because as we step through the frequency band we pass through a side lobe null of the AUT.

EVM is becoming an increasingly important parameter in 5G systems and current 3GPP specifications [89] are moving towards a specified EVM conformance level within a communications cell (Figure 5.105). The need to thus measure the EVM as a function of AUT beam angle will be required for manufacturers of 5G antennas to prove conformity. It is thus important to be able to access the effects of the measurement process on EVM and to optimise the design of a CATR, or any test system, that is intended for communications (5G) testing applications.

References

- [1] Woonton G.A., Borts R.B., Caruthers J.A., 'Indoor measurements of microwave antenna radiation patterns by means of a metal lens', *Journal of Applied Physics*. May 1950;**11**:428–30
- [2] Johnson R.C., 'Antenna range for providing a plane wave for antenna measurements', US Patent 3,302,205, 31 January 1967
- [3] Johnson R.C., Ecker H.A., Moore, R.A., 'Compact range techniques and measurements', *IEEE Transactions on Antennas and Propagation*. September 1969;**11L**:568–76
- [4] Johnson R.C., Ecker H.A., Hollis J.S., 'Determination of far field patterns based on near field measurements', *Proceedings of the IEEE*. December 1973;**61**:1668–94
- [5] Johnson R.C., 'Performance of a compact antenna range', *Antennas and Propagation Society International Symposium*. 1975;**13**:349–52

- [6] Scientific Atlanta Inc., 'The compact range', *Microwave Journal*. 17 October 1974;U:30–2
- [7] Hickman T.G., 'Antenna measurement accuracies on the compact range', *Antennas and Propagation Society International Symposium Digest*, Atlanta, GA; 10–12 June 1974. p. 423
- [8] Vokurka V.J., 'New compact range with cylindrical reflectors and high efficiency', *I.E.Z. Symposium on Microwaves*, Munich; November 1976
- [9] Beeckman P.A., 'Prediction of the Fresnel region field of a compact antenna test range with serrated edges', *IEE Proceedings H*. 1986;**133**:108–14
- [10] Mckay J.P., Rahmat-Samii Y., 'On the determination of quiet zone fields of a compact range antennas with serrated edges', *Proceedings of AMTA* 1989;**13**:8.19–8.24
- [11] Mckay J.P., 'On the optimization of serration-illumination taper combination for compact range reflector antennas', *1990 AMTA Proceedings*. pp. 2.39–2.44
- [12] Joy E.B., Wilson R.E., 'Shaped edge serrations for improved compact range performance', *Proceedings of the 1987 Antenna Measurement Techniques Association Meeting*, Seattle, Washington, DC; 28 September–2 October 1987. pp. 55–62
- [13] Joy E.B., Wilson R.E., 'Low side-lobe reflectors for compact ranges', *Proceedings of the 11th ESTEC Antenna Workshop on Antenna Measurements*, Gothenburg, Sweden; 20–22 June 1988. pp. 95–103
- [14] Schluper H.F., 'Verification method for the serration design of CATR reflectors', *11th AMTA Proceedings*, Monterey, CA; October 1989. pp. 10.9–10.14
- [15] Parini C.G., Philippakis M., 'The use of quiet zone prediction in the design of compact antenna test ranges', *IEE Proceedings – Microwaves, Antennas and Propagation*. 1996;**143**(3):193–9
- [16] Burnside W.D., Gilreath M., Kent B.M., Clerici G., 'Curved edge modification of compact range reflector', *IEEE Transactions on Antennas and Propagation*. 1987;**35**(2):176–82. doi:10.1109/TAP.1987.1144063
- [17] Gupta I.J., Ericksen K.P., Burnside W.D., 'A method to design blended rolled edges for compact range reflectors', *IEEE Transactions on Antennas and Propagation*. 1990;**38**(6).
- [18] Lee T.-H., Burnside W.D., 'Compact range reflector edge treatment impact on antenna and scattering measurements', *IEEE Transactions on Antennas and Propagation*. 1997;**45**(1):57–65. doi:10.1109/8.554241
- [19] Nehme H., Joy E.B., 'Range amplitude error effects on the measurement of low side lobe levels and gain', *Proceedings of the 1990 Antenna Measurement Techniques Association Meeting*, Philadelphia, PA; 8–11 October 1990. pp. 6-13–6-18
- [20] Liu X., Mai Y., Su H., *et al.*, 'Design of tri-reflector compact antenna test range for millimetre/sub-millimetre wave and THz antenna measurement', *International Workshop on Antenna Technology (iWAT)*; 2011. pp. 144–7. doi:10.1109/IWAT.2011.5752382

- [21] Liu X., Quan S., 'Spatial and angular domain simulation of the feed spillover in compact antenna test range', *9th International Symposium on Antennas Propagation and EM Theory (ISAPE)*, IEEE; 2010. pp. 159–62. doi: 10.1109/ISAPE.2010.5696421
- [22] Mahmoud M.S.A., Lee T.-H., Burnside W.D., 'Enhanced compact range reflector concept using an R-card fence: Two-dimensional case', *IEEE Transactions on Antennas and Propagation*. 2001;**49**(3):419–28. doi: 10.1109/8.918616
- [23] Mentzer J.R., 'The use of dielectric lenses in reflection measurements', *Proceedings of the IRE*. February 1953;**41**:252–6
- [24] Olver A.D., Saleeb A.A., 'Lens type compact antenna range', *Electronics Letters*. 5 July 1979;**15**:409, 10
- [25] Menzel W., Huder B., 'Compact range for millimeter-wave frequencies using a dielectric lens', *Electronics Letters*. 13 September 1984;**22**:768–9
- [26] Hirvonen T., Tuovinen J., Raisanen A., 'Lens-type compact antenna test range at MM-waves', *21st European Microwave Conference*. 1991;**2**:1079–83. doi:10.1109/EUMA.1991.336489
- [27] Lonnqvist A., Koskinen T., Hakli J., *et al.*, 'Hologram-based compact range for submillimeter-wave antenna testing', *IEEE Transactions on Antennas and Propagation*. 2005;**53**(10):3151–9. doi:10.1109/TAP.2005.856344
- [28] Hakli J., Koskinen T., Lonnqvist A., *et al.*, 'Testing of a 1.5-m reflector antenna at 322 GHz in a CATR based on a hologram', *IEEE Transactions on Antennas and Propagation*. 2005;**53**(10):3142–50. doi:10.1109/TAP.2005.856343
- [29] Koskinen T., Ala-Laurinaho J., Saily J., *et al.*, 'Experimental study on a hologram-based compact antenna test range at 650 GHz', *IEEE Transactions on Microwave Theory and Techniques*. 2005;**53**(9):2999–3006. doi:10.1109/TMTT.2005.854226
- [30] Hakli J., Koskinen T., Ala-Laurinaho J., Raisanen A.V., 'Dual reflector feed system for hologram-based compact antenna test range', *IEEE Transactions on Antennas and Propagation*. 2005;**53**(12):3940–8. doi:10.1109/TAP.2005.859900
- [31] Masanori I.Y.E., Hiroshi K., Hiroyasu A., *et al.*, 'Current performance and on-going improvements of the 8.2 m Subaru Telescope', *Publications of the Astronomical Society of Japan*. 2004;**56**:381–97
- [32] Parini C.G., Olver A.D., McNair P., Prior C.J., 'The design, construction and use of a millimetrewave compact antenna test range', *Sixth International Conference on Antennas and Propagation ICAP 89* (Conf. Publ. No. 301). 1989;**1**:345–50
- [33] Philippakis M., Parini C.G., 'Two dimensional modelling of antenna pattern measurements in a panelled compact range at millimetrewaves', *Proceedings of the IEEE Antennas and Propagation Society of International Symposium (IEEE-APS)*, Chicago, IL; 1992. pp. 317–20
- [34] Philippakis M., Parini C.G., 'Diffraction effects of a tape covering the gaps of a panelled "compact range" operating at millimetre waves', *IEE Proceedings of the Microwaves, Antennas and Propagation*. 1994;**141**(2):114–22

- [35] Black D.N., Joy E.B., 'A model for the quiet zone effect of gaps in compact range reflectors', *Proceedings of the 1988 Antenna Measurement Techniques Association Meeting*, Atlanta, GA, 12–16 September 1988. pp. 9-15–9-20
- [36] 'Agilent time domain analysis using a network analyzer', Application Note 1287-12; 2012
- [37] Chang D.-C., Liao C.-H., Wu C.-C., 'Compact antenna test range without reflector edge treatment and RF anechoic chamber', *IEEE Antennas and Propagation Magazine*. 2004;**46**(4):27–37. doi:10.1109/MAP.2004.1373997
- [38] Waiyapattanakorn C., Parini C.G., 'Theoretical and experimental investigations of using time domain gating in antenna pattern measurements', *IEE Eighth International Conference on Antennas and Propagation (ICAP)*. 1993;**1**:327–30
- [39] Hartmann J., Habersack J., Steiner H.-J., 'Antenna measurement in compact ranges', *Workshop on Space Borne Antennae Technologies and Measurement Techniques*, 18 April 2002, ISRO, Ahmedabad, India
- [40] Multari M., Migliaccio C., Dauvignac J.-Y., *et al.*, 'Investigation of low cost compact base W-band', *EuCAP Antennas and Propagation*. 2006;1–6. doi:10.1109/EUCAP.2006.4584685
- [41] Philippakis M., Parini C.G., 'Compact antenna range performance evaluation using simulated pattern measurements', *IEE Proceedings on Microwaves, Antennas and Propagation*. 1996;**143**(3):200–6. doi:10.1049/ip-map:19960398
- [42] Philippakis M., 'The effects of diffraction on the performance of compact antenna test ranges', PhD thesis, University of London; 1995
- [43] Clarke R., Brown J., *Diffraction Theory and Antennas*. Sussex, England: Ellis Horwood; 1980
- [44] Parini C.G., Philippakis M., 'The use of quiet zone prediction in the design of compact antenna test ranges', *IEE Proceedings on Microwaves, Antennas and Propagation*. 1996;**143**(3):193–9
- [45] The GRASP reflector antenna software package, TICRA, Denmark, <http://www.ticra.com/products/software/grasp>
- [46] Wilson R.E., Black D.N., Joy E.B., Guler M.G., 'Generating linear probing data from spherical probing data', *Proceedings of the 1992 Antenna Measurement Technique Association Meeting*, Columbus, OH, 19–23 October 1992. pp. 7-22–7-26
- [47] Ala-Laurinaho J., Heinonen J., Häkli J., *et al.*, 'A 650 GHz hologram compact antenna test range, task 5 and 6 report: Fabrication of hologram CATR elements and installation and verification of hologram CATR', ESA contract no. 19131/05/NL/LvH; March 2007
- [48] Tamminen A., Lönnqvist A., Mallat J., Räisänen A.V., 'Monostatic reflectivity and transmittance of radar absorbing materials at 650 GHz', *IEEE Transactions on Microwave Theory and Techniques*. March 2008;**56**(3):632–7
- [49] Capozzoli A., D'Elia G., Liseno A., 'Phaseless characterisation of compact antenna test ranges', *IET Microwaves, Antennas & Propagation*. 2007;**1**(4): 860–6. doi:10.1049/iet-map:20070002

- [50] Balanis C.A., Birtcher C.R., Lam K.W., Vokurka V.J., 'Error determination and analysis techniques for RCS measurements', *1989 AMTA Proceedings*, Monterey, CA
- [51] Lee T.-H., Clark T.L., Burnside W.D., Gupta I.J., 'Critical range evaluation using a diagonal flat plate', *IEEE Transactions on Antennas and Propagation*. 1992;**40**(8):966–74. doi:10.1109/8.163435
- [52] van de Griendt M.A.J., Vokurka V.J., Reddy J., Lemanczyk J., 'Evaluation of a CPTR using an RCS flat plate method', *18th AMTA Proceedings*. 1996;329–34
- [53] Lee T.-H., Burnside W.D., 'Stray signal requirements for compact range reflectors based on RCS measurement errors', *IEEE Transactions on Antennas and Propagation*. 1991;**39**(8):1193–1202. doi:10.1109/8.97355
- [54] Gregson S.F., Dupuy J., Parini C.G., Newell A.C., Hindman G.E., 'Application of mathematical absorber reflection suppression to far-field antenna measurements', *Loughborough Antennas and Propagation Conference (LAPC)*, 2011. pp. 1–4. doi:10.1109/LAPC.2011.6114016
- [55] Gregson S.F., Newell A.C., Hindman G.E., Carey M.J., 'Extension of the mathematical absorber reflection suppression technique to the planar near-field geometry', *2010 AMTA Proceedings*, Atlanta, GA; October 2010
- [56] Gregson S.F., Newell A.C., Hindman G.E., Carey M.J., 'Application of mathematical absorber reflection suppression to planar near-field antenna measurements', *5th European Conference on Antennas and Propagation*, Rome, 11–15 April 2011
- [57] Appel-Hansen J., 'Reflectivity level of radio anechoic chambers', *IEEE Transactions on Antennas and Propagation*. July 1973;AP-21(4):490–8
- [58] Black D.N., Joy E.B., 'Test zone field compensation', *IEEE Transactions on Antennas and Propagation*. April 1995;**43**(4):362–8
- [59] Dirix M., Dallmann T., Pamp J., Heberling D., 'Comparison of APC and feed-APC using field probing measurements of the quiet zone', *7th European Conference on Antennas and Propagation (EuCAP)*, 2013. pp. 4081–4
- [60] Viikari V., Hakli J., Ala-Laurinaho J., Mallat J., Raisanen A.V., 'A feed scanning based APC technique for compact antenna test ranges', *IEEE Transactions on Antennas and Propagation*. 2005;**53**(10):3160–5. doi:10.1109/TAP.2005.856369
- [61] Schluper H.F., 'Direct measurements of stationary antennas on a compact antenna test range', *15th European Microwave Conference*, 1985. pp. 451–6. doi:10.1109/EUMA.1985.333520
- [62] van Norel J., Vokurka V.I., 'Novel APC methods for accurate pattern determination', *15th AMTA Proceedings*, October 1993. pp. 385–9
- [63] Corral C.A., 'Practical issues in advanced antenna pattern comparison', *Antennas and Propagation Society International Symposium Digest*. 1996;**1**:557–60. doi:10.1109/APS.1996.549660
- [64] Gregson S.F., McCormick J., Parini C.G., *Principles of Planar Near-Field Antenna Measurements*. Herts, UK: The Institution of Engineering and Technology; 2007

- [65] McCormick J., Boyce J., Sayers J., Murray J., 'The impact on measurement accuracy of specifying a compact antenna test range for high power testing', *The Second European Conference on Antennas and Propagation*, 2007. pp. 1–6
- [66] 'IEEE Standard Definitions of Terms for Antennas', IEEE Std 145-1993
- [67] Newell A.C., Ward R.D., McFarlane E.J., 'Gain and power parameter measurements using planar near-field techniques', *IEE Antennas and Propagation Society International Symposium*. June 1988; **36(6)**:792–803
- [68] Eriksson H., Svensson B., Magnusson P., 'Gain calibration uncertainties for standard gain horn calibration at a compact antenna test range', *Proceedings of the 5th European Conference on Antennas and Propagation (EUCAP)*, 2011. pp. 3746–50
- [69] 'IEEE Standard Test Procedures for Antennas', ANSI/IEEE Std 149-1979, p. 0_1; 1979
- [70] Shakhtour H., Cornelius R., Heberling D., 'Three antenna gain determination method in compact antenna test ranges', *2013 Loughborough Antennas and Propagation Conference*, 11–12 November 2013. p. 392
- [71] Knott E.F., *Radar Cross Section Measurements*. Springer; 2012. ISBN 1468499068
- [72] Knot E.F., Shaeffer J.F., Tuley M.T., *Radar Cross Section*. 2nd edn. Raleigh, NC: SciTech; 2004, pp. 71–4. ISBN 1-891121-25-1
- [73] Hess D.W., 'Introduction to RCS measurements', *Loughborough Antennas and Propagation Conference*, LAPC 2008. pp. 37–44. doi:10.1109/LAPC.2008.4516860
- [74] Baggett M., Thomas T., 'Obtaining high quality RCS measurements with a very large foam column', *AMTA Symposium Digest*. 2005; **session 1**:9–14
- [75] Finlay C.D., Gregson S., Lyon R.W., McCormick J., 'SPIKE a Physical Optics based code for the analysis of antenna radome interactions', *2007 IET International Conference on Radar Systems*, 2007
- [76] Svensson B., Widenberg B., Viberg M., 'Measurement of a large radome at an antenna compact test range', *11th European Conference on Antennas and Propagation (EUCAP)*, 2017, 2581–2584
- [77] McBride S.T., Nichols S.R., Murphy M., Rodriguez V., Cawthon G.M., 'Changes in the DO-213 standard for commercial nose-radome testing', *AMTA 2016 Proceedings*
- [78] Schmidt C.H., Migl J., Geise A., Steiner H., 'Comparison of payload applications in near field and compact range facilities', *Proc. Antenna Measurement Techniques Association (AMTA) Conference*, October 2015, Long Beach, USA
- [79] Van Rensburg D.J., Newell A., Gregson S., Pelland P., 'Group delay measurement for satellite payload testing', *AMTA Conference*, October 2017, Atlanta, USA
- [80] Habersack J., Kress H., Lindemer W., Steiner H., 'Satellite payload parameter measurements in a compensated compact antenna test range', *Proc. AMTA*, October 1999, Monterey, USA

- [81] Manner O., Wolf H., Lemanczyk J., ‘Payload parameter RF testing’, *Proc. AMTA*, November 2002, Cleveland, USA
- [82] Migl J., Lindemer W., Wogurek W., ‘Low cost satellite payload measurement system’, *Proc. AMTA*, October 2005, Newport, USA
- [83] Dudok E., Steiner H.-J., Smith T., Brumley S., ‘Scanned quiet zone in a compensated antenna test range’, *Proc. 12th AMTA Conference*, 1990, Philadelphia, USA
- [84] Keysight Technologies, ‘Mixer transmission measurements using the frequency converter application in the PNA microwave network analyzers’, Application note 5988-8642EN, Published in USA, July 31, 2014
- [85] Roh W., ‘5G mobile communications for 2020 and beyond – vision and key enabling technologies’, *IEEE WCNC 2014 Keynote*, April 2014
- [86] Pi Z., Khan F., ‘An introduction to millimeter-wave mobile broadband systems’, *IEEE Communications Magazine*. 2011;**49**(6):101–7
- [87] Wang Z., Bovik A.C., Sheikh H.R., Simoncelli E.P., ‘Image quality assessment: From error visibility to structural similarity’, *IEEE Transactions on Image Processing*. 2004;**13**(4):600–12
- [88] ‘Standard’ test images - ‘LAKE’ from http://www.imageprocessingplace.com/root_files_V3/image_databases.htm
- [89] ‘Discussion on OTA EVM requirement’, 3GPP TSG-RAN WG4 Meeting #81, R4-1609526 Reno, Nevada, USA, 14 - 18 November, 2016. from <http://www.3gpp.org/DynaReport/TDocExMtg-R4-81-31683.htm>

Chapter 6

Planar near-field antenna measurements

6.1 Introduction

In Section 2.6, it has been shown that if we can determine the near-field on a surface close to a radiating antenna, we can subsequently determine the radiated far-field. Additionally in Chapter 3, it has been shown that a number of physical geometries allow the sampling of the near-field of an antenna on specific surfaces that are convenient in terms of the hardware required to make the measurements and the necessary processing required to allow the far-field prediction. One of these configurations is the so-called ‘planar near-field antenna test range’. Figure 3.15 illustrates the basic physical geometry of the surface over which data is collected in such a test range as it is usually implemented, although other planar acquisition coordinate systems can be devised (see Figure 3.23).

6.2 Near-field measurement facility

Figure 3.18 illustrates the basic nature of the RF measurement methodology usually involved in data acquisition. The data is obtained by moving a probe/range antenna across a plane in front of the AUT, sampling the data at the required spatial rate, i.e. $< \lambda/2$ [1], where the measured signal from two orthogonal polarisations would be required to be obtained for full characterisation of the AUT near-field. As well as sampling the data at the required sampling interval, it should be observed that the plane over which the data is acquired is finite and as such if a substantial portion of the power generated and radiated by the AUT is not incident on this plane, then, as described later in this chapter, the fidelity of the far-field prediction will be severely impaired.

This implies that the planar near-field range is only a useful tool if it is used for highly directive antennas where it can be assumed that by far the vast majority of the radiated power is incident on the plane over which the data is sampled. However, many antennas are of this nature and the fact that in the course of the measurement process the AUT does not have to be moved does offer considerable advantages in certain circumstances over other measurement geometries where there would be less, as explained later, truncation in the data set.

Conventionally, planar near-field measurement systems operate by sampling the amplitude and phase of the propagating near-field at regular intervals on a plaid

monotonic grid over a planar surface, which is tangential to that of the antenna aperture plane and is located a few wavelengths in front of it. This arrangement is illustrated in Figure 6.1.

The range antenna, or near-field probe, that will be scanned over the plane must be in the propagating near-field region, not the reactive near-field, because evanescent coupling is omitted from the antenna–antenna coupling formulae. An electrically small, i.e. a low gain, low scattering cross-section probe is used to radiate at each of the pre-selected points within the planar surface. Typically, the measurements are made on a lattice that corresponds to a regular rectangular Cartesian grid along paths that are parallel to pre-defined x - and y -axes.

6.2.1 RF sub-system

Acting as a transmitter, the field from the probe produces a quasi-spherical wave within the free-space port of the AUT. Amplitude, phase and polarisation of the radiation from the near-field probe are held constant for all positions of the probe, and a plane wave is synthesised at the surface by the superposition of these quasi-spherical waves. This process is repeated, but the probe antenna is rotated through 90° about the normal to the plane to form an orthogonally polarised plane wave since two orthogonal tangential field components are required to determine the complete polarisation properties of the AUT.

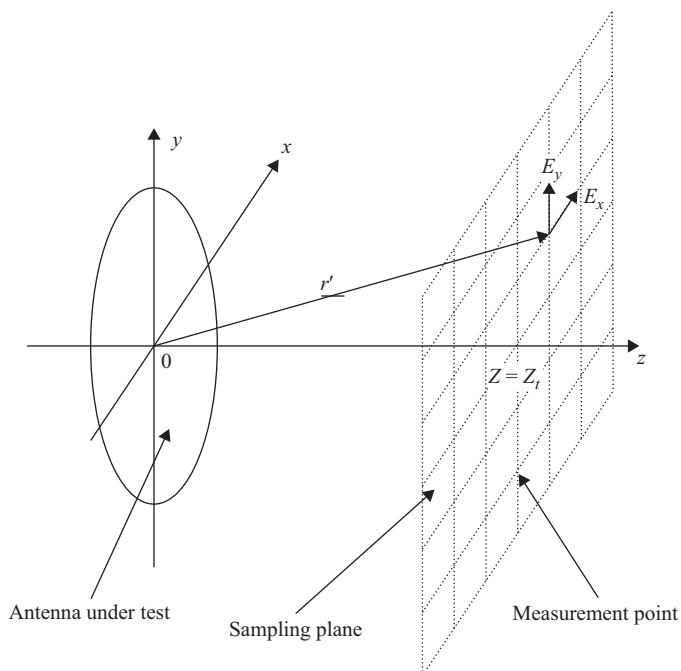


Figure 6.1 *Coordinate system for planar scanning*

Just as the free-space port plane wave is formed through the superposition of a large number of quasi-spherical waves, the response of the AUT to the synthesised plane wave is formed by the superposition of the responses of the AUT to the quasi-spherical waves. The synthesised plane wave can then be steered to other directions by linear phase shifting. This process of phase shifting and summing can, as is elaborated on in the following section, be recognised as a Fourier transform and is carried out using either the Discrete Fourier Transform (DFT) algorithm or when appropriate, the efficient Fast Fourier Transform (FFT) algorithm. Thus, the planar near-field antenna methodology, as well as offering a range configuration where the AUT is static, also provides a convenient and fast far-field prediction process based on the concept of the spatial as opposed to the more usual temporal Fourier transform.

Figure 6.2 shows a typical scheme for a planar near-field range.

As shown in Figures 3.35 and 6.2, the system is essentially a standard Vector Network Analyser (VNA) measurement system controlled via general-purpose interface bus (GPIB) or Ethernet via a central computer. This configuration is based around a VNA operating in remote mixing mode. However, for small systems where cable losses are acceptable, it is possible to work without remote mixing because with short cables, remote mixing becomes merely a way of redistributing the receiver within the chamber to minimise cable losses and improve the system dynamic range.

In the far-field case the necessary dynamic range is principally determined by the type of antenna being tested and must have sufficient dynamic range so that the entire far-field antenna pattern (main beam peak down to lowest side lobe of interest) fits within the system dynamic range. Processing gain of the near-field to far-field transform can suppress noise and increase the usable system dynamic range. This is why near-field ranges can often use poorer absorber than would be the case for an equivalent far-field system.

The multiplexed LO and IF signals are carried from test mixers on flexible phase-stable RF cables (one for each channel) to the RF equipment via flexible conduit. This conduit confines the two RF cables for test channels to constant rolling bends to achieve phase stability. The mechanical dependence arises since the dielectric constant is a function of mechanical stress and strain. When the cables are twisted, the inside of the bend will be compressed and the outside will be stretched, thereby affecting the characteristic impedance that will vary in a complex fashion. Over recent years, the use of a pantograph and rotary joint assembly has become less popular, as the performance of rotary joints degrades with time and imposes limits on the frequency range that the facility can usefully operate.

It should be noted that harmonic mixing does not help ease the phase stability requirements for the moving guided wave path (cable). Although the cables will change the phase of the signal less, since we then take the n th harmonic this will also similarly multiply up the phase change. The amplifiers in Figures 3.35 and 3.36 are likely to be solid-state LNAs to keep weight low, as the probe carriage is generally limited in permitted mass.

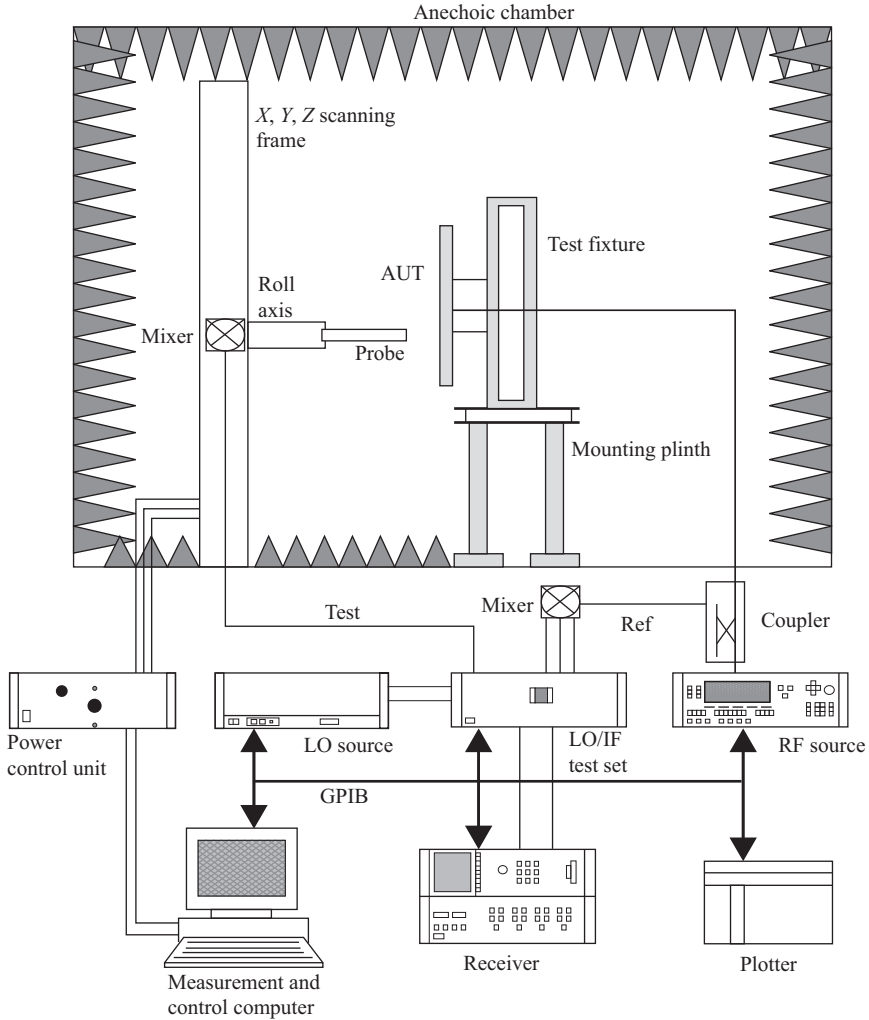


Figure 6.2 Schematic of near-field measurement system

A potential problem with cables is that PTFE dielectric can suffer a nonlinear volumetric change at certain temperatures, which will make phase stability at and around these temperatures difficult to control. The need for a highly controlled environment within the range to ensure stability during the measurement process, including temperature stability, is thus again re-enforced.

The reference and test RF signals obtained from the directional coupler and the AUT are similarly mixed down to an IF frequency, frequently 20 MHz, by the reference and test path mixers. The lengths of the two LO paths are usually

balanced, i.e. of equal length to minimise the impact of phase variations resulting from thermal fluctuations. The concept is that if the two path lengths are the same, the relative phase variation between the respective RF paths will be zero, irrespective of how the temperature fluctuates within the facility. As one arm of the interferometer contains a probe, an AUT, and free space, this can never completely succeed; however, it has been found to be of some use. The IF signal is relatively low in frequency, i.e. 20 MHz, and for convenience it is usually carried from the test mixer to the receiver within the same coaxial cable as the LO signal.

Note: Many VNAs use the time convention,

$$e^{j(\omega t - kz)} \quad (6.1)$$

However, published literature has adopted the opposite (NIST) time convention, namely,

$$e^{j(kz - \omega t)} \quad (6.2)$$

Thus care must be taken to ensure that the correct phase convention is adopted within the transformation process. This book, in common with the majority of works that utilise the angular spectrum, has adopted the positive time dependency of (6.1).

Reciprocity can be invoked to show that it makes no difference whether the AUT is characterised while in transmit or receive mode. However, for passive antennas, it is convenient to transmit from the AUT as the RF source can be placed directly behind the stationary AUT so that signal losses are minimised. In practice, the bandwidth over which the facility as a whole can operate is determined by other factors, principally the planarity and precision of the robotics positioner and the absorption characteristics of the RAM placed within the chamber. A number of VNA vendors offer LO/IF distribution units, but for clarity these have been omitted from these discussions as their function is merely to amplify, level and distribute the RF and LO signals.

6.2.2 Robotics positioner system

Two main design concepts are usually adopted for planar scanners: tower and rail inverted scanners, and box frame scanners. Figure 6.3 shows examples of these two varieties.

Generally, frame scanners offer improved rigidity and positional accuracy over tower and rail designs; however, the metallic frame inevitably introduces additional scattering sources. Thus one of the most attractive advantages of the inverted T is the reduction in possible multi-path.

Note: The frame design was initially favoured for the implementation of many of the smaller PNF scanners designs, but the mechanical constraints imposed by anchoring both axes at both ends made planarity adjustment very difficult. The complexity of this process of alignment eventually led to the development of the

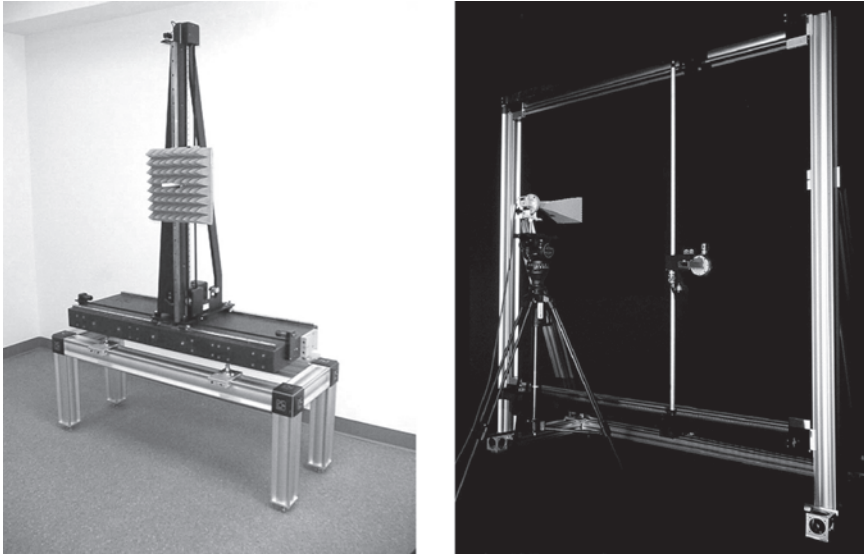


Figure 6.3 Tower and rail inverted T scanner and box frame scanner (Pictures courtesy of NSI-MI Technologies LLC)

inverted T design, where the second axis was constrained at only one end. This design has proved to be much simpler to construct and align.

In most test systems a vertical configuration is chosen, since it affords easy access to the AUT and near-field probe that is crucial when configuring complex active array antennas and acquiring the alignment of the AUT in the range. However, there are special cases where the horizontal plane is employed. In these cases the nature of the AUT and or the possible temperature gradient in the chamber may cause concerns when very large AUTs are to be tested. A good example of this is the unfurlable space-craft antenna where horizontal mounting ensures the reflector surface is not distorted by gravity, see for example Figure 6.8.

Both types of scanner consist of two orthogonal carriages, X and Y , which are supported on a rigid framework to enable the scanning probe to be moved within the xy -scan plane. The probe carriage is mounted on the Y carriage that is located within the X carriage. The scanner size varies enormously, from small (0.8×0.8)-m scanners used for small antennas to the massive (33×16)-m scanners and even bigger.

The position of each of the axes is usually determined using rotary optical encoders that send a train of pulses as the positioners are moved. A typical encoder system transmits 12 192 pulses per inch in the x - and y -axes and 80,000 pulses per inch in the z -axis. The in-plane resolution of the encoders corresponds to an upper frequency limit of 2.88 THz, assuming a positional tolerance of $\lambda/2$. In practice, this is not realised as the planarity, orthogonality and linearity of the axes (discussed in Chapter 10) are very much poorer than this limit. Crucially, as a rule these encoders

are relative rather than absolute so they measure how far the positioner has travelled, rather than where the positioner is. Hence, in the event that the power supply is disrupted, which could occur whenever the control computer is restarted, the absolute position of the scanner can be irrevocably lost.

A data acquisition software suite is used to control the robotics as with the RF sub-system. The acquisition software provides four degrees of freedom, as it controls the electric motors that are used to drive the moving parts of the scanner by means of a power control unit (PCU) via a GPIB card or Ethernet connection. Each motor is used to drive one of the axes of motion x -, y -, z -, or polarisation with the probe carriage being moved with a parabolic velocity profile to minimise mechanical strain. Generally, in order to minimise acquisition times, measurements are made while the probe carriage is in motion, i.e. measurements are made 'on the fly'.

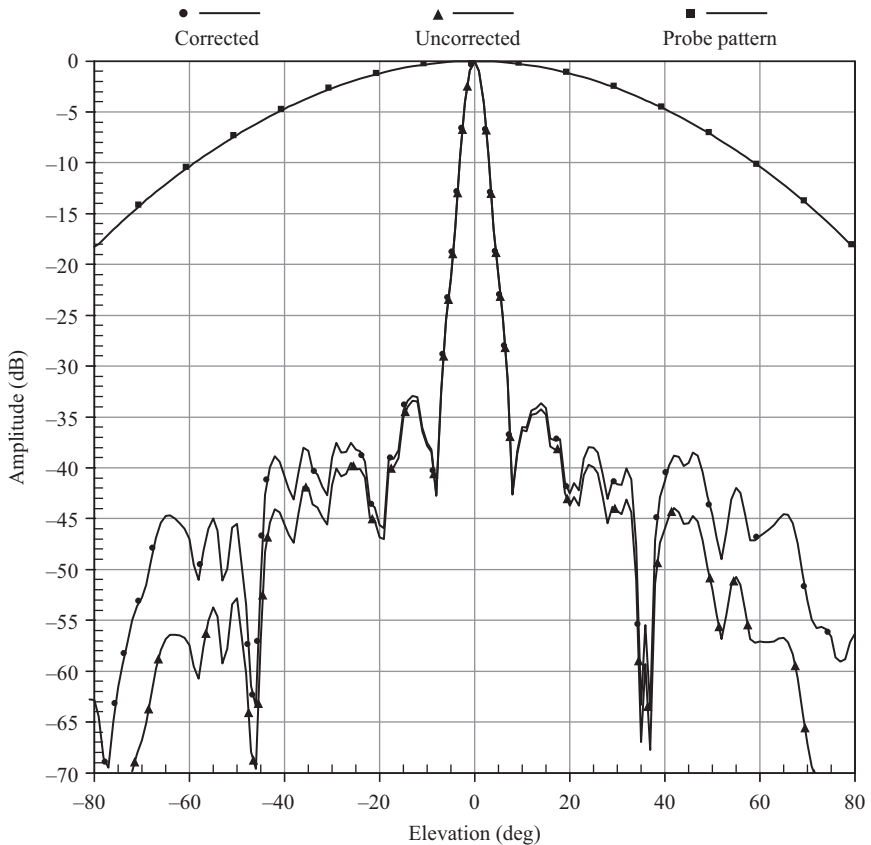


Figure 6.8 Comparison between probe pattern and corrected and uncorrected far-field pattern

6.2.3 *Near-field probe*

Typical near-field probes can include cylindrical waveguide, rectangular waveguide, corrugated horns and pyramidal horns. Two common probe antennas are the dual port choked cylindrical waveguide probe and an open-ended rectangular waveguide probe. Figure 3.32 shows the number of waveguide probes that would be used to cover a range of frequencies. As can be seen from this figure a wide range of probes is required to cover a large bandwidth. This is related to the second requirement listed in Section 3.6.1.4 (No pattern nulls in the forward hemisphere) and the subsequent small size, and the low RCS that is required of the probes. These are further examined in Section 6.5.2.

6.3 **Limitations in the accuracy of the near-field measurement data**

The accuracy with which any prediction of the far-field can be made from the acquired near-field data is dependent on the fidelity with which the measurement system can represent the actual amplitude and phase of the electric field produced by the AUT across the extent of scan plane. Clearly no measurement system has unlimited dynamic range and no noise floor, but as well as these inherent limitations the planar near-field measurement concept is subject to a number of other limitations that are inherent to this and other antenna measurement methodologies.

6.3.1 *Mechanically based limitations*

First, as elaborated on in Chapter 10 on near-field assessment, the measurements are made over a finite scan plane and as such the data is truncated to a section of the surface enclosing the antenna. This means that the data set acquired will be truncated to the angular extent of the size of the angle that subtends the measurement plane relative to the AUT as per Figure 6.4, where as a result of the finite extent of the scan plane $= 2X$ the pattern can only be predicted out to the angle θ_1 .

This truncation means that no prediction of the antenna pattern beyond this angle is possible and, as explained in Chapter 10, this primary truncation can have an impact inside this angle, which is dependent on the prediction of the antenna directivity and pattern within θ_1 [2]. Again, the accuracy with which any prediction can be made is also dependent on other factors related to the nature of the scan plane over which the probe is moved (see Chapter 10). One of these is the accuracy with which the sampling positions can be defined on this scan plane.

Generally with a requirement to sample at $\lambda/2$ spatial intervals, the positional accuracy error is specified as being smaller than $\lambda/50$. If this is not achievable, i.e. either the scan plane is large or the measurement frequency is too high, then often this requirement is relaxed so that the repeatability is better than $\lambda/50$. The positional error is then calibrated, often with the use of laser interferometers, and the positional error corrected within the transformation software, e.g. k -correction [3].

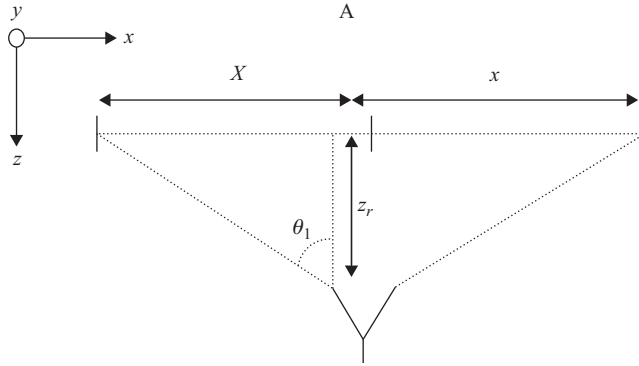


Figure 6.4 Primary truncation of predictable far-field data

Unfortunately unless very carefully implemented [4] this approach is often unsuccessful as most commercially available laser interferometers cannot acquire the position of the probe to the required degree of accuracy while the probe is in motion. Thus, in practice, the tabulated positional errors do not correspond with the actual positional errors while the data of probe samples is on the fly as is usual in antenna measurements.

Note: The positional accuracy can also be affected by vibration within the scanner and the requirement to keep this to a minimum can favour box frame scanners in certain circumstances.

6.3.2 RF system limitations

In the microwave system shown in Figure 6.2, the multiplexed LO and IF signals are carried from test mixers on flexible phase-stable RF cables, one required for each channel, to the RF equipment via flexible conduit. The mechanical dependence of these conduits arises since the dielectric constant is a function of mechanical stress and strain. When the cables are twisted, the inside of the bend will be compressed and the outside will be stretched, thereby affecting the characteristic impedance of the cables. Thus, the necessity of connecting the RF path through a moving probe antenna in the measurement technique will introduce errors associated with the amplitude and particularly the phase of the RF signal is affected by the required movements of the RF probe.

In Tx the near-field measurement technique depends on whether the field measured on the plane is representative of the field that would exist on this plane in the absence of the mechanical and RF measurement system, i.e. if the AUT was only radiating into free space. The limitations so far discussed relate to how accurately the sampling can take place on this plane and how the measured signal can be corrupted in the RF path that transfers the signal to the receiver. However, another source of error is the field that is incident on the scan plane as a result of the presence of structures within and those composing the chamber in which the measurements are to be made.

As described in Chapter 1, the radiation that is incident on the scan plane that is not related to the direct path from the AUT to the plane is referred to as multi-path. In any actual planar scanner, great efforts will be made to reduce multi-path usually by the incorporation of RAM materials. In fact when the installation of the inverted T scanner shown in Figure 6.3 is complete, its appearance would be more like Figure 6.5 where, with an AUT in place, it can be seen that it is installed in a RAM lined room with RAM material placed around all areas of the scanner that could contribute to the production of multi-path.

From Figure 6.5 it can be seen that the effort to reduce multi-path in the measurements has meant that a considerable quantity of RAM is required, depending on the size and configuration of the scanner. Additionally, it can also be seen that, due to the greater preponderance of metal work, a box frame scanner would require considerably more attention to reduce multi-path in its vicinity, a reason for favouring an inverted T type configuration. Clearly great care must be exercised in the design implementation and installation of near-field test ranges so that the integrity of any data sets acquired within the ranges can be relied upon to meet the requirements of the test and measurement procedures.

The factors so far discussed in this chapter relate to requirements for and the limitations of acquiring near-field amplitude and phase data on a plane in the radiative near-field of the AUT. However, we are of course in the majority of circumstances interested in the far-field characteristics of the AUT so a method must be devised whereby this near-field data is transformed in the far-field pattern of the AUT.

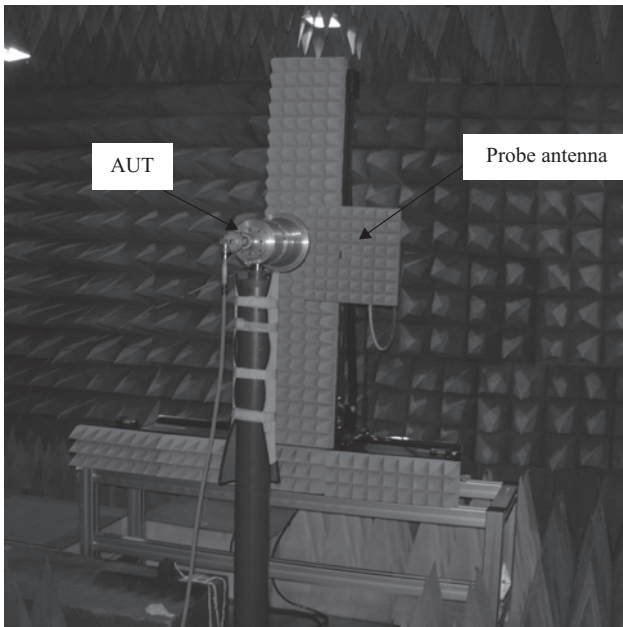


Figure 6.5 Inverted T scanner installed in a chamber (Courtesy of QMUL)

6.4 Solution of Maxwell's equations in Cartesian coordinates

Near-field methodologies require that far-field antenna parameters such as pattern, gain, directivity, polarisation and others be derived analytically from measurements taken over a convenient smooth surface in the near-field of a radiator. For such parameters that cannot be obtained directly from measurements made in the near-field, a transformation from one surface to another is necessitated. This transformation, of monochromatic but otherwise arbitrary waves, can be accomplished by representing the field at an arbitrary point in space as a summation of any elementary wave solutions to Maxwell's equations. Here, the mode coefficients to these solutions are determined by matching the fields over the surface on which the fields are known by using mode orthogonality. Solving this modal expansion for the fields over the surface of a sphere with an infinite radius centred about the AUT results in the far-field pattern.

As already mentioned in Chapter 1, a degree of mathematical convenience can be obtained from selecting a modal basis that is commensurate with the measurement geometry, and in the case of planar measurements this is best accomplished by utilising plane waves and the concept of the plane wave spectrum (PWS).

6.4.1 Plane wave spectrum

In the case of certain types of elementary field, i.e. mode, if the amplitude, phase and direction of propagation of a plane wave are known at one location in space, then the properties of this field can instantly be determined everywhere in space. Thus, if the complex field distribution associated with some radiator can be decomposed into a summation of plane waves propagating in diverse directions, then similarly the properties of the complex field distribution can be determined throughout space from a summation of the properties of the respective plane waves. Thus, the transform of the acquired near-field data in a range is usually based on the plane wave spectrum representation of electromagnetic fields. This generalised interpretation can be shown to stem from the free-space solution of the scalar wave equation, which itself follows directly from classical electromagnetic theory and Maxwell's equations, where the four Maxwell equations are postulated, mathematical generalisations of a great many macroscopic experimental observations of electricity and magnetism.

Any variations in the measured field on the measurement plane for a monochromatic plane wave that occurs at a rate of change that is higher than that which would be observed in a free-space wave travelling tangentially to the plane can only be explained by the projection of the wave onto the plane at different angles. Thus, the measured signal on the plane represents the summation of the various spatial wavelengths produced by the range of angles at which any waves are projected onto the plane. This relationship between the spatial period measured on the plane and the spatial frequency, which can be directly related to an angle of projection onto the plane, is the basis of the transform used to predict the far-field pattern of an

antenna from the measured near-field data on a plane. Thus, just as the temporal period and the temporal frequency are related by a Fourier transform, so likewise are the spatial period and frequency.

This means that a spectrum of monotonic waves, a plane wave spectrum, can be viewed as the summation of plane waves that would produce the asymptotic far-field pattern of the antenna. Thus, the plane wave spectrum can be seen to represent a generic algorithm for obtaining the particular solution to the problem of predicting the far-field pattern of an antenna utilising the boundary conditions represented by infinity on a hemisphere in front of the antenna and the plane on which the data is measured.

This angular spectrum can be obtained directly from the sampled tangential near-field data using

$$\underline{F}_T(k_x, k_y, z = 0) = \int_{-\infty}^{\infty} \int_{-\infty}^{\infty} \underline{E}_T(x, y, z = 0) e^{j(k_x x + k_y y)} dx dy \quad (6.3)$$

The propagating electric field everywhere in the forward half-space can be obtained from the tangential angular spectra as

$$\underline{E}(x, y, z) = \frac{1}{4\pi^2} \int_{-\infty}^{\infty} \int_{-\infty}^{\infty} \left[\underline{F}_T(k_x, k_y) - \hat{e}_z \frac{k_T \cdot \underline{F}_T(k_x, k_y)}{k_z} \right] e^{-j(k_x x + k_y y + k_z z)} dk_x dk_y \quad (6.4)$$

Here, the longitudinal component of the electric field has been obtained from the tangential components using the plane wave condition.

$$F_z(k_x, k_y) = - \frac{k_T \cdot \underline{F}_T(k_x, k_y)}{k_z} \quad (6.5)$$

For the case where only propagating plane wave mode coefficients are considered, as is the case for near-field antenna measurements, the normal component of the propagation vector is obtained from the tangential components,

$$k_z = \sqrt{k_0^2 - k_x^2 - k_y^2} \quad (6.6)$$

If only propagating plane wave mode coefficients are considered then $k_x^2 + k_y^2 \leq k_0^2$. The propagating magnetic field everywhere in space can be obtained from the tangential components of the angular spectra as

$$\begin{aligned} \underline{H}(x, y, z) &= \frac{1}{4\pi^2 \omega \mu} \int_{-\infty}^{\infty} \int_{-\infty}^{\infty} \underline{k} \times \left[\underline{F}_T(k_x, k_y) - \hat{e}_z \frac{k_T \cdot \underline{F}_T(k_x, k_y)}{k_z} \right] \\ &\times e^{-j(k_x x + k_y y + k_z z)} dk_x dk_y \end{aligned} \quad (6.7)$$

At the stationary points $k_x = k_1$ and $k_y = k_2$, the far-field tangential electric field components can be obtained from the tangential angular spectra using

$$\underline{E}(k_x, k_y) \approx j \frac{e^{-jk_0 r}}{\lambda r} \frac{k_z}{k_0} \underline{F}(k_x, k_y) \quad (6.8)$$

Alternatively, when expressed in terms of the propagation vector, the magnetic far zone fields can be obtained from the far zone electric field at the stationary points $k_x = k_1$ and $k_y = k_2$ as

$$\underline{H}(k_x, k_y) = \frac{1}{Z_0 k_0} \underline{k}(k_x, k_y) \times \underline{E}(k_x, k_y) \quad (6.9)$$

This transformation algorithm forms the basis of the methodology used to transform near-field planar measurement data into far-field antenna pattern predictions. Figure 6.6 illustrates the result of implementing the 2D Fourier transform on the measured spatial domain data that would be obtained using a planar scanner.

Note: The explanation above for the relationship between the near-field measurement data and the far-field pattern is necessarily brief and terse; a much fuller and more rigorous explanation can be found in [5].

The transform algorithm described above then allows the prediction of the far-field pattern from the measured near-field data, which will provide an accurate prediction of the far-field pattern provided the measured data is representative of the actual fields produced by the AUT. However, the measurement process introduces a systematic error into the measured near-field data that is related to the characteristics of the probe used to make the measurements. Thus the data in the spectral domain does not faithfully represent the actual far-field pattern until this systematic error can be compensated for.

6.5 Probe pattern compensation

The probe used in near-field scanning is itself an antenna and as such has its own antenna pattern. This has the effect of contributing a systematic error in the form of a singular mapping on top of the actual fields generated by the AUT. Thus the measured near-field data is in fact the convolution of the AUT and probe responses.

Taking account of the convolution theorem, [6] that relates convolution to multiplication in the relation between the function spaces involved in the transform, this means that the predicted far-field data is now the product of the AUT and probe far-field characteristics. This means that in order to realise the correct far-field data for the AUT, the far-field data set needs to be compensated by the removal of the probe far-field response.

Essentially then, this means that the probe pattern at a particular direction in space will correspond to an error at that angle being introduced into any antenna pattern data. This can potentially constitute one of the largest but most

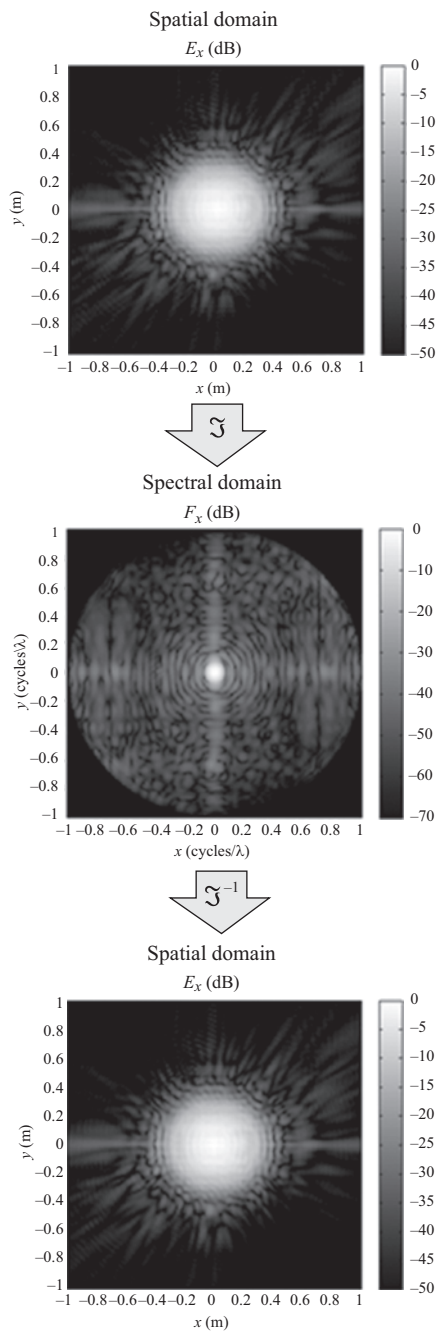


Figure 6.6 Action of the 2D Fourier transform on measured near-field data

repeatable and predictable measurement errors. Thus it is clear that in order to obtain reliable measurements, the electromagnetic properties of the near-field probe must be known very accurately indeed.

6.5.1 *Effect of the probe pattern on far-field data*

The probe pattern can be thought of as a device that spatially filters the fields received from different parts of the AUT. In a planar range as already stated, the effects include something very similar to a direct multiplication of the far-field probe pattern with the far-field AUT pattern and can be shown to be a direct result of the nature of the convolution theorem and can be visualised directly from the mechanical operation of the scanner. It is not usually possible to neglect these effects in a planar range because of the large angles of validity required, and the short measurement distance employed. However, the effects of probe pattern correction can be minimised by utilising a probe of pattern similar to a Hertzian dipole, i.e. a linearly polarised source with an aperture small in comparison to the half wavelength sample spacing.

The general effects of the directivity pattern of the near-field probe on the resulting far-field pattern function of the AUT are illustrated in Figures 6.7 and 6.8.

From these figures, the general effect of the probe pattern on the far-field pattern of the AUT can broadly be determined. The pattern of the probe suppresses the co-polar pattern of the AUT by an amount equal to the directive loss of the probe pattern at the angle of observation.

As has already been shown, this is not a general statement as effects associated with cross-polarisation and polarisation purity have been ignored. Furthermore, it has been assumed that the AUT and the probe are perfectly aligned. However, it is true to say that in the far-field, the effect of the probe on the AUT pattern is a one-to-one mapping, i.e. the pattern of the probe at a given angle will only affect the AUT pattern at that same angle.

From the impact on AUT pattern, produced by the probe pattern, it is clear why pattern nulls in the forward hemisphere of the probe antenna are best avoided, as they are difficult to characterise accurately and they correspond to large correction terms in the far-field antenna pattern that introduce additional uncertainties.

6.5.2 *Scanning probe characteristics*

The above explanation of the impact of the probe characteristics on the integrity of the measurement data clearly indicates why in-depth knowledge of and tight parameter control of probes is necessary. Thus the six criteria listed as probe requirements in Chapter 3 can now be explained in terms of their impact on the measurement process.

1. Time invariant gain and mechanical rigidity: The probe must be resilient against gravitational deformation, etc. Any variation in the electromagnetic performance of the probe between the time when it was characterised and the time when it was used to measure an AUT corresponds to the near-field measurements being corrected with the wrong probe pattern data.

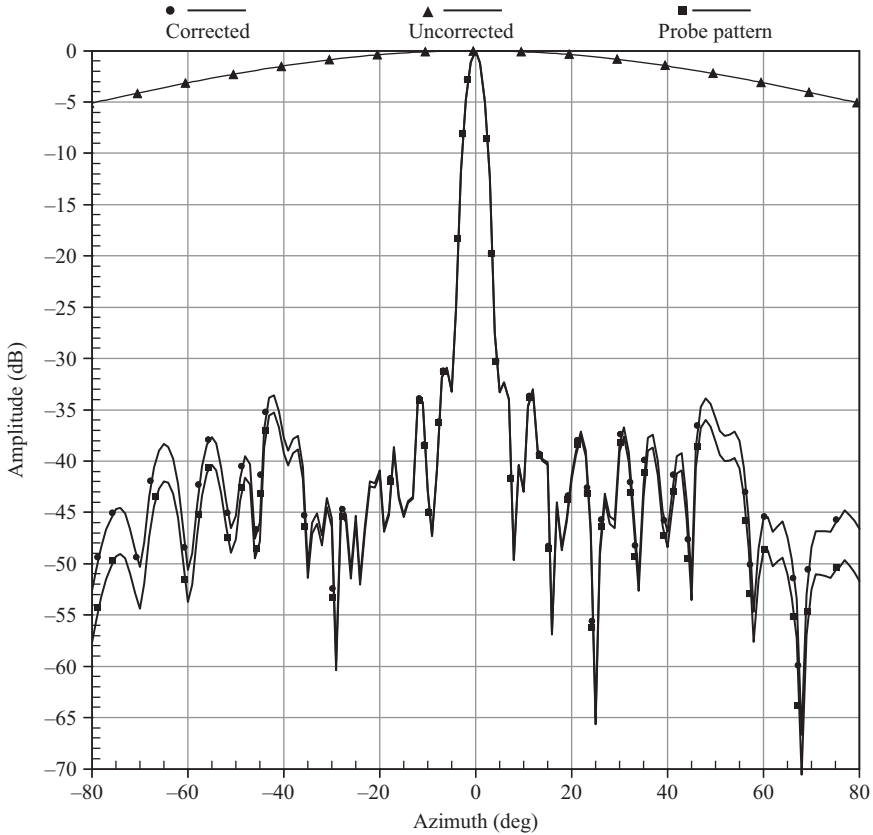


Figure 6.7 Comparison between probe pattern and corrected and uncorrected far-field pattern

2. No pattern nulls in the forward hemisphere corresponding to a low directivity: Electrically and likely physically small probe. Pattern nulls correspond to angles in which the probe is insensitive, i.e. blind, to incoming radiation. This would necessarily correspond to the introduction of large correction terms within the probe compensation process that would render corrected far-field pattern susceptible to spurious signals, i.e. noise. This noise could be introduced either within the antenna measurement process itself, or within the original probe characterisation, e.g. uncertainties associated with the measurement of the null depth.
3. Wide bandwidth: This minimises the necessity to use a multitude of probes to cover the operational bandwidth of the facility, thus reducing the time and uncertainties introduced by the changing and swapping of probes if measurements are required over large bandwidths. Unfortunately, it is not usually possible to satisfy all of the other requirements over an extended bandwidth, i.e. of greater than 20%.

4. Low scattering cross-section and reflection coefficient – i.e. well matched with a small return loss: This is required to minimise the magnitude of the multiple reflections that are set up between the near-field probe and the AUT. Such multiple reflections are omitted from the theoretical treatment of the near-field measurement process and therefore cannot be corrected for. From a practical standpoint, such multiple reflections can result in the introduction of ghost side lobes and can upset the excitation of radiating elements within array antennas. (The importance of this is readily illustrated when the effective area of a planar range is roughly equal to the area of the scan plane.)
5. Good polarisation purity: This is required in order that the various field components can be resolved. Although in principle it is possible to use the probe pattern correction process to effectively improve the polarisation response of the range, it is less demanding, and therefore often more reliable, if a probe with good polarisation purity is employed in the first place.
6. Good front to back ratio: To minimise sensitivity to probe placing and multiple reflections. Unfortunately, in practice this is at odds with item number 2.

In this chapter up to this point, the discussion has centred on the implementation of planar near-field scanning as illustrated in Figure 6.1, the most common geometry employed where the AUT near field is sampled on a rectilinear plaid monotonic grid over a planar surface, which is tangential to that of the antenna. As is illustrated in Figure 3.23, this is not the only planar surface over which it may be convenient to sample the data, and since plane-polar measurements are possible using only a linear translation stage and a polariser or rotator, this geometry is often to be encountered as a technique utilised to provide planer near-field data.

6.6 Plane-polar near-field antenna measurements

Although the plane-rectilinear geometry is by far the most commonly encountered planar implementation, plane-polar [7] and plane-bipolar [8] geometries can also be constructed using mechanically convenient commercially available positioning equipment and are in use in industry and academia.

The combination of the rotation and linear axes enables the probe to trace out a radial vector in two dimensions, thereby allowing the collection of samples across the surface of a plane on a set of concentric rings. Here, samples are taken at regular intervals across a polar grid with, typically, the probe moving in a fixed radial direction and the AUT rotating axially. This arrangement is illustrated in Figure 6.9. Here a large 12 m diameter horizontal plane-polar system is shown testing a large deployable reflector antenna.

In addition to yielding a simplification to the positioning and RF sub-systems, a crucial feature of the technique is the ability of the scan plane diameter to be as much as twice as large as the length of the linear translation axis. Potentially, this enables measurements to be taken across scan planes that are significantly larger in physical extent than the measurement system or even the enclosing test chamber.

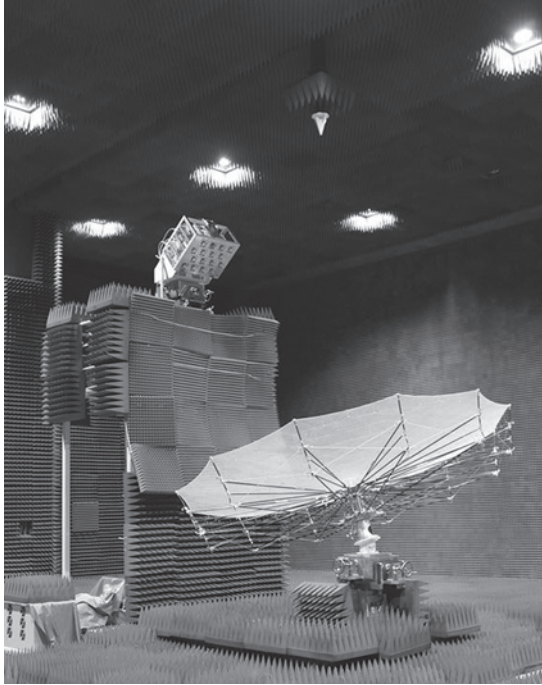


Figure 6.9 Kyoto University horizontal plane-polar system with a 6 m radius (12 m diameter) translation axis (Picture courtesy of Kyoto University & NICT)

Crucially, the plane-polar (and plane-bi-polar) geometries provide additional scope for suppressing range multi-path effects that are not typically available when using conventional plane-rectilinear implementations. As the integrity of the measurement can be compromised in a large part by these reflections, this can constitute another very attractive attribute of these geometries. The following section provides an introduction to the plane-polar near-field to far-field transform and presents some typical results.

6.6.1 Application of spectral methods to plane-polar antenna measurements

As has been shown in Section 6.4.1, and can be extrapolated from (6.3), an angular spectrum of plane waves can be obtained directly from the sampled tangential near-field components using

$$\underline{E}_T(k_x, k_y) = \int_{-\infty}^{\infty} \int_{-\infty}^{\infty} \underline{E}_T(x, y) e^{j(k_x x + k_y y)} dx dy \quad (6.10)$$

It is also known that, from an application of the stationary phase algorithm [9], the asymptotic far electric fields can be easily obtained from the angular spectrum since as $r \rightarrow \infty$

$$\underline{E}(k_x, k_y) \approx j \frac{e^{-jk_0 r}}{\lambda r} \frac{k_z}{k_0} \left[F_T(k_x, k_y) - \frac{k_T \cdot F_T(k_x, k_y)}{k_z} \hat{e}_z \right] \quad (6.11)$$

As is, these equations are not suitable for use with a plane-polar or plane-bi-polar measurement system and some adaption is necessitated. Two methods for accomplishing this task are:

1. Interpolate the data from a plane-polar or plane-bi-polar measurement grid to a plane-rectilinear grid and then utilise the standard techniques of Section 6.4 to obtain the far-field pattern.
2. Recast the near-field to far-field integral transform in terms of the plane-polar or plane-bi-polar coordinate systems.

The principal advantage of utilising interpolation is that the fast Fourier transform can be directly used to significantly improve the efficiency of the transform; however, this is sought at the price of having to interpolate rapidly varying complex near-field data at a very early stage within the transformation processing chain. Conversely, deploying the near-field to far-field transform in each of these measurement geometries removes the requirement for such approximation but will inevitably increase the amount of computational effort required to obtain far-field data. The remainder of this section is devoted to recasting the transmission equation into a plane-polar form.

In fact it turns out that via the use of a multidimensional exchange of variables, it is a comparatively straightforward task to recast the plane wave expansion in a form that is directly applicable to the plane-polar measurement system where the samples are taken on a plaid, monotonic and equally spaced plane-polar grid. The plane-polar coordinate system is presented in Figure 6.10.

In this case the transformation from Cartesian to plane-bi-polar coordinates is a one-to-one mapping, the analytic functions are continuous, the necessary partial derivatives exist and are continuous, and assuming the initial condition is specified in a plane-polar coordinate system where the condition that $r \geq 0$ applies (as will be shown below, this is not a practical limitation) such that $x = r \cos \phi$, $y = r \sin \phi$, with z arbitrary but fixed. Here, the Jacobian can be expressed as [10]

$$\frac{\partial(x, y)}{\partial(r, \phi)} = \begin{vmatrix} \frac{\partial x}{\partial r} & \frac{\partial x}{\partial \phi} \\ \frac{\partial y}{\partial r} & \frac{\partial y}{\partial \phi} \end{vmatrix} = \begin{vmatrix} \cos \phi & -r \sin \phi \\ \sin \phi & r \cos \phi \end{vmatrix} = r(\cos^2 \phi + \sin^2 \phi) = r \quad (6.12)$$

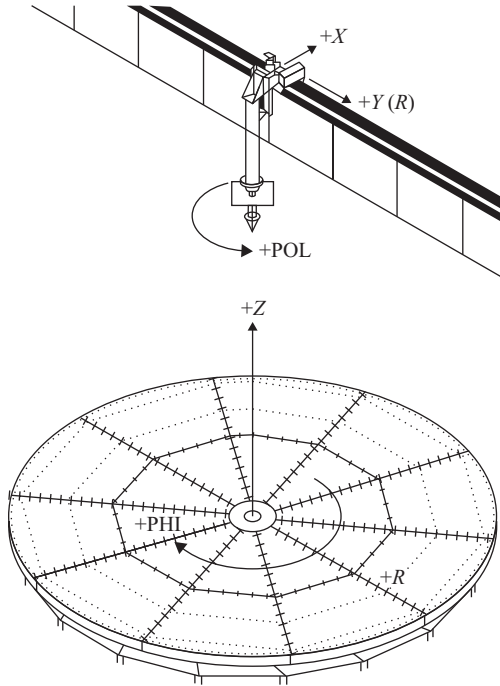


Figure 6.10 Plane-polar schematic showing coordinate system and three axes of motion

Using the exchange of variable formula for double integrals

$$\iint_R f(x,y) dA_{x,y} = \iint_S f(x(u,v), y(u,v)) \left| \frac{\partial(x,y)}{\partial(u,v)} \right| dA_{u,v} \quad (6.13)$$

yields

$$F(k_x, k_y) = \int_0^{2\pi} \int_0^{\infty} f(r, \phi) e^{jk_0 r (u \cos(\phi) + v \sin(\phi))} r dr d\phi \quad (6.14)$$

The transformation from plane-polar to Cartesian unit vectors can be expressed as

$$\hat{e}_x = \cos \phi \hat{e}_r - \sin \phi \hat{e}_\phi \quad (6.15)$$

$$\hat{e}_y = \sin \phi \hat{e}_r + \cos \phi \hat{e}_\phi \quad (6.16)$$

Thus, the Cartesian components of the angular spectrum of plane waves can be obtained directly from the plane-polar electric field components sampled on a

regular plane-polar grid. The corresponding near-fields can be recovered from the plane wave spectrum (PWS) giving

$$\underline{E}(x, y, z) = \frac{1}{4\pi^2} \int_{-k_{y0}}^{k_{y0}} \int_{-k_{x0}}^{k_{x0}} \underline{E}(k_x, k_y, z=0) e^{-jk_0(ux+vy+wz)} dk_x dk_y \quad (6.17)$$

Here, $k_{x0} = k_{y0} = 2\pi/\lambda$. When implemented numerically, the infinitesimal area of a sector of the plane-polar grid must be replaced with a finitely small elemental area. When the angle ϕ is in units of Radians, the area A of a sector can be expressed as

$$A = r^2\phi/2 \quad (6.18)$$

Thus, the elemental segment area of each sample is

$$A = \frac{\phi}{2n} \left[(r + \delta/2)^2 - (r - \delta/2)^2 \right] = r\delta\phi/n \quad (6.19)$$

Here, r is the radius of the sample, δ is the sample spacing, ϕ is the sector angle in radians and n is the number of samples in each 'ring'. The centre point is a special case with an elemental area of

$$A = \frac{\text{Area of sector}}{n} = \frac{1}{2n} \left(\frac{\delta}{2} \right)^2 \phi = \frac{\delta^2\phi}{8n} \quad (6.20)$$

The near-field probe can be conceived of as being a device that spatially filters the fields received from different parts of the AUT. It is not usually possible to neglect these effects in a planar range because of the large angles of validity required, and the comparatively short measurement distance employed. The necessary expressions required to correct the measured near-field data for the directive properties of the measuring probe can be shown to be

$$[A] = \frac{\lambda}{j} [M]^{-1} \cdot [P]^{-1} \cdot [S] e^{jk_z z_0} \quad (6.21)$$

Here, the matrix $[A]$ is used to denote the probe-corrected fields of the AUT, the matrix $[S]$ is the angular spectra derived from the measured near-field, k_z is the z -directed components of the propagation vector and z_0 is the AUT-to-probe separation. Incorporating the probe pattern correction within the near-field to far-field transform developed above commences by recognising that the AUT-to-probe coupling will change differentially from linear scan to linear scan as the AUT is rotated in ϕ across the acquisition interval. Hence, as the probe polarisation rotation angle depends directly on ϕ , the task of applying probe pattern correction has to be moved inside of the double integral with the linear integration being evaluated first.

In order that the probe pattern correction technique can be extended to accommodate the case where the probe has been rotated by an arbitrary, but fixed,

angle ϕ about the positive z -axis of the range, all that is required is to rotate the pattern of the probe and the pattern of the, output, infinitesimal Hertzian dipole, and then to resolve the corrected fields back onto the range polarisation basis. A detailed verification of this can be found in [11]. In this way, probe-corrected far-field data can be obtained with no loss in rigour. Although this approach still requires the use of approximation, i.e. interpolation, in the preparation of the rotated probe pattern, the probe pattern is typically grossly over sampled, and by design will be a low gain, slowly varying far-field pattern function which is easily approximated by piecewise polynomial fitting. Or, alternatively, it could be obtained from analytic models in the event simple open-ended rectangular waveguide probes are employed [12].

It is worth noting that the plane-polar measurement techniques inherently rotate the probe about the range z -axis during an acquisition. Thus, the AUT-probe coupling will change differentially across the acquisition surface. This is not the case with plane-rectilinear scanning where the angular relationship between the probe and the acquisition window is unchanged while characterising each near electric field component. This difficulty can be resolved if the probe is rotated by an equal and opposite amount to counter the rotation and to maintain the angular alignment between the probe and AUT, cf. a Ludwig III spherical far-field measurement. In this way the complexity of the probe compensation as set out above reduces to conventional plane-rectilinear correction as expounded in earlier sections of this chapter. One additional advantage of this counter-rotating scheme is that it significantly eases the demands placed upon the accuracies required for the probe calibration as the principal polarisations of the probe and test antennas remain largely matched for the duration of the measurement. If the probe is not counter-rotated, and does not have a rotationally symmetrical pattern, then the rotation of the probe about the z -axis must be accounted for within the compensation process as presented above.

As an illustration of the effectiveness of the plane-polar measurement configuration, measurement results for a slotted waveguide x -band planar array antenna measured using both a conventional $2.6 \text{ m} \times 2.6 \text{ m}$ vertical scanner and a 1.3 m horizontal plane polar scanner are shown. These systems are presented in Figures 6.11 and 6.12 respectively. *Note:* In both cases a WR90 opened waveguide probe with an AUT to probe separation held constant was used. In each case a WR90 opened rectangular waveguide (OEWG) probe was used with the AUT-to-probe separation kept consistent.

The plane-polar system shown in Figure 6.12 comprises a 0.9 m linear travel stage above an azimuth rotator to provide the scanning motion. Thus, when the motion provided by the linear stage is combined with the rotation provided by the azimuth rotator, a maximum effective scanning area of 1.8 m diameter can be achieved. The plane-polar measured orthogonal tangential near electric field components are presented in the form of false grey-scale checkerboard plots in Figures 6.13 and 6.14. For this measurement, no counter-rotation of the linearly polarised probe was implemented. A non-rotational, symmetric, open-ended rectangular waveguide probe was used to acquire this data, thereby fully exercising the

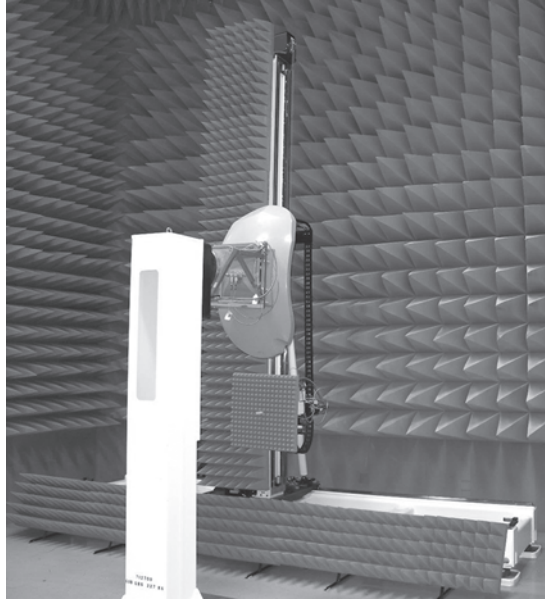


Figure 6.11 NSI-300V-12 \times 12 vertical plane-rectilinear system (Picture courtesy of NSI-MI Technologies LLC)

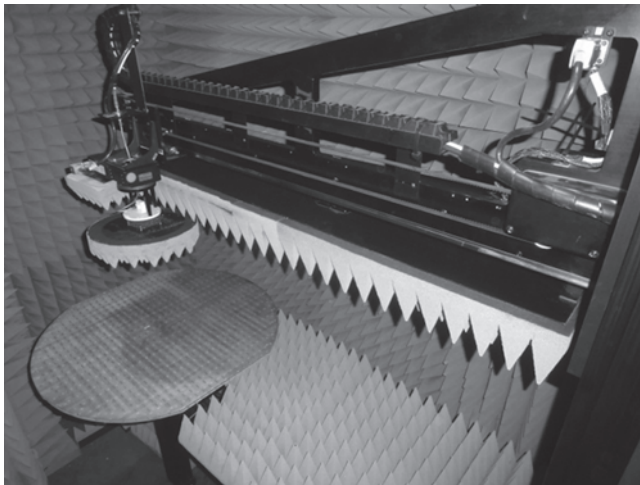


Figure 6.12 NSI-920PP-6 horizontal plane-polar system (Picture courtesy of NSI-MI Technologies LLC)

generality of the plane-polar near-field to far-field transform algorithm as developed above.

Figures 6.15 and 6.16 show that the respective far-field co-polar patterns are in a very encouraging agreement. Here, the patterns are presented in the form of false

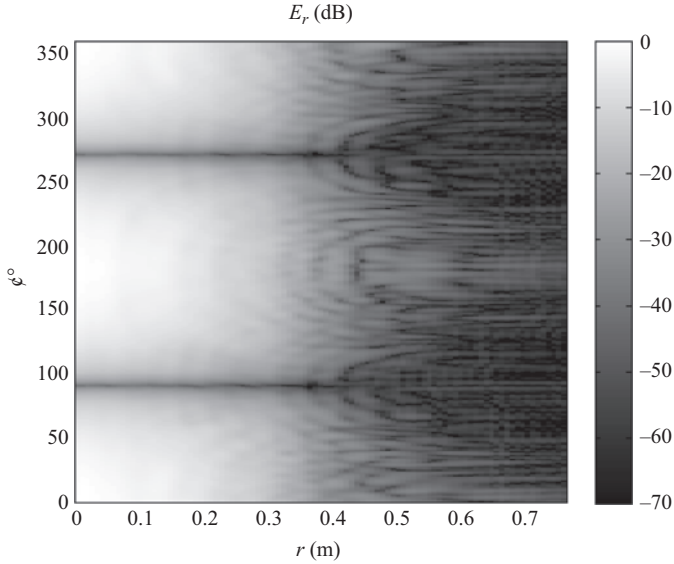


Figure 6.13 E_r polarised measured near electric field component

grey-scale checkerboard plots with the pattern tabulated on a plaid monotonic and equally spaced direction cosine grid, with the electric fields resolved onto a Ludwig II azimuth over elevation polarisation basis, cf. Chapter 4. When acquiring these near-fields, samples were taken at every half wavelength in the linear scan axis, and with an angular increment that corresponded to acquiring one sample at every half wavelength around the circumference of the circular planar sampling interval. This implies that points within the outermost circular cut are over sampled. However, when scanning in the angular ϕ -axis, and taking data on the fly, which is the standard acquisition mode, by using a fast RF sub-system, which is commonly available in the modern laboratory, the scan time is typically limited by the maximum angular velocity of the rotation stage as opposed to the speed of the vector network analyser that is being used. This means that although it is possible to use various strategies to ‘thin’ the amount of measured near-field data, in many cases there is very little practical improvement in acquisition times.

When examining these results, it is important to recognise that the plane-rectilinear and plane-polar measurements were taken using completely different test systems installed within separate chambers. Thus, the differences in low-level, wide-out patterns are most likely attributable to differences in scattering between the respective measurements. The plane-rectilinear system was housed in a partially absorber lined chamber, whereas the plane-polar system had some metallic surfaces exposed, thereby increasing the scattering in some localised directions. Although not shown, the agreement attained between the respective cross-polar patterns was similarly encouraging, with only small differences being observed on

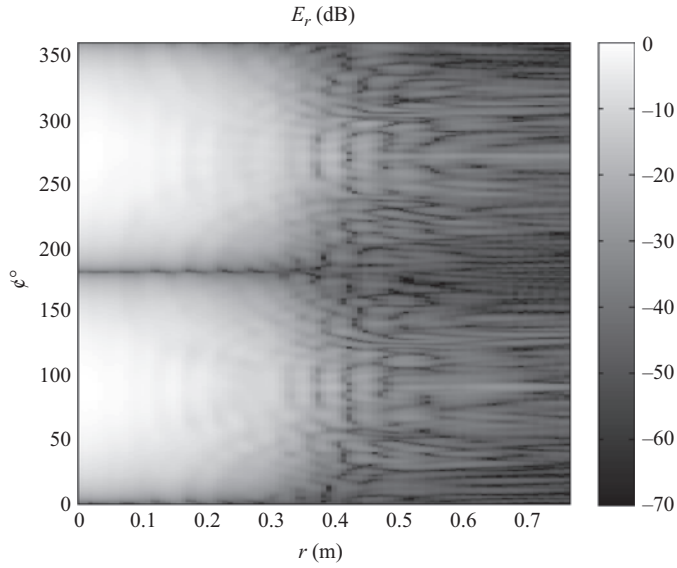


Figure 6.14 E_ϕ polarised measured near electric field component

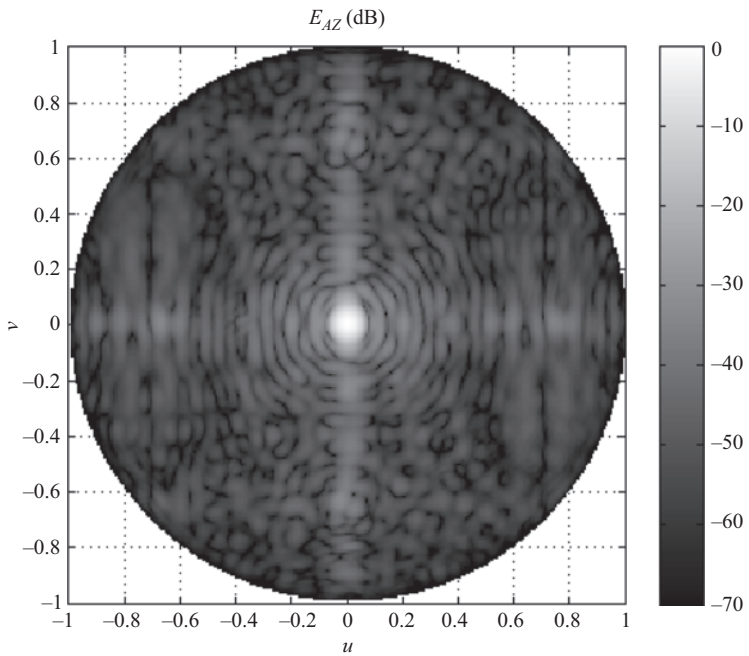


Figure 6.15 Far-field power pattern from plane-rectilinear measurement

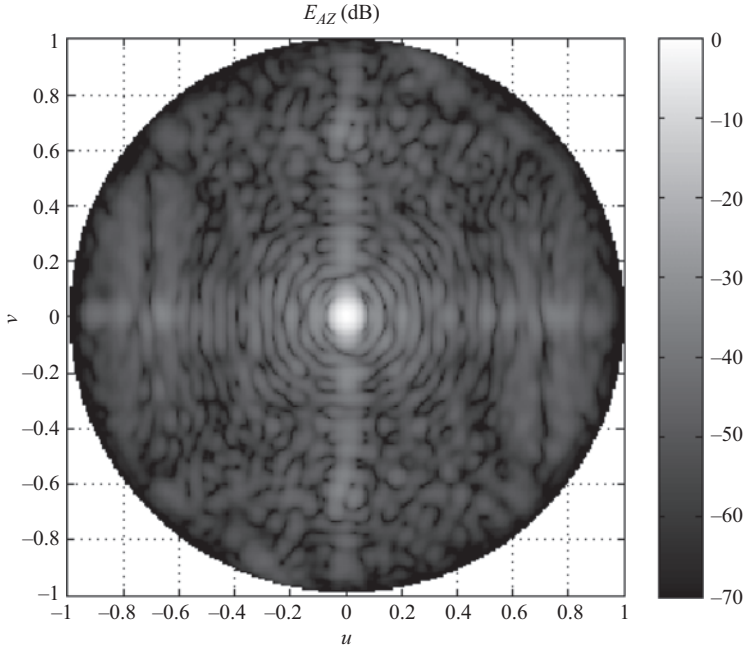


Figure 6.16 Far-field power pattern from plane-polar measurement

boresight, which resulted primarily from the use of a theoretical probe pattern correction that was not able to take account of imperfections in manufacture. This impacted on the polarisation purity of the realised probe.

A comparison of the horizontal, u , cardinal cut is presented in Figure 6.17, where the agreement attained between the plane-polar and plane-rectilinear measurements is similarly encouraging.

By way of further validation, Figures 6.18 and 6.19 contain, respectively, the reconstructed aperture illumination function of the waveguide array as obtained from planar and plane-polar near-field testing. Similarly, Figures 6.20 and 6.21 contain equivalent phase functions. From these figures it is clear that the agreement is very encouraging. The underlying functional form of the respective amplitude and phase patterns are the same, with a very slight difference in horizontal phase taper evident between the plane-rectilinear and plane-polar holograms, indicating slight azimuth misalignment of the AUT when it was installed within the plane-rectilinear range.

6.6.2 Conventional and alternate plane acquisition types

As is evident from the plane-polar coordinate system, plane-polar antenna pattern measurements can be taken using several different acquisition types. Three commonly utilised cases are:

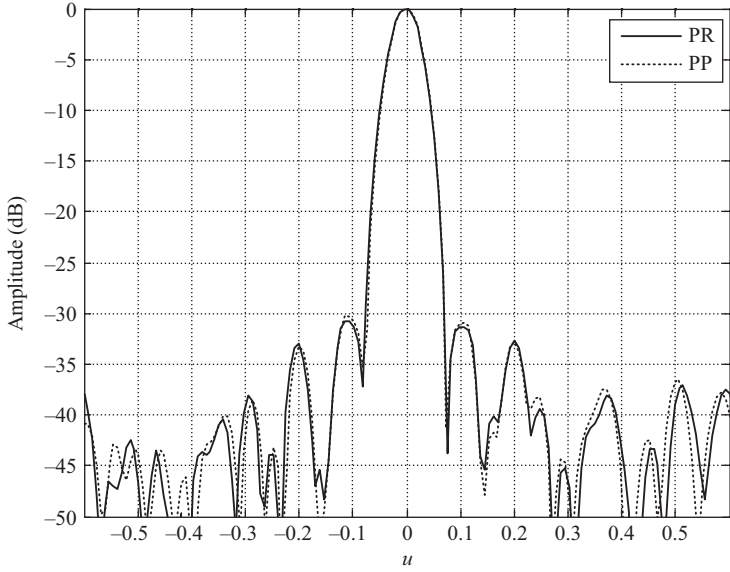


Figure 6.17 Comparison of far-field u cut from plane-rectilinear and plane-polar measurements

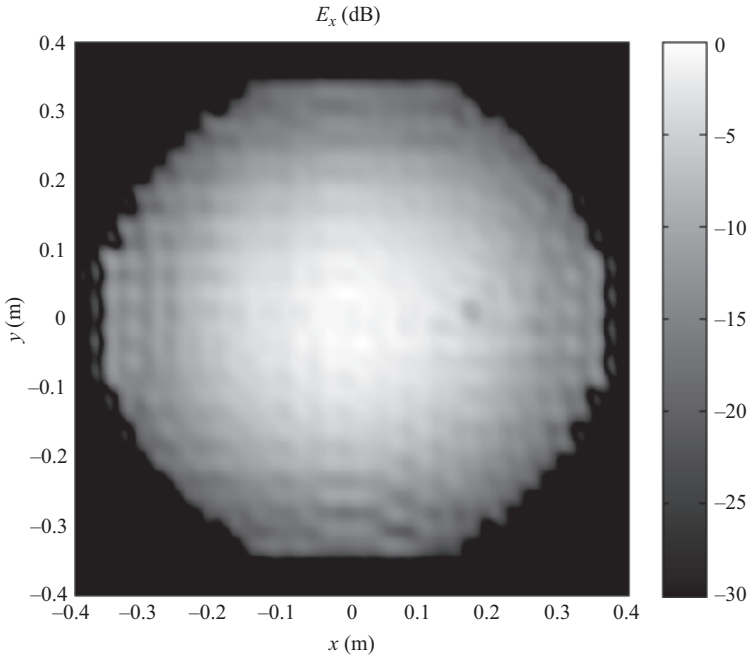


Figure 6.18 Aperture illumination amplitude function from plane-rectilinear measurement

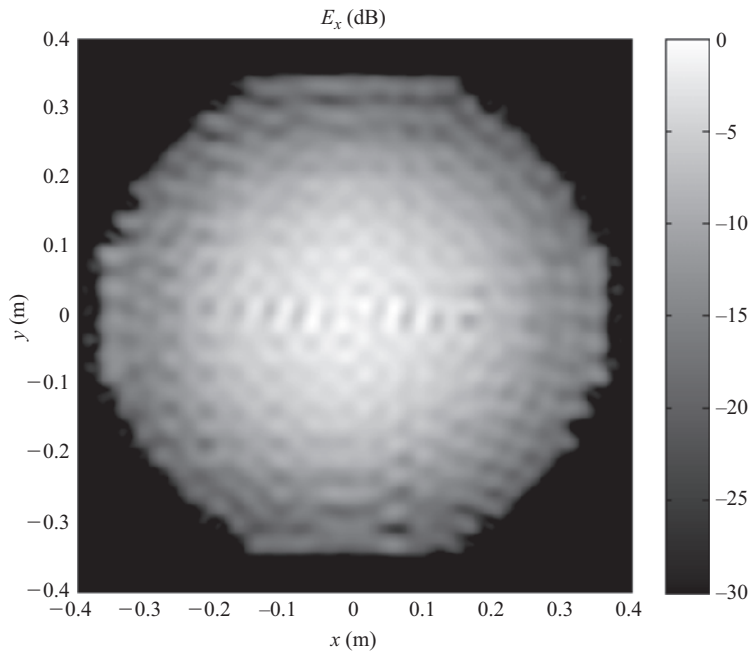


Figure 6.19 Aperture illumination amplitude function from plane-polar measurement

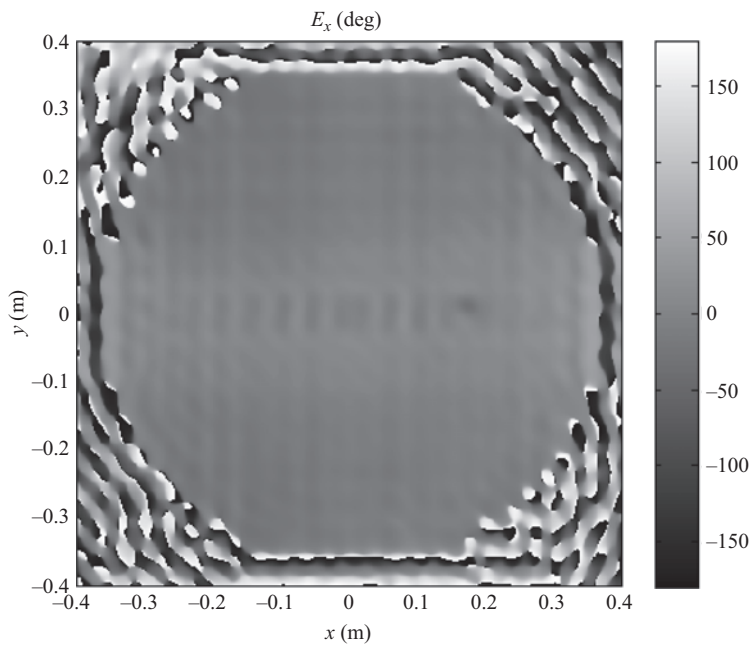


Figure 6.20 Aperture illumination phase function from plane-rectilinear measurement

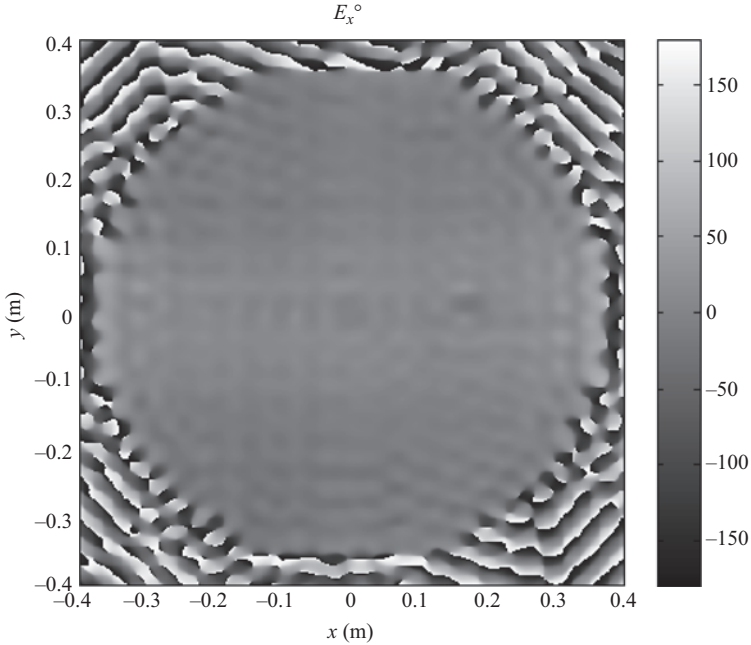


Figure 6.21 Aperture illumination phase function from plane-polar measurement

1. $0 \leq r \leq r_{MAX}$, $-\pi \leq \phi \leq \pi$, (conventional plane),
2. $-r_{MAX} \leq r \leq 0$, $-\pi \leq \phi \leq \pi$, (alternate plane),
3. $-r_{MAX} \leq r \leq r_{MAX}$, $-\pi \leq \phi \leq \pi$, (redundant).

Case 3 requires the ϕ -axis to intersect with the centre of the linear translation stage as illustrated in Figures 6.9 and 6.10. Conversely, Figure 6.12 shows the ϕ -axis in the usual position used for plane-polar measurements (i.e. Case 1) where negative r motion is not possible. Here, when the angles are in radians, the mapping from the ‘alternate’ (or second) plane to the conventional (or first) plane can be expressed mathematically as, $r \rightarrow -r$ and $\phi \rightarrow \phi \pm \pi$. Clearly then, by allowing ϕ to vary by more than modulo 2π or, alternatively, by allowing the polar angle to be centred about a value other than zero, an infinite number of other, trivial, representations become available but these offer no additional utility to those presented above and are not considered further. Although each of these schemes acquires the same scan area, the position of the AUT and the probe within the facility when the data is acquired is different.

This therefore provides a simple and effective way to assess and, potentially, suppress chamber multi-path, i.e. clutter. Figure 6.22 contains a comparison of the conventional and alternate planes (with the alternate plane x -polarised electric near-field data having been mapped into the conventional plane using the aforementioned coordinate transformation) for the case of an x -band slotted waveguide planar array antenna of approximate diameter 10 in. (0.254 m). Here, the patterns

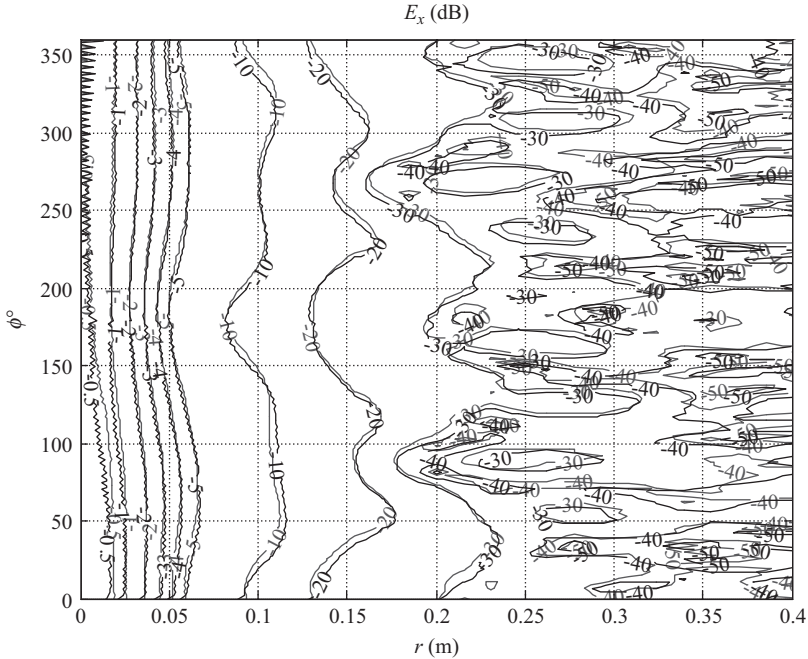


Figure 6.22 Comparison of conventional plane and alternate plane near-field data

have been plotted tabulated on a plaid monotonic plane-polar grid with the near-field being acquired with the probe counter-rotated (in a Ludwig III type acquisition scheme, cf. Chapter 4) so that the AUT and probe field remain polarisation matched throughout the near-field scan. For a correctly aligned system, differences between the respective conventional and alternate contours primarily result from range reflections. A quantitative measure of the similarity between the measured data sets can be obtained by evaluating equivalent multi-path level (EMPL) [13]. The EMPL is half the absolute difference between the patterns expressed in dB and can be thought of as the amplitude necessary to force the two different pattern values to be equal. Here, the differences that result primarily from range clutter peak at the circa -30 dB level with respect to the peak of the pattern. As there are no systematic differences evident, it is possible to confirm that measurement errors resulting from imperfections in range alignment ($r = 0$ offset error – more attention is devoted to this error below), backlash or drift are minimal and can be ignored for the purposes of this comparison exercise. As this measurement is over determined (i.e. containing ‘redundant’ data), it constitutes an excellent candidate for verifying the effectiveness of clutter suppression techniques.

Clearly, it is possible to obtain far-field data using the conventional plane, the alternate plane and the average of the two data sets where the averaging process can be used to suppress the effects of range reflections. However, although a viable

strategy, this would result in a doubling of the measurement time which is undesirable in many applications. Alternatively, as the AUT is an ‘aperture antenna’, it is possible to perform a back propagation of the radiated near-fields to the antenna aperture plane (i.e. infinitesimal planar interface between the conduction current and the displacement current being the majority carrier) before applying a two-dimensional band pass spatial filter function so as to set the fields outside of the antenna’s aperture plane to zero whereupon the filtered far-field pattern can be recovered, cf. Chapter 12. Lastly, the P-MARS mode orthogonalisation and filtering algorithm can be harnessed to obtain multi-path suppressed far-fields [14]. More details on this last option are provided in Chapter 12.

6.6.3 Plane-polar alignment

As with all near-field methodologies, accurate and precise probe positioning is of paramount importance to the success of the technique and comprises an important term within the facility level uncertainty budget, cf. Chapter 10.

In order to perform valid plane-polar near-field measurements, several fundamental alignment requirements must be met:

1. The near-field probe should travel along a linear translation stage (radial axis) while maintaining a constant position in both transverse directions.
2. The vector of the scanner’s ϕ -axis rotator should be orthogonal to and intersect with the direction of probe travel.
3. The vector of the probe’s polarisation rotator should also be orthogonal to the radial axis and anti-parallel to the ϕ -axis.

The position of the probe along the radial axis where the scanner’s polarisation and ϕ -axis are coincident should be defined as its zero position, r_0 . There should be no deviation of this from the true zero, and as the plane-polar system has a pole in the coordinate system, this is a non-arbitrary point in space. A great deal of effort and ingenuity has been devoted to the mechanical alignment of plane-polar antenna test systems, through mechanical and optical measurements, cf. [15]. However, it is also possible to augment these measurements with electrical tests to further verify and refine the systems alignment.

As discussed above, the mechanical ϕ -axis rotator must be correctly aligned with the linear axis and the probe placed in the proper location when performing plane-polar near-field measurements. In some cases it may be impractical to place the optical alignment equipment on the AUT or optical instruments may not be available. In these cases, it may be desirable to check the alignment using electrical measurements on the actual AUT and probe. Appropriate comparison and analysis of two near-field measurements (which can be extracted from a carefully orchestrated single acquisition) that should be identical yield precise measures of some rotator and probe alignment errors.

While in principle these tests are independent of the AUT pattern, as shown in Figure 6.23, judicious choice or placement of the antenna can significantly increase the sensitivity of this procedure. Careful examination of the 180° ϕ scan

acquisition, recalling that the mapping from the ‘alternate’ (or second) plane to the conventional (or first) plane can be expressed mathematically as $r \rightarrow -r$ and $\phi \rightarrow \phi \pm \pi$, illustrates that the $\phi = 180^\circ$ cut represents a repeat measurement of the $\phi = 0^\circ$ cut. This is illustrated in Figure 6.23, which contains a comparison of $\phi = 0^\circ$ and $\phi = 180^\circ$ cuts showing effect of r_0 error on near-field data. That is to say, the point on the linear scan axis that is defined to be zero is not coincident and synonymous with the ϕ rotation axis.

The misalignment is clear from this ‘flip’ test. Perhaps the simplest and most reliable method for determining the displacement between these patterns is to determine the spectral content and examine the relative phase difference. An alternative approach would be to interpolate the measured patterns to sequentially shift the respective patterns and to assess the correspondence by evaluating the cross-correlation coefficient; however, the spectral method is a more direct, noise suppressing technique. The one-dimensional spectral content of the cut can be obtained by evaluating the one-dimensional Fourier transform [16] using,

$$F(u) = \int_{-\infty}^{\infty} f(r)e^{jk_0ur} dr \quad (6.22)$$

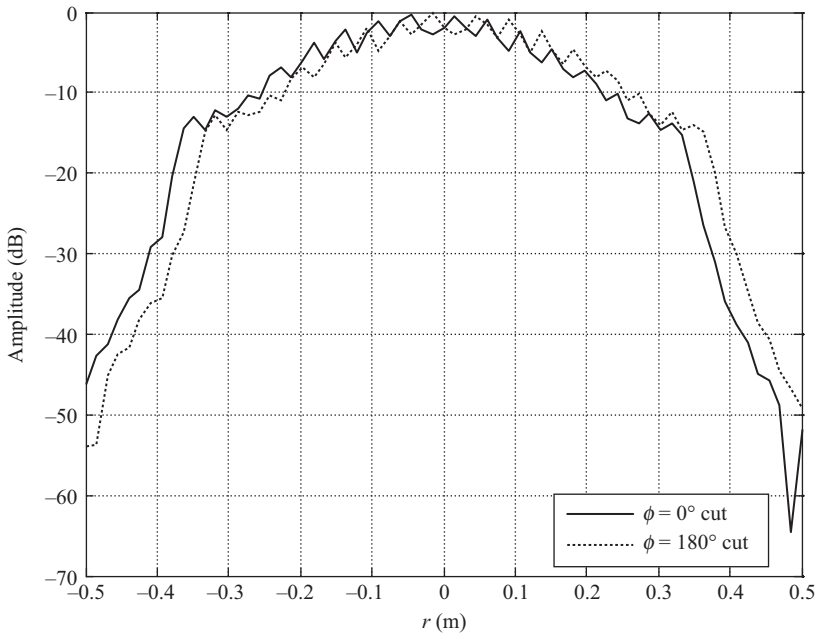


Figure 6.23 Comparison of $\phi = 0^\circ$ and $\phi = 180^\circ$ cuts showing effect of r_0 error on near-field data

Here, the range of the one-dimensional integral collapses so that the Dirichlet conditions [17] and the Nyquist [1] sampling conditions are satisfied, which would be the case for any conventional near-field measurement from which conceivably this data would be extracted. The resulting magnitude and phase spectra are presented in Figures 6.24, 6.25 and 6.26 respectively, where the traces denote spectra arising from the $\phi = 0^\circ$ cut and the $\phi = 180^\circ$ cut. The slight differences in the spectra result in the different truncation suffered by the respective near-field measurements. In the absence of truncation, these two sets of spectra would be identical.

Here, it is assumed that $\phi = 0^\circ$ and $\phi = 180^\circ$ are parallel and anti-parallel respectively with the linear axis of the plane-polar near-field test system. Figure 6.26 shows that, with the shifting properties of the Fourier transform, a linear phase taper is introduced into the far-field pattern. The underlying linear phase function Δ , when expressed in radians, can be determined from the ratio of the respective spectra as (Figure 6.24)

$$\Delta(u) = \text{imag} \left(\ln \left(\frac{F_0(u)}{F_{180}(-u)} \right) \right) \quad (6.23)$$

Here, imag is used to denote a function that returns the imaginary part of the argument, and \ln is the natural logarithm. The slope of $\Delta(u)$ can be obtained numerically by performing a least squares best fit to a linear phase function (i.e.

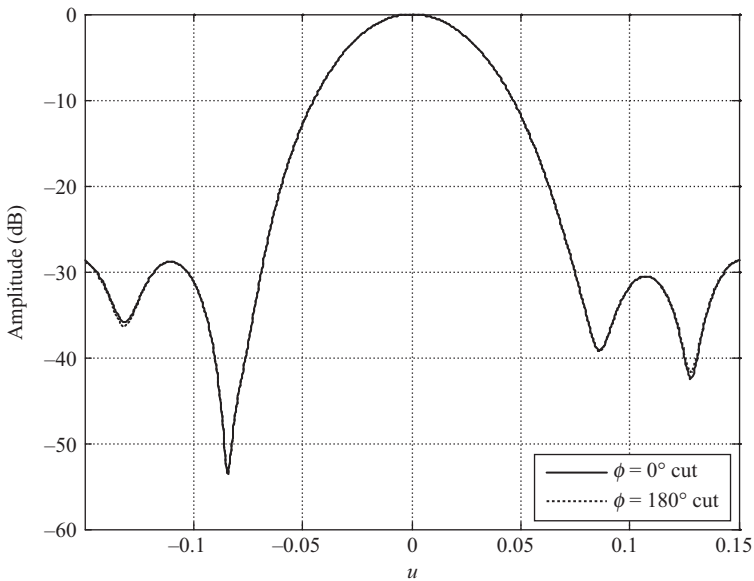


Figure 6.24 Comparison of $\phi = 0^\circ$ and $\phi = 180^\circ$ amplitude spectra showing effect of r_0 error

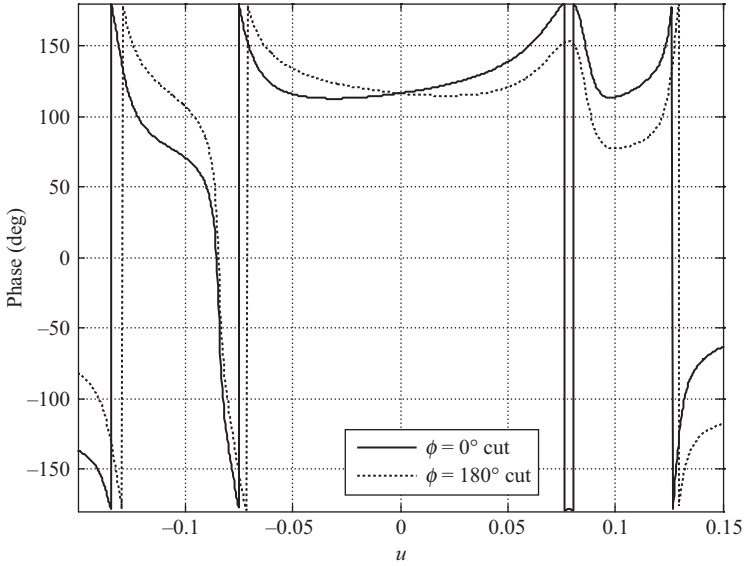


Figure 6.25 Comparison of $\phi = 0^\circ$ and $\phi = 180^\circ$ phase spectra showing effect of r_0 error

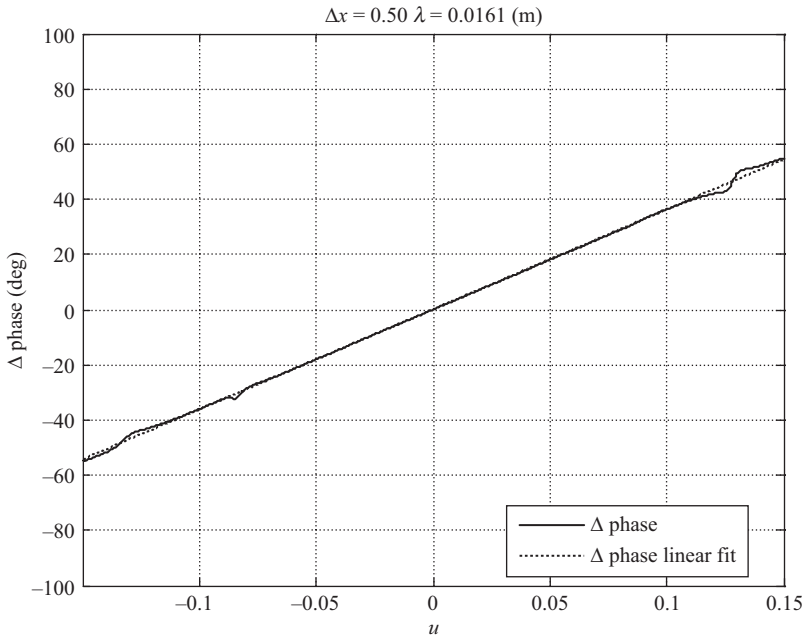


Figure 6.26 Difference between phase spectra of $\phi = 0^\circ$ and $\phi = 180^\circ$ cuts

linear regression), $y = mx + C$ about the spectral region of greatest intensity. Once the gradient, m , of $\Delta(u)$ is known, the linear displacement term can be obtained using

$$r_0 = \Delta x = m/(2k_0) \quad (6.24)$$

Here, the additional factor of a half is included as the displacement is obtained from the difference between the $\phi = 0^\circ$ and $\phi = 180^\circ$ cuts. As each individual cut contains the r_0 error, the phase difference will contain twice the expected error and this factor compensates for that. It has been found that this algorithm can correctly recover the r_0 offset (a half wavelength for the case shown). However, it was also found that much smaller offsets could be reliably recovered, with offsets as small as a twentieth of a wavelength (~ 1.6 mm at 9.375 GHz) being readily resolved. This data therefore confirms that calculation of a phase reference position based on two cuts ($\phi = 0^\circ$ and $\phi = 180^\circ$) taken from a single near-field acquisition can provide a measure of the near-field r_0 error (error in the index offset) without the need to make auxiliary mechanical measurements. This type of calibration can be performed at a single frequency, and the information recovered can then be used for all subsequent measurements at all frequencies to correct for the alignment error. While this method is not able to distinguish between probe translation and AUT translation, by repeating the measurement and instead rotating the probe by 180° a similar procedure can be used to first determine and subsequently remove probe translation effects before then establishing the r_0 [15].

The importance of an r_0 error can be illustrated with the measurement of a narrow beam, slotted waveguide array, with a gain of 35 dB as the AUT with an operating frequency of 9.375 GHz. Plane-polar near electric fields have been simulated for each of these modes with varying r_0 errors being introduced into the simulations. The equivalent far-fields were then determined using standard plane-polar near-field to far-field transformation techniques.

As defined above, the r_0 error was taken to be the linear distance between the zero on the linear scan axis (i.e. the point that is defined to be the pole of the plane-polar coordinate system $r = 0$) and the *true* point where the rotation axis actually intersects with the linear axis. Figure 6.27 contains the great circle cardinal cut as obtained from the 360° ϕ acquisition data with r_0 errors at 0 (ideal reference), $\lambda/20$, $\lambda/10$ and $\lambda/5$. From these figures it is clear that the peak of the pattern noticeably reduces as the r_0 error increases. This is also shown in Figure 6.28 in which the axes of the plot have been adjusted so as to focus on the main beam region of the antenna patterns. From this figure, it is evident that a comparatively small r_0 error, i.e. one-twentieth of a wavelength resulted in a reduction in the peak pattern level of circa 0.1 dB. This would correspond to a comparatively large component in the overall facility level gain uncertainty budget. Furthermore, as the r_0 error increased, the location of the side lobes progressively shifted to wider angles. This behaviour was expected as larger r_0 errors result in an apparent reduction in the spatial extent of the AUT, thereby reducing the measured gain value and increasing the beam-width of the observed far-field pattern.

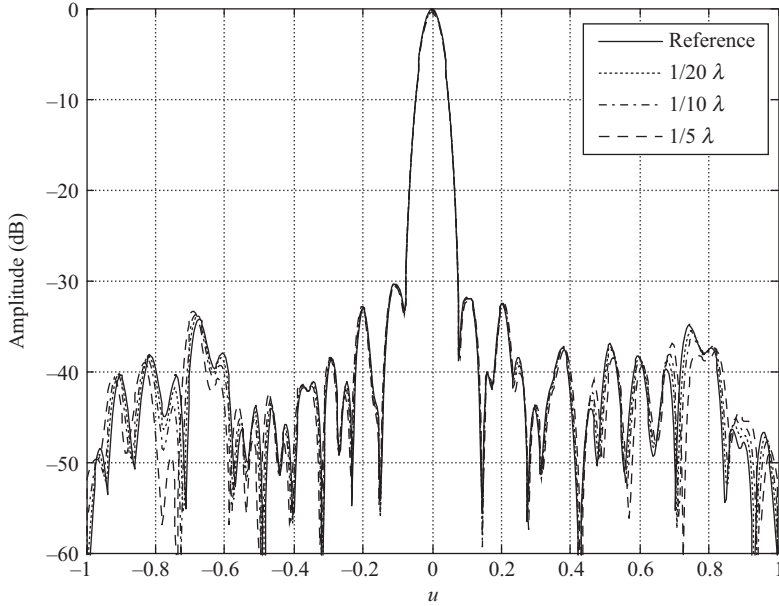


Figure 6.27 Far-field cardinal cut of $360^\circ \phi$ measurements showing pattern for various r_0 errors

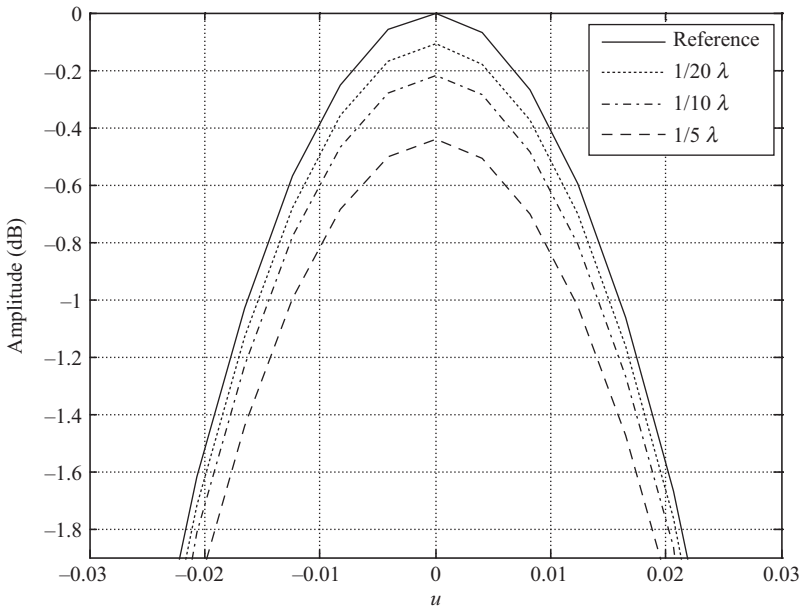


Figure 6.28 Far-field cardinal cut of $360^\circ \phi$ measurements showing beam peak for various r_0 errors

Figures 6.29 and 6.30 contain far-field patterns equivalent to those in Figures 6.27 and 6.28 above; only here the far-field patterns were obtained from the $180^\circ \phi$ acquisition.

From Figure 6.30 it is evident that the peak level is *far* less sensitive to the r_0 error than was the case for $360^\circ \phi$ scan data. The location of the side lobes varies with the r_0 error, exhibiting similar behaviour to the $360^\circ \phi$ scan data. The apparent insensitivity in peak level to the r_0 error for the $180^\circ \phi$ scan data requires further examination, as this behaviour is perhaps not immediately apparent. One explanation for this behaviour can be obtained by considering the effect that this error has on the projected effective area of the antenna as measured in the near-field. For the case of the $360^\circ \phi$ scan, as the r_0 error gets larger, the projected area of the AUT decreases.

Conversely, for the case of the $180^\circ \phi$ scan, the projected area remains constant. This makes sense from the scan type standpoint since for the case of a $180^\circ \phi$ scan mode, an r_0 error merely displaces the AUT in each individual cut with the true ‘width’ of the illumination being preserved as the AUT is, in essence, merely translated linearly from its true position. This is not the case for the 360° scan in which the AUT is apparently shrunk (or conversely enlarged depending on the sign of the r_0 error) with radiated energy being omitted from the measurement. Clearly, although preserving the area of the near-field illumination within the $180^\circ \phi$ scan will yield a more stable far-field peak, a consequence of the non-physical discontinuity in that near-field illumination will inevitably result in the appearance of

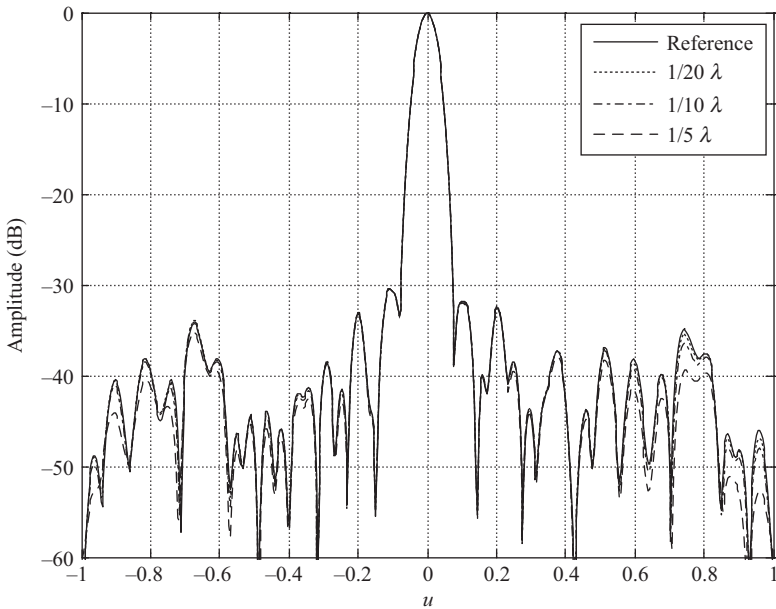


Figure 6.29 Far-field cardinal cut of $360^\circ \phi$ measurements showing pattern for various r_0 errors

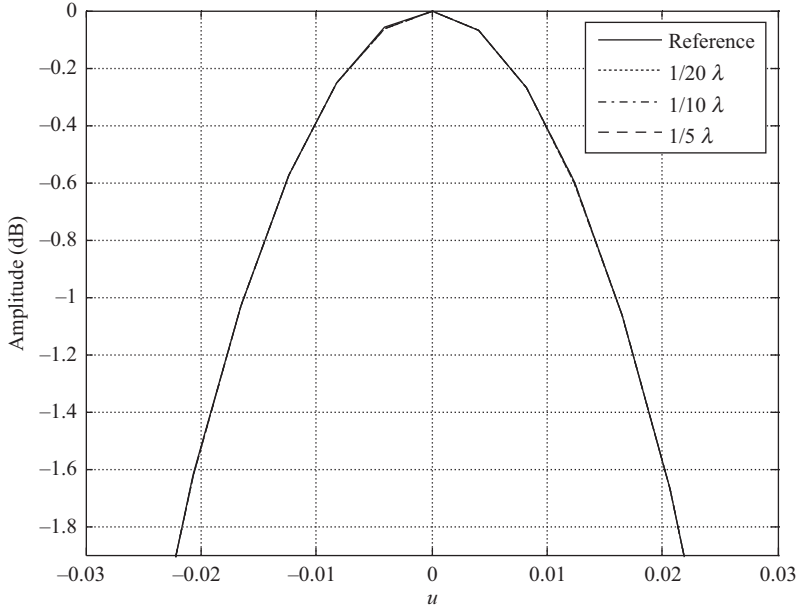


Figure 6.30 *Far-field cardinal cut of 360° ϕ measurements showing pattern for various r_0 errors*

spurious high angular frequency side lobes in the far-field. Thus, correctly determining the r_0 point remains critical if reliable antenna measurements are to be obtained from the plane-polar methodology.

6.6.4 Remaining data acquisition factors of planar scanning

Having established the capabilities, requirements and limitations of planar near-field measurements in terms of RF sub-systems, robotic positioners, near-field probes, planar acquisition geometries and near-to-far-field transforms, it can be realised how data sampled on a planar surface can be effectively used to predict the far-field pattern of an antenna.

Section 6.2 confirms the usual requirements related to the Nyquist sampling criteria for planar near-field measurements. However, near-field measurements can present particular challenges in terms of acquiring suitable sampled data that are related to the measurement methodology and particular attention must be paid to the implications of these challenges if effective near-field measurement results are to be obtained.

6.7 Sampling (interpolation theory) and aliasing

Following the development presented above, it is well known that if the measured field is band limited in the x - and y -axes to k_{x0} and k_{y0} , then a sample spacing of Δx ,

Δy will be sufficient to allow the entire function to be reconstructed from the sampling theory when assuming a plane rectilinear acquisition scheme is adopted [18]. A result of the sampling theorem is that one may consider evaluating the necessary integrals by replacing them with summations with equal sample spacing without introducing an error, the power of the sampling theory lies within recognising that the summation itself is rigorous, providing only that the sample spacing is less than some specific finite value in each axis where the sample spacing in the x - and y -axes is given, respectively, by

$$\Delta x = \frac{\pi}{k_{x0}} \quad (6.25)$$

$$\Delta y = \frac{\pi}{k_{y0}} \quad (6.26)$$

For propagating, i.e. homogeneous plane-wave spectra, the spectrum is limited to

$$k_{x0} = k_{y0} = \frac{2\pi}{\lambda} \quad (6.27)$$

Thus, the sample spacing required to guarantee this, when related to the wavelength, is given by

$$\Delta x = \Delta y = \frac{\pi}{\frac{2\pi}{\lambda}} = \frac{\lambda}{2} \quad (6.28)$$

This implies that, at the baseband, we need two samples per free-space wavelength to uniquely characterise the field across the planar acquisition interval which satisfies the Nyquist sampling theorem. Thus, the limits of integration collapse to a finite interval and the continuous field can be reconstructed from the samples. However, as shown above, in order to apply the sampling theorem, the function must be band-limited. However, the plane-wave spectrum is not *truly* band-limited in the strictest sense although, as we shall now show, a practical band limit does exist since evanescent modes, i.e. non-homogeneous plane waves, attenuate very rapidly as a function of distance. The attenuation when expressed in decibels can be obtained from the propagation vector using

$$A_{dB} = 20 \log_{10}(e^{jk_z z}) \quad (6.29)$$

Here, A is the attenuation expressed in a logarithmic, i.e. dB, form. For evanescent modes, the propagation vector k_z will be complex as, cf. Chapter 4,

$$\gamma = -j\sqrt{u^2 + v^2 - 1} \quad (6.30)$$

where $k_x = k_0 u$ and $k_y = k_0 v$. Thus, the attenuation can be expressed as

$$A_{dB} = 20 \log_{10}\left(e^{k_0 z \sqrt{u^2 + v^2 - 1}}\right) = 20 \log_{10}\left(e^{2\pi(z/\lambda)\sqrt{u^2 + v^2 - 1}}\right) \quad (6.31)$$

Hence, assuming that the attenuation when written in a decibel form is represented by a negative number and, from the law of logarithms,

$$A_{dB} = -54.6 \frac{z}{\lambda} \sqrt{u^2 + v^2 - 1} \tag{6.32}$$

This illustrates that on the unit circle there is *no* attenuation; however, beyond the unit circle the amount of attenuation increases. This is illustrated in Figure 6.31 which contains plots of the attenuation experienced by the modes on circles of various radii, i.e. these are higher order evanescent modes which are being used to illustrate that higher order modes attenuate more rapidly with increasing separation.

The plane-wave spectrum segregates propagating (homogeneous) and non-propagating (non-homogeneous evanescent) plane waves with the evanescent modes being located outside the unit circle, i.e. where $u^2 + v^2 > 1$. This is illustrated in Figure 6.32 which shows the plane-wave spectrum obtained from fields taken within the aperture plane of an AUT, which in this case was an *x*-band pyramidal horn. Figure 6.32 also contains white circles that denote the unit circle, i.e. the interface between propagating (homogeneous) plane waves and reactive (non-homogeneous) plane waves. Two additional circles are plotted with radii of 2 and 3 cycles per wavelength that correspond to the $2K_T/k_0$ and $3K_T/k_0$, respectively. Here, the $2K_T/k_0$ circle corresponds to the $2K_T/k_0$ trace presented in Figure 6.31.

Thus, if one were in possession of an RF sub-system with infinite precision, then it would be possible to detect these reactive fields and finer sample spacing would therefore be needed. However, this absence of the detection of evanescent

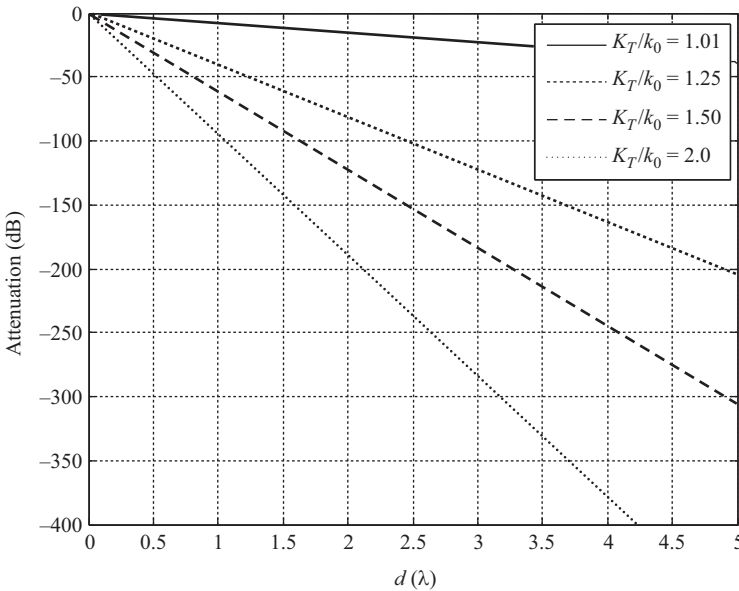


Figure 6.31 Plot of attenuation of evanescent modes as a function of distance

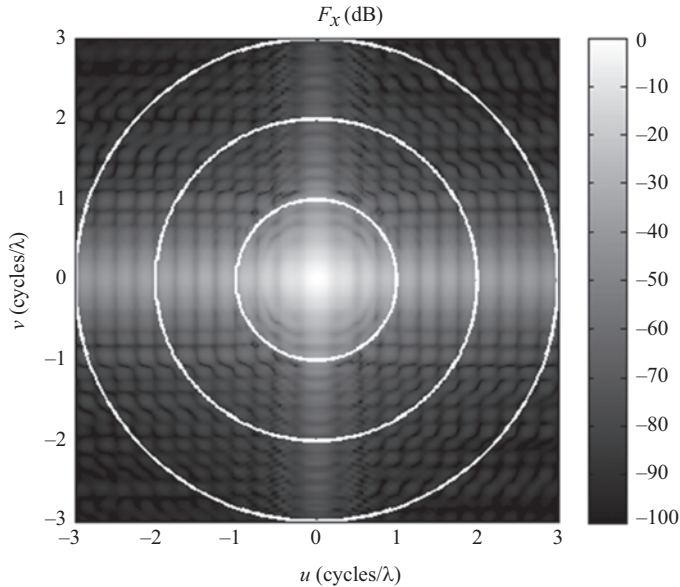


Figure 6.32 Greyscale plot of the intensity of the plane-wave spectrum obtained from samples taken in the aperture plane of a pyramidal horn showing both propagating (visible) and evanescent (non-visible) regions of the plane-wave spectrum

modes imposes a limit to the maximum resolution of the measurement. That is to say, when no evanescent fields are detected, the maximum resolution of the measured field is one-half wavelength. For example, when the separation $d = 3\lambda$, the lowest order reactive field is attenuated resulting in the PWS outside of the unit circle being largely absent, or in practice being dominated by random noise resulting from thermal noise or processing errors, e.g. resulting from truncation or rounding. This is illustrated in Figures 6.33 and 6.34 which contain greyscale checkerboard plots of the magnitude of the plane-wave spectrum as calculated from simulation of an x -band pyramidal horn where the fields were sampled across a plane that was 0.09λ , i.e. just skimming the aperture of the AUT, and 3λ , at a typical measurement distance, from the aperture plane of the horn respectively. In each plot, the unit circle, cf. the Ewald sphere, is plotted in white designating the interface between the propagating, i.e. ‘visible’, and the non-propagating, i.e. ‘invisible’ portions of the spectrum. For the case where the sampling plane is very close to the aperture plane of the AUT, a significant portion of the evanescent field is sampled resulting in the presence of reactive plane-wave component which lie outside of the unit circle, i.e. where $\alpha^2 + \beta^2 > 1$. However, as the separation is increased between the aperture plane of the antenna and the sampling plane, the reactive plane-wave component is greatly attenuated resulting in the absence of field outside the unit circle. However, the propagating field is

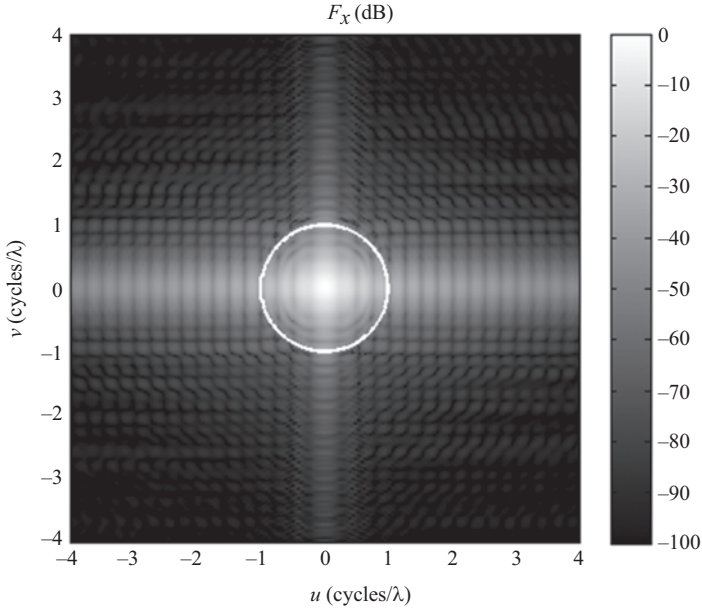


Figure 6.33 PWS for field sampled at a distance of $z = 0.09\lambda$ showing a significant amount of reactive field

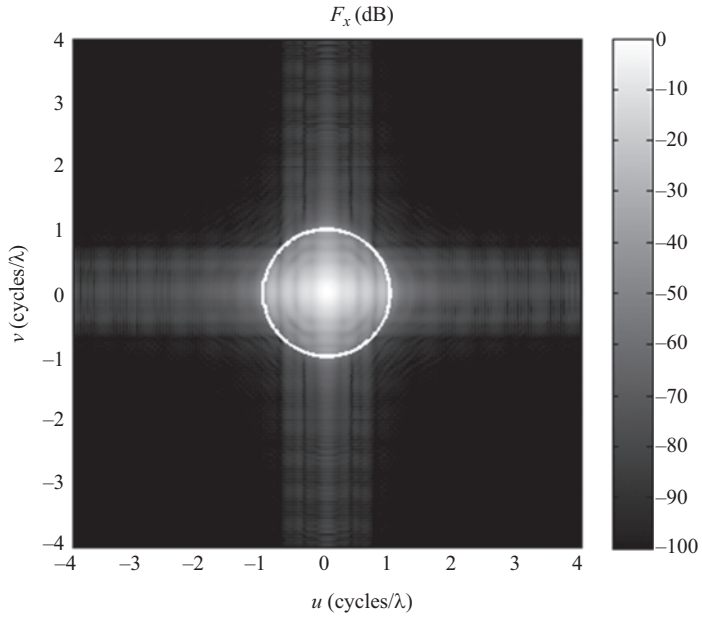


Figure 6.34 PWS for field sampled at a distance of $z = 3\lambda$ showing reactive fields being largely absent

unaffected meaning that the pattern within the unit circle is unchanged between Figures 6.33 and 6.34.

The similarity of the propagating portion of the plane-wave spectra and the difference in the reactive portion of the plane-wave spectra are illustrated in Figure 6.35, where the 0.09λ data set is plotted using a solid line and the 3λ data set is plotted using a dotted line. The vertical dashed lines at ± 1 denote the boundary of the visible portion of the spectrum. Clearly then, the visible part of the spectrum, i.e. the propagation modes, will reach the measurement plane, whereas the evanescent waves will not reach the measurement plane as they are attenuated rapidly with distance.

Thus, the finest detail that can be observed within a measurement is limited by the highest spatial frequency contained within the plane-wave spectrum and is therefore related directly to the wavelength of the RF (i.e. light) that is being used for taking the measurement. If near-field evanescent waves are detected, greater image resolution can be attained. In principle, evanescent can be considered to represent plane-waves which flow back and forth in the aperture plane, that is to say, they are surface waves which store energy until a probe is placed in close proximity whereupon they can couple into that probe and then propagate within the waveguide. An interesting point which is worth noting is that the phase velocity of

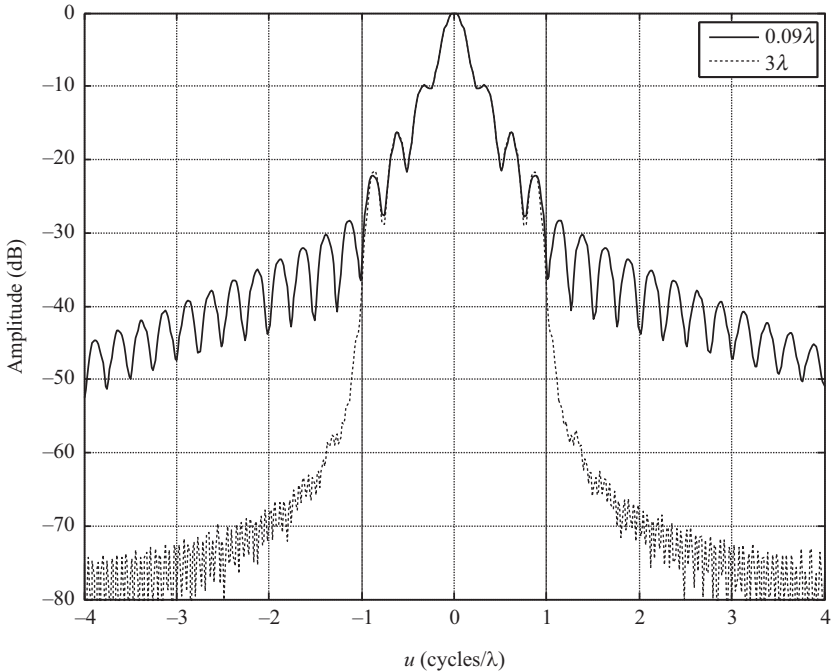


Figure 6.35 Comparison of evanescent fields at different AUT-to-probe separations

the inhomogeneous plane wave is less than that of a homogeneous plane wave. The reason for this is that as the velocity v is determined by the product of the frequency and the wavelength, i.e. $v = f\lambda$ and as f is fixed this implies that $v < c$, the free-space speed of light, then wavelength must also be shorter than that of homogeneous plane-wave. As the wavelength is shorter, we need to use a finer sample spacing to avoid aliasing and will result in higher spatial frequencies in the plane-wave spectrum, which is why we see these components fall outside the unit circle. Thus, free space can be seen to constitute a velocity selecting medium attenuating waves which propagate at velocities other than c .

When we sample a signal, we impose a periodic nature of the spectra of the sampled signal. This is also true here however as we sample in two dimensions, i.e. x - and y -axes, we also impose periodicity in both the k_x and k_y dimensions (or equally, u , v), that is to say, we obtain a periodically repeating spectrum in two axes. This is illustrated in Figure 6.36. Here, the planar near-field data was sampled a wavelength spacing in both the x - and y -axes. As the maximum spectrum is determined from the sample spacing from

$$k_{0x \max} = \left| \frac{\pi}{\delta x} \right| = \left| \frac{\pi}{\lambda} \right| \quad (6.33)$$

Thus, the maximum value of u or v is ± 0.5 . That is to say, the computed spectra repeat beyond ± 0.5 which is evident from inspection of Figure 6.36. Thus,

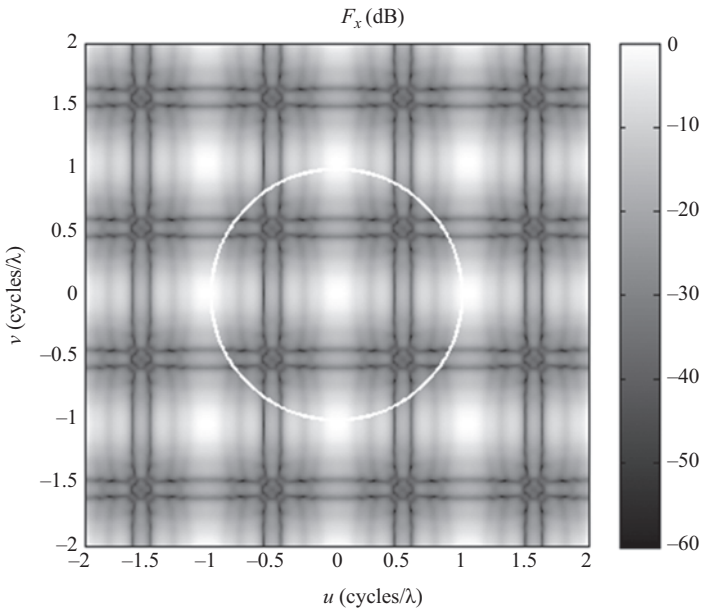


Figure 6.36 Spectrum obtained from sampling in the near-field using $\delta x = \delta y = \lambda$ spacing

at wavelength spacing, the visible portion of the spectral pattern is aliased back into the visible space. At half-wavelength spacing, the pattern is repeated at ± 1.0 and this can be seen illustrated in Figure 6.37 where again the limit of visible space is represented with a unit radius white circle. This implies that only the non-visible portion of the plane-wave spectrum suffers from aliasing. This is a region that is not of interest when determining far-field antenna parameters and is acceptable in many, although not all applications. Lastly, Figure 6.38 presents the spectrum for the case where the near-field was sampled with a quarter wavelength sample spacing. Here, the spectrum repeats beyond ± 2.0 meaning that even AUT-to-probe multiple reflections, etc., would not be aliased into the visible portion of the spectrum in the event that they had been present, see the next section.

6.8 Finer than Nyquist sampling

As expounded within the preceding section, conventional plane rectilinear near-field measurements are acquired using sample spacing on a plane rectilinear grid of one-half wavelength in each axis, the reader is referred to Chapter 3 for a treatment of minimum sampling antenna measurements. However, there are cases where this sampling scheme can be seen to become insufficient with the ensuing far-field patterns suffering from aliasing artefacts which manifest themselves in the form of spurious side lobes in the computed far-field pattern. This effect is illustrated in this

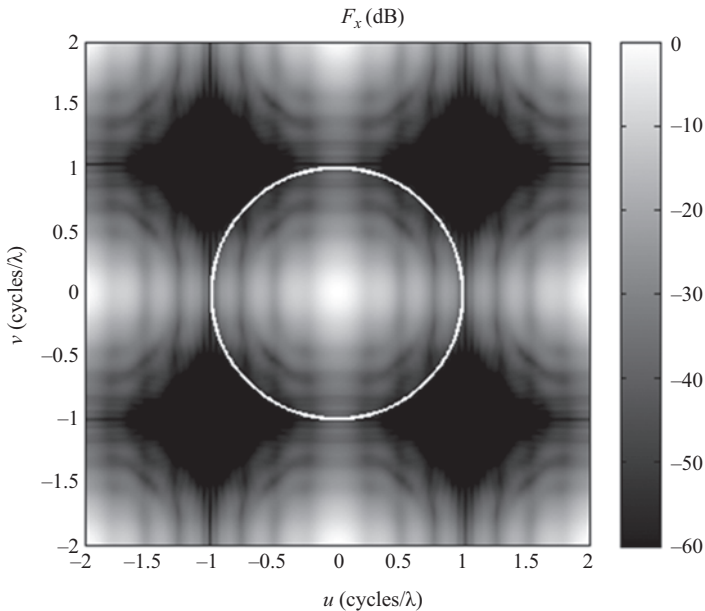


Figure 6.37 Spectrum obtained from sampling in the near-field using $\delta x = \delta y = \lambda/2$ spacing

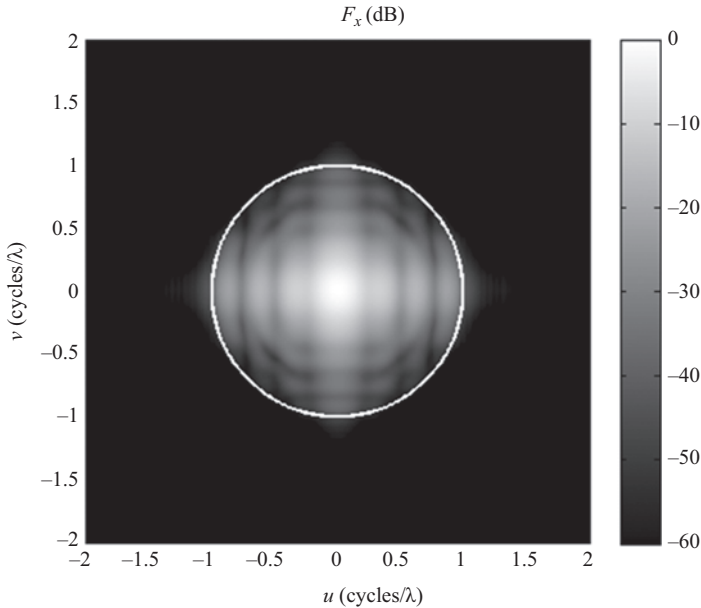


Figure 6.38 Spectrum obtained from sampling in the near-field using $\delta x = \delta y = \lambda/4$ spacing

section together with a method for identifying and compensating for the artefact. Figure 6.39 presents a false-colour checkerboard plot of the amplitude pattern of the angular spectrum obtained from a measurement of a slotted waveguide array antenna that was sampled using half-wavelength sample spacing in the x - and y -axes. Here, as expected, cf. Figure 6.37, the sampling in the spatial domain results in periodicity in the spectral domain. However, in this example, the measured near-fields were modulated by multiple reflections between the scanning probe and the planar array antenna that was being tested. In general, AUT-to-probe multiple reflections will modulate the measured signal and can have a maximum spatial frequency that is double that of the un-modulated transmitted free-fields. In this particular example, elements within the array were laid out on a regular lattice that further modulated the total field that was measured by the near-field probe. In this case, an x -band slotted waveguide array was measured at different sample spacing in the x - and y -axes with an AUT-to-probe separation held fixed at 0.9 wavelengths which resulted in the high level of multiple reflections seen here.

As expected, the main beam and side lobes are aliased outside of visible space, with the maximum extent of visible space being represented with a red unit circle in each plot. Unfortunately, at half-wavelength spacing, some of the AUT-to-probe multiple reflections are aliased back into visible space through the effect of circular convolution. At quarter wavelength, multiple reflections are also shifted outside of visible space as is evident in Figure 6.40. In practice, when measuring periodic antennas, it is worth acquiring a near-field data set at finer than Nyquist sample

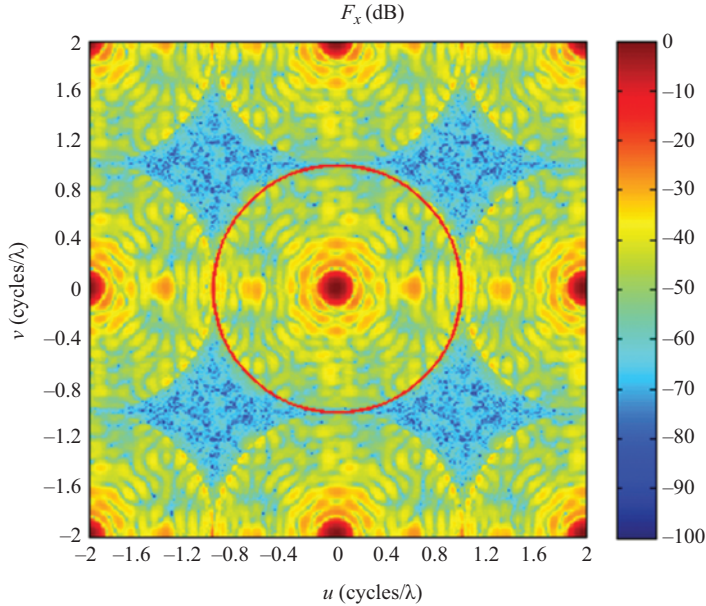


Figure 6.39 $\delta x = \delta y = \lambda/2$, data courtesy of NSI-MI Technologies LLC

spacing and to examine the plane-wave spectrum for the appearance of these side lobes. Once known, the location of the side lobes can be used to specify the correct sample spacing so that the measured pattern is free from these effects. Clearly, increasing the separation between the AUT and the probe will reduce the amount of multiple reflections present within the measurement, however, that will either necessitate in a larger scan area being used or an increase in truncation if it is not possible to increase the span of the measurement in the x - and y -axes.

6.9 Introduction to non-canonical near-field scanning – planar transform example

In general, we take measurements on a canonical surface in electrically close proximity to a radiator. We have a forward equation, as derived above, which we invert to solve for the unknown mode coefficients of the basis functions that are commensurate with the surface that we are testing over. Once we know this set of coefficients, then we can correct them for the effects of the measuring probe. Here, we have assumed that the implementation of probe pattern correction in this way is only possible providing all measurements are performed with a certain probe in a predefined orientation. We then use these compensated coefficients with the forward equation to solve for the field anywhere outside of the near-field sampling surface including the far-field region where we choose a sphere of infinite radius. In each of the formulations, i.e. the planar case treated above, or the cylindrical or

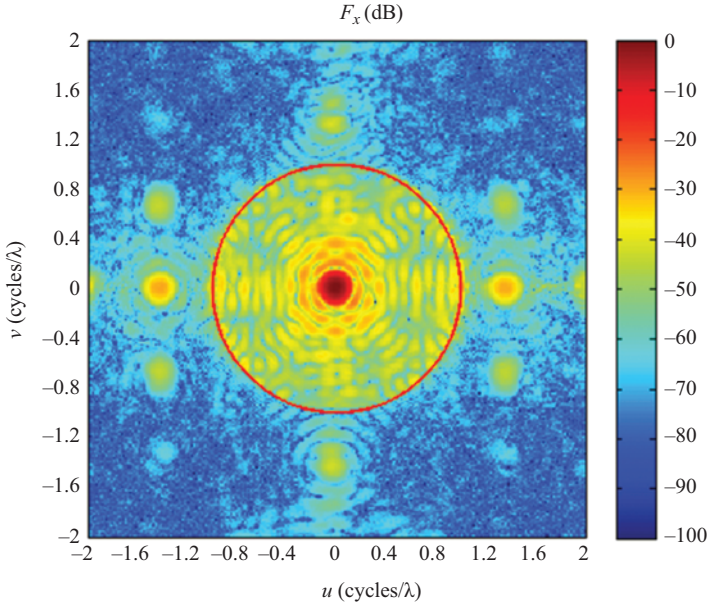


Figure 6.40 $\delta x = \delta y = \lambda/4$, data courtesy of NSI-MI Technologies LLC

spherical cases that are treated below, we can concisely express the relationship between the measurements and the unknown mode coefficients in terms of a matrix equation. As was shown above, the electric field at a point in space can be expressed in terms of an angular spectrum of a plane wave propagating in diverse directions with varying complex amplitudes as

$$\underline{E}(\underline{r}) = \frac{1}{4\pi^2} \int_{-\infty}^{\infty} \int_{-\infty}^{\infty} \underline{F}(\underline{k}) e^{-j\underline{k} \cdot \underline{r}} dk_x dk_y \quad (6.34)$$

Typically, we invert the transmission equation by exploiting mode orthogonality. We shall illustrate this procedure first before progressing to obtain an equivalent solution using an alternative more flexible strategy.

We can try to isolate a single plane-wave coefficient by integrating both sides of this equation with respect to the spatial coordinates thus

$$\begin{aligned} & \int_{-\infty}^{\infty} \int_{-\infty}^{\infty} E(x, y) e^{j(k'_x x + k'_y y)} dx dy \\ &= \int_{-\infty}^{\infty} \int_{-\infty}^{\infty} \left[\frac{1}{4\pi^2} \int_{-\infty}^{\infty} \int_{-\infty}^{\infty} F(k_x, k_y) e^{-j(k_x x + k_y y)} dk_x dk_y \right] e^{j(k'_x x + k'_y y)} dx dy \quad (6.35) \end{aligned}$$

Here, k'_x and k'_y are dummy variables. Exchanging the order of integration and factorising the complex exponentials yields

$$\begin{aligned} & \int_{-\infty}^{\infty} \int_{-\infty}^{\infty} E(x, y) e^{j(k'_x x + k'_y y)} dx dy \\ &= \frac{1}{4\pi^2} \int_{-\infty}^{\infty} \int_{-\infty}^{\infty} \int_{-\infty}^{\infty} \int_{-\infty}^{\infty} F(k_x, k_y) e^{-j((k_x - k'_x)x + (k_y - k'_y)y)} dx dy dk_x dk_y \end{aligned} \quad (6.36)$$

Using the formal integral representation for the two-dimensional Dirac delta function

$$\delta(k_x - k'_x, k_y - k'_y) = \frac{1}{4\pi^2} \int_{-\infty}^{\infty} \int_{-\infty}^{\infty} e^{-j((k_x - k'_x)x + (k_y - k'_y)y)} dx dy \quad (6.37)$$

We see that this reduces to

$$\int_{-\infty}^{\infty} \int_{-\infty}^{\infty} E(x, y) e^{j(k'_x x + k'_y y)} dx dy = \int_{-\infty}^{\infty} \int_{-\infty}^{\infty} F(k_x, k_y) \delta(k_x - k'_x) \delta(k_y - k'_y) dk_x dk_y \quad (6.38)$$

However,

$$\delta(k_x - k'_x, k_y - k'_y) = \begin{cases} 1 & \text{when } k_x = k'_x \text{ and } k_y = k'_y \\ 0 & \text{otherwise} \end{cases} \quad (6.39)$$

Then,

$$\int_{-\infty}^{\infty} \int_{-\infty}^{\infty} E(x, y) e^{j(k'_x x + k'_y y)} dx dy = F(k'_x, k'_y) \quad (6.40)$$

Removing the primes, i.e. by choosing a different set of dummy variables, and reordering yields the required inverted expression for the mode coefficients in terms of a Fourier integral of the measured fields

$$F(k_x, k_y) = \int_{-\infty}^{\infty} \int_{-\infty}^{\infty} E(x, y) e^{j(k_x x + k_y y)} dx dy \quad (6.41)$$

Thus, we have successfully isolated a single plane-wave coefficient and thus inverted the forward equation. In practice, we are able to reconstruct the plane-wave spectrum from a discrete set of samples using the sampling theorem and thus we obtain the discrete form of this expression as required

$$F(k_x, k_y) = \Delta x \Delta y \sum_{n=0}^{N-1} \sum_{m=0}^{M-1} E(n\Delta x, m\Delta y) e^{j(k_x n \Delta x + k_y m \Delta y)} \quad (6.42)$$

However, we are able to obtain an equivalent, more general, form of the transform using linear algebra. As was shown above, when considering a band-limited example or even a quasi-band-limited case, as is usually the situation when antenna testing, we may use the sampling theorem to express the field in the form of a summation of plane waves

$$\underline{E}(\underline{r}_n) = \frac{\Delta k_x \Delta k_y}{4\pi^2} \sum_{m=1}^M \underline{F}(\underline{k}_m) e^{-j\underline{k}_m \cdot \underline{r}_n} \quad (6.43)$$

where \underline{k}_m is the m th propagation vector and \underline{r}_n is the n th position vector such that

$$\underline{r}_n = x_n \hat{e}_x + y_n \hat{e}_y + z_n \hat{e}_z \quad (6.44)$$

$$\underline{k}_n = k_{x,n} \hat{e}_x + k_{y,n} \hat{e}_y + k_{z,n} \hat{e}_z \quad (6.45)$$

Thus, for the planar case with a discrete set of samples $E(r_{1, 2, \dots, n})$, this can be expressed equivalently in a matrix form as

$$\begin{bmatrix} E(\underline{r}_1) \\ E(\underline{r}_2) \\ \vdots \\ E(\underline{r}_n) \end{bmatrix} = \frac{\Delta k_x \Delta k_y}{4\pi^2} \begin{bmatrix} e^{-j(\underline{k}_1 \cdot \underline{r}_1)} & e^{-j(\underline{k}_2 \cdot \underline{r}_1)} & e^{-j(\underline{k}_3 \cdot \underline{r}_1)} & \dots & e^{-j(\underline{k}_m \cdot \underline{r}_1)} \\ e^{-j(\underline{k}_1 \cdot \underline{r}_2)} & e^{-j(\underline{k}_2 \cdot \underline{r}_2)} & e^{-j(\underline{k}_3 \cdot \underline{r}_2)} & \dots & e^{-j(\underline{k}_m \cdot \underline{r}_2)} \\ \vdots & \vdots & \vdots & \ddots & \vdots \\ e^{-j(\underline{k}_1 \cdot \underline{r}_n)} & e^{-j(\underline{k}_2 \cdot \underline{r}_n)} & e^{-j(\underline{k}_3 \cdot \underline{r}_n)} & \dots & e^{-j(\underline{k}_m \cdot \underline{r}_n)} \end{bmatrix} \cdot \begin{bmatrix} F(\underline{k}_1) \\ F(\underline{k}_2) \\ F(\underline{k}_3) \\ \vdots \\ F(\underline{k}_m) \end{bmatrix} \quad (6.46)$$

When expressed compactly in a matrix form, this becomes

$$\underline{v} = \underline{A} \underline{b} \quad (6.47)$$

or, obviously, exactly equivalently as

$$\underline{A} \underline{b} = \underline{v} \quad (6.48)$$

Here, v is a column vector set of measurements, A is a matrix of basis functions, i.e. wave functions, and b is a column vector set of unknown mode coefficients. Typically, we invert the forward transmission equation by exploiting the orthogonality relationship, cf. Chapters 7 and 8. However, it is also possible to solve, i.e. invert, the forward equation using brute force and ignorance by writing

$$b = A^{-1}v \quad (6.49)$$

Again, it is important to note that we have assumed that all measurements were performed with the same probe in the same orientation. If this is not the case, then the probe influence should be included within the forward equation so that its influence is directly considered within the equation system inversion.

In inverting this system of equations, we have assumed that matrix A is a non-singular square matrix and superscript -1 denotes the matrix inverse such that by definition $A^{-1}A = I$, where I is the identity matrix. In general, matrix A will not be square (as we will assume that we have more equations than unknowns) and we will need to find its inverse using some degree of estimation. Fortunately, we can find a pseudo-inverse by using the principle of least squares to obtain an approximate solution. Multiplying by the Hermitian (conjugate) transpose of A , we obtain

$$A^T A b = A^T v \quad (6.50)$$

Here, A^T is the Hermitian transpose of A . Thus, when the columns of A are linearly independent, the product $A^T A$ is invertible and we may write

$$b = (A^T A)^{-1} A^T v \quad (6.51)$$

or

$$b = A^p v \quad (6.52)$$

where A^p denotes the pseudo-inverse matrix that is given by

$$A^p = (A^T A)^{-1} A^T \quad (6.53)$$

As an aside for readers familiar with the programming language MATLAB[®], this is equivalent to using $b = A \setminus v$. Thus, we have obtained the least squares solution for the inversion of our forward transmission equation where we have minimised the quantity

$$\|Ab - v\|^2 \quad (6.54)$$

Thus, when written expressly, we obtain

$$\begin{bmatrix} F(\underline{k}_1) \\ F(\underline{k}_2) \\ F(\underline{k}_3) \\ \vdots \\ F(\underline{k}_m) \end{bmatrix} = \frac{4\pi^2}{\Delta k_x \Delta k_y} A^p \cdot \begin{bmatrix} E(\underline{r}_1) \\ E(\underline{r}_2) \\ \vdots \\ E(\underline{r}_n) \end{bmatrix} \quad (6.55)$$

The merit of this strategy is that we have successfully inverted the forward equation without the need to rely upon mode orthogonality. Although this looks to be a reasonable strategy, the difficulty associated with this is that matrix A will, for any practical measurement, be large and most probably very large. That is to say, the computational effort required to find the pseudo-inverse of A is very significant and grows rapidly as the size of A increases placing very significant demands on the computational resources in terms of run-time and memory. Hence, alternative more efficient methods for computing the pseudo-inverse are generally needed with the iterative conjugate gradient method [19] or the least squares conjugate gradient (LSQR) method [20] being a popular choice. Here, LSQR is a particular implementation of the conjugate gradient method which offers a more attractive solution as will be shown below. A discussion of this algorithm is beyond the scope of this text and is left to the open literature.

By way of an illustration, Figure 6.41 presents the plane-wave spectrum plotted for homogeneous and non-homogeneous plane-wave components as computed using the standard DFT-based transformation developed above. This planar near-field measurement was of an x -band pyramidal horn. Conversely, Figure 6.42 presents the equivalent plane-wave spectrum computed using the matrix inversion technique which was computed using the conjugate gradient method. Here, a relative residual $1.7\text{e-}12$ was achieved with 38 iterations. Increasing the number of iterations did not significantly improve the degree of agreement attained. Clearly, these two results are in very good, but not exact, agreement. Similarly, an encouraging agreement was obtained between the respective phase patterns. To better determine the degree of similarity, the equivalent multipath level (EMPL) was computed to illustrate the degree of similarity between these two results and this can be found presented as a greyscale checkerboard plot in Figure 6.43. The mean EMPL was -70 dB relative to the peak of the pattern which is a very encouraging result. The large amounts of signal outside the unit circle are a result of the very high levels of truncation and the resulting spectral leakage.

For the conjugate gradient method to work, coefficient matrix A must be square, i.e. an $n \times n$ matrix, and should be large and sparse. For the number of rows and columns in A to be equal, this implies that the number of measured points must equal the number of plane-wave coefficients. Note that this is the same constraint that is imposed by the standard FFT algorithm, although not the slower and simpler DFT equivalent. Additionally, it is not possible to have fewer near-field measurements than plane-wave coefficients as this would mean that we have fewer

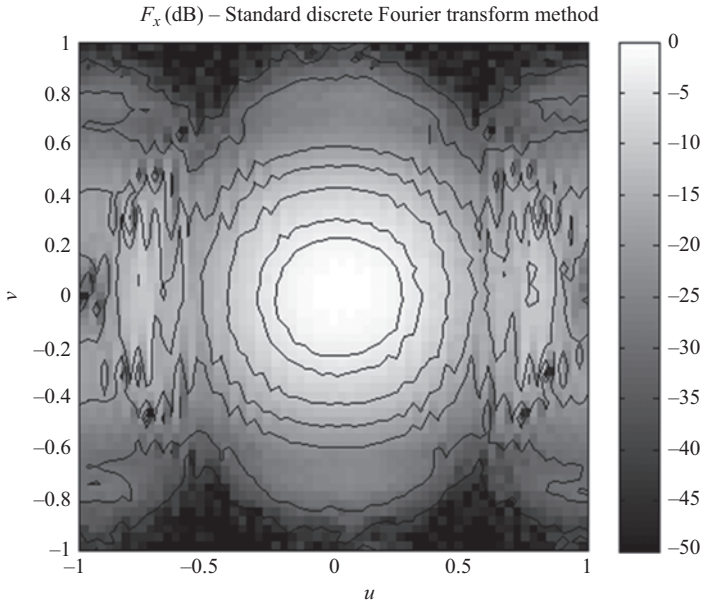


Figure 6.41 Plane-wave spectrum computed using standard Fourier transform method. Note the inclusion of the reactive plane-wave mode coefficients

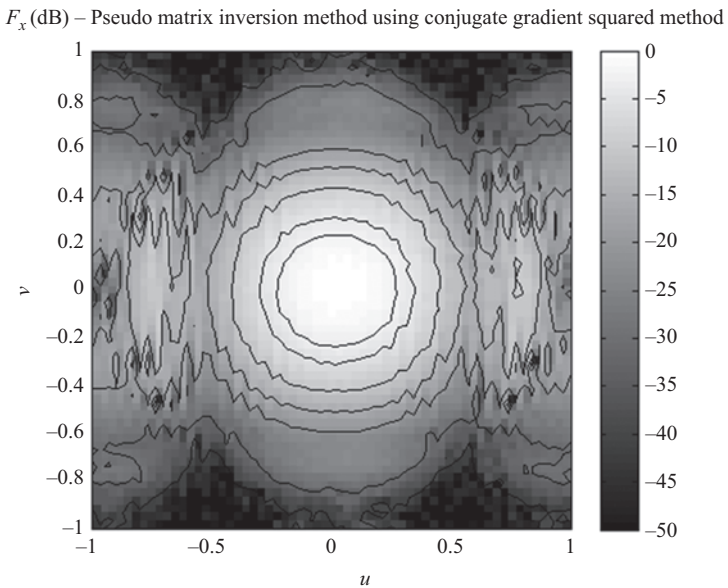


Figure 6.42 Plane-wave spectrum computed using the inverse matrix method. Again note the inclusion of the reactive plane-wave mode coefficients

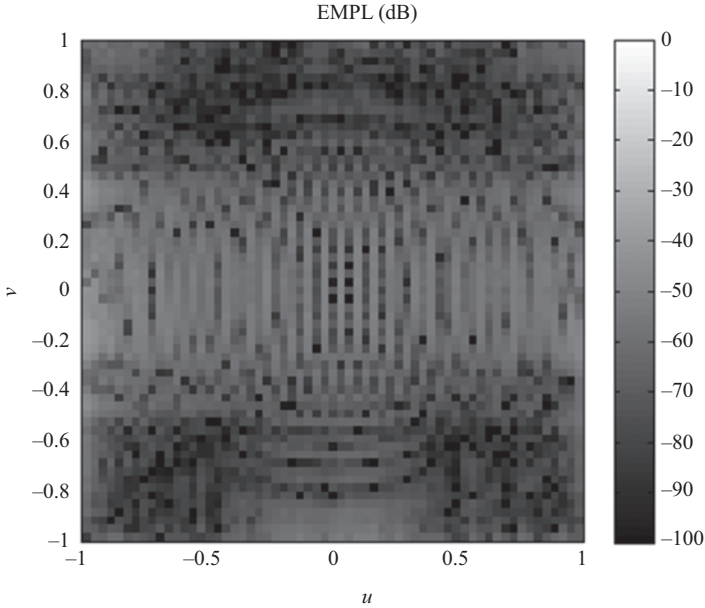


Figure 6.43 Equivalent multipath level plot comparing the degree of agreement attained between transformation algorithms for the propagating and non-propagating mode regions of the plane-wave spectrum

equations than unknowns meaning that this simultaneous equation cannot be solved, i.e. inverted. In practice, we may well wish to have a larger number of points in the angular spectrum than we do in the near-field. This difficulty can be overcome by zero-padding the measured near-field data set in exactly the same manner as we do when using the FFT algorithm. However, this means we have to enlarge the size of the arrays with which we are working further increasing the computational effort and increasing the risk of obtaining unreliable results as a consequence of numerical instabilities.

To illustrate the computational demands associated with this method, it is perhaps worth taking the above, electrically small, case as an example. Here, the measured near-field data set comprised an array of 62 by 62 complex values for each of the two tangential orthogonal polarisations. Selecting a, coarsely sampled, direction cosine space grid comprising 62 by 62 elements implies that the coefficient matrix A contains $62 \times 62 \times 62 \times 62 = 14\,776\,336$ complex elements requiring 236 421 376 bytes of memory. By way of further comparison, for the example considered here, the DFT took 0.067 s, whereas the matrix inversion method took 3.245 s to process. That is to say, when running on the same machine, the matrix inversion algorithm was circa 50 times slower than the DFT-based algorithm. This difference increases even more as the array sizes grow. Although the solution time could be reduced by utilising fewer iterations, there are very few occasions where one would happily sacrifice measurement accuracy. Additionally, the processing can, very

easily, become numerically unstable yielding erroneous results and this is especially true in the event that the initial problem is not posed appropriately.

A more efficient, less resource-intensive and more numerically stable matrix inversion algorithm is the LSQR algorithm of Paige and Saunders [20]. This method has the additional advantage that matrix $[A]$ may be square or rectangular, that is to say, it can be either over-determined or under-determined and may have any rank. In practice, it is often preferable to use the LSQR algorithm as a result of its improved speed, lower memory requirements and greater numerical stability. By way of an illustration of the improved processing time, for the example discussed above, the LSQR algorithm took 0.789 s to perform the necessary matrix inversion which is a significant speed-up when compared to the conventional conjugate gradient method. Practically then, this enables larger array sizes to be handled whilst also reducing the likelihood that the processing will encounter numerical instabilities during its computation.

Although a number of limitations to the matrix inversion method are expounded above, there is a significant benefit in terms of the generality of the approach. Crucially, it is possible to deploy this method over non-canonical surfaces and is our motivation and justification for the increase in effort and complexity. As an example, we shall consider the case of taking planar near-field measurements over an imperfect planar surface. Here, the radiator comprised a simple uniformly illuminated square aperture cut in a perfectly conducting infinite ground plane. A sinusoidal disturbance was introduced into the z -coordinate of the measurement plane of amplitude 0.2 wavelengths simulating an imperfectly flat measurement system, cf. [21,22]. This is significantly larger variation than would be anticipated in practice however an extreme case was chosen to highlight both the effectiveness and the limitations of the correction technique. The resulting electric field was then used to determine the equivalent angular spectra that would include artefacts resulting from these measurement positioning errors. The result of this can be found presented in Figure 6.44. Here, the effect of the comparatively modest positional errors can be seen to have seriously altered the angular spectra. Pattern nulls can be seen to have filled in and it is evident that energy has been moved from the direction of the main beam to other directions altering the level and location of the side lobes. Similarly, Figure 6.45 presents the phase plot that is obtained from using the standard DFT processing which also exhibits significant distortion.

Figures 6.46 and 6.47 show the corresponding results obtained from applying the inverse matrix method. Figures 6.48 and 6.49 present equivalent patterns obtained from using the k -correction method, presented below. Again, this can be compared with the angular spectra of Figures 6.50 and 6.51 which were determined from a near electric field located perfectly on the planar, monotonic, equally spaced, perfectly flat sampling grid. Although not perfect, as a result of processing noise, the improvement in the resulting pattern is clearly significant with the main beam and side lobes regaining much of their symmetry with the well-defined pattern nulls again becoming apparent once again. Only comparatively minor errors are evident within the wide-out side lobes in the inter-cardinal region of smaller field intensities. By way of further comparison, Figures 6.48 and 6.49 contain equivalent

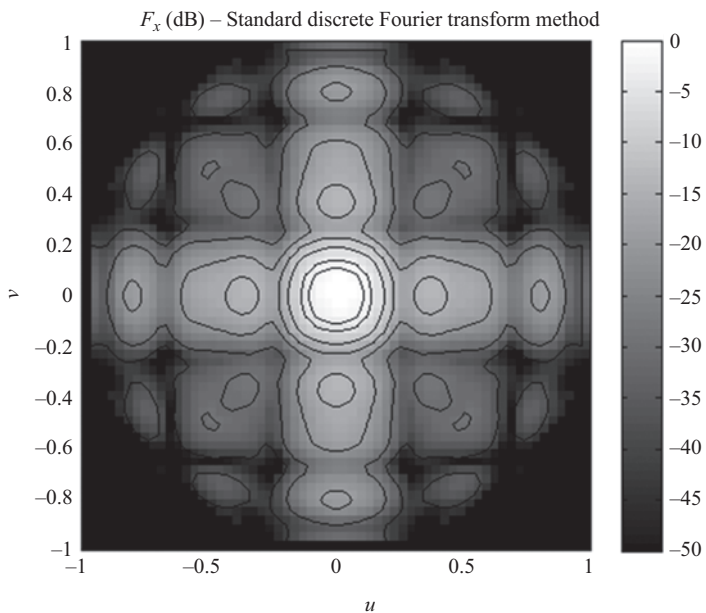


Figure 6.44 Amplitude plot of angular spectra of un-corrected data transformed using standard DFT-based processing with the z -position error

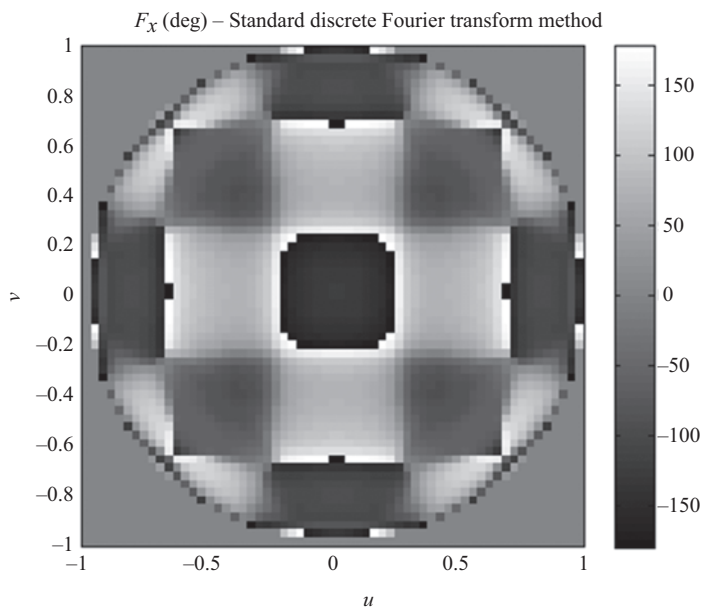


Figure 6.45 Phase plot of angular spectra of un-corrected data transformed using standard DFT-based processing with the z -position error

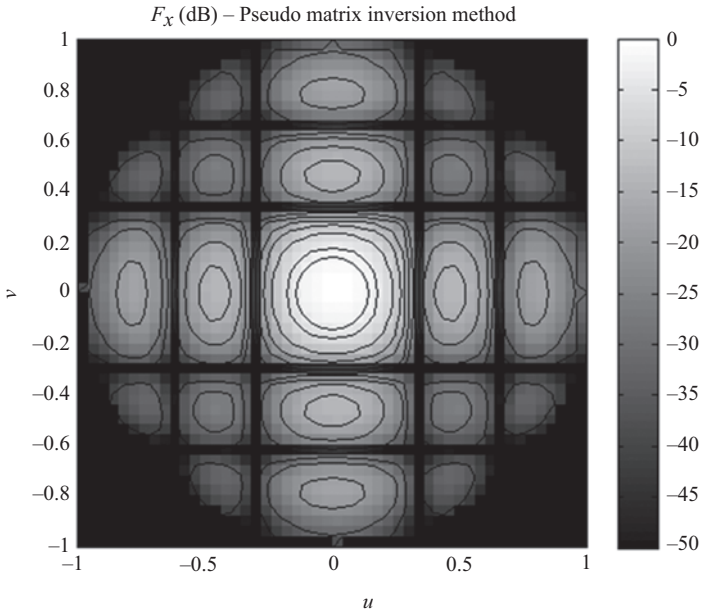


Figure 6.46 Amplitude plot of angular spectra of data transformed using inverse matrix method-based processing with the z-position error

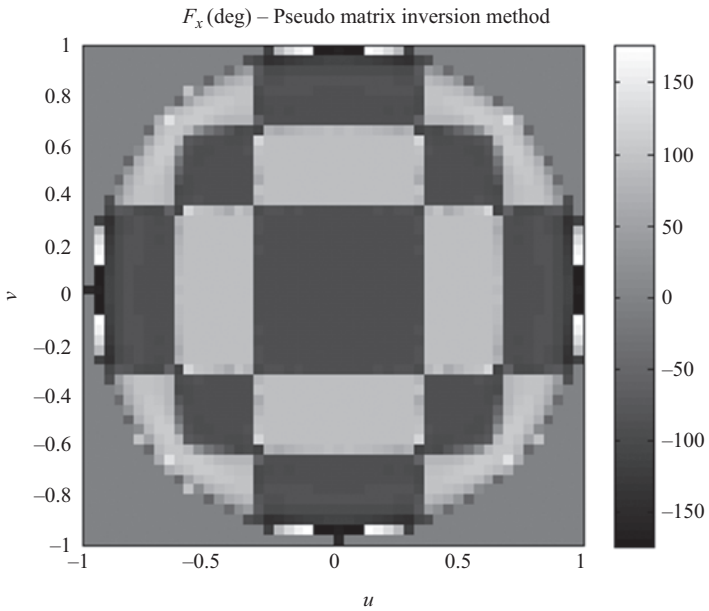


Figure 6.47 Phase plot of angular spectra of data transformed using inverse matrix method-based processing with the z-position error

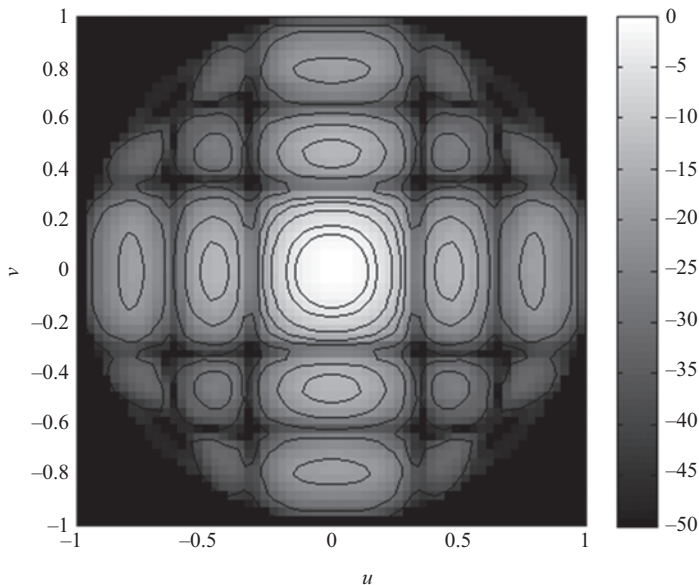


Figure 6.48 Amplitude plot of angular spectra of data transformed using first-order k -correction method-based processing with the z -position error

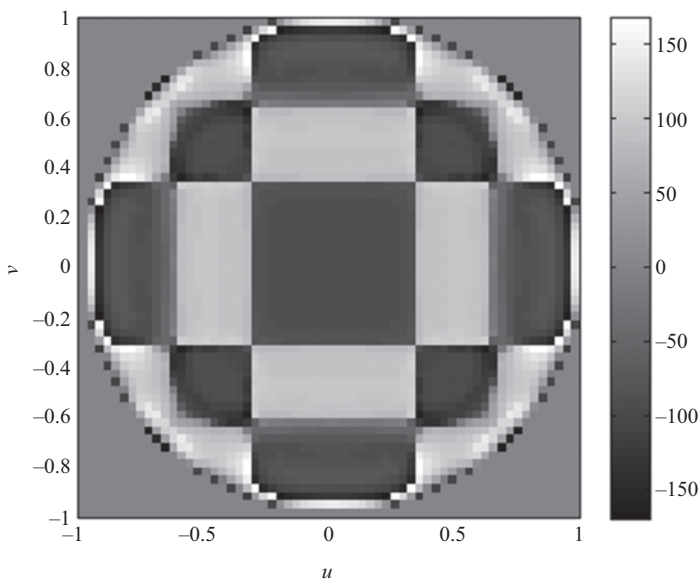


Figure 6.49 Phase plot of angular spectra of data transformed using first-order k -correction method-based processing with the z -position error

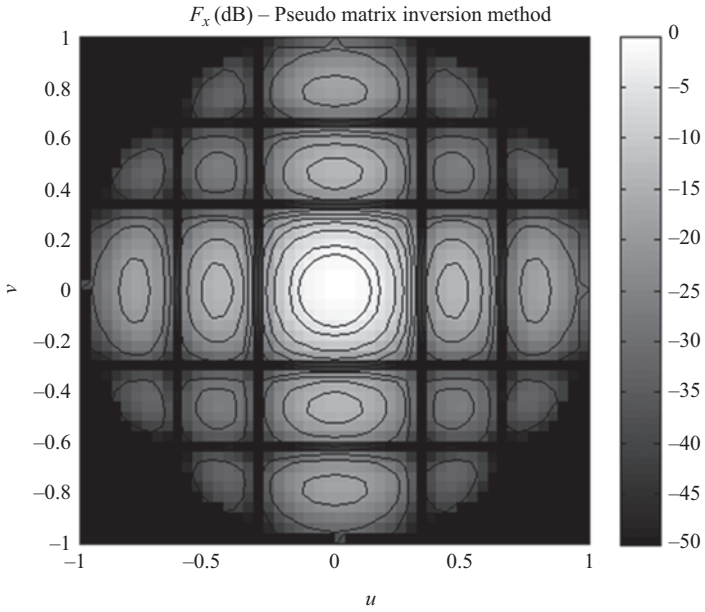


Figure 6.50 Reference amplitude plot of angular spectra of data transformed using the inverse matrix method using near-field data sampled over a perfect plane

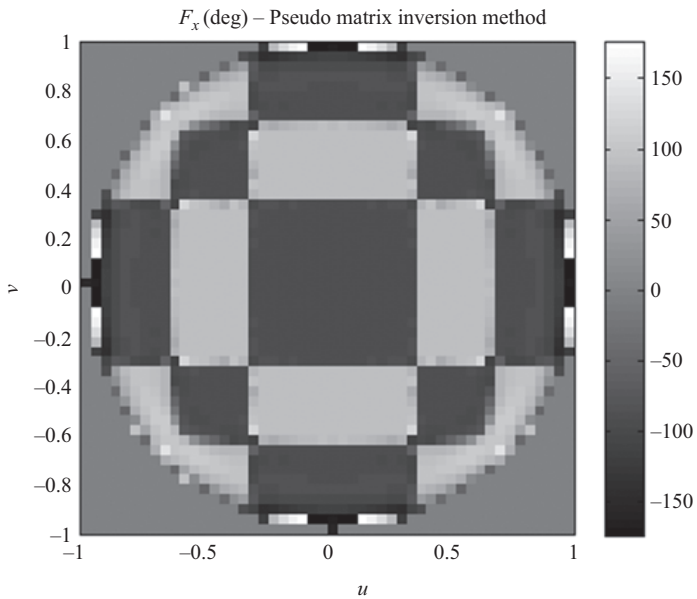


Figure 6.51 Reference phase plot of angular spectra of data transformed using the inverse matrix method using near-field data sampled over a perfect plane

angular spectra only here standard first-order k -correction [21,22] has been used to compensate for the non-planarity of the measurement surface. This is a standard correction technique that is widely deployed within the antenna measurement community. Clearly, the matrix inversion results are in closer agreement with the reference patterns, especially the phase plots further illustrating the advantage of this more computationally intensive, but far more general method. Although impressive as this is, it is perhaps worth remembering that when using the conjugate gradient method or its variants to invert the matrix that this is an approximate method and it assumes that the exact position of the probe is known at the time when the measurement was taken.

A further illustration of the generality of this technique is its deployment to correct for in-plane positioning errors. Traditionally polynomial interpolation or Taylor series correction-based techniques have been used to compensate near-field measurements for the inability of the robot positioning system to acquire the data on a perfect plaid monotonic, and usually equally spaced, grid. To illustrate this, the same configuration as was used above was employed only here the magnitude of the probe displacement error was varied sinusoidally across the measurement plane, i.e. within-plane position measurement errors, where the magnitude of the positional error was 0.4λ , cf. [23]. The result of transforming this data to the far-field using the standard DFT-based technique where the samples were assumed to have been taken at the ideal sampling points can be seen presented in Figure 6.52 which presents the amplitude of the computed plane-wave spectrum. Here, it is

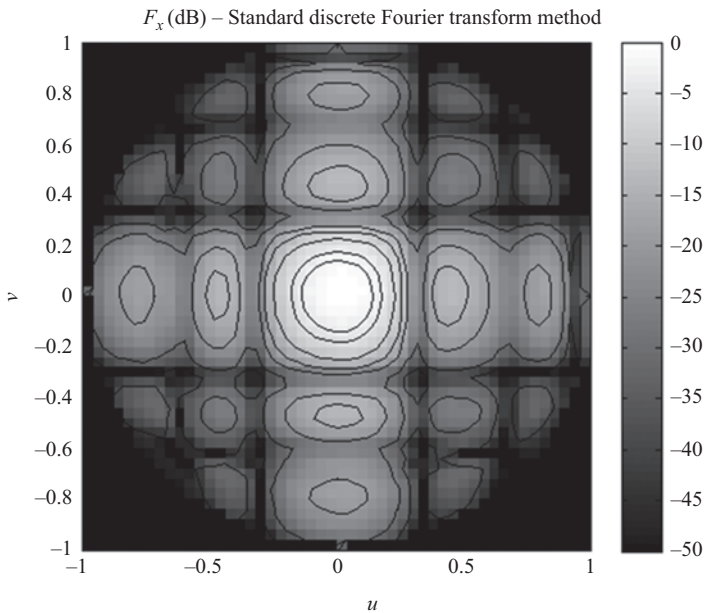


Figure 6.52 Amplitude plot of angular spectra of un-corrected data transformed using standard DFT-based processing with the xy -position error

clear that there is a significant amount of distortion within the pattern on both the main beam and the side lobes, cf. the ideal reference plot of Figure 6.50. Certain side lobes have become displaced and misshapen, and pattern nulls have been partially filled in with the symmetry of the pattern being degraded.

Figure 6.53 presents the amplitude of the angular spectrum as computed by the matrix inversion method. Here, the corrected angular spectrum resembles far more closely the angular spectra obtained from the error-free near-field data presented previously. The shape and location of the main beam and side lobes is far more accurately predicted than was previously the case and the pattern nulls can now be seen to be both deeper and lie in the correct directions. The distortion of the acquisition grid can be quite gross, providing the sampling criteria are satisfied.

As a furthermore extreme and potentially more useful example, it is possible to use this algorithm to process plane-polar, or plane-bi-polar near-field measured data that was considered above. This can be implemented providing the probe is rotationally symmetrical or mechanically counter-rotated during the data acquisition. Plane-polar scanning involves taking measurements on a plane polar grid. Incremental samples are taken by varying the polar angle ϕ and radial displacement r such that the sampled field falls on a raster polar coordinate system where the condition that $r \geq 0$ applies then $u(r, \phi, z = 0) = f(r, \phi)$, where [24]

$$x = r \cos(\phi) \quad (6.56)$$

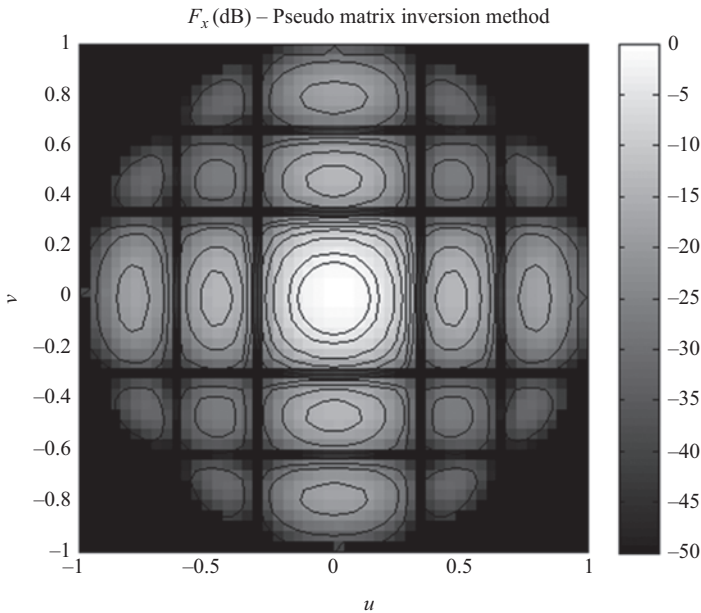


Figure 6.53 Amplitude plot of angular spectra of data transformed using inverse matrix method-based processing with the xy -position error

$$y = r \sin(\phi) \quad (6.57)$$

$$z = z \quad (6.58)$$

This plane-polar coordinate system can be seen presented in Figure 6.54. Example near-field plane-polar data can be seen presented in Figure 6.55 where it has been represented in the form of a greyscale checkerboard plot of the amplitude of the x -polarised component of the near-electric-field.

This data was transformed to the angular spectrum using the matrix inversion method developed above, with the resulting amplitude and phase patterns being presented in Figures 6.56 and 6.57, respectively. This transform was repeated using a standard approach of first interpolating the data to a regular plane-rectilinear grid before computing the angular spectrum using a Fourier transform. The resulting amplitude and phase patterns are presented in Figures 6.58 and 6.59, respectively.

Clearly, these results are in very encouraging agreement, in both amplitude and phase, with only minor differences being evident at wide-out pattern angles nearing the limit of the onset of the first-order truncation effect. When examining the phase plots, it is worth noting that very small differences in the phase angle around $\pm 180^\circ$ will result in a very significant change in the grey-scale value used to depict that point in the plot as a result of the linear greyscale map.

Thus, we have illustrated how this transformation technique can be used to compensate for in-plane and out-of-plane errors providing that the position of the probe is known where we have deployed the LSQR algorithm for the purpose of performing the matrix inversion where its efficiency and numerical stability are paramount to the success of the method. That being said, unreliable angular spectra can be produced in some cases where the near-field contains large amounts of low-

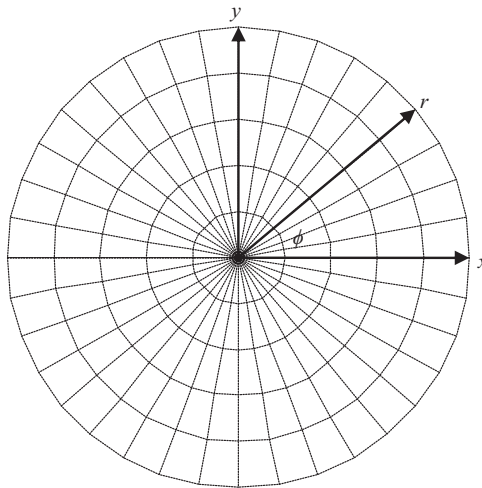


Figure 6.54 *Plane-polar coordinate system*

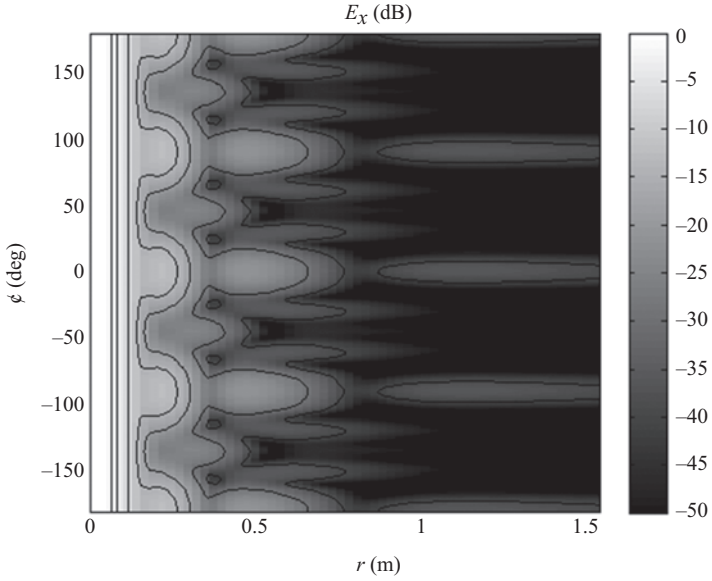


Figure 6.55 Amplitude of the ex-polarised electric field plotted on a plane-polar coordinate system

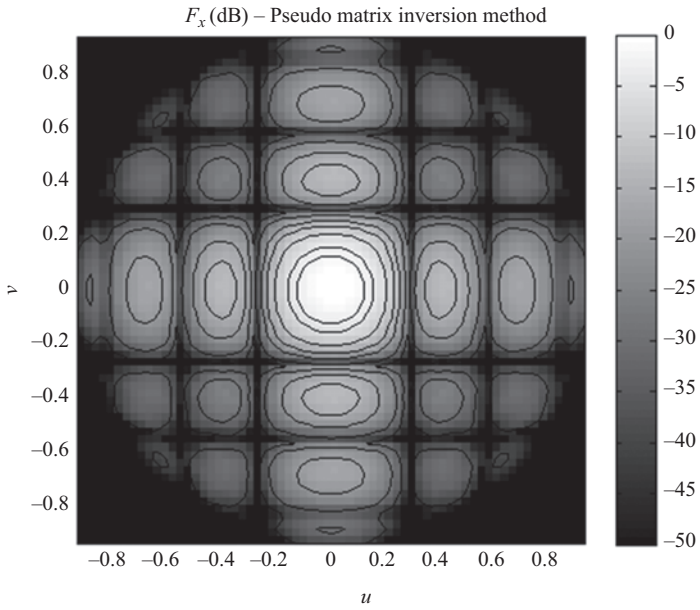


Figure 6.56 Amplitude plot of angular spectra of data transformed using the inverse matrix method

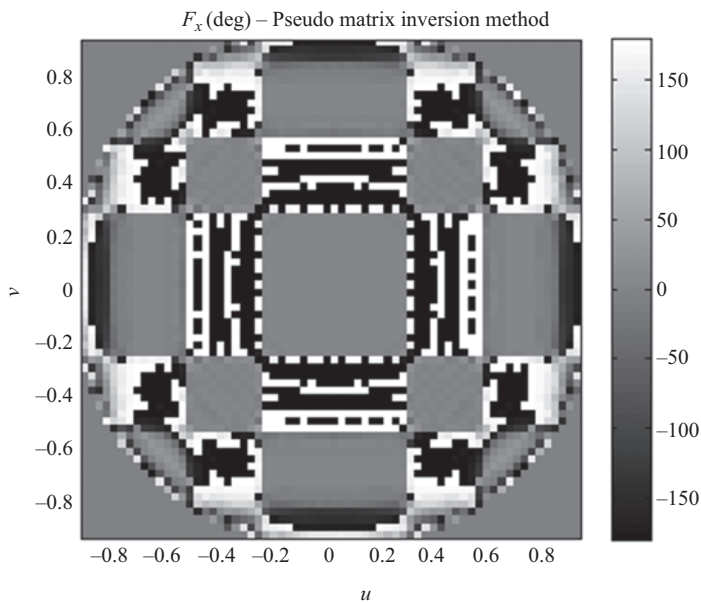


Figure 6.57 Phase plot of angular spectra of data transformed using the inverse matrix method

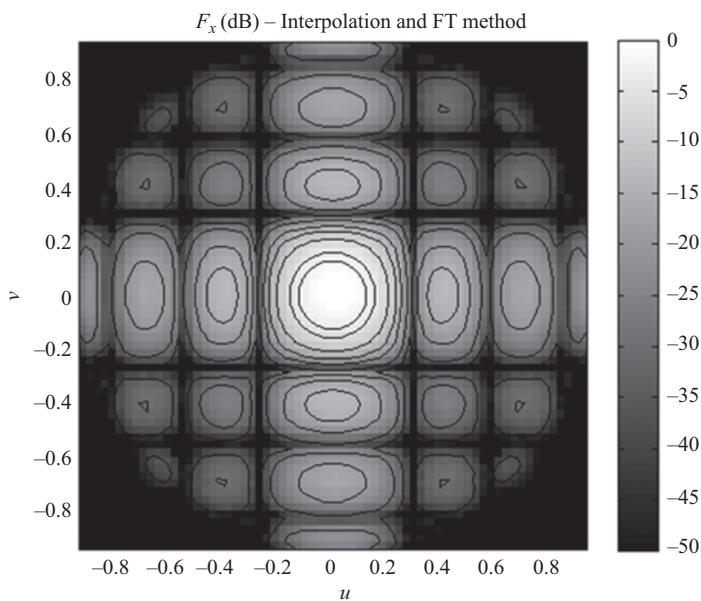


Figure 6.58 Amplitude plot of angular spectra of data transformed using interpolation and Fourier transform-based algorithm

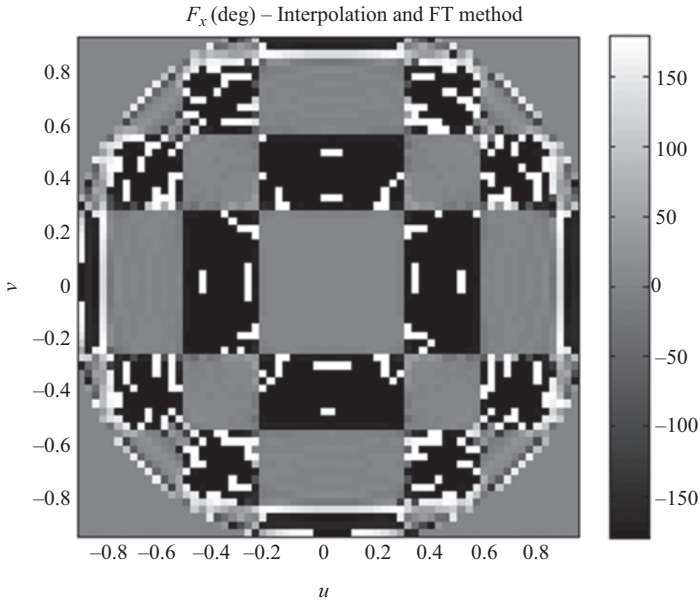


Figure 6.59 Phase plot of angular spectra of data transformed using interpolation and Fourier transform-based algorithm

intensity field points or when the angular spectrum is inappropriately constrained. In summary, this method presents a, conceptually, simple method for processing near-field data which has been acquired over non-canonical, but known, surfaces which may be used to provide reliable far-field data. In Chapter 9, far more sophisticated generalised transform algorithms are introduced where more advanced techniques for speeding up the computation are deployed.

6.10 Electro-optical planar near-field scanning

One of the advantages of the planar near-field technique lies within its ability to place the scanning probe in very close physical proximity to the AUT. The cylindrical and spherical scanning techniques rely upon rotating the AUT about one or more axes and this means that the turning radius imposes a lower limit on the measurement radius which can, for aperture type antennas, be significantly larger than that which could be achieved with planar scanning. This ability to potentially place the probe in very closer mechanical and electrical proximity to the radiator has led to the deployment of a planar positioning system for the purposes of imaging antennas and other radiating structures. Conventionally, placing the AUT and scanning near-field probe so close to one another has led to the introduction of comparatively high levels of multiple reflections, i.e. standing waves, between the AUT and probe which can significantly disturb the very field that one is attempting

to measure. Thus, in cases where accuracy is of paramount importance, especially when measuring low-level side lobes, or very low cross-polar levels, one has generally had to accept the use of separations that are much larger than that suggested purely by the desire to remain outside of the reactive near-field region. This often leads to the use of distances which are far larger than the generally accepted three to five wavelength separation. The recent development of minimally invasive electro-optical (EO) probes seeks to address this shortcoming, cf. Chapter 10.

EO field probes rely upon the principle that imposing an external EM field on a suitable micro-machined, e.g. gallium-arsenide (GaAs), crystal introduces a change in the refractive index within that crystal where the change is proportional to the applied electric field strength. If one were to simultaneously shine a polarised beam of laser light through the crystal, this change in the refractive index would result in a change in the polarisation of that beam. Therefore, the light beam reflected from the probe contains, encoded within it, the electro-optic signal which has been modulated by the impressed RF electric field. In this way, the linear electro-optic effect, also called the Pockels effect [25], may be harnessed as a means of detecting RF and microwave EM fields with the use of a non-conducting minimally invasive probe [26]. This typically small change in polarisation, i.e. linear birefringence, can be used with a suitable arrangement of polarisers, e.g. orthogonally polarised filters, to produce a change in the optical intensity of the illuminating laser light which can be detected with an avalanche photodiode and the amplitude recorded. Here, we are assuming that the birefringent axis of the crystal is at 45° to the axes of the input and output polarisers. The use of a GaAs crystal means that there is no need to use highly reflective metallic probes to scan the field radiated by an antenna, or other structure, thereby reducing the invasiveness of the test system as the EO crystal probe has a relative permittivity of circa 12. As the EO probe is physically small, as it is typically integrated into the optical fibre cable to maximise the optical coupling, it can be used to sense the fields within enclosures or guiding structures. Furthermore, the EO probe is inherently a broadband device with, for example, frequency ranges that span the 200 MHz to 40 GHz range becoming commonplace with the possibility of a single EO probe spanning a frequency range from a few hundred MHz up to W-band.

The EO crystal is mounted on a suitable gradient index lens which in turn is connected to a fibre-optic cable. The input optical probe beam illuminates the crystal which in turn reflects the optical beam back along the optical fibre. This means that an EO system can be used to take frequency domain near-field measurements of antennas or other EM devices [26]. Figure 6.60 contains a photograph of a planar near-field test system which utilises an EO probe-based RF sub-system, whereas Figure 6.61 presents a close-up view of the EO probe scanning a microwave transmission line.

In Figure 6.61, the EO crystal can be seen located at the tip of the optical chain, positioned just above the surface of the microwave transmission line that is being imaged and is less than one cubic mm in volume. EO probes can be constructed to sample the longitudinal or tangential electric field components. Two orthogonal tangential fields can be acquired by rotating the EO probe by 90° about its

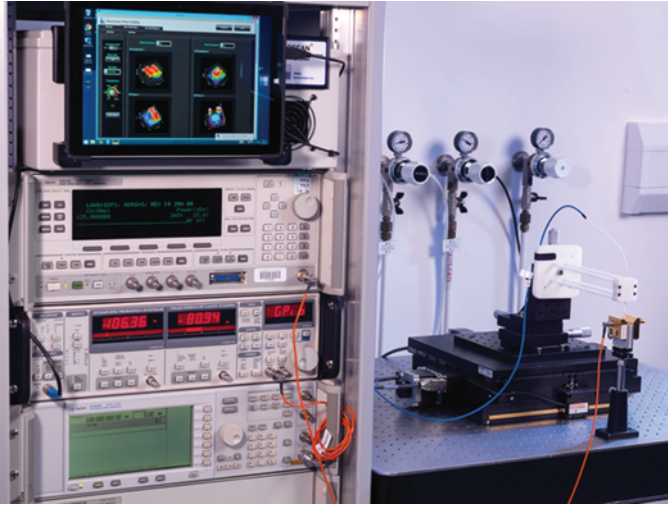


Figure 6.60 Planar electro-optic near-field scanning system with RF sub-system. Pictured at the n3m-labs courtesy of NPL



Figure 6.61 Close-up image of electro-optic probe scanning the very near-fields of a microwave device. The crystal probe can be seen in the centre of the image scanning immediately above the surface of the microwave transmission line. Pictured at the n3m-labs courtesy of NPL

longitudinal axis although the polarisation purity is relatively limited by conventional scanning standards. Thus, EO probe-based systems are capable of measuring the amplitude and phase of an impressed EM field across a frequency band that extends from a few MHz up to mm-wave frequencies although the details of the phase measurement are not well documented in the open literature. In principle then, near-field data acquired in this way is directly amenable for processing with any of the near-field techniques discussed within this text. The single-micrometre

spatial resolution, broad frequency bandwidth and low invasiveness of the EO probe sensor lend the technique to extreme near-field mapping and fault location of microwave integrated circuits. However, as the crystal is of finite size, this means that the light beam reflected from the probe contains an average of the impressed RF electric field where the average is taken across the volume of the probe. Although the spot size of the laser beam can be small, e.g. less than 10 μm , the crystal can be circa 1 mm in depth. Thus, although small, a probe effect is present within the measured EM field that becomes progressively more significant as the frequency of the impressed EM field increases and the wavelength reduces. Further EO imaging applications of this system can be found in the open literature [27,28].

6.11 Summary

This chapter has described the basic geometry and operation of a conventional planar near-field scanner. It has done this by examining the separate sub-systems employed in a scanner facility – primarily the RF sub-system, the robotic positioned sub-system and the range antennas or probes that would be used in the measurement process. In the course of this examination, certain limitations and constraints, e.g. primary and secondary truncations are highlighted in advance of their detailed discussion in Chapter 10.

The solution of Maxwell's equations in Cartesian coordinates has been illustrated in such a way as to be relevant for an explanation of the far-field antenna pattern via the concept of the plane-wave spectrum. Then the impact of the range/probe antenna on the far-field prediction was examined and the convolution theorem invoked so as to allow compensation of the predicted far-field pattern.

Till this point, the chapter has concerned itself with conventional near-field measurements where the probe is scanned over a rectangular Cartesian grid of points that are parallel to the x - and y -axes. However, other planar scanning options are available, i.e. plane-polar and plane bi-polar, and the text has then moved on to an explanation of these alternative scanning techniques. This involves a description of the spectral techniques that can be used to produce a far-field pattern from data that is not acquired on a raster scan. Additionally, the modifications required in probe correction and/or deployments have also been examined and solutions illustrated.

The alignment errors that can be encountered in these alternative techniques were examined and solutions to overcome or mitigate them and, in certain circumstances, exploit them to quantify and correct other errors in the planar measurement process were described. Although we have concentrated on the plane-polar coordinate system, much of the conclusions concerning alignment also apply to the plane bi-polar system.

Attention was then given to the practical implications of the sampling regimes and various transformation algorithms that can be used to address the particular characteristics and limitations of near-field scanning data. This is illustrated by a number of plots that highlight the practical implications of acquiring data in the

near-field and how the deployment of a variety of different sampling and processing techniques can address these issues.

Finally, the new developing techniques related to the use of electro-optical probes for near-field scanning is introduced and the basic mechanisms behind the operation explained and illustrated.

References

- [1] Carlson A.B., *Communication Systems*. Singapore: McGraw-Hill; 1988. pp 344–355. ISBN 0-07-009960-X
- [2] Gregson S.F., McCormick J., Parini C.G., *Principles of Planar Near Field Antenna Measurements*, IET Electromagnetic Waves Series. London: IET; 2007. pp 121–125. ISBN 978-0-86341-756-8
- [3] Gregson S.F., McCormick J., Parini C.G., *Principles of Planar Near Field Antenna Measurements*, IET Electromagnetic Waves Series. London: IET; 2007. pp 312–315. ISBN 978-0-86341-756-8
- [4] Hindman G.E., *Positional Correction on Large Near Field Scanners Using an Optical Tracker System*. AMTA; October 1994
- [5] Gregson S.F., McCormick J., Parini C.G., *Principles of Planar Near Field Antenna Measurements*, IET Electromagnetic Waves Series. London: IET; 2007. pp 90–112. ISBN 978-0-86341-756-8
- [6] Steward E.G., *Fourier Optics: An Introduction*, 2nd edn. Hemel Hempstead; Ellis Horwood; 1987. pp 84–88. ISBN 0-7458-0128
- [7] Rahmat-Sami Y., “A plane-polar approach for far-field construction from near-field measurements.” *IEEE Transactions on Antennas and Propagation*, March 1980; AP-29(2):216–230
- [8] Yaccarino R.G., Rahmat-Sami Y., Williams L.I., “The bi-polar planar near-field measurement technique. Part II: Near-field to far-field transformation and holographic imaging methods.” *IEEE Transactions on Antennas and Propagation*, February 1994; 42:196–204
- [9] Gregson S.F., McCormick J., Parini C.G., *Principles of Planar Near Field Antenna Measurements*, IET Electromagnetic Waves Series. London: IET; 2007. pp 95–101. ISBN 978-0-86341-756-8
- [10] Hazewinkel M. (ed), *Jacobi Matrix, Encyclopaedia of Mathematics*. Springer. 2001. ISBN 978-0-86341-736-8
- [11] Gregson S.F., McCormick J., Parini C.G., *Principles of Planar Near Field Antenna Measurements*, IET Electromagnetic Waves Series. London: IET; 2007. pp 143–148. ISBN 978-0-86341-756-8
- [12] Gregson S.F., McCormick J., Parini C.G., *Principles of Planar Near Field Antenna Measurements*, IET Electromagnetic Waves Series. London: IET; 2007. p 189. ISBN 978-0-86341-756-8
- [13] McCormick J., Gregson S.F., Parini C.G., “Quantitative measures of comparison between antenna pattern data sets.” *IEE Proceedings on Antenna and Propagation*, 2005:539–550. doi:101049/ji-map: 2004 45005

- [14] Gregson S.F., Newell A.C., Hindman G.E., Pellard P., *Range Multipath Reduction in Planar Near-Field Antenna Measurements*. AMTA, October 2012
- [15] Carey M., Pellard P., Gregson S.F., Shinohara N., *Mechanical and Electrical Alignment Techniques for Plane-Polar Near-Field Antenna Measurements*. AMTA, October 2013
- [16] Champeney D.C., *Fourier Transforms in Physics, Student Monographs in Physics*. Bristol and Boston: Adam Hilger; 1985. pp 1–55. ISBN 0-85374-794-2
- [17] Carlson A.B., *Communication Systems*. Singapore: McGraw Hill; 1988. pp 29–31. ISBN 0-07-009960-X
- [18] Gregson S.F., McCormick J., Parini C.G., *Principles of Planar Near Field Antenna Measurements*, IET Electromagnetic Waves Series. London: IET; 2007. pp 120–121. ISBN-978-0-86341-756-8
- [19] Hestenes M.R., Stiefel E., “Methods of conjugate gradients for solving linear systems”, *Journal of Research of the National Bureau of Standards*, December 1952; 49(6):409–436
- [20] Paige C.C., Saunders M.A., “LSQR: An algorithm for sparse linear equations and sparse least squares”, *ACM Transactions on Mathematical Software*, March 1982; 8(1):43–71
- [21] Gregson S.F., McCormick J., Parini C.G., *Principles of Planar Near Field Antenna Measurements*, IET Electromagnetic Waves Series. London: IET; 2007. pp 312–314. ISBN 978-0-86341-756-8
- [22] Corey L.E., Joy E.B., “On computation of electromagnetic fields on planar surfaces from fields on nearby surfaces”, *IEEE Transactions on Antennas Propagation*, March 1981; AP-29:402
- [23] Gregson S.F., McCormick J., Parini C.G., *Principles of Planar Near Field Antenna Measurements*, IET Electromagnetic Waves Series. London: IET; 2007. pp 305–312. ISBN 978-0-86341-756-8
- [24] Gregson S.F., McCormick J., Parini C.G., *Principles of Planar Near Field Antenna Measurements*, IET Electromagnetic Waves Series. London: IET; 2007. pp 150–151. ISBN 978-0-86341-756-8
- [25] Hecht E., *Optics*, 2nd edn. Addison-Wesley Publishing Company; 1984. pp 318–319. ISBN 0-201-11611-1
- [26] Lee D.-J., Kim S., Song D.-R., Hong Y.-P., “Photonic-assisted on wafer millimetre-wave imaging system”, in *Proc. 41st Int. Conf. Infrared, Millim., Terahertz Waves*, 2016, pp 1–2
- [27] Urbonas J., Kim K., Aaen P.H., “Direct E-field measurement and imaging of oscillations within power amplifiers”, *IEEE Transactions on Instrumentation And Measurement (Early Access)*, September 2018:1–8
- [28] Urbonas J., Kim K., Aaen P.H., “An electro-optic pulsed NVNA load–pull system for distributed E-field measurements”, *IEEE Transactions on Microwave Theory and Techniques*, June 2018; 66(6)

Chapter 7

Cylindrical near-field antenna measurements

7.1 Introduction

The right circular cylindrical near-field measurement system is formed from the intersection of a linear translation stage and a rotation stage where the linear translation axis is parallel to the axis of rotation. A right circular cylinder is taken to be a 3D object comprising two congruent circles (that is to say two surfaces that have the same dimensions and shape) as parallel bases and a connecting lateral surface. The centres of the two circles form a line that is perpendicular to the bases. The combination of single rotation and single linear axes enables the probe to trace out a conceptual cylindrical surface in three dimensions, thereby allowing the collection of samples on a set of coaxial rings. Here, samples are taken at regular intervals across a cylindrical grid with, typically, the probe moving in a fixed linear direction, and the antenna under test (AUT) rotating in parallel. Typically, the linear axis and rotation axes are aligned to the local gravity vector. This not only simplifies the alignment of the axes of the robotic positioning system, but also ensures that the AUT does not suffer a variation in the effect of gravity during an acquisition. In addition to yielding a simplification to the positioning and RF sub-systems, this geometry enables complete azimuth patterns to be obtained providing a wide out antenna pattern including front-to-back ratio, while maintaining the gravitational vector with respect to the AUT during the course of an acquisition. This makes this a particularly attractive proposition for testing gravitationally sensitive, e.g. space antenna assemblies. Thus, the cylindrical technique is most appropriate for fan-beam type antennas where the finite length of the linear scan axis and the inevitable truncation that result from this are of minimal importance.

Figure 7.1 contains a schematic representation of a typical cylindrical near-field antenna test system where the conceptual, truncated, cylindrical raster sampling strategy is shown.

By way of a further illustration, Figure 7.2 contains a picture of a cylindrical near-field antenna test system that is shown testing an offset reflector antenna. The vertical linear axis can be seen to the right of the image with a waveguide probe mounted on the carriage. The rotation stage onto which the AUT is mounted is obscured by absorber.

Figure 7.3 contains a grey-scale checkerboard plot of the measured cylindrical near-field amplitude of a fan-beam antenna. Here, complete 360° angular cuts were taken that spanned a linear axis of 1.56 m in length.

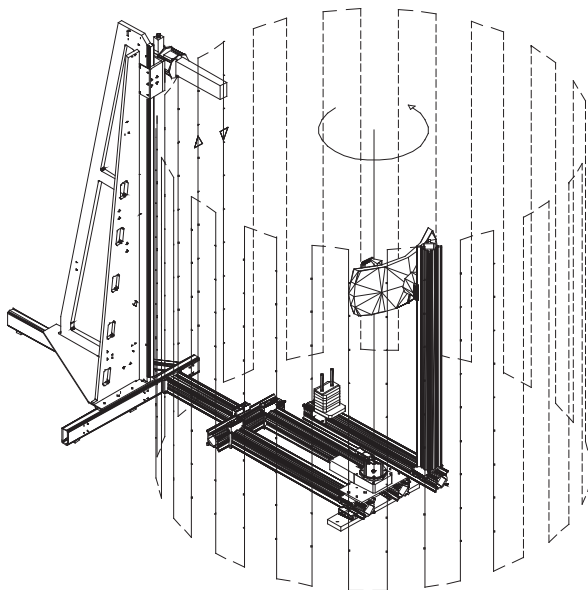


Figure 7.1 Schematic of cylindrical near-field antenna test system showing conceptual scanning surface enclosing AUT

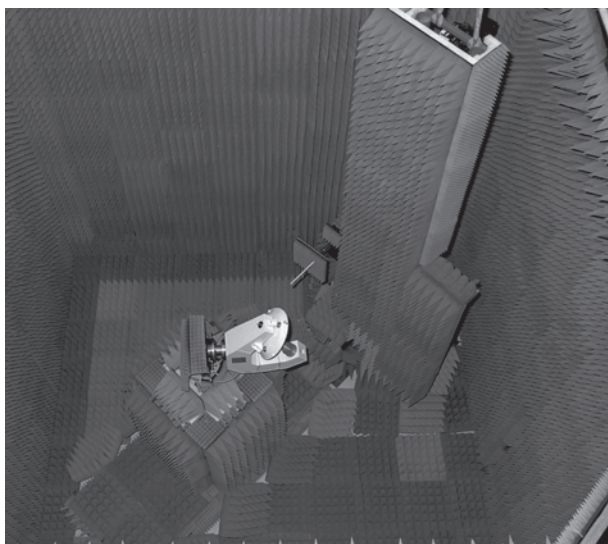


Figure 7.2 Large vertical cylindrical near-field test system (Picture courtesy of the David Florida Laboratory, Canadian Space Agency)

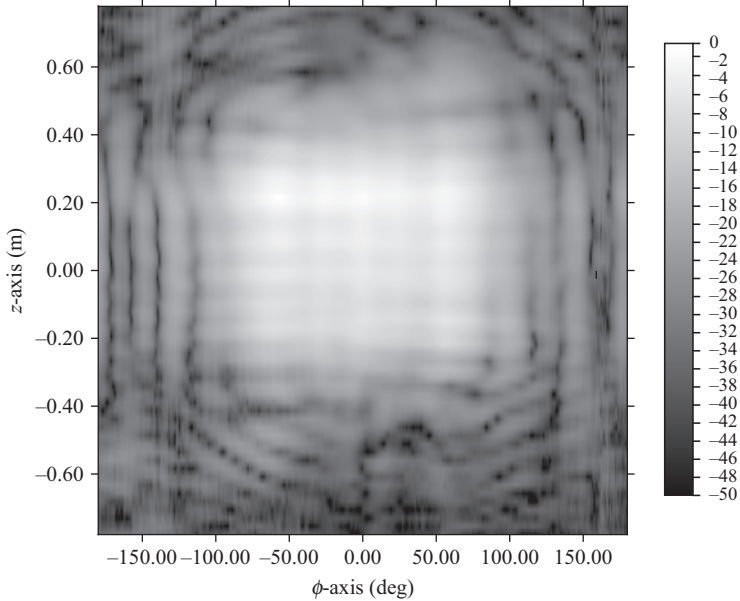


Figure 7.3 Cylindrical near-field False Cour plot of measured amplitude pattern of fan-beam antenna

The corresponding far-field cardinal cuts have been presented in Figure 7.4 where the truncated elevation axis (this axis corresponded to the vertical linear scan axis) is evident.

As will be shown within this chapter, the electromagnetic fields outside an arbitrary test antenna radiating into free space can be expanded into a set of orthogonal cylindrical mode coefficients (CMCs) and these modes and coefficients can then be used to obtain the electric and magnetic fields everywhere in space outside of a conceptual cylindrical surface which encloses the radiator. It will also be shown that these CMCs can be determined from the measured data in a very efficient manner through the use of the fast Fourier transform (FFT). Once obtained, these mode coefficients can be corrected for the spatial filtering properties of the measuring near-field probe and used to determine the true AUT transmitting CMCs. It will then be shown that a highly efficient FFT-based summation process can be utilised to obtain the asymptotic far electric and magnetic fields, thus all the stages of the process illustrated in Figure 3.37 defining the generic near-field measurement process, as described in Section 3.62, can be undertaken using a cylindrical measurement geometry.

It is thus proved that parameters such as the far-field antenna pattern function, axial ratio, tilt angle, directivity of the AUT can all be obtained from two orthogonal tangential near electric field components. This formulation, therefore, enables highly accurate, practical, cylindrical near-field techniques to be

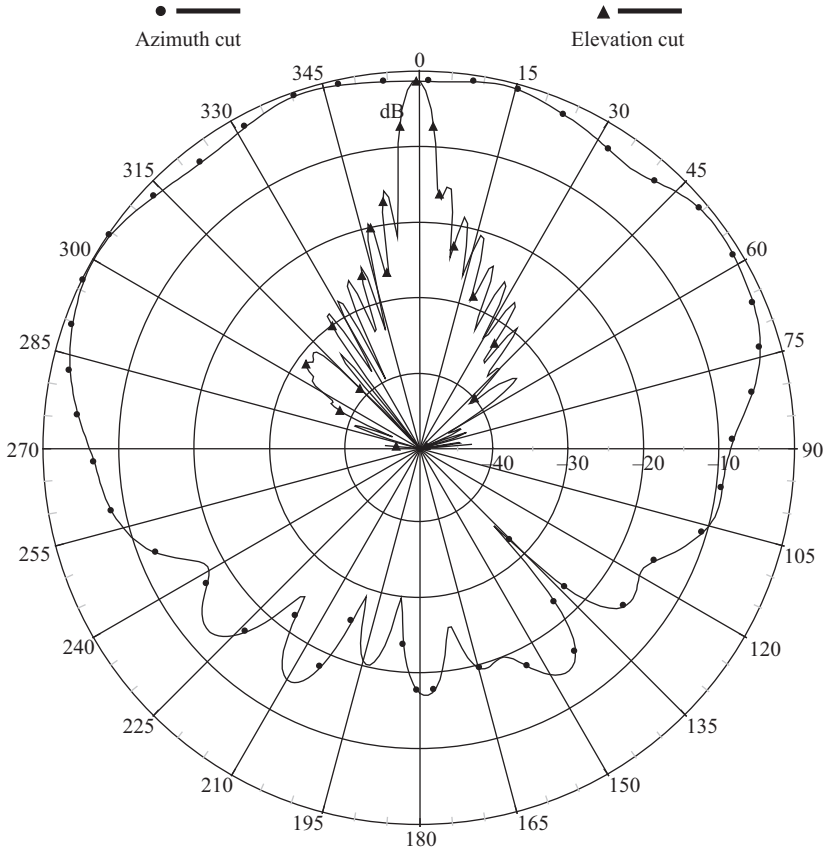


Figure 7.4 Comparison of far-field cardinal cuts obtained from CNF measurements of a fan-beam antenna

implemented. The geometry that will be used during the development of this cylindrical formulation is presented in Figure 7.5.

Here, for a right circular cylindrical coordinate system, as depicted in Figure 7.5, we can write that

$$x = \rho \cos \phi \tag{7.1}$$

$$y = \rho \sin \phi \tag{7.2}$$

$$z = z \tag{7.3}$$

where $\rho \geq 0$, $0 \leq \phi \leq 2\pi$, $-\infty \leq z \leq \infty$. In a rectangular coordinate system, the point P can be expressed as $P(x, y, z)$. Conversely, in a right cylindrical coordinate system the point P can be expressed as $P(\rho, \phi, z)$ where the relationship between

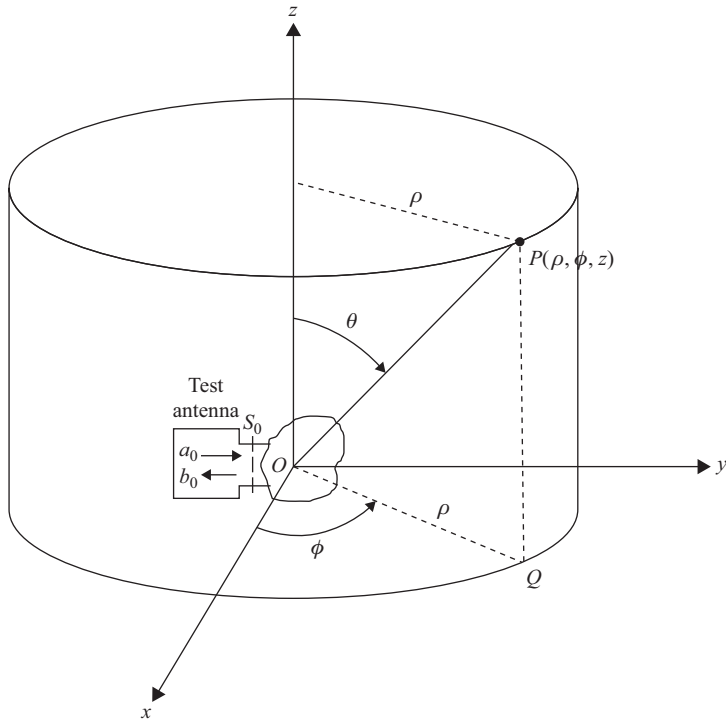


Figure 7.5 Geometry for the formulation of standard cylindrical near-field theory showing test antenna in its own coordinate system

the two systems is established through this triad of equations. Conversely from rearranging the above equations, we obtain the inverse relationships, namely

$$\rho = \sqrt{x^2 + y^2} \tag{7.4}$$

$$\phi = \arctan\left(\frac{y}{x}\right) \tag{7.5}$$

$$z = z \tag{7.6}$$

Here, we take advantage of the two argument arctangent functions so that quadrant ambiguity can be eliminated yielding angles that span the complete 2π range. As the electric and magnetic fields are vector quantities, we also need to obtain expressions that allow the respective vector field components to be converted from rectangular to cylindrical coordinate systems and vice versa. This can be accomplished easily using the standard expression,

$$\hat{e}_1 = \frac{\partial \underline{r} / \partial u_1}{|\partial \underline{r} / \partial u_1|} \tag{7.7}$$

From Figure 7.5 it is clear that in cylindrical coordinates, the position vector \underline{r} can be expressed as

$$\underline{r} = \rho \cos \phi \hat{\underline{e}}_x + \rho \sin \phi \hat{\underline{e}}_y + z \hat{\underline{e}}_z \quad (7.8)$$

Then

$$\frac{\partial \underline{r}}{\partial \rho} = \cos \phi \hat{\underline{e}}_x + \sin \phi \hat{\underline{e}}_y \quad (7.9)$$

Since $\left| \frac{\partial \underline{r}}{\partial \rho} \right| = 1$

$$\hat{\underline{e}}_\rho = \cos \phi \hat{\underline{e}}_x + \sin \phi \hat{\underline{e}}_y \quad (7.10)$$

Similarly

$$\frac{\partial \underline{r}}{\partial \phi} = -\rho \sin \phi \hat{\underline{e}}_x + \rho \cos \phi \hat{\underline{e}}_y \quad (7.11)$$

As $\left| \frac{\partial \underline{r}}{\partial \phi} \right| = \rho$

$$\hat{\underline{e}}_\phi = -\sin \phi \hat{\underline{e}}_x + \cos \phi \hat{\underline{e}}_y \quad (7.12)$$

Hence we can write this in matrix form as

$$\begin{bmatrix} \hat{\underline{e}}_\rho \\ \hat{\underline{e}}_\phi \\ \hat{\underline{e}}_z \end{bmatrix} = \begin{bmatrix} \cos \phi & \sin \phi & 0 \\ -\sin \phi & \cos \phi & 0 \\ 0 & 0 & 1 \end{bmatrix} \cdot \begin{bmatrix} \hat{\underline{e}}_x \\ \hat{\underline{e}}_y \\ \hat{\underline{e}}_z \end{bmatrix} \quad (7.13)$$

Conversely, as this is an orthogonal and normalised matrix, we can obtain the inverse relationship by taking the transpose of the square matrix, thus

$$\begin{bmatrix} \hat{\underline{e}}_x \\ \hat{\underline{e}}_y \\ \hat{\underline{e}}_z \end{bmatrix} = \begin{bmatrix} \cos \phi & -\sin \phi & 0 \\ \sin \phi & \cos \phi & 0 \\ 0 & 0 & 1 \end{bmatrix} \cdot \begin{bmatrix} \hat{\underline{e}}_\rho \\ \hat{\underline{e}}_\phi \\ \hat{\underline{e}}_z \end{bmatrix} \quad (7.14)$$

As the coordinate and unit vector relationships are now established, these can be used with Maxwell's equations in order that a solution to the vector wave equation can be sought using this coordinate system. The following section establishes that the general vector wave equation can be reduced to the scalar wave equation in cylindrical coordinates, and that this equation can be solved using the method of separation of variables. In this way, elementary cylindrical vector wave functions are constructed that are shown to be amenable for use as the basis of standard cylindrical, and subsequently by extension of conical, near-field theory.

7.2 Solution of Maxwell's equation in cylindrical coordinates

As was shown earlier in Chapter 2, Maxwell's field equations can be used to obtain the vector wave equation

$$\nabla^2 \underline{E} = -k^2 \underline{E} \quad (7.15)$$

As was noted above, as only alternating, sinusoidal, time-harmonic quantities are to be considered the time dependency of the complex representations of the electromagnetic field vectors can be taken to be of the form $e^{j\omega t}$ (i.e. a 'positive' time dependency), where $\omega = 2\pi f$ is the angular frequency and f represents the temporal frequency measured in Hertz. Both f and ω are positive and greater than zero. As before a complex exponential form of time dependency is assumed, and as is usually the case when using this notation, the time factor is suppressed, that is to say, the complex exponentials are cancelled on either side of the relevant expressions. Some caution is taken at this point. Many texts adopt the opposite time dependency to that being assumed herein. As the time dependency is generally suppressed, this difference is not always instantly apparent. Some changes within formulae are introduced, and these can include opposite signs within the complex exponentials and in the case of the cylindrical near-field theory the use of Hankel functions of the first kind as opposed to Hankel functions of the second kind. When comparing between various references, awareness of this sort of variation is absolutely *crucial*.

Let us now assume that the field can be expressed in the form of

$$\underline{E}(\rho, \phi, z) = E_\rho(\rho, \phi, z)\hat{\underline{e}}_\rho + E_\phi(\rho, \phi, z)\hat{\underline{e}}_\phi + E_z(\rho, \phi, z)\hat{\underline{e}}_z \quad (7.16)$$

Then as the vector Laplacian operator can be expressed in cylindrical coordinates as [1]

$$\nabla^2 \underline{E} = \left(\nabla^2 E_\rho - \frac{E_\rho}{\rho^2} - \frac{2}{\rho^2} \frac{\partial E_\phi}{\partial \phi} \right) \hat{\underline{e}}_\rho + \left(\nabla^2 E_\phi - \frac{E_\phi}{\rho^2} + \frac{2}{\rho^2} \frac{\partial E_\rho}{\partial \phi} \right) \hat{\underline{e}}_\phi + (\nabla^2 E_z) \hat{\underline{e}}_z \quad (7.17)$$

The underlying reason for the form of the z -component is that the z -axis is a Cartesian axis. This is a very useful property that we will exploit within our development of the cylindrical near-field technique. Thus, rearranging yields

$$\begin{aligned} & \left(\nabla^2 E_\rho - \frac{E_\rho}{\rho^2} - \frac{2}{\rho^2} \frac{\partial E_\phi}{\partial \phi} \right) \hat{\underline{e}}_\rho + \left(\nabla^2 E_\phi - \frac{E_\phi}{\rho^2} + \frac{2}{\rho^2} \frac{\partial E_\rho}{\partial \phi} \right) \hat{\underline{e}}_\phi + (\nabla^2 E_z) \hat{\underline{e}}_z \\ & = -k^2 E_\rho \hat{\underline{e}}_\rho - k^2 E_\phi \hat{\underline{e}}_\phi - k^2 E_z \hat{\underline{e}}_z \end{aligned} \quad (7.18)$$

Hence the vector wave equation can be reduced to three simultaneous scalar partial differential equations yielding

$$\nabla^2 E_\rho - \frac{E_\rho}{\rho^2} - \frac{2}{\rho^2} \frac{\partial E_\phi}{\partial \phi} = -k^2 E_\rho \quad (7.19)$$

$$\nabla^2 E_\phi - \frac{E_\phi}{\rho^2} + \frac{2}{\rho^2} \frac{\partial E_\rho}{\partial \phi} = -k^2 E_\phi \quad (7.20)$$

$$\nabla^2 E_z = -k^2 E_z \quad (7.21)$$

Here, in each of these expressions, the Laplacian is of a *scalar* quantity (that is in cylindrical coordinates). This is in contrast to general wave equation which contained a Laplacian of a *vector* quantity. Crucially, the z -polarised cylindrical component is an uncoupled second-order partial differential equation which can be solved. As these are simultaneous equations, it is possible to select any one of these and then to find its solution. Thus, we are free to select whichever is the most convenient of these equations and then to find its solution. The third expression comprises an uncoupled second-order partial differential equation. The other two equations are coupled second-order partial differential equations which are more difficult to solve. Thus, the solution of this uncoupled equation will become the subject of the remainder of this section.

The scalar wave equation can be expressed in cylindrical coordinates as follows. The Laplacian can be expressed in cylindrical coordinates using [2]

$$\nabla^2 \psi = \frac{1}{h_1 h_2 h_3} \left[\frac{\partial}{\partial u_1} \left(\frac{h_2 h_3}{h_1} \frac{\partial \psi}{\partial u_1} \right) + \frac{\partial}{\partial u_2} \left(\frac{h_3 h_1}{h_2} \frac{\partial \psi}{\partial u_2} \right) + \frac{\partial}{\partial u_3} \left(\frac{h_1 h_2}{h_3} \frac{\partial \psi}{\partial u_3} \right) \right] \quad (7.22)$$

where, for cylindrical coordinates, $u_1 = \rho$, $u_2 = \phi$, $u_3 = z$, $\hat{e}_1 = \hat{e}_\rho$, $\hat{e}_2 = \hat{e}_\phi$, $\hat{e}_3 = \hat{e}_z$, $h_1 = h_\rho = 1$, $h_2 = h_\phi = \rho$, and $h_3 = h_z = 1$. Thus

$$\nabla^2 \psi = \frac{1}{\rho} \left[\frac{\partial}{\partial \rho} \left(\rho \frac{\partial \psi}{\partial \rho} \right) + \frac{\partial}{\partial \phi} \left(\frac{1}{\rho} \frac{\partial \psi}{\partial \phi} \right) + \frac{\partial}{\partial z} \left(\rho \frac{\partial \psi}{\partial z} \right) \right] \quad (7.23)$$

Simplifying this yields

$$\nabla^2 \psi = \frac{1}{\rho} \frac{\partial}{\partial \rho} \left(\rho \frac{\partial \psi}{\partial \rho} \right) + \frac{1}{\rho^2} \frac{\partial^2 \psi}{\partial \phi^2} + \frac{\partial^2 \psi}{\partial z^2} \quad (7.24)$$

The first term is the derivative of a product. Thus, using the rule for differentiating a product

$$\frac{d}{dx} [uv] = v \frac{du}{dx} + u \frac{dv}{dx} \quad (7.25)$$

Hence

$$\frac{\partial}{\partial \rho} \left(\rho \frac{\partial \psi}{\partial \rho} \right) = \frac{\partial \psi}{\partial \rho} + \rho \frac{\partial^2 \psi}{\partial \rho^2} \quad (7.26)$$

Thus, in cylindrical coordinates, the scalar Laplacian can be expressed as

$$\nabla^2 \psi = \frac{\partial^2 \psi}{\partial \rho^2} + \frac{1}{\rho} \frac{\partial \psi}{\partial \rho} + \frac{1}{\rho^2} \frac{\partial^2 \psi}{\partial \phi^2} + \frac{\partial^2 \psi}{\partial z^2} \quad (7.27)$$

When expanded, the scalar wave equation in cylindrical coordinates can be written as

$$\frac{\partial^2 \psi}{\partial \rho^2} + \frac{1}{\rho} \frac{\partial \psi}{\partial \rho} + \frac{1}{\rho^2} \frac{\partial^2 \psi}{\partial \phi^2} + \frac{\partial^2 \psi}{\partial z^2} = -k^2 \psi \quad (7.28)$$

Here, $\psi(\rho, \phi, z)$ is a scalar function that is used to denote a field component.

7.3 Solution of the scalar wave equation in cylindrical coordinates

Within this section, we are going to attempt to solve this equation by harnessing the method of separation of variables. We are therefore going to assume that a solution can be found of the form:

$$\psi(\rho, \phi, z) = R(\rho)\Phi(\phi)Z(z) \quad (7.29)$$

Substituting the assumed solution into the scalar Helmholtz equation

$$\frac{\partial^2 \psi}{\partial \rho^2} + \frac{1}{\rho} \frac{\partial \psi}{\partial \rho} + \frac{1}{\rho^2} \frac{\partial^2 \psi}{\partial \phi^2} + \frac{\partial^2 \psi}{\partial z^2} = -k^2 \psi \quad (7.30)$$

yields

$$\begin{aligned} \Phi(\phi)Z(z) \frac{\partial^2 R(\rho)}{\partial \rho^2} + \Phi(\phi)Z(z) \frac{1}{\rho} \frac{\partial R(\rho)}{\partial \rho} + R(\rho)Z(z) \frac{1}{\rho^2} \frac{\partial^2 \Phi(\phi)}{\partial \phi^2} \\ + R(\rho)\Phi(\phi) \frac{\partial^2 Z(z)}{\partial z^2} = -k^2 R(\rho)\Phi(\phi)Z(z) \end{aligned} \quad (7.31)$$

Dividing throughout by the solution yields

$$\frac{1}{R(\rho)} \frac{\partial^2 R(\rho)}{\partial \rho^2} + \frac{1}{R(\rho)} \frac{1}{\rho} \frac{\partial R(\rho)}{\partial \rho} + \frac{1}{\Phi(\phi)} \frac{1}{\rho^2} \frac{\partial^2 \Phi(\phi)}{\partial \phi^2} + \frac{1}{Z(z)} \frac{\partial^2 Z(z)}{\partial z^2} = -k^2 \quad (7.32)$$

or

$$\frac{1}{R(\rho)} \frac{\partial^2 R(\rho)}{\partial \rho^2} + \frac{1}{R(\rho)} \frac{1}{\rho} \frac{\partial R(\rho)}{\partial \rho} + \frac{1}{\Phi(\phi)} \frac{1}{\rho^2} \frac{\partial^2 \Phi(\phi)}{\partial \phi^2} + \frac{1}{Z(z)} \frac{\partial^2 Z(z)}{\partial z^2} + k^2 = 0 \quad (7.33)$$

Using the argument that was first deployed when solving the wave equation in rectangular coordinates, the fourth term is not a function of ρ or ϕ . Also, and as all of the terms sum to zero, it must also not be a function of z . Thus, we can set this term equal to a convenient constant that is yet to be determined. Thus, as we are free to choose the constant, we can make this equal to the square of a

constant for convenience (and consistency with the planar case) and we may write that

$$\frac{1}{Z(z)} \frac{\partial^2 Z(z)}{\partial z^2} = -k_z^2 \quad (7.34)$$

This equation is called the harmonic equation and its solutions are called harmonic functions. As was the case for the planar case, as treated in Chapter 6, these solutions can take the form of $\sin(k_z z)$, $\cos(k_z z)$, $\exp(jk_z z)$ or $\exp(-jk_z z)$ where any two of these are linearly independent. Substituting this separation constant into the scalar Helmholtz equation yields

$$\frac{1}{R(\rho)} \frac{\partial^2 R(\rho)}{\partial \rho^2} + \frac{1}{R(\rho)} \frac{1}{\rho} \frac{\partial R(\rho)}{\partial \rho} + \frac{1}{\Phi(\phi)} \frac{1}{\rho^2} \frac{\partial^2 \Phi(\phi)}{\partial \phi^2} - k_z^2 + k^2 = 0 \quad (7.35)$$

Multiplying throughout with ρ^2 yields

$$\frac{\rho^2}{R(\rho)} \frac{\partial^2 R(\rho)}{\partial \rho^2} + \frac{\rho}{R(\rho)} \frac{\partial R(\rho)}{\partial \rho} + \frac{1}{\Phi(\phi)} \frac{\partial^2 \Phi(\phi)}{\partial \phi^2} + (k^2 - k_z^2) \rho^2 = 0 \quad (7.36)$$

Now, the third term is independent of ρ or z and thus, similarly, it too can be set equal to a constant of our choice. Hence

$$\frac{1}{\Phi(\phi)} \frac{\partial^2 \Phi(\phi)}{\partial \phi^2} = -m^2 \quad (7.37)$$

Or

$$\frac{d^2 \Phi(\phi)}{d\phi^2} + m^2 \Phi(\phi) = 0 \quad (7.38)$$

This again is a harmonic oscillator equation. As was found before, the solutions of this expression are of the form,

$$\Phi_m^\pm = \Phi_0 e^{\pm jm\phi} \quad (7.39)$$

However, since we clearly have a periodic boundary condition we require any physical solution to have the same value when $\phi = 0$ as when $\phi = 2\pi$. More generally, this boundary condition requires the physical solution to have the same value at ϕ as it has for $\phi \pm 2\pi$, thus

$$e^0 = 1 = e^{jm2\pi} \quad (7.40)$$

Alternatively, by using Euler's identity this can be expressed as [3]

$$1 = \cos(m2\pi) + j \sin(m2\pi) \quad (7.41)$$

Thus, this equation can only hold when m is an integer. This is different to the z equation case where the separation constant could take on integer *and* non-integer

values. Thus, the scalar Helmholtz equation in cylindrical coordinates reduces to an equation in ρ only and the equation is therefore separated as required

$$\frac{\rho^2}{R(\rho)} \frac{\partial^2 R(\rho)}{\partial \rho^2} + \frac{\rho}{R(\rho)} \frac{\partial R(\rho)}{\partial \rho} - m^2 + (k^2 - k_z^2)\rho^2 = 0 \quad (7.42)$$

This can be rewritten in a more recognisable form by multiplying through with $R(\rho)$ and since this is now an ordinary differential equation we obtain

$$\rho^2 \frac{d^2 R(\rho)}{d\rho^2} + \rho \frac{dR(\rho)}{d\rho} + [(k^2 - k_z^2)\rho^2 - m^2]R(\rho) = 0 \quad (7.43)$$

For convenience, if we define a new constant k_ρ as

$$k_\rho^2 = k^2 - k_z^2 \quad (7.44)$$

Then we can write that

$$\rho^2 \frac{d^2 R(\rho)}{d\rho^2} + \rho \frac{dR(\rho)}{d\rho} + [(k_\rho \rho)^2 - m^2]R(\rho) = 0 \quad (7.45)$$

With

$$\frac{d^2 \Phi(\phi)}{d\phi^2} + m^2 \Phi(\phi) = 0 \quad (7.46)$$

where m is an integer, and

$$\frac{d^2 Z(z)}{dz^2} + k_z^2 Z(z) = 0 \quad (7.47)$$

The ϕ and z equations are harmonic equations, which give rise to harmonic functions, cf. the Cartesian case discussed in the preceding chapter. However, the ρ equation is definitely not a harmonic equation. It is, however, a modified (i.e. parametric) version of Bessel's equation. This can be seen by making a simple linear exchange of variables. Using the substitution

$$s = k_\rho \rho \quad (7.48)$$

where we can also write that

$$\frac{ds}{d\rho} = \frac{d(k_\rho \rho)}{d\rho} = k_\rho \quad (7.49)$$

The derivatives within our differential equation can be exchanged using the following operator substitutions and using the chain rule we obtain

$$\frac{dR}{d\rho} = \frac{dR}{ds} \frac{ds}{d\rho} = \frac{dR}{ds} k_\rho \quad (7.50)$$

And from using the chain rule for higher derivatives we see that

$$\frac{d^2R}{d\rho^2} = \frac{d}{d\rho} \left(\frac{dR}{ds} \frac{ds}{d\rho} \right) = \frac{d^2R}{ds^2} \left(\frac{ds}{d\rho} \right)^2 + \frac{dR}{ds} \frac{d^2s}{d\rho^2} = \frac{d^2R}{ds^2} k_\rho^2 + 0 \quad (7.51)$$

Thus, we can exchange the variables in our parametric Bessel equation, from $d\rho$ to ds and from $k_\rho\rho$ to s and transform it into the standard form since

$$\left(\frac{s}{k_\rho} \right)^2 \frac{d^2R(\rho)}{ds^2} k_\rho^2 + \left(\frac{s}{k_\rho} \right) \frac{dR(\rho)}{ds} k_\rho + [s^2 - m^2]R(\rho) = 0 \quad (7.52)$$

Simplifying yields Bessel's equation

$$s^2 \frac{d^2R(\rho)}{ds^2} + s \frac{dR(\rho)}{ds} k_\rho + [s^2 - m^2]R(\rho) = 0 \quad (7.53)$$

for which the solutions are well known

The point $s = 0$ is a singular regular point for this equation and we can therefore expand its solution as a Frobenius series [4]. Commonly used solutions are Bessel functions $J_m(s)$, Neumann functions which are also known as Bessel functions of the second kind, $Y_m(s)$, Hankel functions of the first kind $H_m^{(1)}(s)$ and Hankel functions of the second kind $H_m^{(2)}(s)$. In each of these functions we recall that $s = k_\rho\rho$. The subscript m is known as the order of the Bessel function and although we can define Bessel functions of non-integer order, as was shown earlier, the values of m in this boundary value problem *are* integers. Any two of these functions are linearly independent solutions of Bessel's equation, so in general a linear combination of any two of these is used as solution with the particular choice being dependent upon the particular boundary value problem that is being treated.

Typically, Bessel functions are used to represent standing waves, whereas Hankel functions are used to represent travelling waves. Thus, for the case of free-field measurements which is our area of application, we can expect that Hankel functions will be the solution of greatest utility. Since the anticipated solution to the Helmholtz equation in cylindrical coordinates was expressed as the product of three functions, i.e.

$$\psi(\rho, \phi, z) = R(\rho)\Phi(\phi)Z(z) \quad (7.54)$$

the solution can be expressed as

$$\psi_{k_\rho, m, k_z}(\rho, \phi, z) = R(\rho)\Phi(\phi)Z(z) \quad (7.55)$$

Or more specifically as in this case, the most appropriate solution, or elementary wave function, is of the form,

$$\psi_{k_\rho, m, k_z}(\rho, \phi, z) = Z_m^{(i)}(k_\rho\rho)h(m\phi)h(k_z z) \quad (7.56)$$

where we recall that the separation constants are related through the equation

$$k_\rho^2 = k^2 - k_z^2 \quad (7.57)$$

And

$$Z_m^{(i)}(k_\rho \rho) = \begin{cases} J_m(k_\rho \rho) & \text{when } i = 1 \\ Y_m(k_\rho \rho) & \text{when } i = 2 \\ H_m^{(1)}(k_\rho \rho) & \text{when } i = 3 \\ H_m^{(2)}(k_\rho \rho) & \text{when } i = 4 \end{cases} \quad (7.58)$$

A more general solution can be formed from these elemental wave functions as linear combinations of wave functions must also be solutions of the Helmholtz equation. We may therefore sum over the various possibilities, thus

$$\psi(\rho, \phi, z) = \sum_m \sum_{k_z} B_{m, k_z} Z_m^{(i)}(k_\rho \rho) h(m\phi) h(k_z z) \quad (7.59)$$

Here B is a constant to be determined from the boundary conditions. In the limit, the summation can tend to an integral across the separation constant k_z in which case the general solution can be expressed as

$$\psi(\rho, \phi, z) = \sum_{m=-\infty}^{\infty} \int_{-\infty}^{\infty} B_m(k_z) Z_m^{(i)}(k_\rho \rho) h(m\phi) h(k_z z) dk_z \quad (7.60)$$

Here we have chosen to integrate across k_z as the cylindrical near-field measurements yield data, i.e. the boundary conditions, that are a function of ϕ and z with ρ fixed. If instead, the measurement had been taken with ρ varying and z fixed, as would be the case when taking plane-polar measurements, then it would have been more appropriate to take the integration in k_ρ . In either case, the summation is retained in ϕ as only integer values of m are needed which is a requirement of the physically imposed periodic boundary conditions. As will be shown later, this solution can be used to construct Fourier integrals which have many attractive properties.

Before progressing, it is important that the mathematical properties and physical interpretation of the various functions are well understood so that the correct choice can be made for a particular application at hand. Let us first consider solutions of the form,

$$h(k_z z) = e^{-jk_z z} \quad (7.61)$$

Here, for a fixed frequency, the z -directed propagation constant cannot vary independently as

$$k_z = \pm \sqrt{k^2 - k_\rho^2} \quad (7.62)$$

Thus, k_z can take on real *and* imaginary values. For a positive suppressed time dependency, when k_z is positive and real, this represents waves propagating in the positive z direction that are unattenuated. Conversely, when k_z is negative and real, this represents waves propagating in the negative z direction that are unattenuated.

However, if k_z is complex, as is the case when $k_r^2 > k^2$, these represent waves that are either attenuated or amplified depending on whether the imaginary part is positive or negative as

$$e^{-jk_z z} = e^{-j(\alpha+j\beta)z} = e^{-j\alpha z} e^{\beta z} \tag{7.63}$$

Here α is used to denote the real part of k_z , whereas β denotes the imaginary part of k_z . From inspection of this expression it is clear that when the real part of k_z is positive and the imaginary part is positive then this represents waves that are propagating in the negative z direction and that are augmented, i.e. increasing. If instead, the real part of k_z is positive and the imaginary part is negative then this represents waves that are propagating in the negative z direction and that are attenuated. If instead, the real part is identically zero, and the imaginary part is non-zero, then this represents evanescent fields, i.e. which are non-homogenous waves. Thus, for $k_\rho^2 \leq k^2$ the positive root is chosen to ensure that the waves propagate outward in the positive z direction, while the negative imaginary root is chosen when $k_\rho^2 > k^2$ so that the waves decay exponentially as they propagate outwards in the positive z direction and remain finite when $z \rightarrow \infty$.

If the opposite sign had been chosen then this would have represented as an exponentially increasing wave that would become infinitely large as $z \rightarrow \infty$ which is prohibited. Hence

$$k_z = \begin{cases} \sqrt{k^2 - k_\rho^2} & \text{when } k_\rho^2 < k^2 \\ -j\sqrt{k_\rho^2 - k^2} & \text{otherwise} \end{cases} \tag{7.64}$$

Hence, the solution of the scalar wave equation in cylindrical coordinates can be expressed as

$$\psi(\rho, \phi, z) = \sum_{m=-\infty}^{\infty} \int_{-\infty}^{\infty} B_m(k_z) Z_m^{(i)}(k_\rho \rho) h(m\phi) e^{-jk_z z} dk_z \tag{7.65}$$

Next we can consider the ϕ solution which is also a harmonic equation; however, here only discrete values of the separation constant m are admitted.

$$h(m\phi) = e^{\pm jm\phi} \tag{7.66}$$

Since the vales of m are allowed to take on both positive and negative values, there is no need to retain both the positive and negative solutions explicitly. Thus, without loss of generality, we are able to express the solution of the scalar wave equation as

$$\psi(\rho, \phi, z) = \sum_{m=-\infty}^{\infty} \int_{-\infty}^{\infty} B_m(k_z) Z_m^{(i)}(k_\rho \rho) e^{jm\phi} e^{-jk_z z} dk_z \tag{7.67}$$

The final step is to select the appropriate function for $Z_m^{(i)}$ where for our application we recall that the argument of the function is $s = k_\rho \rho$,

$$Z_m^{(i)}(s) = \begin{cases} J_m(s) & \text{when } i = 1 \\ Y_m(s) & \text{when } i = 2 \\ H_m^{(1)}(s) & \text{when } i = 3 \\ H_m^{(2)}(s) & \text{when } i = 4 \end{cases} \quad (7.68)$$

where from the method of Frobenius, for positive values of m , the Bessel function of the first kind is [5]

$$J_m(s) = \sum_{n=0}^{\infty} \frac{(-1)^n}{n!(n+m)!} \left(\frac{s}{2}\right)^{2n+m} \quad (7.69)$$

However, Bessel functions with negative orders, i.e. values of m , are also needed if a complete set of wave functions are to be available. However, as m is an integer in our case, we may write that negative values of m can be obtained from the Bessel function of positive m using

$$J_{-m}(s) = (-1)^m J_m(s) \quad (7.70)$$

This relation is obtained by substituting m by $-m$ in the series representation of the first-order Bessel function. In our application, a second solution can be obtained from a limiting procedure; the result of this can be expressed as [5]

$$Y_m(s) = \frac{J_m(s) \cos(m\pi) - J_{-m}(s)}{\sin(m\pi)} \quad (7.71)$$

By way of an illustration of the properties of these functions, Figures 7.6 and 7.7 contain plots of Bessel functions of the first and second kinds for several values of positive m .

As has been noted earlier, for wave propagation, it is often convenient to introduce two further functions which are formed from a combination of these functions. Thus, Hankel functions of the first and second kinds are defined as

$$H_m^{(1)}(s) = J_m(s) + jY_m(s) \quad (7.72)$$

$$H_m^{(2)}(s) = J_m(s) - jY_m(s) \quad (7.73)$$

As before, the order of the function is defined by the integer m . Hankel functions of negative order can be calculated from Hankel functions of positive order from the following identity:

$$H_{-m}^{(1)}(s) = e^{j\pi|m|} H_{|m|}^{(1)}(s) \quad (7.74)$$

$$H_{-m}^{(2)}(s) = e^{-j\pi|m|} H_{|m|}^{(2)}(s) \quad (7.75)$$

Thus, the real part of the Hankel function shares the properties of the Bessel function of the first kind, whereas the imaginary part of the Hankel function shares

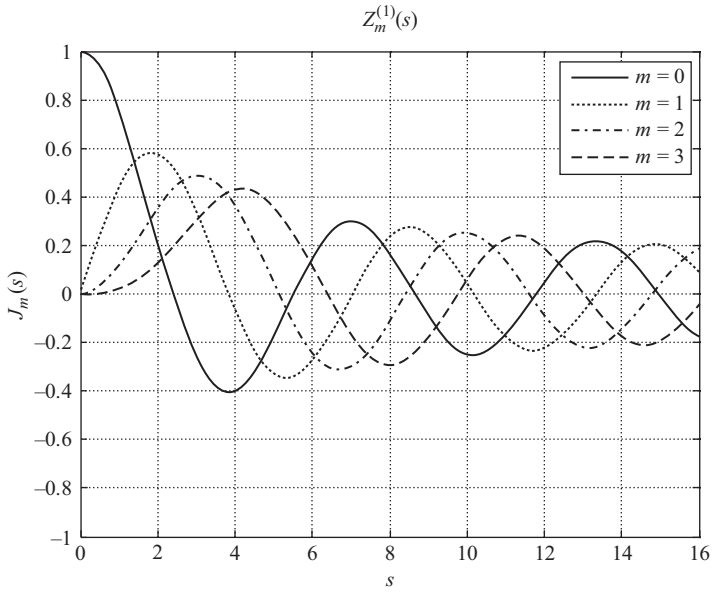


Figure 7.6 Bessel functions of the first kind plotted for several positive integer values of m

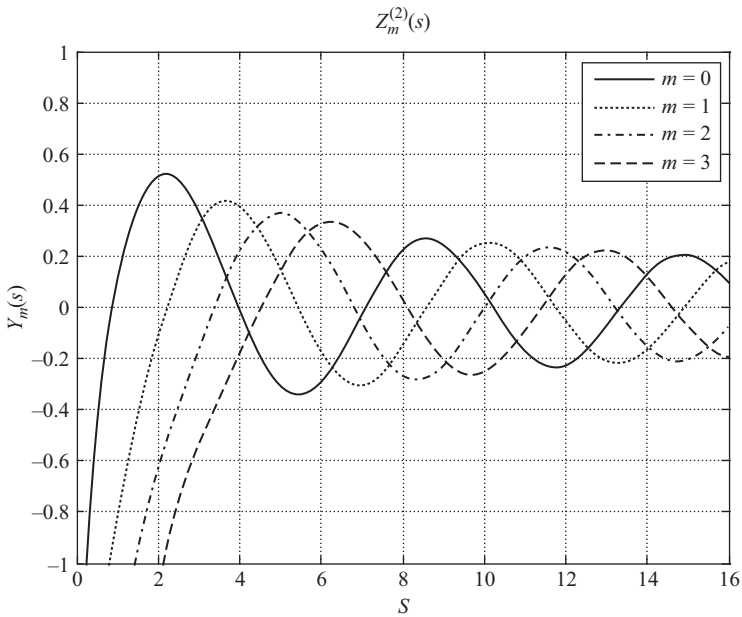


Figure 7.7 Bessel functions of the second kind plotted for several positive integer values of m

the properties of the Bessel function of the second kind. Thus, it is perhaps more illustrative to inspect the magnitude and argument of the Hankel functions. Figure 7.8 contains a plot of the magnitude of the Hankel function of the first kind for various positive integer values of m . Conversely, Figure 7.9 contains a plot of the argument of the Hankel function of the first kind for various positive integer values of m , where the phase angle has been plotted in decimal degrees. Figures 7.10 and 7.11 show equivalent plots for the Hankel function of the second kind.

From inspection of Figures 7.6 and 7.11, the following qualitative analogies can be made. Bessel functions of the first and second kinds, i.e. J_m and Y_m respectively, exhibit oscillatory behaviour for real values of s . This is true for the sinusoidal functions and thus they represent standing waves. Conversely, the Hankel functions of the first and second kinds represent travelling waves for s real. Hankel functions of the first kind denote waves propagating in the negative ρ direction, whereas Hankel functions of the second kind denote waves propagating in the positive ρ direction. These observations are summarised in the following expressions:

$$J_m(s) \text{ analogous to } \cos(s) \tag{7.76}$$

$$Y_m(s) \text{ analogous to } \sin(s) \tag{7.77}$$

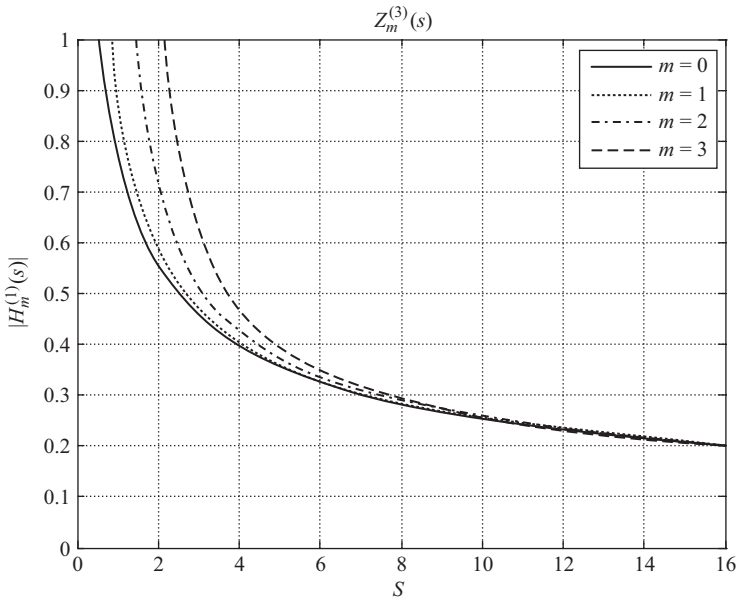


Figure 7.8 Magnitude of Hankel functions of the first kind plotted for several positive integer values of m

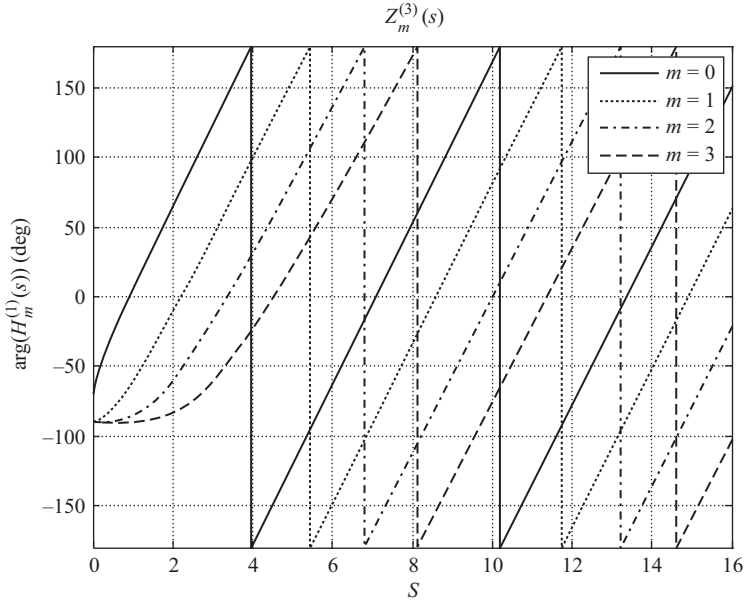


Figure 7.9 Argument of Hankel functions of the first kind plotted for several positive integer values of m

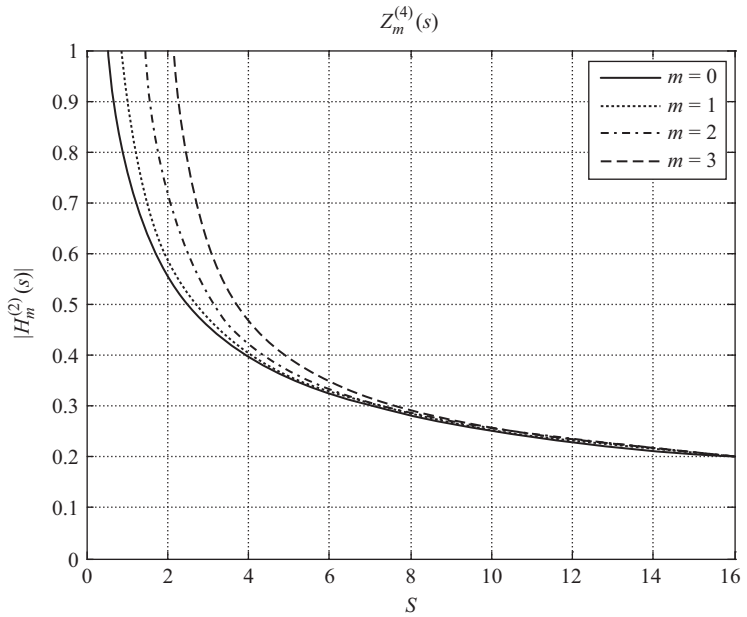


Figure 7.10 Magnitude of Hankel functions of the second kind plotted for several positive integer values of m

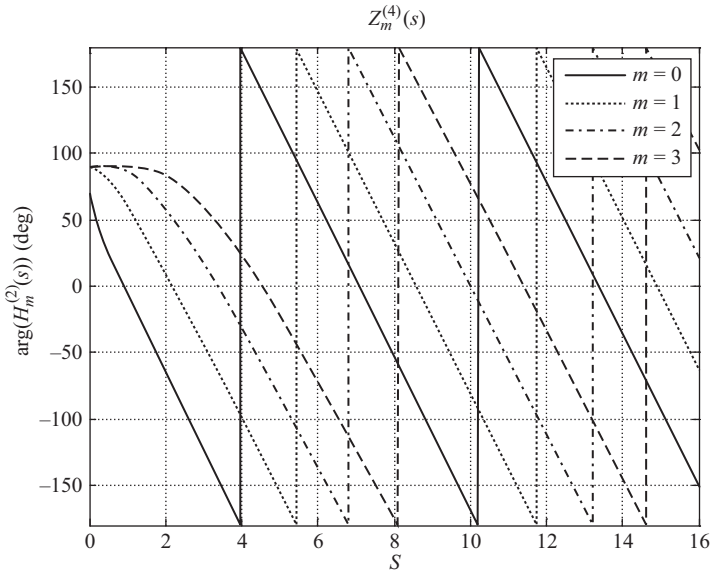


Figure 7.11 Argument of Hankel functions of the second kind plotted for several positive integer values of m

$$H_m^{(1)} \text{ analogous to } e^{js} \tag{7.78}$$

$$H_m^{(2)} \text{ analogous to } e^{-js} \tag{7.79}$$

As was the case when selecting appropriate wave functions for the z -axis, we are interested in travelling wave solutions. Thus, Hankel functions of the second kind are the only functions which possess the appropriate behaviour as $\rho \rightarrow \infty$ when $k\rho$ is positive real or imaginary. Specifically, when s is real, this corresponds to an outward travelling wave; when s is imaginary, this corresponds to an evanescent field; and when s is complex, this corresponds to an attenuated travelling wave. If the opposite (suppressed) time dependency had been chosen then Hankel functions of the first kind would have been the appropriate choice. Thus, the reader is cautioned when comparing results from texts that have differing assumed, and usually suppressed, time dependencies. Finally, we are able to express the solution of the scalar wave equation as

$$\psi(\rho, \phi, z) = \sum_{m=-\infty}^{\infty} \int_{-\infty}^{\infty} B_m(k_z) H_m^{(2)}(k_\rho \rho) e^{jm\phi} e^{-jk_z z} dk_z \tag{7.80}$$

Thus, when keeping in mind the properties of the Hankel functions, it is possible to recognise this as a Fourier integral in the z direction and a Fourier type series in the ϕ direction. Here, k_z specifies a ‘direction of propagation’ since the phase of the

cylindrical wave in the z direction is given by $\exp(-jk_z z)$. The next section will develop methods for constructing vector fields from these scalar wave functions.

7.4 Construction of vector fields

In order that a vector field can be constructed, it is necessary to develop elementary cylindrical vector wave functions that are derived from the elementary cylindrical scalar wave functions. The radiated electric field in free space can be split into transverse electric (TE) and transverse magnetic (TM) parts with respect to the cylindrical z -axis. Specifically this can be expressed as [6]

$$\begin{aligned}\underline{E} &= \nabla \times \hat{\underline{e}}_z \psi_1 + \frac{1}{k} \nabla \times (\nabla \times \hat{\underline{e}}_z \psi_2) \\ &= \nabla \times \hat{\underline{e}}_z \psi_1 + k \hat{\underline{e}}_z \psi_2 + \frac{1}{k} \nabla \left(\frac{\partial(\psi_2)}{\partial z} \right)\end{aligned}\quad (7.81)$$

Here, ψ_1 and ψ_2 are related to the TE and TM parts of the electric field respectively. Thus, we can define two elementary vector wave functions

$$\underline{M}_{mk_z}^{(2)} = \nabla \times \hat{\underline{e}}_z \psi_1 \quad (7.82)$$

$$\underline{N}_{mk_z}^{(2)} = \frac{1}{k} \nabla \times (\nabla \times \hat{\underline{e}}_z \psi_2) \quad (7.83)$$

In cylindrical coordinates, the curl operator can be expressed as

$$\nabla \times \underline{A} = \left(\frac{1}{\rho} \frac{\partial A_z}{\partial \phi} - \frac{\partial A_\phi}{\partial z} \right) \hat{\underline{e}}_\rho + \left(\frac{\partial A_\rho}{\partial z} - \frac{\partial A_z}{\partial \rho} \right) \hat{\underline{e}}_\phi + \left(\frac{1}{\rho} \frac{\partial(\rho A_\phi)}{\partial \rho} - \frac{1}{\rho} \frac{\partial A_\rho}{\partial \phi} \right) \hat{\underline{e}}_z \quad (7.84)$$

However, as the scalar field only acts in the z direction, this becomes

$$\nabla \times A_z \hat{\underline{e}}_z = \frac{1}{\rho} \frac{\partial A_z}{\partial \phi} \hat{\underline{e}}_\rho - \frac{\partial A_z}{\partial \rho} \hat{\underline{e}}_\phi \quad (7.85)$$

Thus

$$\underline{M}_{mk_z}^{(2)} = \frac{1}{\rho} \frac{\partial \psi_1}{\partial \phi} \hat{\underline{e}}_\rho - \frac{\partial \psi_1}{\partial \rho} \hat{\underline{e}}_\phi \quad (7.86)$$

Substituting the elemental scalar wave function yields

$$\underline{M}_{mk_z}^{(2)} = \frac{1}{\rho} \frac{\partial H_m^{(2)}(k_\rho \rho)}{\partial \phi} e^{jm\phi} e^{-jk_z z} \hat{\underline{e}}_\rho - \frac{\partial H_m^{(2)}(k_\rho \rho)}{\partial \rho} e^{jm\phi} e^{-jk_z z} \hat{\underline{e}}_\phi \quad (7.87)$$

or

$$\underline{M}_{mk_z}^{(2)} = \frac{1}{\rho} H_m^{(2)}(k_\rho \rho) e^{-jk_z z} \frac{\partial e^{jm\phi}}{\partial \phi} \hat{\underline{e}}_\rho - e^{jm\phi} e^{-jk_z z} \frac{\partial H_m^{(2)}(k_\rho \rho)}{\partial \rho} \hat{\underline{e}}_\phi \quad (7.88)$$

Hence, taking the derivatives and factorising yields

$$\underline{M}_{mk_z}^{(2)} = \left[\frac{jm}{\rho} H_m^{(2)}(k_\rho \rho) \hat{\underline{e}}_\rho - \frac{\partial H_m^{(2)}(k_\rho \rho)}{\partial \rho} \hat{\underline{e}}_\phi \right] e^{jm\phi} e^{-jk_z z} \quad (7.89)$$

Now, the derivative of a Hankel function in this case is merely differentiation of a function and we have standard tools available for tackling those types of problems. Thus, as before, let $s = k_\rho \rho$ so that

$$\frac{ds}{d\rho} = \frac{d(k_\rho \rho)}{d\rho} = k_\rho \quad (7.90)$$

Recalling the standard formula so that

$$\frac{dH}{d\rho} = \frac{dH}{ds} \frac{ds}{d\rho} = \frac{dH}{ds} k_\rho \quad (7.91)$$

We, therefore, obtain the following operator substitution,

$$\frac{\partial H_m^{(2)}(k_\rho \rho)}{\partial \rho} = k_\rho \frac{\partial H_m^{(2)}(s)}{\partial s} = k_\rho H_m^{(2)'}(k_\rho \rho) \quad (7.92)$$

where $H_m^{(2)'}$ ($k_\rho \rho$) represents the derivative with respect to the argument of the Hankel function of the second kind. Thus

$$\underline{M}_{mk_z}^{(2)} = \left[\frac{jm}{\rho} H_m^{(2)}(k_\rho \rho) \hat{\underline{e}}_\rho - k_\rho H_m^{(2)'}(k_\rho \rho) \hat{\underline{e}}_\phi \right] e^{jm\phi} e^{-jk_z z} \quad (7.93)$$

If needed, a similar argument can be used to derive the derivative of the Hankel function of the first kind. Be aware that some workers prefer to explicitly retain the derivative of the Hankel function so as to explicitly state with what the derivative is with respect to. This would make the vector elementary wave function

$$\underline{M}_{mk_z}^{(2)} = \left[\frac{jm}{\rho} H_m^{(2)}(k_\rho \rho) \hat{\underline{e}}_\rho - \frac{\partial H_m^{(2)}(k_\rho \rho)}{\partial \rho} \hat{\underline{e}}_\phi \right] e^{jm\phi} e^{-jk_z z} \quad (7.94)$$

However, that is a cumbersome nomenclature and one which is not particularly helpful when developing computer code to implement the cylindrical mode expansion, which is of course the final objective here. Thus, as we have explicitly defined the derivative we will retain this rather more compact form. Specifically, the operator substitution

$$H_m^{(i)'}(s) = \frac{d}{ds} \left(H_m^{(i)}(s) \right) = H_{m-1}^{(i)}(s) - \frac{m}{s} H_m^{(i)}(s) \quad (7.95)$$

where i can take on the value $i = 1$ or $i = 2$ only with $s \neq 0$. As will be shown, this is a particularly convenient expression that we will use during the numerical implementation of the cylindrical mode expansion. The \underline{N} elementary vector wave

function is obtained using an analogous procedure. Thus, recalling the definition of the second elementary vector wave equation

$$\underline{N}_{mk_z}^{(2)} = \frac{1}{k} \nabla \times (\nabla \times \hat{\underline{e}}_z \psi_2) \quad (7.96)$$

Using the previously obtained results, we can write that

$$\underline{N}_{mk_z}^{(2)} = \frac{1}{k} \nabla \times \left(\left[\frac{j m}{\rho} H_m^{(2)}(k_\rho \rho) \hat{\underline{e}}_\rho - k_\rho H_m^{(2)'}(k_\rho \rho) \hat{\underline{e}}_\phi \right] e^{jm\phi} e^{-jk_z z} \right) \quad (7.97)$$

However, obtaining the second elementary vector wave function using this strategy results in expressions that contain higher-order derivatives of the Hankel function which are inconvenient. Thus, we shall employ an alternative strategy which will alleviate this difficulty. The \underline{N} elementary wave function can be expressed in an alternative form [6]:

$$\underline{N}_{mk_z}^{(2)} = \frac{1}{k} \nabla \times (\nabla \times \hat{\underline{e}}_z \psi_2) = k \hat{\underline{e}}_z \psi_2 + \frac{1}{k} \nabla \left(\frac{\partial(\psi_2)}{\partial z} \right) \quad (7.98)$$

where the derivative with respect to the z direction can be obtained as

$$\frac{\partial(\psi_2)}{\partial z} = \frac{\partial}{\partial z} \left(H_m^{(2)}(k_\rho \rho) e^{jm\phi} e^{-jk_z z} \right) = -jk_z H_m^{(2)}(k_\rho \rho) e^{jm\phi} e^{-jk_z z} \quad (7.99)$$

The gradient operator in cylindrical coordinates can be expressed as

$$\nabla \psi = \hat{\underline{e}}_\rho \frac{\partial \psi}{\partial \rho} + \hat{\underline{e}}_\phi \frac{1}{\rho} \frac{\partial \psi}{\partial \phi} + \hat{\underline{e}}_z \frac{\partial \psi}{\partial z} \quad (7.100)$$

Hence

$$\begin{aligned} \underline{N}_{mk_z}^{(2)} &= k \hat{\underline{e}}_z H_m^{(2)}(k_\rho \rho) e^{jm\phi} e^{-jk_z z} + \frac{1}{k} \hat{\underline{e}}_\rho \frac{\partial}{\partial \rho} \left(-jk_z H_m^{(2)}(k_\rho \rho) e^{jm\phi} e^{-jk_z z} \right) \\ &\quad + \frac{1}{k} \hat{\underline{e}}_\phi \frac{1}{\rho} \frac{\partial}{\partial \phi} \left(-jk_z H_m^{(2)}(k_\rho \rho) e^{jm\phi} e^{-jk_z z} \right) \\ &\quad + \frac{1}{k} \hat{\underline{e}}_z \frac{\partial}{\partial z} \left(-jk_z H_m^{(2)}(k_\rho \rho) e^{jm\phi} e^{-jk_z z} \right) \end{aligned} \quad (7.101)$$

Evaluating the derivatives in each direction yields

$$\begin{aligned} \underline{N}_{mk_z}^{(2)} &= k H_m^{(2)}(k_\rho \rho) e^{jm\phi} e^{-jk_z z} \hat{\underline{e}}_z - \frac{1}{k} j k_z \frac{\partial H_m^{(2)}(k_\rho \rho)}{\partial \rho} e^{jm\phi} e^{-jk_z z} \hat{\underline{e}}_\rho \\ &\quad + \frac{1}{k} \frac{1}{\rho} m k_z H_m^{(2)}(k_\rho \rho) e^{jm\phi} e^{-jk_z z} \hat{\underline{e}}_\phi - \frac{1}{k} k_z^2 H_m^{(2)}(k_\rho \rho) e^{jm\phi} e^{-jk_z z} \hat{\underline{e}}_z \end{aligned} \quad (7.102)$$

Factorising yields

$$\begin{aligned} \underline{N}_{mk_z}^{(2)} = & \left(-\frac{jk_z}{k} \frac{\partial H_m^{(2)}(k_\rho \rho)}{\partial \rho} \hat{\underline{e}}_\rho + \frac{mk_z}{k\rho} H_m^{(2)}(k_\rho \rho) \hat{\underline{e}}_\phi \right. \\ & \left. + \frac{k^2}{k} H_m^{(2)}(k_\rho \rho) \hat{\underline{e}}_z - \frac{k_z^2}{k} H_m^{(2)}(k_\rho \rho) \hat{\underline{e}}_z \right) e^{jm\phi} e^{-jk_z z} \end{aligned} \quad (7.103)$$

or

$$\begin{aligned} \underline{N}_{mk_z}^{(2)} = & \left(-\frac{jk_z}{k} \frac{\partial H_m^{(2)}(k_\rho \rho)}{\partial \rho} \hat{\underline{e}}_\rho + \frac{mk_z}{k\rho} H_m^{(2)}(k_\rho \rho) \hat{\underline{e}}_\phi \right. \\ & \left. + \left(\frac{k^2 - k_z^2}{k} \right) H_m^{(2)}(k_\rho \rho) \hat{\underline{e}}_z \right) e^{jm\phi} e^{-jk_z z} \end{aligned} \quad (7.104)$$

Using the definition of k_ρ^2

$$k_\rho^2 = k^2 - k_z^2 \quad (7.105)$$

This can be expressed in a more compact form:

$$\underline{N}_{mk_z}^{(2)} = \left(-\frac{jk_z}{k} \frac{\partial H_m^{(2)}(k_\rho \rho)}{\partial \rho} \hat{\underline{e}}_\rho + \frac{mk_z}{k\rho} H_m^{(2)}(k_\rho \rho) \hat{\underline{e}}_\phi + \frac{k_\rho^2}{k} H_m^{(2)}(k_\rho \rho) \hat{\underline{e}}_z \right) e^{jm\phi} e^{-jk_z z} \quad (7.106)$$

Finally, using the derivative of the Hankel function in place of the Hankel function

$$\frac{\partial H_m^{(2)}(k_\rho \rho)}{\partial \rho} = k_\rho \frac{\partial H_m^{(2)}(s)}{\partial s} = k_\rho H_m^{(2)'}(k_\rho \rho) \quad (7.107)$$

The second elementary vector wave function can be expressed as

$$\underline{N}_{mk_z}^{(2)} = \left(-\frac{jk_z}{k} k_\rho H_m^{(2)'}(k_\rho \rho) \hat{\underline{e}}_\rho + \frac{mk_z}{k\rho} H_m^{(2)}(k_\rho \rho) \hat{\underline{e}}_\phi + \frac{k_\rho^2}{k} H_m^{(2)}(k_\rho \rho) \hat{\underline{e}}_z \right) e^{jm\phi} e^{-jk_z z} \quad (7.108)$$

Hence, as the general expression for a radiated electric field can be expressed by a linear combination of the \underline{M} and \underline{N} vector wave functions, we may write that

$$\underline{E}(\rho, \phi, z) = \sum_{m=-\infty}^{\infty} \int_{-\infty}^{\infty} \left[B_m^1(k_z) \underline{M}_{mk_z}^{(2)}(\rho, \phi, z) + B_m^2(k_z) \underline{N}_{mk_z}^{(2)}(\rho, \phi, z) \right] dk_z \quad (7.109)$$

with

$$\underline{M}_{mk_z}^{(2)} = \left[\frac{jm}{\rho} H_m^{(2)}(k_\rho \rho) \hat{\underline{e}}_\rho - k_\rho H_m^{(2)'}(k_\rho \rho) \hat{\underline{e}}_\phi \right] e^{jm\phi} e^{-jk_z z} \quad (7.110)$$

and

$$\underline{N}_{mk_z}^{(2)} = \frac{1}{k} \left(-jk_z k_\rho H_m^{(2)'}(k_\rho \rho) \hat{e}_\rho + \frac{mk_z}{\rho} H_m^{(2)}(k_\rho \rho) \hat{e}_\phi + k_\rho^2 H_m^{(2)}(k_\rho \rho) \hat{e}_z \right) e^{jm\phi} e^{-jk_z z} \quad (7.111)$$

The coefficients B_m^1 and B_m^2 , which are also known as Cylindrical Mode Coefficients (CMC), are complex numbers that are weighting coefficients for the vector wave functions and that are not functions of the scanning variables z and ϕ . They are, however, functions of the polarisation index, the ϕ index n and the Fourier variable k_z . These are the only quantities in these formulae that depend upon the test antenna. If these coefficients were known for the test antenna then these equations would allow the electric field to be evaluated everywhere radiating in free space outside of a conceptual cylinder that is centred about the origin of the measurement coordinate system that encloses the majority of the current sources where the radius of this cylinder is defined to be a , and is called the maximum radial extent (MRE) or also the minimum radius cylinder (MRC). The magnetic field can be similarly obtained from the same set of CMCs from using the Maxwell Faraday equation

$$\underline{H}(\rho, \phi, z) = \frac{-1}{j\omega\mu} \nabla \times \underline{E}(\rho, \phi, z) \quad (7.112)$$

Thus, the magnetic field can be obtained from

$$\underline{H}(\rho, \phi, z) = \frac{-1}{j\omega\mu} \sum_{m=-\infty}^{\infty} \int_{-\infty}^{\infty} \left[B_m^1(K_z) \nabla \times \underline{M}_{mk_z}^{(2)}(\rho, \phi, z) + B_m^2(K_z) \nabla \times \underline{N}_{mk_z}^{(2)}(\rho, \phi, z) \right] dk_z \quad (7.113)$$

Now from the definitions of the vector solutions as set out above, we have that

$$\underline{N}_{mk_z}^{(2)}(\rho, \phi, z) = \frac{1}{k} \nabla \times \underline{M}_{mk_z}^{(2)}(\rho, \phi, z) \quad (7.114)$$

Similarly [7]

$$\underline{M}_{mk_z}^{(2)}(\rho, \phi, z) = \frac{1}{k} \nabla \times \underline{N}_{mk_z}^{(2)}(\rho, \phi, z) \quad (7.115)$$

Thus, the magnetic fields can be obtained using the analogous equation

$$\underline{H}(\rho, \phi, z) = \frac{-k}{j\omega\mu} \sum_{m=-\infty}^{\infty} \int_{-\infty}^{\infty} \left[B_m^1(k_z) \underline{N}_{mk_z}^{(2)}(\rho, \phi, z) + B_m^2(k_z) \underline{M}_{mk_z}^{(2)}(\rho, \phi, z) \right] dk_z \quad (7.116)$$

where the CMCs B_m^1 and B_m^2 depend upon the AUT. Thus, the principal objective of this work is to determine these coefficients for a given test antenna and so inverting the above equations is where our attention must next be focused. The \underline{M} and \underline{N} vectors wave functions were chosen as they possess certain orthogonality

properties that are convenient and, as we will show, can be used to invert these integrals. The derivation of these relationships is the subject of the next section.

7.5 Derivation of cylindrical mode coefficients from cylindrical near-field data

In practice, one does not have the CMCs. Instead, one has to determine these from measured near-field data. In order that this can be accomplished, the expressions that were obtained within the preceding section need to be inverted through the use of three useful orthogonality relations. Deriving these expressions will be the first task tackled within this section.

7.5.1 Orthogonality properties of cylindrical wave vectors

Three orthogonality relationships are needed for the \underline{M} and \underline{N} vector wave functions in order that the field equations can be inverted to enable the CMCs to be determined from measured cylindrical near-fields. These orthogonality relations are derived within the following sections before being used to obtain expressions for the CMCs in terms of two measured orthogonal tangential near electric field components.

7.5.1.1 Property A

The first orthogonality property can be expressed as

$$\int_{-\infty}^{\infty} \int_0^{2\pi} \left(\underline{M}_{mk_z}^{(2)} \times \underline{M}_{m'k'_z}^{(2)} \right) \cdot \hat{\underline{e}}_{\rho} d\phi dz = 0 \quad (7.117)$$

Here, the primed quantities are used to distinguish the respective m and k_z variables and are not used to denote derivatives, cf. the notation used for the Hankel functions. As was shown above

$$\underline{M}_{mk_z}^{(2)} = \left[\frac{j m}{\rho} H_m^{(2)}(k_{\rho} \rho) \hat{\underline{e}}_{\rho} - k_{\rho} H_m^{(2)'}(k_{\rho} \rho) \hat{\underline{e}}_{\phi} \right] e^{j m \phi} e^{-j k_z z} \quad (7.118)$$

Here, it is evident that \underline{M} has *no* z -directed component. Thus, the cross-product of this vector with itself can therefore *only* have a z -directed component. Thus, the scalar product of the z -directed and ρ -directed vectors will be zero as these are orthogonal vectors. Hence the integral must also be identically zero thereby verifying the first orthogonality property. Note that this is true even if the arguments of the respective Hankel functions are different.

7.5.1.2 Property B

The second orthogonality property can be expressed as

$$\int_{-\infty}^{\infty} \int_0^{2\pi} \left(\underline{N}_{mk_z}^{(2)} \times \underline{N}_{m'k'_z}^{(2)} \right) \cdot \hat{\underline{e}}_{\rho} d\phi dz = 0 \quad (7.119)$$

Here, as before, the primed quantities are used to distinguish the respective m and k_z variables and are not used to denote derivatives, cf. the notation used for the Hankel functions. The integrand within the above expression can be significantly simplified using the following standard vector identity,

$$(\underline{B} \times \underline{C}) \cdot \underline{A} = \underline{C} \cdot (\underline{A} \times \underline{B}) \quad (7.120)$$

Thus

$$\left(\underline{N}_{mk_z}^{(2)} \times \underline{N}_{m'k'_z}^{(2)} \right) \cdot \hat{\underline{e}}_\rho = \underline{N}_{m'k'_z}^{(2)} \cdot \left(\hat{\underline{e}}_\rho \times \underline{N}_{mk_z}^{(2)} \right) \quad (7.121)$$

This is convenient as a unit vector crossed with another vector will result in a vector with components that act purely within a single plane in space. Since

$$\underline{N}_{mk_z}^{(2)} = \frac{1}{k} \left(-jk_z k_\rho H_m^{(2)'}(k_\rho \rho) \hat{\underline{e}}_\rho + \frac{mk_z}{\rho} H_m^{(2)}(k_\rho \rho) \hat{\underline{e}}_\phi + k_\rho^2 H_m^{(2)}(k_\rho \rho) \hat{\underline{e}}_z \right) e^{jm\phi} e^{-jk_z z} \quad (7.122)$$

Then

$$\hat{\underline{e}}_\rho \times \underline{N}_{mk_z}^{(2)} = \frac{1}{k} \left[-\left(k_\rho^2 H_m^{(2)}(k_\rho \rho) \right) \hat{\underline{e}}_\phi + \left(\frac{mk_z}{\rho} H_m^{(2)}(k_\rho \rho) \right) \hat{\underline{e}}_z \right] e^{jm\phi} e^{-jk_z z} \quad (7.123)$$

The required integral can be obtained from taking the scalar dot product of this, and the elementary cylindrical vector mode function yielding

$$\left(\underline{N}_{mk_z}^{(2)} \times \underline{N}_{m'k'_z}^{(2)} \right) \cdot \hat{\underline{e}}_\rho = \frac{1}{k^2} \left[\frac{mk_z k_\rho^2}{\rho} H_{m'}^{(2)}(k_\rho \rho) H_m^{(2)}(k_\rho \rho) - \frac{m'k'_z k_\rho^2}{\rho} H_{m'}^{(2)}(k_\rho \rho) H_m^{(2)}(k_\rho \rho) \right] e^{jm'\phi} e^{-jk'_z z} e^{jm\phi} e^{-jk_z z} \quad (7.124)$$

Factorising yields

$$\left(\underline{N}_{mk_z}^{(2)} \times \underline{N}_{m'k'_z}^{(2)} \right) \cdot \hat{\underline{e}}_\rho = \frac{k_\rho^2}{k^2} \left[mk_z H_{m'}^{(2)}(k_\rho \rho) H_m^{(2)}(k_\rho \rho) - m'k'_z H_{m'}^{(2)}(k_\rho \rho) H_m^{(2)}(k_\rho \rho) \right] e^{j(m'+m)\phi} e^{-j(k'_z+k_z)z} \quad (7.125)$$

Now, when integrating this with respect to ϕ and z , the quantity within the brackets will be constant, thus the integral can be expressed as

$$\int_{-\infty}^{\infty} \int_0^{2\pi} \text{const} e^{j(m'+m)\phi} e^{-j(k'_z+k_z)z} d\phi dz \quad (7.126)$$

Thus, the integral can be split into two 1D integrals, namely

$$\int_{-\infty}^{\infty} \int_0^{2\pi} \text{const} e^{j(m'+m)\phi} e^{-j(k'_z+k_z)z} d\phi dz = \text{const} \int_0^{2\pi} e^{j(m'+m)\phi} d\phi \int_{-\infty}^{\infty} e^{-j(k'_z+k_z)z} dz \tag{7.127}$$

Evaluating the first integral and assuming that $m \neq -m'$ then

$$\int_0^{2\pi} e^{j(m'+m)\phi} d\phi = \left[-\frac{j}{m'+m} e^{j(m'+m)\phi} \right]_0^{2\pi} = -\frac{j}{m'+m} + \frac{j}{m'+m} = 0 \tag{7.128}$$

This is true provided m and m' are both integers which in this application they are. When $m = -m'$, the integral is non-zero, as is shown in the following section. Similarly, for the integral in z , this can be recognised as being an integral representation of the Dirac delta function [8] namely

$$\delta(t-x) = \frac{1}{2\pi} \int_{-\infty}^{\infty} e^{j(t-x)z} dz \tag{7.129}$$

Rearranging this so as to match our expression yields

$$2\pi\delta(-k_z - k'_z) = \int_{-\infty}^{\infty} e^{-j(k_z+k'_z)z} dz \tag{7.130}$$

which is zero everywhere except at $-k_z - k'_z$. Thus, the product of the ϕ - and z -integrals is zero everywhere except when $m' = -m$ and when $k'_z = -k_z$. An alternative way to view the z -integral is to evaluate the z -integral providing $k_z \neq -k'_z$ which yields

$$\int_{-\infty}^{\infty} e^{-j(k'_z+k_z)z} dz = \left[\frac{j}{k'_z + k_z} e^{-j(k'_z+k_z)z} \right]_{-\infty}^{\infty} \tag{7.131}$$

For which the magnitude and phase remain finite for all values of z . This follows from noting that the magnitude of a complex exponential is unity and the argument is wrapped modulo 2π . Thus, the product of the ϕ and z integrals will be zero providing $m \neq -m'$ and $k_z = -k'_z$. However, when $m' = -m$ and when $k'_z = -k_z$, the complex exponentials equate to unity and the integral is non-zero unless the terms within the parentheses are also equal to zero. Under these circumstances, the terms within the parenthesis that we must consider are

$$mk_z H_{m'}^{(2)}(k_\rho \rho) H_m^{(2)}(k_\rho \rho) - m' k'_z H_{m'}^{(2)}(k_\rho \rho) H_m^{(2)}(k_\rho \rho) \tag{7.132}$$

However, when $m' = -m$ and when $k'_z = -k_z$ this becomes

$$mk_z H_{-m}^{(2)}(k_\rho \rho) H_m^{(2)}(k_\rho \rho) - mk_z H_{-m}^{(2)}(k_\rho \rho) H_m^{(2)}(k_\rho \rho) \quad (7.133)$$

Note that the arguments of the Hankel functions are exactly equal in this case since k_ρ depends upon k_z by definition. Thus, the sum equates to zero. The second orthogonality relationship is therefore confirmed. Again, this relation holds even if the arguments of the respective Hankel functions are different since in those cases $k_z \neq -k'_z$ and the complex exponential in the definite ϕ integral will be identically zero.

7.5.1.3 Properties C and D

The third orthogonality property we need can be obtained from crossing the N and M functions and integrating as before, where the integrand can be significantly simplified using the following standard vector identity,

$$(\underline{B} \times \underline{C}) \cdot \underline{A} = \underline{B} \cdot (\underline{C} \times \underline{A}) = -\underline{B} \cdot (\underline{A} \times \underline{C}) \quad (7.134)$$

Thus, the integrand in the preceding equation can be expressed equivalently as

$$\left(\underline{N}_{mk_z}^{(2)} \times \underline{M}_{m'k'_z}^{(2)} \right) \cdot \hat{\underline{e}}_\rho = -\underline{N}_{mk_z}^{(2)} \cdot \left(\hat{\underline{e}}_\rho \times \underline{M}_{m'k'_z}^{(2)} \right) \quad (7.135)$$

Again, this is convenient since this will result in a vector with components that act purely within a single plane in space. Here, as \underline{M} has only ρ - and ϕ -directed components this will result in

$$\hat{\underline{e}}_\rho \times \underline{M}_{m'k'_z}^{(2)} = -k'_\rho H_m^{(2)'} e^{jm'\phi} e^{-jk'_z z} \hat{\underline{e}}_z \quad (7.136)$$

Here, the argument of the Hankel function has been suppressed for the sake of brevity. As before, the required integral can be obtained from taking the scalar dot product of this, and the elementary cylindrical vector mode function yielding

$$\begin{aligned} \left(\underline{N}_{mk_z}^{(2)} \times \underline{M}_{m'k'_z}^{(2)} \right) \cdot \hat{\underline{e}}_\rho &= \underline{N}_{mk_z}^{(2)} \cdot \left(k'_\rho H_m^{(2)'} e^{jm'\phi} e^{-jk'_z z} \hat{\underline{e}}_z \right) \\ &= \frac{k_\rho^2 k'_\rho}{k} H_m^{(2)} H_m^{(2)'} e^{jm\phi} e^{-jk_z z} e^{jm'\phi} e^{-jk'_z z} \\ &= \frac{k_\rho^2 k'_\rho}{k} H_m^{(2)} H_m^{(2)'} e^{j(m+m')\phi} e^{-j(k_z+k'_z)z} \end{aligned} \quad (7.137)$$

Now, when integrating this with respect to ϕ and z , only the complex exponentials are variables, all of the remaining factors are constants with respect to the integration; thus, as with the second relation we are able to consider this integral separately. Thus, evaluating the ϕ integral and assuming that $m \neq -m'$ then again we may write that providing they are also integers

$$\int_0^{2\pi} e^{j(m'+m)\phi} d\phi = 0 \quad (7.138)$$

However, when $m = -m'$ this becomes

$$\int_0^{2\pi} e^{j(m'+m)\phi} d\phi = \int_0^{2\pi} d\phi = [\phi]_0^{2\pi} = 2\pi \tag{7.139}$$

Next we must consider the integral in z . Here we have to evaluate

$$\int_{-\infty}^{\infty} e^{-j(k_z+k'_z)z} dz \tag{7.140}$$

However, as before, where rearranging this so as to match our expression yields

$$2\pi\delta(-k_z - k'_z) = \int_{-\infty}^{\infty} e^{-j(k_z+k'_z)z} dz \tag{7.141}$$

Thus, when $m = -m'$ and $k_z = -k'_z$, we may write that

$$\int_{-\infty}^{\infty} \int_0^{2\pi} \left(\underline{N}_{mk_z}^{(2)} \times \underline{M}_{m'k'_z}^{(2)} \right) \cdot \hat{\underline{e}}_{\rho} d\phi dz = \frac{k_{\rho}^2 k'_{\rho}}{k} H_m^{(2)} H_{m'}^{(2)'} 4\pi^2 \delta(-k_z - k'_z) \tag{7.142}$$

Substituting in $m = -m'$ and noting that the argument of the Hankel function and the argument of the derivative of the Hankel function are equal yields the required integral result:

$$\int_{-\infty}^{\infty} \int_0^{2\pi} \left(\underline{N}_{mk_z}^{(2)} \times \underline{M}_{m'k'_z}^{(2)} \right) \cdot \hat{\underline{e}}_{\rho} d\phi dz = \frac{4\pi^2 k_{\rho}^3}{k} H_m^{(2)} H_{-m}^{(2)'} \delta(-k_z - k'_z) \tag{7.143}$$

Thus, the complete orthogonality property can be expressed as

$$\begin{aligned} & \int_{-\infty}^{\infty} \int_0^{2\pi} \left(\underline{N}_{mk_z}^{(2)} \times \underline{M}_{m'k'_z}^{(2)} \right) \cdot \hat{\underline{e}}_{\rho} d\phi dz \\ &= \begin{cases} \frac{4\pi^2 k_{\rho}^3}{k} H_m^{(2)} H_{-m}^{(2)'} \delta(-k_z - k'_z) & \text{for } m' = -m \\ 0 & \text{otherwise} \end{cases} \end{aligned} \tag{7.144}$$

where it is understood that the delta function belongs under an integral sign. Following directly from this relationship we can write Property D as

$$\begin{aligned} & \int_{-\infty}^{\infty} \int_0^{2\pi} \left(\underline{M}_{m'k'_z}^{(2)} \times \underline{N}_{mk_z}^{(2)} \right) \cdot \hat{\underline{e}}_{\rho} d\phi dz \\ &= \begin{cases} -\frac{4\pi^2 k_{\rho}^3}{k} H_m^{(2)} H_{-m}^{(2)'} \delta(-k - zk'_z) & \text{for } m' = -m \\ 0 & \text{otherwise} \end{cases} \end{aligned} \tag{7.145}$$

which is the final orthogonality property that is needed. It is noted that the condition that is applied to these orthogonality relation can be expressed equivalently using the Kronecker delta which is zero unless $m' = -m$ in which case it equates to unity. Hence, using this notation these relationships can be restated more compactly as

$$\int_{-\infty}^{\infty} \int_0^{2\pi} \left(\underline{N}_{mk_z}^{(2)} \times \underline{M}_{m'k'_z}^{(2)} \right) \cdot \hat{\underline{e}}_{\rho} d\phi dz = \frac{4\pi^2 k_{\rho}^3}{k} H_m^{(2)} H_{-m'}^{(2)\prime} \delta_{-mm'} \delta(-k_z - k'_z) \tag{7.146}$$

$$\int_{-\infty}^{\infty} \int_0^{2\pi} \left(\underline{M}_{m'k'_z}^{(2)} \times \underline{N}_{mk_z}^{(2)} \right) \cdot \hat{\underline{e}}_{\rho} d\phi dz = -\frac{4\pi^2 k_{\rho}^3}{k} H_m^{(2)} H_{-m'}^{(2)\prime} \delta_{-mm'} \delta(-k_z - k'_z) \tag{7.147}$$

where the Kronecker delta is defined as

$$\delta_{-mm'} = \begin{cases} 1 & \text{if } m' = -m \\ 0 & \text{if } m' \neq -m \end{cases} \tag{7.148}$$

7.5.2 *Determining cylindrical mode coefficients from measured near electric field components*

In order that the vector cylindrical wave coefficients can be determined from measurement, the field equation that was derived in the previous section needs to be inverted. This can be accomplished by using the orthogonality relations that were derived within the preceding section. Two sets of CMCs are needed to represent the field radiated into free space and we must obtain each of these. The following sections contain the required derivations for obtaining the B^1 and B^2 CMCs from tangential measured near electric fields.

7.5.2.1 **Derivation of B^1 cylindrical mode coefficients**

Consider crossing the \underline{N} elementary vector wave function into the near electric field. This can be achieved by evaluating

$$\underline{N}_{m',k'_z}^{(2)} \times \underline{E}(\rho, \phi, z) \tag{7.149}$$

where

$$\underline{E}(\rho, \phi, z) = \sum_{m=-\infty}^{\infty} \int_{-\infty}^{\infty} \left[B_m^1(k_z) \underline{M}_{m,k_z}^{(2)}(\rho, \phi, z) + B_m^2(k_z) \underline{N}_{m,k_z}^{(2)}(\rho, \phi, z) \right] dk_z \tag{7.150}$$

Hence suppressing the arguments of the Hankel functions for brevity yields

$$\begin{aligned} \underline{N}_{m',k'_z}^{(2)} \times \underline{E}(\rho, \phi, z) &= \sum_{m=-\infty}^{\infty} \int_{-\infty}^{\infty} \left[B_m^1(k_z) \underline{N}_{m',k'_z}^{(2)} \times \underline{M}_{m,k_z}^{(2)} \right. \\ &\quad \left. + B_m^2(k_z) \underline{N}_{m',k'_z}^{(2)} \times \underline{N}_{m,k_z}^{(2)} \right] dk_z \end{aligned} \quad (7.151)$$

Dotting this with the ρ -directed unit vector and integrating across the imaginary scanning cylinder yields

$$\begin{aligned} &\int_{-\infty}^{\infty} \int_0^{2\pi} \left(\underline{N}_{m',k'_z}^{(2)} \times \underline{E}(\rho_0, \phi, z) \right) \cdot \hat{\underline{e}}_{\rho} d\phi dz \\ &= \int_{-\infty}^{\infty} \int_0^{2\pi} \left(\sum_{m=-\infty}^{\infty} \int_{-\infty}^{\infty} \left[B_m^1(k_z) \underline{N}_{m',k'_z}^{(2)} \times \underline{M}_{m,k_z}^{(2)} \right] dk_z \right) \cdot \hat{\underline{e}}_{\rho} d\phi dz \\ &\quad + \int_{-\infty}^{\infty} \int_0^{2\pi} \left(\sum_{m=-\infty}^{\infty} \int_{-\infty}^{\infty} \left[B_m^2(k_z) \underline{N}_{m',k'_z}^{(2)} \times \underline{N}_{m,k_z}^{(2)} \right] dk_z \right) \cdot \hat{\underline{e}}_{\rho} d\phi dz \end{aligned} \quad (7.152)$$

Here, ρ_0 denotes the radius of the scanning cylinder. Exchanging the order of integration and summation yields

$$\begin{aligned} &\int_{-\infty}^{\infty} \int_0^{2\pi} \left(\underline{N}_{m',k'_z}^{(2)} \times \underline{E}(\rho_0, \phi, z) \right) \cdot \hat{\underline{e}}_{\rho} d\phi dz \\ &= \sum_{m=-\infty}^{\infty} \int_{-\infty}^{\infty} \int_{-\infty}^{\infty} \int_0^{2\pi} \left[B_m^1(k_z) \underline{N}_{m',k'_z}^{(2)} \times \underline{M}_{m,k_z}^{(2)} \right] \cdot \hat{\underline{e}}_{\rho} d\phi dz dk_z \\ &\quad + \sum_{m=-\infty}^{\infty} \int_{-\infty}^{\infty} \int_{-\infty}^{\infty} \int_0^{2\pi} \left[B_m^2(k_z) \underline{N}_{m',k'_z}^{(2)} \times \underline{N}_{m,k_z}^{(2)} \right] \cdot \hat{\underline{e}}_{\rho} d\phi dz dk_z \end{aligned} \quad (7.153)$$

Thus, this is now in a form that the orthogonality properties that were developed within the preceding section can be applied. Using Property B yields

$$\begin{aligned} &\int_{-\infty}^{\infty} \int_0^{2\pi} \left(\underline{N}_{m',k'_z}^{(2)} \times \underline{E}(\rho_0, \phi, z) \right) \cdot \hat{\underline{e}}_{\rho} d\phi dz \\ &= \sum_{m=-\infty}^{\infty} \int_{-\infty}^{\infty} \int_{-\infty}^{\infty} \int_0^{2\pi} \left[B_m^1(k_z) \underline{N}_{m',k'_z}^{(2)} \times \underline{M}_{m,k_z}^{(2)} \right] \cdot \hat{\underline{e}}_{\rho} d\phi dz dk_z \end{aligned} \quad (7.154)$$

Using Property C

$$\int_{-\infty}^{\infty} \int_0^{2\pi} \left(\underline{N}_{m, k_z}^{(2)} \times \underline{M}_{m', k'_z}^{(2)} \right) \cdot \widehat{\underline{e}}_{\rho} d\phi dz$$

$$= \begin{cases} \frac{4\pi^2 k_{\rho}^3}{k} H_m^{(2)} H_{-m}^{(2)'} \delta(-k_z - k'_z) & \text{for } m' = -m \\ 0 & \text{otherwise} \end{cases} \quad (7.155)$$

Yields (note that the use of primes in the orthogonality relation and the field expression are interchanged with one another)

$$\int_{-\infty}^{\infty} \int_0^{2\pi} \left(\underline{N}_{m', k'_z}^{(2)} \times \underline{E}(\rho_0, \phi, z) \right) \cdot \widehat{\underline{e}}_{\rho} d\phi dz$$

$$= \frac{4\pi^2 k_{\rho}^3}{k} \int_{-\infty}^{\infty} H_{-m}^{(2)} H_m^{(2)'} B_m^1(k_z) \delta(-k_z - k'_z) dk_z \quad (7.156)$$

Thus, from the definition of the Dirac delta function and assuming $f(t)$ is continuous at t_0 , we know that

$$\int_{-\infty}^{\infty} f(t) \delta(t - t_0) dt = f(t_0) \quad (7.157)$$

Thus, the orthogonality property of the elementary vector wave functions has the effect of tapping off the value of the multiplying function at the sampling point as determined by the argument of the delta function. Recalling that $\delta(t) = \delta(-t)$

$$\int_{-\infty}^{\infty} \int_0^{2\pi} \left(\underline{N}_{m', k'_z}^{(2)} \times \underline{E}(\rho_0, \phi, z) \right) \cdot \widehat{\underline{e}}_{\rho} d\phi dz = \frac{4\pi^2 k_{\rho}^3}{k} H_{-m}^{(2)} H_m^{(2)'} B_m^1(-k'_z) \quad (7.158)$$

Rearranging this yields

$$B_m^1(-k'_z) = \frac{k}{4\pi^2 k_{\rho}^3 H_{-m}^{(2)}(k_{\rho} \rho_0) H_m^{(2)'}(k_{\rho} \rho_0)} \int_{-\infty}^{\infty} \int_0^{2\pi} \left(\underline{N}_{m', k'_z}^{(2)} \times \underline{E}(\rho_0, \phi, z) \right) \cdot \widehat{\underline{e}}_{\rho} d\phi dz \quad (7.159)$$

Here, the argument of the Hankel function has been reintroduced. The vector operation within the integrand will result in a scalar quantity that is formed from difference between the z -polarised electric field component multiplied with the ϕ component of the vector wave function and the ϕ -polarised electric field component multiplied with the z -component of the wave function. That is to say, when

suppressing the dependency of the field components for the sake of brevity, the integrand can be expressed as

$$\left(\underline{N}_{m', k'_z}^{(2)} \times \underline{E} \right) \cdot \hat{\underline{e}}_\rho = -H_{m'}^{(2)}(k_\rho \rho_0) \frac{1}{k} \left[\frac{m' k'_z}{\rho_0} E_z + k_\rho^2 E_\phi \right] e^{jm'\phi} e^{-jk'_z z} \quad (7.160)$$

Substituting this into the preceding expression for the CMC and recalling that $m = -m'$ and that $k_z = -k'_z$ yields the desired result

$$B_m^1(k_z) = \frac{-1}{4\pi^2 k_\rho^3 H_m^{(2)'}(k_\rho \rho_0)} \times \int_{-\infty}^{\infty} \int_0^{2\pi} \left(\frac{mk_z}{\rho_0} E_z(\rho_0, \phi, z) + k_\rho^2 E_\phi(\rho_0, \phi, z) \right) e^{-jm\phi} e^{jk_z z} d\phi dz \quad (7.161)$$

7.5.2.2 Derivation of B^2 cylindrical mode coefficients

A similar procedure is used to obtain the second orthogonal set of CMCs. Here, however, the strategy is to cross the \underline{M} function into the expression for the electric field and then to integrate. This can be achieved by evaluating

$$\underline{M}_{m', k'_z}^{(2)} \times \underline{E}(\rho, \phi, z) \quad (7.162)$$

Again suppressing the argument of the Hankel function for brevity yields

$$\underline{M}_{m', k'_z}^{(2)} \times \underline{E}(\rho, \phi, z) = \sum_{m=-\infty}^{\infty} \int_{-\infty}^{\infty} \left[B_m^1(k_z) \underline{M}_{m', k'_z}^{(2)} \times \underline{M}_{m, k_z}^{(2)} + B_m^2(k_z) \underline{M}_{m', k'_z}^{(2)} \times \underline{N}_{m, k_z}^{(2)} \right] dk_z \quad (7.163)$$

Dotting this with the ρ -directed unit vector and integrating across the imaginary scanning cylinder yields

$$\begin{aligned} & \int_{-\infty}^{\infty} \int_0^{2\pi} \left(\underline{M}_{m', k'_z}^{(2)} \times \underline{E}(\rho_0, \phi, z) \right) \cdot \hat{\underline{e}}_\rho d\phi dz \\ &= \int_{-\infty}^{\infty} \int_0^{2\pi} \left(\sum_{m=-\infty}^{\infty} \int_{-\infty}^{\infty} \left[B_m^1(k_z) \underline{M}_{m', k'_z}^{(2)} \times \underline{M}_{m, k_z}^{(2)} \right] dk_z \right) \cdot \hat{\underline{e}}_\rho d\phi dz \\ &+ \int_{-\infty}^{\infty} \int_0^{2\pi} \left(\sum_{m=-\infty}^{\infty} \int_{-\infty}^{\infty} \left[B_m^2(k_z) \underline{M}_{m', k'_z}^{(2)} \times \underline{N}_{m, k_z}^{(2)} \right] dk_z \right) \cdot \hat{\underline{e}}_\rho d\phi dz \end{aligned} \quad (7.164)$$

Again, exchanging the order of integration and summation and this time using orthogonality Property A yields

$$\begin{aligned}
 & \int_{-\infty}^{\infty} \int_0^{2\pi} \left(\underline{M}_{m',k'_z}^{(2)} \times \underline{E}(\rho_0, \phi, z) \right) \cdot \hat{\underline{e}}_{\rho} d\phi dz \\
 &= \sum_{m=-\infty}^{\infty} \int_{-\infty}^{\infty} \int_{-\infty}^{\infty} \int_0^{2\pi} \left[B_m^2(k_z) \underline{M}_{m',k'_z}^{(2)} \times \underline{N}_{m,k_z}^{(2)} \right] \cdot \hat{\underline{e}}_{\rho} d\phi dz dk_z
 \end{aligned} \tag{7.165}$$

Recalling Property D

$$\begin{aligned}
 & \int_{-\infty}^{\infty} \int_0^{2\pi} \left(\underline{M}_{m',k'_z}^{(2)} \times \underline{N}_{mk_z}^{(2)} \right) \cdot \hat{\underline{e}}_{\rho} d\phi dz \\
 &= \begin{cases} -\frac{4\pi^2 k_{\rho}^3}{k} H_m^{(2)} H_{-m}^{(2)'} \delta(-k_z - k'_z) & \text{for } m' = -m \\ 0 & \text{otherwise} \end{cases}
 \end{aligned} \tag{7.166}$$

where again we assume that the product acting on the Delta function is well behaved and enables the result of the integral to be expressed as

$$\int_{-\infty}^{\infty} \int_0^{2\pi} \left(\underline{M}_{m',k'_z}^{(2)} \times \underline{E}(\rho_0, \phi, z) \right) \cdot \hat{\underline{e}}_{\rho} d\phi dz = -\frac{4\pi^2 k_{\rho}^3}{k} H_m^{(2)} H_{-m}^{(2)'} B_m^2(-k'_z) \tag{7.167}$$

Or writing the second set of CMCs in terms of an integral of the elementary vector mode functions and the electric field yields

$$B_m^2(-k'_z) = -\frac{k}{4\pi^2 k_{\rho}^3 H_m^{(2)} H_{-m}^{(2)'}} \int_{-\infty}^{\infty} \int_0^{2\pi} \left(\underline{M}_{m',k'_z}^{(2)} \times \underline{E}(\rho_0, \phi, z) \right) \cdot \hat{\underline{e}}_{\rho} d\phi dz \tag{7.168}$$

Examining the integrand and expressing the terms in component form yields

$$\left(\underline{M}_{m',k'_z}^{(2)} \times \underline{E} \right) \cdot \hat{\underline{e}}_{\rho} = -k_{\rho} H_m^{(2)'}(k_{\rho} \rho_0) E_z e^{jm'\phi} e^{-jk'_z z} \tag{7.169}$$

Substituting this into the previous result and recalling that $m = -m'$ and $k_z = -k'_z$ yields

$$B_m^2(k_z) = \frac{k}{4\pi^2 k_{\rho}^2 H_m^{(2)}(k_{\rho} \rho_0)} \int_{-\infty}^{\infty} \int_0^{2\pi} E_z(\rho_0, \phi, z) e^{-jm\phi} e^{jk_z z} d\phi dz \tag{7.170}$$

Finally, we obtain the principal formula for determining CMCs from two orthogonal transverse near electric field components. These are

$$B_m^1(k_z) = \frac{-1}{4\pi^2 k_\rho^3 H_m^{(2)'}(k_\rho \rho_0)} \times \int_{-\infty}^{\infty} \int_0^{2\pi} \left(\frac{mk_z}{\rho_0} E_z(\rho_0, \phi, z) + k_\rho^2 E_\phi(\rho_0, \phi, z) \right) e^{-jm\phi} e^{jk_z z} d\phi dz \quad (7.171)$$

$$B_m^2(k_z) = \frac{k}{4\pi^2 k_\rho^2 H_m^{(2)}(k_\rho \rho_0)} \int_{-\infty}^{\infty} \int_0^{2\pi} E_z(\rho_0, \phi, z) e^{-jm\phi} e^{jk_z z} d\phi dz \quad (7.172)$$

From this it is clear that for the case where measurements are taken using an infinitesimal electric dipole probe, the probe correction problem reduces to the limiting case of an application of the orthogonality relationships for the \underline{M} and \underline{N} elemental vector wave functions. This is also true for the planar and spherical cases. Once these mode coefficients have been obtained, it is possible to calculate the electric field radiated into free space everywhere *outside* of a conceptual, infinitely long cylinder of radius ρ_0 , i.e. where $\rho \geq \rho_0$ using

$$\underline{E}(\rho, \phi, z) = \sum_{m=-\infty}^{\infty} \int_{-\infty}^{\infty} \left[B_m^1(k_z) \underline{M}_{m, k_z}^{(2)}(\rho, \phi, z) + B_m^2(k_z) \underline{N}_{m, k_z}^{(2)}(\rho, \phi, z) \right] dk_z \quad (7.173)$$

For the case where measurements are taken using an infinitesimal Hertzian dipole probe, these equations enable the near-field to far-field transform to be accomplished through the application of a cylindrical mode expansion of the fields. It follows that for theoretical or computational electromagnetic applications, these formulae are very useful. However, evaluating the formula for the electric fields is formidable but can be dramatically simplified when the fields are only required to be determined in the true far-field. This is the subject of the next section.

7.6 Derivation of asymptotic far-field parameters from cylindrical mode coefficients

As was shown in the preceding section, it is possible to compute the field radiated into free space from a set of CMCs anywhere in space outside of a conceptual right circular cylinder that encloses the current sources so that $\rho > a$, where a denotes the MRC. These equations can be modified so that they automatically produce the asymptotic far-field as this is often of greatest interest in practice [9]. The first step is to utilise the large argument value of the Bessel function of the first and second

kinds. These can be expressed, respectively, as [10]

$$J_m(x) \approx \sqrt{\frac{2}{\pi x}} \cos\left(x - \frac{m\pi}{2} - \frac{\pi}{4}\right) \quad (7.174)$$

$$Y_m(x) \approx \sqrt{\frac{2}{\pi x}} \sin\left(x - \frac{m\pi}{2} - \frac{\pi}{4}\right) \quad (7.175)$$

From the definition of the Hankel function of the second kind, the large argument asymptotic form of this function can be obtained from

$$H_m^{(2)}(x) \approx \sqrt{\frac{2}{\pi x}} \left[\cos\left(x - \frac{m\pi}{2} - \frac{\pi}{4}\right) - j \sin\left(x - \frac{m\pi}{2} - \frac{\pi}{4}\right) \right] \quad (7.176)$$

Or equivalently using Euler's formula, this can be written more compactly as

$$H_m^{(2)}(x) \approx \sqrt{\frac{2}{\pi x}} e^{-j\left(x - \frac{m\pi}{2} - \frac{\pi}{4}\right)} = (j)^m \sqrt{\frac{2}{\pi x}} e^{-j\left(x - \frac{\pi}{4}\right)} \quad (7.177)$$

Now, the asymptotic large argument derivative of the Hankel function with respect to the argument can be obtained by using the standard relation namely

$$\frac{dH_m^{(2)}(ax)}{dx} = aH_{m-1}^{(2)}(ax) - \frac{m}{x}H_m^{(2)}(ax) \quad (7.178)$$

Again, substituting the large argument form of the Hankel function into this yields

$$\frac{dH_m^{(2)}(ax)}{dx} = a(j)^{m-1} \sqrt{\frac{2}{\pi x}} e^{-j\left(x - \frac{\pi}{4}\right)} - \frac{m}{x} (j)^m \sqrt{\frac{2}{\pi x}} e^{-j\left(x - \frac{\pi}{4}\right)} \quad (7.179)$$

Or

$$\frac{dH_m^{(2)}(ax)}{dx} = aj^{-1}H_m^{(2)}(ax) - \frac{m}{x}H_m^{(2)}(ax) \quad (7.180)$$

In the limit, where $x \rightarrow \infty$ this can be approximated by the useful formula

$$\frac{dH_m^{(2)}(ax)}{dx} = H_m^{(2)'}(ax) = -jaH_m^{(2)}(ax) \quad (7.181)$$

These two substitutions can be used to obtain expressions for the electric field in the far-field where the argument of both the Hankel function and its derivative are large. When the product $k_\rho \rho \rightarrow \infty$, the \underline{M} and \underline{N} elementary vector wave functions can be expressed as

$$\underline{M}_{mk_z}^{(2)} = j \left[\frac{m}{\rho} \hat{\underline{e}}_\rho + k_\rho \hat{\underline{e}}_\phi \right] H_m^{(2)}(k_\rho \rho) e^{jm\phi} e^{-jk_z z} \quad (7.182)$$

And with the same restriction

$$\underline{N}_{mk_z}^{(2)} = \frac{1}{k} \left(-k_z k_\rho \hat{\underline{e}}_\rho + \frac{mk_z}{\rho} \hat{\underline{e}}_\phi + k_\rho^2 \hat{\underline{e}}_z \right) H_m^{(2)}(k_\rho \rho) e^{jm\phi} e^{-jk_z z} \quad (7.183)$$

For notational convenience, let us define the following two vector functions:

$$\underline{M}_{mk_z} = j \left[\frac{m}{\rho} \hat{\underline{e}}_\rho + k_\rho \hat{\underline{e}}_\phi \right] \quad (7.184)$$

$$\underline{N}_{mk_z} = \frac{1}{k} \left(-k_z k_\rho \hat{\underline{e}}_\rho + \frac{mk_z}{\rho} \hat{\underline{e}}_\phi + k_\rho^2 \hat{\underline{e}}_z \right) \quad (7.185)$$

Thus, using these definitions, the far electric field radiating into free space can be expressed as

$$\begin{aligned} \underline{E}(\rho, \phi, z) = \sum_{m=-\infty}^{\infty} \int_{-\infty}^{\infty} & \left[B_m^1(k_z) \underline{M}_{mk_z} \right. \\ & \left. + B_m^2(k_z) \underline{N}_{mk_z} \right] (j)^m \sqrt{\frac{2}{\pi k_\rho \rho}} e^{-j(k_\rho \rho - \frac{\pi}{4})} e^{jm\phi} e^{-jk_z z} dk_z \end{aligned} \quad (7.186)$$

Hence, by exchanging the order of integration and summation, the far electric field can be written in terms of these functions and the mode coefficients as

$$\begin{aligned} \underline{E}(\rho, \phi, z) = \int_{-\infty}^{\infty} & \sqrt{\frac{2}{\pi k_\rho \rho}} e^{j\frac{\pi}{4}} \sum_{m=-\infty}^{\infty} (j)^m \\ & \times \left[B_m^1(k_z) \underline{M}_{mk_z} + B_m^2(k_z) \underline{N}_{mk_z} \right] e^{jm\phi} e^{-jk_\rho \rho} e^{-jk_z z} dk_z \end{aligned} \quad (7.187)$$

These equations can perhaps be interpreted more easily if we define a new vector quantity

$$\underline{\varepsilon}_{k_z}(\rho, \phi) = \sqrt{\frac{2}{\pi k_\rho \rho}} e^{j\frac{\pi}{4}} \sum_{m=-\infty}^{\infty} (j)^m \left[B_m^1(k_z) \underline{M}_{mk_z} + B_m^2(k_z) \underline{N}_{mk_z} \right] e^{jm\phi} \quad (7.188)$$

Hence, the far electric fields can be expressed equivalently, and more compactly, as

$$\underline{E}(\rho, \phi, z) = \int_{-\infty}^{\infty} k_\rho \underline{\varepsilon}_{k_z}(\rho, \phi) \frac{e^{-jk_\rho \rho}}{k_\rho} e^{-jk_z z} dk_z \quad (7.189)$$

In this form, it is clear that this is a Fourier relationship where k_z is the Fourier variable with z and k_z being conjugate variables. That is

$$\underline{E}(\rho, \phi, z) = \mathfrak{F}^{-1} \left\{ k_\rho \underline{\varepsilon}_{k_z}(\rho, \phi) \frac{e^{-jk_\rho \rho}}{k_\rho} \right\} \quad (7.190)$$

Here, \mathfrak{F}^{-1} is used to denote the inverse Fourier transform. Similarly, \mathfrak{F} will be used to denote the Fourier transform operation. As this is a Fourier relationship, we may instantly bring to bear the enormous power of analysis borne from Fourier theory. One such tool is the convolution (or sometimes Faltung, which is German for folding) theorem. This theorem, as examined in Section 6.5 and elaborated on in [5] and [6], states that the Fourier transform of a convolution is given by the product of the individual Fourier transforms. Conversely, the Fourier transform of a product is given by the convolution of the individual transforms. This is the case here since Fourier transforming both sides of this expression yields the following expression where it is evident that right-hand side comprises a multiplication of two functions namely

$$\mathfrak{F} \left\{ \underline{E}_{r \rightarrow \infty}(\rho, \phi, z) \right\} = k_\rho \underline{\varepsilon}_{k_z}(\rho, \phi) \frac{e^{-jk_\rho \rho}}{k_\rho} \tag{7.191}$$

Thus, taking the inverse transform (so as to recover the original equation) and using the convolution theorem yields

$$\underline{E}_{r \rightarrow \infty}(\rho, \phi, z) = \mathfrak{F}^{-1} \left\{ k_\rho \underline{\varepsilon}_{k_z}(\rho, \phi) \right\} \otimes \mathfrak{F}^{-1} \left\{ \frac{e^{-jk_\rho \rho}}{k_\rho} \right\} \tag{7.192}$$

where the symbol \otimes is used to denote the convolution operation. Specifically, the convolution of two functions is defined by the integral

$$f(z) \otimes h(z) = \frac{1}{2\pi} \int_{-\infty}^{\infty} f(\xi) h(z - \xi) d\xi \tag{7.193}$$

where ξ is a dummy variable. Since the integration is in ξ , as far as the integration process itself is concerned, the z variable is, momentarily, regarded as being a constant. Hence

$$\underline{E}_{r \rightarrow \infty}(\rho, \phi, z) = \frac{1}{2\pi} \int_{-\infty}^{\infty} \mathfrak{F}_\xi^{-1} \left\{ k_\rho \underline{\varepsilon}_{k_z}(\rho, \phi) \right\} \mathfrak{F}_{z-\xi}^{-1} \left\{ \frac{e^{-jk_\rho \rho}}{k_\rho} \right\} d\xi \tag{7.194}$$

Now, the second inverse Fourier transform, that is to say the transform of a complex exponential, can be shown to be the integral representation of the zeroth-order Hankel function of the second kind. Specifically this transform can be expressed as

$$\mathfrak{F}_{z-\xi}^{-1} \left\{ \frac{e^{-jk_\rho \rho}}{k_\rho} \right\} = \int_{-\infty}^{\infty} \frac{e^{-jk_\rho \rho}}{k_\rho} e^{jk_z(z-\xi)} dk_z \tag{7.195}$$

From the large argument Hankel function of the second kind, which was derived above, the zeroth-order function, i.e. when $m = 0$, can be expressed as

$$H_0^{(2)}(x) \approx \sqrt{\frac{2}{\pi x}} e^{j\frac{\pi}{4}} e^{-jx} \tag{7.196}$$

Hence

$$\pi H_0^{(2)}(x) \approx \sqrt{\frac{2\pi}{x}} e^{j\frac{\pi}{4}} e^{-jx} \quad (7.197)$$

When

$$x = k\sqrt{(z - \xi)^2 + \rho^2} = k\sqrt{z^2 - 2z\xi + \xi^2 + \rho^2} \quad (7.198)$$

Now from the cylindrical geometry, z and ρ can be related to the polar spherical angle θ using

$$z = r \cos \theta \quad (7.199)$$

$$\rho = r \sin \theta \quad (7.200)$$

Hence using a standard trigonometric identity, we can write that

$$x = k\sqrt{\xi^2 - 2r\xi \cos \theta + r^2} = kr \left(\left(\frac{\xi}{r} \right)^2 - \frac{2\xi \cos \theta}{r} + 1 \right)^{1/2} \quad (7.201)$$

The first few terms of the Taylor series expansion can be written as

$$(1 + \alpha)^m = 1 + m\alpha + \frac{m(m-1)}{2!} \alpha^2 + \dots \quad (7.202)$$

Thus, using this expansion and retaining *just* the first term, we obtain

$$x = kr \left[1 + \frac{1}{2} \left(\left(\frac{\xi}{r} \right)^2 - \frac{2\xi \cos \theta}{r} \right) \right] = kr + \frac{k\xi^2}{2r} - k\xi \cos \theta \quad (7.203)$$

Thus, ignoring the inverse r terms as these will tend to zero as r tends to infinity in the complex exponential and retaining just the first term in the square root factor yields

$$\pi H_0^{(2)}(x) \underset{r \rightarrow \infty}{\approx} \sqrt{\frac{2\pi}{kr}} e^{j\frac{\pi}{4}} e^{-jkr} e^{jk\xi \cos \theta} \quad (7.204)$$

Hence, the far electric field can be expressed as

$$\underline{E} \underset{r \rightarrow \infty}{(\rho, \phi, z)} = \sqrt{\frac{1}{2\pi kr}} e^{j\frac{\pi}{4}} e^{-jkr} \int_{-\infty}^{\infty} \mathfrak{F}_{\xi}^{-1} \left\{ k_{\rho} \underline{E}_{k_z}(\rho, \phi) \right\} e^{jk\xi \cos \theta} d\xi \quad (7.205)$$

Now, the last integral represents the Fourier transform of an inverse Fourier transform. Hence the resultant is the original function scaled by a factor of 2π to preserve the normalisation and is evaluated at $k_z = k \cos \theta$ as in this case ξ and

$k \cos \theta$ are the conjugate variables with $k \cos \theta$ varying linearly, as opposed to varying linearly with the polar angle.

$$\underline{E}_{r \rightarrow \infty}(\rho, \phi, z) = \sqrt{\frac{2\pi}{kr}} e^{j\frac{\pi}{4}} e^{-jkr} k_{\rho} \underline{\varepsilon}_{k_z}(\rho, \phi) \quad (7.206)$$

Recalling our original definition for k_{ρ} and using a simple trigonometric identity means that we can relate this to the polar angle as

$$k_{\rho} = \sqrt{k^2 - k_z^2} = k \sqrt{1 - (\cos \theta)^2} = k \sin \theta \quad (7.207)$$

Hence

$$\underline{E}_{r \rightarrow \infty}(\rho, \phi, z) = \sqrt{\frac{2\pi}{kr}} e^{j\frac{\pi}{4}} e^{-jkr} k \sin \theta \underline{\varepsilon}_{k_z}(\rho, \phi) \quad (7.208)$$

Rewriting this in terms of the CMCs yields

$$\underline{E}_{r \rightarrow \infty}(\rho, \phi, z) = j2k \sin \theta \sqrt{\frac{1}{kr k_{\rho} \rho}} e^{-jkr} \sum_{m=-\infty}^{\infty} (j)^m \left[B_m^1(k_z) \underline{M}_{mk_z} + B_m^2(k_z) \underline{N}_{mk_z} \right] e^{jm\phi} \quad (7.209)$$

In component form this becomes

$$E_{\phi}(\rho, \phi, z) = j2k \sin \theta \sqrt{\frac{1}{kr k_{\rho} \rho}} e^{-jkr} \sum_{m=-\infty}^{\infty} (j)^m \left[B_m^1(k_z) j k_{\rho} + B_m^2(k_z) \frac{m k_z}{k_{\rho}} \right] e^{jm\phi} \quad (7.210)$$

or

$$E_{\phi}(\rho, \phi, z) = \frac{j2}{r} e^{-jkr} \sum_{m=-\infty}^{\infty} (j)^m \left[B_m^1(k_z) j k \sin \theta + B_m^2(k_z) \frac{m \cos \theta}{r \sin \theta} \right] e^{jm\phi} \quad (7.211)$$

As the B^2 CMCs are scaled by a factor of r^{-1} , in the far-field that are invariably smaller than the B^1 coefficients, thus in the far-field we can express the ϕ -polarised far electric fields purely in terms of the B^1 coefficients and thus we may write that

$$E_{\phi}(r, \phi, \theta) = -2k \sin \theta \frac{e^{-jkr}}{r} \sum_{m=-\infty}^{\infty} (j)^m B_m^1(k \cos \theta) e^{jm\phi} \quad (7.212)$$

Here, and as per the usual convention, the unimportant far-field spherical phase factor and inverse r term are usually suppressed in each of the far-field components. Thus, we obtain the usually quoted formula

$$E_{\phi}(r, \phi, \theta) = -2k \sin \theta \sum_{m=-\infty}^{\infty} (j)^m B_m^1(k \cos \theta) e^{jm\phi} \quad (7.213)$$

This process can now be repeated for the θ -polarised field component; however, here we have a further complication as the \underline{M} and \underline{N} quantities are expressed in terms of the cylindrical unit vectors. Thus, we need to transform these into an equivalent spherical form. The relationship between cylindrical and spherical unit vectors can be expressed as [11]

$$\widehat{\underline{e}}_{\theta} = \widehat{\underline{e}}_{\rho} \cos \theta - \widehat{\underline{e}}_z \sin \theta \quad (7.214)$$

$$\widehat{\underline{e}}_{\phi} = \widehat{\underline{e}}_{\phi} \quad (7.215)$$

When transformed into polar-spherical components, the θ -polarised component of \underline{M} and \underline{N} can be expressed as

$$\underline{M}_{mk_z} = j \frac{m \cos \theta}{\rho} \widehat{\underline{e}}_{\theta} \quad (7.216)$$

$$\begin{aligned} \underline{N}_{mk_z} &= -\frac{1}{k} \left(k_z k_{\rho} \cos \theta + k_{\rho}^2 \sin \theta \right) \widehat{\underline{e}}_{\theta} \\ &= -k \left(\cos^2 \theta \sin \theta + \sin^2 \theta \sin \theta \right) \widehat{\underline{e}}_{\theta} \\ &= -k \sin \theta \widehat{\underline{e}}_{\theta} \end{aligned} \quad (7.217)$$

The θ -polarised far electric field component can be expressed as

$$E_{\theta}(\rho, \phi, z) = \frac{j2}{r} e^{-jkr} \sum_{m=-\infty}^{\infty} (j)^m \left[B_m^1(k_z) \frac{jm \cos \theta}{r \sin \theta} - B_m^2(k_z) k \sin \theta \right] e^{jm\phi} \quad (7.218)$$

Here, as a result of the r^{-1} factor in the equation the far-field B^1 , CMCs are smaller than the B^2 coefficients. We can therefore express the ϕ -polarised far electric fields purely in terms of the B^2 coefficients, and thus we may write that

$$E_{\theta}(r, \phi, \theta) = -2k \sin \theta \frac{e^{-jkr}}{r} \sum_{m=-\infty}^{\infty} (j)^m j B_m^2(k \cos \theta) e^{jm\phi} \quad (7.219)$$

Thus, the asymptotic far-field pattern can be obtained from a simple summation of mode coefficients as follows:

$$E_{\theta}(r, \phi, \theta) = -j2k \sin \theta \sum_{m=-\infty}^{\infty} j^m B_m^2(k \cos \theta) e^{jm\phi} \quad (7.220)$$

$$E_{\phi}(r, \phi, \theta) = -2k \sin \theta \sum_{m=-\infty}^{\infty} j^m B_m^1(k \cos \theta) e^{jm\phi} \quad (7.221)$$

In the far-field, as a consequence of the plane-wave condition, i.e. these are transverse electromagnetic waves, thus $\underline{k} \cdot \underline{E} = \underline{k} \cdot \underline{H} = 0$ and we can therefore write that

$$E_r(r, \phi, \theta) = 0 \quad (7.222)$$

With

$$\underline{H}_{r \rightarrow \infty}(r, \phi, \theta) = \frac{1}{Z_0} \hat{e}_r \times \underline{E}(r \rightarrow \infty, \theta, \phi) \quad (7.223)$$

where Z_0 denotes the impedance of free space. Thus

$$H_\theta(r, \phi, \theta) = \frac{2k \sin \theta}{Z_0} \sum_{m=-\infty}^{\infty} j^m B_m^1(k \cos \theta) e^{jm\phi} \quad (7.224)$$

$$H_\phi(r, \phi, \theta) = -j \frac{2k \sin \theta}{Z_0} \sum_{m=-\infty}^{\infty} j^m B_m^2(k \cos \theta) e^{jm\phi} \quad (7.225)$$

$$H_r(r, \phi, \theta) = 0 \quad (7.226)$$

Here, and as per the usual convention, the unimportant far-field spherical phase factor and inverse r term have been suppressed and it is understood that $k_z = k \cos \theta$. From these expressions we can see that the s -index in $B_m^s(k \cos \theta)$ specifies the polarisation of the wave since $s = 1$ modes produce ϕ -component (horizontal) far-fields and $s = 2$ modes produce θ -component (vertical) far-fields (with horizontal and vertical designations assuming that the z -axis is vertical as shown in Figure 7.5). The useful aspect of these expressions is that they represent a summation of the CMCs, with no numerical integration or evaluation of Hankel functions necessitated. Here, as was demonstrated earlier, the CMCs themselves are computed by evaluating

$$B_m^1(k_z) = \frac{-1}{4\pi^2 k_\rho^3 H_m^{(2)'}(k_\rho \rho_0)} \times \int_{-\infty}^{\infty} \int_0^{2\pi} \left(\frac{mk_z}{\rho_0} E_z(\rho_0, \phi, z) + k_\rho^2 E_\phi(\rho_0, \phi, z) \right) e^{-jm\phi} e^{jk_z z} d\phi dz \quad (7.227)$$

$$B_m^2(k_z) = \frac{k}{4\pi^2 k_\rho^2 H_m^{(2)}(k_\rho \rho_0)} \int_{-\infty}^{\infty} \int_0^{2\pi} E_z(\rho_0, \phi, z) e^{-jm\phi} e^{jk_z z} d\phi dz \quad (7.228)$$

Thus, for the ideal case where the tangential orthogonal cylindrical near electric field components are sampled with an infinitesimal electric dipole probe, the complete electromagnetic six-vector can be obtained outside of the conceptual measuring cylinder. As the complete electromagnetic six-vector is obtained, it is possible to compute any asymptotic far-field parameter, e.g. total radiated power, gain, directivity, tilt angle, axial ratio, complex polarisation ratio and so on. This, therefore, provides the basis for modern cylindrical near-field antenna testing. The next section will extend this formulation so that non-ideal probes, that is to say real-world probes such as open-ended rectangular waveguides, can be used to acquire near-field data. These are probes for which the output of the probe is not

proportional to a single vector component of the incident field at a point in space but instead are determined from a weighted average of all vector components across some finite non-zero area.

7.7 Development of the transmission formula

Probe-compensated near-field measurements on a cylinder with arbitrary probe pattern compensation were first presented in the open literature in [12] and the development presented in the subsequent sections follows a procedure similar to that outlined therein. The derivation of the transmission equation is accomplished as follows:

1. Express the antenna fields in cylindrical coordinates using elemental vector mode functions.
2. Write the scattering matrix for the antenna and probe in their respective coordinate systems.
3. Derive the joining equations, using field expressions in each coordinate system.
4. Use joining equations and scattering matrix for each antenna to derive the transmission equation.
5. Solve the transmission equation for the unknown test antenna CMCs.
6. Sum the test antenna CMCs to obtain the asymptotic far-fields.

A detailed derivation of this development is presented in the following section together with an illustration of the effect of probe compensation in cylindrical near-field measurements. This section concludes with a necessary derivation of a vector translation theorem.

7.7.1 The coupling equation – derivation of probe-compensated cylindrical near-field antenna measurements

Using the mathematical apparatus that we have established earlier, and from linear superposition, it is possible to write the fields between the AUT and the probe in the form

$$\underline{E}(\rho, \phi, z) = \sum_{m=-\infty}^{\infty} \int_{-\infty}^{\infty} \left\{ \left[b_m^1(k_z) \underline{M}_{m,k_z}^{(2)}(\rho, \phi, z) + b_m^2(k_z) \underline{N}_{m,k_z}^{(2)}(\rho, \phi, z) \right] + \left[a_m^1(k_z) \underline{M}_{m,k_z}(\rho, \phi, z) + a_m^2(k_z) \underline{N}_{m,k_z}(\rho, \phi, z) \right] \right\} dk_z \quad (7.229)$$

$$\underline{H}(\rho, \phi, z) = \frac{-1}{j\omega\mu} \nabla \times \underline{E}(\rho, \phi, z) \quad (7.230)$$

Here, modes with coefficients denoted with b_m^1 and b_m^2 are associated with the fields from the AUT, whereas the modes with coefficients denoted by a_m^1 and a_m^2 are

associated with the fields from the probe antenna. As will be shown, the relationship between the wave amplitude in the waveguide feed of the AUT and the wave amplitude in the waveguide feed of the probe can be obtained from the source scattering matrix formulation. The defining equation for S parameters can be expressed in matrix notation as

$$[b] = [S] \cdot [a] \tag{7.231}$$

In this application, the transducer scattering matrix encapsulates the linear behaviour of the antenna to all possible excitations from impressed incident waves. That is to say, the set of outgoing wave amplitudes $[b]$ will be determined linearly by a set of incident voltage wave-amplitudes $[a]$ and can be taken as a definition of linearity for the AUT. The scattering matrix representation of test antenna probe interaction can be found presented in Figure 7.12. Here, un-primed variables refer to the test antenna’s scattering matrix, whereas primed variables relate to the probe’s scattering matrix.

Using the configuration depicted in Figure 7.12, the source scattering matrix equation can be expressed (in expanded form) for the test antenna as [13]

$$b_0 = \Gamma_0 a_0 + \sum_{m=-\infty}^{\infty} \int_{-\infty}^{\infty} [R_m^1(k_z) a_m^1(k_z) + R_m^2(k_z) a_m^2(k_z)] dk_z \tag{7.232}$$

$$b_m^1(k_z) = T_m^1(k_z) a_0 + \sum_{v=-\infty}^{\infty} \int_{-\infty}^{\infty} [S_{m,v}^{1,1}(k_z, k'_z) a_v^1(k'_z) + S_{m,v}^{1,2}(k_z, k'_z) a_v^2(k'_z)] dk'_z \tag{7.233}$$

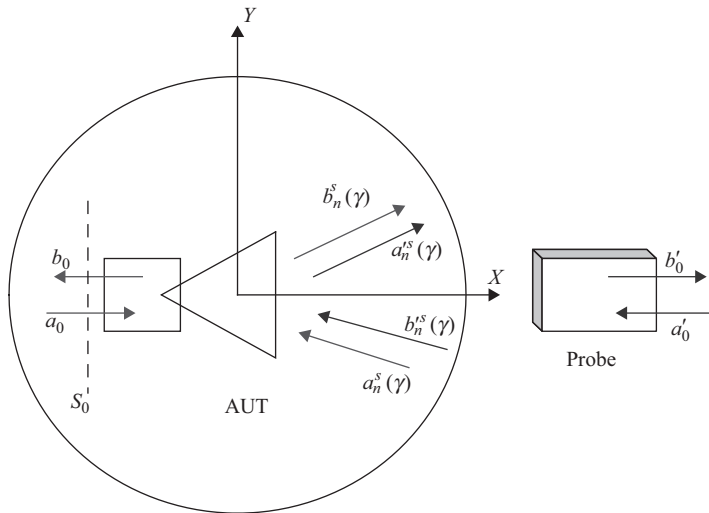


Figure 7.12 Schematic representation of cylindrical scattering matrix formulation

$$b_m^2(k_z) = T_m^2(k_z)a_0 + \sum_{v=-\infty}^{\infty} \int_{-\infty}^{\infty} \left[S_{m,v}^{2,1}(k_z, k'_z) a_v^1(k'_z) + S_{m,v}^{2,2}(k_z, k'_z) a_v^2(k'_z) \right] dk'_z \quad (7.234)$$

Here, Γ_0 is the voltage reflection coefficient of the AUT defined at the surface S_0 . Here, R denotes the receiving properties of the AUT, T denotes the transmitting properties of the AUT and S denotes the scattering properties of the AUT. When multiple reflections between the test antenna and the probe are neglected, that is to say when $a_v^1(k'_z) = a_v^2(k'_z) = 0$, the field leaving the antenna can be expressed as

$$b_m^1(k_z) = T_m^1(k_z)a_0 \quad (7.235)$$

$$b_m^2(k_z) = T_m^2(k_z)a_0 \quad (7.236)$$

This assumption is valid provided the scattered field is small when compared to the incident fields. Although this is often the case in practice, this is an approximation whose impact must be assessed. Therefore, evaluation of this comprises one term within the facility-level range assessment, cf. Chapter 10. This assumption is common to all forms of near-field measurements irrespective of the particular coordinate system being considered. The importance of these expressions is that they imply that if T_m^1 and T_m^2 can be determined, then probe-corrected far-fields for the test antenna can be obtained from the b_m^1 and b_m^2 CMCs using the summation process developed in the preceding section. The next step in determining the T_m^1 and T_m^2 mode coefficients from measured data involves relating the probe and AUT coordinate systems and scattering matrices.

7.7.2 Probe and test antenna

Let us define a cylindrical coordinate system that is fixed to the probe and that is coaxial with the AUT's coordinate system. Here, coordinates that are associated with the probe are denoted with primes. The geometry of this arrangement can be found presented schematically in Figure 7.13.

Now, in the same way as we did for the AUT, we are able to write the source scattering matrix for the probe as

$$b'_o(\phi_0, z_0) = \Gamma'_0 a'_0 + \sum_{m=-\infty}^{\infty} \int_{-\infty}^{\infty} \left[R'_m{}^1(k_z) a'_m{}^1(k_z) + R'_m{}^2(k_z) a'_m{}^2(k_z) \right] dk_z \quad (7.237)$$

As was shown in Figure 7.12, b'_o is the output of the probe which is recorded as the probe scans across the conceptual cylindrical sampling surface. As can be deduced from the mechanical acquisition process, cf. Figure 7.1, the probe coordinate system is merely the AUT's coordinate system rotated about the z -axis by an amount ϕ_0 , and translated along the z -axis by a distance z_0 . Thus, ϕ_0 and z_0 vary during the course of the cylindrical near-field measurement while the radius remains fixed so

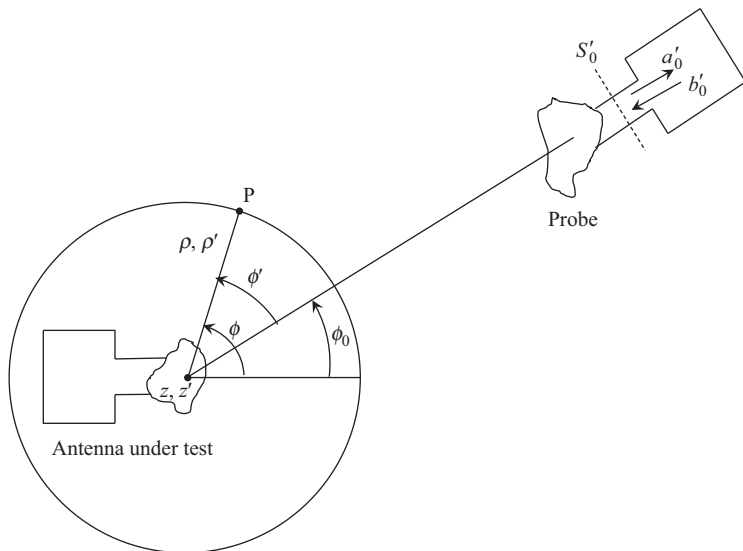


Figure 7.13 Schematic representation of the transmission system for cylindrical probe compensation derivation

that

$$\rho' = \rho \tag{7.238}$$

$$\phi' = \phi - \phi_0 \tag{7.239}$$

$$z' = z - z_0 \tag{7.240}$$

Here, ϕ_0 and z_0 vary such that

$$0 \leq \phi_0 \leq 2\pi \tag{7.241}$$

$$-\infty \leq z_0 \leq \infty \tag{7.242}$$

Clearly, the fields at a point in space are the same irrespective of the coordinate system used to specify them. Thus

$$\underline{E}'(\rho', \phi', z') = \underline{E}(\rho, \phi, z) \tag{7.243}$$

Hence

$$\underline{E}'(\rho, \phi - \phi_0, z - z_0) = \underline{E}(\rho, \phi, z) \tag{7.244}$$

Although not stated here, similar expressions can be written down for the equivalent magnetic fields. Writing the fields explicitly in terms of the respective cylindrical wave coefficients yields

$$\begin{aligned} \underline{E}(\rho, \phi, z) = \sum_{m=-\infty}^{\infty} \int_{-\infty}^{\infty} \left\{ \left[b_m^1(k_z) \underline{M}_{m, k_z}^{(2)}(\rho, \phi, z) + b_m^2(k_z) \underline{N}_{m, k_z}^{(2)}(\rho, \phi, z) \right] \right. \\ \left. + \left[a_m^1(k_z) \underline{M}_{m, k_z}(\rho, \phi, z) + a_m^2(k_z) \underline{N}_{m, k_z}(\rho, \phi, z) \right] \right\} dk_z \end{aligned} \quad (7.245)$$

$$\begin{aligned} \underline{E}'(\rho', \phi', z') = \sum_{m=-\infty}^{\infty} \int_{-\infty}^{\infty} \left\{ \left[a_m^1(k_z) \underline{M}_{m, k_z}^{(2)}(\rho', \phi', z') + a_m^2(k_z) \underline{N}_{m, k_z}^{(2)}(\rho', \phi', z') \right] \right. \\ \left. + \left[b_m^1(k_z) \underline{M}_{m, k_z}(\rho', \phi', z') + b_m^2(k_z) \underline{N}_{m, k_z}(\rho', \phi', z') \right] \right\} dk_z \end{aligned} \quad (7.246)$$

where

$$\underline{M}_{mk_z}^{(2)} = \left[\frac{jm}{\rho} H_m^{(2)}(k_\rho \rho) \hat{\underline{e}}_\rho - k_\rho H_m^{(2)'}(k_\rho \rho) \hat{\underline{e}}_\phi \right] e^{jm\phi} e^{-jk_z z} \quad (7.247)$$

and

$$\underline{N}_{mk_z}^{(2)} = \frac{1}{k} \left(-jk_z k_\rho H_m^{(2)'}(k_\rho \rho) \hat{\underline{e}}_\rho + \frac{mk_z}{\rho} H_m^{(2)}(k_\rho \rho) \hat{\underline{e}}_\phi + k_\rho^2 H_m^{(2)}(k_\rho \rho) \hat{\underline{e}}_z \right) e^{jm\phi} e^{-jk_z z} \quad (7.248)$$

Equating coefficients using the orthogonality properties of the elementary cylindrical wave functions yields

$$b_m^s(k_z) \underline{M}_{m, k_z}^{(2)}(\rho, \phi, z) = a_m^s(k_z) \underline{M}_{m, k_z}^{(2)}(\rho', \phi', z') \quad (7.249)$$

and

$$a_m^s(k_z) \underline{M}_{m, k_z}^{(2)}(\rho, \phi, z) = b_m^s(k_z) \underline{M}_{m, k_z}^{(2)}(\rho', \phi', z') \quad (7.250)$$

where s is used as a polarisation index which is equal to 1, or 2, only. Thus

$$\begin{aligned} b_m^s(k_z) e^{jm\phi} e^{-jk_z z} &= a_m^s(k_z) e^{jm\phi'} e^{-jk_z z'} \\ &= a_m^s(k_z) e^{jm(\phi - \phi_0)} e^{-jk_z(z - z_0)} \end{aligned} \quad (7.251)$$

Cancelling like terms yields

$$b_m^s(k_z) = a_m^s(k_z) e^{-jm\phi_0} e^{jk_z z_0} \quad (7.252)$$

or equivalently

$$a_m^s(k_z) = b_m^s(k_z) e^{jm\phi_0} e^{-jk_z z_0} \quad (7.253)$$

Similarly

$$b_m^s(k_z) = a_m^s(k_z) e^{jm\phi_0} e^{-jk_z z_0} \quad (7.254)$$

This behaviour can also be interpreted as arising from the shifting property of the Fourier relationship that exists between the sampled fields and the corresponding CMCs. Crucially, these equations express the relationship between the probe and antenna coefficients. Thus, these relations can be used to link the two scattering matrix equations to give the required transmission formula. Now, in the same way as we did for the AUT, we are now able to write the source scattering matrix for the probe as

$$b'_0(\phi_0, z_0) = \Gamma'_0 a'_0 + \sum_{m=-\infty}^{\infty} \int_{-\infty}^{\infty} \left[R'_m{}^1(k_z) a'^1_m(k_z) + R'^2_m(k_z) a'^2_m(k_z) \right] dk_z \quad (7.255)$$

Here, b'_0 is the output of the probe which is recorded as the probe scans across the conceptual cylindrical sampling surface. Using the relationship connecting the probe and AUT scattering equations we obtain

$$b'_0(\phi_0, z_0) = \Gamma'_0 a'_0 + \sum_{m=-\infty}^{\infty} \int_{-\infty}^{\infty} \left[R'_m{}^1(k_z) b^1_m(k_z) + R'^2_m(k_z) b^2_m(k_z) \right] e^{jm\phi_0} e^{-jk_z z_0} dk_z \quad (7.256)$$

As before, when multiple reflections between the test antenna and the probe are neglected this can be expressed in terms of the transmitting properties of the AUT yielding

$$b'_0(\phi_0, z_0) = \Gamma'_0 a'_0 + a_0 \sum_{m=-\infty}^{\infty} \int_{-\infty}^{\infty} \left[R'_m{}^1(k_z) T^1_m(k_z) + R'^2_m(k_z) T^2_m(k_z) \right] \times e^{jm\phi_0} e^{-jk_z z_0} dk_z \quad (7.257)$$

Let us now assume that the input to the probe is zero, that is to say when $a'_0 = 0$, which would be the case when the AUT is transmitting and the probe is terminated with a perfectly matched load. In this case the transmission formula reduces to

$$b'_0(\phi_0, z_0) = a_0 \sum_{m=-\infty}^{\infty} \int_{-\infty}^{\infty} \left[R'_m{}^1(k_z) T^1_m(k_z) + R'^2_m(k_z) T^2_m(k_z) \right] e^{jm\phi_0} e^{-jk_z z_0} dk_z \quad (7.258)$$

This is the transmission formula for the case of *negligible* multiple reflections between the AUT and the probe. This integral has to be inverted in order to be able to express the unknown T^1_m and T^2_m AUT transmit CMCs in terms of the measured amplitude and phase b'_0 . Fortunately, as this is a Fourier integral and a Fourier series, this can be immediately inverted to yield

$$R'_m{}^1(k_z) T^1_m(k_z) + R'^2_m(k_z) T^2_m(k_z) = \frac{1}{4\pi^2 a_0} \int_{-\infty}^{\infty} \int_0^{2\pi} b'_0(\phi_0, z_0) e^{-jm\phi_0} e^{jk_z z_0} d\phi_0 dz_0 \quad (7.259)$$

Thus, by evaluating this integral it is possible to compute this for as many values of m and k_z as are required. The number and range of values of m and k_z are discussed below when examining the sampling theorem for cylindrical near-field antenna measurements. Clearly, this integral can be evaluated using the efficient FFT algorithm and that too is discussed in the following sections. However, there is one remaining difficulty as there are two unknown values of the AUT transmitting coefficients (T_m^1, T_m^2) produced by a single integration. This can be resolved if a second measurement is taken as this would enable the construction of two simultaneous equations which could then be solved for the unknown AUT transmit coefficients. Thus, for the second cylindrical near-field measurement, we may write the corresponding expression

$$R''_m(k_z)T_m^1(k_z) + R''^2_m(k_z)T_m^2(k_z) = \frac{1}{4\pi^2 a_0} \int_{-\infty}^{\infty} \int_0^{2\pi} b''_0(\phi_0, z_0) e^{-jm\phi_0} e^{jk_z z_0} d\phi_0 dz_0 \quad (7.260)$$

Here, the values of b''_0 can most easily be obtained by using the same probe and merely rotating it about its boresight direction by 90° . Alternatively, a second probe with a different pattern could be used; however, it is more convenient in most applications to use a mechanical rotation stage to simply reposition a single probe between successive cylindrical near-field scans. Typically then, the b'_0 measured amplitude and phases would correspond to measurements taken with the principal polarisation of the probe being aligned with the unit \underline{e}_ϕ vector, and the b''_0 corresponding to the case where the principal polarisation of the probe being aligned with the unit \underline{e}_z vector. Thus, provided the receiving characteristic of the two probes are known, the simultaneous equations can be solved for the AUT transmitting functions as follows. In matrix form, as we did with the planar case, these simultaneous equations can be expressed as

$$\begin{bmatrix} I'_m(k_z) \\ I''_m(k_z) \end{bmatrix} = \begin{bmatrix} R'^1_m(k_z) & R'^2_m(k_z) \\ R''^1_m(k_z) & R''^2_m(k_z) \end{bmatrix} \cdot \begin{bmatrix} T_m^1(k_z) \\ T_m^2(k_z) \end{bmatrix} \quad (7.261)$$

where

$$I'_m(k_z) = \frac{1}{4\pi^2 a_0} \int_{-\infty}^{\infty} \int_0^{2\pi} b'_0(\phi_0, z_0) e^{-jm\phi_0} e^{jk_z z_0} d\phi_0 dz_0 \quad (7.262)$$

$$I''_m(k_z) = \frac{1}{4\pi^2 a_0} \int_{-\infty}^{\infty} \int_0^{2\pi} b''_0(\phi_0, z_0) e^{-jm\phi_0} e^{jk_z z_0} d\phi_0 dz_0 \quad (7.263)$$

Thus, provided this does not result in a singular matrix, these simultaneous equations can be inverted by evaluating the inverse of the square matrix as

$$\begin{bmatrix} T_m^1(k_z) \\ T_m^2(k_z) \end{bmatrix} = \begin{bmatrix} R'^1_m(k_z) & R'^2_m(k_z) \\ R''^1_m(k_z) & R''^2_m(k_z) \end{bmatrix}^{-1} \cdot \begin{bmatrix} I'_m(k_z) \\ I''_m(k_z) \end{bmatrix} \quad (7.264)$$

where, from linear algebra we know that the inverse of a (not necessarily orthogonal and normalised) matrix can be obtained from

$$\begin{bmatrix} R'_m(k_z) & R''_m(k_z) \\ R''_m(k_z) & R''_m(k_z) \end{bmatrix}^{-1} = \frac{1}{(R'_m(k_z)R''_m(k_z) - R''_m(k_z)R''_m(k_z))} \cdot \begin{bmatrix} R''_m(k_z) & -R''_m(k_z) \\ -R''_m(k_z) & R'_m(k_z) \end{bmatrix} \quad (7.265)$$

This is valid provided the denominator of the multiplying factor is non-zero. This denominator is actually the determinant of the original square matrix and would be zero in the event the original matrix is singular. Avoidance of this difficulty is generally assured provided each probe responds predominantly to one polarisation, i.e. e_ϕ or e_z respectively. Thus, each scan must be taken using a different probe or, with the same probe only using a different orientation, e.g. with the probe having been rotated by 90° about its z -axis. Assuming the matrix determinant is non-zero, the AUT transmit coefficients can be obtained from

$$\begin{bmatrix} T'_m(k_z) \\ T''_m(k_z) \end{bmatrix} = \frac{1}{(R'_m(k_z)R''_m(k_z) - R''_m(k_z)R''_m(k_z))} \cdot \begin{bmatrix} R''_m(k_z) & -R''_m(k_z) \\ -R''_m(k_z) & R'_m(k_z) \end{bmatrix} \cdot \begin{bmatrix} I'_m(k_z) \\ I''_m(k_z) \end{bmatrix} \quad (7.266)$$

Finally, writing this explicitly for the two sets of linearly independent AUT transmit coefficients we obtain

$$T'_m(k_z) = \frac{R''_m(k_z)I'_m(k_z) - R''_m(k_z)I''_m(k_z)}{(R'_m(k_z)R''_m(k_z) - R''_m(k_z)R''_m(k_z))} \quad (7.267)$$

and

$$T''_m(k_z) = \frac{R'_m(k_z)I''_m(k_z) - R''_m(k_z)I'_m(k_z)}{(R'_m(k_z)R''_m(k_z) - R''_m(k_z)R''_m(k_z))} \quad (7.268)$$

Thus, provided the receiving coefficients of the probes are known, the AUT transmit coefficients can be determined from the measured amplitude and phases at the probe, i.e. $b'_0(\phi_0, z_0)$ and $b''_0(\phi_0, z_0)$. The last task to address before the probe-compensated cylindrical near-field theory is complete is to obtain the probe-receiving coefficients in the AUT coordinate system from known probe transmitting coefficients specified in the probe coordinate system and to derive the requisite vector elemental cylindrical wave functions.

The probe compensation scheme developed above requires that the probe coefficients are provided in a coordinate system that is centred on the measurement axis. From the shifting property of the Fourier transform that relates the measured cylindrical near-field data and the CMCs, we can expect that a rotation in the ϕ -axis

corresponds to a linear phase change in the mode domain that is applied in the m -axis. Similarly, a displacement in the z -axis would similarly correspond to a linear phase change to the CMCs purely in the k_z axis. Thus, applying a translation in two of the three orthogonal cylindrical axes can be implemented rigorously in the mode domain in a trivial way. However, a translation in the radial direction would change the distribution of modes in a fundamental way. This can be seen intuitively from a consideration of the sampling theorem which is treated in detail in the following section. A probe centred at the probe coordinate system would be expected to contain only a very few, low-order CMCs. However, as the probe is displaced away from the origin of its coordinate system, a larger number of higher-order mode coefficients would be required in order that the more rapidly varying phase function is correctly represented. Thus, even an electrically small probe antenna, which contains perhaps only a first-order mode, when displaced away from its origin by a distance that is equal to the radius of the conceptual cylindrical near-field measurement surface, will contain mainly higher-order modes. This is also true for spherical near-field measurements as illustrated in Figure 8.33 in Volume 2. Thus, when the probe compensation is applied to the spectrum of CMCs, every mode is affected and not just a few low-order coefficients. This is a very crucial feature of the translation of origins that is central to cylindrical (and also spherical) probe compensation formula. The translated probe receive coefficients can be obtained using a summation formula [14,15]. This formula is based upon Graf's addition theorem [15] which states that a displaced cylindrical harmonic function can be constructed from a linear superposition (i.e. which in this case is an infinite summation) of un-displaced cylindrical harmonic functions. This formula can therefore be used to enable cylindrical mode coefficients that are expressed in terms of a cylindrical coordinate system that is centred outside of the probe to be related to the cylindrical mode coefficients that are expressed in terms of a cylindrical coordinate system that is centred on the probe.

However, in an alternative method that will be further developed in Chapter 12, it is possible to displace a radiator by transforming to the asymptotic far-field, and then by applying a differential phase change, cf. Section 12.4.1. As shown above, this transform between modes and far-fields can be implemented numerically through the use of one-dimensional fast Fourier transform; this method is both rigorous and highly efficient. Furthermore, as most probe patterns are derived from far-field measurements, which are typically taken using spherical systems, the starting point for preparing the probe cylindrical mode expansion is in fact far-field data. Thus, this phase change can be conveniently applied early on within the data processing chain, i.e. before transforming to determine the transmit probe cylindrical mode coefficients. However, irrespective of how the translation of origins is actually implemented, the displacement is equal to the measurement radius of the cylindrical near-field measurements that this data is to be used to correct. The receive coefficients can be obtained from the transmit coefficients using the reciprocity relation [16]

$$R_n^s(k_z) = (-1)^n \frac{4\pi k_\rho^2 Z_g}{k Z_0} T_{-n}^s(-k_z) \quad (7.269)$$

Here, Z_0 is the impedance of free space and Z_g is the impedance of the single mode in the waveguide transmission line. These expressions can be used to obtain translated probe receiving coefficients for each of the two probes whereupon they can be used with the probe compensation formula that was developed above. The next section provides an illustration of the effect and significance that probe correction has on an example cylindrical near-field antenna measurement.

7.7.3 *Effect of probe compensation in cylindrical near-field measurements*

This section contains an illustration of the typical effect of probe pattern compensation in cylindrical near-field measurements. Figures 7.14 and 7.15 contain cardinal cuts that show the far-field antenna patterns which were obtained from cylindrical near-field measurements with and without probe compensation. Here, it can be seen that when acquiring data from an AUT, which in this case is a medium gain x -band planar-slotted waveguide array antenna, the effect of probe compensation is most significant in the vertical elevation axis which is the axis that is most closely associated with the linear-scan axis. This follows from the comparatively small AUT-to-probe separation and the large linear span which corresponds to field being incident on the probe from comparatively large incidence angles. Thus, the directive properties of the probe, that is to say the angular sensitivity of the probe, are most crucial in the linear axis. For the angular scanning axis, the AUT is rotated such that the field incident on the near-field probe arrives from a far smaller range of incidence angles than was the case for the orthogonal axis. Thus, the sensitivity

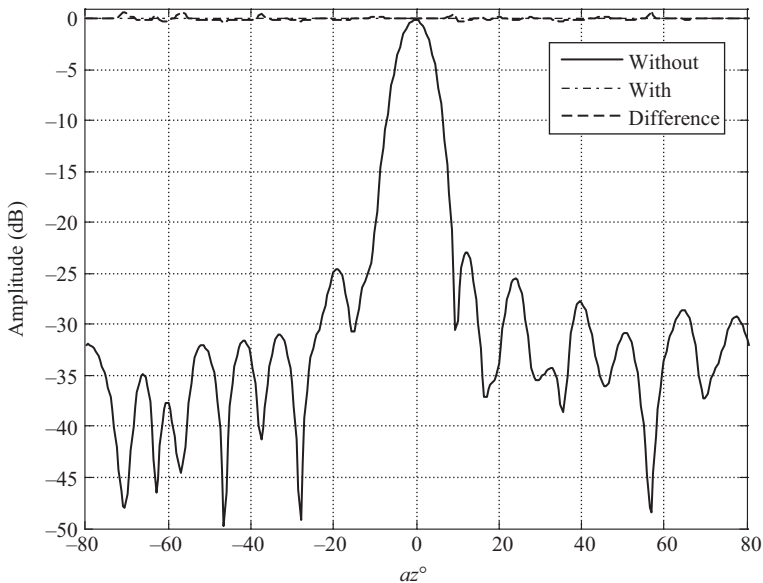


Figure 7.14 *Comparison of azimuth cuts with and without probe compensation*

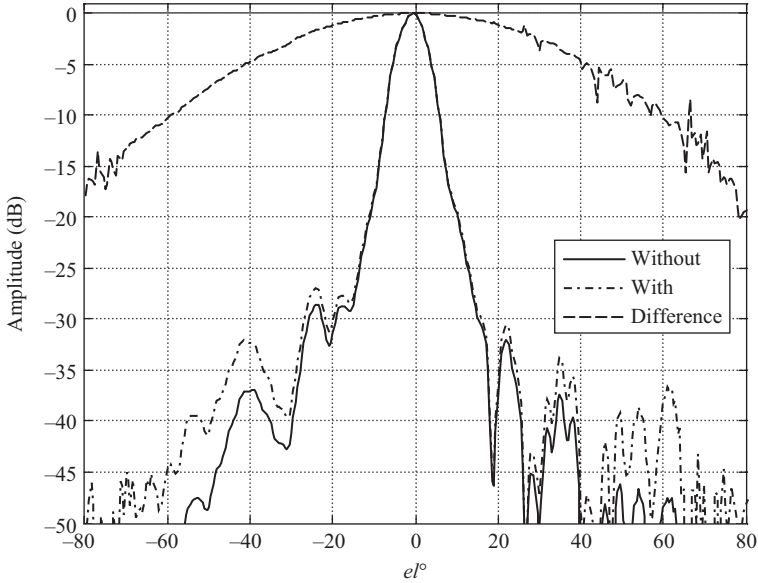


Figure 7.15 Comparison of elevation cuts with and without probe compensation

of the probe as a function of angle is less pronounced. This can be seen illustrated in the results presented in Figure 7.14 where the effect of probe compensation in the ϕ -axis is very limited. Indeed, providing the probe pattern illumination is constant across the conceptual minimum cylinder, then in the ϕ -axis, probe compensation can be ignored. Conversely, for the θ -axis, as shown in Figure 7.15, the effect is far more pronounced and equates broadly to the planar case that was treated earlier in Chapter 6. Thus, the observations regarding the characteristics of a planar near-field probe are equally applicable here. That is to say, a probe that is intended for use with cylindrical testing should have a broad pattern that does not contain pattern nulls within the forward half-space as this would result in excessively large correction coefficients being used within the compensation procedure. This can lead to numerical instabilities or loss of sensitivity in the corresponding far-field directions. Similarly, errors within the calibration of the probe pattern will be introduced into cylindrical measurements that are corrected with this data and the error approximately corresponds to a one-to-one mapping in the θ -axis.

The form of the probe compensation can perhaps be better interpreted if the formulae are written in a slightly different form. Let us rewrite the probe correction formula as

$$T_m^1(k_z) = \frac{\frac{I'_m(k_z)}{R_m^1(k_z)} - \frac{R_m^2(k_z)I''_m(k_z)}{R_m^1(k_z)R_m^2(k_z)}}{\left(1 - \frac{R_m^2(k_z)R_m^1(k_z)}{R_m^1(k_z)R_m^2(k_z)}\right)} \quad (7.271)$$

Let two complex polarisation ratios be defined as:

$$\mathfrak{R}'_m(k_z) = \frac{R'_m(k_z)}{R''_m(k_z)} \quad (7.272)$$

$$\mathfrak{R}''_m(k_z) = \frac{R''_m(k_z)}{R''_m(k_z)} \quad (7.273)$$

Thus, the probe compensated AUT transmit coefficients can be obtained using

$$T^1_m(k_z) = \frac{\frac{I'_m(k_z)}{R'_m(k_z)} - \frac{I''_m(k_z)}{R''_m(k_z)} \frac{1}{\mathfrak{R}'_m(k_z)}}{1 - \frac{\mathfrak{R}''_m(k_z)}{\mathfrak{R}'_m(k_z)}} \quad (7.274)$$

Similarly

$$T^2_m(k_z) = \frac{\frac{I''_m(k_z)}{R''_m(k_z)} - \frac{I'_m(k_z)}{R'_m(k_z)} \mathfrak{R}''_m(k_z)}{1 - \frac{\mathfrak{R}''_m(k_z)}{\mathfrak{R}'_m(k_z)}} \quad (7.275)$$

This is a form that is analogous to that which is used to represent the planar, or spherical, probe compensation formula and is a version that is often used when compiling range assessments, cf. Chapter 10. From inspection of these equations we can see that when one assumes that probe no. 1 (denoted by single primes) is H -polarised (E_ϕ) and probe no. 2 (denoted by double primes) is V -polarised (E_θ), we see that the ratio of $\mathfrak{R}''_s/\mathfrak{R}'_s$ approaches 0 and thus

$$T^1_m(k_z) \approx \frac{I'_m(k_z)}{R'_m(k_z)} - \frac{I''_m(k_z)}{R''_m(k_z)} \frac{1}{\mathfrak{R}'_m(k_z)} \quad (7.276)$$

And similarly

$$T^2_m(k_z) \approx \frac{I''_m(k_z)}{R''_m(k_z)} - \frac{I'_m(k_z)}{R'_m(k_z)} \mathfrak{R}''_m(k_z) \quad (7.277)$$

Both of these equations now consist of two terms, the first being what can be called a 'pattern correction' term and the second a 'polarisation correction' term, cf. the detailed discussion presented in Chapter 8.

7.7.4 Calculation of probe cylindrical mode coefficients from far-field data

The equivalent CMCs that represent the displaced antenna can be obtained from an inversion of equations that compute the far-field from the CMCs. As was shown earlier, asymptotic far-field data can be obtained using

$$E_\theta(r, \phi, \theta) \underset{r \rightarrow \infty}{=} -j2k \sin \theta \sum_{m=-\infty}^{\infty} j^m B_m^2(k \cos \theta) e^{jm\phi} \quad (7.278)$$

$$E_{\phi}(r, \phi, \theta) = -2k \sin \theta \sum_{m=-\infty}^{\infty} j^m B_m^1(k \cos \theta) e^{jm\phi} \quad (7.279)$$

Thus, as this is a Fourier series, its inverse transform can be immediately written down as

$$B_m^1(k \cos \theta) = -\frac{j^{-m}}{4\pi k \sin \theta} \int_0^{2\pi} E_{\phi}(r, \phi, \theta) e^{-jm\phi} d\phi \quad (7.280)$$

$$B_m^2(k \cos \theta) = -j \frac{j^{-m}}{4\pi k \sin \theta} \int_0^{2\pi} E_{\theta}(r, \phi, \theta) e^{-jm\phi} d\phi \quad (7.281)$$

The factor of 2π is introduced in the denominator to preserve the normalisation of the resulting CMCs. These transforms can be evaluated numerically through the use of the efficient 1D inverse FFT, or trapezoidal FFT. These equations enable the probe CMCs to be obtained from far-field data. Far-field probe data would need to be provided having been tabulated on an appropriately spaced far-field grid, which in this case corresponds to a plaid, monotonic and equally spaced azimuth over elevation coordinate system with the fields resolved onto a Ludwig II azimuth over elevation (az/el) polarisation basis, cf. the appendices for a detailed treatment of polarisation bases. This definition corresponds to the spherical (r, ϕ, θ) grid that is used within the standard cylindrical derivation with the positive z -axis vertical, cf. Figure 7.5. The far-field data can be either measured on this grid, or alternatively, approximation, e.g. piecewise polynomial interpolation can be used to produce data that is tabulated as required. The relationship between the az/el coordinates and the polar spherical coordinates can be expressed as

$$az = \phi \quad (7.282)$$

$$el = \frac{\pi}{2} - \theta \quad (7.283)$$

Thus, the relationship between the unit vectors in these two coordinate systems can be expressed as

$$\hat{\underline{e}}_{az} = \hat{\underline{e}}_{\phi} \quad (7.284)$$

$$\hat{\underline{e}}_{el} = -\hat{\underline{e}}_{\theta} \quad (7.285)$$

These equations are also utilised with the development of the cylindrical mathematical absorber reflection suppression and far-field mathematical absorber reflection techniques that are developed in Chapter 12.

One important aspect to the preparation of the probe pattern for use in the compensation of near-field measurements is to ensure that the probe pattern phase reference is located in the centre of the aperture at the tip of the probe. This ensures that when the measurement radius, etc., is measured, the distance used is the

distance from the origin of the measurement coordinate system (which in this case is measured from the assumed vertical ϕ -axis to the tip of the probe). This appears self-evident for the example of an open-ended rectangular waveguide probe; however, this is also true for non-aperture type probes, e.g. log-periodic dipole array (LPDA) antennas or open-boundary dual ridge tapered horns. For these types of probes, the active radiating portion of the structure will generally move along the probes, z -axis as a function of frequency. However if, as part of the auxiliary probe pattern calibration measurements, the probe is acquired across its frequency band with the tip always located exactly at the origin of the measurement coordinate system, which for a spherical test system is the intersection of the θ - and ϕ -axes, then this means that when this pattern data is used to compensate measurements taken using this probe, any displacement in the location of the active portion of the probe will be correctly compensated for.

Probably the most commonly used probe for cylindrical near-field testing comprises an open-ended rectangular waveguide section that is excited by the dominant TE_{10} mode. The well-behaved broad pattern function that is free from nulls in the forward hemisphere, has good polarisation purity, and exhibits a low scattering cross-section make these devices particularly well suited to being used as general purpose near-field probes. Two commonly used non-aperture type, broadband, probe antennas can be seen in Figures 7.16 and 7.17. Neither of these probes has a single aperture; however, if the above procedure is used both can be successfully used for the acquisition of cylindrical near-field data provided the probe pattern is not overly narrow and the side lobes too low, then they can be effectively used as probes. If the pattern falls off too rapidly with angle, then the probe is insensitive to a wave incident from these directions, and consequently the compensation coefficients become too large and the measurement becomes insensitive for these (primarily elevation) directions. For the case of the LPDA antenna, as the frequency increases, the radiating centre moves progressively towards the tip of the

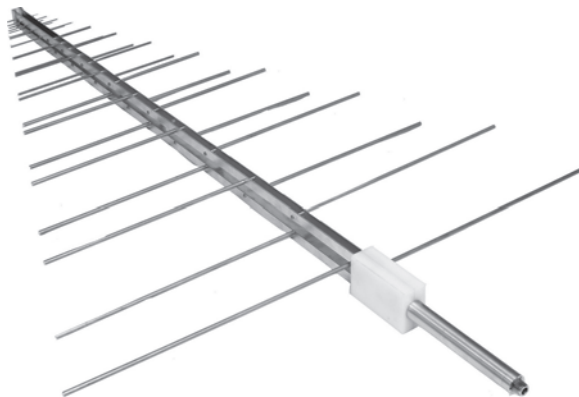


Figure 7.16 0.20–3 GHz log-periodic dipole array antenna used as a broadband probe (Image courtesy of RF-Spin)

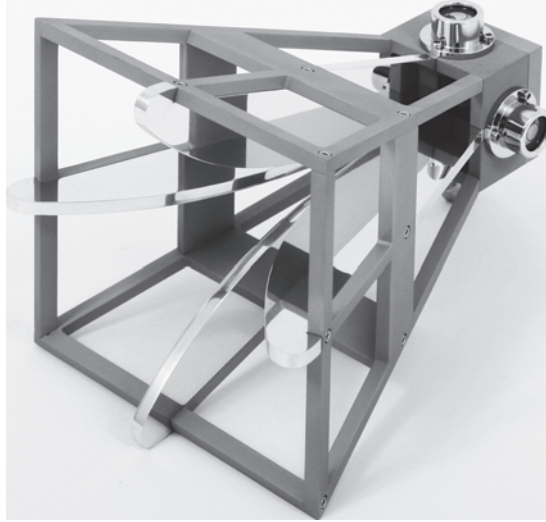


Figure 7.17 2–6 GHz dual-port quad-ridge open boundary horn used as broadband probe (Image courtesy of RF-Spin)

probe where the shortest dipole elements are located with the longer elements acting as reflectors. This is the converse behaviour to that of the open boundary quad-ridge horn (QRH). In this case, as the frequency increases, the ‘radiating’ portion of the device moves away from the ‘aperture’ of the probe down the throat of the horn towards the region where the separation between the ridges becomes narrow. In either case, provided the auxiliary calibration is performed as described earlier, and the radius of the cylindrical measurement is taken from the axis of rotation to the tip of the probe, no further parallax-correction, etc., is needed. A detailed treatment of probe and probe characterisation is presented in Chapter 12.

7.8 Sampling requirements for cylindrical near-field measurements

Band limits of the AUT pattern in the θ direction define a data point spacing in z like the planar case. Also, the Fourier variable k_z can be limited to $\pm k_0$ (equivalently, where $k_\rho = 0$) as these are the highest-order propagating modes. As the sample spacing, i.e. resolution, is determined from the maximum value of k_z , we can write that

$$\delta z = \frac{\pi}{k} = \frac{\lambda}{2} \quad (7.286)$$

where λ denotes the wavelength. This corresponds to taking one sample per half wavelength for a homogeneous wave propagating in the $\pm z$ direction which is the

fastest rate of change of phase for a non-evanescent wave, cf. Nyquist's result that equi-spaced data should be sampled with at least two points per cycle of highest frequency component, see Chapter 6 [1]. Due to the exponential decrease in the reactive cylindrical modes the maximum m value (cf. the spherical case as developed in Chapter 8) can be expressed in terms of the free-space wavenumber and the MRC, r_t , as

$$M = kr_t + M_0 \quad (7.287)$$

Here, M_0 is a positive integer that is a safety margin that depends upon the accuracy required. A value of $M_0 = 10$ is sufficient for many test applications not involving super-directive antennas. Figure 7.18 contains a schematic representation of the plan-view of a cylindrical test system. Here, the AUT can be seen to be displaced from the ϕ -axis. The MRC is centred on the axis of rotation and is sufficiently large in diameter to be able to circumscribe the majority of the current sources. The measurement radius is coaxial with the MRC but must be larger than the MRC to prevent mechanical interference between the AUT and the probe. The cylindrical near-field theory as developed above will work for any measurement radius that is larger than the MRC; however, when the AUT-to-probe separation is larger than this by several wavelengths, reactive coupling of evanescent modes is minimised and the aforementioned sampling criteria is valid. That is to say

$$\rho_0 > r_t + n\lambda \quad (7.288)$$

where n is a positive number ≥ 0 . As has been shown within the development of the planar theory, reactive fields are attenuated very rapidly with distance and when $n \geq 3$, all appreciable reactive modes are effectively attenuated before they reach

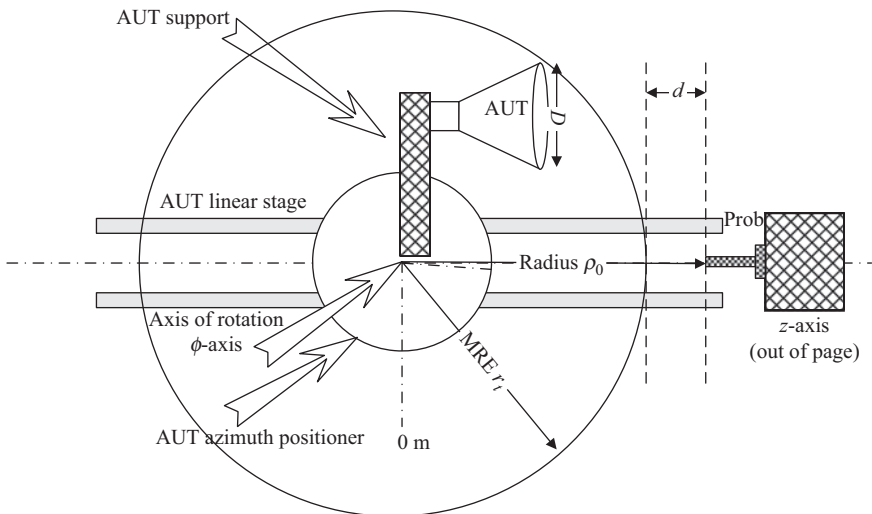


Figure 7.18 *Illustration of MRE = MRC in cylindrical near-field measurements*

the probe. The angular sample spacing, in radians, is determined from the highest-order cylindrical mode that contains appreciable amounts of power and is thus,

$$\Delta\phi \leq \frac{\pi}{M} \quad (7.289)$$

when $M \gg 1$. Thus, when $kr_t \gg M_0$, then this equates to taking samples at every half wavelength around the circumference of the cylinder defined by the MRC,

$$\Delta\phi \leq \frac{\pi}{kr_t + M_0} \approx \frac{\lambda}{2r_t} \quad (7.290)$$

Here, the angular sample spacing is expressed in radians. Thus, the maximum mode index, M , is driven by the frequency, size and mounting offset of the AUT being considered and is independent of the measurement radius. It is found that when testing antennas outside of the reactive near-field, higher order cylindrical modes, specifically those corresponding to the region outside of a circle defined by

$$m^2 + (k_z r_t)^2 = M^2 \quad (7.291)$$

will be attenuated very rapidly and the infinite summations can be truncated to a finite number without incurring appreciable error. This can also be expressed as

$$m^2 + (k_z r_t)^2 = (kr_t + M_0)^2 \quad (7.292)$$

Thus, in practice the amplitude of the CMCs is found to attenuate rapidly outside the circle defined by the circle of radius kr_t , which is shown in white in Figure 7.19. This concept is used extensively in Chapter 12 when developing the cylindrical Mathematical Absorber Reflection Suppression (C-MARS) technique multipath suppression technique.

Hence, we have shown that the practical upper bounds on the sampling interval equate to taking one sample per half wavelength across the surface of the conceptual minimum cylinder. It is important to note at this stage that we are not completely free in our choice of $\Delta\phi$. While we need to ensure that we satisfy the sampling criteria, we also need to ensure that the ϕ span constitutes a closed sampling interval, that is to say the maximum and minimum angular limits do not overlap, or leave a gap, as this would result in an appreciable error being introduced into the computed CMCs and resulting far-field pattern data. Clearly, and as is the case with planar testing, larger AUT-to-probe separations necessitate larger linear scan axes for a given maximum far-field valid angle which is merely a consequence of limiting measurement truncation in this axis.

As stated earlier, there are no limits in the theory that require a measurement distance, d , of 3 wavelengths or greater. However, when testing at reduced separations, the required data point spacing to correctly sample the fine structure of the evanescent field will decrease, requiring some experimentation to determine what the spacing should be, and often increases the measurement time. In the planar case, the reduced distance will increase the angular region of validity, or reduce the scan lengths, which are good reasons to move as close as possible. However, at

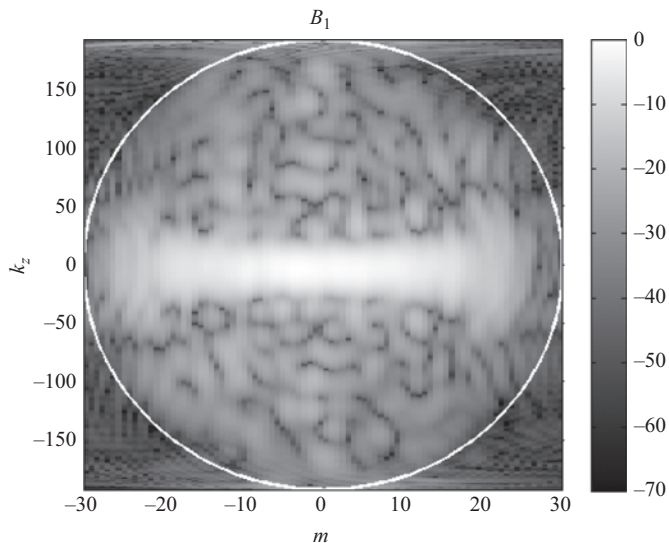


Figure 7.19 Cylindrical mode coefficients attenuate rapidly outside the circle of radius k_a – shown in white

shorter ranges, the multiple reflection error may increase significantly and this is one of the reasons for choosing the larger distance. Thus, due to these band limits, the integration required to obtain the CMCs, etc., can be replaced by summation without approximation and the discrete, or more usually fast Fourier transform can be used to compute the CMCs.

The specification of the sample spacing in the angular and linear axes enables the specification of a plaid, monotonic and equally spaced lattice of points (ρ_0 , $m\Delta\phi$, $n\Delta z$) at which samples are to be taken where m and n are integers such that $0 \leq m \leq M-1$ and $0 \leq n \leq N-1$ with M and N being positive integers. Here, it is assumed that the measured fields are zero when $z < 0$ and $z > (N-1)\Delta z$. In practice, this can only be achieved if the linear scan-axis is infinitely long. However, for most practical cases, the test antenna would be installed within a truncated conceptual measuring cylinder so that there is no appreciable radiation propagating in the $\pm z$ direction. That is to say, the AUT must have directive gain in this axis and N must be set to a suitably large value. It has been found that truncation in the z -axis at a fairly high level of field circa -10 dB leads to the introduction of a spurious ripple on the far-field θ -axis radiation pattern. This effect is most noticeable in side lobe level variation, and in the computed antenna directivity, which will therefore also affect the predicted gain value. However, it can be stated that the overall far-field ϕ -axis pattern obtained with a severely z -shortened cylindrical near-field data may be acceptable for many applications. Further improvements are possible through the use of near-field filter functions to soften the effect of scan height truncation. So that this can be illustrated, Figure 7.20

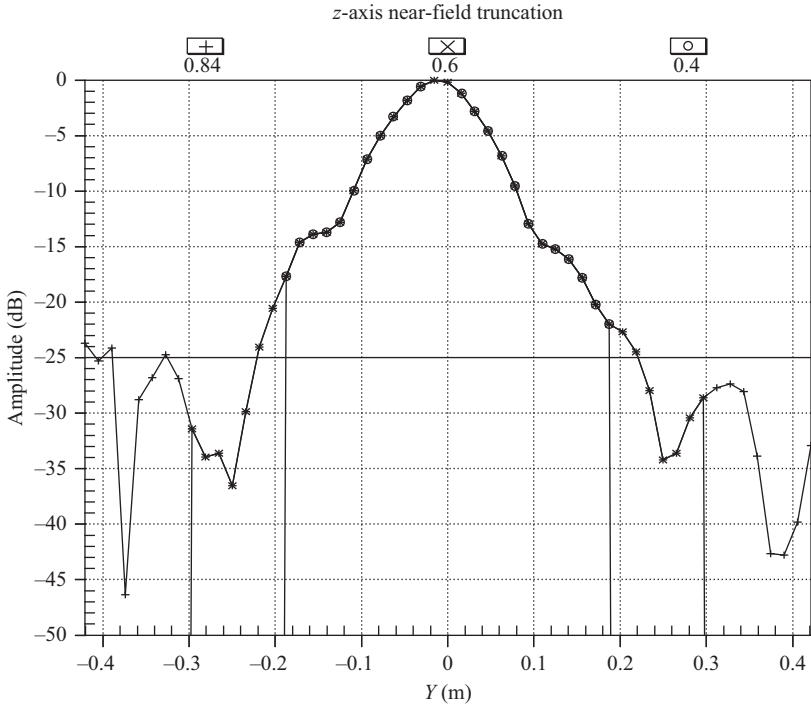


Figure 7.20 Near-field data for a vertical cut, with varying z -axis truncation

contains a z -axis cut of measured cylindrical near-field data. Here, the three data sets have been truncated in the linear axis and correspond to a span in the linear axis of 0.84 m, 0.6 m and 0.4 m respectively. This data was transformed to the far-field using the standard probe-corrected cylindrical processing as developed earlier. The resulting far-field θ - and ϕ -axis cuts are presented in Figures 7.21 and 7.22, respectively. Here, the variation in the θ -axis (elevation) cut is most pronounced. This is expected as the z -axis truncation corresponds most closely to this far-field axis. As the truncation is increased, the maximum far-field angle out to which reliable data is available reduces and the degree of spurious high-frequency ripple also increases. Variation in the ϕ -axis (azimuth) cut is also evident even though this axis is not truncated in the near-field. This follows from the anti-reductionist relationship between the near- and far-fields. As expected, however, the degree of change is less than was the case for the θ -axis.

Table 7.1 shows the computed directivity values for the various truncation cases considered earlier. It is clear that the reduced scan area artificially raises the measured directivity value. However, these are *gross* examples of truncation and in practice some degree of truncation level may be tolerable in some applications. Methods for establishing the degree of error, mostly using perturbation-based techniques, are established in Chapter 10.

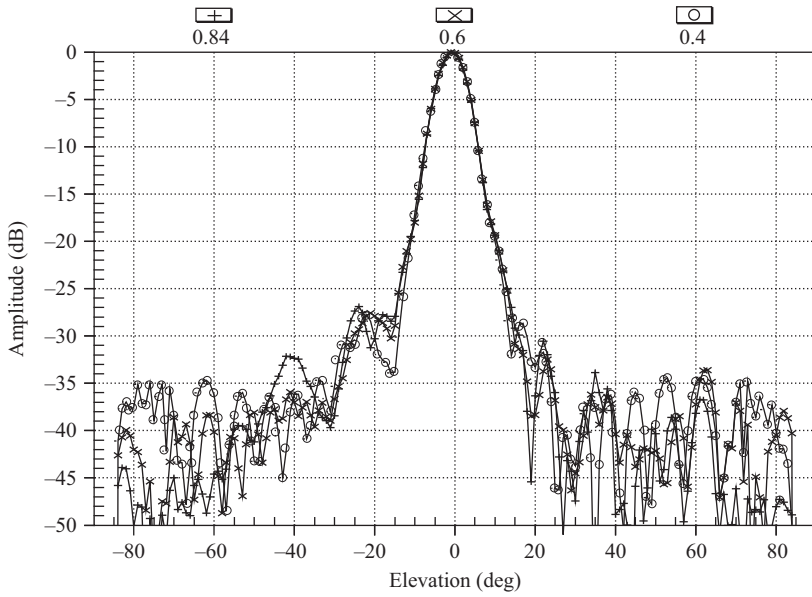


Figure 7.21 Far-field elevation (θ) pattern cuts for truncated height data sets

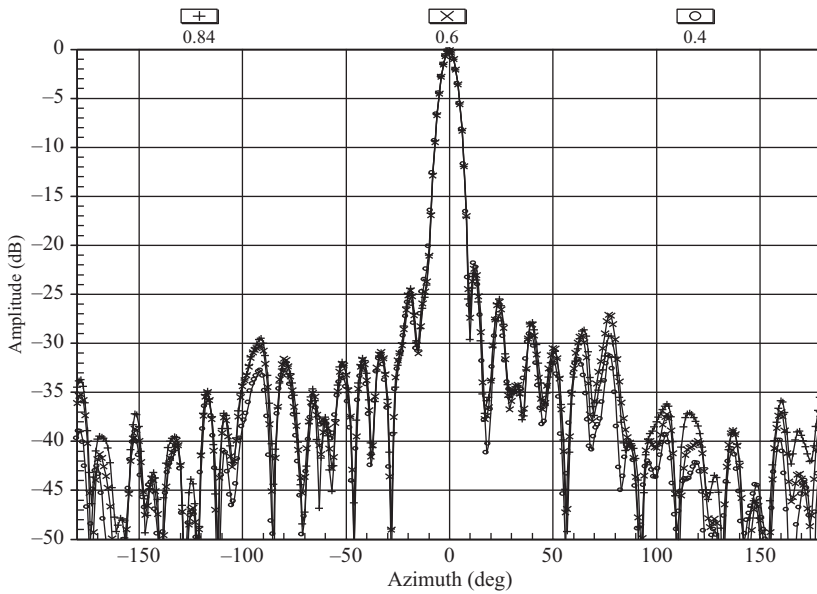


Figure 7.22 Far-field azimuth (ϕ) pattern cuts for truncated height data sets

Table 7.1 Computed directivity versus z-axis truncation

CNF scan height (m)	Measured directivity (dBi)
0.84	27.95
0.6	27.88
0.4	28.05

The necessary integrals can be evaluated efficiently by using the FFT algorithm. When using the FFT to evaluate the integral for the CMCs, the integral transform domain data will be produced on a grid such that the maximum value of k_z can be determined using

$$|k_{z0}| = \left| \frac{\pi}{\Delta z} \right| \tag{7.293}$$

Thus, the sample spacing can be obtained using, cf. the planar case developed earlier

$$\Delta k_z = \frac{2k_{z0}}{N} = \frac{2\pi}{N\Delta z} \tag{7.294}$$

where N is the number of points in the k_z axis. Hence

$$k_{z,n} = k_{z0} + n\Delta k_z = n \frac{2\pi}{N\Delta z} - \frac{\pi}{\Delta z} \tag{7.295}$$

Thus, in terms of direction cosines we obtain the usual expression for the lattice coordinate

$$\frac{k_{z,n}}{k} = \frac{\lambda}{N\Delta z} \left[n - \frac{N}{2} \right] \tag{7.296}$$

Note that when using a standard FFT algorithm, the DC point, i.e. the component that corresponds to a cylindrical wave propagating in the xy -plane, is placed at the first element in the array, not midway between elements. Since the polar spherical angle is related to k_z , the Fourier transform parameter for the z -part of the cylindrical modes through

$$k_z = k \cos \theta \tag{7.297}$$

This implies that the far-fields will be provided on a lattice of (θ, ϕ) points with θ determined by

$$\theta_n = \arccos \left(\frac{k_{z,n}}{k} \right) \tag{7.298}$$

hence

$$k_{\rho,n} = \sqrt{k^2 - k_{z,n}^2} \tag{7.299}$$

Thus, as n is an integer, the points will be distributed evenly in ‘cosine space’, and non-equally in angle space, cf. again the planar case treated earlier. The use of the FFT algorithm requires that for the first time we must consider evaluating non-integer order Hankel (and potentially Bessel) functions. The reason for this is that, beyond the use of zero padding to increase the array bounds of the near-field data arrays, as the number of points returned by a FFT must equal the number of points provided to the algorithm, we are not therefore free to arbitrarily choose the sample spacing of the transformed arrays. Computationally, this is not too inconvenient as routines for the computation of Hankel functions of non-integer orders are available and the expression for evaluating negative-order functions and the derivative of the Hankel functions are also valid for non-integer orders. For the mode index axis, m , a similar treatment can also be employed, thus and using analogous notation to the k_z case considered earlier

$$|m_0| = \left| \frac{\pi}{\Delta\phi} \right| \quad (7.300)$$

With

$$\Delta m = \frac{2m_0}{M} = \frac{2\pi}{M\Delta\phi} \quad (7.301)$$

where M is the number of points in the m -axis, and i is a positive integer, thus

$$m_i = m_0 + i\Delta m = \frac{i2\pi}{M\Delta\phi} - \frac{\pi}{\Delta\phi} \quad (7.302)$$

The angular axis is assumed to comprise a closed sampling interval, otherwise further truncation will be introduced. Thus, we are not free to choose the ϕ -axis span, sample spacing and number of samples with complete freedom. It is also important to recall that here it is assumed that there is no angular harmonic m greater than $\pi/\Delta\phi$. Using these relationships, the integrals required to compute the CMCs can be replaced as FFT-type summations, thereby allowing highly efficient cylindrical near-field to far-field transform algorithms to be deployed.

7.9 Implementation of cylindrical near-field to far-field transformation

In the preceding sections a detailed development of the cylindrical near-field to far-field transform process is presented. Although the mathematical development is lengthy and in places involved, the resulting formula and the corresponding computer algorithm are not too complex. The transformation process is illustrated later where example data is passed through the standard cylindrical algorithm in an attempt to highlight the important steps and features of the process. Figures 7.23 and 7.24 are respectively the horizontal (ϕ) and vertically (z) polarised measured cylindrical near-field amplitude patterns that have been presented in the form of a

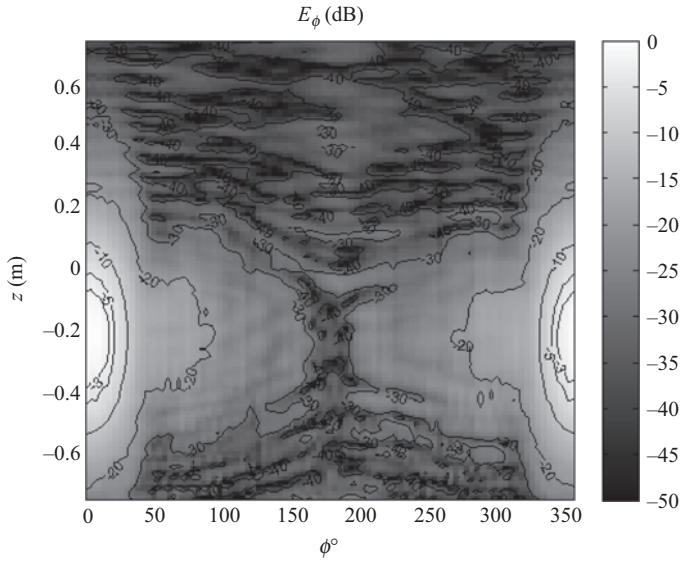


Figure 7.23 Horizontally (ϕ) polarised measured cylindrical near-field amplitude data

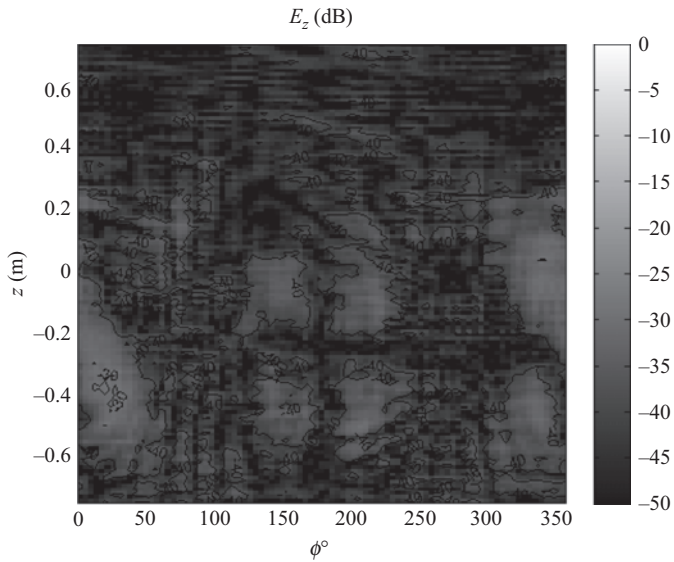


Figure 7.24 Vertically (z) polarised measured cylindrical near-field amplitude data

grey-scale checkerboard plot. Although not shown, corresponding phase data is also recorded as part of the acquisition.

For this example, the near-field data was taken at 8 GHz. The MRC was 0.1270 m, making $k_0 \approx 167 \text{ m}^{-1}$. Thus, the highest-order CMC was 31 meaning that all modes of orders $-31 \leq m \leq 31$ were computed during the transformation. This implied that the angular sampling increment should be no greater than 5.7° and so an actual sample spacing of 4° was used when acquiring this near-field data. In the linear axis a sample spacing of 0.0187 m should be used to satisfy the Nyquist criteria and in actuality this measurement was slightly oversampled as an actual sample spacing of 0.0120 m was used during the acquisition.

Using the formula derived earlier, the CMCs can be computed. Figures 7.25 and 7.26 respectively show plots of the $S = 1$ and $S = 2$ polarised CMCs which have again been presented in terms of a greyscale checkerboard plot. Here, the amplitude has been presented in dB form. CMCs are complex quantities and as such possess a phase pattern that has not been presented. Here, as only radiated, rather than reactive, fields contribute to the asymptotic far-field pattern, CMCs have only been computed and plotted over the range $-k_0 \leq k_z \leq k_0$. Similarly, modes have only been computed up to $|m| \leq m_{max}$, where m_{max} is determined by the angular sample spacing.

Once the measured electric fields have been expanded onto a set of cylindrical modes, these modes can be corrected for the directive properties of the measuring probe. In this example, a WR90 open-ended rectangular waveguide section excited by the fundamental TE_{10} mode was used as a near-field probe. As required by the cylindrical near-field theory as developed earlier, two different probes are

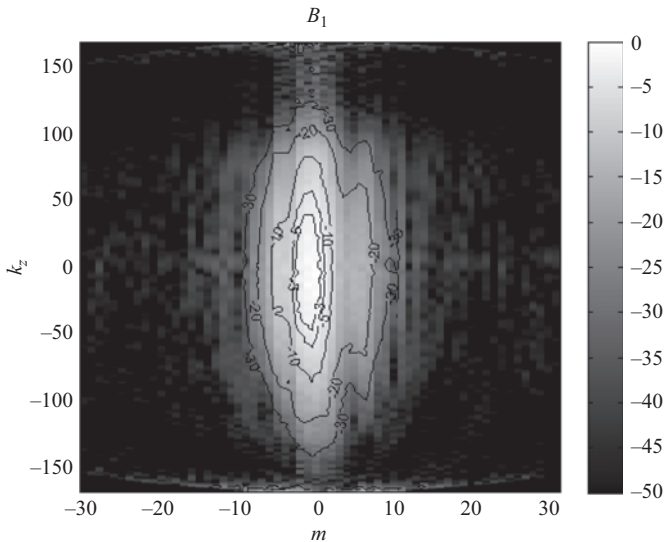


Figure 7.25 $S = 1$ polarised measured cylindrical mode coefficients

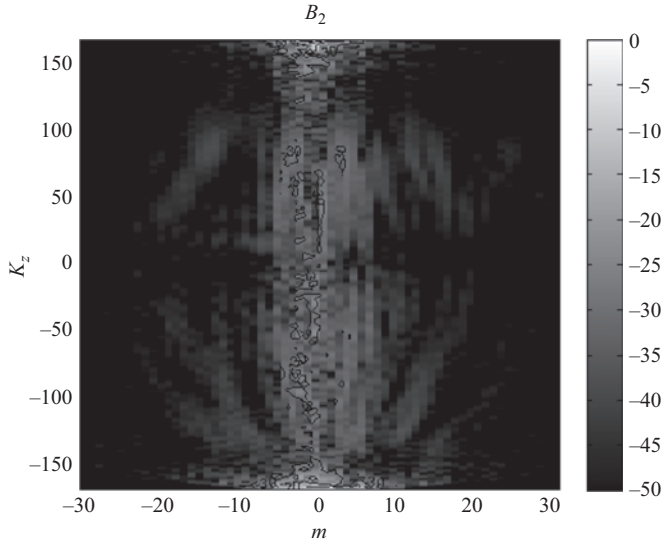


Figure 7.26 $S = 2$ polarised measured cylindrical mode coefficients

necessary to implement probe correction; two measurements were made where the probe had been rotated by 90° about its length between successive measurements. This is the reason why two orthogonal components of the near electric field were measured. Once the measured cylindrical modes have been compensated for the measuring probe, two new sets of modes corresponding to the AUT are obtained. These can be found presented in Figures 7.27 and 7.28 which correspond to the $S = 1$ and $S = 2$ polarisations, respectively. From comparison of these and the equivalent plots prior to probe correction, it can be seen that the greatest change can be observed in the k_z axis. This phenomenon is apparent as the far-field pattern is obtained through a summation in m , with the k_z axis essentially only being relabelled between mode domain and the far-field. Probe correction in cylindrical near-field measurements typically has the greatest impact in the θ -axis which corresponds to the (vertical) linear z -axis. As with the planar case that was treated in the previous chapter, this follows from the comparatively short-range length and the large subtended elevation angles observed at the probe. Conversely, in the ϕ -axis, the probe is nominally always receiving AUT-radiated fields from the boresight direction and hence the comparatively minor change observed in the m -axis.

Once the probe-corrected AUT CMCs have been obtained, these can be summed to compute the asymptotic far-field pattern. The ϕ - and θ -polarised far electric field components can be found presented in Figures 7.29 and 7.30, respectively. Here, the patterns have been plotted as a function of ϕ and θ on a plaid, monotonic and equally spaced polar spherical grid, cf. Figure 7.5.

Here, the peak of the pattern has been normalised to 0 dB with the θ -polarised, i.e. cross-polar, pattern being plotted with respect to the peak of the ϕ -polarised, i.e.

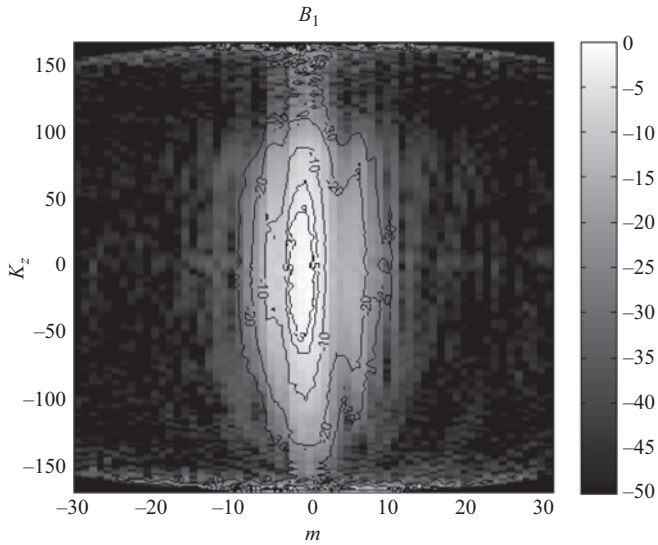


Figure 7.27 $S = 1$ polarised probe-corrected cylindrical mode coefficients

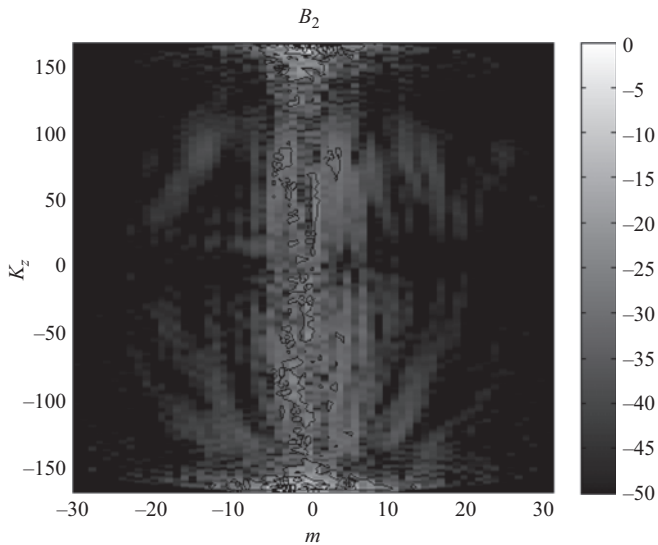


Figure 7.28 $S = 2$ polarised probe-corrected cylindrical mode coefficients

co-polar, pattern. In Figures 7.29 and 7.30, the ϕ -axis has been shifted so that the $\phi = 0^\circ$ (boresight) direction lies in the centre of the plot in agreement with general convention. The following section presents an interesting extension of the standard cylindrical near-field transform as outlined earlier that enables near-field data to be

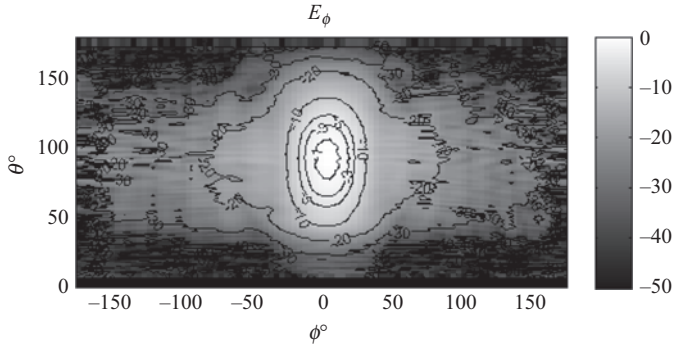


Figure 7.29 ϕ -Polarised probe-corrected far-field antenna pattern

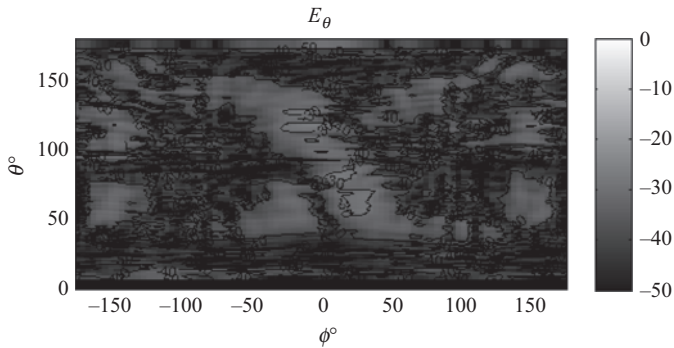


Figure 7.30 θ -Polarised probe-corrected far-field antenna pattern

acquired over the surface of a cone and transformed to provide probe-corrected far-field data. A data processing (i.e. flow) diagram for the probe-corrected cylindrical near-field to far-field transform can be seen presented in Figure 7.31. As a final part of the cylindrical processing, two further commonly implemented steps have been shown in this flow diagram. The first of these is the change in polarisation basis and a detailed treatment of coordinate systems, polarisation basis can be found presented in the appendices. The second is the inverse transform from the far-field back to the antenna aperture plane which is a commonly used method of non-invasive, non-destructive diagnostics. Detailed information regarding this can be found presented in Chapter 12 on advanced antenna measurement techniques. These two topics are more general topics that are used with other near-field geometries being, as they are, not limited to the cylindrical implementation.

7.10 Conical near-field antenna measurements

Conceptually, the right conical measurement system is perhaps most closely related to the well-documented, well-understood cylindrical near-field scanning technique.

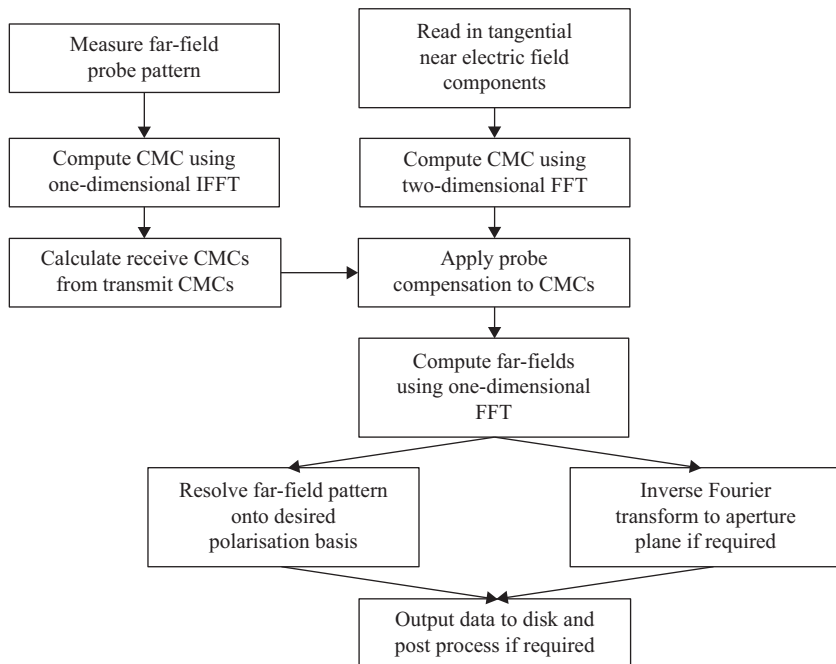


Figure 7.31 Flow diagram for cylindrical near-field to far-field transform

Only here, the axis of rotation of the AUT and the linear translation stage which carries the probe are no longer constrained to be exactly parallel to one another. By taking samples incrementally on a raster grid by varying the azimuthal (ϕ) angle and linear displacement, the near electric field can be sampled over the surface of a right cone [17]. An example of this arrangement can be seen presented in Figure 7.32. Here, a standard NSI-200V-5 \times 5 combination planar-cylindrical antenna test system is being used to acquire conical near-field data.

Here, the vertical axis of the 1.5 m by 1.5 m planar scanner has been tilted from the vertical using a precision tilting fixture that allowed for 0° or 30° half cone-angle, which is the angle between the local gravity vector and the linear axis. As conical measurements were made, the (horizontal) x -axis was not used during the acquisitions. The rotational ϕ -axis of the cylindrical system remains vertical and is aligned to the local gravity vector. The WR-90 open-ended rectangular waveguide probe is aligned so that its z -axis (axis coaxial to the waveguide section) is horizontal. Thus, the probe is used to acquire horizontal and vertical near electric fields which correspond to the standard cylindrical ϕ - and z -polarised unit vectors. The AUT was an x -band standard gain horn (SGH). The acquisitions were made using standard cylindrical data acquisition software with no modification to the software being required with only the addition of the cone being needed to be recorded. The implementation of the conical transform can be derived from the integral used to



Figure 7.32 Conical near-field antenna measurements being acquired using an NSI-MI Technologies LLC combination planar-cylindrical positioning system

determine the CMCs from the measured fields. By noting that the measurement radii are a function of the z -axis, we can write that

$$B_m^1(k_z) = \frac{-1}{4\pi^2 k_\rho^3} \int_{-\infty}^{\infty} \int_0^{2\pi} \frac{1}{H_{-m}^{(2)'}(k_\rho \rho_0(z))} \left(\frac{mk_z}{\rho_0(z)} E_z(\rho_0(z), \phi, z) + k_\rho^2 E_\phi(\rho_0(z), \phi, z) \right) e^{im\phi} e^{jk_z z} d\phi dz \quad (7.303)$$

$$B_m^2(k_z) = \frac{k}{4\pi^2 k_\rho^2} \int_{-\infty}^{\infty} \int_0^{2\pi} \frac{1}{H_m^{(2)}(k_\rho \rho_0(z))} E_z(\rho_0(z), \phi, z) e^{im\phi} e^{jk_z z} d\phi dz \quad (7.304)$$

The far-fields are obtained from the B^1 and B^2 CMCs using the usual summation process developed earlier. Clearly, for the case where probe pattern correction is needed, this would also be needed to be implemented within the z -integral. In this way, the near-field to far-field transform is implemented by performing a cylindrical mode expansion on each infinitesimal thin cylindrical scan (i.e. ring) in turn and then using the principle of linear super-position to obtain the resulting modal expansion. It is possible to transform each ring of data to the far-field and then to integrate the fields there to obtain equivalent results; however, the computational effort required is greater in this case.

In practice, the number of CMCs can be truncated to a finite number which equates approximately to half wavelength sampling over the surface of a conceptual cylinder that is centred on the origin of the measurement coordinate system, and that encloses the majority of the current sources. This is also true for the conical case. Thus, the maximum mode index M is given by $M = kr_t + M_0$, where r_t is the MRC and M_0 is a safety margin that depends upon the accuracy required. A value of $M_0 = 10$ is sufficient for many applications not involving super-directive antennas. Also, as was the case for the cylindrical geometry, the Fourier variable k_z can be limited to $\pm k_0$ (equivalently, where $k_\rho = 0$) as these are the highest-order propagating modes. As the sample spacing, i.e. resolution, is determined from the maximum value of k_z , we can write that $\delta_z = \pi/k_0 = \lambda/2$, where λ denotes the wavelength. Thus, for the conical case, the angular sample spacing is held fixed for all values of z at an amount determined by the size of the MRC, with samples being taken at every half wavelength along the linear scan axis, that is over the surface of the cone, i.e. not along the rotation axis where the two amounts differ by a factor of the cosine of the half cone angle.

To illustrate the conical measurement system, the system shown in Figure 7.32 was used to acquire a conical and cylindrical near-field measurement of the same test antenna. The first measurement consisted taking a conventional cylindrical near-field measurement and this was to be used as the baseline measurement against which the conical test case could be compared. The second measurement, as illustrated, involved tilting the vertical axis of the scanner through 30° so that an equatorial conical near-field measurement could be made. This case was selected so that the basic conical near-field to far-field transform could be verified against the baseline cylindrical case. Measured cylindrical and conical near-field amplitude data of the horizontally (i.e. ϕ) polarised electric field can be found presented in Figures 7.33 and 7.34, respectively.

These measured data sets were transformed to the far-field using the algorithm outlined earlier where the results shown in Figures 7.35 and 7.36 were obtained. These results can be compared directly with the results shown in Figures 7.29 and 7.30.

As is evident from inspection of the plots of the near-field measured patterns, the data sets are all truncated to some degree in the nominally vertical linear axis which will inevitably lead to some leakage in the far-field pattern. First, and as is the case with planar scanning, the first-order truncation effect will result in the error within the pattern being effectively infinitely large outside of some angular limit which can be approximated by geometry (cf. an infinite frequency, geometrical optics approximation). Second, the holistic nature of the relationship that exists between the near-field and far-field regions will result in the introduction of some ripple into the far-field pattern within even this angular range.

Unfortunately, as these measurements were preliminary in nature, they were not conducted within a screened anechoic environment and as such, the multi-path within the measurements did differ between each measurement configuration which degraded the agreement attained. This was particularly crucial as both the orientation of the AUT and the probe changed between measurements. Crucially,

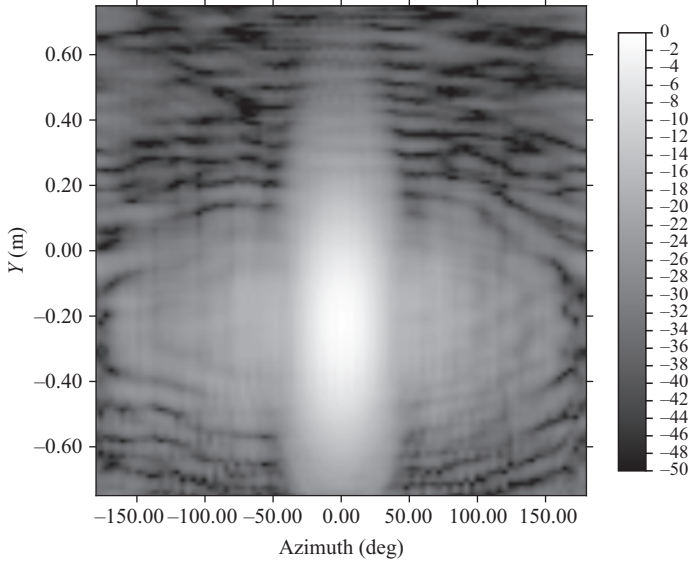


Figure 7.33 Cylindrical near-field amplitude data of the ϕ -polarised near electric field component

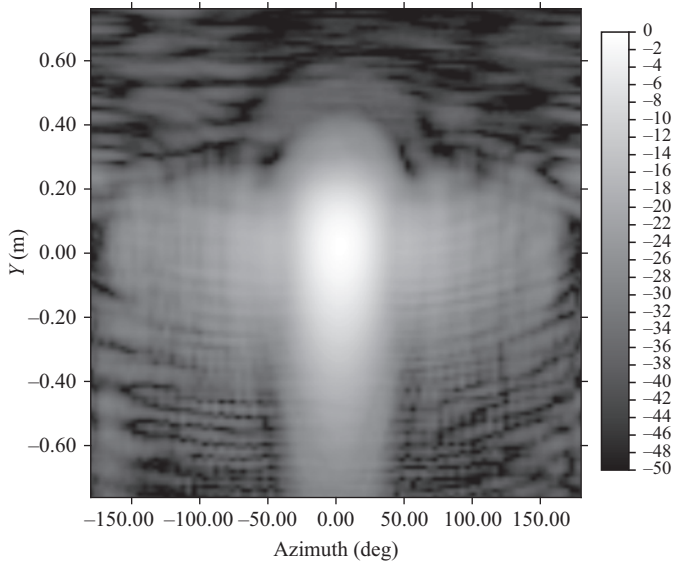


Figure 7.34 Conical near-field amplitude data of the ϕ -polarised near electric field component

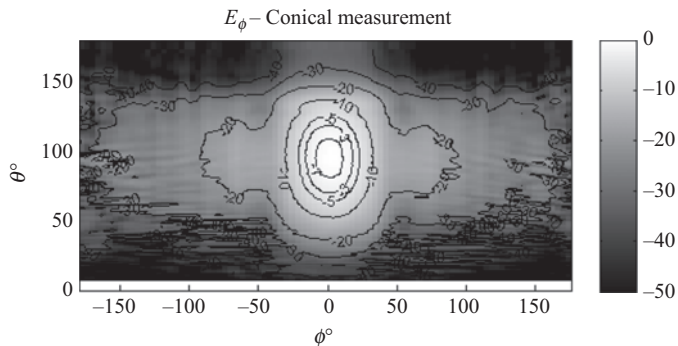


Figure 7.35 ϕ -Polarised far-field antenna pattern

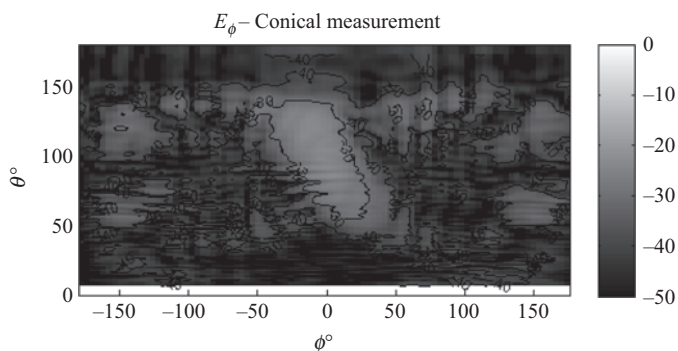


Figure 7.36 θ -Polarised far-field antenna pattern

the radii of the cylindrical, and particularly the conical, measurements were not accurately determined during these measurements which are the most likely cause of the small discrepancies in the location of the side lobes. Further verification of this technique can be found presented in [17].

Ideally, the boresight of the AUT would be orientated so that it points directly through the tip of the cone, i.e. in a polar mode (cf. the equatorial mode measurements discussed herein) so that the undesirable effects of truncation are minimised. In practice, however, any imperfection in the alignment of the conical system could result in the introduction of significant errors in the corresponding far-field pattern. This is a consequence of the fact that, naturally, the boresight direction of the AUT, and thus the region of greatest field intensity, will be directed towards the tip of the cone, which is where the set of radial conical linear cuts intersect and where the alignment issues are most critical. Obviously, this can be eased by orientating the AUT so that it ‘looks’ out through the side of the cone thus avoiding the tip region, but this is perhaps an inelegant solution. One alternative that has been used with considerable success is the closely related poly-planar measurement

technique. For the poly-planar case, a truncated pyramid, i.e. a pyramidal frustum, was employed to resolve this difficulty. Here, however, an analogous conical frustum would be used which is a frustum created by slicing the top of a right cone where the cut is made parallel to the base of the cone. Here, the cap that is used to replace the tip of the conic section constitutes a conventional plane-polar measurement. It is intended to displace the intersection between the individual cuts from the region of greatest field intensity to a less sensitive location. Thus, in the event that the adjacent scans do not intersect perfectly, the resulting positional error will impact less on the far-field pattern.

It is often preferable when taking near-field antenna measurements that the selected measurement geometry is selected which is commensurate with the geometry of the AUT. Thus, this technique would be particularly well suited to the characterisation of base-station antennas, or arrays installed behind tangent ogive radomes, such as those commonly employed with nose-mounted fire-control radars which generally constitutes an electrically large test article that often presents the experimentalist with both electromagnetic and mechanical challenges. Details of this are left to the open literature, e.g. [18] and [19].

7.11 Summary

This chapter has presented a development of the standard probe-corrected cylindrical near-field antenna measurement theory. While a detailed understanding of the cylindrical near-field theory is perhaps not generally required for most testing applications, an understanding of the theory and its implications will be valuable in solving measurement problems and insuring good data is acquired and reliable far-field data produced. The great advantage of the cylindrical approach is that it is instantly applicable to testing antennas for which it is desired to compute the complete 360° far-field azimuthal pattern. This is a significant advantage when compared to the planar approach for which the far-field pattern is only obtainable over a half-space without recourse to repeating the measurement and post-processing. However, the cylindrical approach is limited in the polar axis as the field at $\theta = 0^\circ$ and 180° is excluded, both practically due to the finite length of any realised linear translation axis and theory as the Hankel functions are not defined for these angles. That being noted, as shown earlier, any antenna that is tested broadside for which there is some reasonable gain, the θ -axis can provide complete azimuthal (ϕ -axis) far-field pattern data. However, for the class of antennas that do not satisfy this directivity requirement, recourse must be sought in spherical near-field antenna testing which is developed within the following chapter. Further very detailed information on cylindrical near-field antenna testing can be found in [9] and [12] which contain much of the original ground-breaking work that underpinned this technology. Much of the mathematical framework and many of the concepts that are necessitated by the spherical theory are in common with that presented earlier. Thus, development of the cylindrical near-field theory provides a perspicuous introduction to the probe-compensated spherical near-field theory.

References

- [1] Morse P.M., Feshbach H., *Methods of Theoretical Physics*. New York: McGraw-Hill Book Company, Inc.; 1953. p. 116 (Library of Congress Card Number: 52-11515)
- [2] Spiegel M.R., *Theory on Problems of Vector Analysis and an Introduction to Tensor Analysis*. Schaum's Outline Series. New York: Schaum Publishing Co.; 1959
- [3] Abramowitz M., Stegun I.A. (eds.), *Handbook of Mathematical Functions with Formulas, Graphs, and Mathematical Tables*. New York: Dover Publications; 1964. p. 74 (Standard Book Number: 486-61272-4)
- [4] Kreyszig E., *Advanced Engineering Mathematics*. 8th edn. New York: John Wiley & Sons; 1999. p. 218. ISBN 0-471-15496-2
- [5] Harrington R.F., *Time-Harmonic Electromagnetic Fields*. IEEE Press, Wiley-Interscience, New York: John Wiley & Sons, Inc.; 2001. p. 460. ISBN 0-471-20806-X
- [6] Morse P.M., Feshbach H., *Methods of Theoretical Physics*. New York: McGraw-Hill Book Company, Inc.; 1953. p. 1766 (Library of Congress Card Number: 52-11515)
- [7] Stratton J.A., *Electromagnetic Theory*. IEEE Press Series on Electromagnetic Wave Theory. New Jersey: Wiley-Interscience, John Wiley & Sons, Inc; 2007. p. 393. ISBN-10 0-470-13153-5
- [8] Arfken G.B., Weber H.J., *Mathematical Methods for Physicists*. 4th edn. San Diego: Academic Press; 1995. p. 81. ISBN 0-12-059816-7
- [9] Yaghjian A.D., *Near-Field Antenna Measurements on a Cylindrical Surface: A Source Scattering-Matrix Formulation*. Boulder, CO: Electromagnetics Division, Institute for Basic Standards, National Bureau of Standards; 1977. p. 20 (NBS Technical Note 696)
- [10] Harrington R.F., *Time-Harmonic Electromagnetic Fields*. New York: IEEE Press, Wiley-Interscience, John Wiley & Sons, Inc.; 2001. p. 462. ISBN 0-471-20806-X
- [11] Balanis C.A., *Advanced Engineering Electromagnetics*. New York: John Wiley & Sons; 1989. p. 923. ISBN 0-471-62194-3
- [12] Leach W.M., Paris D.T., 'Probe compensated near-field measurements on a cylinder', *IEEE Transactions on Antennas and Propagation*. July 1973; **AP-21**(4) 435-445
- [13] Kerns D.M., *Scattering-Matrix Description and Near-Field Measurements of Electroacoustic Transducers*. Boulder, CO: Electromagnetics Division; 1974. p. 13 (National Bureau of Standards Technical Note 651)
- [14] Rudge A.W., Milne K., Olver A.D., Knight P., *The Handbook of Antenna Design*. London, UK: Peter Peregrinus Ltd, IEE Electromagnetic Waves Series 15; 1982. p. 612. ISBN 0-906048-82-6
- [15] Abramowitz M., Stegun I.A. (eds.), *Handbook of Mathematical Functions with Formulas, Graphs, and Mathematical Tables*. New York: Dover Publications. 1964. p. 363 (Standard Book Number: 486-61272-4)

- [16] Rudge A.W., Milne K., Olver A.D., Knight P., *The Handbook of Antenna Design*. London, UK: Peter Peregrinus Ltd, IEE Electromagnetic Waves Series 15; 1982. p. 614. ISBN 0-906048-82-6
- [17] Gregson S.F., Hindman G.E., ‘Conical near-field antenna measurements’, *Antenna Measurement Techniques Association 2008 Symposium*. Boston, MA: 2008
- [18] Gregson S.F., Parini C.G., Dupuy J., ‘Measuring wide angle antenna performance using small cylindrical scanners’, *The Third European Conference on Antennas and Propagation (EuCAP)*, 23–27 March 2009
- [19] Dixon W.C., Janse van Rensburg D., *Evaluation of Radome Performance from Cylindrical Near-Field Measurements*. Antenna Measurement Techniques Association; 2003

This page intentionally left blank

Index

- active electronically scanned antenna (AESA) 22
- advanced antenna pattern correction (AAPC) 244
- angle convention for rotation stages 105
- angular momentum 11
- antenna coupling
 - mechanism behind: *see*
 - electromagnetic (EM) theory and mechanism behind antenna coupling
 - phenomena of 1–3
- antenna cross-section 10–13
- antenna effective area: *see* antenna cross-section
- antenna pattern comparison (APC) methods 244–6
- antenna plotting system (APS) 98, 182
- antenna port definition 59–61
- antenna test range RF test equipment 85
 - generic near-field antenna
 - measurement process 98–100
- RF instrumentation for test ranges
 - amplifiers 91
 - attenuators 94
 - couplers 93
 - down conversion mixers and up conversion multipliers 88–90
 - integrated facility
 - instrumentation 95–8
 - probes 92–3
 - receivers and sources 87–8
 - RF cables 94
 - switches 93–4
- antenna under test (AUT) 103–4, 108, 111, 138, 159, 182, 361
 - aperture 66
 - AUT-to-probe multiple reflections 342
 - coordinate system 64
 - cylindrical scanning 84
 - free space radiation pattern 63
 - near-field 297, 311
 - planar near-field scanner 80–2
 - spherical near-field ranges 79–80
 - Tx and Rx measurements 65
- arcsine-space plotting coordinate system 116–18
- asymptotic far-field parameters, derivation of
 - from cylindrical mode coefficients 401–9
- attenuators 94
- axial ratio (AR) 148–56, 160
- azimuth, conversion from polar spherical to
 - over elevation bases 143–5
- azimuth, elevation and roll angles 168–9
- azimuth bases, conversion from polar spherical to elevation over 145–6
- azimuth over elevation coordinate system 106–8
- azimuth over elevation polarisation basis 131, 134
- ‘backward-wave’ coupler 93
- bandwidth, defined 9
- Bessel equation 377

- blended rolled edges 199–202
 - quiet zone versus knife edge reflector 201
- box frame scanner 301–2, 306
- broadband probes
 - 0.20–3 GHz log-periodic dipole array antenna 422
 - 2–6 GHz dual-port quad-ridge open boundary horn 423
- Cartesian coordinates 107, 178
- Cartesian polarisation basis 126–7
- characterisation via measurement process 3–6, 22–3
- circuit-element characteristics 9
- circular polarisation 143, 156–60
 - left- and right-hand 18
- coherent detector 87
- compact antenna test range (CATR)
 - 74–7, 100, 187
 - dual cylindrical reflector 218
 - dual shaped reflector 218–20
 - elements of 188
 - end-to-end testing and the compensated CATR 272–4
 - hologram 207–9, 221
 - improving measured patterns 239
 - lens 221
 - radar cross-section measurements in 253–7
 - radome measurements in 261–5
 - satellite and telecommunications payload testing in 271–2
 - single-offset reflector 218
 - tri-reflector 220–1
 - working of 223–33
- compact range measurements 187
 - electromagnetic fields, collimation of 190–4
 - feed spillover 205
 - hologram CATRs 207–9
 - lenses as collimators 205–7
 - reflector edge diffraction 194
 - reflector surface errors and panel gaps 209–13
 - time gating and absorber-less chamber 213–17
- OTA testing for 5G antennas 277–90
- quiet zones and performance evaluation 221
- CATR, working of 223–33
 - evaluation using RCS of known target 236–9
 - feed scanning for static AUT measurements 245–6
 - improving measured CATR patterns 239
 - measurement by field probing 233–5
 - phase-less quiet zone scanning 235–6
- radar cross-section (RCS)
 - measurements 252
 - in CATR 253–7
 - model towers 259
 - sources of error in CATR 257, 259
 - target imaging 260–1
 - time gating for 259–60
- radiation pattern and power
 - parameter measurement 246
 - power parameter measurement 248–52
 - radiation pattern measurement 246–8
- radome testing 261
 - boresight shift, measurement of 269
 - flash lobe, measurement of 269–70
 - mechanically scanned AUTs 265–6
 - pattern distortion, measurement of 269
 - radome measurements in 261–5
 - reflectivity, measurement of 266–8
 - transmission efficiency, measurement of 268–9

- ranges and design issues 217
 - dual cylindrical reflector CATR 218
 - dual shaped reflector CATR 218–20
 - hologram CATR 221
 - lens CATR 221
 - single-offset reflector CATR 218
 - tri-reflector CATR 220–1
- satellite testing 271–7
 - EIRP measurement 275–6
 - end-to-end testing and the compensated CATR 272–4
 - group delay measurements 276–7
 - G/T measurements 275–6
 - SFD measurements 275
 - telecommunications payload testing in a CATR 271–2
- compensated CATR (CCR) 271–2
- complex polarisation ratios 420
- complex polarisation vectors 157
- complex vector, complex conjugate of 156
- complex vector algebra 156
- complex vector wave equations 40
- conical near-field antenna measurements 435–41
- convolution theorem 309, 364, 404
- coordinate systems 14, 18, 103
 - arcsine-space plotting 116–18
 - azimuth over elevation 106–8
 - direction cosine 114–16
 - and elemental solid angles 120
 - elevation over azimuth 108–9
 - one-dimensional great circle pattern cuts 120–4
 - for planar scanning 298
 - polar spherical 109–11
 - transformation between 118–20
 - true-view 111–14
- co-polar pattern 125
- Coulomb force law 31
- coupling equation 409–11
- cross polarisation, defined 124
- cross-polar pattern 125
- cylindrical mathematical absorber reflection suppression (C-MARS) 425
- cylindrical mode coefficients (CMCs) 239, 369, 390, 425, 429, 432, 437
 - derivation of asymptotic far-field parameters from 401–9
 - derivation of CMCs
 - from cylindrical near-field data 391–401
 - from measured near-electric field components 396–401
- cylindrical near-field (CNF) antenna measurements 367
- cylindrical near-field scanning (CNFS) 82–3
- cylindrical near-field to far-field transformation, implementation of 430–5
 - derivation of asymptotic far-field parameters from cylindrical mode coefficients 401–9
 - derivation of cylindrical mode coefficients from measured near-electric field components 396–401
 - orthogonality properties of cylindrical wave vectors 391–6
- Maxwell's equation, solution of 373–5
- sampling requirements for 423–30
- scalar wave equation, solution of 375–86
- transmission formula, development of 409
 - calculation of probe cylindrical mode coefficients from far-field data 420–3
 - coupling equation 409–11
 - probe and test antenna 411–18
 - probe compensation, effect of 418–20
- vector fields, construction of 386–91

- Dirac delta function 393
- direct gain measurement 251–2
- direction cosine coordinate system 114–16
- direction cosine matrices 164
 - in the rotation of coordinate systems 162–8
- direction cosine matrix 170
- direction cosines 107
- directivity 10–11, 248
- Discrete Fourier Transform (DFT) 299, 348, 350, 352, 356
- dual cylindrical reflector CATR 218
- dual offset CATR geometry 252
- dual shaped reflector CATR 218–20

- Earth-centred Earth fixed (ECEF) coordinate system 176, 182
- Earth maps, plotting antenna patterns on 176–84
- effective isotropic radiated power (EIRP) 246, 252, 274–5
- Eiffel, Alexandre Gustave 31
- electrical boresight system 98
- electric and magnetic potentials 42
 - retarded potentials 43–53
 - static potentials 43
- electric charge and EM fields 30–3
- electromagnetic (EM) theory and mechanism behind antenna coupling 2, 29
 - antenna port definition 59–61
- electric and magnetic potentials 42
 - retarded potentials 43–53
 - static potentials 43
- electric charge and EM fields 30–3
- field equivalence principle 54–6
- inapplicability of source excitation as measurement methodology 53
- Maxwell's classical EM field theory 29–30
- Maxwell's equations 38–42
- power flux in EM field 34–7
 - reflection and scattering of electromagnetic fields by extended objects 58–9
 - vector electromagnetic fields, characterising 56–8
- electromagnetic fields, collimation of 190–4
 - feed spillover 205
 - hologram CATRs 207–9
 - lenses as collimators 205–7
 - reflector edge diffraction 194
 - blended rolled edges 199–202
 - serrated edge reflectors 194–9
 - shaped feed illumination 202–5
 - reflector surface errors and panel gaps 209–13
 - time gating and absorber-less chamber 213–17
- electromagnetic field theory (EFT) 1, 29–30
- electromagnetic interaction between antennas 10–13
- electro-optical (EO) probes 362–3
- electro-optical planar near-field scanning 361–4
- electro-optic probe scanning very near-fields 363
- electro-optic signal 362
- elemental solid angles, coordinate systems and 120
- elevation, conversion from polar spherical to
 - over azimuth bases 145–6
- elevation bases, conversion from polar spherical to azimuth over 143–5
- elevation over azimuth coordinate system 108–9
- elliptical polarisation 148–56
- equivalent isotropically radiated power (EIRP) 248
- equivalent multipath level (EMPL) 32, 243, 348
- error vector magnitude (EVM) 280, 283, 290
- Ethernet 299, 303

- Euler angles 169–71
- Euler's identity 376
- ex-polarised electric field 358–9
- Faraday, Michael 2
- far-field chambers 71–3
- far-field measurements 103
- far-field positioners 104
- far-field power pattern
 - from plane-polar measurement 322
 - from plane-rectilinear measurement 321
- far-field probe data 421
- far-field ranges 66–8
 - alternatives to 73
 - compact antenna test range (CATR) 74–7
 - tapered anechoic chambers 73–4
- far-fields 18–20, 57
- fast Fourier transform (FFT) 215, 299, 315, 348, 350, 369, 429
- feed scanning for static AUT
 - measurements 245–6
- feed spillover 193, 205
- field equivalence principle 54–6
- field probing 233–5
- 'flower petal' serrations, randomised 198
- F-MARS technique 241, 243, 245
- 'forward-wave' coupler 93
- Fourier integrals 379
 - of measured fields 345
- Fourier theory 404
- Fourier transform 224, 299, 308, 404
 - one-dimensional 328
- free-space antenna measurement
 - techniques 20
- free-space characteristics 9
- free-space conditions 68–73
- free space radiation pattern 13–17, 63
- frequency multiplying modules 90–1
- frequency span 215
- frequency sweep 215
- Fresnel diffraction patterns 195
- Friis transmission formula 251
- gain 9–10, 63, 150
 - measurement
 - using substitution technique 250
 - realised 249–50
- gain over frequency (G/F) 273
- gain over noise temperature (G/T)
 - measurements 275–6
- gallium-arsenide (GaAs) 362
- Gall Peters projection 161
- gauge transformations 46
- Gaussian-beam-mode (GBM) theory 225
- Gauss's Theorema Egregium 111, 161–2
- general-purpose interface bus (GPIB) 299, 303
- generic near-field measurement
 - process 98–100
- geometric optics (GO) field 199, 202
- geometric theory of diffraction (GTD) 200
- geostationary orbit 178
- gimbal mount 265
- gradient operator in cylindrical
 - coordinates 388
- Graf's addition theorem 417
- great circle pattern cuts, one-dimensional 120–4
- Green's function 46, 56
- Green's theorem 42
- group delay (GD) measurements 276–7
- Hankel functions 373, 378, 381, 383–5, 387–9, 391, 394–5, 397–9, 402, 404, 430
- hardware time gating 215–16
- harmonic equation 376
- Heisenberg uncertainty principle 11
- Helmholtz equation 42, 376, 378–9
- Hertzian dipole 56
- hologram CATRs 207–9, 221
- horizontally polarised antenna 17–18
- Huygen's principle 54

- IEEE299 69
- impedance mismatch 249
- indirect measurements 77–85
 - cylindrical near-field scanning (CNFS) 82–3
 - planar near-field scanner (PNFS) 80–2
 - spherical near-field range 79–80
- information theory, development of 4
- interpolation, utilising 315
- inverse Fourier transform 404–5
- inverse matrix method 349, 351, 353, 355, 357, 359–60
- inverted T scanner 302, 306
- I/Q demodulator 87
- ISAR (inverse synthetic aperture radar) 237–8, 261
- isometric rotation of coordinate systems 161
 - azimuth, elevation and roll angles 168–9
 - Euler angles 169–71
 - Gauss's Theorema Egregium 161–2
 - plotting antenna patterns on Earth maps 176–84
 - quaternions 171–4
 - use of direction cosine matrices in the rotation of coordinate systems 162–8
 - viewer plotting antenna patterns, orientation of 174–6
- iterative conjugate gradient method 348
- Jacobi–Bessel expansion of aperture field 235
- k-correction method 351, 354
- Kelvin, Lord 4
- Kirchhoff integral theorem 42
- known target
 - evaluation using RCS of 236–9
- Laplacian operator 41, 373
- Larmor equation 37, 46
- least squares conjugate gradient (LSQR) method 348, 351, 358
- left-handed circular polarisation (LHCP) 18
- lens CATR 221
- lenses as collimators 205–7
- linear and circular polarisation bases 156–60
- linear dipole antenna 6
- local oscillator (LO) signal 85
- log-periodic dipole array (LPDA) 422
- Lorentz force law 32
- Lorentz gauge 46
- Ludwig I polarisation basis 126–7
- Ludwig II definitions, conversion between 146–8
- Ludwig II polarisation basis 131–7
- Ludwig III polarisation basis 137–43
- magnetic potential 43
- mathematical absorber reflection suppression (MARS) 239–44
- maximum radial extent (MRE) 390
- Maxwell Faraday equation 390
- Maxwell's classical EM field theory 29–30
- Maxwell's equation 23, 38–42, 98
 - solution of
 - in Cartesian coordinates 307–9, 364
 - in cylindrical coordinates 373–5
- measurable properties of antennas 6–9
 - antenna cross-section 10–13
 - antenna gain and directivity 9–10
 - far-field 18–20
 - free-space radiation pattern 13–17
 - measurement limitations 22–3
 - phase in measurement 20–1
 - polarisation 17–18
 - reciprocity 21–2
- measurement 24
 - and alignment 63–4
 - characterisation via 3–6
 - definition 4
 - indirect 77–85
 - cylindrical near-field scanning (CNFS) 82–3

- planar near-field scanner (PNFS)
 - 80–2
 - spherical near-field range 79–80
- limitations 22–3
- mapping process 5
- scanning, geometries for 84–5
- set theoretic model of 5
- measurement methodology,
 - inapplicability of source excitation as 53
- metallic isolating structure 100
- minimum radius cylinder (MRC) 390, 424
- near-field acquisition surface
 - geometries 78
- near-field measurement system 92, 297
 - generic near-field measurement process 98–100
 - near-field probe 304
 - RF sub-system 298–301
 - robotics positioner system 301–3
 - scanning probe 92
 - schematic of 300
- near-field scanning 24
- Neumann functions 378
- non-canonical near-field scanning 343–61
- Nyquist sampling, finer than 341–3
- Nyquist sampling theorem 335
- offset parabolic reflector antenna 7
- one-dimensional great circle pattern cuts 120–4
- one-to-one mapping 92, 315
- orthogonal frequency-division multiplexing (OFDM)
 - simulating a communications system using 278–90
- orthogonality property 395
 - of cylindrical wave vectors 391–6
- OTA testing for 5G antennas 277
 - simulating a communications system using OFDM 278–90
- passive transformation matrices 162–4
- ‘pattern correction’ term 420
- pattern plotting 103
 - coordinate systems 103
 - arcsine-space plotting 116–18
 - azimuth over elevation 106–8
 - direction cosine 114–16
 - and elemental solid angles 120
 - elevation over azimuth 108–9
 - one-dimensional great circle pattern cuts 120–4
 - polar spherical 109–11
 - transformation between 118–20
 - true-view 111–14
- isometric rotation of coordinate systems 161
 - azimuth, elevation and roll angles 168–9
- Earth maps, plotting antenna patterns on 176–84
- Euler angles 169–71
- Gauss’s Theorema Egregium 161–2
- orientation of viewer plotting antenna patterns 174–6
- quaternions 171–4
- use of direction cosine matrices in 162–8
- polarisation bases 124
 - conversion between LII definitions 146–8
 - conversion from polar spherical to azimuth over elevation bases 143–5
 - conversion from polar spherical to elevation over azimuth bases 145–6
- elliptical polarisation, axial ratio and tilt angle 148–56
- linear and circular polarisation bases 156–60
- Ludwig I 126–7
- Ludwig II 131–7
- Ludwig III 137–43

- measures of polarisation
 - discrimination 160
 - polar spherical 127–31
- phase in measurement 20–1
- phase-less quiet zone scanning 235–6
- phi-over-theta ‘model tower’
 - positioning system 131
- physical size of antenna 6
- physical theory of diffraction (PTD)
 - 200
- planar electro-optic near-field scanning
 - system with RF sub-system 363
- planar field probe 234
- planar near-field (PNF) antenna
 - measurements 297
 - Cartesian coordinates, solution of
 - Maxwell’s equations in 307,
 - 364
 - plane wave spectrum 307–9
 - electro-optical planar near-field
 - scanning 361–4
 - finer than Nyquist sampling 341–3
 - limitations in accuracy of 304
 - mechanically based limitations
 - 304–5
 - RF system limitations 305–6
 - near-field measurement facility 297
 - near-field probe 304
 - RF sub-system 298–301
 - robotics positioner system 301–3
 - non-canonical near-field scanning
 - 343–61
 - plane-polar near-field antenna
 - measurements 313
 - aperture illumination amplitude
 - function 324
 - aperture illumination phase
 - function from 325
 - application of spectral methods
 - to 314–22
 - conventional and alternate plane
 - acquisition types 322–7
 - plane-polar alignment 327–34
 - remaining data acquisition factors
 - of planar scanning 334
 - probe pattern compensation 309
 - far-field data, effect of probe
 - pattern on 311
 - scanning probe characteristics
 - 311–13
 - sampling (interpolation theory) and
 - aliasing 334–41
 - planar near-field scanner (PNFS) 80–2
 - planar patch array antenna 8
 - plane-polar coordinate system 315,
 - 358–9
 - plane-polar field probe 234
 - plane-polar measurement 318, 322
 - plane-polar scanning 357
 - plane-rectilinear measurement
 - aperture illumination amplitude
 - function from 323
 - aperture illumination phase function
 - from 324
 - far-field power pattern from 321
 - plane-wave spectra 339, 349
 - plane wave spectral components
 - (PWSC) 236
 - plane wave spectrum (PWS) 307–9,
 - 317, 338
 - Pockels effect 362
 - polarisation 9–11, 17–18, 63–4
 - polarisation bases 124
 - axial ratio 148–56
 - conversion 143
 - between LII definitions 146–8
 - from polar spherical to azimuth
 - over elevation bases 143–5
 - from polar spherical to elevation
 - over azimuth bases 145–6
 - elliptical polarisation 148–56
 - linear and circular polarisation
 - bases 156–60
 - Ludwig I 126–7
 - Ludwig II 131–7
 - Ludwig III 137–43
 - polarisation discrimination,
 - measures of 160
 - polar spherical 127–31
 - tilt angle 148–56

- 'polarisation correction term,' 420
- polarisation matrix 256
- polarisation purity 313
- polar spherical coordinate system 109–11
- polar spherical polarisation basis 127–31
- positive constant 41
- power flux density 9
- power flux in EM field 34–7
- power parameters
 - measurement 248–52
 - direct gain measurement 251–2
 - EIRP measurement 252
 - gain measurement using the substitution technique 250
 - saturating flux density measurement 252
 - three-antenna gain method 250–1
- Poynting vector 36, 58
- principle of constancy of the light speed 30
- principle of relativity 30
- probe-compensated near-field measurements 409
- probe cylindrical mode coefficients, calculation of
 - from far-field data 420–3
- probe pattern compensation 309
 - far-field data, effect of probe pattern on 311
 - scanning probe characteristics 311–13
- probe pattern correction technique 317
- pseudo time gating: *see* software time gating

- quadrature amplitude modulation (QAM) 278
- quadrature channel detector 87
- quadrature detector 87
- quaternions 171–4
- quiet zone 187
 - CATR, working of 223–33
 - evaluation using RCS of known target 236–9
 - feed scanning for static AUT measurements 245–6
 - improving measured CATR patterns 239
 - antenna pattern comparison (APC) methods 244–5
 - mathematical absorber reflection suppression (MARS) 239–44
 - measurement by field probing 233–5
 - performance evaluation 221
 - phase-less quiet zone scanning 235–6
- radar adsorbent material (RAM) 69, 301, 306
 - measure of 69
 - reflectivity 69
- radar cross-section (RCS) 187
 - versus aspect angle 260
 - in CATR 253–7
 - versus cross range 261
 - versus down range 261
 - error sources for 257, 259
 - versus frequency 261
 - image formation 261
 - measurements 252
 - model towers 259
 - versus range 261
 - target imaging 260–1
 - time gating for 259–60
- radiating near-field 20
- radiation efficiency of the antenna 10
- radiation pattern measurement 246–8
- radiation pattern of the antenna 15
- radome measurement ranges 270
- radomes for fire control radars 262
- range RF system, fundamental basis of 85
- ranges and design issues 217
 - dual cylindrical reflector CATR 218
 - dual shaped reflector CATR 218–20
 - hologram CATR 221
 - lens CATR 221
 - single-offset reflector CATR 218
 - tri-reflector CATR 220–1
- reactive near-field aspects 2

- receive sub-system 3, 17
- reciprocity 21–2, 301
- rectangular pyramidal horn antenna 8
- reflector edge diffraction 193
 - blended rolled edges 199–202
 - serrated edge reflectors 194–9
 - shaped feed illumination 202–5
- reflector surface errors and panel gaps 209–13
- remote standard antenna (RSA) 137–8
- retarded potentials 34, 43–53
- RF multipliers 90
- RF test system 85
- RF to IF mixer configuration 88
- right-hand circular polarisation (RHCP) 18
- robotics positioner system 301–3
- roll-over-elevation-over-azimuth positioner system 104
- rotation methodologies 64–6
- Rx sub-system 3, 17–18

- sampling (interpolation theory) and aliasing 334–41
- satellite testing
 - EIRP measurement 275–6
 - end-to-end testing and the compensated CATR 272–4
 - group delay measurements 276–7
 - G/T measurements 275–6
 - SFD measurements 275
 - telecommunications payload testing in CATR 271–2
- Saturating Flux Density (SFD) 246, 248, 252, 275
- scalar wave equation, solution of
 - in Cartesian coordinates 307
 - in cylindrical coordinates 375–86
- scanning measurements 78
 - geometries for 84–5
- scanning probe, characteristics of 92
- serrated edge reflectors 194–9, 202
- serrated rim reflector CATRs 196
- seven axis positioner 65
- shaped feed illumination 202–5
- shielding values 69
- single-offset reflector CATR 218, 253
 - feed spillover in 205
- single reflector CATR 75–6
- slant-linear polarised field 18
- slotted waveguide planar array antenna 7
- software time gating 214–15
- source-scattering matrix equation 410
- spectral methods 328
 - for plane-polar antenna measurements 314–22
- spherical coordinate system 109–11
- spherical near-field range 79–80
- spherical rotation systems 105
- spherical scanning, practical implementation of 80
- spin angular momentum 11
- spin-linear value 160
- standard gain horn (SGH) 108, 436
- static potentials 43
- Stratton–Chu equations 59
- sub-satellite longitude 178
- synchronous/coherent detection 88

- tapered anechoic chambers 73–4
- Taylor series 356
- telecommunications payload testing in CATR 271–2
- test zone: *see* quiet zone
- Theta-Phi coordinate system 104
- three-antenna gain method 250–1
- three-dimensional antenna measurements 105
- tilt angle 148–56
- time gating 194
 - and absorber-less chamber 213–17
 - for radar cross-section 259–60
- tower and rail inverted T scanner 301–2
- transfer characteristics 9
- transformation between coordinate systems 118–20
- transformation matrices 162–4, 168
- transmission formula, development of 409

- calculation of probe cylindrical mode coefficients from far-field data 420–3
- coupling equation 409–11
- cylindrical near-field measurements, effect of probe compensation in 418–20
- probe and test antenna 411–18
- transmit sub-system 3, 17–18
- transverse electric (TE) part 386
- transverse electromagnetic (TEM) 61
- transverse magnetic (TM) part 386
- transverse wave equation 41
- tri-reflector CATR 220–1
 - simulated performance of 205
- true-view coordinate system 111–14
- twin reflector CATR, plan view of 74
- Tx sub-system 3, 17–18
- unit vectors, inverse transformations of 158
- un-primed coordinate system 165
- vector electromagnetic fields, characterising 56–8
- vector fields, construction of 386–91
- vector Helmholtz equation 41
- vector network analyser (VNA) measurement system 85, 215, 299
- vector potential 56
- viewer plotting antenna patterns, orientation of 174–6
- wall reflections 193–4
- WGS84 ECEF model 181
- World Geodetic System 84 (WGS84) ellipsoid model 181

Theory and Practice of Modern Antenna Range Measurements

2nd Expanded Edition, Volume 1

This greatly expanded, co-authored, two-volume text provides a comprehensive introduction and explanation of both the theory and practice of modern antenna measurements, from their most basic postulates and assumptions, to the intricate details of their applications in various demanding modern measurement scenarios.

Starting with an initial examination of the properties of antennas that allow them to enhance the free-space interaction of electronic systems, the authors then introduce direct far-field and indirect far-field forms of antenna measurements and their various implementations. Detailed descriptions are given of the direct far-field measurement technique CATR (Compact Antenna Test Ranges), Body-Centric measurements, and detailed developments of standard planar, cylindrical, spherical and non-canonical near-field techniques; and includes a through treatment of near-field range error budgets which are an indispensable part of antenna metrology. The books conclude with recent advances in measurement techniques such as aperture diagnostics, phase-less antenna metrology, error correction, and range multi-path suppression techniques. Extensive examples illustrate the concepts and techniques covered.

This second edition is thoroughly expanded and now includes new chapters on near-field to far-field transforms from non-canonical surfaces, electromagnetic modelling of CATRs and near-field antenna measurement systems. In addition there is an expanded chapter on coordinate systems, polarization bases and antenna pattern plotting and new sections on more specialized topics such as 5G and Radome measurements.

About the Authors

Professor Clive Parini is Professor of Antenna Engineering at Queen Mary University of London, UK.

Professor Stuart Gregson is Director of Operations & Research at Next Phase Measurements and an Honorary Visiting Professor in the School of Electronic Engineering and Computer Science of Queen Mary University of London, UK.

Dr John McCormick is an Antenna Engineer with Leonardo MW, Edinburgh, UK.

Dr Daniël Janse van Rensburg is Snr VP of RF Products and Applications at NSI-MI Technologies, Suwanee, Georgia, USA. He is also Adjunct Professor at the University of Ottawa, Canada.

Professor Thomas Eibert is Professor of High-Frequency Engineering at the Technical University of Munich, Germany.

ISBN 978-1-83953-126-2



SciTech Publishing an imprint of the IET
The Institution of Engineering and Technology
theiet.org
978-1-83953-126-2